THE EFFECT OF CARBIDE-FORMING ELEMENTS ON THE METAL DUSTING RATE IN HYDROCARBON ENVIRONMENTS

Gideon Albertus Slabbert

A dissertation submitted to the Faculty of Engineering and the Built Environment, University of the Witwatersrand, in fulfilment of the requirements for the degree of Master of Science in Engineering

Johannesburg 2012

DECLARATION

I, Gideon Albertus Slabbert, declare that this dissertation is my own unaided work, except where otherwise acknowledged. It is being submitted for the degree of Master of Science in Engineering at the University of the Witwatersrand, Johannesburg. It has not been submitted previously at this, or any other university for any degree or examination.

_____ _____

Signature Date

ABSTRACT

Metal dusting occurs in carburizing atmospheres at intermediate temperatures (approximately between 430°C and 900°C), with the maximum rate of attack occurring at about 600°C to 700°C, depending on alloys and environments. Attack is in the form of small pits or general uniform waste that yields a crumbly residue (dust) composed of graphite, metal, carbides and oxides (called coke).

The objective of this work was to determine the influence of carbide-forming elements, like titanium and niobium, on the metal dusting rate of commercial alloys. These results are used in development of alloys to combat metal dusting. Similar grades of stainless steels were exposed to metal dusting conditions and their performance compared. For austenitic stainless steels, **Type 304L** stainless steel was compared to **Type 321** (i.e. essentially Type 304 with titanium added) and **Type 316L** stainless steel compared to that of **Type 316Ti** (Type 316 with titanium added). The performance of a ferritic grade with similar chromium content as Type 304L and Type 316L was also included (i.e. **Type 430**), and also compared to a stabilised grade, **Type 441** (Type 430 with both titanium and niobium as carbide-formers). This indicated the characteristics of chromium and carbon migration, the formation of carbides, and their subsequent oxidation, on the mechanism for metal dusting.

The results indicated that the alloys that contained carbide-forming elements initially degraded to a lesser extent. In addition, it was also observed that the ferritic alloys were initially more resistant compared to the austenitic alloys. This is counterintuitive, since Type 316L is regarded as being more “corrosion resistant” than Type 430. The increased corrosion resistance is attributed to greater mobility of chromium in a ferritic structure, compared to an austenitic structure, to replace chromium that is used to form and repair chromium oxide scale on the surface. This is also important information that will help with alloy development.

The importance of a high chromium content, and other elements that promote a stable oxide film at the operating conditions, as well as a ferritic structure, are highlighted as possibilities to develop alloys to mitigate attack by metal dusting. The negative effect of carbide-forming elements during prolonged exposure indicates that those elements should be avoided.

ACKNOWLEDGEMENTS

I would like to thank the following people and organisations, without which this work would not have been possible:

- The South African Department of Science and Technology (DST) and the Advanced Metals Initiative (AMI) and the Ferrous Metals Development Network (FMDN) are gratefully acknowledged for providing support.
- Mintek, for their support and permission to publish these results.
- My supervisor, Prof. Lesley Cornish for her guidance, encouragement and mentorship, and to the DST/NRF Centre of Excellence in Strong Materials for supporting her.
- To Columbus Stainless, for providing material for testing.
- To the Advanced Materials Division at Mintek, especially Marandela Mulaudzi, Richard Couperthwaite, Veronica Morudu and Thulani Ndwandwe.
- To Dr Jianqiang Zhang from the University of New South Wales, Sydney, Australia, for continuous support and advice.
- And to my family, Tertia for putting up with me and providing encouragement, my children, Anina and Stefan, and to my parents, Jan and Cecilia for their unfailing support and love at all times. This work is a direct result of your support, and I thank you.

TABLE OF CONTENTS

1. INTRODUCTION 1
2. LITERATURE REVIEW 5
   2.1. Oxidation 6
   2.2. Sulphidation 9
   2.3. Carburisation 10
   2.4. Metal dusting 11
      2.4.1. Gaseous carbon activity 13
      2.4.2. Mechanisms of metal dusting 15
      2.4.3. Protection by oxide scaling 27
      2.4.4. Effects of surface conditions and finish 30
3. PROJECT DESCRIPTION 33
   3.1. Hypothesis statement 33
   3.2. Project objectives 33
   3.3. Research question 33
   3.4. Experimental methods 33
      3.4.1. Test alloys 33
      3.4.2. Sample preparation 35
      3.4.3. Test procedures 35
      3.4.4. Methods of analysis 37
4. RESULTS 48
   4.1. Six day exposure test 48
      4.1.1. Visual examination 48
      4.1.2. Mass loss 52
      4.1.3. Metallography 54
      4.1.4. Scanning Electron Microscopy 62
      4.1.5. Transmission Electron Microscopy 64
   4.2. Seven day exposure period 68
      4.2.1. Visual examination 68
      4.2.2. Mass loss 75
      4.2.3. Metallography 76
      4.2.4. Scanning Electron Microscopy 88

4.2.5. X-ray diffraction 111
4.3. Fourteen day test 114
4.3.1. Visual examination 114
4.3.2. Mass loss 122
4.3.3. Metallography 124
4.3.4. Scanning Electron Microscopy 134
4.3.5. X-ray diffraction 143
4.4. Thirty day Test 147
4.4.1. Visual examination 147
4.4.2. Mass loss 156
4.4.3. Metallography 158
4.4.4. Scanning Electron Microscopy 177
4.4.5. X-ray diffraction 245
4.4.6. Characterisation of coke 249
5. DISCUSSION 251
6. CONCLUSIONS AND RECOMENDATIONS 259
7. REFERENCES 262
APPENDIX 1 266

LIST OF FIGURES

Figure 1.1. Process flow of a typical modern petroleum refinery to produce domestic and industrial fuels [NiI1]. 2

Figure 2.1. Typical effect of temperature on high temperature sulphidation of steels and stainless steels (Modified McConomy) [1986Gut]. 10

Figure 2.2. Equilibria constants versus temperature for gas-phase carbon producing reactions [2010You]. 15

Figure 2.3. Schematic illustration of the metal dusting mechanism on iron and low-alloy steels [1998Gra1]. 17

Figure 2.4. Mass transfer model for coke filament growth from carbides [2010You]. 19

Figure 2.5. Dependence of coking and dusting rates on p_{CO} in $H_2/CO/H_2O$ mixtures [2010You]. 20

Figure 2.6. Coke deposition and metal wastage kinetics for electropolished 25Cr alloys at 680°C in $CO/H_2/H_2O$ [2002Toh]. 22

Figure 2.7. Schematic illustration of the metal dusting mechanism on high alloyed steels and CrFeNi-alloys taken from (a) [1995Gra1] and (b) [2003Gra]. 24

Figure 2.8. Mechanisms of metal dusting as it appears on stainless steels, including an active corrosion process with carbon and oxygen (Type III), in combination with fragmentation by graphitization (Type II) [2004Sza]. 25

Figure 2.9. Processes occurring on high alloy materials during local oxide scale failure leading to a growing metal dusting pit [2011You]. 29

Figure 2.10. Effect of grain size on the metal dusting behaviour of Type 304 at 600°C in H_2-24CO-2H_2O [2007Lai]. 30

Figure 2.11. Thermogravimetric testing of alloy 800 (Fe-21Cr-32Ni) in H_2-24CO-2H_2O at 600°C in different surface conditions [2003Gra2]. 31

Figure 2.12. Thermogravimetric testing of Type 310 (Fe-25Cr-20Ni) in H_2-24CO-2H_2O at 600°C in different surface conditions [2003Gra2]. 32

Figure 2.13. Metal dusting behaviour for alloy 601 in H_2-49CO-2H_2O at 650°C for different surface conditions [1997Klo]. 32

Figure 3.1. Schematic diagram of the metal dusting test rig. 39

Figure 3.2. Photograph of the metal dusting test rig. 40

Figure 3.3. Schematic diagram illustrating how the samples were sectioned for characterisation. 43

Figure 3.4. Schematic diagram illustrating how the different samples were analysed. 44

Figure 4.1. Photograph of the samples after the 6-day exposure. 49

Figure 4.2. Close-up photograph of the samples and coking associated with the 316L samples shown in Figure 4.1. 50

Figure 4.3. Photograph of the 304L and 321 austenitic samples after the 6-day test. 50

Figure 4.4. Photograph of the 316L and 316Ti austenitic samples after the 6-day test. 51
Figure 4.5. Photograph of the 430 and 441 ferritic samples after the 6-day test. 51
Figure 4.6. Micrograph of a cross-section through the 321-5 sample. 55
Figure 4.7. Higher magnification of the 321-5 sample shown in Figure 4.6. 55
Figure 4.8. Micrograph of a cross-section through the 316-5 showing coking and shallow attack. 56
Figure 4.9. Micrograph of localised intergranular attack on Sample 316-5. 56
Figure 4.10. Higher magnification micrograph the attack on Sample 316-5 shown in Figure 4.9. 57
Figure 4.11. Micrograph of shallow attack and products on Sample 316-5. 57
Figure 4.12. Micrograph of a second phase forming on the grain boundaries (arrow), intergranular attack and grain-dropping on Sample 316-6. 58
Figure 4.13. Micrograph of mostly shallow uniform attack on Sample 316Ti-5. 58
Figure 4.14. Micrograph of shallow attack and associated corrosion products on Sample 316Ti-5. 59
Figure 4.15. Etched micrograph showing the general carbide distribution in Sample 430-5. 60
Figure 4.16. Etched micrograph of Sample 430-5 showing a degree of carburisation near the surface. 60
Figure 4.17. Etched micrograph of Sample 441-5 showing the carbide distribution and the titanium carbo-nitrides (arrows). 61
Figure 4.18. Higher magnification micrograph of Sample 441-5 shown in Figure 4.17. 61
Figure 4.19. SEM-SE image of a pit on the 316-6 sample after the third test that was run for 6 days. 62
Figure 4.20. SEM-SE image of the coking on the 316L samples. 63
Figure 4.21. Higher magnification of the carbon filaments and associated carbide particles (arrows) shown in Figure 4.20. 63
Figure 4.22. TEM image of a carbon filament and carbide particle (dark particle) from the 316L samples. 64
Figure 4.23. TEM image of a carbon filament from the 316L samples illustrating that they are hollow tubes (carbon nanotubes). 65
Figure 4.24. TEM image of a carbon filament from the 316L samples illustrating the walls of the hollow tube. 65
Figure 4.25. Higher magnification of Figure 4.24 demonstrating that the filaments are “multi-walled carbon nanotubes” (MWCNTs). 66
Figure 4.26. TEM image of carbon filaments and several carbide particles (dark particles) from the 6-day test. 67
Figure 4.27. Higher magnification of a carbide particle from the 6-day test showing the faceted nature. 67

Figure 4.28. Photograph of the samples in the ceramic boat after exposure to the 7-day test. 69
Figure 4.29. Close-up photograph showing coking associated with the austenitic samples. 69
Figure 4.30. Photograph of the 304L and 321 samples exposed to the 7-day test. 70
Figure 4.31 Close-up of the 304L sample showing only light tarnishing with no coking. 70
Figure 4.32. Close-up photograph of the 321 sample showing only light tarnishing and no coking. 71
Figure 4.33. Photograph of the 316L and 316Ti samples showing tarnishing and minor pits on the surface of both alloys. 71
Figure 4.34. Reverse sides of the 316L and 316Ti samples showing tarnishing and minor pits on a 316L sample. 72
Figure 4.35. Close-up of filament growth on a 316Ti sample. 72
Figure 4.36. Photograph of the 430 and 441 samples. 73
Figure 4.37. Close-up of a 430 sample showing only light tarnishing. 73
Figure 4.38. Photograph of a 441 sample showing less tarnishing than the 430 samples. No coking was evident. 74
Figure 4.39. Micrograph of a cross-section through Sample 304-1 sample showing a pit and coking. 76
Figure 4.40. Higher magnification of Sample 304-1 showing shallow attack. 77
Figure 4.41. Cross section of Sample 321-1 (copper plated) showing no significant metal wastage. 77
Figure 4.42. Higher magnification of shallow grain boundary attack on Sample 321-1. 78
Figure 4.43. Micrograph of shallow attack on Sample 321-1. 78
Figure 4.44. Micrograph of the titanium carbo-nitrides in Sample 321-1. 79
Figure 4.45. Higher magnification of Sample 321-1 showing attack associated with the titanium carbo-nitride precipitates. 79
Figure 4.46. Micrograph of etched Sample 321-1 showing carburisation on grain boundaries. 80
Figure 4.47. Higher magnification of the carbide distribution near the centre of the cross-section of Sample 321-1. 80
Figure 4.48. Micrograph of a pit in Sample 316 -1. 81
Figure 4.49. Higher magnification micrograph of Figure 4.48 showing the intergranular nature of the attack. 82
Figure 4.50. Micrograph of a pit at a corner on Sample 316-2. 82
Figure 4.51. Micrograph of the titanium carbo-nitride precipitates in Sample 316Ti-1. 83
Figure 4.52. Higher magnification micrograph showing selective attack of the titanium carbo-nitride precipitates in Sample 316Ti-1. 83
Figure 4.53. Micrograph of the carburisation in Sample 430-1. 84

Figure 4.54. Higher magnification micrograph of the carbide distribution near the centre of the cross-section of Sample 430-1. 85

Figure 4.55. Micrograph of Sample 441-1 showing the titanium carbo-nitride precipitate distribution. 85

Figure 4.56. Micrograph showing shallow attack and carburisation associated with the damaged oxide layer in Sample 441-1. 86

Figure 4.57. Micrograph of Sample 441-1 in the etched condition. 86

Figure 4.58. Higher magnification micrograph of shallow attack on Sample 441-1 in the etched condition. 87

Figure 4.59. Higher magnification micrograph of the titanium carbo-nitrides in the matrix of Sample 441-1 (etched). 87

Figure 4.60. SEM-BSE image of the surface of Sample 304-1. 88

Figure 4.61. SEM-BSE image of the lighter areas shown in Figure 4.60. 89

Figure 4.62. Higher magnification SEM-BSE image of the lighter areas shown in Figure 4.61. 89

Figure 4.63. SEM-BSE image of the darker areas on Sample 304-1 shown in Figure 4.60. 90

Figure 4.64. Higher magnification SEM-BSE image of Sample 304-1 shown in Figure 4.63. 90

Figure 4.65. SEM-BSE image of grain boundary attack and white particles on the surface of Sample 304-1. 91

Figure 4.66. EDX spectrum of the white particles (including some matrix) on the surface of Sample 304-1 shown in Figure 4.65. 91

Figure 4.67. SEM-BSE image of the surface of Sample 321-1. 92

Figure 4.68. SEM-BSE image of the light areas on Sample 321-1 shown in Figure 4.67. 93

Figure 4.69. Higher magnification SEM-BSE image of Sample 321-1 shown in Figure 4.68. 93

Figure 4.70. SEM-BSE image of the dark areas on Sample 321-1 shown in Figure 4.67. 94

Figure 4.71. Higher magnification SEM-BSE image of the dark areas on Sample 321-1 shown in Figure 4.67. 94

Figure 4.72. SEM-BSE image of the surface of Sample 316-1. 95

Figure 4.73. Higher magnification SEM-BSE image of the light areas on Sample 316-1 shown in Figure 4.72. 96

Figure 4.74. Higher magnification SEM-BSE image of the dark areas shown in Figure 4.72. 96

Figure 4.75. SEM-BSE image of the initiation of pitting on the surface of Sample 316-1. 97

Figure 4.76. SEM-BSE image of the surface of Sample 316Ti-1. 98

Figure 4.77. Higher magnification SEM-BSE image of Sample 316Ti-1 shown in Figure 4.76. 98

Figure 4.78. Higher magnification SEM-BSE image of the lighter areas on Sample 316Ti-1 shown in Figure 4.76. 99

Figure 4.79. Higher magnification SEM-BSE image of the darker areas on Sample 316Ti-1 shown in Figure 4.76. 99

Figure 4.80. SEM-BSE image of the surface near the edge of Sample 316Ti-1. 100

Figure 4.81. SEM-BSE image of the lighter areas of Sample 316Ti-1 shown in Figure 4.80. 100

Figure 4.82. SEM-BSE image of intergranular attack associated with the darker areas in Sample 316Ti-1 shown in Figure 4.80. 101

Figure 4.83. EDX spectrum of the light particles (including some matrix) on Sample 316Ti-1 shown in Figure 4.82. 101

Figure 4.84. SEM-BSE image of the surface of Sample 430-1. 102

Figure 4.85. Higher magnification SEM-BSE image of Sample 430-1 shown in Figure 4.84. 103

Figure 4.86. SEM-BSE image of the surface of Sample 441-1. 103

Figure 4.87. SEM-BSE image of the lighter areas on Sample 441-1 shown in Figure 4.86. 104

Figure 4.88. Higher magnification SEM-BSE image of Sample 441-1 shown in Figure 4.87. 104

Figure 4.89. SEM-BSE image of darker areas on Sample 441-1 shown in Figure 4.86 (in BSE mode). 105

Figure 4.90. SEM-SE image of similar areas shown in Figure 4.89. 105

Figure 4.91. Higher magnification SEM-BSE image of the darker area in Sample 441-1 shown in Figure 4.89 and Figure 4.90. 106

Figure 4.92. SEM-BSE image of a cross-section through Sample 304-1. 107

Figure 4.93. Higher magnification SEM-BSE image of Sample 304-1 shown in Figure 4.92. 107

Figure 4.94. SEM-BSE image of pitting by intergranular attack and grain dropping in Sample 316-2. See also Figure 4.50. 108

Figure 4.95. Higher magnification SEM-BSE image of intergranular attack in Sample 316-2 shown in Figure 4.94. 108

Figure 4.96. Higher magnification of grains exposed by grain dropping in Sample 316-2shown in Figure 4.94, with some attack at the grain boundaries, twins and crystallographic planes. 109

Figure 4.97. EDX spectrum of the oxide on the surface of Sample 316-2 shown in Figure 4.95. 109

Figure 4.98. SEM-BSE image of a cross-section of Sample 316Ti–2. 110

Figure 4.99. Higher magnification SEM-BSE image of Sample 316Ti-2 shown in Figure 4.98. 110

Figure 4.100. X-ray spectrum of the surface of Sample 304-2, showing peaks and volume %. 111
Figure 4.101. X-ray spectrum of the surface of Sample 321-2. 112
Figure 4.102. X-ray spectrum of the surface of Sample 316L-2, showing peaks and volume %. 112
Figure 4.103. X-ray spectrum of the surface of Sample 316Ti-2. 113
Figure 4.104. X-ray spectrum of the surface of Sample 430-2. 113
Figure 4.105. X-ray spectrum of the surface of Sample 441-2. 114
Figure 4.106. Photograph of all the coupons in the boat showing the extent of coke formation. 115
Figure 4.107. Close-up photograph of the coking shown in Figure 4.106. 115
Figure 4.108. Photograph of the 304L and 321 samples exposed in the 14-day test. 116
Figure 4.109. Close-up photograph of the 321-4 sample showing coke formation on the surface. 116
Figure 4.110. Photograph of the rear surfaces of the 304L and 321 samples shown in Figure 4.108, showing pit formation on 304-4 (arrow). 117
Figure 4.111. Close-up photograph of the 316L coupons after exposure showing coking and filament growth on the surface. 118
Figure 4.112. Photograph of the 316L and 316Ti samples exposed for 14-days. 118
Figure 4.113. Photograph of the rear surfaces of the 316L and 316Ti samples showing coking and pitting on the surfaces. 119
Figure 4.114. Close-up photograph of coking and pitting on the 316L samples. 119
Figure 4.115. Close-up photograph of coking on the 316Ti samples. 120
Figure 4.116. Photograph of the Types 430 and 441 samples exposed for 14 days. 121
Figure 4.117. Photograph of Sample 430-3 showing filament growth. 121
Figure 4.118. Photograph of the coke formation associated with the ferritic samples (430 in this instance). 122
Figure 4.119. Micrograph of a cross-section through Sample 304-3. 124
Figure 4.120. Micrograph of a cross-section through Sample 316-3 showing significant metal wastage by intergranular attack. 125
Figure 4.121. Higher magnification micrograph of intergranular attack in Sample 316-3 shown in Figure 4.120. 125
Figure 4.122. Micrograph of localised intergranular attack in Sample 316-3. 126
Figure 4.123. Micrograph of localised intergranular attack in Sample 316-4. 126
Figure 4.124. Higher magnification micrograph of the metal wastage on Sample 316-4 shown in Figure 4.123. 127
Figure 4.125. Micrograph of a pit in Sample 316Ti-3. 127
Figure 4.126. Micrograph of Sample 316Ti-3 shown in Figure 4.125. 128

Figure 4.127. Higher magnification of the intergranular attack and metal wastage in Sample 316Ti-3 shown in Figure 4.126. 128

Figure 4.128. Micrograph of localised attack in Sample 316Ti-4. 129

Figure 4.129. Higher magnification micrograph of intergranular attack in Sample 316Ti-4 shown in Figure 4.128. 129

Figure 4.130. Micrograph of attack in Sample 430-3 associated with the coke formation shown in Figure 4.117. 130

Figure 4.131. Etched micrograph of Sample 430-3 showing carburisation at the surfaces of the sample. 131

Figure 4.132. Etched micrograph of Sample 430-3 showing the carbide distribution in the centre through the thickness. 131

Figure 4.133. Micrograph of unetched Sample 441-3 showing no attack. 132

Figure 4.134. Etched microstructure of Sample 441-3 showing the titanium carbo-nitride distribution. 132

Figure 4.135. Higher magnification of the distribution of the titanium carbo-nitride precipitates in Sample 441-3. 133

Figure 4.136. High magnification micrograph of the carbide distribution and titanium carbo-nitride precipitation (arrows) in Sample 441-3 and associated coking (dark). 133

Figure 4.137. SEM-SE image in secondary mode showing coke filaments shown in Figure 4.117, with filaments fractured during sample preparation for SEM, leaving the “base” of the growth. 134

Figure 4.138. SEM-SE image of the surface of Sample 430-4. 135

Figure 4.139. Higher magnification SEM-SE image of Sample 430-4 shown in Figure 4.138 showing different particles [(1) fine needles, (2) chunky and faceted particles and (3) light particles]. 135

Figure 4.140. SEM-BSE image of coking and possible pit initiation on the surface in Sample 430-4. 136

Figure 4.141. SEM-SE image in secondary mode of coke filaments shown in Figure 4.118, with carbide particles at the tips. 136

Figure 4.142. Higher magnification SEM-SE image of the region shown in Figure 4.141. 137

Figure 4.143. EDX spectrum of “metal dust” particles shown in Figure 4.142. 137

Figure 4.144. SEM-SE image of a pit on the surface in Sample 316-3 (after cleaning). 138

Figure 4.145. SEM-SE image of a pit in Sample 316-4 (not cleaned). 139

Figure 4.146. SEM-SE image of the carbon products inside the pits shown in Figure 4.145 showing the carbon filaments with carbide particles at tips. 139

Figure 4.147. Higher magnification SEM-SE image of Figure 4.146. 140

Figure 4.148. TEM image of some of the carbon filaments shown in Figure 4.141, with the dark particle in top right hand corner being a carbide “metal dust”. 141

Figure 4.149. TEM image showing a higher magnification of the region in Figure 4.148, clearly showing that the carbon filaments are tubular. 142

Figure 4.150. (a) is an BSE image of the region, and associated X-ray maps of (b) iron, (c) chromium and (d) nickel. 143

Figure 4.151. X-ray spectrum and volume % of the surface of Sample 304-4..... 144

Figure 4.152. X-ray spectrum and volume % of the surface of Sample 321-4..... 144

Figure 4.153. X-ray spectrum and volume % of the surface of Sample 316L-4. 145

Figure 4.154. X-ray spectrum of the surface of Sample 316Ti-4. 145

Figure 4.155. X-ray spectrum of the surface of Sample 430-4..... 146

Figure 4.156. X-ray spectrum of the surface of Sample 441-4..... 146

Figure 4.157. Photograph of the samples in the ceramic boat after the 30-day exposure test. 147

Figure 4.158. Close-up photograph of the coking comparing the austenitic alloys to the ferritic alloys. 148

Figure 4.159. Close-up photograph of the coking comparing the austenitic alloys to the ferritic alloys. 148

Figure 4.160. Photograph of the 304L and 321 samples after the 30-day exposure. The samples on the left-hand side have been cleaned with a soft nylon brush. 149

Figure 4.161. Close-up photograph of the cleaned 304-7 sample showing pitting at the edges. 149

Figure 4.162. Photograph of the 321-8 sample that was not cleaned, showing a uniform coke layer. 150

Figure 4.163. Photograph of Sample 321-7 after being cleaned with a brush in running water, showing the shiny black layer retained on the surface..... 150

Figure 4.164. Photograph of the 316L and 316Ti samples exposed for 30 days. The samples on the LHS have been cleaned, and show extensive pitting. 151

Figure 4.165. Photograph of Sample 316-8 that was not cleaned. 152

Figure 4.166. Photograph of Sample 316-7 after cleaning, showing the extent of the pitting. 152

Figure 4.167. Photograph of Sample 316Ti-7 after cleaning, showing the extent of the pitting. 153

Figure 4.168. Photograph of the 430 and 441 samples after exposure for 30 days. 154

Figure 4.169. Photograph showing the difference between the 430 and 441 samples that were cleaned (LHS) and those that were not cleaned (RHS)..... 154

Figure 4.170.Close-up photograph of the 430-7 sample that was cleaned, showing attack on the edges. 155

Figure 4.171. Close-up photograph of Sample 441-7 after being cleaned, showing tenacious carbon build-up and associated pitting. 155

Figure 4.172. Micrograph of a cross-section through Sample 304-7 showing localised attack. 158

Figure 4.173. Micrograph of Sample 304-7 showing more widespread attack. 159
Figure 4.174. Higher magnification micrograph of the attack in Sample 304-7. 159
Figure 4.175. Micrograph of carburisation and associated attack in Sample 304-7. 160
Figure 4.176. Micrograph of a cross-section through Sample 321-7 showing no localised attack. 160
Figure 4.177. Micrograph of carburisation and widespread attack in Sample 321-8. 161
Figure 4.178. Higher magnification of the carburisation and attack in Sample 321-8 shown in Figure 4.177. 161
Figure 4.179. Micrograph in the unetched condition showing the internal carburisation in Sample 321-8 (inside dashed line). 162
Figure 4.180. Micrograph of a cross-section through Sample 316-7 showing wide-spread attack. 163
Figure 4.181. Micrograph of Sample 316-7 in another area as shown in Figure 4.180 showing uniform nature of attack. 163
Figure 4.182. Higher magnification micrograph of Sample 316-7 showing uniform nature of attack. 164
Figure 4.183. Micrograph of Sample 316-7 showing intergranular attack and grain dropping. 164
Figure 4.184. Micrograph of attack in Sample 316-8. 165
Figure 4.185. Higher magnification micrograph of Sample 316-8 showing intergranular attack. 165
Figure 4.186. Micrograph of attack in Sample 316Ti-8. 166
Figure 4.187. Higher magnification micrograph of Sample 316Ti-8 shown in Figure 4.186. 166
Figure 4.188. Higher magnification micrograph of Sample 316Ti-8 shown in Figure 4.187 (the globular features (arrows) are alcohol stains, seeping from the intergranular attack). 167
Figure 4.189. Micrograph of internal carburisation and attack in Sample 430-7 (etched). 168
Figure 4.190. Higher magnification micrograph of Sample 430-7 shown in Figure 4.189 (etched). 168
Figure 4.191. Micrograph between two areas of localised attack in Sample 430-7 (etched). 169
Figure 4.192. Higher magnification micrograph near the surface just below the pit in Sample 430-7 (etched). 169
Figure 4.193. Micrograph of Sample 430-7 in the carburised zone (etched). 170
Figure 4.194. Micrograph of the interface between the carburised zone and matrix in Sample 430-7 (etched). 170
Figure 4.195. Micrograph of sample near the centre of Sample 430-7 showing the general carbide distribution (etched). 171

Figure 4.196. Micrograph of Sample 441-7, showing significant surface relief near the edges after polishing. 172
Figure 4.197. Micrograph of Sample 441-7 showing relief around the edges, due to poor edge retention from polishing and associated coking. 172
Figure 4.198. Micrograph of a cross-section through Sample 441-7 (etched). 173
Figure 4.199. Micrograph showing extensive carburisation in Sample 441-7 (etched), initiating from localised sites. 173
Figure 4.200. Micrograph in another area of Sample 441-7 (etched), showing uniform carburisation. 174
Figure 4.201. Micrograph showing uniform carburisation at the edge of Sample 441-7 (etched) (this area is similar to Figure 4.196). 174
Figure 4.202. Higher magnification micrograph of carburisation in Sample 441-7 initiating from localised sites. 175
Figure 4.203. Higher magnification image of Sample 441-7 of the intergranular nature at the progressing front shown in Figure 4.202. 175
Figure 4.204. Higher magnification image of the carburisation near the edge of Sample 441-7. 176
Figure 4.205. Micrograph of the attack associated with the titanium carbo-nitride precipitates in Sample 441-7. 176
Figure 4.206. Higher magnification image of Sample 441-7 shown in Figure 4.205. 177
Figure 4.207. SEM-BSE image of the surface of Sample 304-8. 178
Figure 4.208. Higher magnification SEM-BSE image of the surface of Sample 304-8 showing protrusions on the surface and individual particles. 179
Figure 4.209. Higher magnification SEM-BSE image of the surface of Sample 304-8. 179
Figure 4.210. SEM-SE image of a pit in the surface in Sample 304-8 that was covered with corrosion product, which was an oxide (i.e. not coke), as shown in Figure 4.211. 180
Figure 4.211. EDX spectrum of product inside pit shown in Figure 4.210. 180
Figure 4.212. SEM-BSE image of the surface of Sample 321-8. 181
Figure 4.213. SEM-SE image of the coke layer covering parts of the surface on Sample 321-8 (the light particle near the centre was not analysed). 181
Figure 4.214. SEM-BSE image of the surface of Sample 321-8. 182
Figure 4.215. Higher magnification SEM-BSE image of the surface of Sample 321-8. 182
Figure 4.216. EDX spectrum of the surface of Sample 321-8 shown in Figure 4.215. 183
Figure 4.217. EDX spectrum of the coke layer on Sample 321-8, shown in Figure 4.213. 183
Figure 4.218. SEM-SE image of pitting on the surface of Sample 316-8. 184
Figure 4.219. SEM-BSE image of the surface of Sample 316-8. 185
Figure 4.220. SEM-BSE image inside a pit of Sample 316-8. 185

Figure 4.221. Higher magnification SEM-BSE image of Sample 316-8. 186
Figure 4.222. EDX spectrum of the surface of Sample 316-8. 186
Figure 4.223. EDX spectrum of the surface of a pit on Sample 316-8. 187
Figure 4.224. SEM-SE image of pitting on the surface on Sample 316Ti-8. 188
Figure 4.225. SEM-SE image of general attack and pitting on Sample 316Ti-8. 188
Figure 4.226. SEM-BSE image of the pitting and uniform attack on the surface of Sample 316Ti-8. 189
Figure 4.227. Higher magnification SEM-BSE image of the surface of Sample 316Ti-8. 189
Figure 4.228. SEM-BSE image of the surface of Sample 316Ti-8 showing the initiation of pitting. 190
Figure 4.229. EDX spectrum of the uniform corroded surface of Sample 316Ti-8. 190
Figure 4.230. EDX spectrum of the darker areas on the surface of Sample 316Ti-8 shown in Figure 4.228. 191
Figure 4.231. SEM-BSE image of the surface of Sample 430-8. 192
Figure 4.232. Higher magnification image of the surface of Sample 430-8. 192
Figure 4.233. Higher magnification SEM-BSE image of the surface of Sample 430-8. 193
Figure 4.234. SEM-SE image of a pit in Sample 430-8. 193
Figure 4.235. SEM-BSE image of the same pit in Sample 430-8 (Figure 4.234). 194
Figure 4.236. Higher magnification SEM-BSE image of inside the pit in Sample 430-8. 194
Figure 4.237. EDX spectrum of the surface in Sample 430-8. 195
Figure 4.238. EDX spectrum of the pit in Sample 430-8 shown in Figure 4.236. 195
Figure 4.239. SEM-BSE image of the surface of Sample 441-8. 196
Figure 4.240. Higher magnification SEM-BSE image of the surface of Sample 441-8. 197
Figure 4.241. SEM-BSE image of pitting in Sample 441-8. 197
Figure 4.242. Higher magnification SEM-BSE image of a pit in Sample 441-8. 198
Figure 4.243. EDX spectrum of the surface of Sample 441-8. 198
Figure 4.244. EDX spectrum inside a pit (area analysis) in Sample 441-8. 199
Figure 4.245. SEM-BSE image of a cross-section through a corroded area of Sample 304-7. 200
Figure 4.246. EDX spectrum of position A shown in Figure 4.245 of Sample 304-7. 200
Figure 4.247. EDX line scan on Sample 304-7 as shown in Figure 4.245. 201
Figure 4.248. SEM-BSE image of the protective oxide layer on Sample 304-7. 201
Figure 4.249. EDX line scan through Sample 304-7 as shown in Figure 4.248. 202
Figure 4.250. SEM-BSE image of attack in Sample 321-8. 203
Figure 4.251. Higher magnification SEM-BSE image of attack on Sample 321-8. 204

Figure 4.252. EDX line scan of Sample 321-8 as shown in Figure 4.251. 204
Figure 4.253. Higher magnification (SEM-BSE) of the uniform attack in Sample 321-8 205
Figure 4.254. EDX spectrum of the protective chromium oxide layer on Sample 321-8 as shown in Figure 4.253. 205
Figure 4.255. EDX spectrum of the oxide outside the chromia layer of Sample 321-8 as shown in Figure 4.253 206
Figure 4.256. SEM-BSE image of the matrix of Sample 321-8 showing carburisation on the grain boundaries and attack around the titanium carbo-nitride precipitate. 206
Figure 4.257. EDX spectrum of the titanium carbo-nitride precipitate in Sample 321-8 (Figure 4.256). 207
Figure 4.258. Bulk analysis of Sample 321-8 showing no evidence of nickel. 207
Figure 4.259. SEM-BSE image of uniform corrosion by intergranular attack, and subsequent degradation of the grains in Sample 316-8. 209
Figure 4.260. Higher magnification SEM-BSE image of the carbides (arrows) and attack on Sample 316-8. 210
Figure 4.261. Higher magnification SEM-BSE image of the carbides (arrows) and associated attack in Sample 316-8. 210
Figure 4.262. High magnification SEM-BSE image of the carbides (arrows), grain boundary attack and progressive attack of the grains in Sample 316-8. 211
Figure 4.263. EDX Spectrum of products (white phase) on the grain boundaries of Sample 316-8 (including some matrix) 211
Figure 4.264. SEM-BSE image of the general nature of the metal wastage on Sample 316-8, showing the white phase on the grain boundaries was still evident in the corroded area. 212
Figure 4.265. Higher magnification image of the attack on Sample 316-8. 212
Figure 4.266. EDX line scan of Sample 316-8 as shown in Figure 4.265. 213
Figure 4.267. EDX line scan in similar area as shown in Figure 4.266, but over a longer distance. 213
Figure 4.268. EDX spectrum of the large light phase on the grain boundary of Sample 316-8 as shown in Figure 4.265. 214
Figure 4.269. EDX spectrum of the corroded region adjacent to the large light phase on the grain boundary of Sample 316-8 as shown in Figure 4.265. 214
Figure 4.270. SEM-BSE image of Sample 316-8 indicating positions where various EDX analyses were made. 215
Figure 4.271. EDX analysis of Point 1 in Sample 316-8 as shown in Figure 4.270. 215
Figure 4.272. EDX analysis of Point 2 in Sample 316-8 as shown in Figure 4.270. 216
Figure 4.273. EDX analysis of Point 3 in Sample 316-8 as shown in Figure 4.270. 216
Figure 4.274. EDX analysis of Point 4 in Sample 316-8 as shown in Figure 4.270. 217
Figure 4.275. SEM-BSE image of attack in Sample 316Ti-8 218

Figure 4.276. Higher magnification SEM-BSE image of attack in Sample 316Ti-8. 218
Figure 4.277. Higher magnification SEM-BSE image of grain boundary precipitation and associated attack in Sample 316Ti-8. 219
Figure 4.278. Higher magnification SEM-BSE image of products on the surface of Sample 316Ti-8. 219
Figure 4.279. SEM-BSE image of grain boundary attack in Sample 316Ti-8. 220
Figure 4.280. Higher magnification SEM-BSE image of attack in Sample 316Ti-8 as shown in Figure 4.279. 220
Figure 4.281. EDX spectrum of the outside oxide on Sample 316Ti-8 as shown in Figure 4.278. 221
Figure 4.282. EDX spectrum of the white phase in the outside oxide layers in Sample 316Ti-8 as shown in Figure 4.278. 221
Figure 4.283. EDX spectrum of the white phase on the grain boundaries in Sample 316Ti-8 as shown in Figure 4.280. 222
Figure 4.284. SEM-BSE image of carburisation at local breakdown of the protective oxide layer in Sample 430-7, and the onset of metal wastage by metal dusting. 223
Figure 4.285. Higher magnification SEM-BSE image of pitting and carburisation in Sample 430-7. 224
Figure 4.286. Higher magnification SEM-BSE image of carburisation at the pitting of Sample 430-7 shown in Figure 4.285. 224
Figure 4.287. SEM-BSE image of the oxide associated with the pit on Sample 430-7. 225
Figure 4.288. High magnification SEM-BSE image of carburisation below the pit in Sample 430-7. 225
Figure 4.289. SEM-BSE image in carburised zone in Sample 430-7 showing the carbide morphology. 226
Figure 4.290. SEM-BSE image of carbides in the matrix of Sample 430-7. 226
Figure 4.291. EDX spectrum in the carburised zone, close to the surface in Sample 430-7. 227
Figure 4.292. EDX spectrum of white phase in oxide layer in Sample 430-7 as shown in Figure 4.287. 227
Figure 4.293. EDX spectrum of the oxide layer close to the metal surface in Sample 430-7 as shown in Figure 4.287. 228
Figure 4.294. EDX spectrum of the outside oxide layer in Sample 430-7 as shown in Figure 4.287. 228
Figure 4.295. SEM-BSE image of localised carburisation and associated initiation of a pit in Sample 430-7, showing the position of the line scan performed. 230
Figure 4.296. EDX line scan in Sample 430-7 as shown in Figure 4.295. 230
Figure 4.297. SEM-BSE image of general (uniform) attack in Sample 430-8. 231
Figure 4.298. High magnification SEM-BSE image of the oxide layer in Sample 430-8 shown in Figure 4.297. 231

Figure 4.299. EDX spectrum of the oxide layer on Sample 430-8 as shown in Figure 4.298.....232
Figure 4.300. EDX spectrum of the coke above the oxide layer in Sample 430-8 as shown in Figure 4.297.....232
Figure 4.301. EDX spectrum of the metal below oxide layer of Sample 430-8 containing about 15% chromium.....233
Figure 4.302. SEM-BSE image of the matrix of Sample 441-7.....234
Figure 4.303. Higher magnification SEM-BSE image of internal attack forming coke (black) associated with titanium carbo-nitride precipitates (dark) in Sample 441-7.....235
Figure 4.304. SEM-BSE image of localised carburisation in Sample 441-7.....235
Figure 4.305. EDX analysis along the line shown in Figure 4.304 of Sample 441-7.....236
Figure 4.306. SEM-BSE image of oxide in a pit and associated carburisation in Sample 441-7, showing positions where EDX analyses were performed.....236
Figure 4.307. SEM-BSE image of the interface between the grain boundary and internal carburisation in Sample 441-7.....237
Figure 4.308. SEM-BSE image of interface between grain boundary carburisation and matrix structure in Sample 441-7.....237
Figure 4.309. EDX analysis of the substrate underneath the oxide layer in Sample 441-7 shown in Figure 4.306 (Position A).....238
Figure 4.310. EDX analysis of a chromium- and silicon-rich phase in the oxide layer on Sample 441-7 shown in Figure 4.306 (Position B).....238
Figure 4.311. EDX analysis of the chromium-rich phase in the oxide layer in Sample 441-7 shown in Figure 4.306 (Position C).....239
Figure 4.312. EDX analysis of the iron-rich phase in the oxide layer in Sample 441-7 shown in Figure 4.306 (Position D).....239
Figure 4.313. SEM-BSE image of an area where the protective chromium oxide layer (arrow) was still relatively intact on Sample 441-8.....240
Figure 4.314. SEM-BSE image of localised attack in Sample 441-8.....241
Figure 4.315. EDX spectrum of the oxide associated with the attack on Sample 441-8 as shown in Figure 4.314 (Position A).....241
Figure 4.316. EDX spectrum of the white product in the oxide shown in Figure 4.314 in Sample 441-8 (Position B).....242
Figure 4.317. EDX spectrum of the particles at the grain boundaries of Sample 441-8 (Position C).....242
Figure 4.318. SEM-BSE image of the initiation of metal dusting and the surface of Sample 441-8.....243
Figure 4.319. Higher magnification SEM-BSE image of the white phase at the surface of Sample 441-8 shown in Figure 4.318.....244
Figure 4.320. SEM-BSE image of the white phase at the surface of Sample 441-8.....244

Figure 4.321. X-ray spectrum of the surface of Sample 304-8 showing peaks and volume %. 246
Figure 4.322. X-ray spectrum of the surface of Sample 321-8. 246
Figure 4.323. X-ray spectrum of the surface of Sample 316-8. 247
Figure 4.324. X-ray spectrum of the surface of Sample 316Ti-8. 247
Figure 4.325. X-ray spectrum of the surface of Sample 430-8. 248
Figure 4.326. X-ray spectrum of the surface of Sample 441-8 248
Figure 4.327. X-ray spectrum of the coke associated with the austenitic samples. 249
Figure 4.328. Raman spectrograph of the coke associated with the austenitic samples (labelled as Sample 1). 250
Figure 5.1. Graph of the corrosion rates for up to 30 days. 252
Figure 5.2. Corrosion rates of the 304L, 321, 430 and 441 samples exposed for up to 30 days. 253
Figure 5.3. X-ray spectra of the 304L samples exposed for 7 days, 14 days, 30 days and un-exposed (from top to bottom respectively) 254
Figure 5.4. X-ray spectra of the 321 samples exposed for 7 days, 14 days, 30 days and un-exposed (from top to bottom respectively) 254
Figure 5.5. X-ray spectra of the 316L samples exposed for 7 days, 14 days, 30 days and un-exposed (from top to bottom respectively) 255
Figure 5.6. X-ray spectra of the 316Ti samples exposed for 7 days, 14 days, 30 days and un-exposed (from top to bottom respectively) 255
Figure 5.7. X-ray spectra of the 430 samples exposed for 7 days, 14 days, 30 days and un-exposed (from top to bottom respectively) 256
Figure 5.8. X-ray spectra of the 441 samples exposed for 7 days, 14 days, 30 days and un-exposed (from top to bottom respectively) 256

LIST OF TABLES

Table 1.1. Corrosive substances found in many refining processes, as indicated in Figure 1.1 [NiI1]. 3

Table 2.1. Maximum service temperatures for common engineering alloys in air [NiI2, 2012Hol]. 8

Table 2.2. Gas phase equilibria relevant to carburising and metal dusting [2010You]. 14

Table 2.3. Alloys studied by Szakálos with operating mechanisms [2004Sza]. 16

Table 3.1. Nominal compositions of the alloys tested (wt%); values indicate maxima unless ranges are specified. 34

Table 3.2. Details of sample exposure and evaluation. 45

Table 4.1. Mass change data after the 6-day test. 53

Table 4.2. Mass change data for the 7-day test. 75

Table 4.3. Mass change data for the 14-day test. 123

Table 4.4. Mass change data for the 30-day test. 157

THE EFFECT OF CARBIDE-FORMING ELEMENTS ON THE METAL DUSTING RATE IN HYDROCARBON ENVIRONMENTS

1. INTRODUCTION

South Africa, like most other countries, is heavily reliant on crude oil as a major energy source to fuel the economy. During petroleum refining, raw crude is separated by fractional distillation into petroleum gas, naphtha (petrol), middle distillates (kerosene and jet fuel), gas oils (cracking stocks) lubricating oils, and residual oils used for fuel oils, asphalt, or thermal crack stocks (coking). All the streams from crude distillation are further processed or treated to convert the many fractionated materials to saleable or useful petrochemical stocks. These processes involve the separation of gases and absorption or removal of unwanted substances such as carbon monoxide, ammonia and hydrogen sulphide. Figure 1.1 is a typical flow diagram of a refinery [NiI1]. The corrosive species are underlined in Figure 1.1, and further described in Table 1.1 [NiI1].

Petroleum refining is increasingly becoming more sophisticated in comparison to the single shell stills of the 1800s. Chemical and mechanical engineering advances are being sought to increase product yields and improve plant operating reliability. Methods are being developed to remove potential pollutants, like sulphur and lead, from processes and products. Changing national interests among oil-producing countries are affecting sources of crude supplies. One result of these changes is a growing emphasis on materials engineering [NiI1]. Raw crude entering a refinery contains several forms of sulphur, water, salts, organic, nitrogen, and organic acids which split, combine or convert into numerous corrosive combinations. These corrosive species lead to particular forms (mechanisms) of corrosion in different areas of the refinery. It is the responsibility of corrosion and materials engineers to provide cost-effective solutions, while risks are managed to prevent unexpected failures. Due to the flammable nature of the process streams, failure is often disastrous, leading to fire and widespread damage to adjacent equipment, pollution and other environmental issues, injury and health and safety concerns, loss of income due to plant down time, etc..

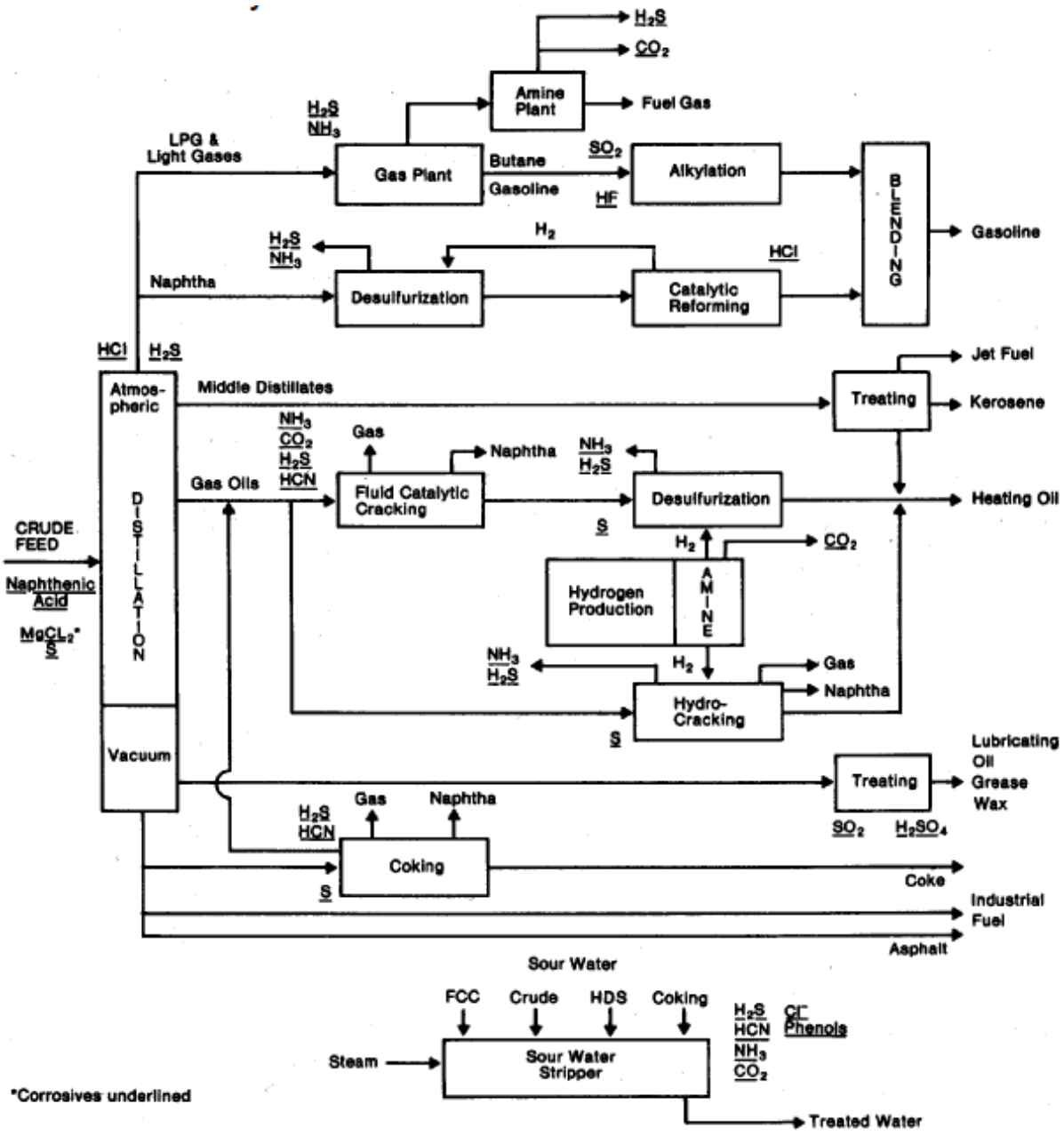


Figure 1.1. Process flow of a typical modern petroleum refinery to produce domestic and industrial fuels [NiI1].

Table 1.1. Corrosive substances found in many refining processes, as indicated in Figure 1.1 [NiI1].

Compound	Description
Sulphur	Present in raw crude, it causes high-temperature sulphidation of metals. It combines with other elements to form aggressive compounds such as sulphides and sulphates, sulphurous, polythionic, and sulphuric acid.
Naphthenic acid	A collective name for organic acids found primarily in crude oils from western United States, certain Texas and Gulf Coast and a few Mid-East oils.
Polythionic acid	Sulphurous acids formed by the interaction of sulphides, moisture, and oxygen. This generally occurs when the equipment is shut down.
Chlorides	Present in the form of salts ($MgCl_2$ and $CaCl_2$), originating from crude oil, catalysts and cooling water.
Carbon dioxide	Occurs in steam reforming of hydrocarbon in hydrogen plants, and in some catalytic cracking plants. CO_2 combines with moisture to form carbonic acid.
Ammonia	Nitrogen in feedstock combines with hydrogen to form ammonia. Ammonia is also sometimes used for neutralisation, which in turn may combine with other elements to form corrosive compounds like ammonium chloride.
Cyanides	Usually generated in the cracking of high nitrogen feed stocks. When present, corrosion rates are likely to increase.
Hydrogen chloride	Formed through the hydrolysis of $MgCl_2$ and $CaCl_2$ and is formed in many overhead (vapour) streams. On condensation, it forms aggressive hydrochloric acid.
Sulphuric acid	Used as catalyst in alkylation plants and is formed in some process streams containing sulphur trioxide, water and oxygen.
Hydrogen	Can lead to blistering and embrittlement of steel. It also readily combines with other species to form corrosive compounds.
Phenols	Found primarily in sour water strippers.
Oxygen	Originates in crude, aerated water, or packing gland leaks. Causes oxidation and scaling in high temperature environments of under-alloyed materials.
Carbon	At high temperature, results in carburisation, which causes embrittlement or metal dusting in some alloys.

One particular form of corrosion that is still posing many challenges is metal dusting (MD). A definition of metal dusting and the various factors involved in metal dusting were presented by Hochman [1972Hoc]:

1. Environment: Gas phase, potentially carburizing and reducing with or without oxygen.
2. Temperature: Usually 450-800°C.
3. Form: Localized or general pitting and/or general overall surface wastage; surface usually carburized.
4. Product: Dust or powder composed of graphite mixed with metal, metal carbides and metal oxides.

This type of high temperature corrosion is insidious, since when initiated, the metal dusting pit growth rate may reach at least a millimetre per month on stainless steels and an order of magnitude higher on low alloyed steels. It is a widespread problem in the petrochemical industry, particularly in cracker furnaces and reforming units, i.e. in hydrocarbon synthesis gas containing predominantly CO and H_2 with some water vapour. This means that basically all production facilities of monomers, which are the raw materials for polymer production, like polyethylene, may be subjected to metal dusting. Other chemical processes where organic compounds are reacting, such as in butane dehydrogenation, hydrodealkalation, acetic acid cracking and pyridine production are also subjected to metal dusting [1995Gra1]. Industrial processes within the heat-treating industry, energy production (coal gasification plants) and ammonia plants are other examples. During recent years, MD has attracted considerable attention due to development of new processes in the petrochemical industry, as well as in electric power generation. Furthermore, the limitation of the materials of construction prohibits the use of more energy favourable processes at higher temperatures.

This project will therefore be undertaken to contribute to the existing understanding of metal dusting. Better understanding of the mechanism will help to develop and specify cost-effective engineering materials that are more resistant to metal dusting environments.

2. LITERATURE REVIEW

Corrosion has been defined in different ways, but a common definition states that corrosion is the undesirable deterioration of a material due to reaction with its environment [1967Fon, 2004McE]. Different materials behave differently in different environments, leading to particular forms of corrosion. Corrosion reactions may be conveniently classified as either 'Wet Corrosion' or 'Dry Corrosion'. Wet corrosion, as the name implies, occurs only in the presence of aqueous solutions or electrolytes. Dry corrosion occurs when no liquid is present, or the temperature is above the dew point of the environment [1967Fon, 2012Hol].

Wet corrosion is an electrochemical process, and electrochemical reactions are used to explain it. Wet corrosion, as the name suggests, occurs only in the presence of aqueous solutions (which include condensation from moisture) or electrolytes, and is the most commonly encountered type of corrosion. Wet corrosion can be further categorised by the appearance of the corroded metal. These categories include the following (often referred to as the eight forms of corrosion):

- Uniform or general corrosion
- Galvanic corrosion
- Crevice corrosion
- Pitting corrosion
- Intergranular corrosion
- Selective de-alloying
- Erosion corrosion
- Stress corrosion cracking (SCC)

Dry corrosion, or direct chemical combination, occurs above the environment dew point. Dry corrosion is usually associated with high temperatures, and gases are the usual corrodents. Examples of dry corrosion include:

- Oxidation
- Sulphidation
- Carburisation

- Metal dusting.

2.1. Oxidation

All common metals and alloys are unstable in air or oxygen and react to form oxides, even at room temperature. This chemical reaction between metal and oxygen is referred to as oxidation. Unlike most chemical reactions, oxidation of many important alloys creates an oxide film that, as it thickens, forms an increasingly effective barrier between the metal and the gas. The rate of oxidation is controlled by diffusion of metal outward or oxygen inward through the oxide. This diffusion is dependent on temperature, temperature fluctuations, the integrity of the oxide layer, and the presence of other gases in the atmosphere [1967Fon, 2012Hol].

A summary of the salient facts concerning the high-temperature oxidation of alloys commonly used in refinery process units is as follows [2012Hol]:

- The maximum temperature at which carbon steel has adequate, long-term resistance to scaling in an oxidising atmosphere is about 550°C. The primary factors affecting high temperature oxidation are metal temperature and alloy composition. Oxidation of carbon steel begins to become significant above about 480°C.
- Oxidation rates are often not constant with time. The oxide scale can act as a diffusion barrier, so that the oxidation rate progressively drops as the scale layer builds up.
- Temperature cycling substantially increases the scaling rate of many high-temperature, heat-resistant alloys because of spalling of the scale. This is more significant for austenitic alloys due to the larger difference in thermal expansion between the matrix and the oxide scale, compared to ferritic steels for instance.
- The oxidation resistance of steels is approximately proportional to the chromium content, but the resistance of a chromium-bearing steel is further enhanced by small additions of silicon, aluminium, titanium and niobium.
- Traces of sulphur gases in the high-temperature environment may increase the scaling rate of both low- and high-alloy steels. High-nickel, heat-resistant steels and nickel-based alloys should be used with caution in hot gases containing appreciable quantities of sulphur.

- Oxidation resistance is only one of several criteria to be used in selecting materials for high-temperature applications. Good high-temperature mechanical properties, freedom from development of brittle metallurgical constituents, and resistance to process-side corrosion also are usually necessary.

Most alloys, including carbon steels and low alloy steels, suffer general thinning due to oxidation. Usually the component will be covered on the outside surface with an oxide scale depending on the temperature and exposure time. The 300 Series SS and nickel alloys generally have a very thin dark scale unless exposed to extremely high temperatures where metal loss rates are excessive. Resistance to oxidation is best achieved by upgrading to a resistant alloy. Chromium is the primary alloying element that affects resistance to oxidation. Other alloying elements, including silicon and aluminium are effective, but their concentrations are limited due to adverse effects on mechanical properties. They are often used in special alloys for applications as heater supports, burner tips and components for combustion equipment. Maximum recommended service temperatures for alloys are given in Table 2.1 [NiI2, 2012Hol]. An interesting observation from Table 2.1 is that the recommended maximum temperature for ferritic materials for intermittent use is higher than for continuous use (isothermal versus cyclic treatments), however, the allowable temperature for intermittent use for austenitic materials is lower. The resistance of materials to oxidation is linked to the development and maintenance of a protective oxide layer on the surface. Alloys designed for high temperature applications therefore have elements that promote stable oxide layers like chromium, aluminium and silicon. However, thermal cyclic treatments cause thermal stresses in the oxide layer that break the film and exposes “fresh” unprotected substrate that can be oxidised. The difference between the thermal expansion coefficient for austenite and oxide scale is larger than between ferrite and the oxide scale. Thermal cyclic treatments (intermittent use) of austenitic materials will therefore break oxide scales more readily than for ferritic materials, which is why the recommended temperature for intermittent temperature usage for austenitic materials is lower than for continuous usage.

Table 2.1. Maximum service temperatures for common engineering alloys in air [NiI2, 2012Hol].

Alloy	Structure	Continuous Temperature (^oC)	Intermittent Temperature (^oC)
Carbon Steel	Ferrite	550	-
C - ½ Mo	Ferrite	565	-
1 Cr - ½ Mo	Ferrite	585	-
1¼ Cr - ½ Mo	Ferrite	595	-
2¼ Cr - 1 Mo	Ferrite	635	-
3 Cr - 1 Mo	Ferrite	635	-
5 Cr - ½ Mo	Ferrite	650	-
5 Cr - ½ Mo - 1½Si	Ferrite	700	-
7 Cr - ½ Mo	Ferrite	675	-
9 Cr - 1 Mo	Ferrite	700	-
Type 410 (12 Cr)	Martensite	705	815
Type 405 (12 Cr -¼ Al)	Ferrite	705	815
Type 430 (17 Cr)	Ferrite	815	870
Type 446 (27 Cr)	Ferrite	1095	1175
Type 304 (18 Cr - 8 Ni)	Austenite	925	870
Type 316 (18 Cr - 8 Ni - 3 Mo)	Austenite	925	870
Type 321 (18 Cr - 8 Ni -½ Ti)	Austenite	925	870
Type 347 (18 Cr - 8 Ni 1 Cb)	Austenite	925	870
Type 309 (25 Cr - 12 Ni)	Austenite	1095	980
Type 310 (25 Cr - 20 Ni)	Austenite	1150	1035

2.2. Sulphidation

Sulphidation is the corrosion of carbon steel and other alloys resulting from their reaction with sulphur compounds in high temperature environments. The presence of hydrogen accelerates corrosion. The following materials are commonly affected [2012Hol]:

- All iron based materials, including carbon steel, low alloy steels and stainless steels.
- Nickel based alloys are also affected to varying degrees, depending on composition, particularly depending on the chromium content.
- Copper based alloys sulphide at lower temperatures than carbon steel.

Major factors affecting the sulphidation rate are alloy composition, temperature and concentration of corrosive sulphur compounds. Susceptibility of an alloy to sulphidation is determined by its ability to form protective sulphide scales.

Sulphidation of iron-based alloys usually begins at metal temperatures above 260°C. The typical effects of increasing temperature, chromium content, and sulphur content on metal loss are shown in the modified McConomy curves, Figure 2.1 [1986Gut]. In general, the resistance of carbon steel and other alloys is determined by chromium content of the material. Increasing chromium contents significantly increase resistance to sulphidation. 300 Series stainless steels, such as Types 304, 316, 321 and 347 are highly resistant in most refining process environments. Nickel based alloys are similar to stainless steels in that similar levels of chromium provide similar resistance to sulphidation (regardless of the nickel level).

Crude oils, coal and other hydrocarbon streams contain sulphur at various concentrations. Total sulphur content is made up of many different sulphur-containing compounds. Sulphidation is primarily caused by H_2S and other reactive sulphur species as a result of the thermal decomposition of sulphur compounds at high temperatures. Some sulphur compounds react more readily to form H_2S, so it can be misleading to predict corrosion rates

based on weight % sulphur alone. A sulphide scale on the surface of the component offers varying degrees of protection depending on the alloy and the severity of the process stream.

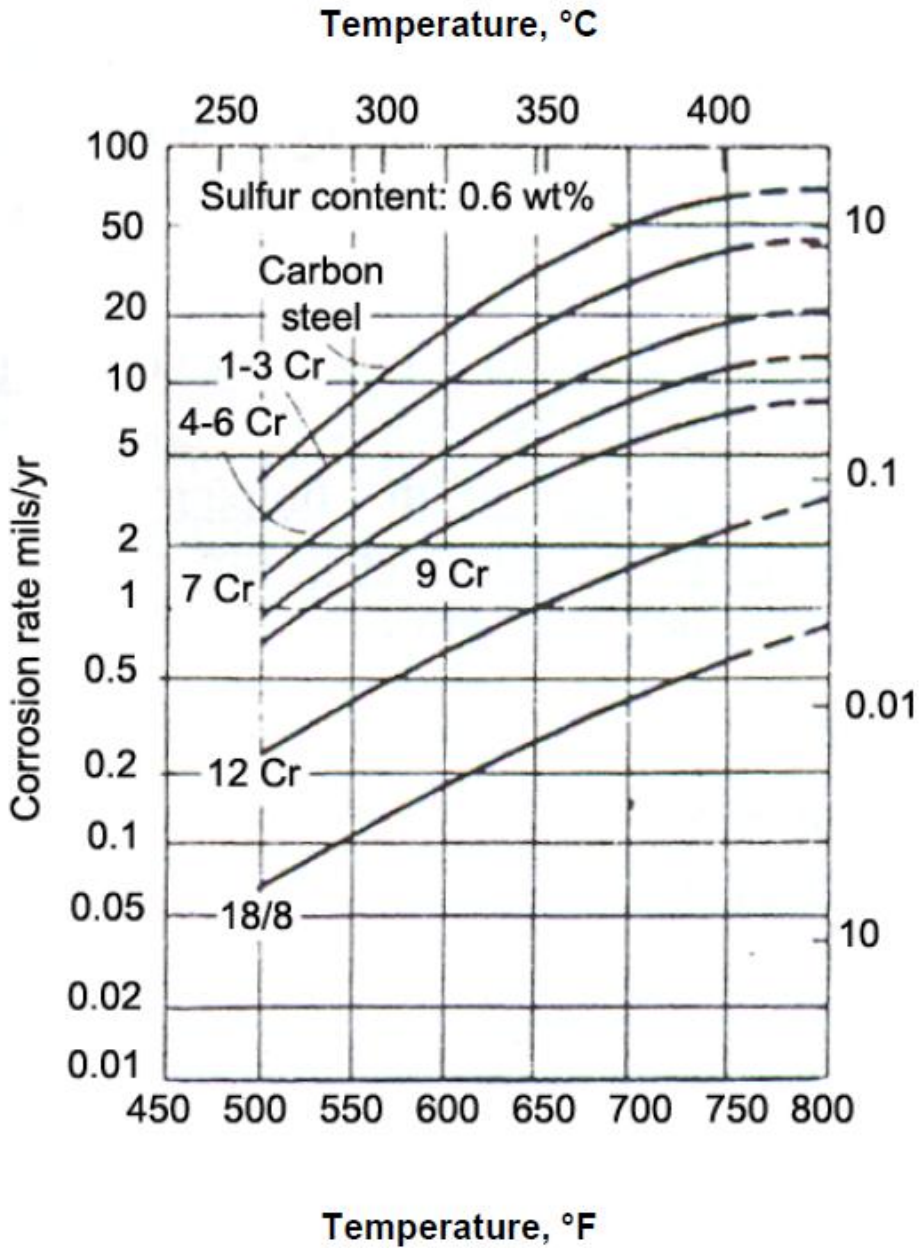


Figure 2.1. Typical effect of temperature on high temperature sulphidation of steels and stainless steels (Modified McConomy) [1986Gut].

2.3. Carburisation

Carburisation occurs when carbon is absorbed into a material at elevated temperature while in contact with a carbonaceous material or carburising environment. The carbon activity is

generally less than 1 (a_c<1), but large enough to stabilise metal carbides. These reactions are rapid and destructive [2012Hol].

Carbon steel and low alloy steels, 300 and 400 Series SS, Cast Stainless Steels (HK and HP [both iron-based heat resisting alloy castings]) and Fe-Ni based alloys (e.g. Alloys 600 and 800) are affected in refineries. Three conditions must be satisfied [2012Hol]:

- exposure to a carburising environment
- temperature high enough to allow diffusion of carbon into the metal (typically above 590°C)
- a susceptible material.

Conditions favouring carburisation include a high gas phase carbon activity (hydrocarbons, coke, gases rich in CO, CO_2, methane, ethane) and low oxygen potential (minimal O_2 or steam). Initially, carbon diffuses into the component at a high rate, and then tapers off as the depth of carburisation increases.

In carbon steels and low alloy steels, carbon reacts to form a hard brittle structure that may crack or spall upon cooling. The 300 Series SS are more resistant than carbon steel and the low alloy steels, due to higher chromium and nickel content. Carburisation can result in the loss of high temperature creep ductility, loss of ambient temperature mechanical properties (specifically toughness/ductility), loss of weldability and corrosion resistance.

2.4. Metal dusting

Metal dusting is a form of carburisation resulting in accelerated localised pitting which occurs in carburising gases and/or process streams containing carbon and hydrogen. For metal dusting, the gas is supersaturated with carbon (a_c>1). Pits usually form on the surface and may contain soot or graphite dust. Low alloy steels, 300 Series SS, nickel based and heat resisting alloys are primarily affected by metal dusting. There is currently no known metal alloy that is immune to metal dusting under all conditions [2012Hol].

Process stream composition, operating temperature and alloy composition are critical factors. Metal dusting is preceded by carburisation and is characterised by rapid metal wastage. This involves a complex series of reactions involving a reducing gas, including hydrogen, methane, propane and CO. It usually occurs in the operating temperature range of about 480-820°C, the upper temperature limit being a function of the thermodynamics of carbon formation, and the lower limit being a function of the kinetics of diffusion of carbon into the metal matrix [2012Hol].

The mechanism of metal dusting is considered to be different for ferritic and austenitic materials and therefore needs to be treated separately. For ferrous alloys, the process can be described as follows [1998Gra1]:

- Saturation of the metal matrix by carburisation
- Precipitation of metal carbides at the metal surface and grain boundaries
- Deposition of graphite from the atmosphere onto the metal carbides at the surface, thus decreasing the carbon activity
- Carbides are only stable at high carbon activity, thus promoting decomposition of the metal carbides under the graphite to a mixture of carbon and metal particles
- Further deposition of graphite is catalysed by the metal particles on the surface
- Volume changes associated with these transformations generate high internal stresses resulting in disintegration of the surface into a 'dust' of filamentary carbon and metal particles

In high nickel alloys, it is thought that metal dusting occurs without the formation of metal carbides. It can also occur under alternating reducing and oxidising conditions.

Affected units on refineries primarily include fired heater tubes, thermowells and furnace components operating in carburising environments have experienced metal dusting. Metal dusting has been reported in catalytic reforming unit heater tubes, gas reforming waste heat boiler tubes and tube-sheets, coker heaters, gas turbines, methanol reforming unit outlet piping and thermal hydrodealkylation furnaces and reactors [2012Hol].

In low alloy steels, the wastage can be uniform, but is usually in the form of small pits filled with a crumbly residue of metal oxides and carbides. The corrosion product is a voluminous carbon dust containing metal particles and sometimes metal oxides and carbides. Frequently, this dust will be swept away by the flowing process stream, leaving behind only the thinned or pitted metal.

In stainless and high alloy steels, however, the attack is frequently local, appearing as deep, round pits. Metallography shows that the metal is heavily carburised under the attacked surface.

There is currently no known metal alloy that is immune to metal dusting under all conditions [2012Hol]. Protection is conferred by a tightly adherent oxide scale of chromium (Cr_2O_3), silica (SiO_2) or alumina (Al_2O_3), which presents a physical barrier to the inward diffusion of carbon. An aluminium diffusion treatment to the base metal substrate can thus be beneficial in some applications, but high chromium-containing alloys appear to offer most promise so far, with excellent results having been reported with castings of 50/50 Cr-Ni alloy [2012Hol].

A degree of success has been reported with the use of high-velocity oxy-fuel (HVOF) thermal spray coatings, high in chromium content, to protect the base metal in certain applications, such as tube-sheets. Other successful mitigating actions include the use of refractory coatings and various design options to keep the base metal out of the susceptible metal dusting temperature range [2012Hol].

2.4.1. Gaseous carbon activity

There are three common gas-phase reactions that produce carbon. These include [2010You]:

Synthesis gas reaction:

$$CO + H_2 = H_2O + C \qquad \textit{Equation 2.1}$$

The Boudouard reaction:

$$2CO = CO_2 + C \qquad \textit{Equation 2.2}$$

Hydrocarbon cracking, for example:

$$CH_4 = 2H_2 + C \qquad \textit{Equation 2.3}$$

The standard free energies of the above three reactions are listed in Table 2.2 [2010You]. It should be noted that all three reactions are very slow, as homogeneous gas-phase processes and will not reach equilibrium in a typical laboratory reactor, unless catalysed. Although most metals of interest in engineering applications are catalytically active to these reactions (i.e. iron, nickel, cobalt, and their alloys), their oxide scales are inert. This is why the formation of a stable oxide film is important to resist metal dusting attack.

Table 2.2. Gas phase equilibria relevant to carburising and metal dusting [2010You].

Reaction	$\Delta G°_f = A + BT$ (J)	
	A	B
$CO + H_2 = H_2O + C$	-135 515	142.37
$2CO = CO_2 + C$	-170 700	174.50
$CH_4 = 2H_2 + C$	87 399	-108.74

Temperature has a marked, but very different effect on the three reactions listed above, as shown in Figure 2.2. Therefore, methane (and other hydrocarbons in general), can only produce high carbon activities at very high temperatures. On the other hand, carbon activity is increasingly raised as the temperature is lowered for the synthesis gas and Boudouard reactions [2010You].

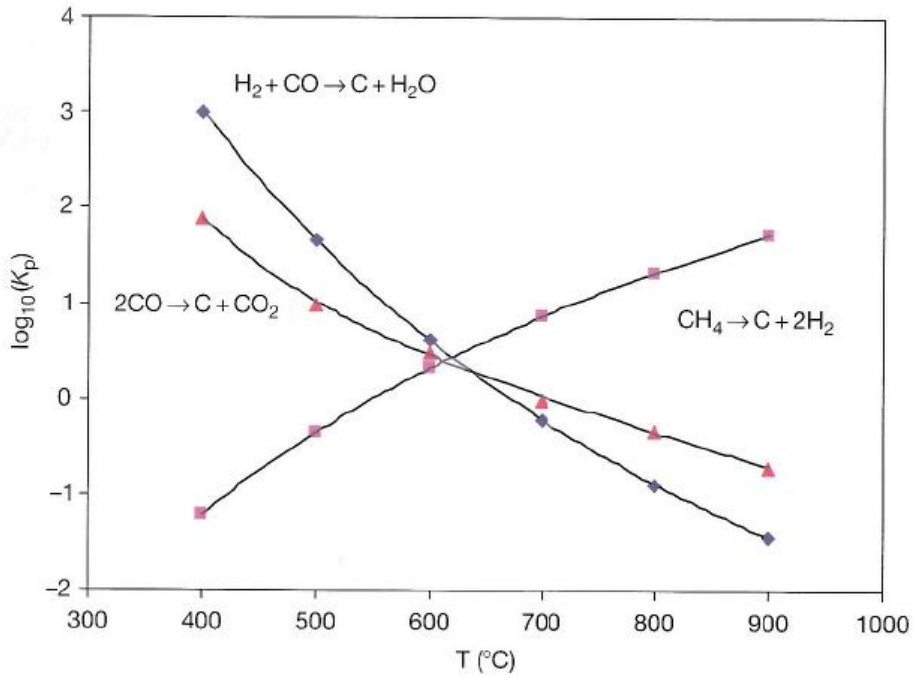


Figure 2.2. Equilibria constants versus temperature for gas-phase carbon producing reactions [2010You].

Due to the fact that these reactions are difficult to equilibrate, they become supersaturated with carbon – i.e. $a_c > 1$. A practical example of this is synthesis gas produced in a steam reforming unit, which generally has $a_c < 0.5$. As the gas is cooled from the reaction temperature, the rate of Equation 2.1 is so slow that the gas fails to adjust its composition by depositing carbon. The gas-phase carbon activity as calculated from Equation 2.4 can therefore be much greater than 2.1 [2010You].

$$a_c[1] = \frac{K_{(1)} p_{H_2} p_{CO}}{p_{H_2O}} \qquad \textit{Equation 2.4}$$

2.4.2. Mechanisms of metal dusting

The phenomenon of metal dusting may be divided into three main mechanisms, denoted Type I, Type II and Type III.

Type I, first described by Hochman *et al.* [1966Hoc, 1972Hoc] and further detailed by Grabke [1995Gra1, 1998Gra1], involves decomposition of metastable cementite. Type II may be described as disintegration of a carbon supersaturated phase by internal

graphitization, and was first described by Hultgren and Hillert [1953Hul] and studied in detail by Pippel *et al.* [1995Pip, 1998Pip]. Type III, which operates on high alloyed steels and Ni-based alloys, was first proposed by Szakálos [2002Sza1] and further described [2002Sza2, 2003Sza, 2002Sza3], involves selective oxidation of alloyed carbides, i.e. not pure Fe-carbides.

A secondary mechanism may be added, namely carbon nanotube formation, Type IV. It may be described as a continued fragmentation of the corrosion products and involves carbon nanotube formation, as was mentioned by Szakálos [2004Sza]. There is seldom only one metal dusting mechanism operating on steels or Ni-based alloys. For example, Types III and II operate in conjunction on austenitic stainless steels and Ni-based alloys [2002Sza1, 2002Sza2, 2002Sza3, 2003Sza, 2006Sza].

A summary of the alloys studied and operating mechanisms are given in Table 2.3 [2004Sza]. A ranking has been made, with the most dominating mechanism in the steady state process listed first.

Table 2.3. Alloys studied by Szakálos with operating mechanisms [2004Sza].

Alloy type	Commercial grade	Operating mechanisms	Reference
Fe	(Ultra pure Fe)	II + I	[2003Sza]
FeCr	TP 446, 26Cr-steel	III + II + I	[2003Sza]
FeCrAl	APM, 0C404	III + II	[1999Sza, 2003Sza]
FeNiCr	AISI 304L, 253MA	III + II	[1999Sza, 2002Sza1, 2002Sza2, 2003Sza]
NiFeCrAl	Alloy 602CA	III + II	[2006Sza]

2.4.2.1. Metal dusting of iron

Metal dusting on iron has been known for more than 120 years, and has been studied particularly by Hochman *et al.* [1966Hoc, 1972Hoc] and Grabke [1995Gra1, 1998Gra1]. When iron is exposed to carbon-rich gas at oxygen potentials too low to form iron oxide, the metal catalyses reactions such as Equations 2.1 to 2.3, but the resulting carbon is dissolved in the metal. Hochman and Grabke [1966Hoc, 1972Hoc, 1995Gra1, 1998Gra1] suggested that this leads to carbon super saturation of the iron and subsequent formation of metastable cementite. Once the iron surface is covered with cementite, carbon deposits on the carbide, the carbon activity at the cementite surface is then reportedly unity (i.e. not the

supersaturated value of the gas phase), which means that it becomes unstable and decomposes via Equation 2.5 to produce finely divided iron and carbon (graphite).

$$Fe_3C = 3Fe + C \qquad \textit{Equation 2.5}$$

The process is schematically illustrated in Figure 2.3 in steps (a) to (d) as follows [1998Gra1]:

(a) Oversaturation of the metal phase (matrix) with dissolved carbon or by carburization

(b) Formation of Fe_3C at the surface with growth from the interior

(c) Deposition of graphitic carbon onto the Fe_3C surface, $a_c \rightarrow 1$

(d) Decomposition of the Fe_3C, and carbon deposition by catalytic action of the metal particles, arising from Fe_3C decomposition.

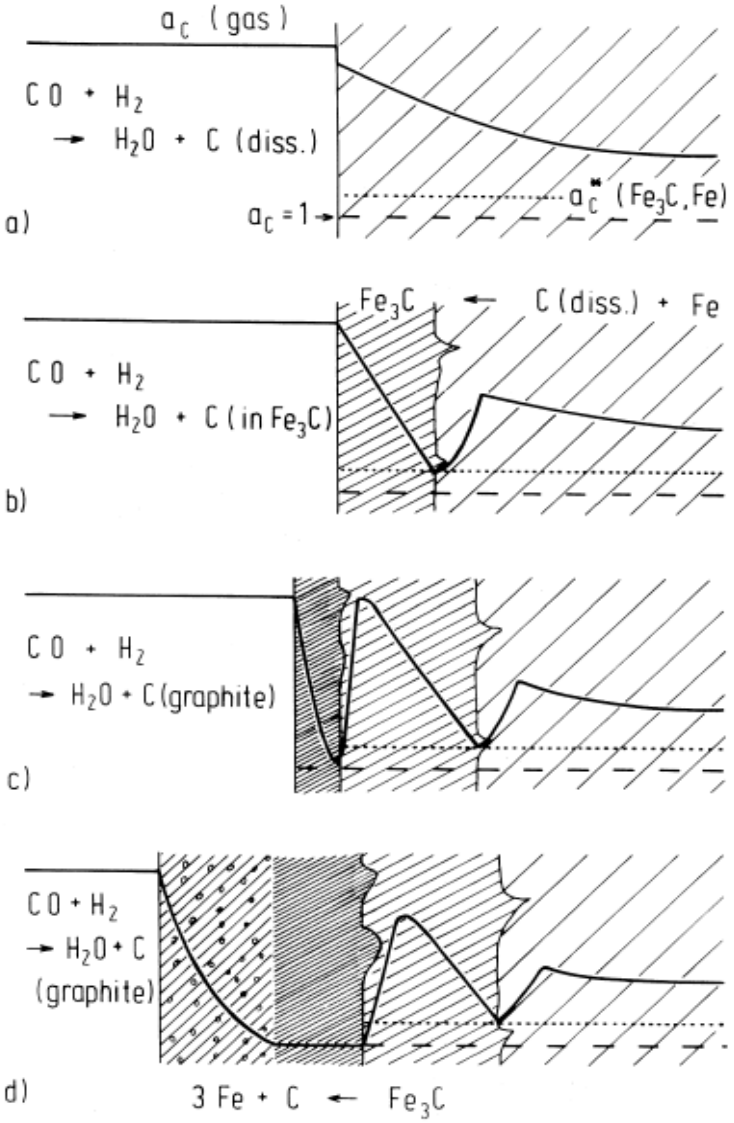


Figure 2.3. Schematic illustration of the metal dusting mechanism on iron and low-alloy steels [1998Gra1].

The iron particles formed due to the decomposition of the cementite are catalytically active and accelerate carbon decomposition. The kinetics of carbon decomposition was observed in the short term to follow a quadratic rate law shown in Equation 2.6 [1994Gra1]:

$$\Delta W_C / A = k_C t^2 \qquad \textit{Equation 2.6}$$

where $\Delta W_C / A$ is the carbon weight per unit area, k_C is the equilibrium constant for the carbon reaction and t is time. Later, the rate becomes linear. The form of Equation 2.6 was explained by Grabke *et al.* [1994Gra1] as being due to the generation of catalytically active particles by metal consumption in the dusting process:

$$\Delta W_M / A = k_d t \qquad \textit{Equation 2.7}$$

The term $\Delta W_M / A$ is metal wastage expressed as mass loss per unit area, k_d is the metal disintegration (dusting) rate constant and t is time. If the catalytic particles are of uniform surface area and activity, then the rate of carbon deposition is proportional to the mass of metal consumed:

$$\frac{d(\Delta W_C / A)}{dt} = k \times k_d t \qquad \textit{Equation 2.8}$$

The term k is a rate constant. Integration of Equation 2.8 yields Equation 2.6. In the long term, individual particles are encapsulated by carbon and deactivated as catalysts. The rate at which this happens approximately balances the rate of new particle generation, as coking rates become approximately constant [2010You].

Most of the coke deposit is reported to be filamentary [2010You]. The filaments were reported to have faceted cementite particles at their tips. The particles are oriented with their [001] direction parallel to the carbon tube axis [2003Toh]. This allows cementite planes in the {010} and {100} families to be parallel to the tube axis. The d-spacing of the (020) plane is 0.337 nm and that of the (300) plane is 0.169 nm. These correspond closely to the (0002) and (0004) d-spacings of graphite (0.337 and 0.168 nm respectively). Therefore, it is suggested that alignment of these planes to the graphite basal planes (which form the multiple walls of the nanotube), leads to formation of low-energy graphite-carbide interfaces and a preferred growth orientation for the carbon tubes.

A mass transport model for filamentary coke deposit is shown in Figure 2.4 [2010You]. The faceted carbides formed are in contact with the gas, and catalyse carbon deposition/production. This carbon diffuses through the cementite particle to the cementite-graphite interface, where growth of the carbon nanotube continues.

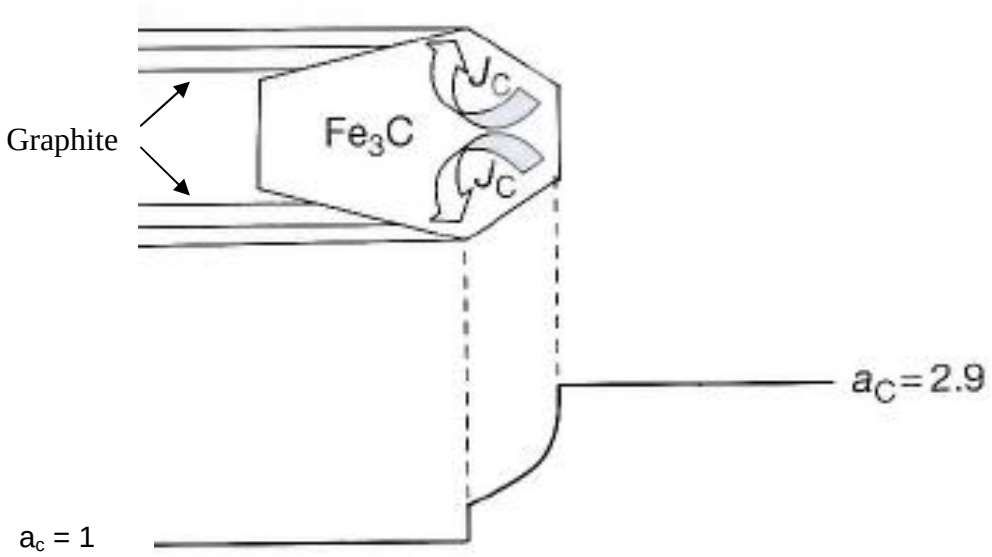


Figure 2.4. Mass transfer model for coke filament growth from carbides [2010You].

2.4.2.2. Metal dusting of low alloy steels

On iron and low alloy steels, the attack may start with wide pits, but becomes more or less general, so that uniform wastage is observed. The metal dusting mechanism for low alloy steels are similar to that of pure iron [2010You], although the rate has been observed to be slightly faster than for pure iron, as shown in Figure 2.5. The reason for the faster dusting rates is not clear. The chromium content is not high enough to form a stable protective oxide on these alloys, although the oxygen partial pressure is high enough to oxidise the chromium. The chromium-rich particles are probably encapsulated in the cementite layer where they act as nuclei for graphite precipitation, thereby accelerating cementite disintegration.

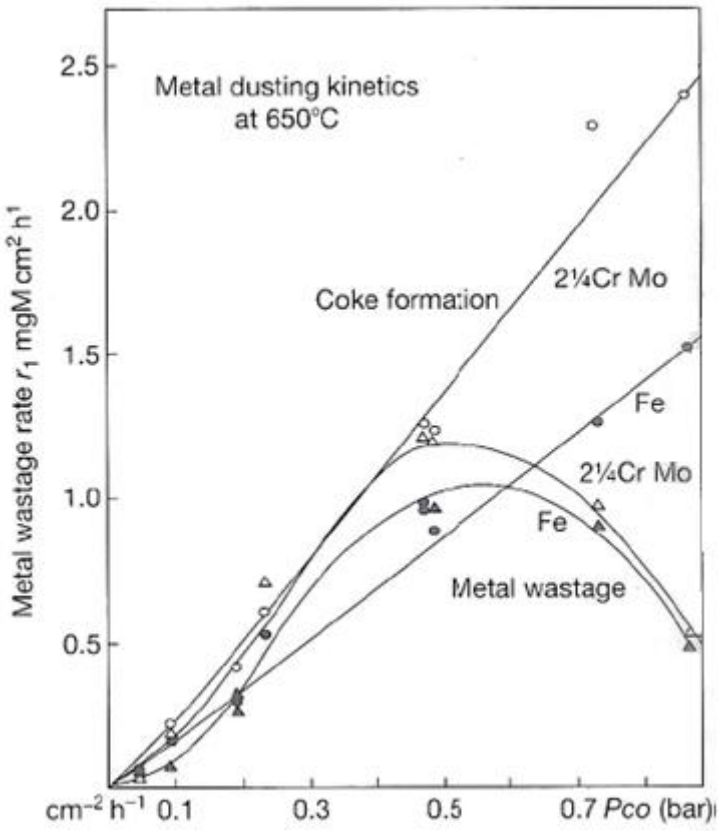


Figure 2.5. Dependence of coking and dusting rates on p_{CO} in $H_2/CO/H_2O$ mixtures [2010You].

The dusting mechanism, similar to that for iron, therefore involves intermediate formation of the unstable cementite [1993Gra2, 1994Gra1, 1994Gra2, 1998Gra1, 1998Gra3], as shown in Figure 2.3, and the following steps take place:

(i) Carbon transfer and oversaturation of the metal matrix,

(ii) Formation of cementite M_3C (M = Fe, Cr or Ni) at the surface and at grain boundaries. The cementite layer is a diffusion barrier for further carbon ingress, causing increased a_c, and

(iii) Nucleation of graphite on the surface, causing decrease of $a_c \rightarrow 1$. The cementite becomes unstable and starts to decompose by inward growth of graphite:

$$M_3C \rightarrow 3M + C \qquad \textit{Equation 2.9}$$

In the decomposition of cementite, the carbon atoms attach to graphite planes, which grow more or less vertically into the cementite. The metal atoms migrate through the graphite and agglomerate under formation of fine metal particles (~20mm), which catalyse carbon deposition from the gas phase, often under growth of carbon filaments from the metal particles.

Szakálos [2004Sza] concluded that it is not possible to explain the driving forces or the steady state process of metal dusting by decomposition of metastable cementite (Type I). However, there might be an intact or unbroken cementite layer during the initial stages of metal dusting, while the steady-state process is governed by fragmentation due to graphitisation (Type II).

The mechanism can be retarded and altered by the presence of sulphur [1995Gra2, 2001Gra]. Adsorption of sulphur on the metal surface hinders the transfer of carbon into solid solution, i.e. step (a), and also the carbon deposition is retarded. But more important, the nucleation of graphite is impeded and reaction step (c) may not take place at all, or is delayed for a long time. In this way, cementite is stabilized and its properties concerning thermodynamics, diffusion and stoichiometry could be studied [2000Sch1, 2000Sch2]. Suppression of metal dusting depends on carbon and sulphur activity in the atmosphere, carburising gas CO or CH_4, temperature and time [1995Gra2, 2000Sch1, 2000Sch2, 2001Gra].

2.4.2.3. Metal dusting of ferritic chromium steels

The behaviour of ferritic chromium steels exposed to $CO/H_2/H_2O$ gas mixtures depend on whether a chromia scale is formed and retained [2010You]. This is similar for the corrosion resistance of stainless steels in aqueous corrosive environments. If the chromium content is too low to form a Cr_2O_3 scale, the steel will dust at the same rate as a low alloy steel as explained above (for instance a 2¼ Cr-1Mo type alloy). If the steels form a continuous, adherent chromia scale, resistance to dusting under isothermal conditions is very good, because the scale prevents carbon entry. The factors that determine the resistance of the alloys to metal dusting are those factors that influence its ability to quickly form a continuous Cr_2O_3 scale by diffusing chromium to the surface [2010You].

The effect of temperature on the diffusion coefficient of chromium, D_{Cr} was demonstrated by Grabke *et al.* [1993Gra2]. Steels with 17 to 26% chromium showed complete resistance to dusting at 600°C to 650°C, but showed metal dusting attack at 550°C. The susceptibility to dusting therefore increases as the temperature and D_{Cr} decrease. The greater D_{Cr} in ferritic steels (than austenitics) ensures that ferritic alloys can heal or repair damaged oxide layers

more efficiently than austenitic alloys with a similar chromium content. This leads to improved dusting resistance as shown in Figure 2.6 [2002Toh].

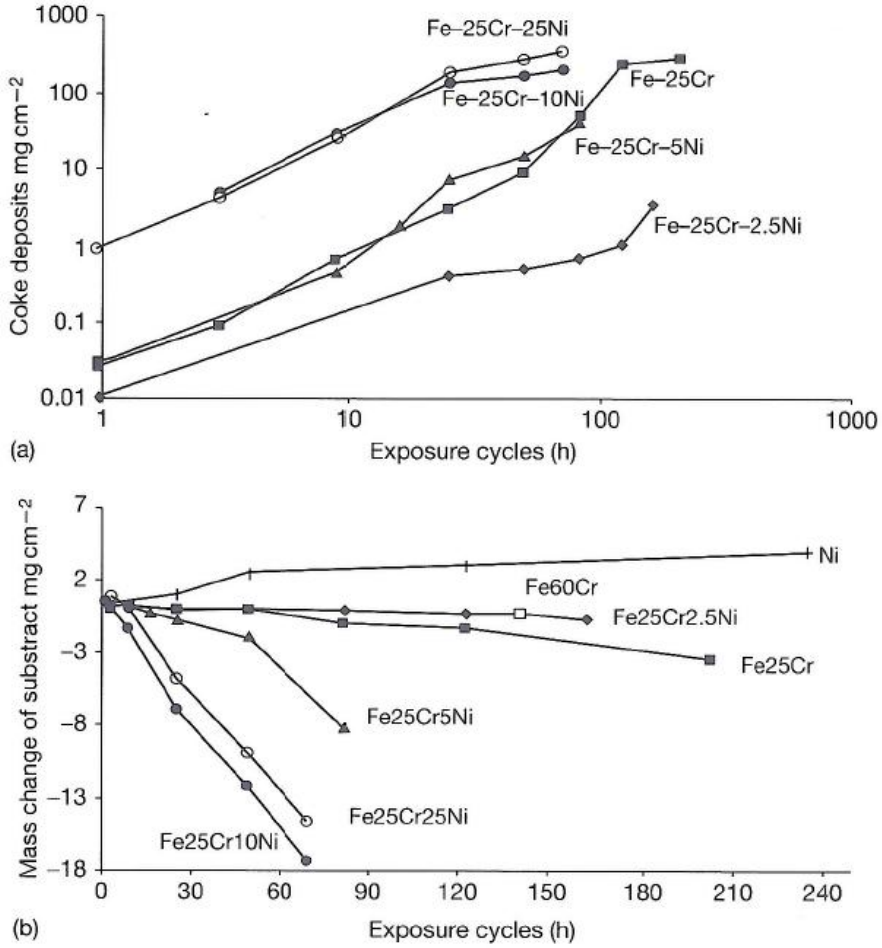


Figure 2.6. Coke deposition and metal wastage kinetics for electropolished 25Cr alloys at 680°C in $CO/H_2/H_2O$ [2002Toh].

Since the resistance to dusting is increased as D_{Cr} is increased, the effective value for D_{Cr} can be increased at lower temperatures by creating a deformed and fine-grained alloy surface. This is done by surface grinding, shot peening, etc., and has been shown to lead to better dusting resistance [2010You].

However, alloys which develop continuous protective chromia scales are subject to long-term dusting attack. Under isothermal exposure, growth stress accumulation in the scale

eventually leads to mechanical failure [2010You]. A series of such events can exhaust the capacity of an alloy to heal or regrow its protective scale, and metal dusting follows. Discontinuous exposures and short-term thermal cycling combine the effects of accumulated growth stress and thermal shock. These result in chromium depletion. Further breakdown of the chromia scale allows carbon to enter the chromium-depleted metal. Rapid inward diffusion of carbon leads to internal precipitation of chromium carbides, thereby preventing subsequent rehealing of the scale. The depleted iron matrix forms a cementite layer, which disintegrates producing cementite particles to catalyse further coke deposition – i.e. similar mechanism as iron and low alloy steels once the chromium is depleted, and tied up as internal carbides. The result is a pitted surface. Continued attack results in the pits to widen and coalesce until the attack is eventually general [2010You].

If the alloy chromium is high enough, dusting of ferritics can be prevented [2010You]. An Fe-60Cr alloy survived 1000 one hour cycles at 680°C, forming only Cr_2O_3, which was impermeable to carbon. Furthermore, the chromia was catalytically inactive, and no coke deposited.

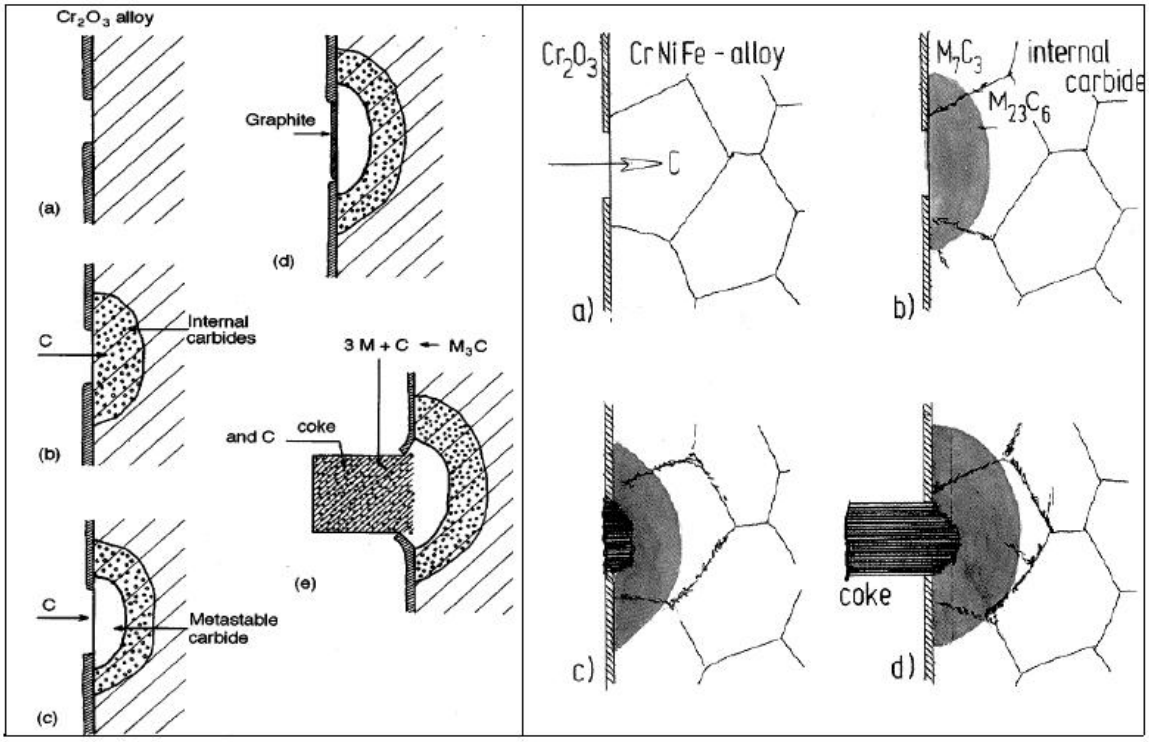
2.4.2.4. Metal dusting of higher alloyed steels

The mechanism for metal dusting of nickel alloys differs from that of ferritic material in that cementite is not formed, and the corresponding nickel carbide is unstable. Grabke *et al.* [1996Gra] found that the dusting of binary Fe-Ni alloys varied in reaction morphology and rate with the nickel content. Low nickel alloys behaved like pure iron, forming a surface layer of cementite, whereas higher nickel alloys graphitised directly without forming a carbide. The nickel content required to suppress cementite formation was reported as 30wt% [1996Gra], and also as 5 to 10wt% [2003Pip].

In publications by Grabke [1995Gra1, 2003Gra], metal dusting of high alloyed steels and CrFeNi-alloys were described with a schematic representation, as shown in Figure 2.7. The proposed mechanism includes the following principal steps:

- Carbon diffuses into the structure, primarily at breaks in the chromium oxide layer.

- Carburization and formation of very fine Cr-rich M_7C_3-carbides (grey zone) and $M_{23}C_6$ carbides in the grain boundaries.
- Formation of possibly metastable $(Fe,Ni)_3C$ cementite in the Cr-depleted matrix, followed by cementite decomposition (Type I) and direct fragmentation by graphitisation (Type II). The corrosion products would thus be cementite or Fe/Ni particles, graphite and Cr-rich carbide particles.
- Oxidation of the corrosion products in the coke, i.e. oxidation of the very fine Cr-rich carbides, which subsequently would give very fine spinel/chromia particles in the coke.



(a) (b)

Figure 2.7. Schematic illustration of the metal dusting mechanism on high alloyed steels and CrFeNi-alloys taken from (a) [1995Gra1] and (b) [2003Gra].

The proposed mechanism (Type III mechanism) is based on the concept of active corrosion by carbon and oxygen. Carbon reacts with metal and metal carbides are formed. These carbides dissolve and oxidise selectively, and free carbon is released which forms carbides/graphite. This process may be compared to chlorine-induced active corrosion where metal chlorides are formed which oxidise, and chlorine is released to form more metal chlorides [1992Ree].

The Type III mechanism was first identified on an AISI 304L type stainless steel exposed at 650°C in a CO-containing gas mixture [2002Sza1, 2004Sza]. SEM studies of the metal dusting reaction front in cross-section were comparable to the sketch in Figure 2.8 [2004Sza]. This shows simultaneous operation of mechanisms III (oxidation of carbides) and II (graphitization). These two processes work in collaboration; the carbides dissolve since there is a decreasing Cr-gradient towards the Cr-containing oxide, and the process is promoted by the fine structured austenitic layer with graphite flakes (Zone 4) which provide fast Cr diffusion paths [2002Sza1, 2004Sza].

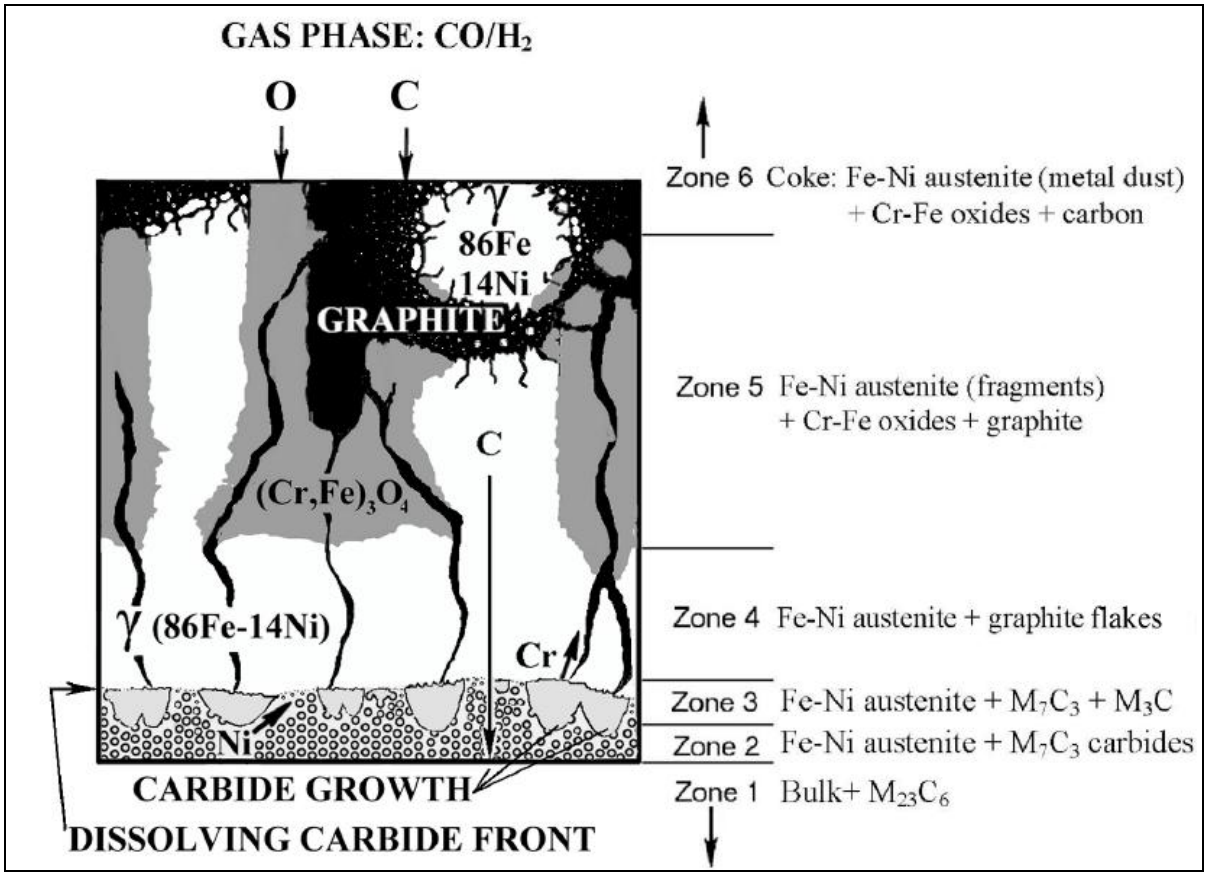


Figure 2.8. M*echanisms of metal dusting as it appears on stainless steels, including an active corrosion process with carbon and oxygen (Type III), in combination with fragmentation by graphitization (Type II) [2004Sza].*

Starting with un-carburized AISI 304L steel, the metal dusting steps were divided into six zones [2004Sza]:

1) Carburized bulk with $M_{23}C_6$ carbides, which forms at lower carbon activities.
2) Carburized bulk with M_7C_3 carbides.

3) Dissolving carbide front with M_7C_3 and M_3C.
4) Cr-depleted zone ("white phase"), Fe-Ni austenite border with graphite flakes.
5) Corrosion products: Cr-Fe oxides, metal fragments in micrometre-size and carbon.
6) Coke, continued corrosion of the corrosion products by the Type II mechanism, i.e. disintegration of the metal fragments into smaller and smaller metal dust and finally, nanometre-sized particles formation of carbon nanotubes.

The process of metal dusting that yields the six zones described above initiates with the selective oxidation of chromium to produce a chromium-depleted subsurface alloy region [2010You]. If sufficient chromium remains, the chromia scale reheals. If the oxygen partial pressure is too low for nickel or iron oxides to form, then carbon enters the alloy to precipitate chromium carbides. At these low temperatures, the diffusion coefficient for chromium is small, with the result that the carbides formed are also small. Removal of chromium from the matrix renders future healing of the surface scale impossible, facilitating more gas entry into the chromium depleted region. The metal is essentially a Fe-Ni alloy, and at high nickel concentrations undergoes graphitisation and disintegration similar to pure nickel.

Thermal cycling metal dusting studies on Fe-*x*Ni-25Cr alloys revealed very different metal dusting rates with varying nickel contents [2002Toh]. This is shown graphically in Figure 2.6. A 2.5% Ni alloy is ferritic and formed a cementite surface layer which disintegrated into cementite dust. Alloys with 5% and 10% Ni had duplex structures ($\alpha + \gamma$), in which the austenite was more rapidly carburised than the ferrite. Dusting produced nanoparticles of M_3C from the 5% Ni alloys and both M_3C and austenite from the 10% Ni alloy. The 25% Ni alloy was fully austenitic and disintegrated to produce austenite dust. The shift from carbide to austenite particles with increasing nickel content is the same as that for binary Fe-Ni alloys [1996Grab].

The variation of dusting rate with Fe/Ni ratios shown in Figure 2.6 [2002Toh] reflects mainly the difference in the diffusion coefficient of chromium accompanying the change from ferritic to austenitic structures. Therefore, rehealing was more effective and the frequency of dusting initiation less in the alloy sequence $\alpha > \alpha + \gamma > \gamma$. At still higher nickel levels, the

improved performance was attributed to lowering of the alloy carbon permeability [2010You].

From increasing research on austenitic alloys, it seems that higher nickel levels are beneficial and that a minimum chromium concentration of about 25% is required [1993Gra, 1996Gra, 1998Gra, 2000Bak, 2000Mai]. At these levels, scale breakdown allows formation of two internal carbide zones, usually spheroidal M_7C_3 near the surface and lamellar or Widmanstätten $M_{23}C_6$ at greater depths [2002Toh]. Alloy additions of silicon and aluminium improve the ability of the scale system to exclude carbon by forming oxide subscales [1993Gra, 2000Bak, 1999Mai, 2004Zen, 1998Stra]. Addition of carbide-forming elements (Mo, W, Nb) form stable carbides. Their ability to getter carbon allows unreacted chromium to reheal the surface scale, delaying the onset of dusting [1998Stra]. However, subsequent oxidation of these refractory metal carbides leads to volume expansion and disruption of the protective scale [1988Lit].

Szakalos *et al*. have pointed out that the fine internal carbides formed after scale failure can be oxidised, leading to disruption of the metal and contributing to the dusting process [2003Sza]. This is the "green rot" corrosion process [1959Bet], in which the large volume expansion accompanying carbide oxidation fractures the metal. The two possible reactions for internal carbides near the surface are the oxidation process and simple dissolution, providing a chromium flux toward the surface. The competition between the two processes will depend on oxygen and carbon permeabilities and the chromium diffusion coefficient. The gas composition will also influence the rate of carbon and oxygen dissolution into the metal.

Active corrosion by carbon and oxygen is probably the major degradation mechanism in chromia-forming engineering alloys exposed in CO-containing atmospheres independent of the water vapour content. It is also shown that this mechanism is operative for Cr-containing alumina formers [2002Sza1, 2004Sza].

2.4.3. Protection by oxide scaling

Surface oxide scales play an important role in the long-term performance of alloys under dusting conditions. Using radioactive carbon, it has been shown that the solubility of carbon

in Cr_2O_3 and Al_2O_3 at 1000°C is below the detection limit of 0.01 ppm [1985Wol]. Scales of these oxides are therefore expected to provide effective diffusion barriers to carbon. Furthermore, most observations suggest that these oxides provide no significant catalytic effect for carbon deposition from the gas [2005Nis]. For such an oxide to continue as a diffusion barrier, it must retain its mechanical integrity as well as chemical stability.

The oxides of iron, cobalt and nickel are unstable at low oxygen potentials of typical dusting atmospheres [2011You]. However, Cr_2O_3, Al_2O_3, SiO_2 and $FeCr_2O_4$ are all stable, and the heat resisting alloys commonly used should therefore be expected to resist metal dusting. However, most of these alloys do fail. One reason is the relative low temperatures involved and the consequently low alloy diffusion rate. A second reason is that most heat resisting alloys are designed to form external, rather than internal oxides. However, in gases such as synthesis gas, the competing processes are external oxide scaling and carbon attack [2011You]. Selective oxidation of chromium produces a Cr_2O_3 scale and a chromium-depleted subsurface alloy layer, until local scale damage allows gas access to the metal.

Oxide scales at high temperatures are evolving systems, in which accumulated intrinsic growth stresses interact with stress relief mechanisms, as shown by acoustic emission and microstructural investigations for purely oxidising conditions [1987Kha, 1987Scu]. The results of Raman investigations [2007Roh] revealed a chromia peak shift, indicating a high level of compressive stresses in the scale was developed under metal dusting conditions. The present understanding of the stress relief mechanisms in the oxide under these conditions assumes temporary microcracking and subsequent microcrack healing due to the on-going oxidation, resulting in a nano- or microcavity network filled with molecular species from the gas [1987Scu, 1987Atk].

The outcome of carbon penetration of the scale will depend on the carbon activity, as well as the other conditions at the scale-alloy interface. A schematic diagram of the mechanisms leading to pitting as a consequence of oxide scale failure is given in Figure 2.9 [2011You].

- Figure 2.9.1 shows intact oxide scale, or scale interspersed with fine graphite precipitates.

- Figure 2.9.2 shows scale cracks that form by intrinsic oxide growth stresses (or by graphite precipitation and growth).
- Figure 2.9.3 shows the widening of the scale cracks and further cracking by graphite growth at scale cracks/delaminations.
- Figure 2.9.4 shows pit formation as a consequence of local scale cracking processes, followed by graphite formation. "Repassivation" can take place in the case of sufficient resupply of protective oxide scale forming alloying elements from the alloy interior.

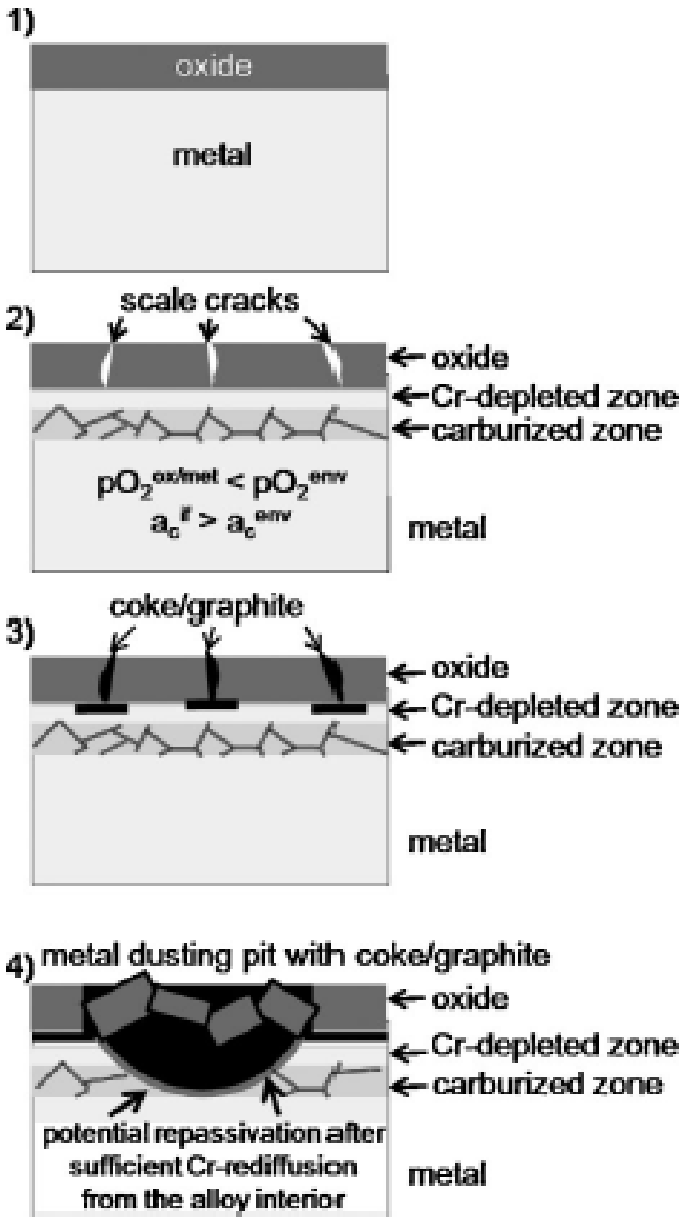


Figure 2.9. Processes occurring on high alloy materials during local oxide scale failure leading to a growing metal dusting pit [2011You].

2.4.4. Effects of surface conditions and finish

From the above section, it is clear that the formation of a good, protective chromium oxide scale is a very effective way to provide protection against metal dusting attack. Since the temperature for metal dusting attack is relatively low, and chromium diffusion is low at these temperatures, rapid formation of a good protective scale is critical. Accordingly, the concentration of chromium at the surface is important. A high chromium concentration at the metal surface provides faster formation of protective chromia scale. Therefore, alloys with a higher bulk chromium concentration are more resistant to metal dusting. Also, for the same reason, fine-grained structures exhibit better metal dusting resistance compared to coarse grained structures, as illustrated in Figure 2.10 [2007Lai]. This is because the grain boundaries provide fast diffusion paths for the chromium to reach to the metal surface. A fine-grained material will have more grain boundaries and thus more chromium reaching the surface to form a better chromium oxide scale faster than coarse-grained material, therefore, resisting metal dusting attack better [2007Lai].

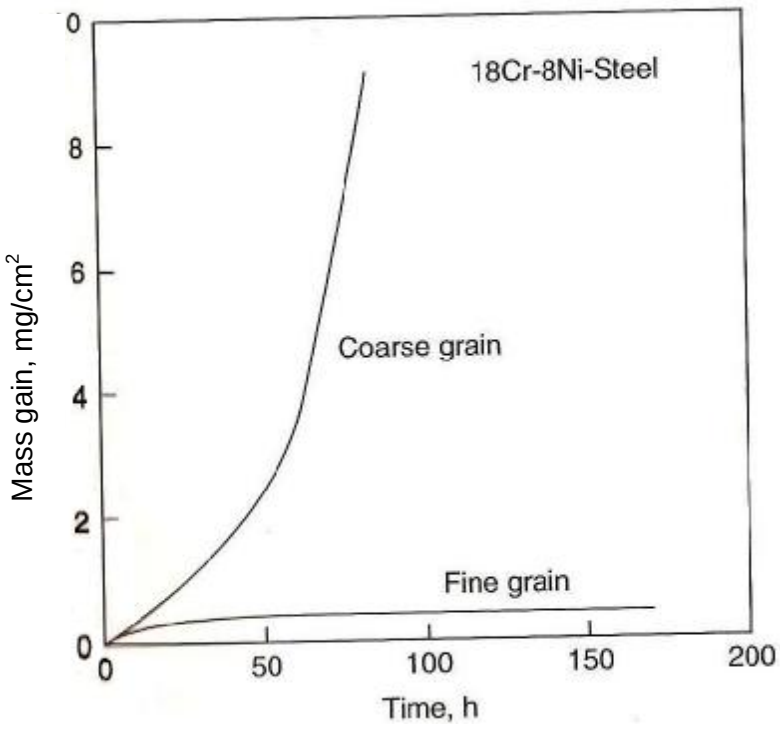


Figure 2.10. Effect of grain size on the metal dusting behaviour of Type 304 at 600°C in H_2-24CO-2H_2O [2007Lai].

The surface of the metal can also be prepared by grinding or machining to produce a thin cold-worked layer with a high density of dislocations. These dislocations also provide fast diffusion paths for the chromium to reach the metal surface to form protective chromia scale. As a result, metal dusting is greatly improved when the surface is ground or machined, as shown in Figure 2.11 and Figure 2.12 [2003Gra2]. For both Alloy 800 and 310 stainless steel, the as-ground specimen was more resistant to metal dusting than the as-received surfaces (cold rolled) and the electropolished surfaces. The electropolished surfaces were the worst because of removal of mechanical damage (chemical dissolution), as well as possible surface depletion of chromium during electropolishing. Type 310 stainless steel performed better than Alloy 800 in these tests, due to the higher chromium content.

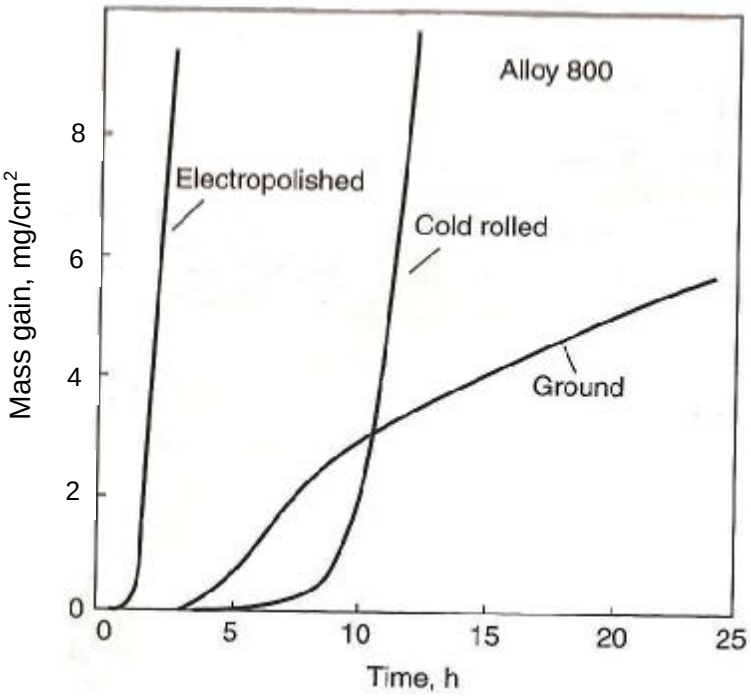


Figure 2.11. Thermogravimetric testing of alloy 800 (Fe-21Cr-32Ni) in H_2-24CO-2H_2O at 600°C in different surface conditions [2003Gra2].

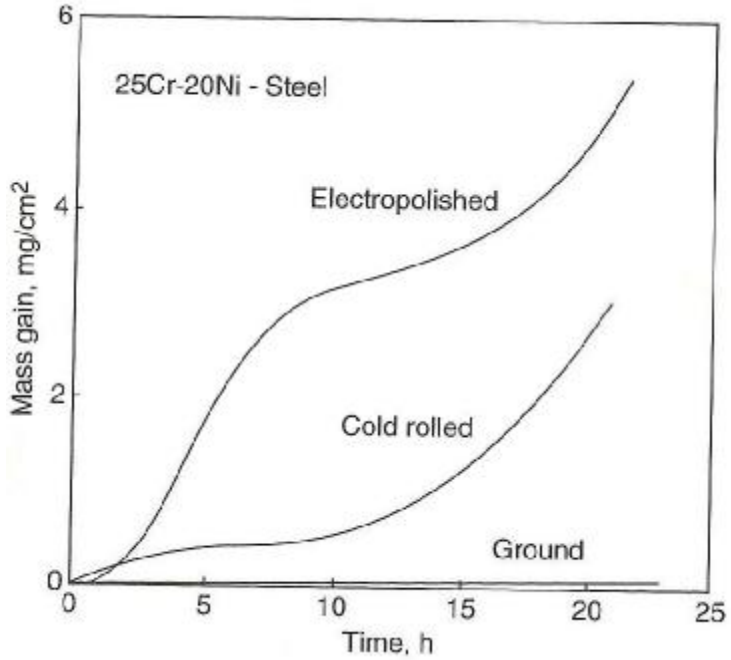


Figure 2.12. Thermogravimetric testing of Type 310 (Fe-25Cr-20Ni) in H_2-24CO-2H_2O at 600°C in different surface conditions [2003Gra2].

For Alloy 601, specimens with a ground surface finish also showed better resistance to metal dusting than those with an electropolished surface finish, as shown in Figure 2.13 [1997Klo]. The "black" sample (i.e. a black annealed sample that was not subsequently pickled and passivated) performed as poorly as the electropolished sample, and both exhibited surface chromium depletion due to annealing in air. The formation of chromium oxide scales during annealing in air results in some chromium depletion at the surface.

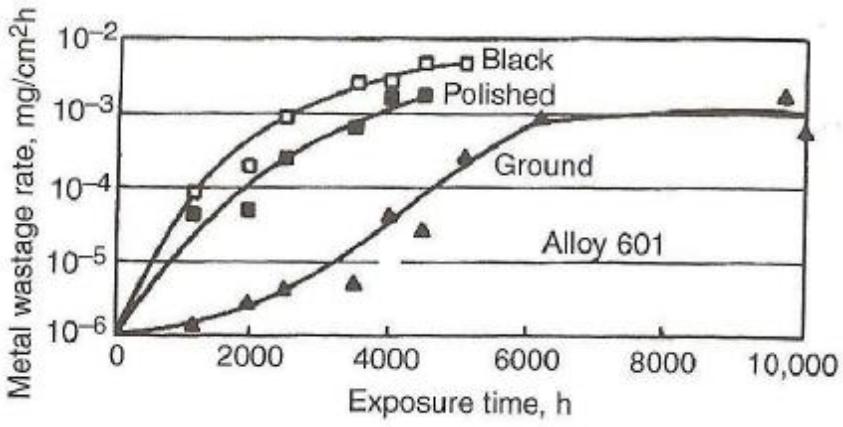


Figure 2.13. Metal dusting behaviour for alloy 601 in H_2-49CO-2H_2O at 650°C for different surface conditions [1997Klo].

3. PROJECT DESCRIPTION

3.1. Hypothesis statement

The understanding of the metal dusting mechanism will aid with the development of new coatings and materials to combat metal dusting.

3.2. Project objectives

The objectives of this MSc project focussed on the expansion of the knowledge base of metal dusting from a fundamental mechanistic point of view. This was done by focussing on the effect of carbide-forming elements in austenitic and ferritic structures on the metal dusting rate.

3.3. Research question

Does the formation of more stable carbides, e.g. those in Type 441, reduce the metal dusting rate associated with the proposed mechanism for Type III metal dusting?

3.4. Experimental methods

3.4.1. Test alloys

The research approach of the project was to expose different stainless steels with an equivalent amount of chromium, but in different alloys that contained different carbide formers, under a controlled metal dusting environment, to determine how they deteriorate with exposure time. Therefore, the following commercial alloys were chosen:

3.4.1.1. Austenitic alloys

- **Type 304L** stainless steel was used as reference material and its performance compared against that of **Type 321** (i.e. essentially Type 304 with Ti added).
- Similarly, the performance of **Type 316L** stainless steel was compared to that of **Type 316Ti** (i.e. essentially Type 316 with Ti added). Although the chromium content is generally slightly lower and the nickel content slightly higher in Type 316L compared to Type 304L, the difference is probably negligible, which means

that the influence of molybdenum can also be assessed by comparing the performance of Type 304L to 316L. Molybdenum is also a carbide-former.

3.4.1.2. Ferritic alloys

- **Type 430** stainless steel also has about 18% chromium, similar to the austenitic alloys mentioned above, and was therefore also included in the test program. Type 430 does not contain any nickel (or other austenite stabilisers), and therefore has a ferritic structure. Comparison between Types 304L and 430 therefore allowed direct assessment of the influence of the matrix structure on the metal dusting rate.
- The performance of Type 430 was compared to that of **Type 441** (essentially Type 430 with Ti and Nb added – i.e. dual stabilised grade).

These factors affected the characteristics of chromium migration and the formation of oxide scales, carbon migration, the formation of carbides and their subsequent oxidation, on the different alloy systems. The nominal compositions of the alloys forming part of this dissertation are listed in Table 3.1.

Table 3.1. Nominal compositions of the alloys tested (wt%); values indicate maxima unless ranges are specified.

	Type 304L	Type 321	Type 316L	Type 316Ti	Type 430	Type 441
C	0.030	0.080	0.030	0.080	0.120	0.030
Cr	17.5-19.5	17.0-19.0	16.0-18.0	16.0-18.0	16.0-18.0	17.5-18.5
Ni	8.0-12.0	9.0-12.0	10.0-14.0	10.0-14.0	0.75	-
Mo	-	-	2.0-3.0	2.0-3.0	-	-
Ti	-	5(C+N) to 0.7	-	5(C+N) to 0.7	-	0.1 to 0.6
Nb	-	-	-	-	-	0.3+3C

3.4.2. Sample preparation

All the alloys tested were sourced from Columbus Stainless, and were of similar approximate thickness to ensure that they had been subjected to similar processing conditions during manufacture. All the alloys were in the cold rolled condition. The alloys were sectioned into samples 20 x 20 mm and a 5 mm hole was drilled in the centre to suspend the samples in the furnace. It is clear from Section 2.4.4 that the surface condition plays a major role in the metal dusting resistance, where ground surfaces are more resistant due to providing greater mobility of chromium to repair surface protective scales, so the samples were tested in the ground condition. This was done to closer simulate the condition of material surfaces encountered in practice, and to allow a more direct comparison between the different alloys. The samples were all ground to a 320 grit silicon carbide finish.

The dimensions of the samples were then measured with a digital calliper to the nearest 0.01mm and the samples stored in plastic bags. Immediately prior to testing, the samples were degreased with acetone and weighed to the nearest 0.1 mg.

3.4.3. Test procedures

A test rig was purpose-built to control the gas compositions at elevated temperatures in the metal dusting regime. For this, a horizontal ceramic tube furnace was used with 316 gas pipelines capable of supplying a mixture of two gases simultaneously. Mass flow controllers were used to regulate gas flow rates to obtain the desired mixing ratios. Water vapour was supplied by using a HPLC pump. All the gas tubes passing the water vapour were wrapped with heating tape that was maintained at 120°C. Three gases were used throughout all the tests performed. Firstly, nitrogen was passed through the furnace once the samples were loaded to flush any oxygen in the system and reduce the oxygen partial pressure. The system was flushed with nitrogen for a minimum of one hour, before the temperature was increased to the set temperature. In this study, the temperature was set at 680°C, which yielded an actual temperature in the hot zone of the furnace of 650°C. Once the furnace reached the set temperature, the CO and H_2 flow rates were adjusted using mass flow controllers that regulated the gas mixtures. The gas was mixed, together with the water vapour, and passed through the furnace. The gas flow rate and temperature was maintained constant throughout the different exposure periods used (i.e. isothermal testing). Although most research papers

referenced earlier used thermal cycling treatments, isothermal testing was deliberately chosen in this study. Thermal cycling speeds up the metal dusting process by breaking the protective oxide scale that can cause carbon to diffuse into the metal matrix. The breaking of the oxide scale occurs during cooling, due to the different expansion coefficients between the matrix and the oxide. The difference between the expansion coefficient for austenite and the oxide scale is larger than that between ferritc materials and the oxide [2005Out]. This is why the recommended service temperatures for intermittent (cyclic) use for ferritic materials are lower than for continuous use, yet for austenitics, the recommended temperatures for intermittent use are lower than for continuous use. Therefore, because austenitic and ferritic materials were tested in this exposure program, an isothermal regime was used. Furthermore, for the intended simulated environments in petrochemical plants, the processes are continuous and not batch processes. The equipment in the plant will therefore not be subjected to cyclic temperature conditions that could cause protective oxide scales to crack prematurely.

The specific gas mixture used for all the tests performed were 18.9%CO-79.1% H_2-2%H_2O. At 650°C, the carbon activity for this gas mixture is 11.75 assuming CO + H_2 = H_2O + C is the dominant reaction.

Safety features that were built into the system included:

- All the gas cylinders were kept outside the laboratory. The gases were transported to the furnace via stainless steel tubes.
- The test rig (furnace, mass flow controllers, etc.) was built inside a fume cabinet.
- A CO detector was installed adjacent to the furnace and coupled to a solenoid valve at the CO regulator. Detection of more than 50 ppm CO sounded an alarm and automatic shutdown of the CO line.
- A pressure regulator was fitted to the gas lines and the pressure set at 2 bar. An increase in the pressure in the pipeline (like tube blockages, etc.) would cause the pressure to vent through the pressure regulator.
- A knockout pot was also installed at the exit of the furnace to cool the gas and separate the water and gas.

A schematic flow diagram of the test rig is given in Figure 3.1 and a photograph of the layout is shown in Figure 3.2.

3.4.4. Methods of analysis

The following methods were used to evaluate the samples subsequent to testing:

- Visual examination and photographic record.
- Weight change to assess coking and metal wastage.
- Optical microscopy microstructure in the etched and unetched condition of each alloy.
- Scanning electron microscopy (SEM) with energy-dispersive X-ray spectroscopy (EDX) of the surface and cross-sections.
- Transmission electron microscopy (TEM) with energy-dispersive X-ray spectroscopy (EDX) of the coke.
- X-ray diffraction (XRD) for phase identification and crystal structure.
- Raman spectroscopy to characterise coke.

Duplicate coupons of each alloy were exposed to each test performed. After each exposure period, the samples were removed from the furnace and their visual appearance noted. A photographic record was also kept of all the samples. Both the specimens were re-weighed after the test to give an indication of mass change. An increase in mass is an indication of the extent of oxidation and coking, and a mass-loss is an indication of the degree of metal loss. Thereafter, one of the specimens were cleaned with a nylon nailbrush under running water and reweighed to measure the mass-loss of the samples due to metal loss (wastage).

Since the metal wastage rate was only calculated using one sample, no statistical analysis was included (i.e. no errors). However, since sequential tests were performed over a period of time, the different data points were used to verify the overall validity of points. Since the samples were not chemically cleaned with acids to remove all corrosion products, these results cannot be taken as absolute.

Since the exposed surface area of the samples, as well as the exposure time, will affect the mass-loss figures and make direct comparison difficult based purely on mass, the metal wastage rate was expressed in terms of penetration rate for a given time (i.e. mm/year). This is the standard way to express corrosion rate calculations (ASTM G31 - 12: Standard Guide for Laboratory Immersion Corrosion Testing of Metals). The results are expressed as penetration rates, and assume therefore that the mass-loss was recorded uniformly over the entire surface of the samples. Since the corrosion attack was localised, the penetration rates were not interpreted to predict the expected penetration rate per year. The results are therefore used as comparison between the different alloys as another tool, in conjunction with the other characterisation methods employed.

The equation to calculate the corrosion rate, as given in ASTM G31, is given below:

$$Corrosion \cdot rate\left(mm/y\right) = \frac{87600 \times Mass \cdot loss\left(g\right)}{Density\left(g/cm^3\right) \times Area\left(cm^2\right) \times Time\left(h\right)} \qquad \textit{Equation 2.10}$$

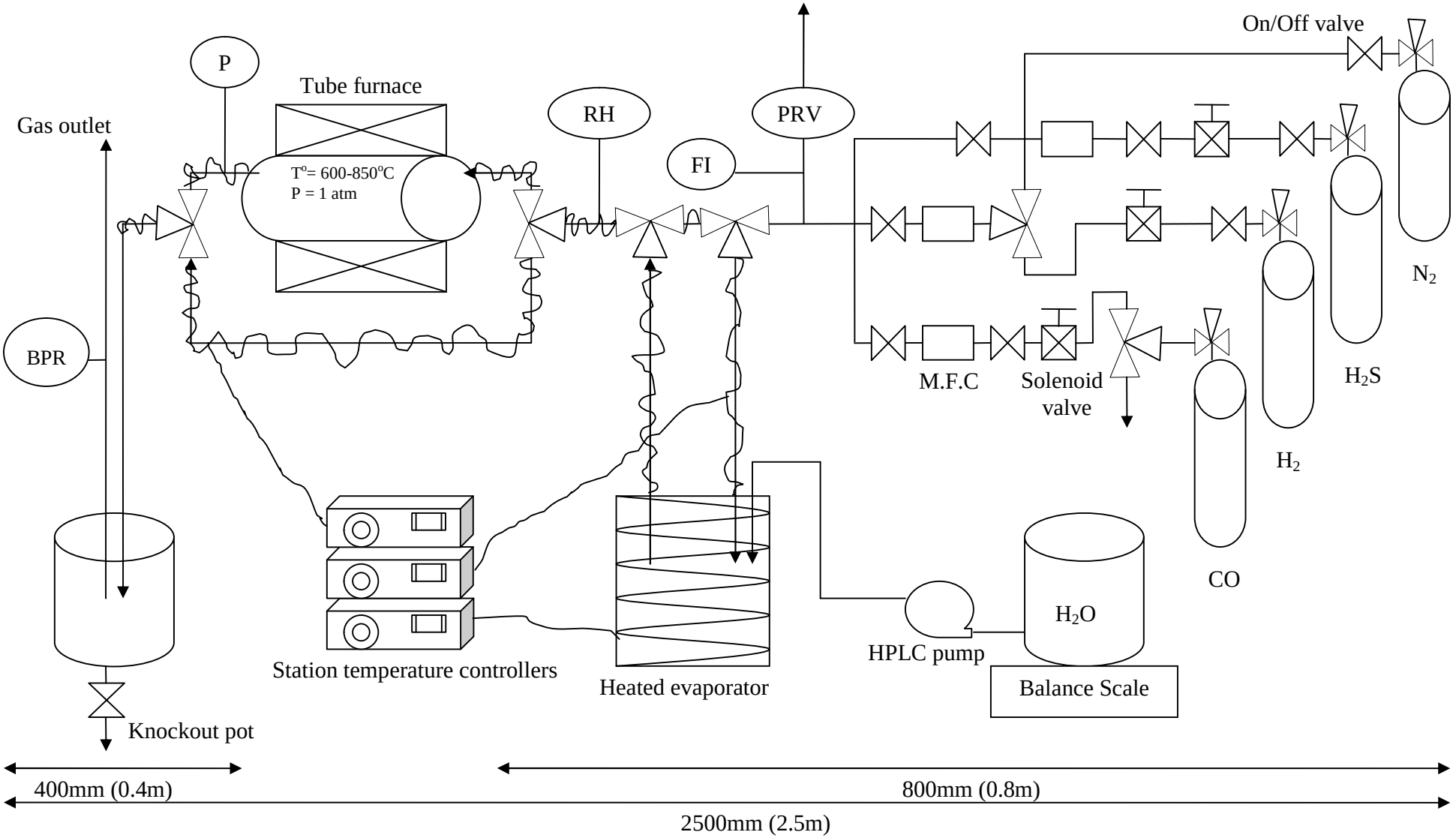


Figure 3.1. Schematic diagram of the metal dusting test rig.



Figure 3.2. Photograph of the metal dusting test rig.

Thereafter, each sample was sectioned in half, and the cross-section of one half was electrolytically copper coated (to protect the surface) and mounted for metallography. The other half was again sectioned in two (i.e. one quarter of the original sample size), and one quarter used for surface analysis on the SEM, and the other quarter used for XRD analysis. Figure 3.3 is a schematic diagram illustrating how each sample was sectioned for further analysis, and Figure 3.4 illustrates how each sample was treated and characterised. From the duplicate specimens tested for each alloy for each test, the **odd** numbers were treated as described in the left-hand column (i.e. cleaned), and the **even** numbers were treated as described by the right-hand column (i.e. not cleaned).

For XRD analysis, the samples were analysed with a PANalytical X'Pert pro powder diffractometer with X'Celerator detector and variable divergence-and fixed receiving slits with Fe filtered Co-Kα radiation. The X-ray tube voltage and current used were 35kV and 45mA respectively. The specimens were scanned with a step size of 0.017°, 10 seconds per step and total measurement time of about 10 minutes. The phases were identified using X'Pert Highscore software.

Samples of the coke produced during the tests were analysed with a JEOL-2100F field emission electron microscope (TEM) to characterise the morphology and EDX was used to identify metallic particles in the coke. The coke was dispersed in ethanol and placed in an ultrasonic bath. The droplets of the dispersed solution were then placed on a copper grid for evaluation on the TEM.

Samples of the coke were also analysed by Raman spectroscopy. Raman spectra were acquired using a PerkinElmer RamanStation 400 bench top Raman spectrometer. The excitation source was a near-infrared 785 nm laser (100 mW at the sample), with a spot size of 100 μm. A spectral range of 100-3200 cm^{-1} was employed. The detector was a temperature controlled Charged Coupled Device (CCD) detector (-50°C) incorporating a 1024 x 256 pixel sensor. Spectra were acquired using Spectrum software and images were acquired using Spectrum IMAGE software, both supplied by PerkinElmer.

The one half of each specimen tested intended for metallography was firstly electrolytically coated with copper. This was done to retain corrosion products and ensure good edge-retention – since most of the analysis was focussed at the surface. Generally, nickel plating is used for this purpose; however, since some of the alloys contained nickel, copper was used to ensure corrosion products were not incorrectly characterised. The copper plating was performed as follows:

Solution:

- $CuSO_4.5H_2O$ 200-240 g/L
- H_2SO_4 45-75 g/L
- HCl 0.02-0.1 g/L

Conditions:

- Temperature 40-50°C
- Current density 2-10 A/dm^2
- Anode Copper

Subsequent to copper plating, the samples were hot mounted in a conductive Black Polyfast resin, specifically for SEM analysis. Mounted specimens were successively ground to 1200 grit silicon carbide (SiC) paper, and then polished to 1 µm finish on diamond cloths. The samples that were cleaned to assess the metal wastage rate were etched, whereas the un-cleaned samples (containing reaction products on the surfaces of the specimens) were retained for evaluation in the un-etched condition.

Surface and microstructural analyses of the samples were performed on a FEI Nova NanoSEM 200 scanning electron microscope, equipped with energy dispersive X-ray spectroscopy (SEM-EDX). Images were produced in both backscattered and secondary electron modes. Since all the samples were plated in a solution containing H_2SO_4 and HCl, most of the samples also contained elemental traces of sulphur and chloride. Since these elements did not originate from the metal dusting process, they were not regarded in this study.

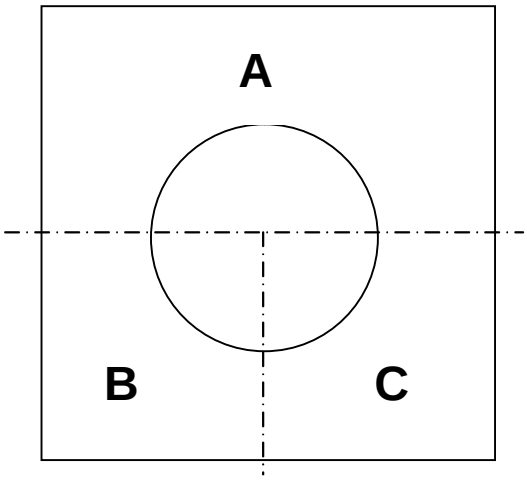


Figure 3.3. Schematic diagram illustrating how the samples were sectioned for characterisation.

The samples were therefore exposed and evaluated as described in Table 3.2. The sample labels refer to the Columbus Stainless internal specification for the respective alloys, followed by the unique number given for the sample. Therefore, Sample 30412-1 refers to Type 304L stainless steel, number 1 in this test matrix. Similarly, Samples 32113-*x* refers to Type 321, Samples 31613-*x* refers to Type 316L, Samples 31663-*x* refers to Type 316Ti, Samples 43012-*x* refers to Type 430 and Samples 44101-*x* refers to Type 441 stainless steel. Samples 1 to 8 were exposed for varying lengths of time in the furnace, while Sample 13 was not exposed in the furnace. Sample 13 was used as a reference sample to assess the degree of metal dusting attack.

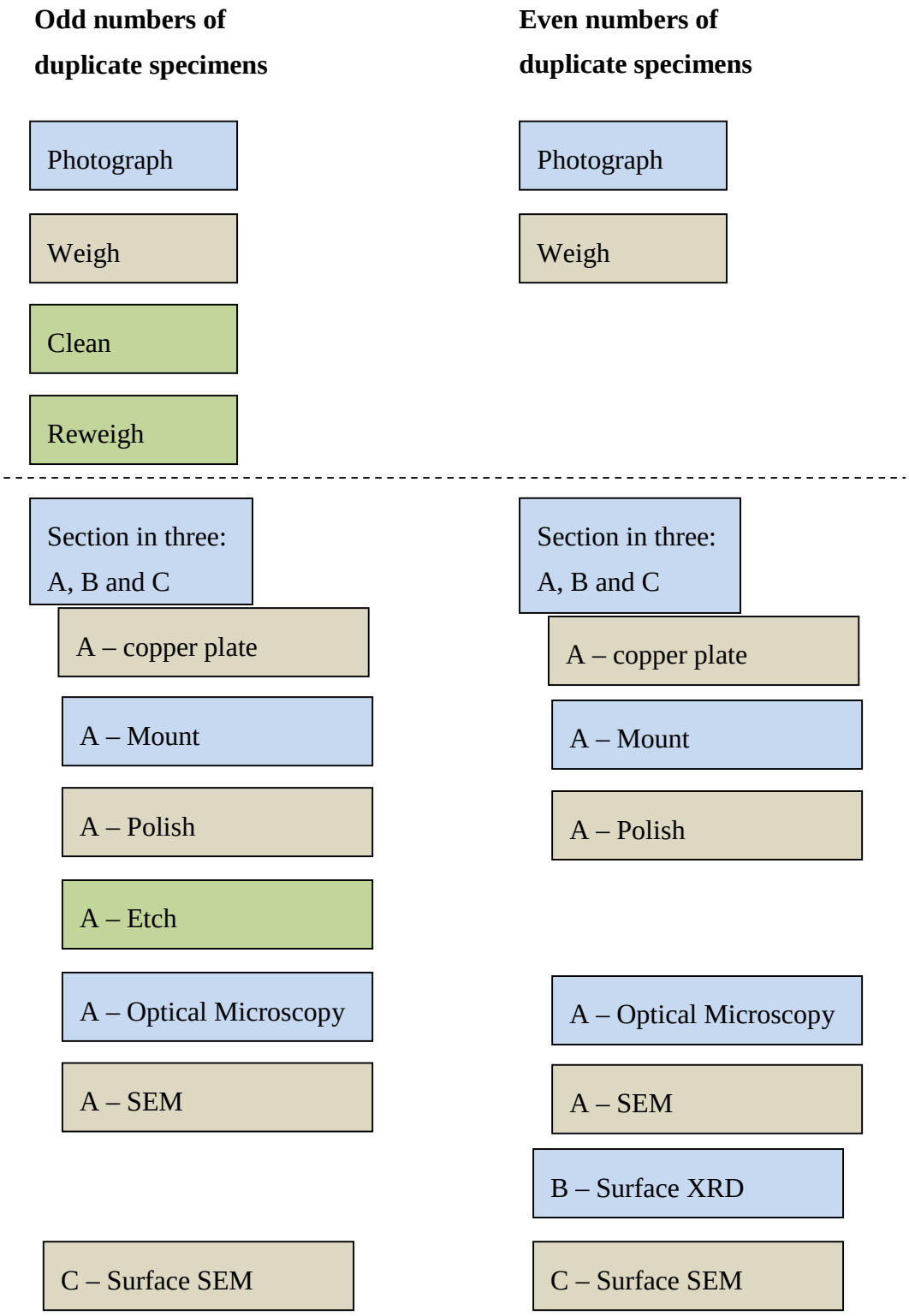


Figure 3.4. Schematic diagram illustrating how the different samples were analysed.

Table 3.2. Details of sample exposure and evaluation.

Label	Grade	Exposure Days (h)	Clean	Optical Microscopy	Etch	SEM	XRD
30412-1	304L	7 (168)	Yes	Yes	Yes	Yes	No
30412-2	304L	7 (168)	No	Yes	No	Yes	Yes
30412-3	304L	14 (336)	Yes	Yes	Yes	Yes	No
30412-4	304L	14 (336)	No	Yes	No	Yes	Yes
30412-5	304L	6 (144)	Yes	Yes	Yes	Yes	No
30412-6	304L	6 (144)	No	Yes	No	Yes	No
30412-7	304L	30 (720)	Yes	Yes	Yes	Yes	No
30412-8	304L	30 (720)	No	Yes	No	Yes	Yes
30412-13	304L	No	No	Yes	Yes	Yes	Yes
32113-1	321	7 (168)	Yes	Yes	Yes	Yes	No
32113-2	321	7 (168)	No	Yes	No	Yes	Yes
32113-3	321	14 (336)	Yes	Yes	Yes	Yes	No
32113-4	321	14 (336)	No	Yes	No	Yes	Yes
32113-5	321	6 (144)	Yes	Yes	Yes	Yes	No
32113-6	321	6 (144)	No	Yes	No	Yes	No
32113-7	321	30 (720)	Yes	Yes	Yes	Yes	No
32113-8	321	30 (720)	No	Yes	No	Yes	Yes
32113-13	321	No	No	Yes	Yes	Yes	Yes
31613-1	316L	7 (168)	Yes	Yes	Yes	Yes	No
31613-2	316L	7 (168)	No	Yes	No	Yes	Yes
31613-3	316L	14 (336)	Yes	Yes	Yes	Yes	No
31613-4	316L	14 (336)	No	Yes	No	Yes	Yes
31613-5	316L	6 (144)	Yes	Yes	Yes	Yes	No
31613-6	316L	6 (144)	No	Yes	No	Yes	No

Label	Grade	Exposure Days (h)	Clean	Optical Microscopy	Etch	SEM	XRD
31613-7	316L	30 (720)	Yes	Yes	Yes	Yes	No
31613-8	316L	30 (720)	No	Yes	No	Yes	Yes
31613-13	316L	No	No	Yes	Yes	Yes	Yes
31663-1	316Ti	7 (168)	Yes	Yes	Yes	Yes	No
31663-2	316Ti	7 (168)	No	Yes	No	Yes	Yes
31663-3	316Ti	14 (336)	Yes	Yes	Yes	Yes	No
31663-4	316Ti	14 (336)	No	Yes	No	Yes	Yes
31663-5	316Ti	6 (144)	Yes	Yes	Yes	Yes	No
31663-6	316Ti	6 (144)	No	Yes	No	Yes	No
31663-7	316Ti	30 (720)	Yes	Yes	Yes	Yes	No
31663-8	316Ti	30 (720)	No	Yes	No	Yes	Yes
31663-13	316Ti	No	No	Yes	Yes	Yes	Yes
43012-1	430	7 (168)	Yes	Yes	Yes	Yes	No
43012-2	430	7 (168)	No	Yes	No	Yes	Yes
43012-3	430	14 (336)	Yes	Yes	Yes	Yes	No
43012-4	430	14 (336)	No	Yes	No	Yes	Yes
43012-5	430	6 (144)	Yes	Yes	Yes	Yes	No
43012-6	430	6 (144)	No	Yes	No	Yes	No
43012-7	430	30 (720)	Yes	Yes	Yes	Yes	No
43012-8	430	30 (720)	No	Yes	No	Yes	Yes
43012-13	430	No	No	Yes	Yes	Yes	Yes
44101-1	441	7 (168)	Yes	Yes	Yes	Yes	No
44101-2	441	7 (168)	No	Yes	No	Yes	Yes
44101-3	441	14 (336)	Yes	Yes	Yes	Yes	No

Label	Grade	Exposure Days (h)	Clean	Optical Microscopy	Etch	SEM	XRD
44101-4	441	14 (336)	No	Yes	No	Yes	Yes
44101-5	441	6 (144)	Yes	Yes	Yes	Yes	No
44101-6	441	6 (144)	No	Yes	No	Yes	No
44101-7	441	30 (720)	Yes	Yes	Yes	Yes	No
44101-8	441	30 (720)	No	Yes	No	Yes	Yes
44101-13	441	No	No	Yes	Yes	Yes	Yes

4. RESULTS

Tests were completed for 6 days, 7 days, 14 days and 30 days continuous exposure in the furnace. In all the tests, all the coupons were inserted simultaneously into the furnace. Although the degree of coking could not be accurately measured, it did allow assessment of the extent of attack on the coupons of the different alloys.

4.1. Six day exposure test

The test performed for six days was the third test performed on the samples, after the tests performed for seven days and fourteen days respectively. It is described first since it was the shortest test. This test was therefore performed on the samples labelled “5” and “6” (Table 3.2).

4.1.1. Visual examination

Figure 4.1 is a photograph of the samples after exposure for six days in the furnace, and also demonstrates how the samples were suspended in a ceramic boat with ceramic rods. Some coke formation was associated with the austenitic samples, as also shown in Figure 4.2.

Figure 4.3 shows Types 304L and 321 samples. No significant attack or difference in degree of tarnishing between the two alloys could be identified. Figure 4.4 shows Types 316L and 316Ti samples. Small isolated pits were found on the samples of both alloys. The Type 316L samples were tarnished to a greater degree than the Type 316Ti samples.

Figure 4.5 shows the ferritc samples, with Type 430 on the top row and Type 441 on the bottom row. No significant attack was evident, but the Type 430 samples appeared more tarnished (surface oxidation) than Type 441 (containing carbide-formers).

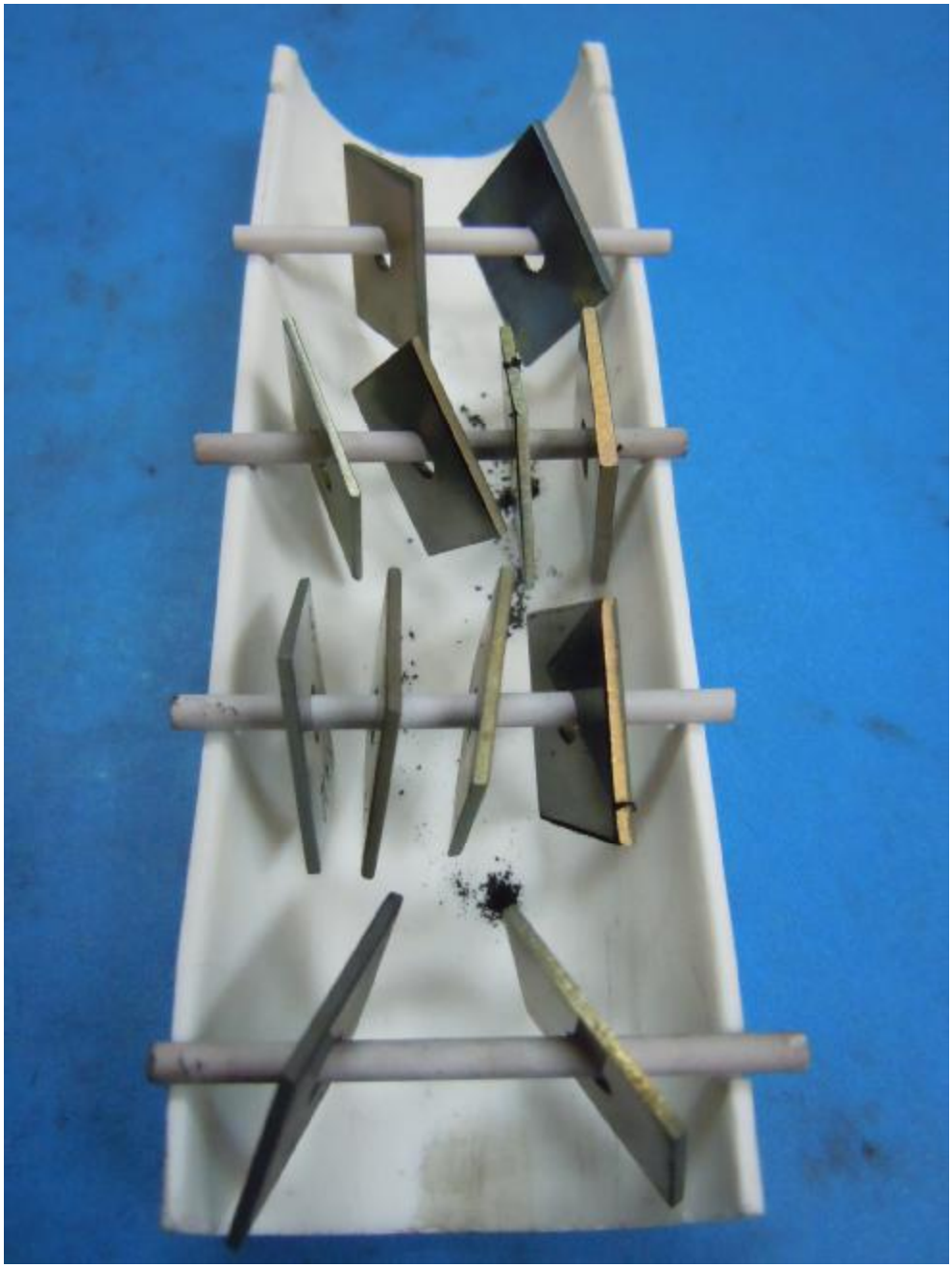


Figure 4.1. Photograph of the samples after the 6-day exposure.



Figure 4.2. Close-up photograph of the samples and coking associated with the 316L samples shown in Figure 4.1.



Figure 4.3. Photograph of the 304L and 321 austenitic samples after the 6-day test.



Figure 4.4. Photograph of the 316L and 316Ti austenitic samples after the 6-day test.



Figure 4.5. Photograph of the 430 and 441 ferritic samples after the 6-day test.

4.1.2. Mass loss

The weights of the samples (Table 4.1) did not change significantly during the six day exposure test, but generally, for the samples in the un-cleaned condition, it appeared that the grades containing carbide-formers gained more weight. The Types 304L and 316L samples exhibited the same amount of coke, and their equivalent grades, with titanium added, had a higher amount of coking. The amount of coking on Type 430 was similar to the austenitic grades without carbide-formers (Types 304L and 316L), but no coking was recorded for the grade containing carbide formers (i.e. Type 441).

Table 4.1. Mass change data after the 6-day test.

Sample		304L	304L	321	321	316L	316L	316Ti	316Ti	430	430	441	441
		5	6	5	6	5	6	5	6	5	6	5	6
Density	**g/cm^3**	7.9	7.9	7.8	7.8	8.0	8.0	8.0	8.0	7.8	7.8	7.7	7.7
Length	**mm**	20.40	20.82	20.45	20.76	20.69	20.29	20.36	20.77	20.79	20.57	20.41	20.71
Width	**mm**	20.18	20.40	20.43	19.88	20.20	19.86	20.50	20.66	20.38	20.51	20.32	20.47
Thickness	**mm**	1.21	1.14	1.40	1.36	1.43	1.40	1.83	1.83	1.45	1.43	1.38	1.38
Radius	**mm**	5.20	5.07	5.00	5.00	5.00	5.08	5.17	5.08	5.17	5.03	5.00	5.00
Area	**cm^2**	8.69	8.95	9.03	8.89	9.06	8.69	9.33	9.29	9.15	9.13	8.95	9.14
Mass before	**g**	3.5078	3.4158	4.2416	4.0725	4.3125	4.0746	5.4222	5.7111	4.2812	4.2798	3.9789	4.0942
Mass after	**g**	3.5081	3.4160	4.2423	4.0726	4.3124	4.0749	5.4222	5.7116	4.2811	4.2797	3.9792	4.0948
Mass loss	**g**	-0.0003	-0.0002	-0.0007	-0.0001	0.0001	-0.0003	0	-0.0005	0.0001	0.0001	-0.0003	-0.0006
Time	**h**	144	144	144	144	144	144	144	144	144	144	144	144
Corr. rate	**mm/y**	-0.0027	-0.0017	-0.0060	-0.0009	0.0008	-0.0026	0	-0.0041	0.0009	0.0009	-0.0026	-0.0052
Corr. rate	**Average**	**-0.0022**		**-0.0035**		**-0.0009**		**-0.0020**		**0.0009**		**-0.0039**	
Cleaned mass	**g**	3.508	-	4.2419	-	4.3123	-	5.4218	-	4.281	-	3.9792	-
Cleaned mass loss	**g**	-0.0002	-	-0.0003	-	0.0002	-	0.0004	-	0.0002	-	-0.0003	-
Cleaned Corr. rate	**mm/y**	**-0.0018**	**-**	**-0.0026**	**-**	**0.0017**	**-**	**0.0033**	**-**	**0.0017**	**-**	**-0.0026**	-
Coking mass	**g**	0.0001	-	0.0004	-	0.0001	-	0.0004	-	0.0001	-	0.0000	-
Coking rate	**mg/cm^2/day**	**0.0019**	**-**	**0.0074**	**-**	**0.0018**	**-**	**0.0071**	**-**	**0.0018**	**-**	**0.0000**	**-**

4.1.3. Metallography

No significant attack was evident on the cross-sections prepared for the Types 304L or 321 samples that were exposed for six days. Figure 4.6 and Figure 4.7 are micrographs through a Type 321 sample, showing no attack at the surfaces.

Figure 4.8 is a micrograph of a cross-section through a Type 316L sample. Shallow attack was evident over most of the surfaces, with coking and corrosion products on the surface. Local areas where corrosion initiated to form pitting corrosion were also found, as shown in Figure 4.9 and Figure 4.10. The intergranular nature of the attack was clearly evident with associated grain-dropping. It was also evident that as well as the grain boundaries, twin boundaries were also preferentially attacked. Once more of the grains had dropped out, this would be an isolated pit on the surface. Figure 4.11 is a higher magnification image of the general attack, showing that this attack was also preferential on the grain boundaries. Figure 4.12 is another micrograph of localised attack showing a second phase on the grain boundaries, associated with the intergranular attack. A phase was also present ahead of the 'reaction front'. This is possibly the carburisation process. Figure 4.13 and Figure 4.14 are cross-sections through a 316Ti sample showing that the attack was uniform over most of the surfaces, and no localised attack was found on these samples.

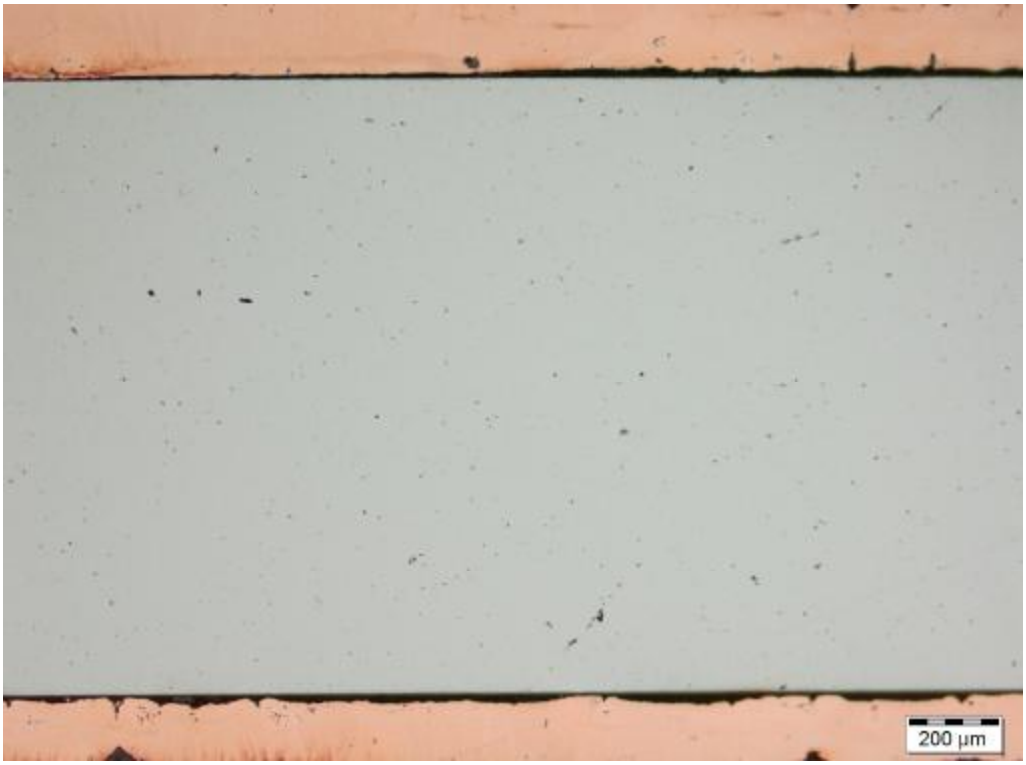


Figure 4.6. Micrograph of a cross-section through the 321-5 sample.

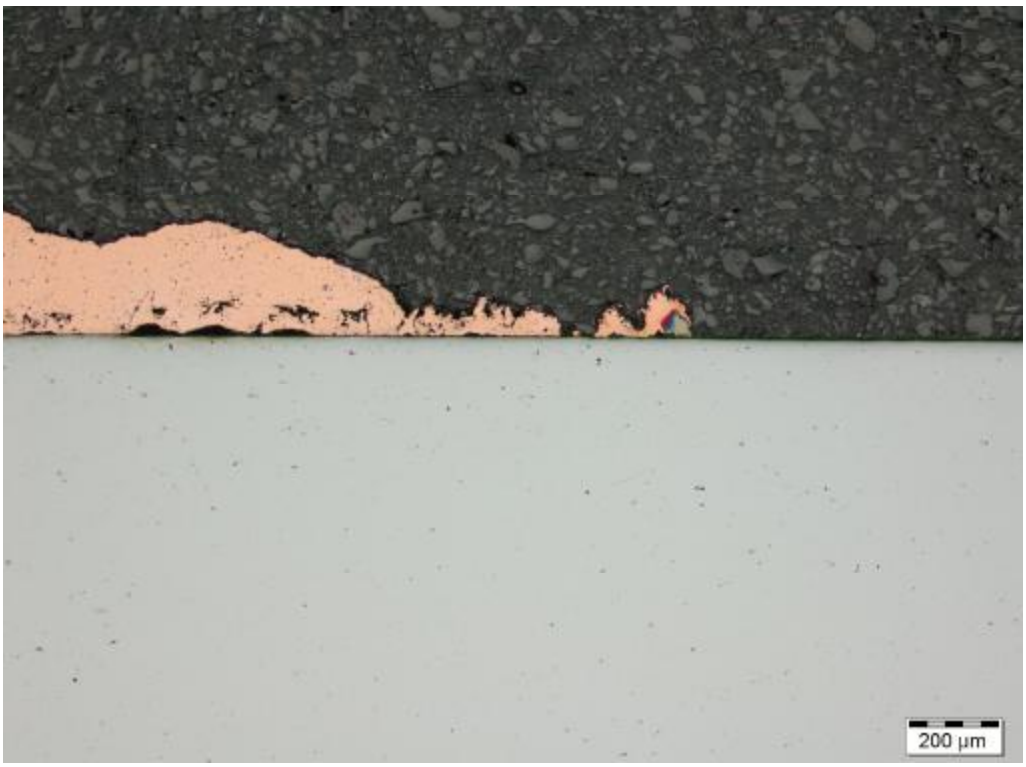


Figure 4.7. Higher magnification of the 321-5 sample shown in Figure 4.6.

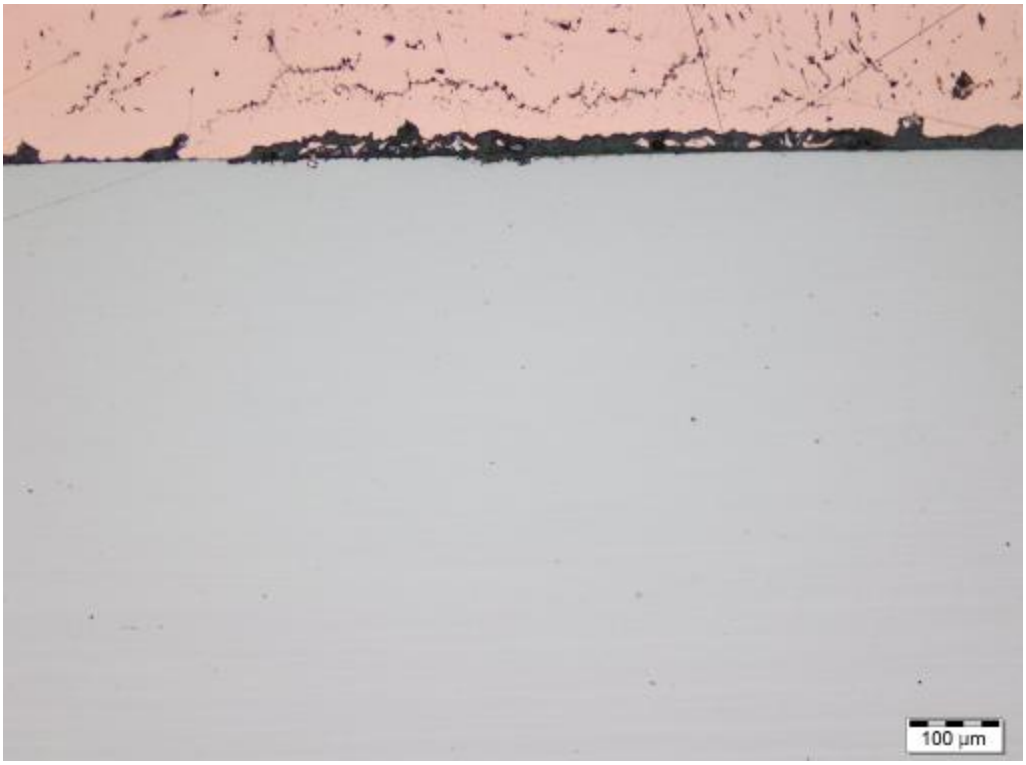


Figure 4.8. Micrograph of a cross-section through the 316-5 showing coking and shallow attack.

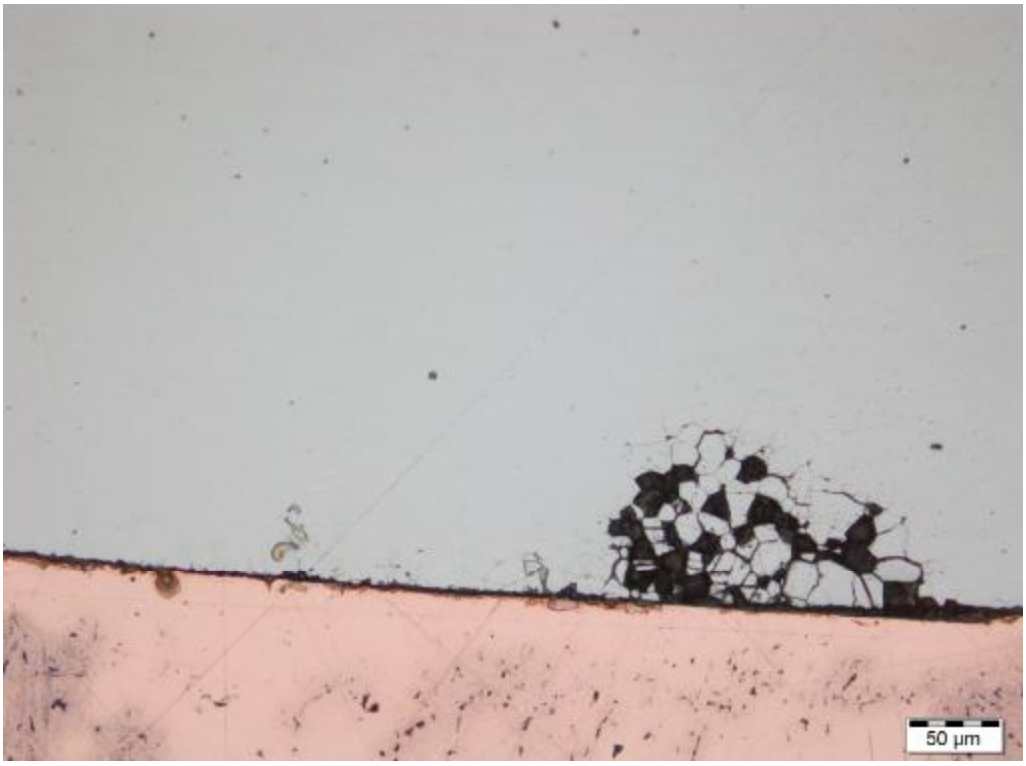


Figure 4.9. Micrograph of localised intergranular attack on Sample 316-5.

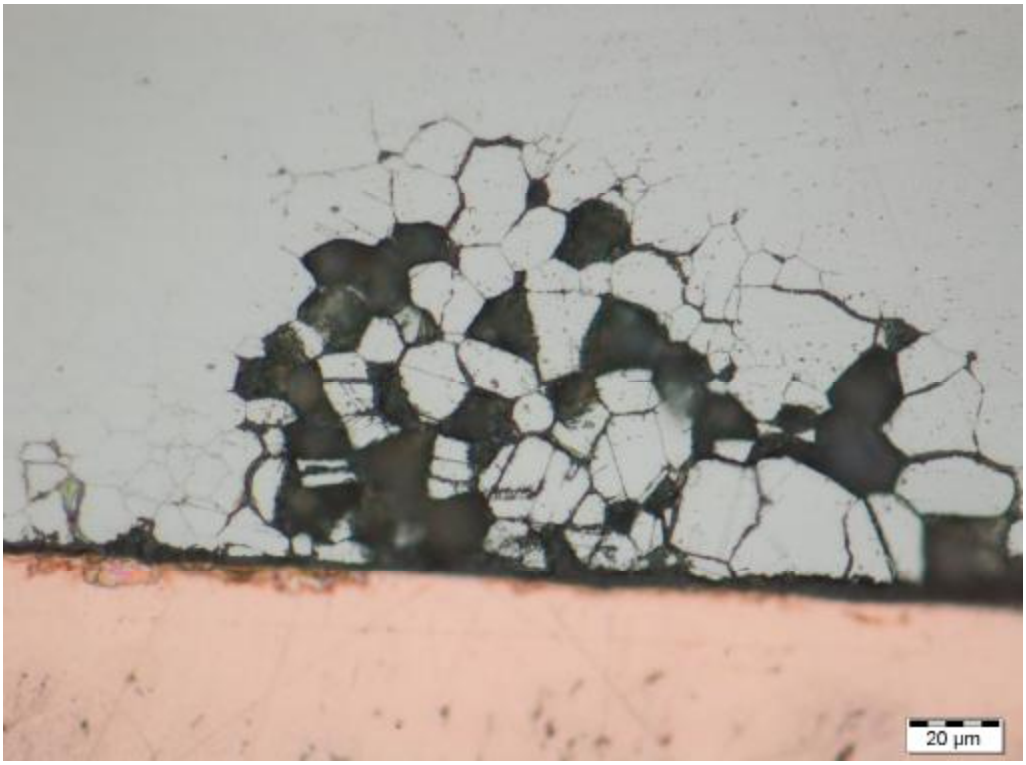


Figure 4.10. Higher magnification micrograph the attack on Sample 316-5 shown in Figure 4.9.

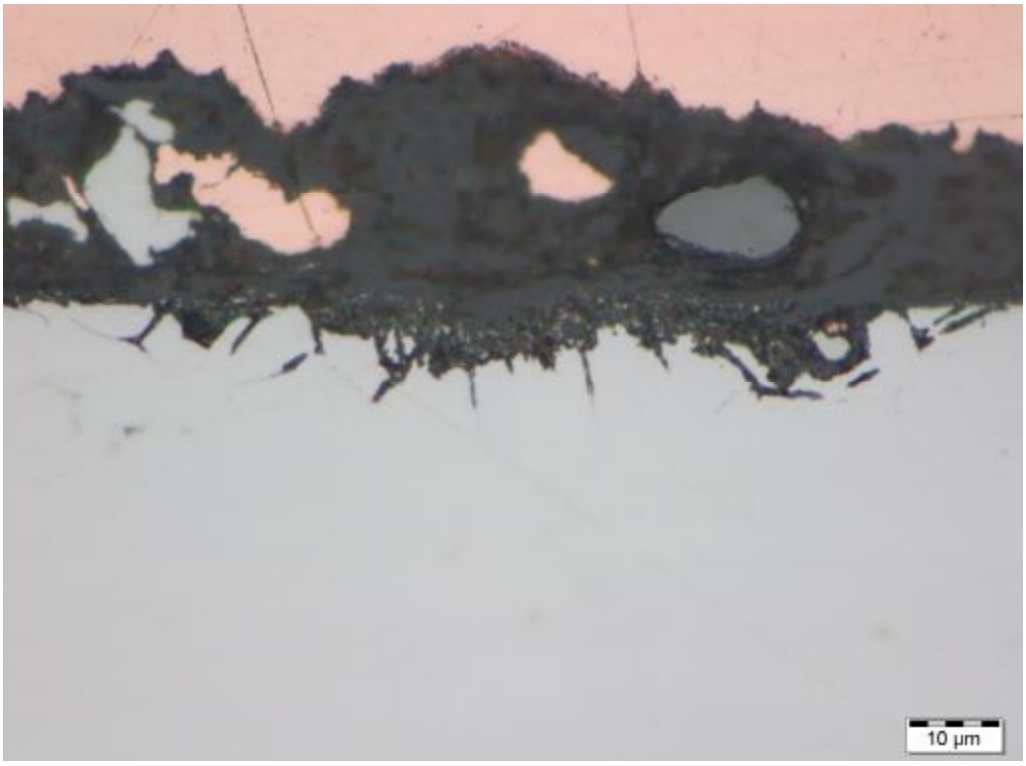


Figure 4.11. Micrograph of shallow attack and products on Sample 316-5.

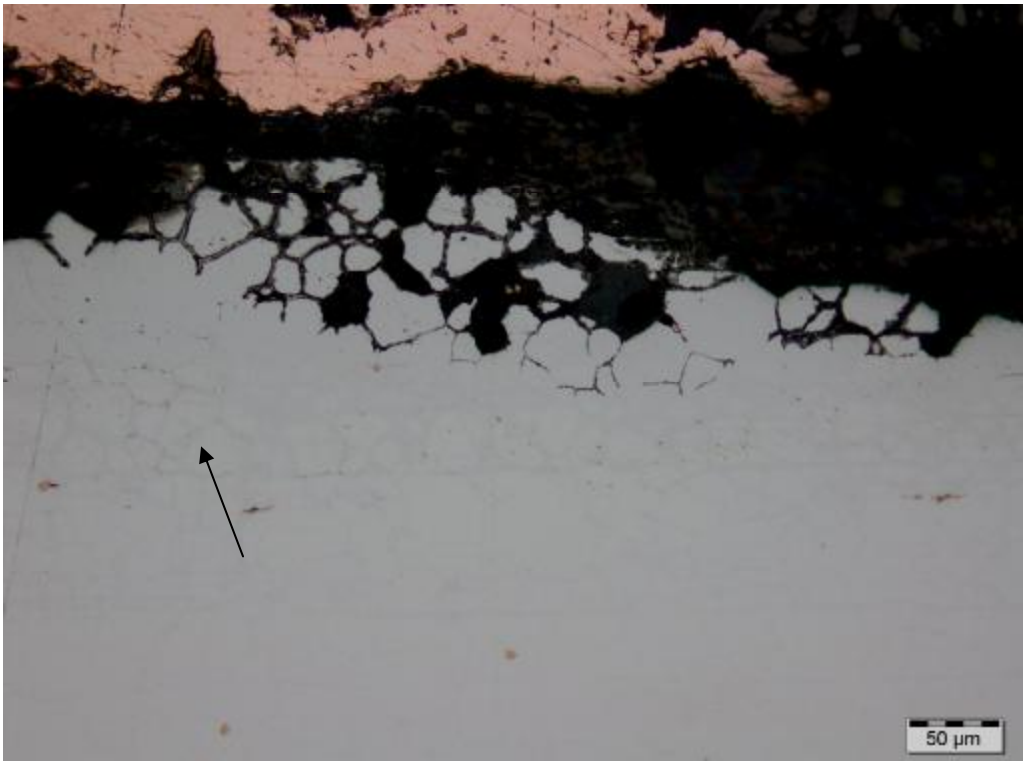


Figure 4.12. Micrograph of a second phase forming on the grain boundaries (arrow), intergranular attack and grain-dropping on Sample 316-6.

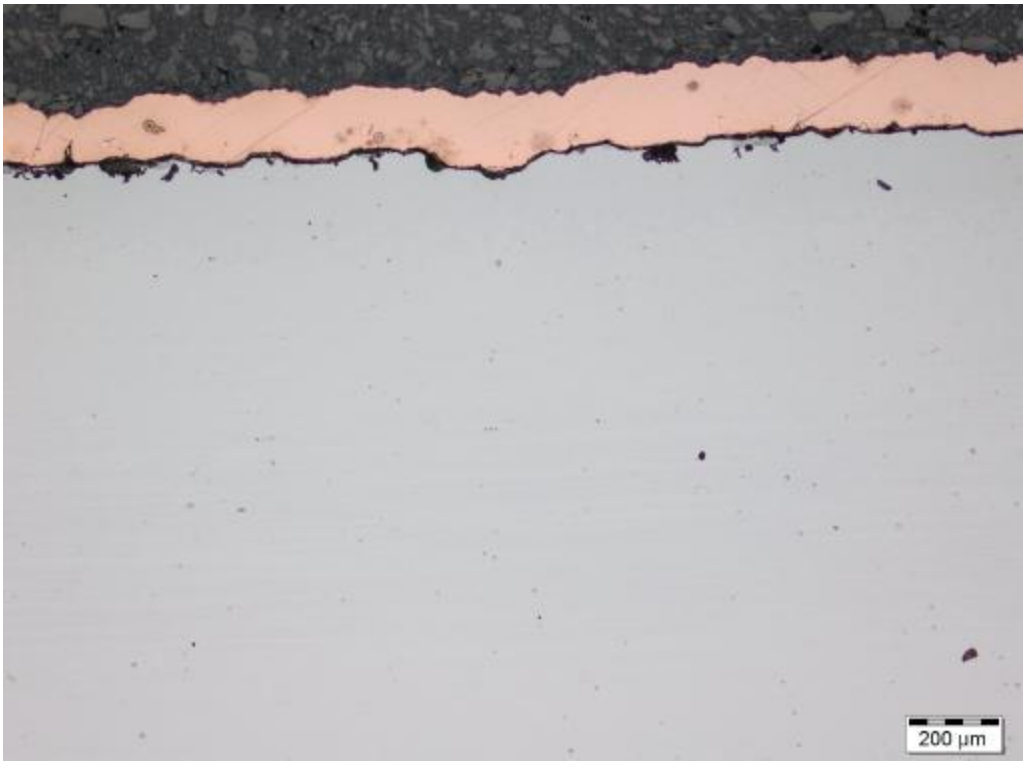


Figure 4.13. Micrograph of mostly shallow uniform attack on Sample 316Ti-5.



Figure 4.14. Micrograph of shallow attack and associated corrosion products on Sample 316Ti-5.

Figure 4.15 is a micrograph showing the carbide distribution in the Type 430 stainless steel exposed for 6 days in the etched condition. Figure 4.16 is a micrograph near the surface showing the increased amount of carbides near the surface. However, no breaks in the oxide scale occurred, and there was no localised carburisation. Figure 4.17 and Figure 4.18 are micrographs of etched Type 441 material exposed for six days. Intergranular and intragranular carbide precipitation was evident, as well as selective attack associated with the large titanium carbo-nitride precipitates on the grain boundaries. This indicates that the oxide has been damaged at these localised positions. The grains were recrystallised, and not in the as-rolled condition.

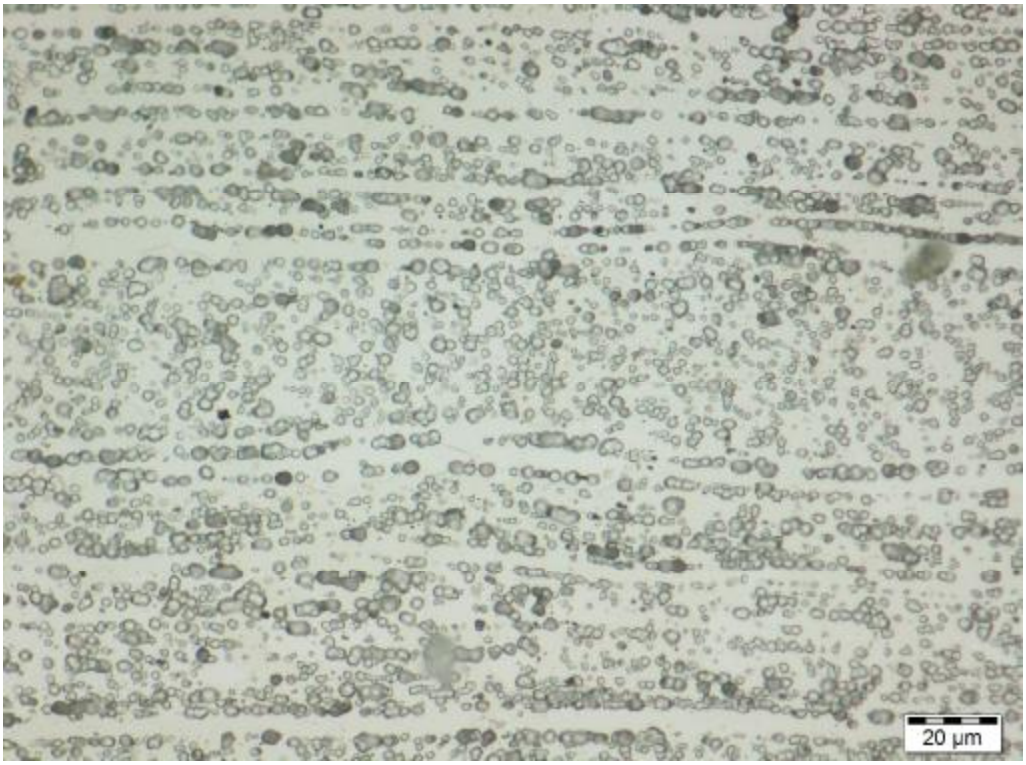


Figure 4.15. Etched micrograph showing the general carbide distribution in Sample 430-5.

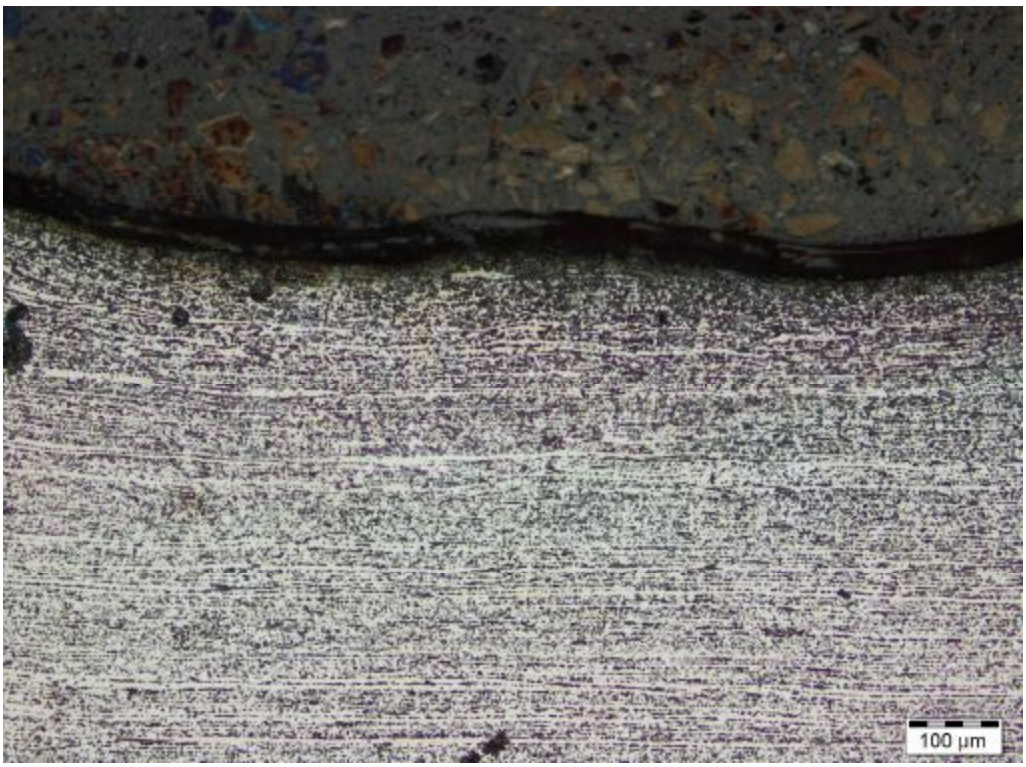


Figure 4.16. Etched micrograph of Sample 430-5 showing a degree of carburisation near the surface.

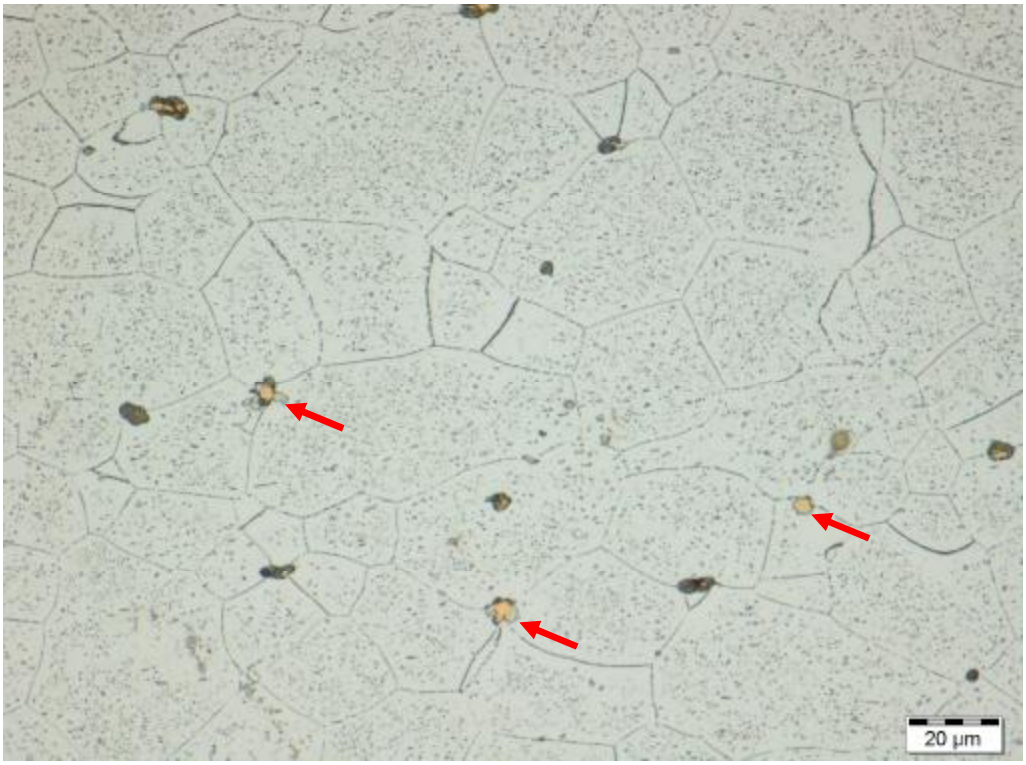


Figure 4.17. Etched micrograph of Sample 441-5 showing the carbide distribution and the titanium carbo-nitrides (arrows).

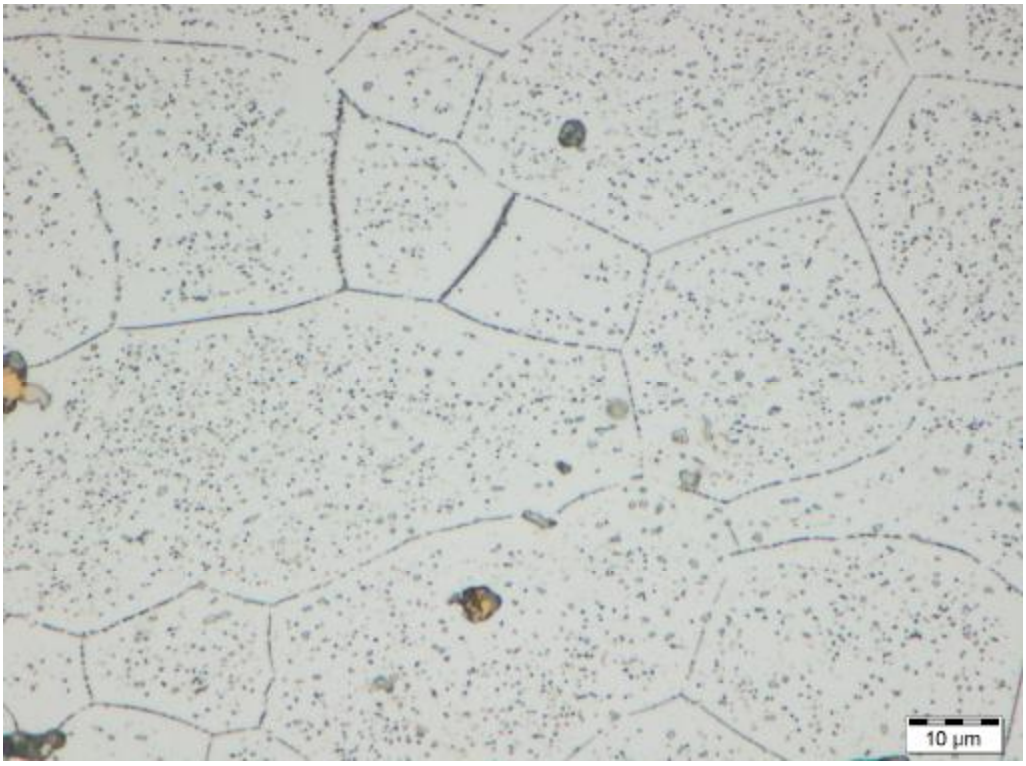


Figure 4.18. Higher magnification micrograph of Sample 441-5 shown in Figure 4.17.

4.1.4. Scanning Electron Microscopy

Figure 4.19 is a SEM image of a pit in Sample 316-6 that was not cleaned. The localised attack was evident with the original ground surface clearly surrounding the hemispherical pit. No other corrosive attack was evident, apart from the pit. Figure 4.20 and Figure 4.21 are SEM images of the carbon filaments inside the pit, with Figure 4.21 taken at 100 000X magnification showing the carbide particles at the end of the filaments.

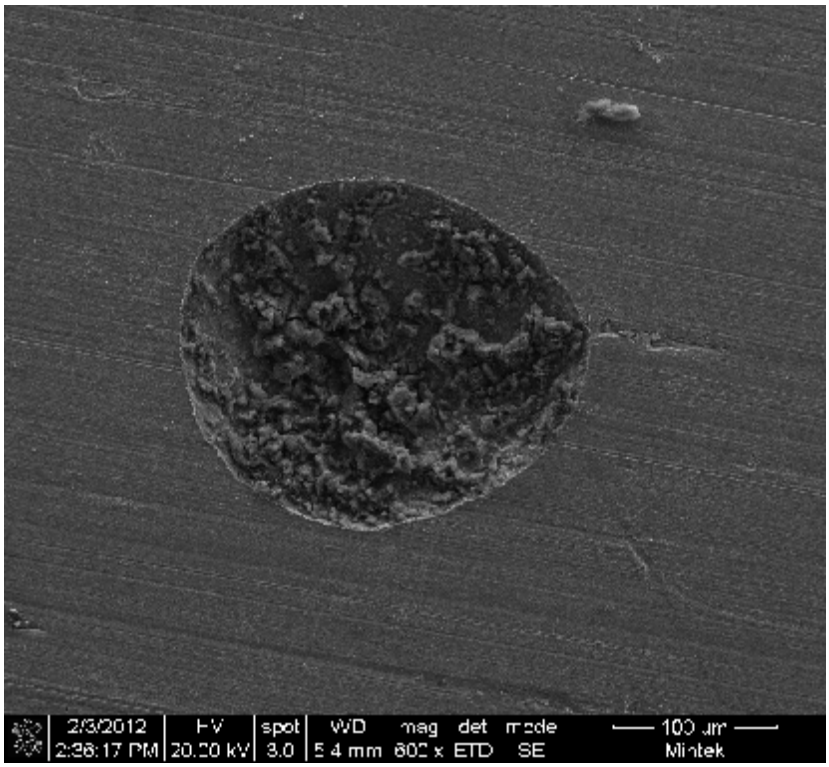


Figure 4.19. SEM-SE image of a pit on the 316-6 sample after the third test that was run for 6 days.

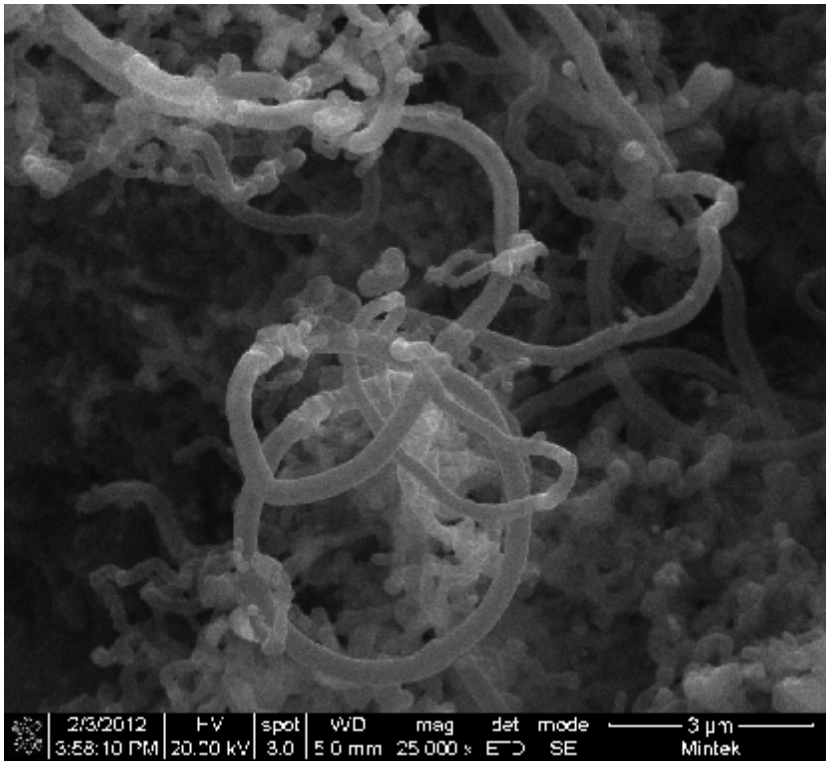


Figure 4.20. SEM-SE image of the coking on the 316L samples.

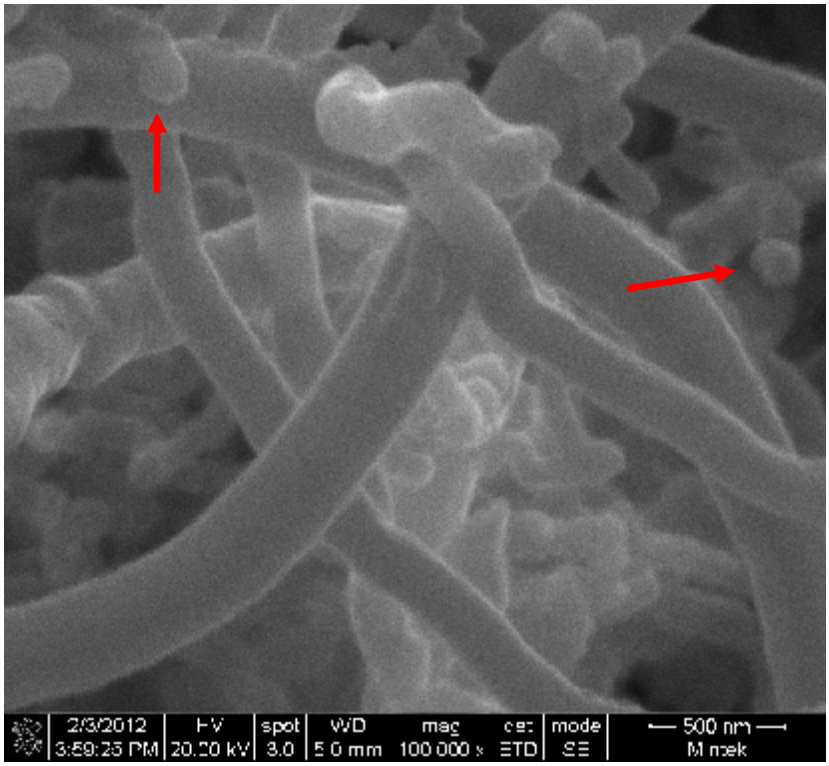


Figure 4.21. Higher magnification of the carbon filaments and associated carbide particles (arrows) shown in Figure 4.20.

4.1.5. Transmission Electron Microscopy

Figure 4.22 and Figure 4.23 are TEM images of the filaments removed from the Type 316L samples exposed for six days, which demonstrate that the filaments were hollow tubes. Figure 4.24 and Figure 4.25 are higher magnification TEM images of the filaments showing that the diameters of the filaments were about 60 nm, and that the walls of the filaments consisted of multiple layers. These hollow carbon filaments are commonly referred to as multiple walled carbon nanotubes (MWCNTs). Figure 4.26 and Figure 4.27 are TEM images of the corrosion products associated with the filaments, demonstrating their faceted nature. These particles were most likely faceted carbides – referring to the "dust" from metal dusting.

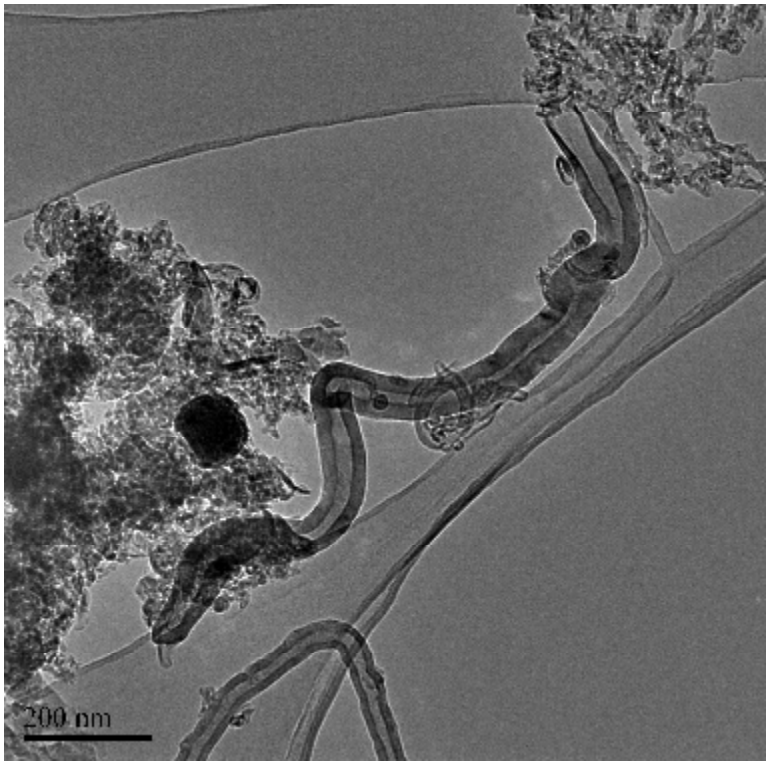


Figure 4.22. TEM image of a carbon filament and carbide particle (dark particle) from the 316L samples.

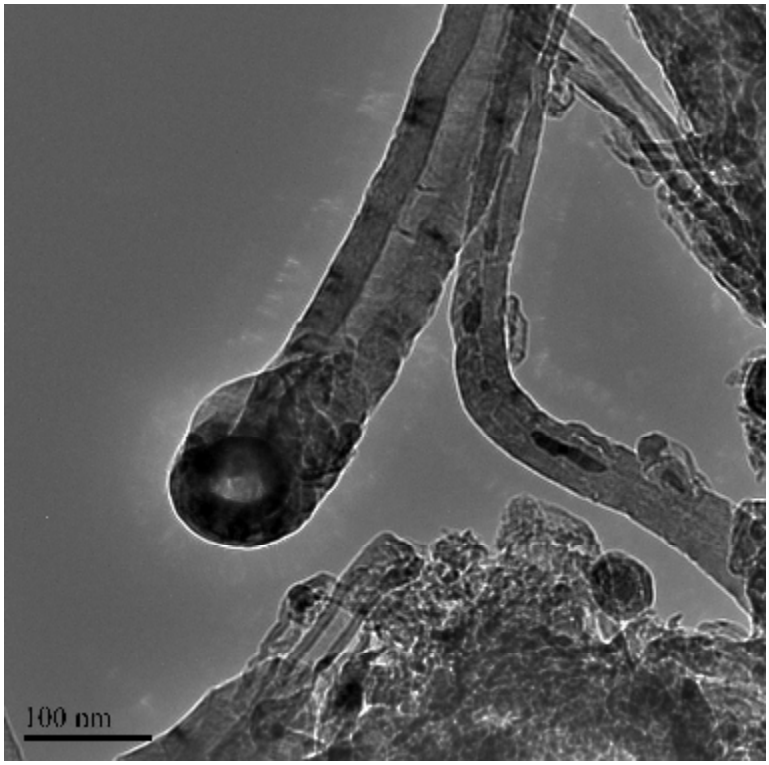


Figure 4.23. TEM image of a carbon filament from the 316L samples illustrating that they are hollow tubes (carbon nanotubes).

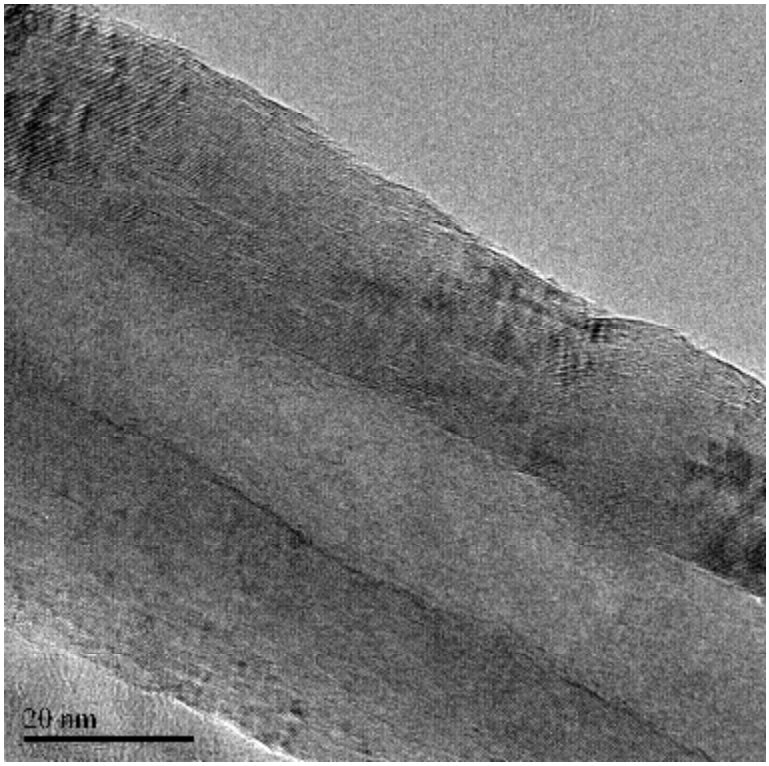


Figure 4.24. TEM image of a carbon filament from the 316L samples illustrating the walls of the hollow tube.

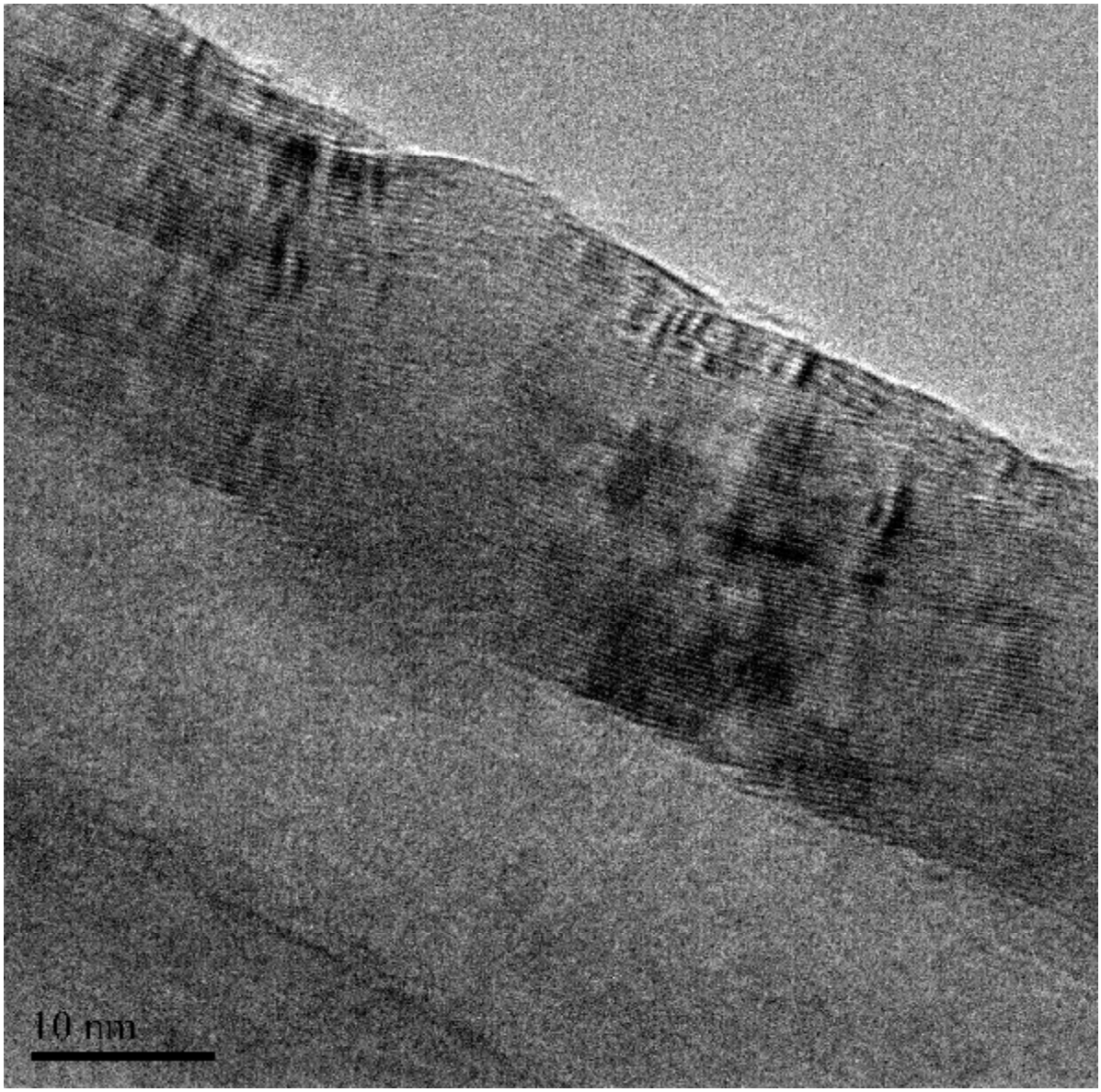


Figure 4.25. Higher magnification of Figure 4.24 demonstrating that the filaments are "multi-walled carbon nanotubes" (MWCNTs).

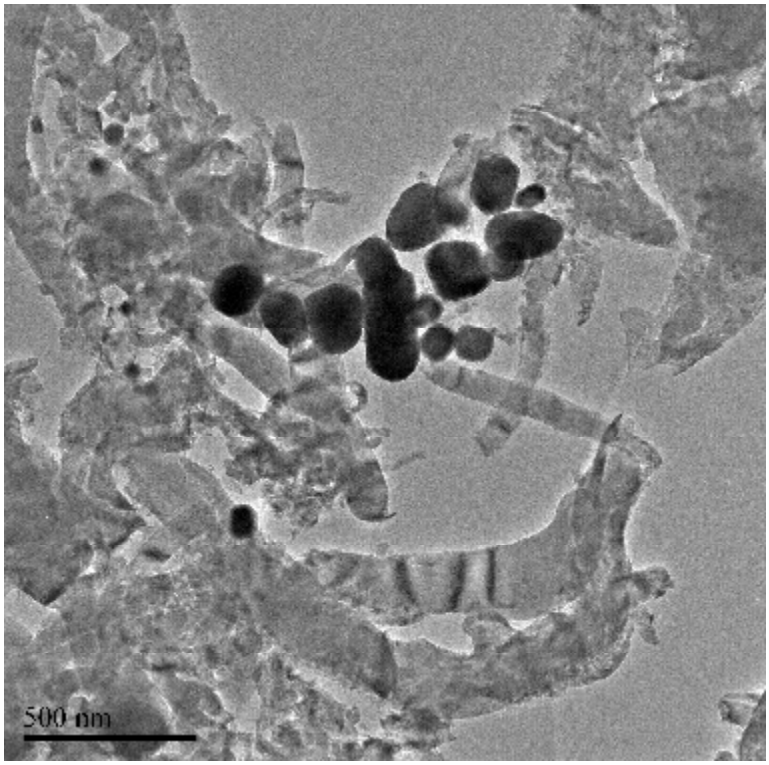


Figure 4.26. TEM image of carbon filaments and several carbide particles (dark particles) from the 6-day test.

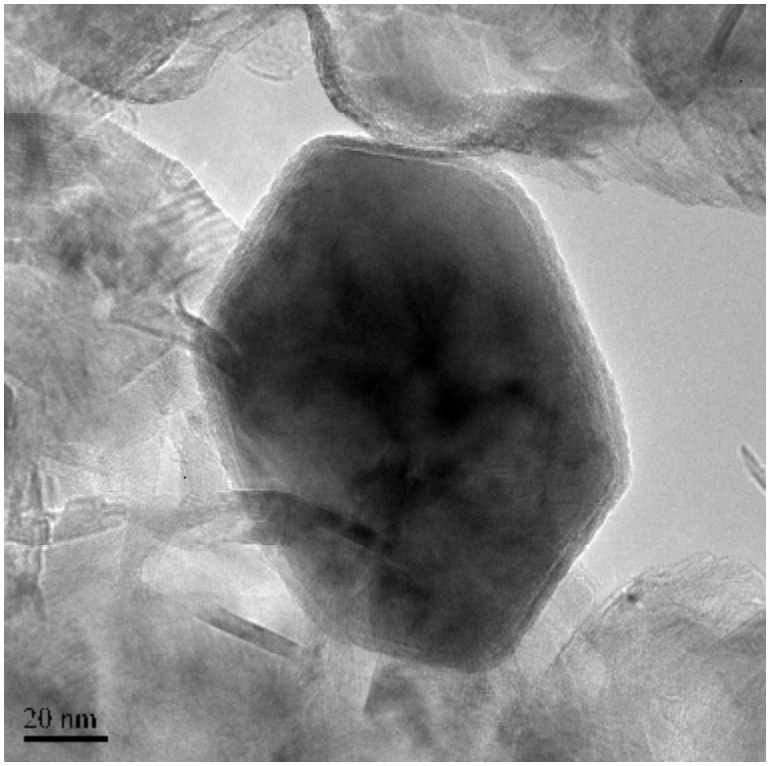


Figure 4.27. Higher magnification of a carbide particle from the 6-day test showing the faceted nature.

4.2. Seven day exposure period

The seven day test was the first test performed, and was performed on all the samples labelled 1 and 2. The results were similar to the six day test (Section 4.1), with no significant coking evident on any of the coupons. Only minor discolouration was evident on all the coupons, and none of the coupons showed appreciable mass changes – suggesting that no significant corrosive attack took place.

4.2.1. Visual examination

Figure 4.28 and Figure 4.29 are photographs of the samples as removed from the furnace. Similar to the six day test, only minor coking was associated with the 316L samples. Figure 4.30 shows the Types 304L and 321 samples. The 304L samples appeared slightly more tarnished than the 321 samples, as demonstrated in the close-up photographs shown in Figure 4.31 and Figure 4.32.

Figure 4.33 is a photograph of the types 316L and 316Ti samples exposed for 7 days showing the greater degree of tarnishing associated with the 316L samples. Isolated pits were evident on both alloys. Figure 4.34 shows the rear sides of the samples, with more pits in the 316L samples compared to 316Ti. Figure 4.35 is a close-up photograph of carbon filament growth associated with a pit on the 316Ti sample.

Figure 4.36 is a photograph of the Types 430 and 441 samples exposed for seven days. Again, the 430 samples were tarnished to a greater degree than the 441 samples, as shown in Figure 4.37 and Figure 4.38 respectively. There was no coking on the Type 441 sample.

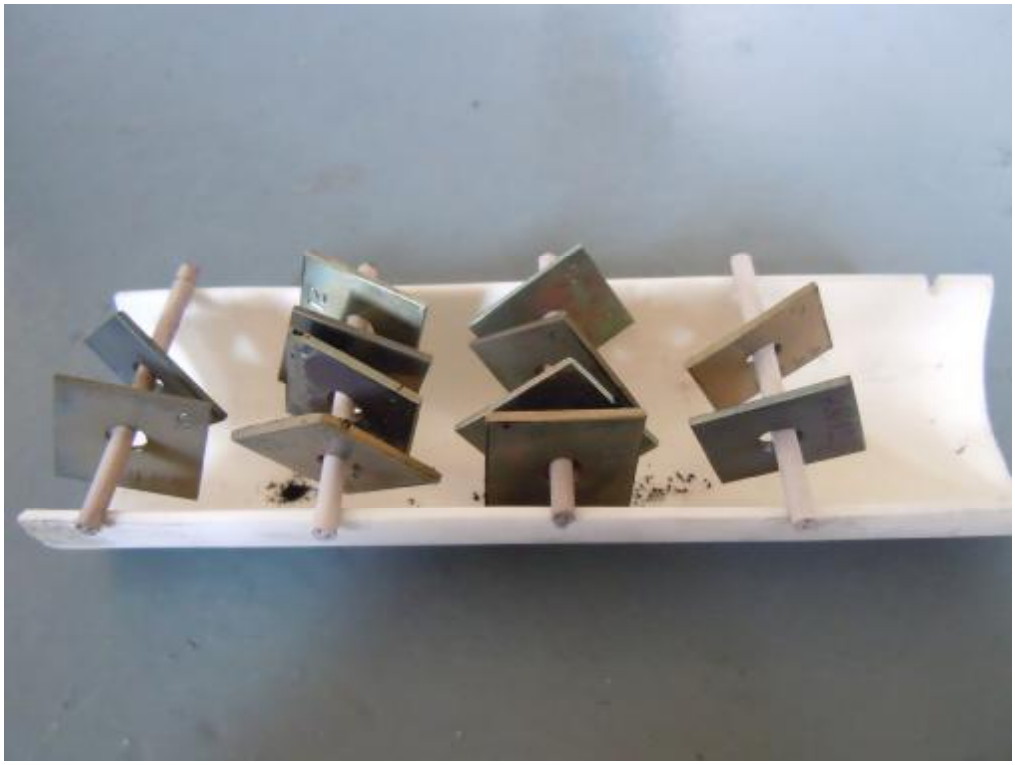


Figure 4.28. Photograph of the samples in the ceramic boat after exposure to the 7-day test.

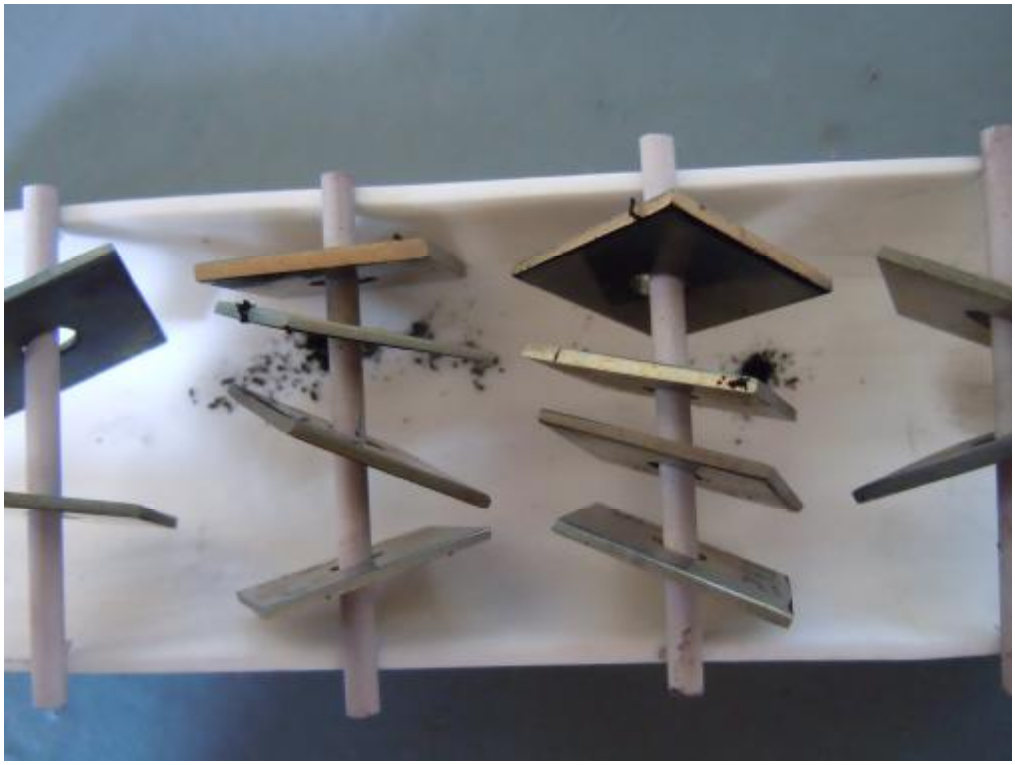


Figure 4.29. Close-up photograph showing coking associated with the austenitic samples.



Figure 4.30. Photograph of the 304L and 321 samples exposed to the 7-day test.



Figure 4.31 Close-up of the 304L sample showing only light tarnishing with no coking.



Figure 4.32. Close-up photograph of the 321 sample showing only light tarnishing and no coking.



Figure 4.33. Photograph of the 316L and 316Ti samples showing tarnishing and minor pits on the surface of both alloys.



Figure 4.34. Reverse sides of the 316L and 316Ti samples showing tarnishing and minor pits on a 316L sample.

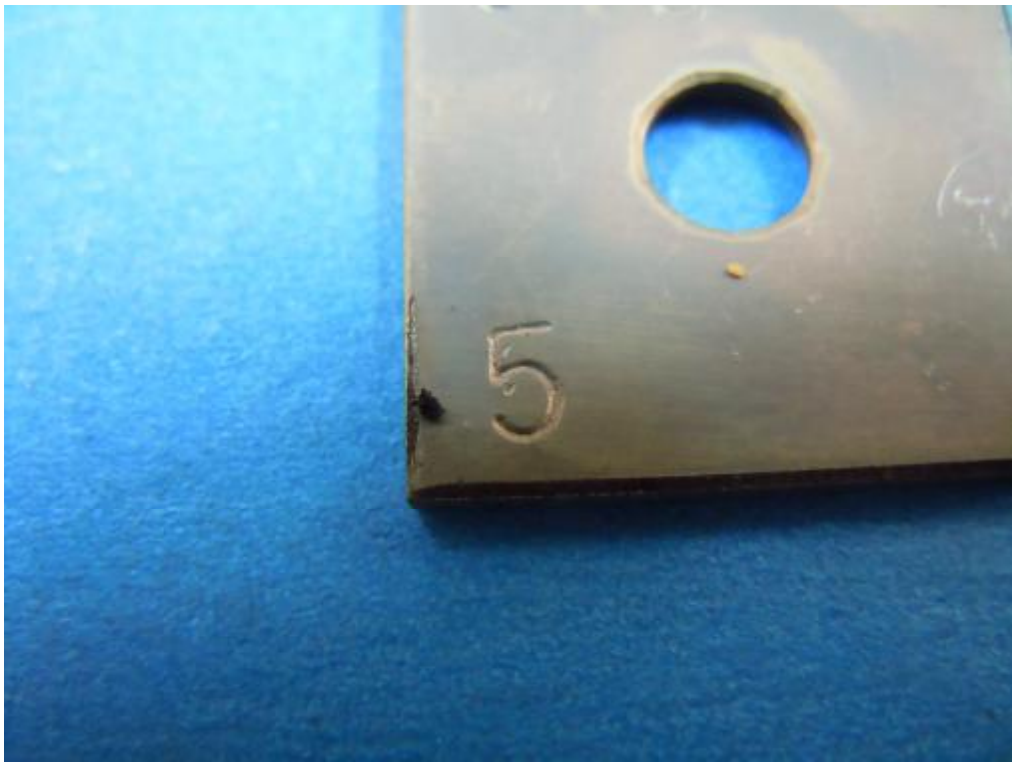


Figure 4.35. Close-up of filament growth on a 316Ti sample.



Figure 4.36. Photograph of the 430 and 441 samples.



Figure 4.37. Close-up of a 430 sample showing only light tarnishing.

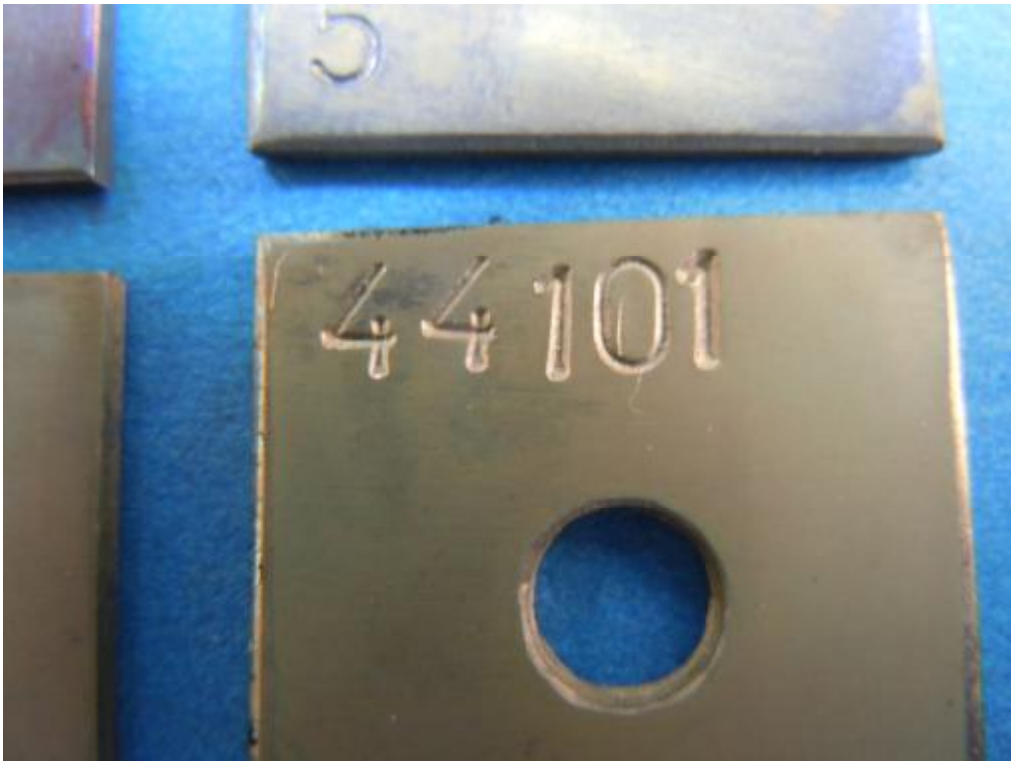


Figure 4.38. Photograph of a 441 sample showing less tarnishing than the 430 samples. No coking was evident.

4.2.2. Mass loss

Similar to the test performed on the six day samples, no significant mass changes occurred of the samples as removed from the furnace (Table 4.2). However, the tendency was generally for the austenitic grades containing the carbide-formers to have gained more weight, while the ferritic samples did not exhibit a mass change. Due to the fact that these samples did not exhibit a mass change, these coupons were not cleaned subsequently to exposure.

Table 4.2. Mass change data for the 7-day test.

Sample		304L	304L	321	321	316L	316L	316Ti	316Ti	430	430	441	441
		1	2	1	2	1	2	1	2	1	2	1	2
Density	**g/cm^3**	7.9	7.9	7.8	7.8	8.0	8.0	8.0	8.0	7.8	7.8	7.7	7.7
Length	**mm**	20.25	20.55	20.58	20.57	20.76	20.00	20.73	20.70	21.54	20.88	20.59	20.61
Width	**mm**	19.47	19.39	20.35	20.50	20.29	19.98	20.58	20.62	20.44	20.12	20.42	20.42
Thickness	**mm**	1.12	1.13	1.32	1.30	1.41	1.37	1.87	1.86	1.45	1.43	1.37	1.42
Radius	**mm**	5.18	5.15	5.00	5.00	5.00	5.19	5.00	5.17	5.17	5.18	5.14	5.02
Area	**cm^2**	8.26	8.36	8.99	9.03	9.11	8.57	9.61	9.56	9.51	9.06	9.03	9.11
Mass before	**g**	3.1015	3.1688	4.0795	4.0121	4.3666	4.0089	5.7636	5.7349	4.5229	4.1506	4.1104	4.2258
Mass after	**g**	3.1015	3.1685	4.0798	4.0123	4.3664	4.0090	5.7640	5.7353	4.5229	4.1506	4.1105	4.2257
Mass loss	**g**	0	0.0003	-0.0003	-0.0002	0.0002	-0.0001	-0.0004	-0.0004	0	0	-0.0001	0.0001
Time	**h**	168	168	168	168	168	168	168	168	168	168	168	168
Corr. rate	**mm/y**	0.0000	0.0024	-0.0022	-0.0015	0.0014	-0.0008	-0.0027	-0.0027	0.0000	0.0000	-0.0008	0.0007
Corr. rate	**Average**	0.0012		-0.0019		0.0003		-0.0027		0.0000		0.0000	

4.2.3. Metallography

Figure 4.39 and Figure 4.40 are micrographs of cross-sections removed through the Type 304L samples exposed for seven days. Minor attack (shallow pits) and coking were evident on the surface with minor detached oxides. Figure 4.41 is a micrograph removed through the 321 sample showing no significant attack. Higher magnification revealed minor localised attack (shallow pits), as shown in Figure 4.42 and Figure 4.43. Figure 4.44 and Figure 4.45 are micrographs showing preferential carburisation or coking associated with the titanium carbo-nitrides, which formed in layers. Figure 4.46 and Figure 4.47 are micrographs showing the degree of carburisation on the grain boundaries of the etched Type 321 samples.

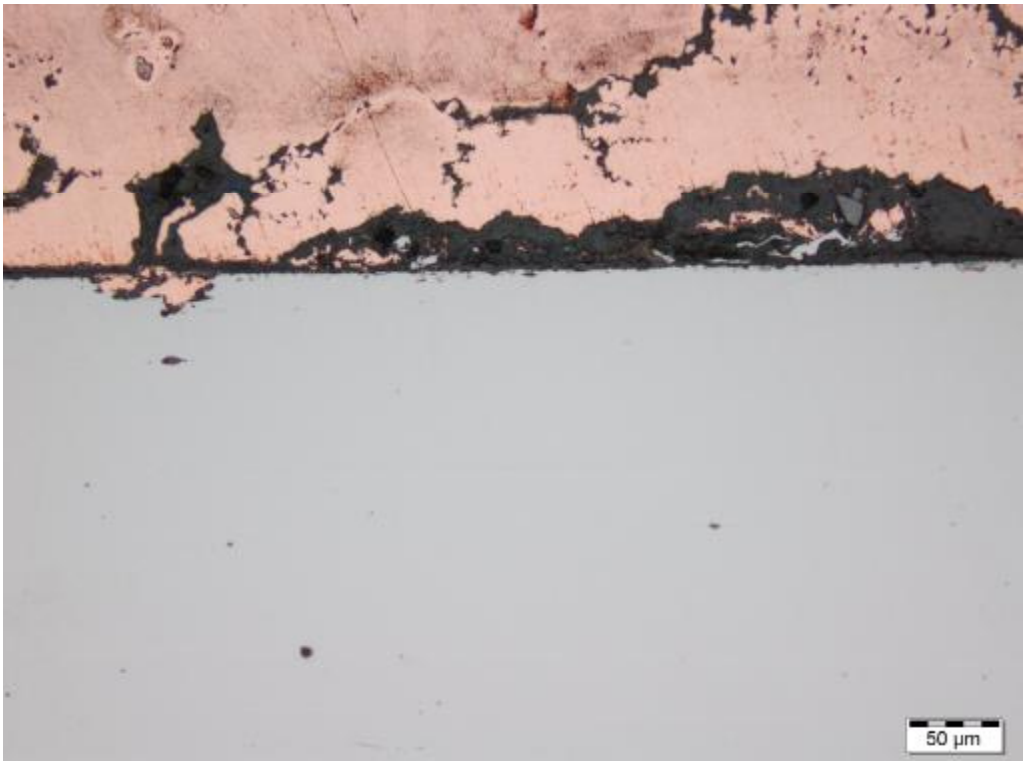


Figure 4.39. Micrograph of a cross-section through Sample 304-1 sample showing a pit and coking.

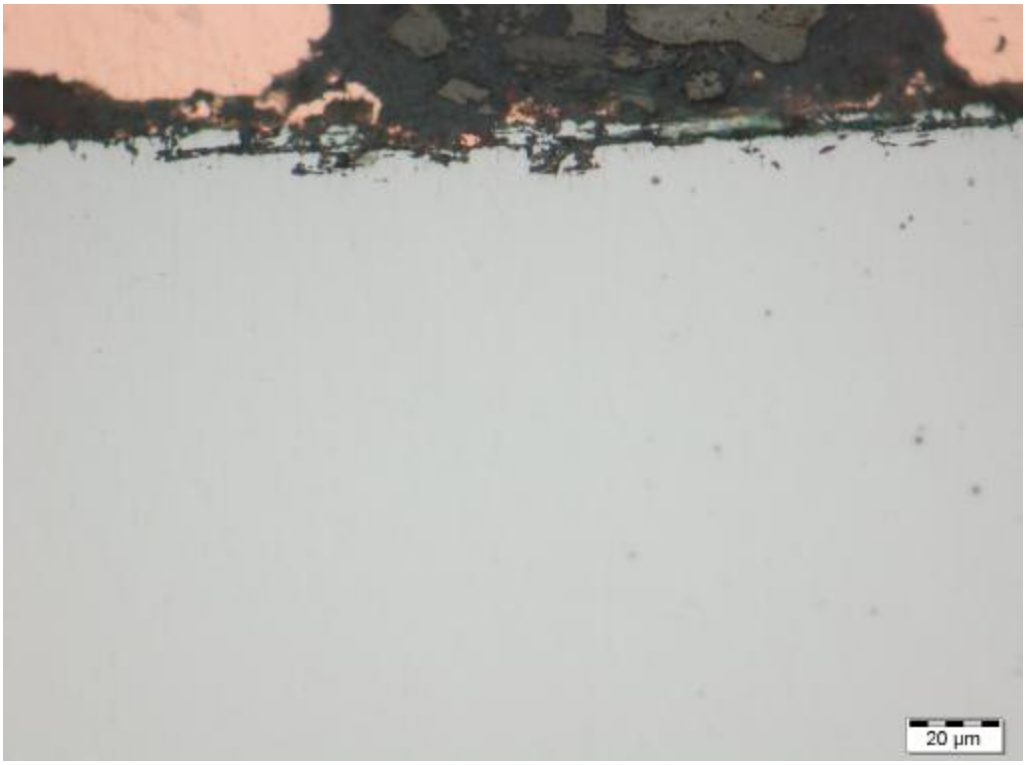


Figure 4.40. Higher magnification of Sample 304-1 showing shallow attack.



Figure 4.41. Cross section of Sample 321-1 (copper plated) showing no significant metal wastage.

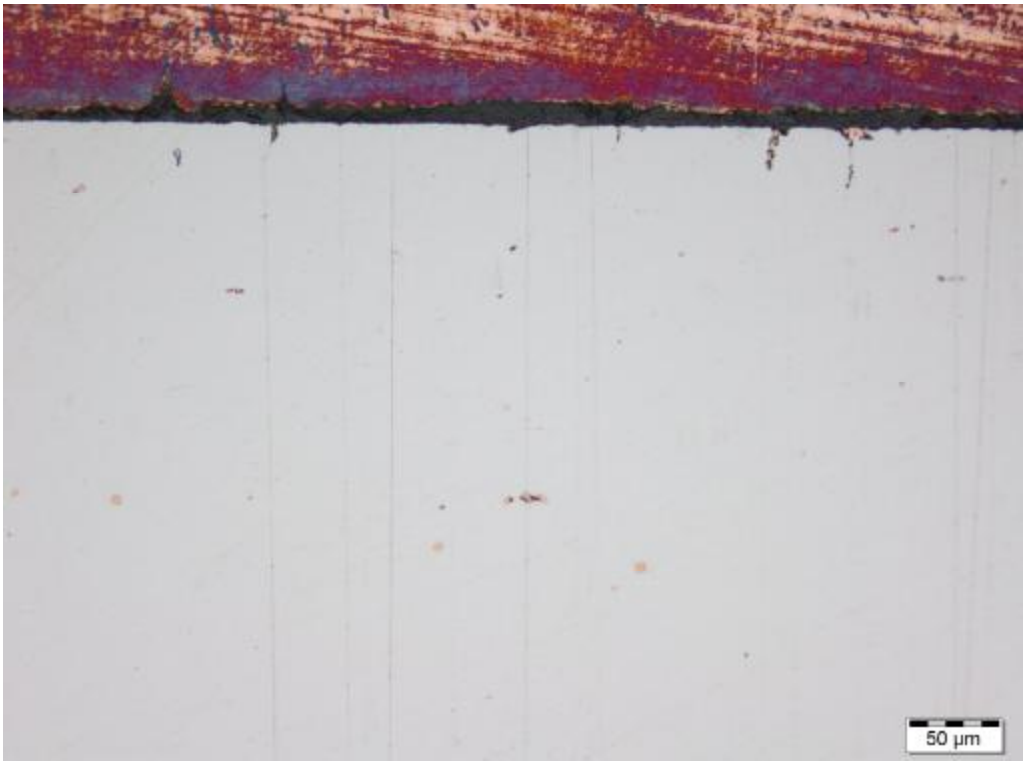


Figure 4.42. Higher magnification of shallow grain boundary attack on Sample 321-1.

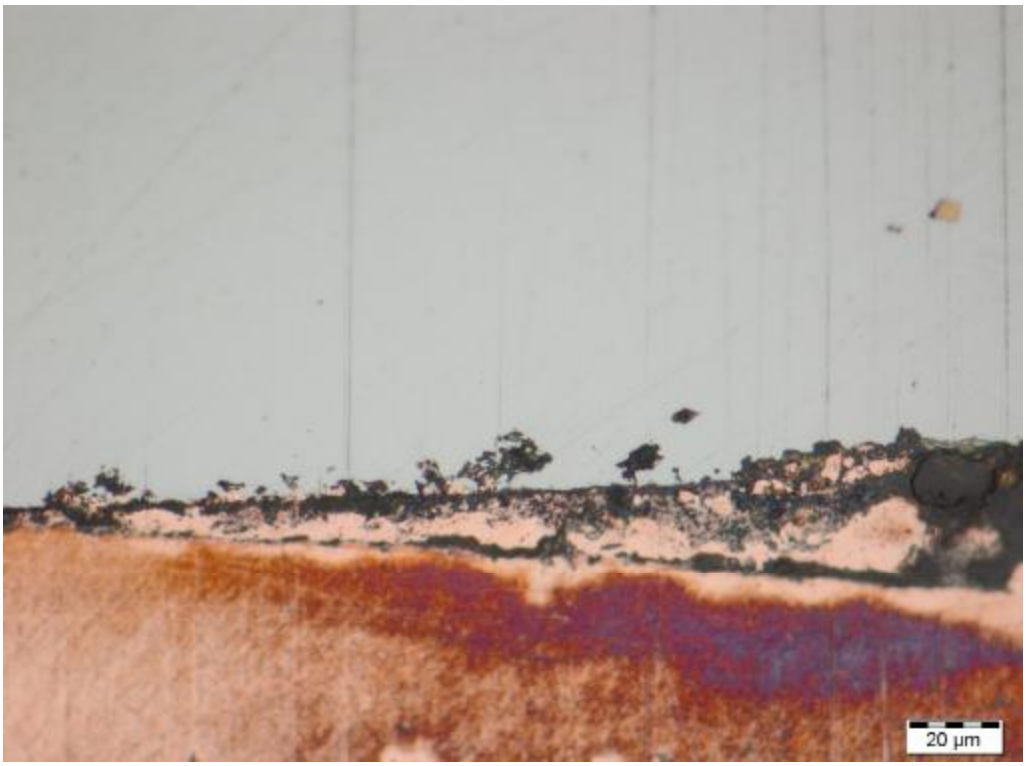


Figure 4.43. Micrograph of shallow attack on Sample 321-1.

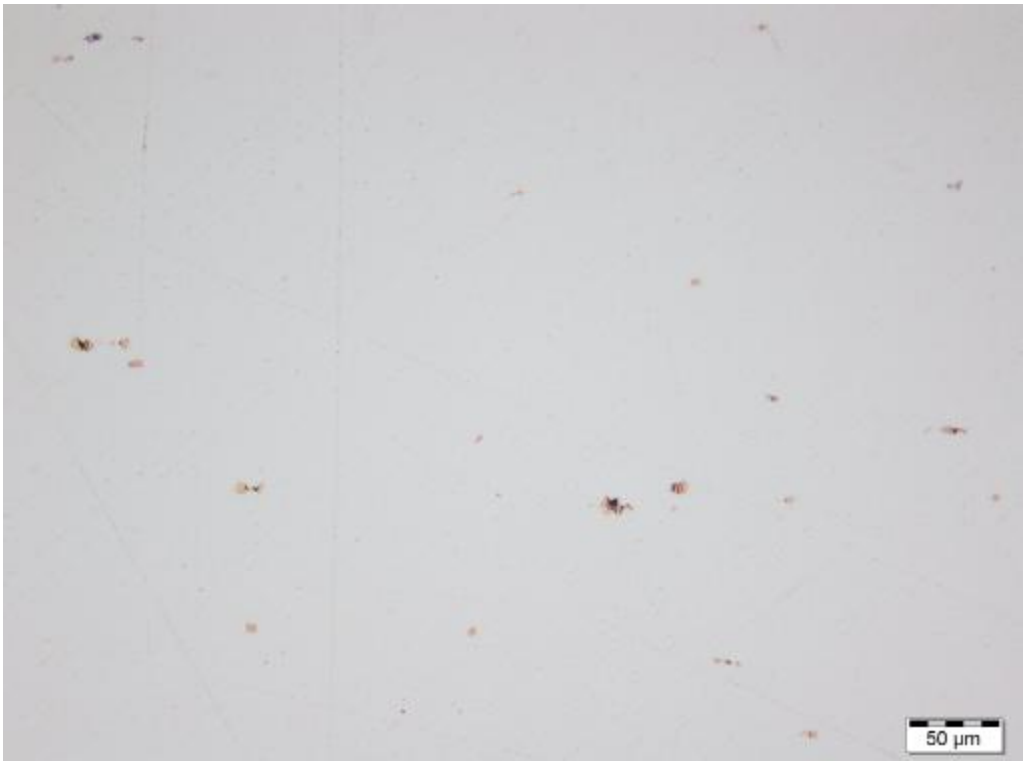


Figure 4.44. Micrograph of the titanium carbo-nitrides in Sample 321-1.



Figure 4.45. Higher magnification of Sample 321-1 showing attack associated with the titanium carbo-nitride precipitates.

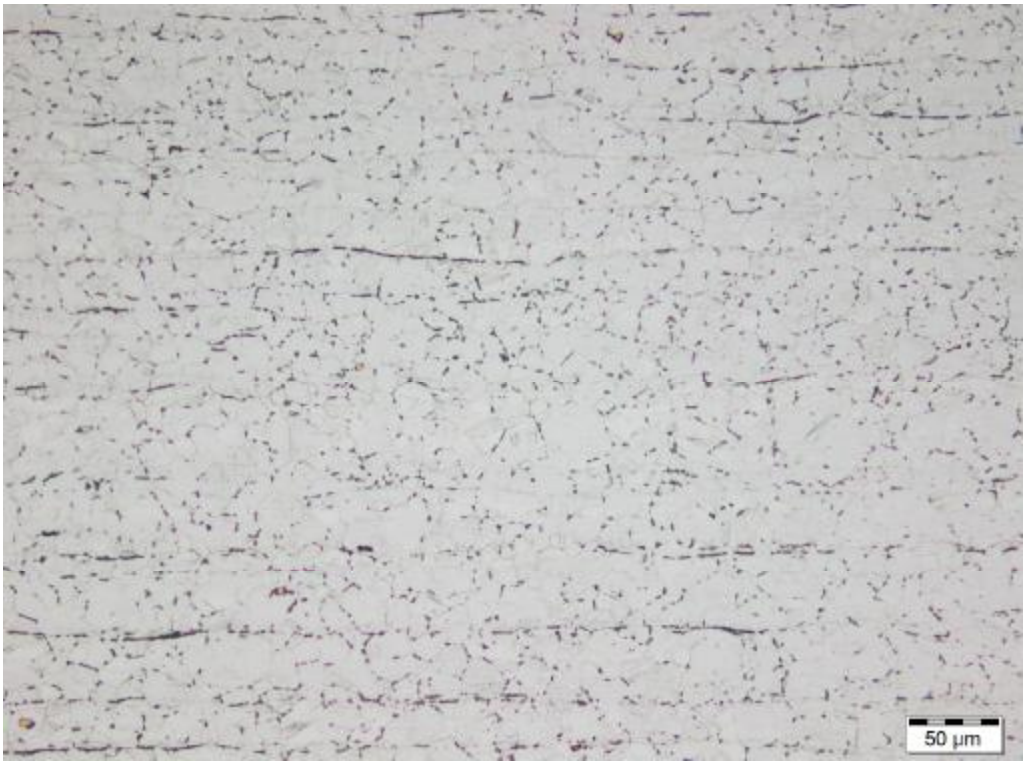


Figure 4.46. Micrograph of etched Sample 321-1 showing carburisation on grain boundaries.

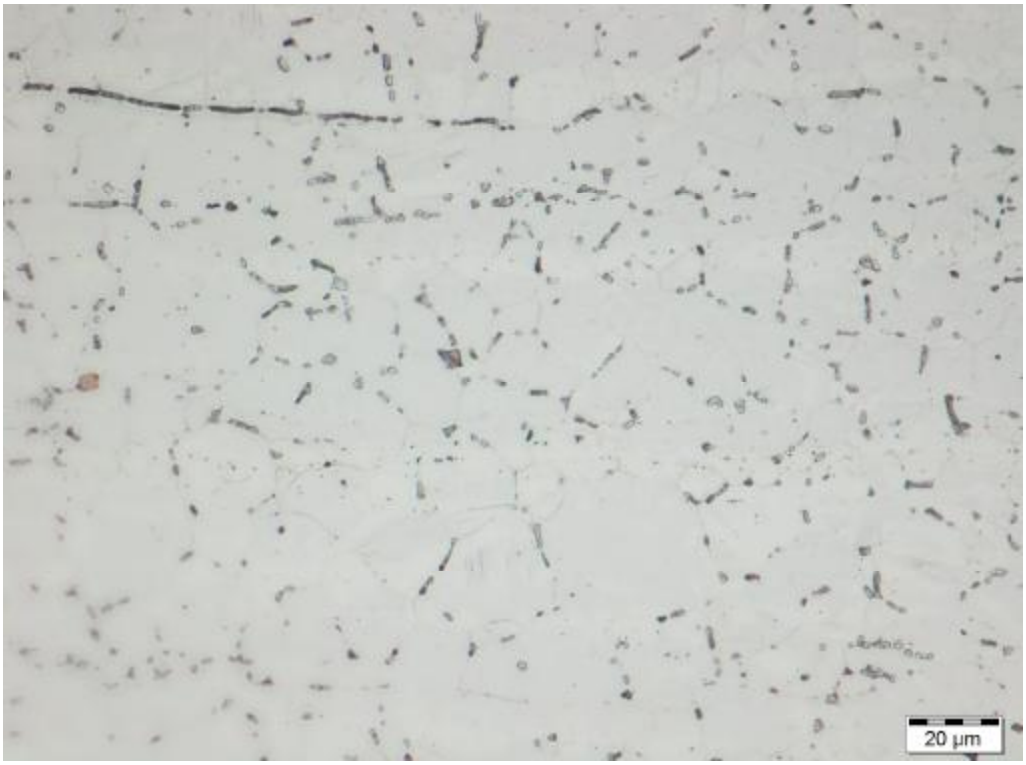


Figure 4.47. Higher magnification of the carbide distribution near the centre of the cross-section of Sample 321-1.

Figure 4.48 and Figure 4.49 are micrographs of cross-sections removed through the 316L samples showing localised attack in the form of intergranular corrosion. Cracks at the grain boundaries that were associated with the attack were evident, suggesting that mechanical stresses associated with the corrosion products were likely to have contributed in the degradation mechanism. Figure 4.50 is a micrograph of a pit near the edge of the sample also showing intergranular attack. The products and loose grains had disappeared (possibly by the sample preparation), leaving only a relatively clean pit. No surface attack was found associated with the 316Ti sample, but the titanium carbo-nitride precipitates also showed selective carburisation, similar to the 321 samples, as shown in Figure 4.51 and Figure 4.52. The titanium carbo-nitride distribution was layered, being associated with the thermo-mechanical processing of the sheet.

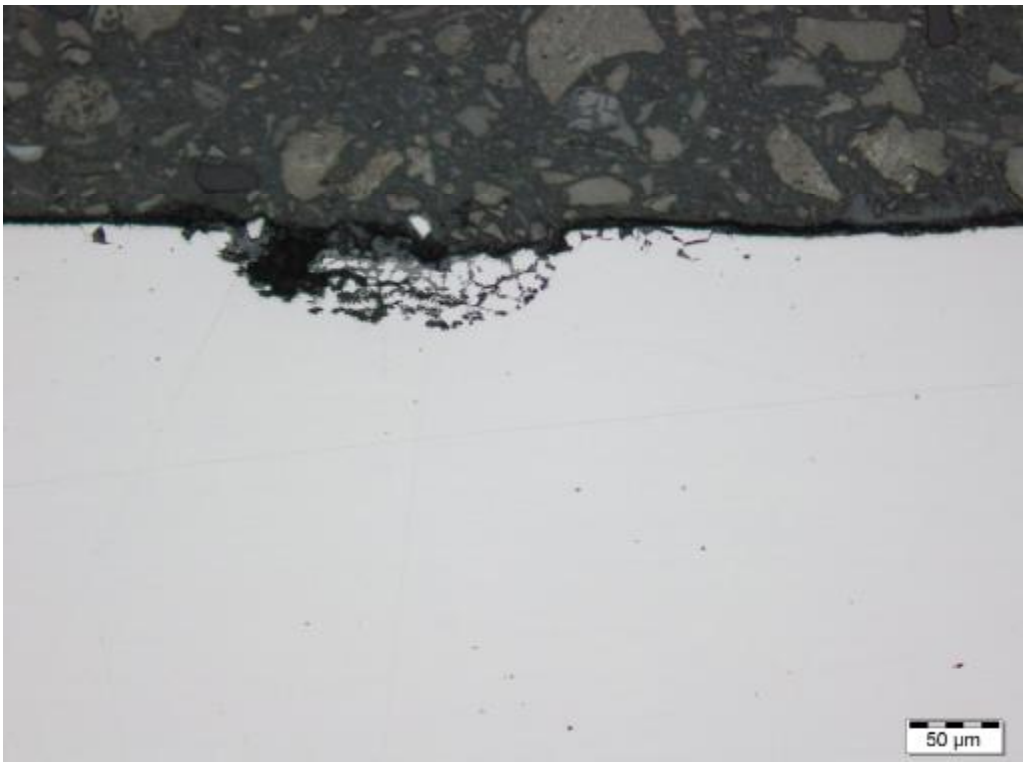


Figure 4.48. Micrograph of a pit in Sample 316 -1.

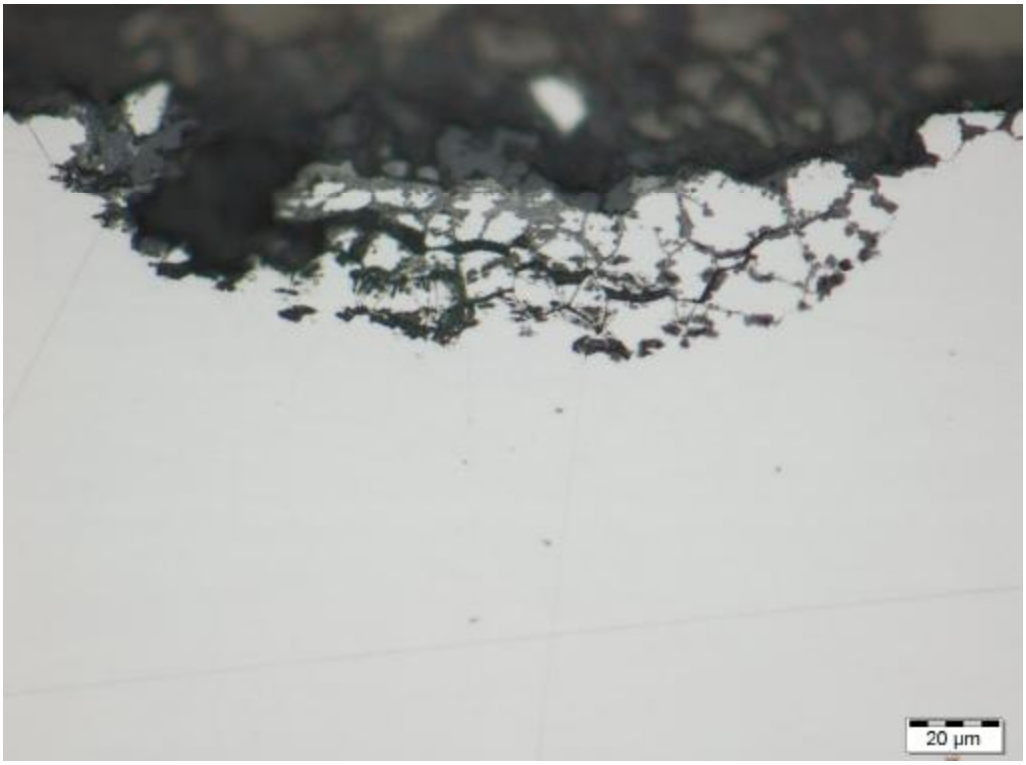


Figure 4.49. Higher magnification micrograph of Figure 4.48 showing the intergranular nature of the attack.

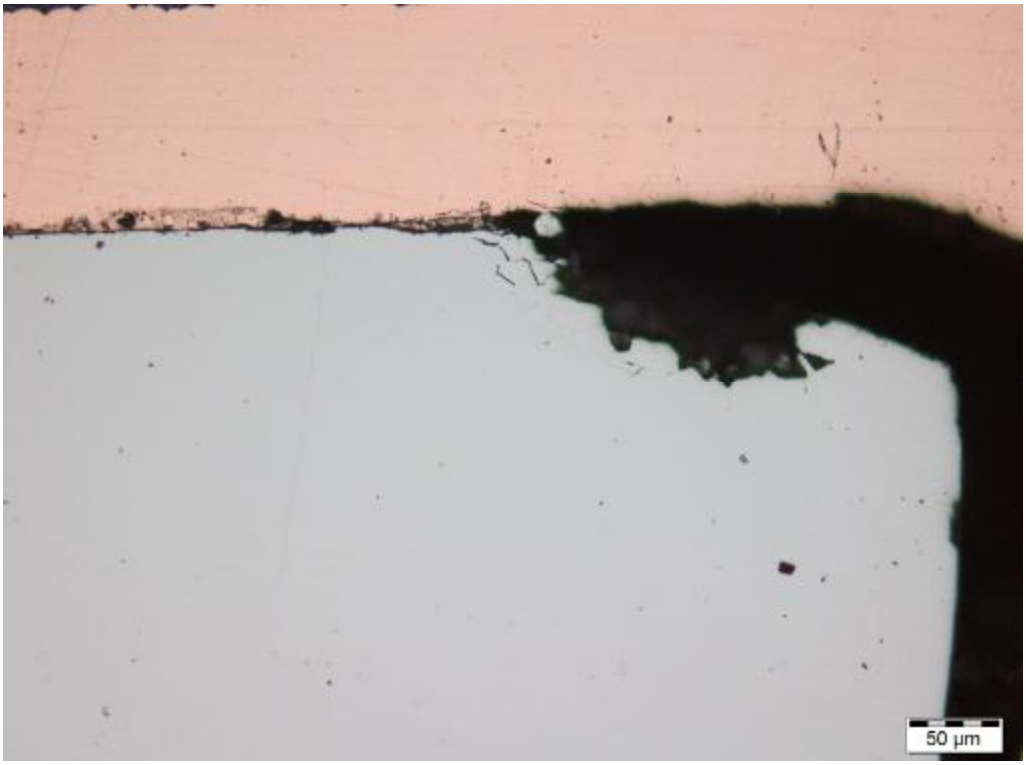


Figure 4.50. Micrograph of a pit at a corner on Sample 316-2.



Figure 4.51. Micrograph of the titanium carbo-nitride precipitates in Sample 316Ti-1.



Figure 4.52. Higher magnification micrograph showing selective attack of the titanium carbo-nitride precipitates in Sample 316Ti-1.

No surface attack was found on either of the Types 430 or 441 samples. Micrographs showing the carbide distribution in etched Type 430 are shown in Figure 4.53 and Figure 4.54 showing the layered structure typical of as-rolled samples. Figure 4.55 to Figure 4.57 show the selective carburisation of the titanium carbo-nitrides in the Type 441 stainless steel and the shallow attack. Figure 4.56 shows the internal carburisation (inside the dashed line) that resulted from the breaks in the oxide layer and subsequent attack. Figure 4.58 is an etched microstructure showing a thick chromium oxide film covering a carbide phase that formed at the surface. Figure 4.59 is a higher magnification micrograph of the titanium carbo-nitride precipitates in the matrix of the Type 441 sample, and also illustrates that the grains were recrystallized. The bimodal distribution consists of large titanium carbo-nitride precipitates, and smaller (iron and chromium) carbides. Not all the grain boundaries had precipitates.



Figure 4.53. Micrograph of the carburisation in Sample 430-1.

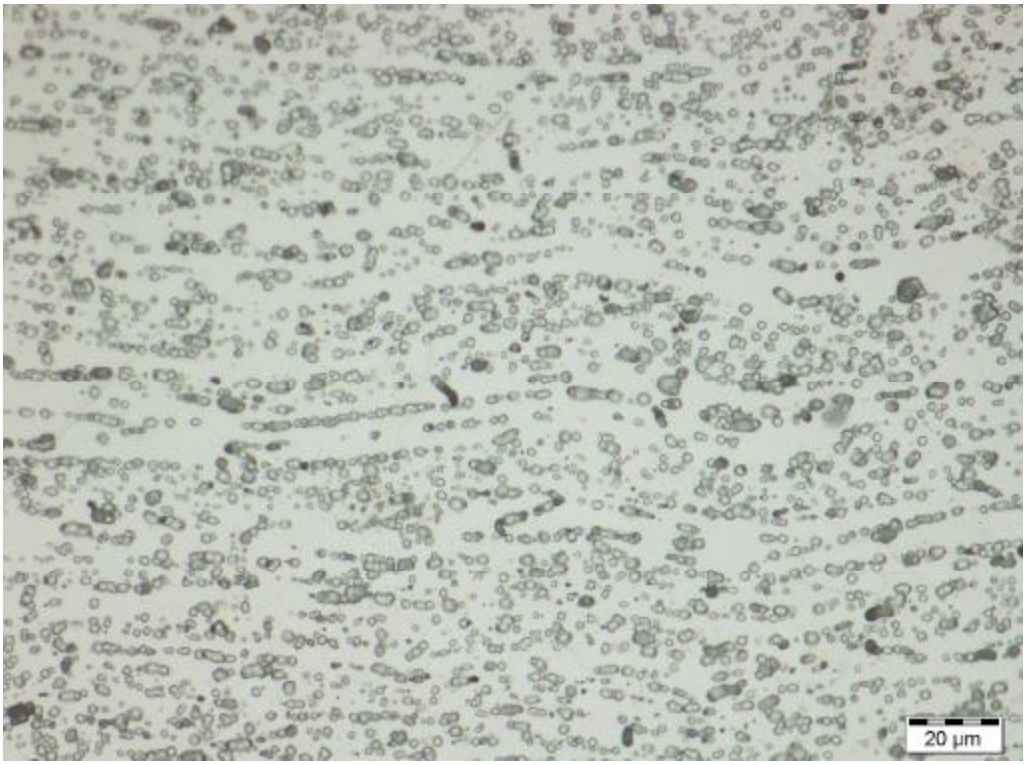


Figure 4.54. Higher magnification micrograph of the carbide distribution near the centre of the cross-section of Sample 430-1.



Figure 4.55. Micrograph of Sample 441-1 showing the titanium carbo-nitride precipitate distribution.

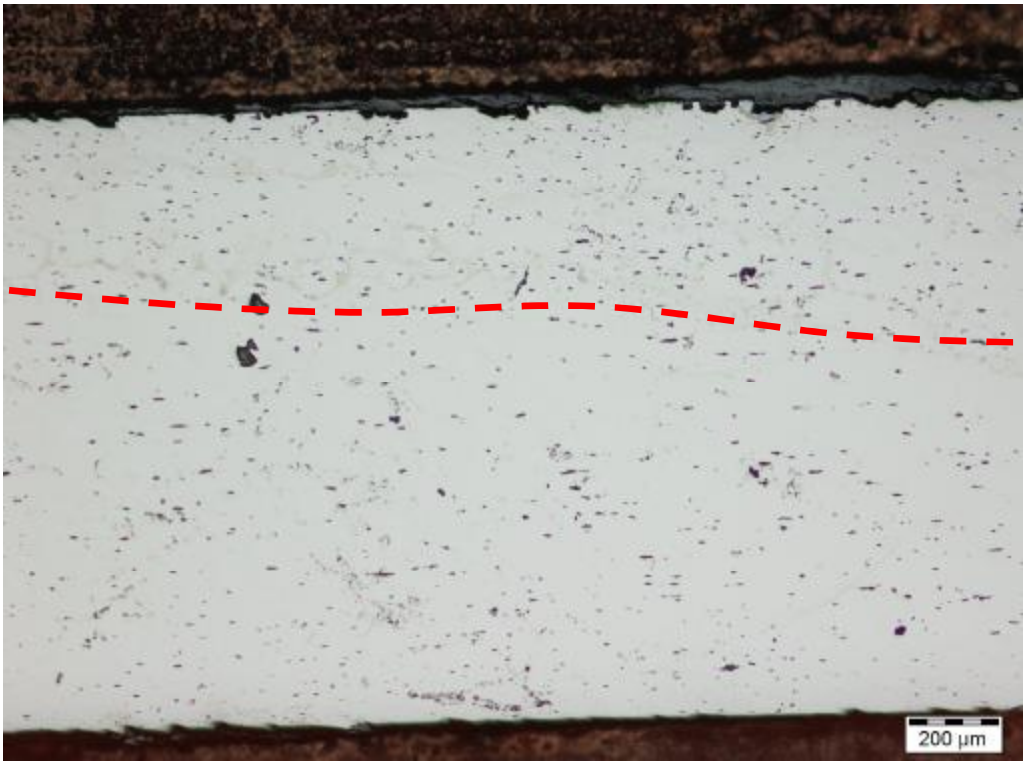


Figure 4.56. Micrograph showing shallow attack and carburisation associated with the damaged oxide layer in Sample 441-1.



Figure 4.57. Micrograph of Sample 441-1 in the etched condition.

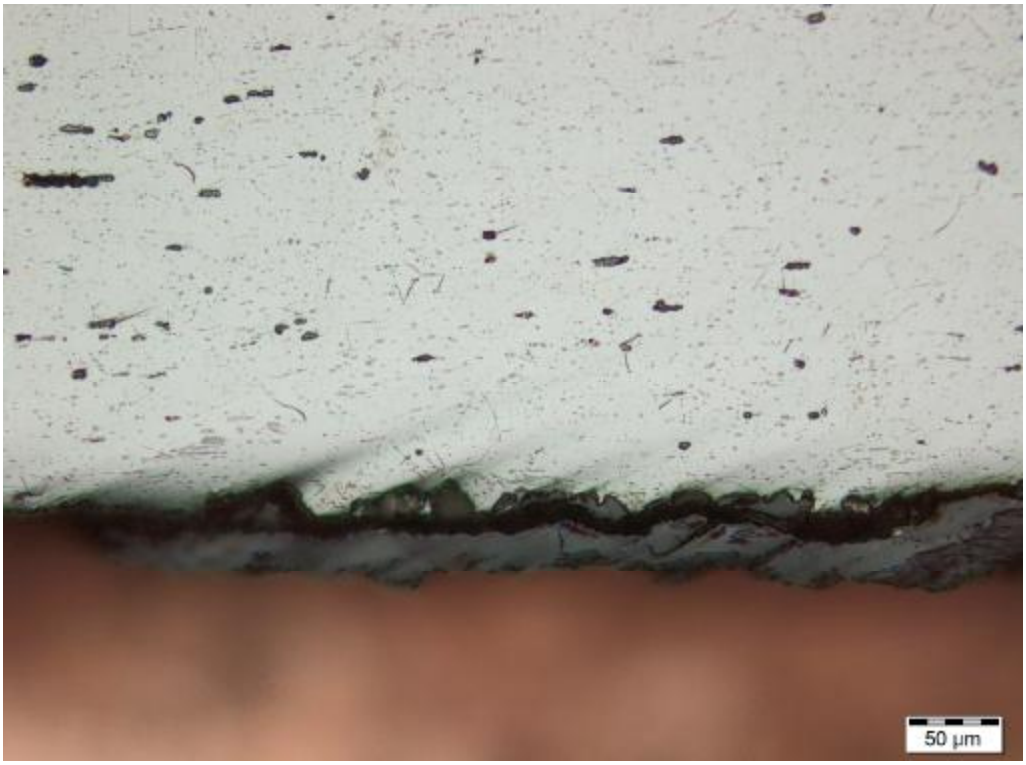


Figure 4.58. Higher magnification micrograph of shallow attack on Sample 441-1 in the etched condition.

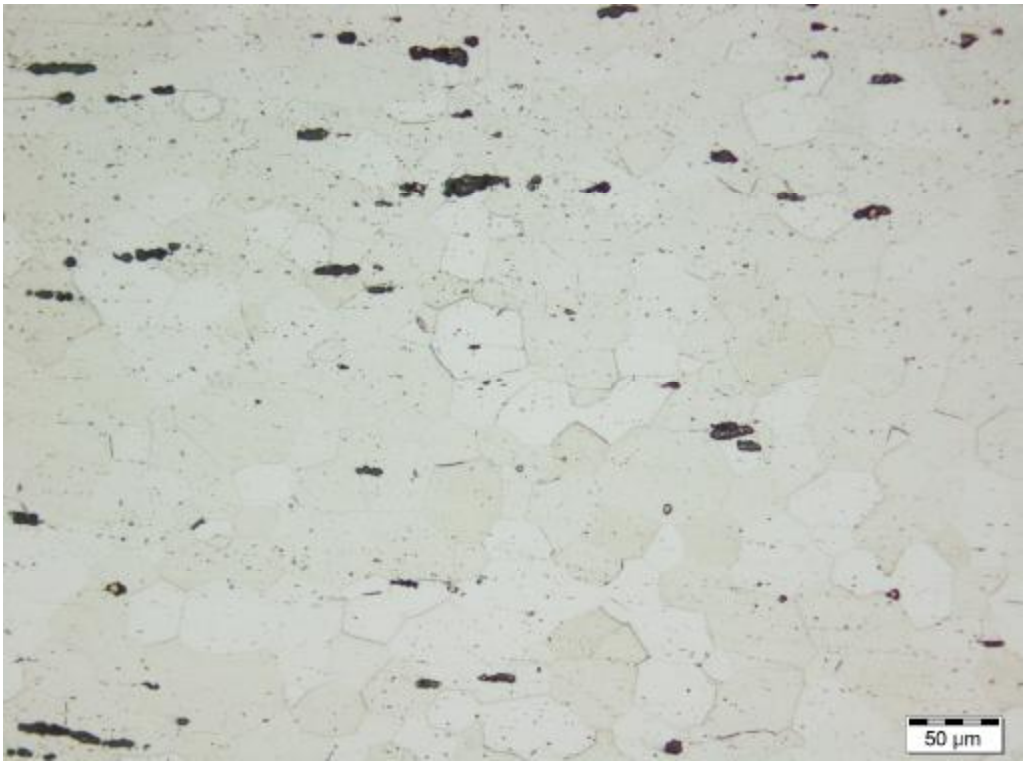


Figure 4.59. Higher magnification micrograph of the titanium carbo-nitrides in the matrix of Sample 441-1 (etched).

4.2.4. Scanning Electron Microscopy

Figure 4.60 is an SEM image of the surface of the Type 304L sample that was exposed for seven days in the furnace, showing light and darker areas. Figure 4.61 and Figure 4.62 are SEM images of the lighter areas, showing that these areas were relatively smooth (the grinding marks can be seen). Figure 4.63 and Figure 4.64 are SEM images of the darker areas, illustrating that these areas were relatively rougher, with more of the white needle-like phase and also more pits. Figure 4.65 is a SEM image from near the edge of the 304L sample showing intergranular attack associated with a dark area. White spheroidal particles were also present and associated with the attack. Figure 4.66 is an EDX spectrum of the white phase, illustrating that it primarily consists of iron and chromium, with oxygen and carbon also present. It is likely that this phase is a metal carbide, but this was not conclusively proven, due to the fact that carbon from the coking was present over most of the surfaces. However, since the white phase particles were much less than 3 µm across, there would have been substantial pick-up of the substrate. The chromium content was lower than the substrate, indicating that particles were not chromium carbides.

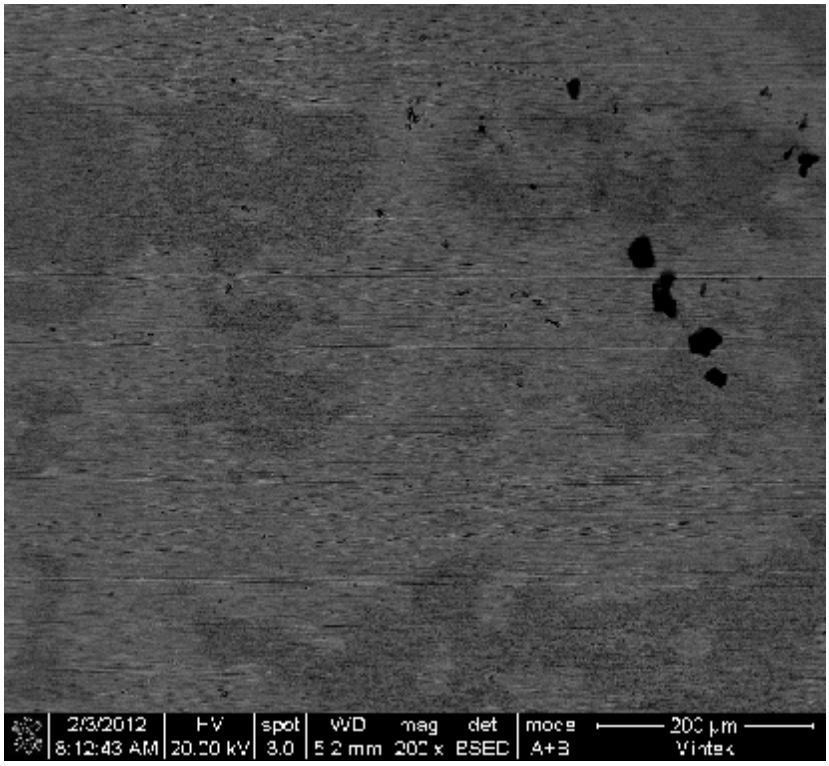


Figure 4.60. SEM-BSE image of the surface of Sample 304-1.

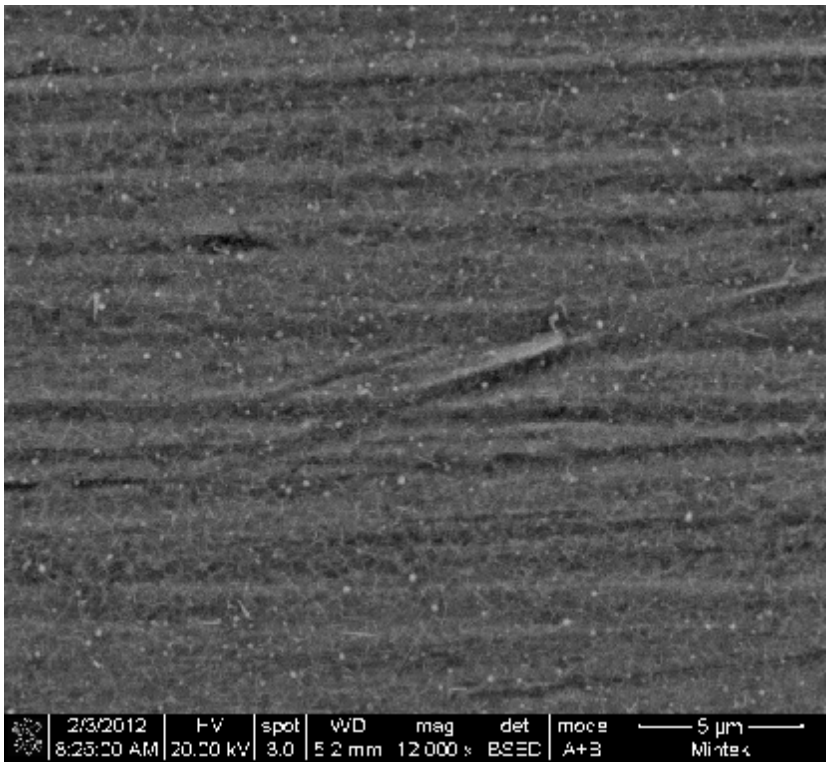


Figure 4.61. SEM-BSE image of the lighter areas shown in Figure 4.60.

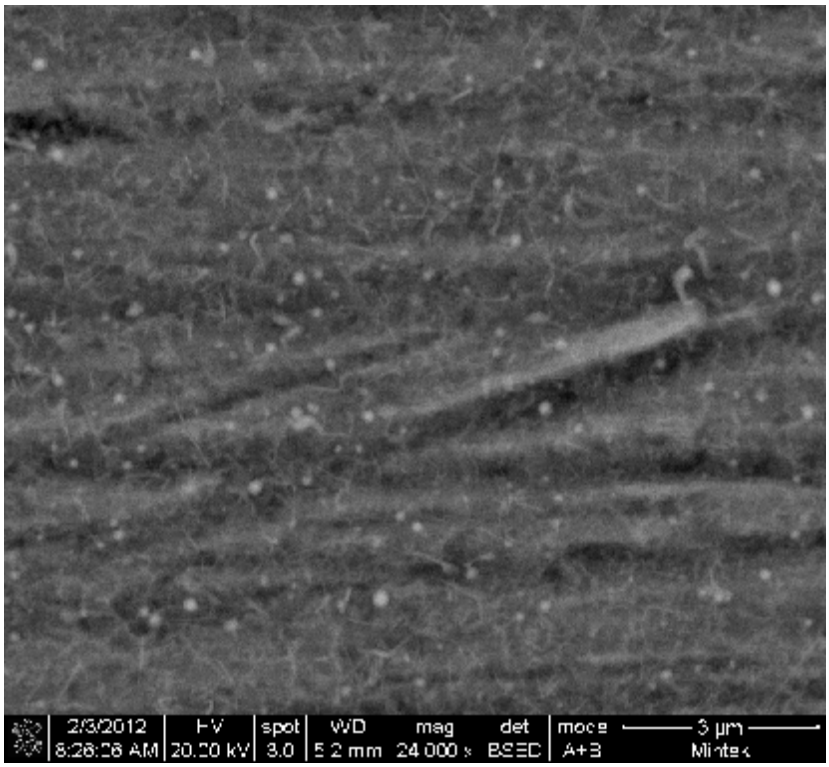


Figure 4.62. Higher magnification SEM-BSE image of the lighter areas shown in Figure 4.61.

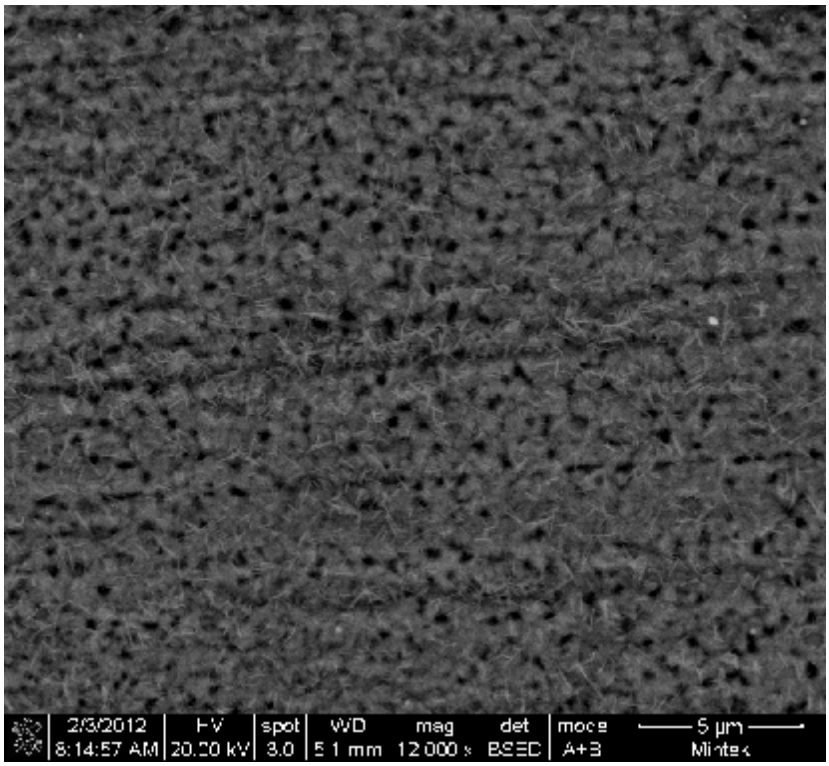


Figure 4.63. SEM-BSE image of the darker areas on Sample 304-1 shown in Figure 4.60.

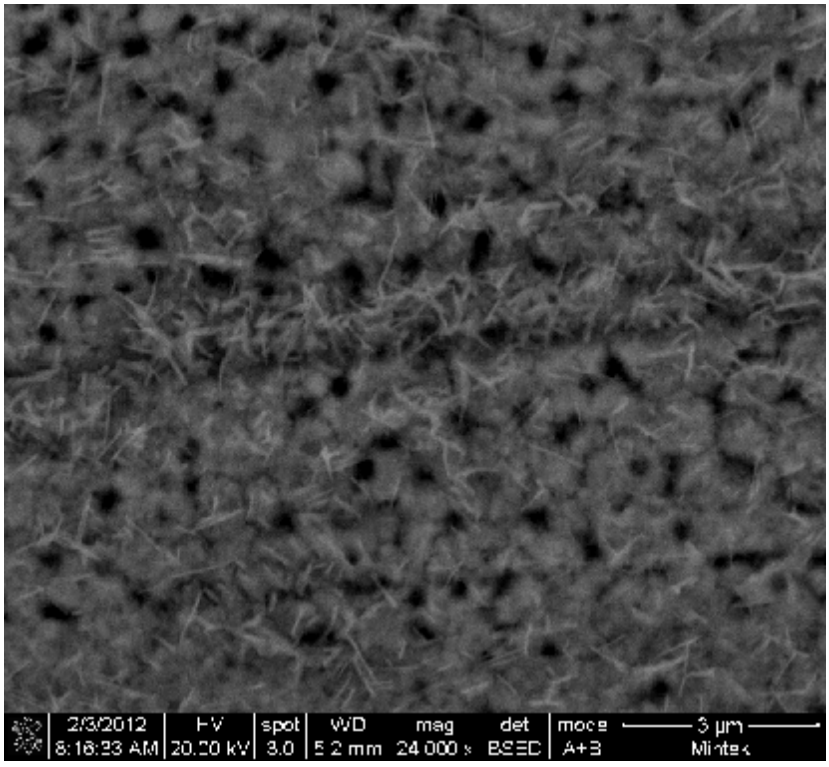


Figure 4.64. Higher magnification SEM-BSE image of Sample 304-1 shown in Figure 4.63.

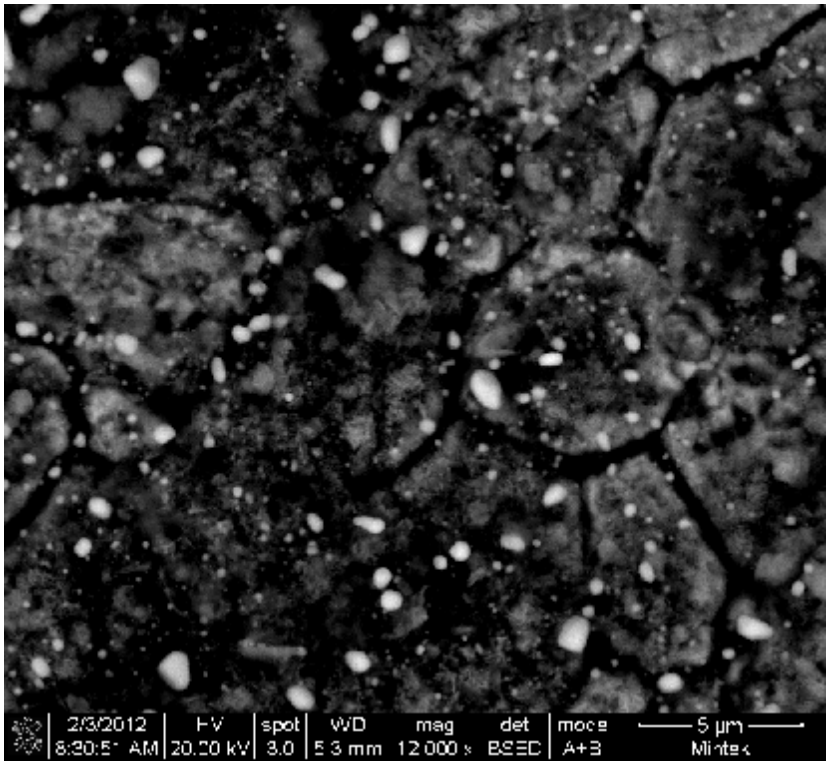


Figure 4.65. SEM-BSE image of grain boundary attack and white particles on the surface of Sample 304-1.

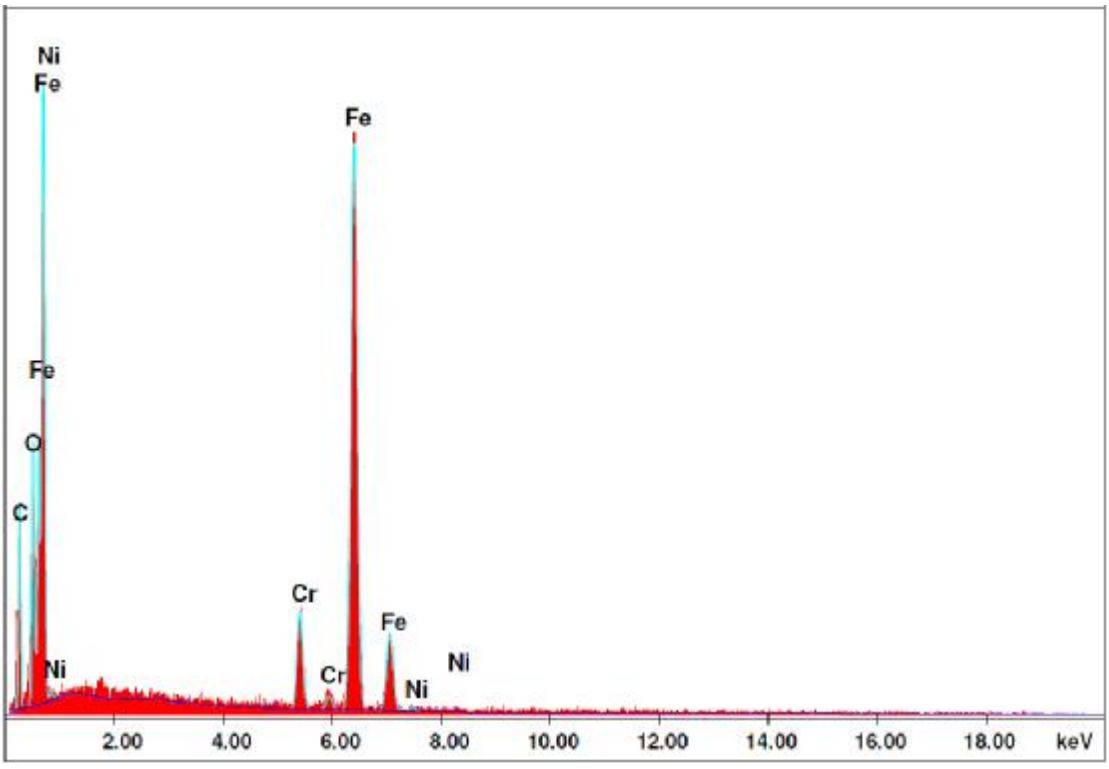


Figure 4.66. EDX spectrum of the white particles (including some matrix) on the surface of Sample 304-1 shown in Figure 4.65.

Figure 4.67 is an SEM image of the surface of the Type 321 sample exposed for seven days, which also showed light and dark areas. Figure 4.68 and Figure 4.69 are SEM images of the lighter areas showing a relative smooth surface compared to the darker areas, shown in Figure 4.70 and Figure 4.71. The particles associated with the light areas were more faceted than on the Type 304L samples analysed. It is not clear whether they are platelets. The particles associates with the dark areas were less faceted, and could be associated with the growth of thick oxide scale.

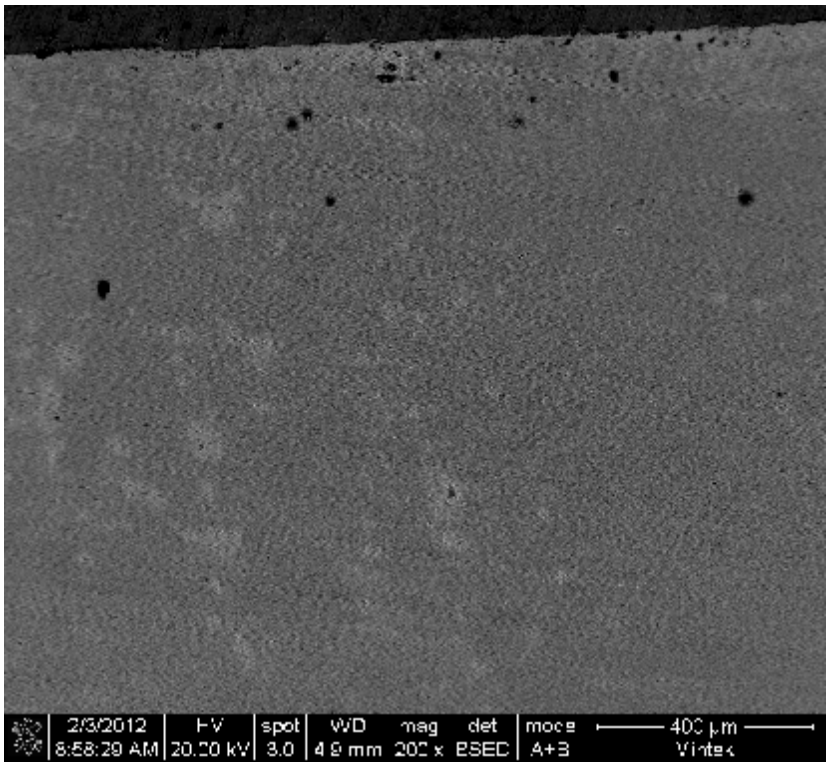


Figure 4.67. SEM-BSE image of the surface of Sample 321-1.

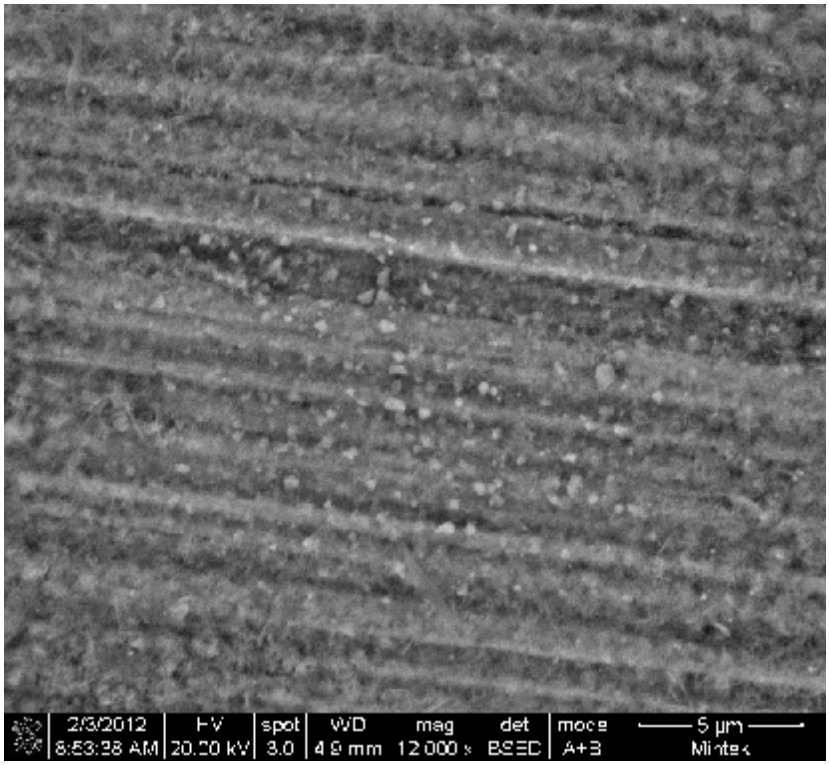


Figure 4.68. SEM-BSE image of the light areas on Sample 321-1 shown in Figure 4.67.

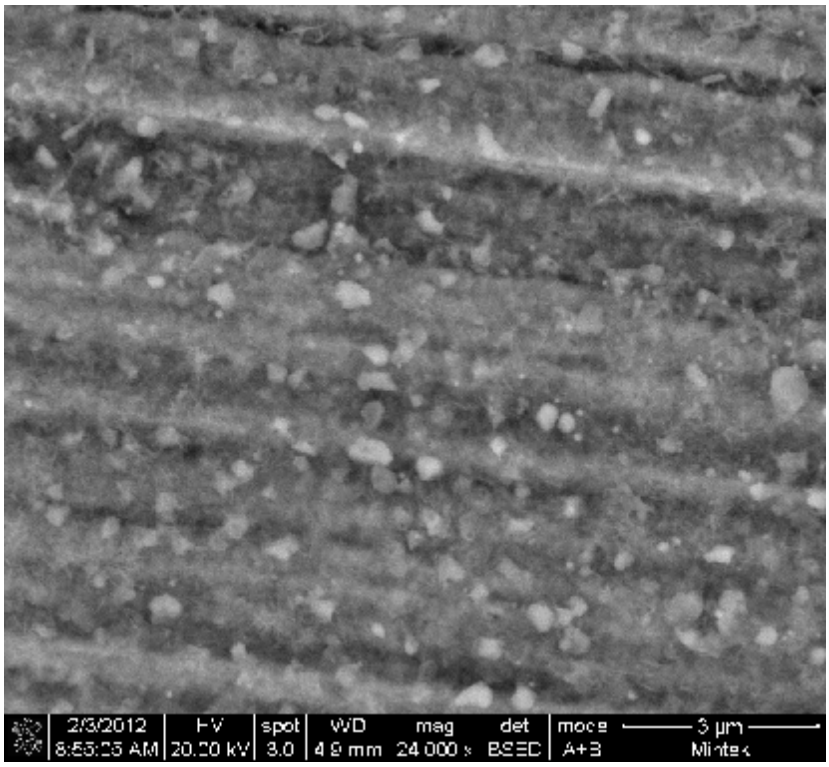


Figure 4.69. Higher magnification SEM-BSE image of Sample 321-1 shown in Figure 4.68.

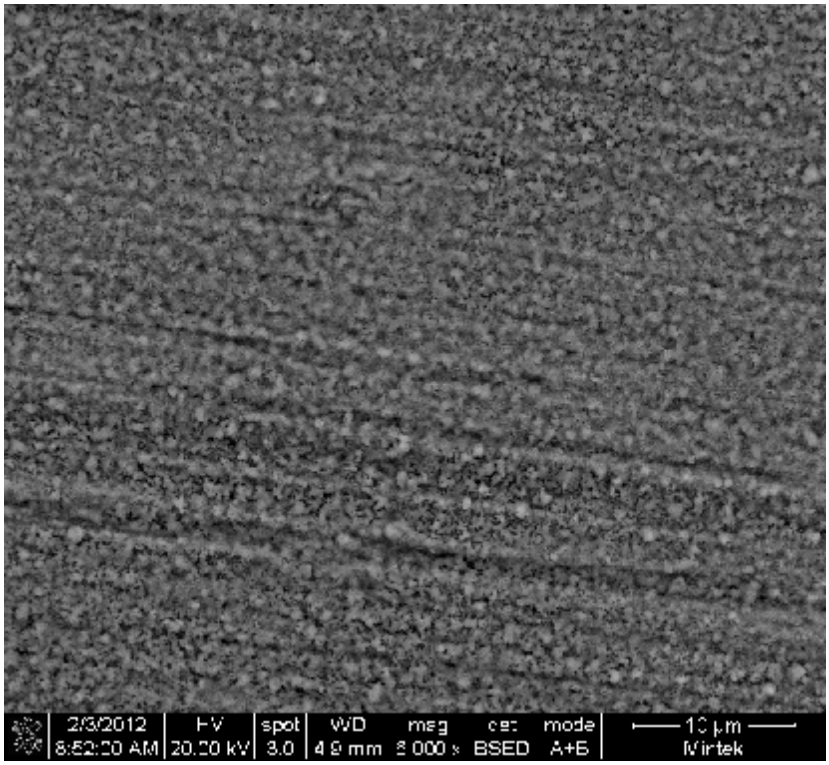


Figure 4.70. SEM-BSE image of the dark areas on Sample 321-1 shown in Figure 4.67.

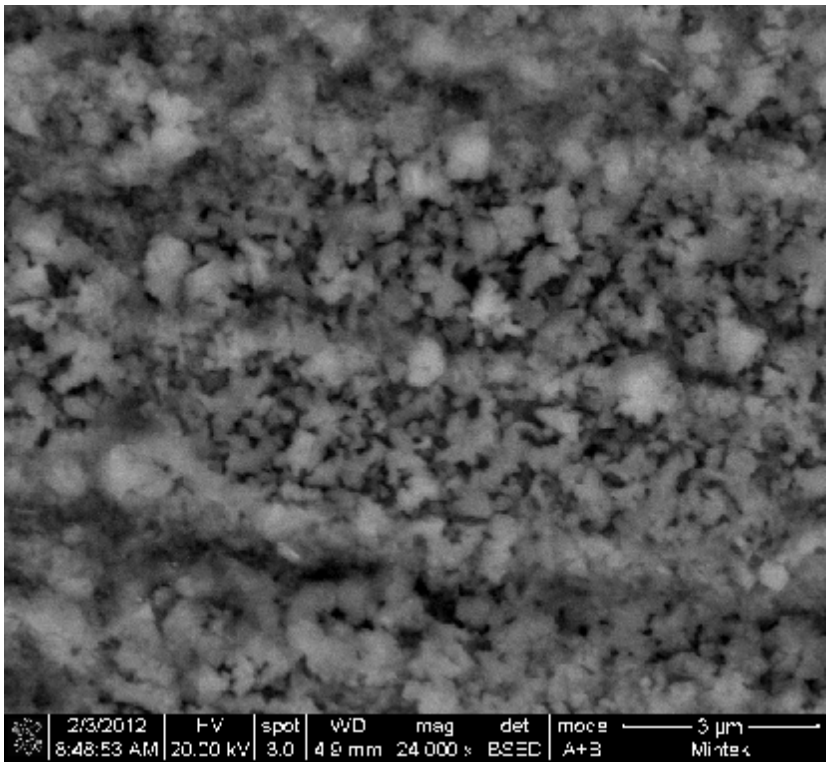


Figure 4.71. Higher magnification SEM-BSE image of the dark areas on Sample 321-1 shown in Figure 4.67.

Figure 4.72 is a SEM image of the surface of a Type 316L sample that was exposed for seven days. Figure 4.73 is an SEM image of a lighter area showing a smooth surface with white precipitates, and Figure 4.74 is an image of a darker area showing a greater degree of attack, being rougher. The darker appearance could also be associated with the growth of thick oxide scale on the surface, and is just gaps between the individual oxide grains. Figure 4.75 is a SEM image of an area where pitting initiated. The white particles associated with the pitting appeared generally larger than those particles away from the pitting attack.

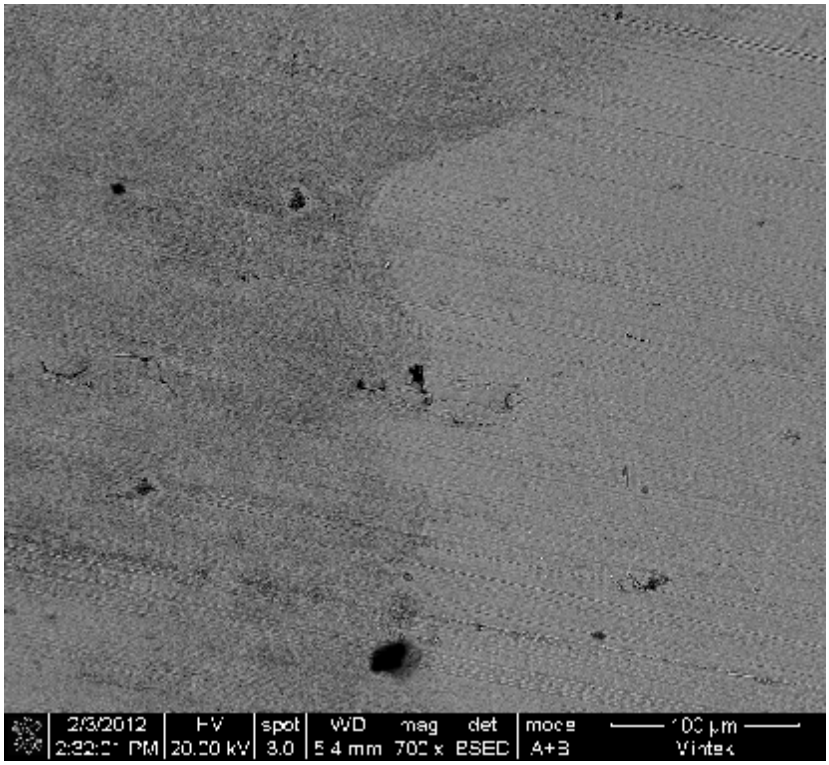


Figure 4.72. SEM-BSE image of the surface of Sample 316-1.

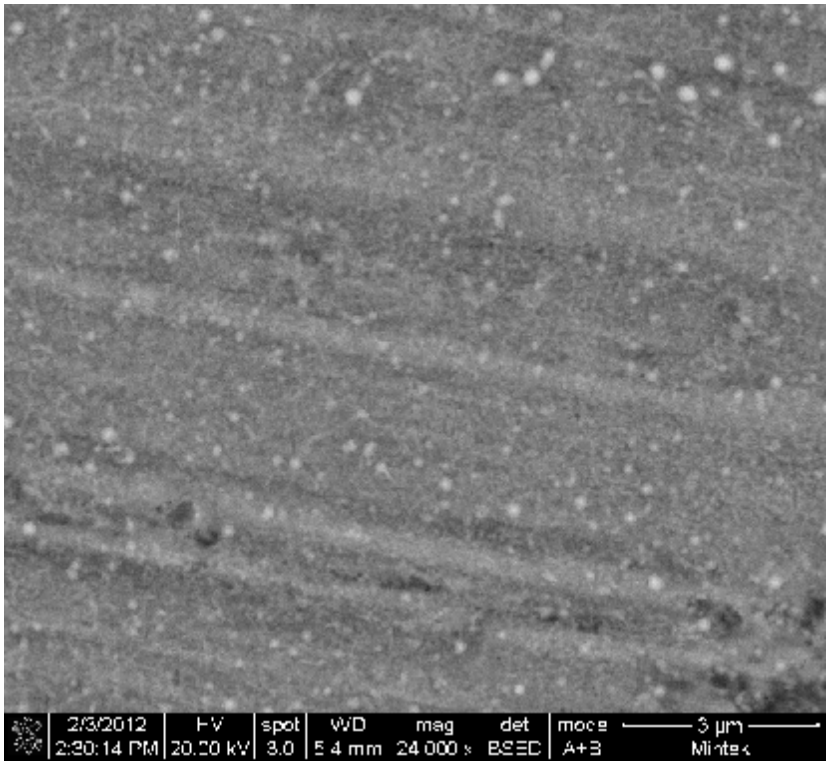


Figure 4.73. Higher magnification SEM-BSE image of the light areas on Sample 316-1 shown in Figure 4.72.

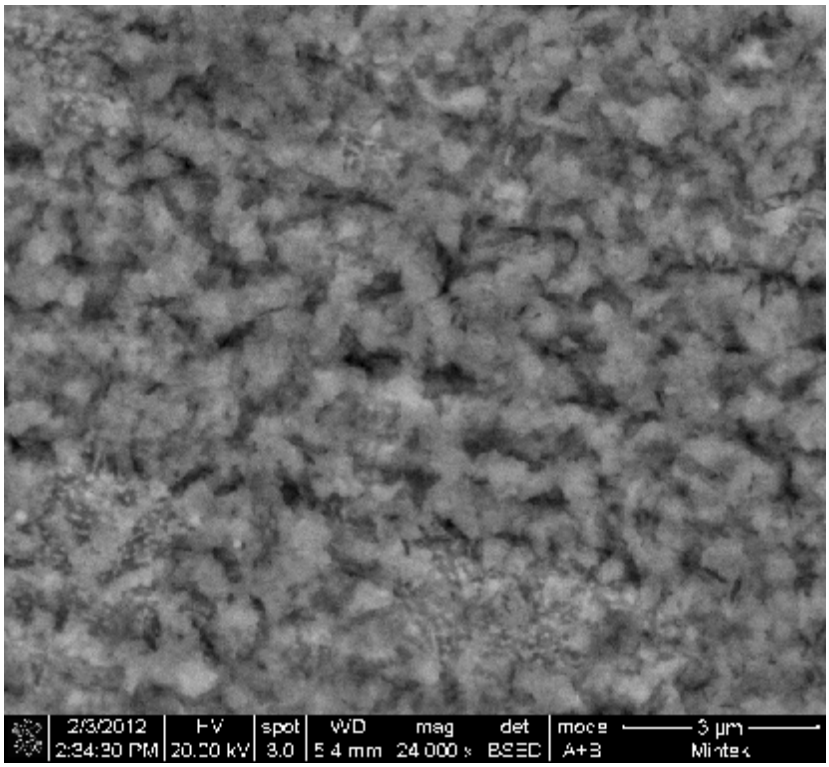


Figure 4.74. Higher magnification SEM-BSE image of the dark areas shown in Figure 4.72.

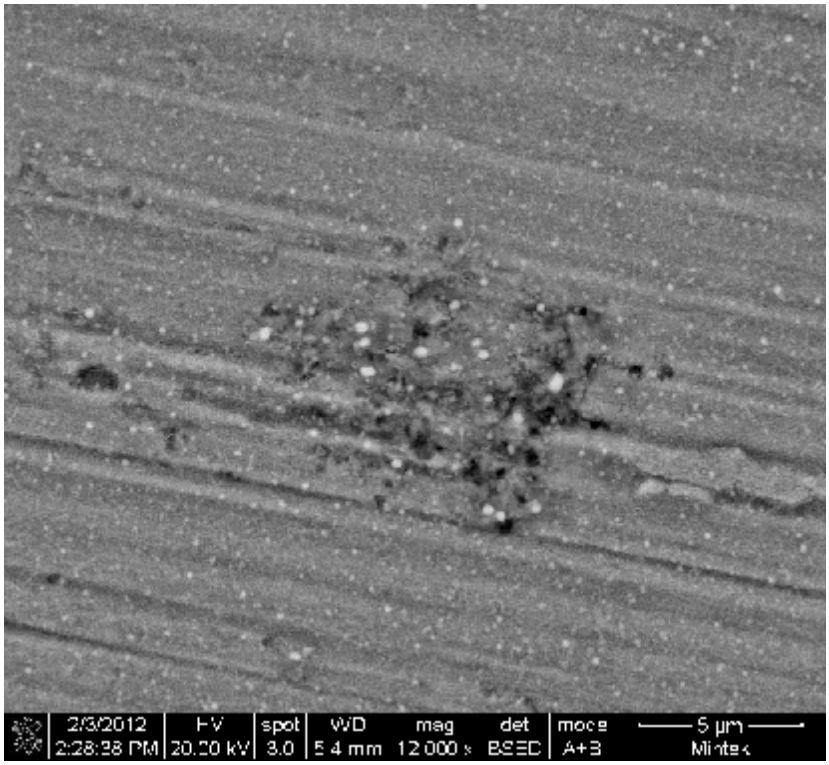


Figure 4.75. SEM-BSE image of the initiation of pitting on the surface of Sample 316-1.

Figure 4.76 and Figure 4.77 are SEM images of the surface of a Type 316Ti sample exposed for seven days to the furnace, also showing some scratches. Figure 4.78 is a higher magnification image of a lighter area and Figure 4.79 of a darker area, both also showing a needle-like phase, with the darker area having more. Again, the darker area was rougher and therefore associated with a greater degree of attack. Figure 4.80 is an SEM image of the 316Ti near the edge showing more attack than elsewhere on the sample. Figure 4.81 is an image of a relative lighter area and Figure 4.82 shows greater attack in the form of intergranular attack, also showing the facetted nature of the white particles. Figure 4.83 is an EDX spectrum of the white particles associated with the attack, consisting predominantly of iron and chromium (even though some matrix would also have been included), similar to the particles found on the Type 304L sample (Figure 4.66).

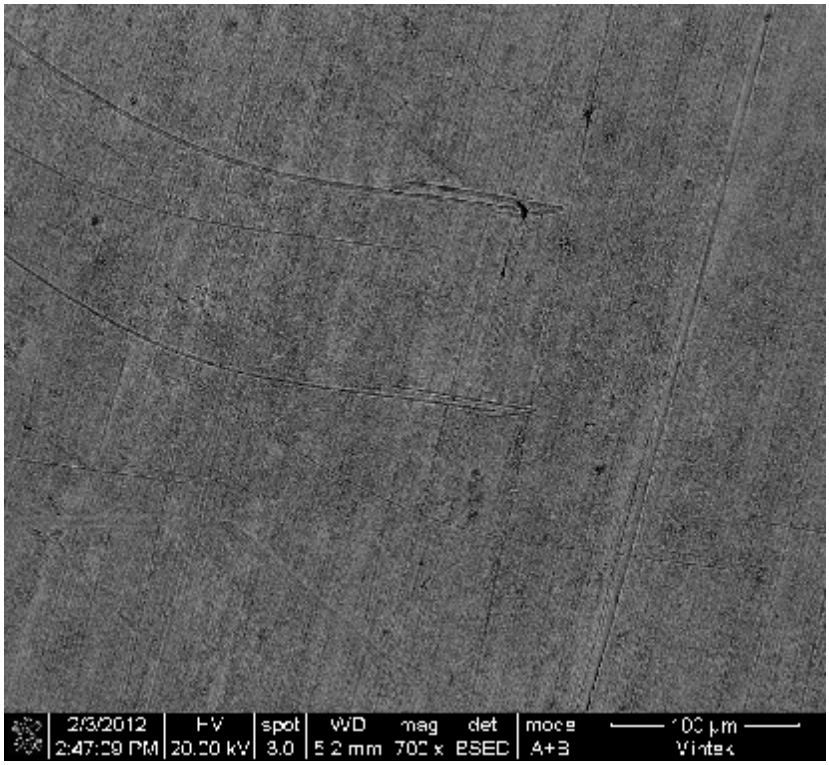


Figure 4.76. SEM-BSE image of the surface of Sample 316Ti-1.

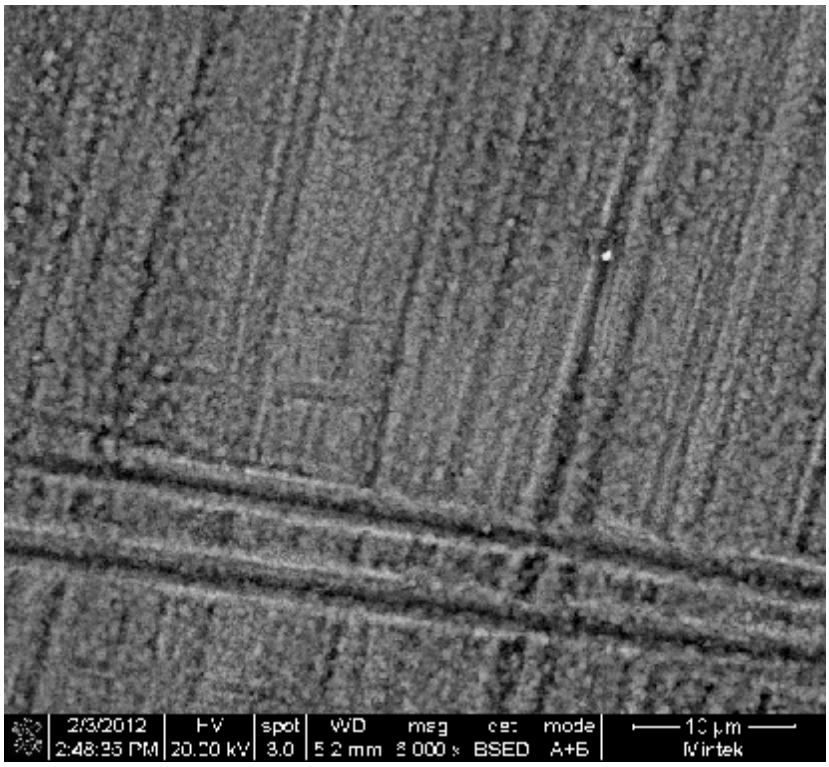


Figure 4.77. Higher magnification SEM-BSE image of Sample 316Ti-1 shown in Figure 4.76.

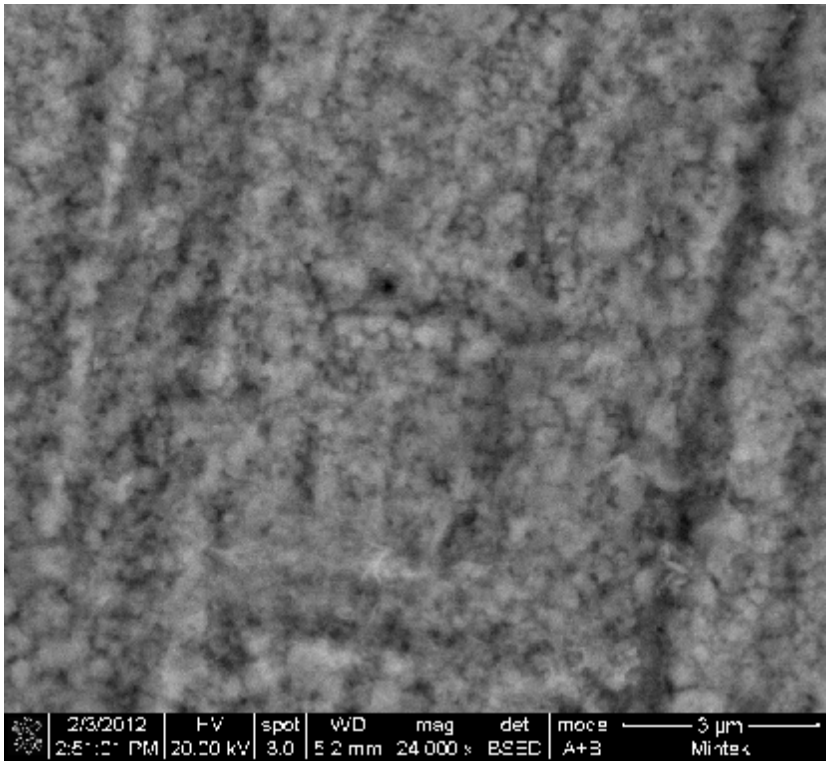


Figure 4.78. Higher magnification SEM-BSE image of the lighter areas on Sample 316Ti-1 shown in Figure 4.76.

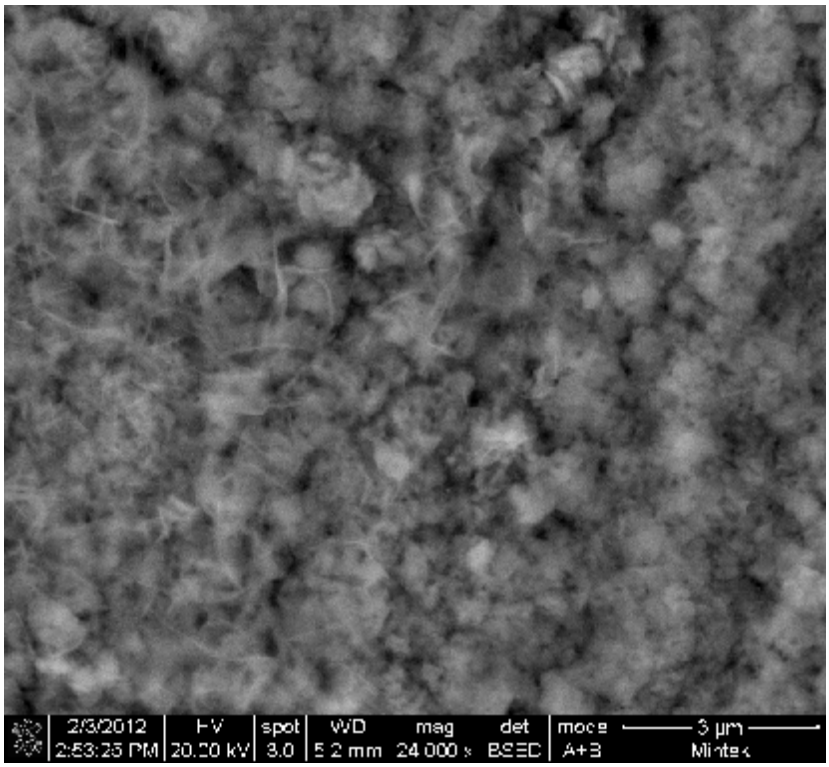


Figure 4.79. Higher magnification SEM-BSE image of the darker areas on Sample 316Ti-1 shown in Figure 4.76.

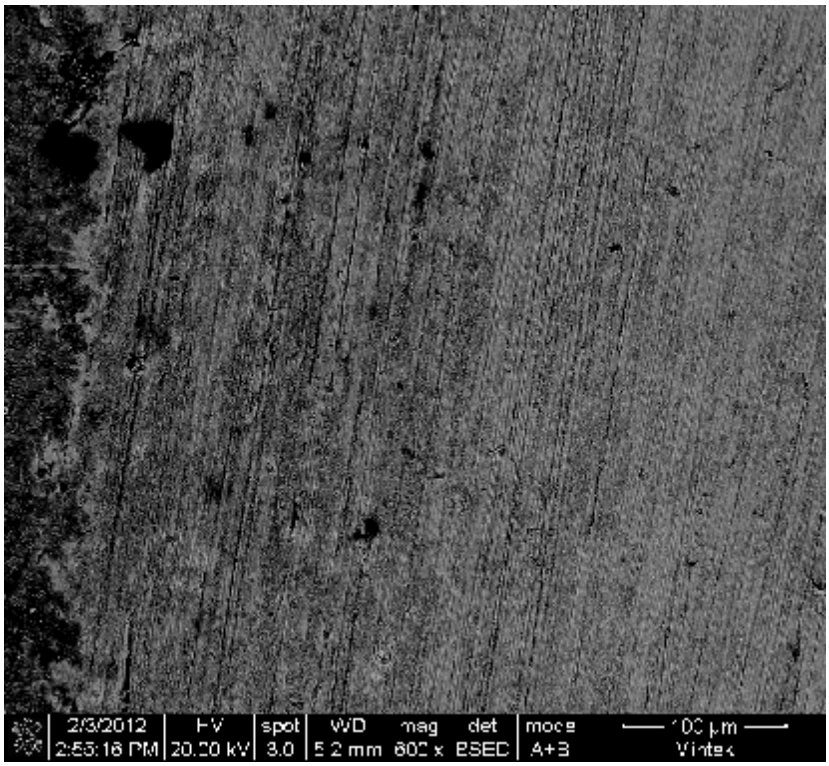


Figure 4.80. SEM-BSE image of the surface near the edge of Sample 316Ti-1.

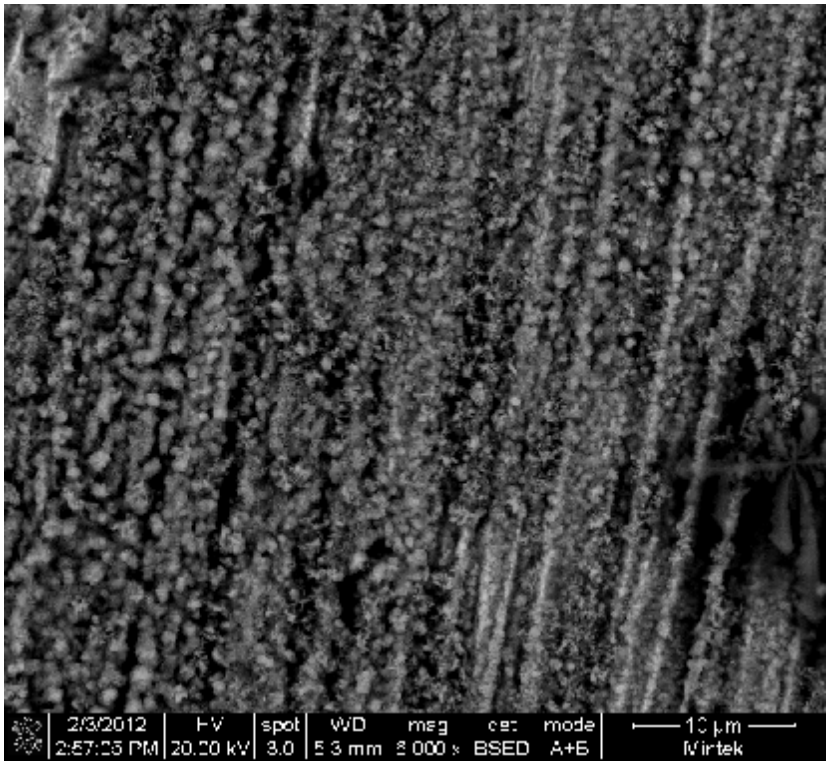


Figure 4.81. SEM-BSE image of the lighter areas of Sample 316Ti-1 shown in Figure 4.80.

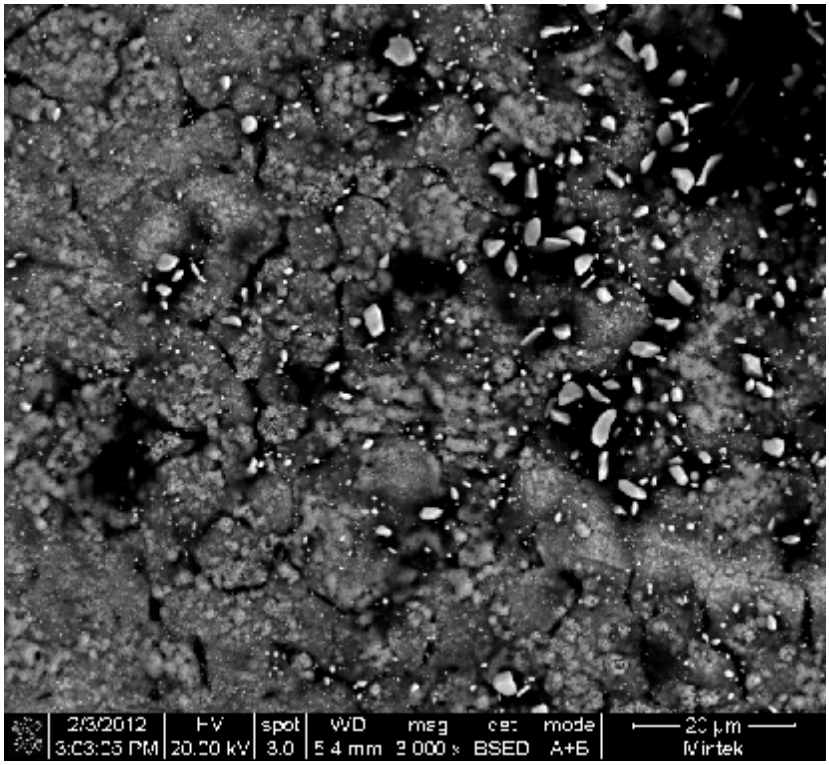


Figure 4.82. SEM-BSE image of intergranular attack associated with the darker areas in Sample 316Ti-1 shown in Figure 4.80.

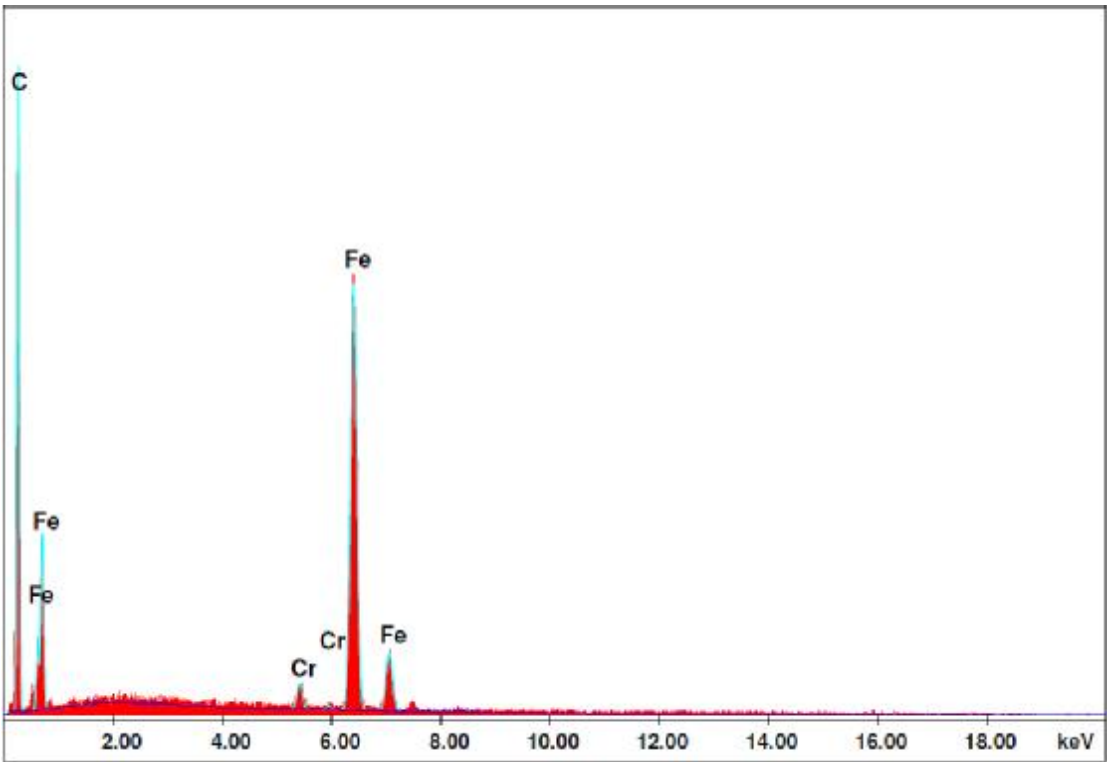


Figure 4.83. EDX spectrum of the light particles (including some matrix) on Sample 316Ti-1 shown in Figure 4.82.

Figure 4.84 and Figure 4.85 are SEM images of the surface of a Type 430 sample exposed for seven days to the furnace. No attack or lighter / darker areas were found on the surface of the sample. There were globular and a finer needle-like phases on the surfaces. Figure 4.86 is an SEM image of a Type 441 samples exposed for seven days. No significant attack was also found on these samples, but lighter and darker areas were identified. Figure 4.87 and Figure 4.88 are images of lighter areas that were generally smoother. Figure 4.89 is an SEM image of a darker area and Figure 4.90 is a SEM of the same area. Figure 4.91 is a higher magnification SEM image of the darker area showing the rougher surface finish associated with a greater degree of attack. Some of the particles appeared to be plates.

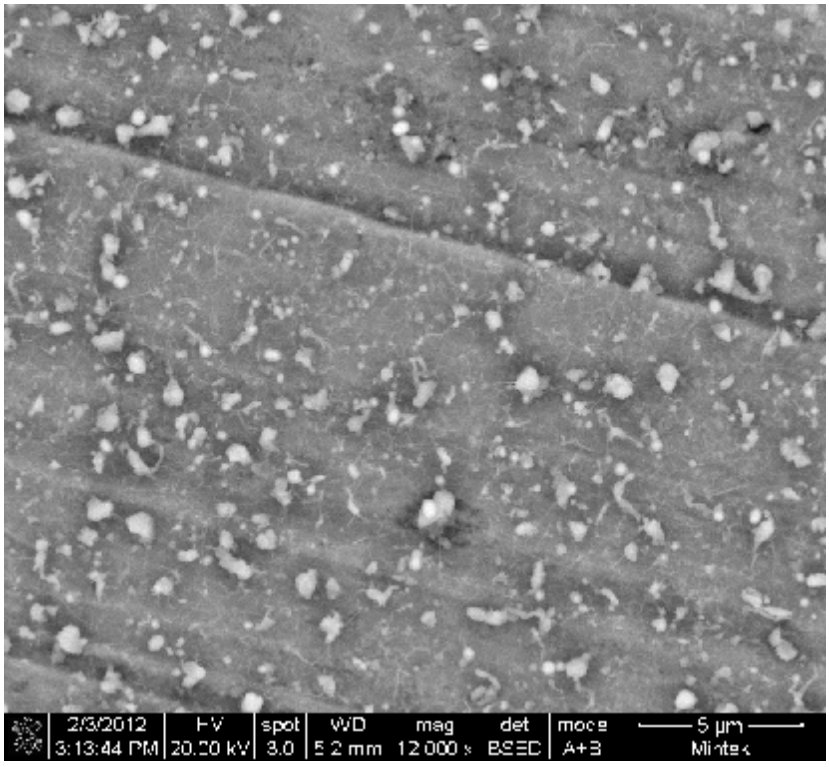


Figure 4.84. SEM-BSE image of the surface of Sample 430-1.

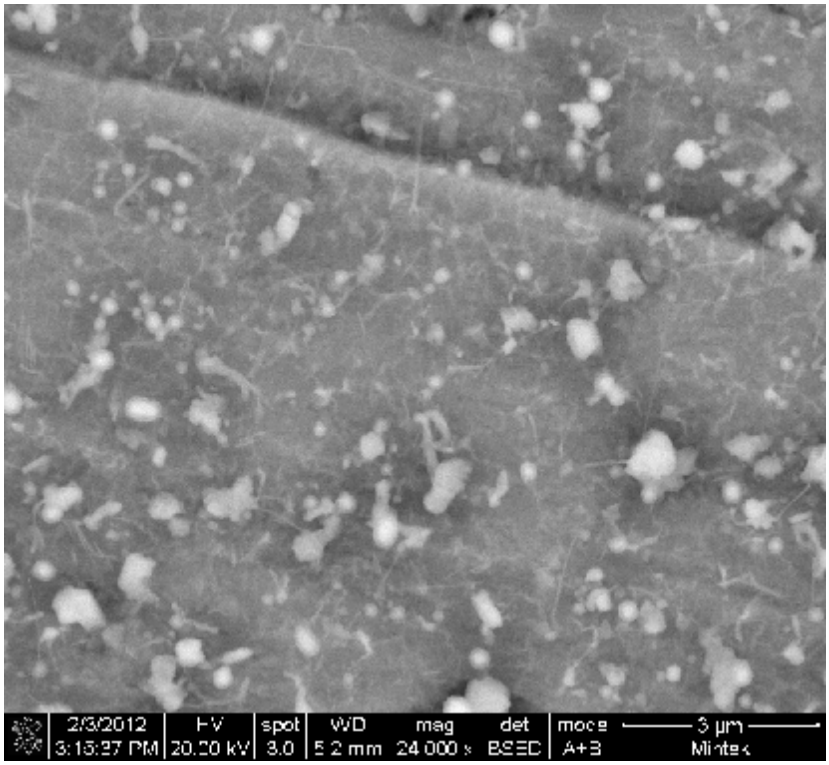


Figure 4.85. Higher magnification SEM-BSE image of Sample 430-1 shown in Figure 4.84.

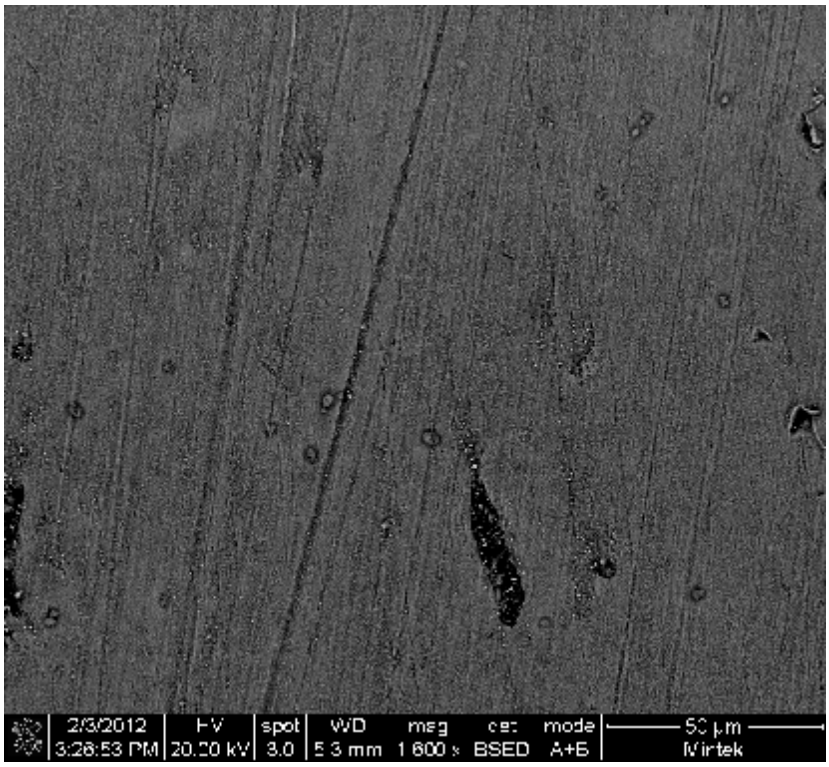


Figure 4.86. SEM-BSE image of the surface of Sample 441-1.

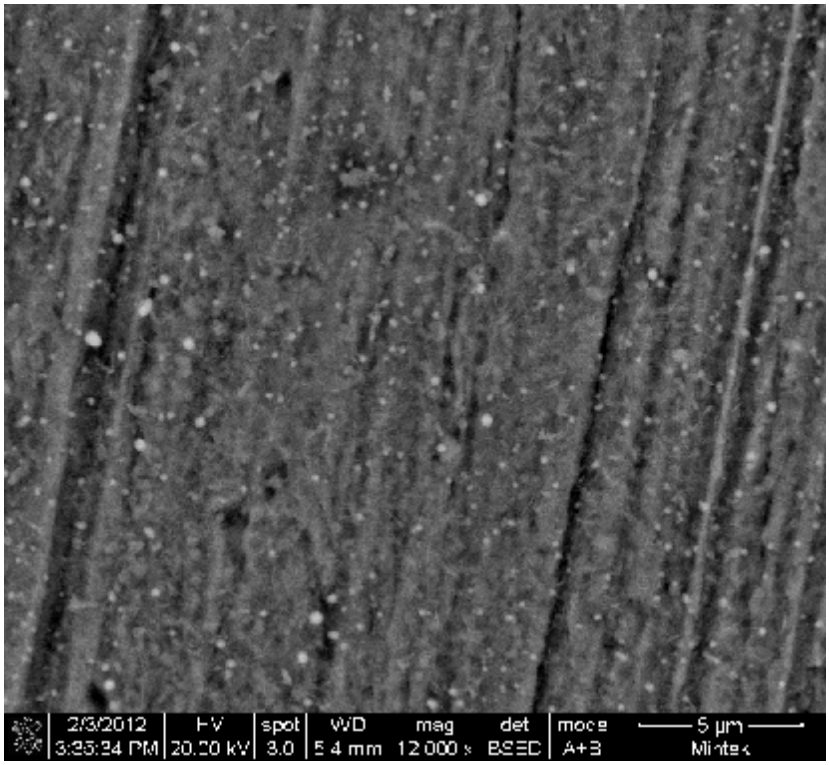


Figure 4.87. SEM-BSE image of the lighter areas on Sample 441-1 shown in Figure 4.86.

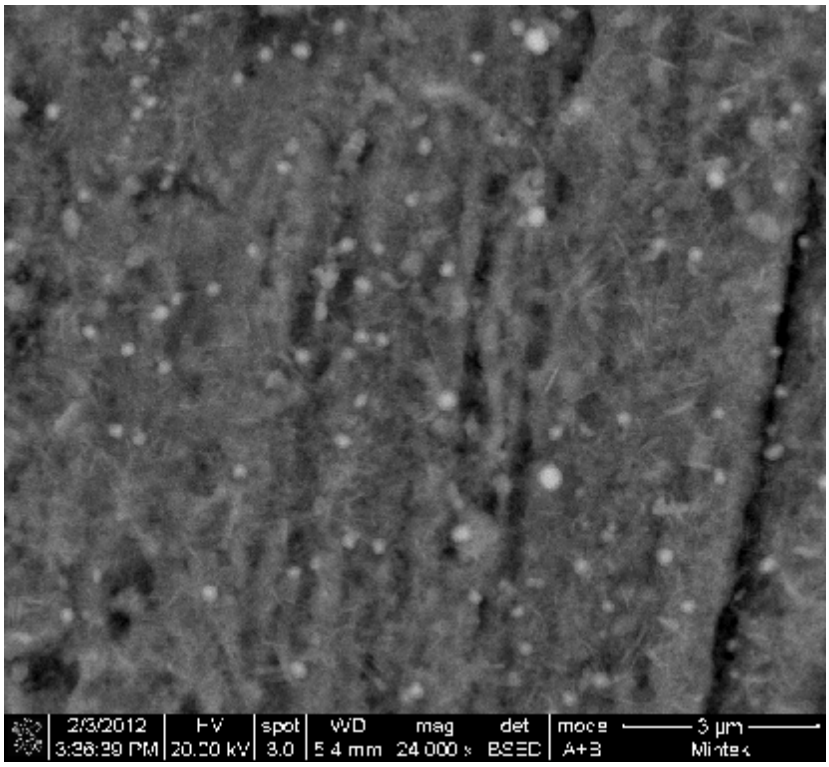


Figure 4.88. Higher magnification SEM-BSE image of Sample 441-1 shown in Figure 4.87.

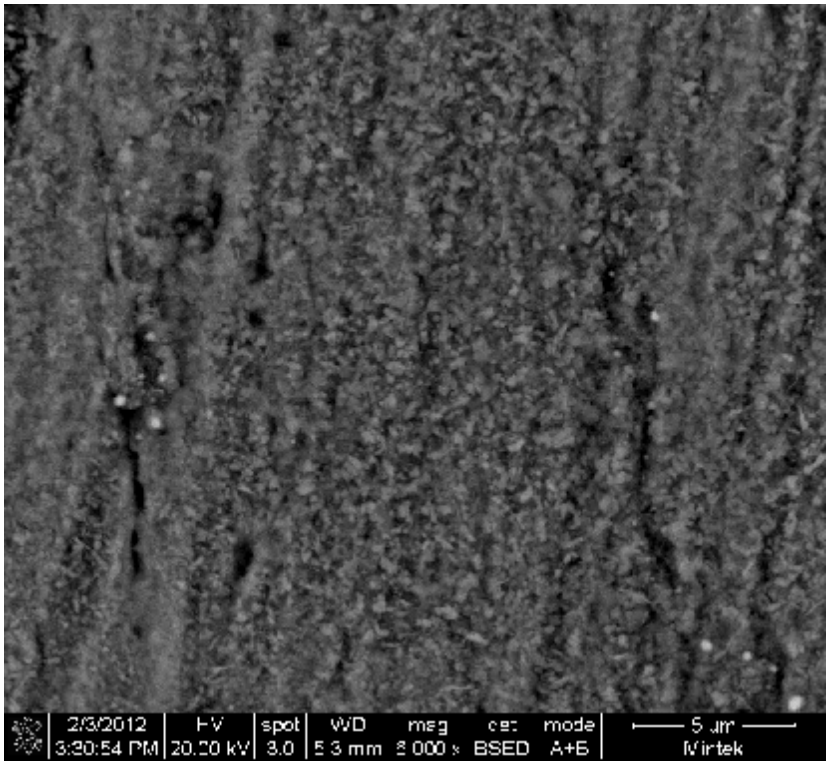


Figure 4.89. SEM-BSE image of darker areas on Sample 441-1 shown in Figure 4.86 (in BSE mode).

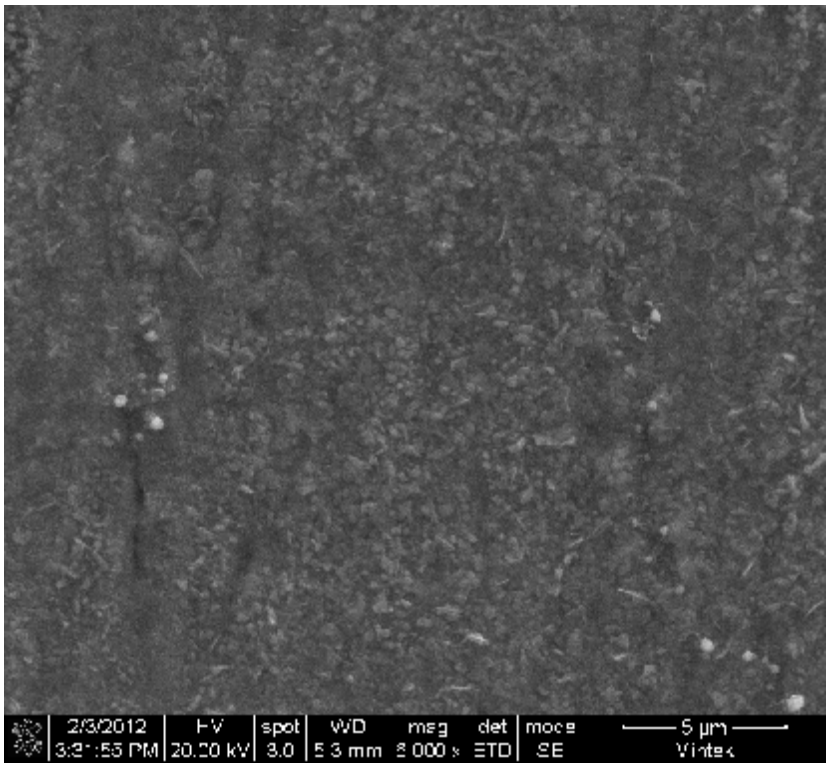


Figure 4.90. SEM-SE image of similar areas shown in Figure 4.89.

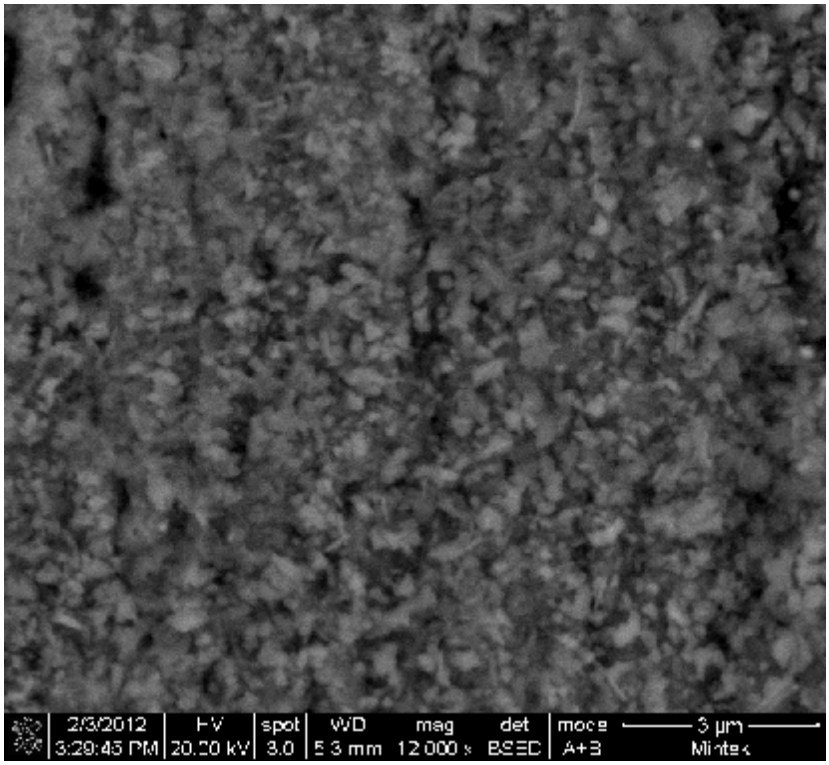


Figure 4.91. Higher magnification SEM-BSE image of the darker area in Sample 441-1 shown in Figure 4.89 and Figure 4.90.

Figure 4.92 and Figure 4.93 are SEM images of cross-sections removed from a Type 304L sample that was exposed for seven days to the furnace. The copper plating process did not work efficiently on the coke deposits, as these positions took very long to coat, and in some instances, did not coat at all, as shown in Figure 4.92. The oxide was relatively thick in this area, being about 3 µm thick. Only minor attack was evident on the surface of the samples, in the form of small pits. Figure 4.94 to Figure 4.96 are SEM images of cross-sections removed through the Type 316L sample showing localised attack, in the form of intergranular corrosion. The exposed grains of the material were relatively clean, revealing no significant attack of the grains, apart from at the twin grain boundaries or precipitates on parallel crystallographic planes (Figure 4.96). Figure 4.97 is an EDX spectrum of the oxide on the surface of the 316L sample showing that it is enriched with chromium. The copper and sulphur originates from the copper plating process. Figure 4.98 is an SEM image of Type 316Ti sample, showing no significant attack on the surface of this sample. Figure 4.99 is a higher magnification image of the titanium carbo-nitride precipitates, showing a degree of carburisation associated with the precipitate interfaces.

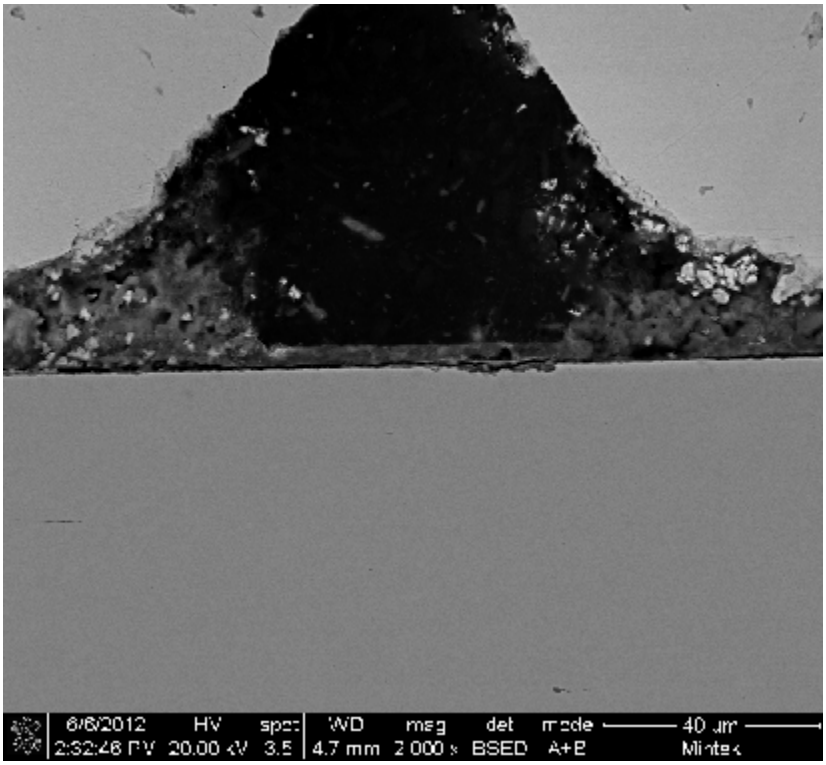


Figure 4.92. SEM-BSE image of a cross-section through Sample 304-1.

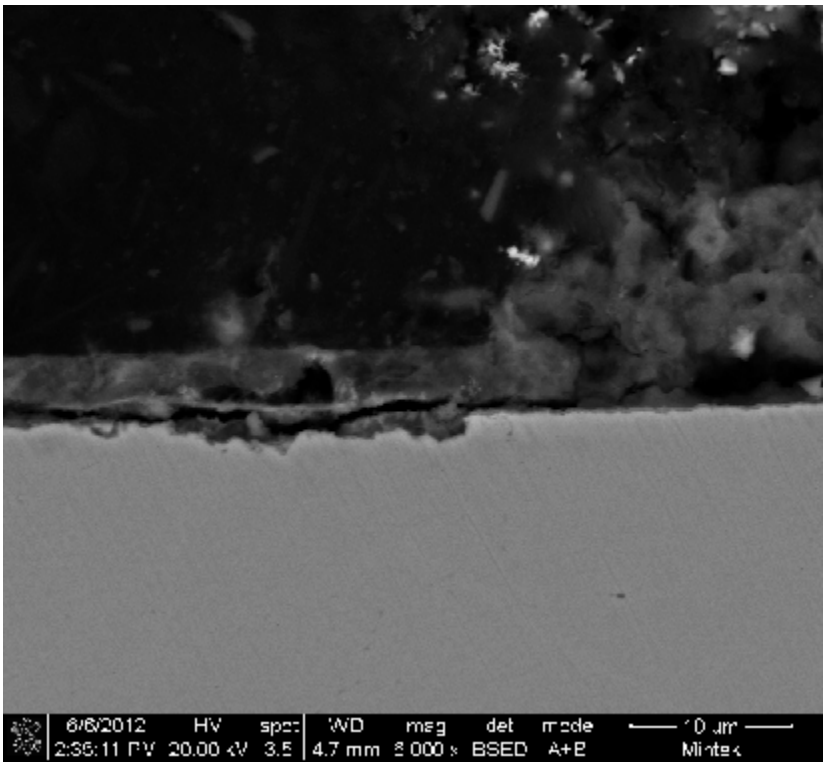


Figure 4.93. Higher magnification SEM-BSE image of Sample 304-1 shown in Figure 4.92.

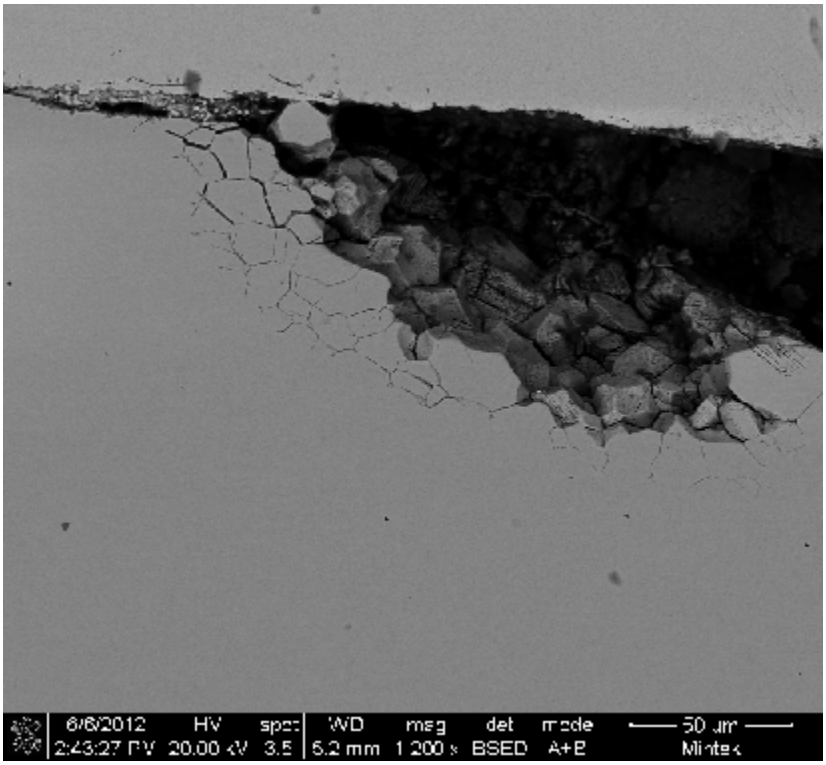


Figure 4.94. SEM-BSE image of pitting by intergranular attack and grain dropping in Sample 316-2. See also Figure 4.50.

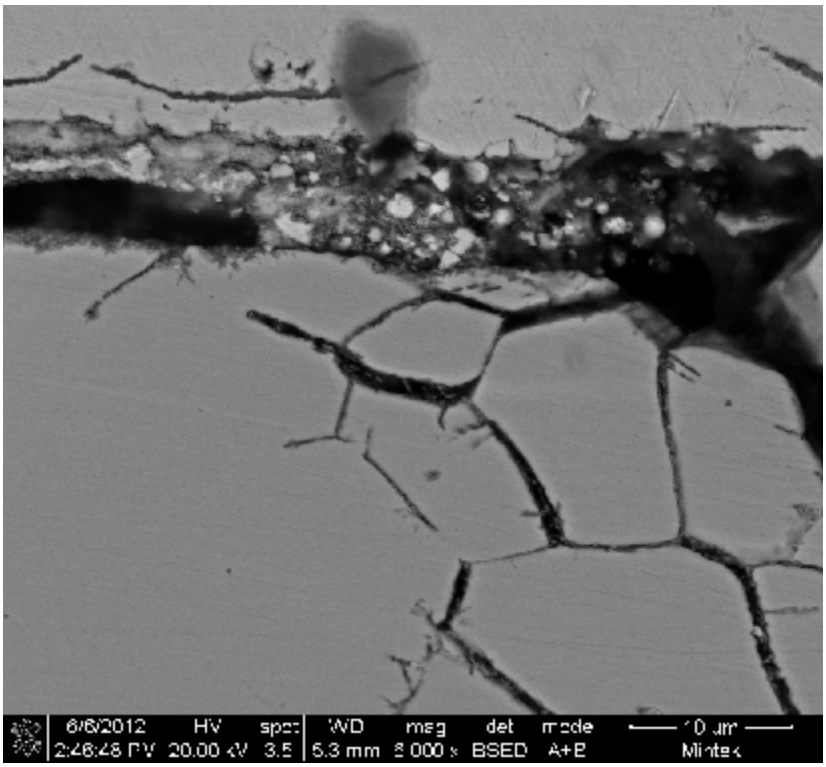


Figure 4.95. Higher magnification SEM-BSE image of intergranular attack in Sample 316-2 shown in Figure 4.94.

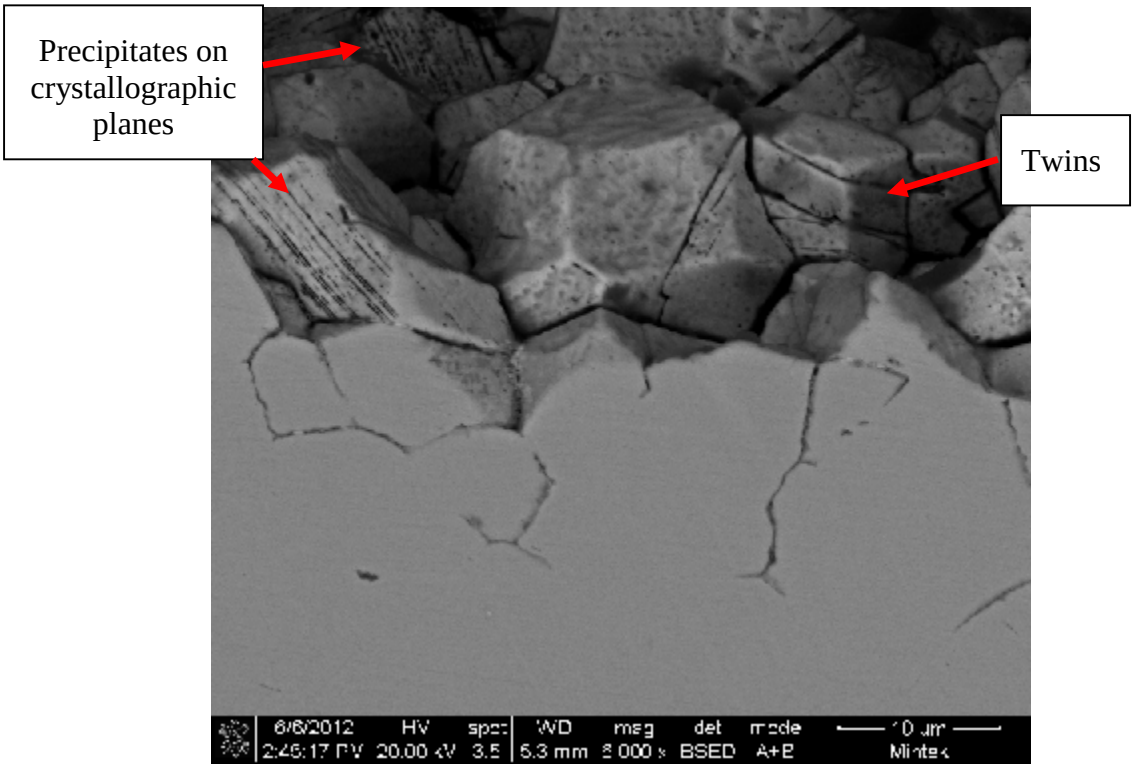


Figure 4.96. Higher magnification of grains exposed by grain dropping in Sample 316-2shown in Figure 4.94, with some attack at the grain boundaries, twins and crystallographic planes.

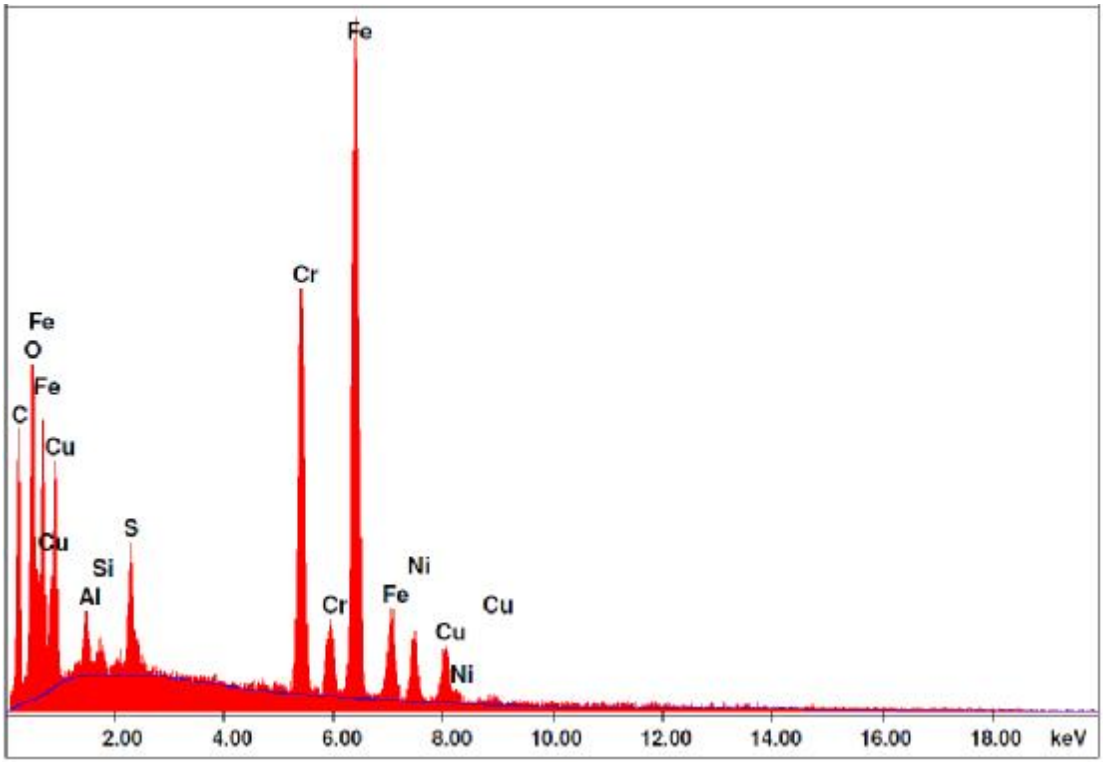


Figure 4.97. EDX spectrum of the oxide on the surface of Sample 316-2 shown in Figure 4.95.

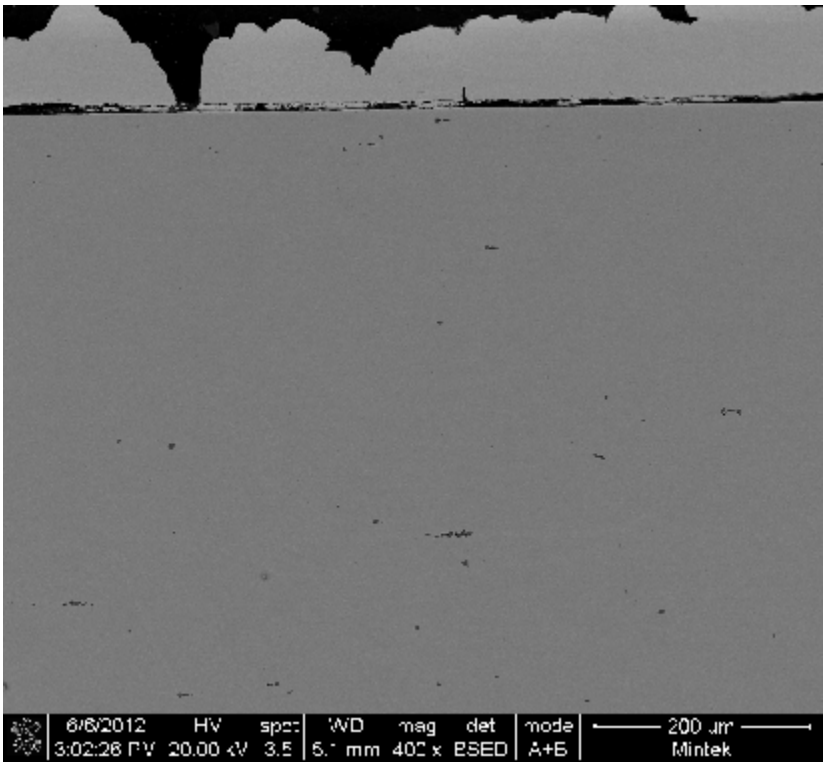


Figure 4.98. SEM-BSE image of a cross-section of Sample 316Ti–2.

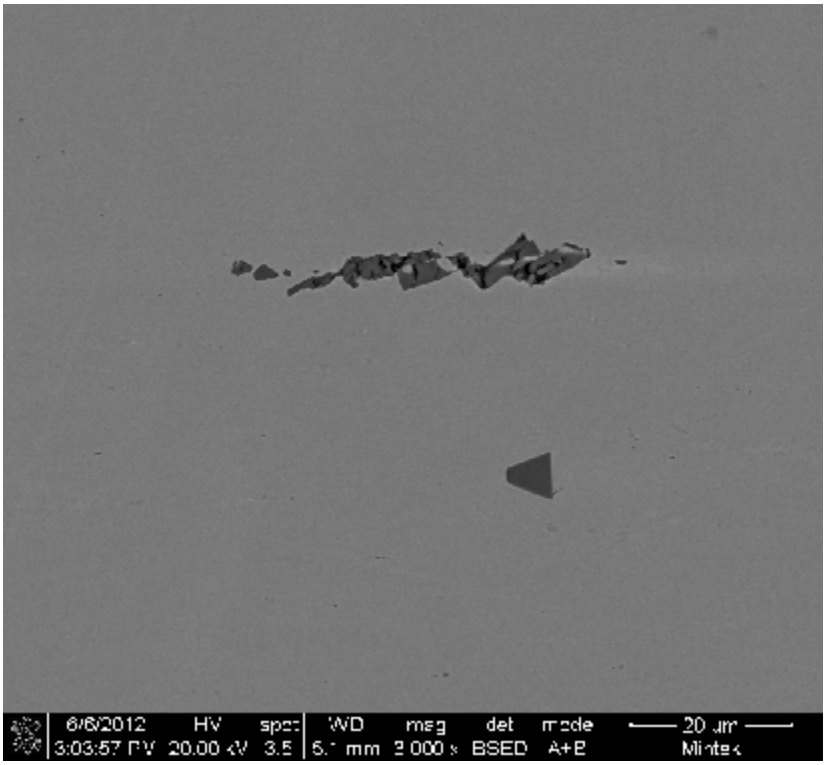


Figure 4.99. Higher magnification SEM-BSE image of Sample 316Ti-2 shown in Figure 4.98.

4.2.5. X-ray diffraction

Figure 4.100 is an X-ray spectrum of the surface of the 304L sample after exposure for seven days. The structure predominantly consisted of austenite, as expected, although another phase, identified as ferrite, was also detected. This was a higher volume of ferrite than expected for this sample (8.6%). Figure 4.101 is an X-ray spectrum of the 321 sample exposed for seven days. Only a ferrite phase was identified in this sample. This result was unexpected, and was not regarded as a reliable result for this sample. Further work is suggested to clarify this result. Figure 4.102 and Figure 4.103 are X-ray spectra of Types 316L and 316Ti samples, respectively after exposure for seven days. Both these samples predominantly consisted of austenite. Figure 4.104 and Figure 4.105 are X-ray spectra of the surfaces of Types 430 and 441, respectively. Both these samples consisted predominantly of ferrite, as expected for these samples.

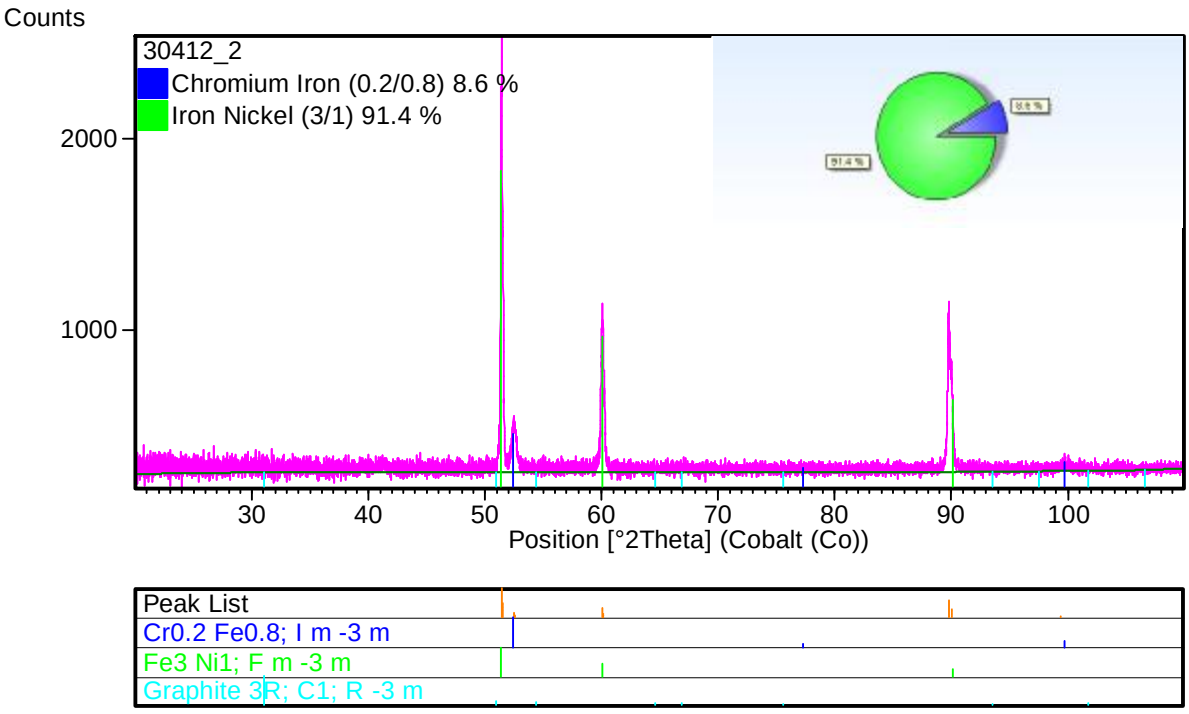


Figure 4.100. X-ray spectrum of the surface of Sample 304-2, showing peaks and volume %.

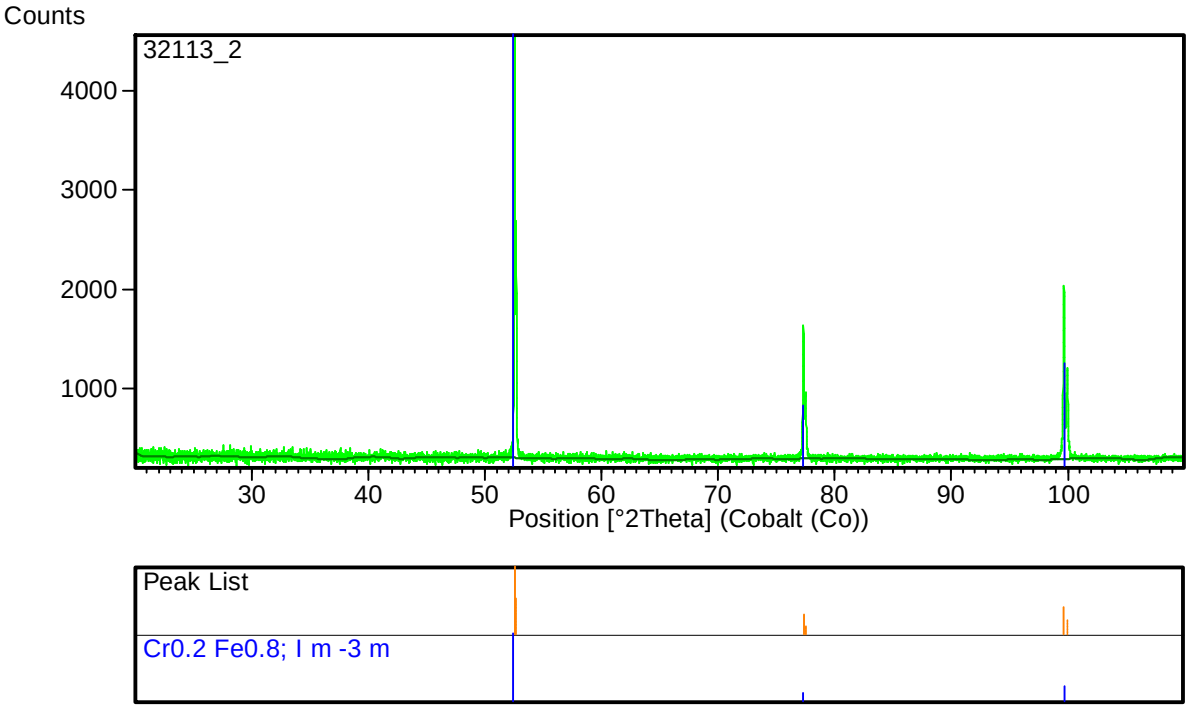


Figure 4.101. X-ray spectrum of the surface of Sample 321-2.

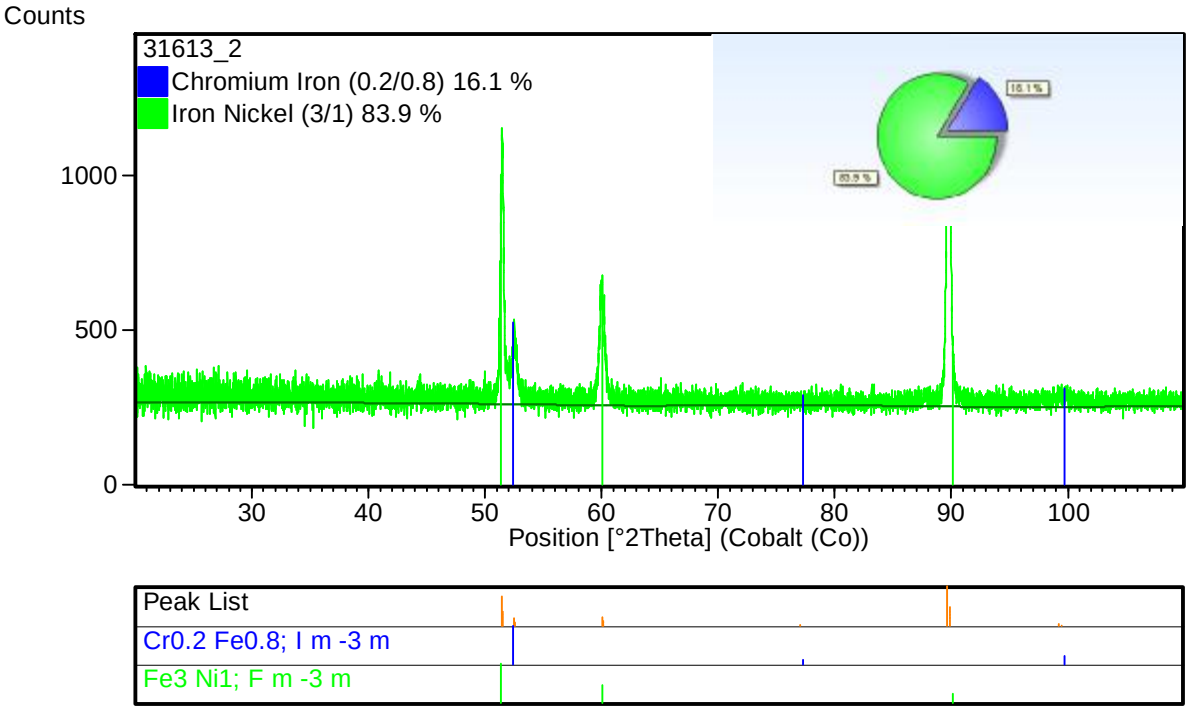


Figure 4.102. X-ray spectrum of the surface of Sample 316L-2, showing peaks and volume %.

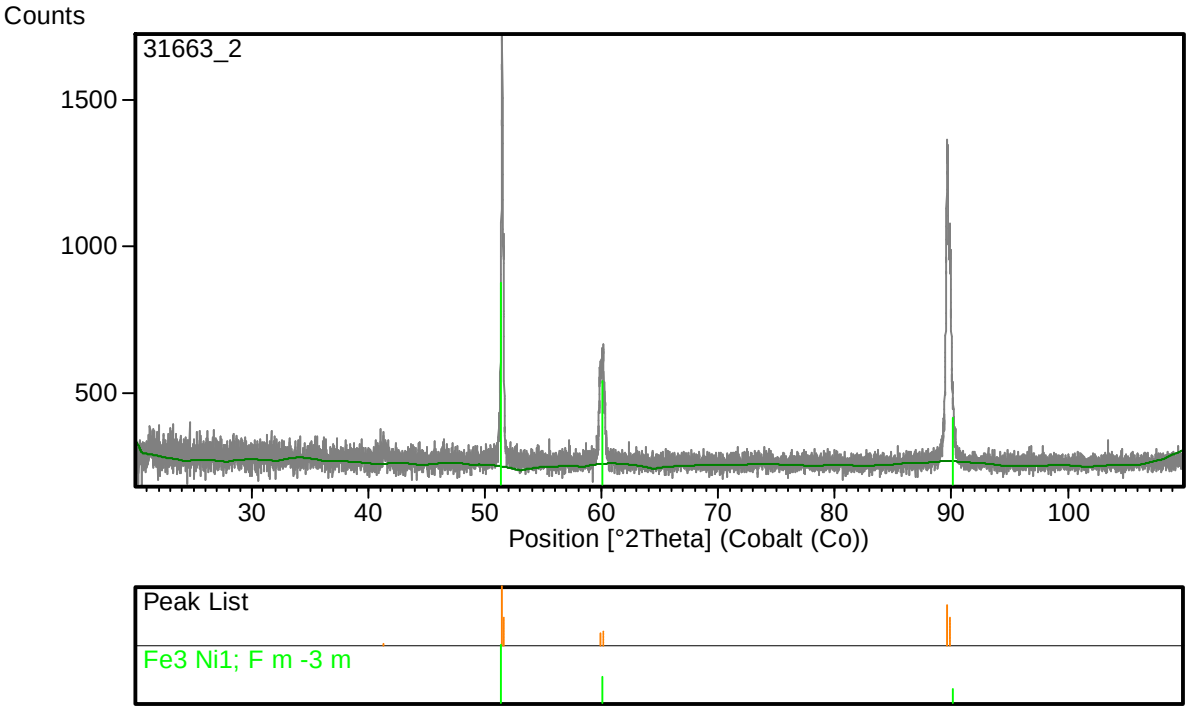


Figure 4.103. X-ray spectrum of the surface of Sample 316Ti-2.

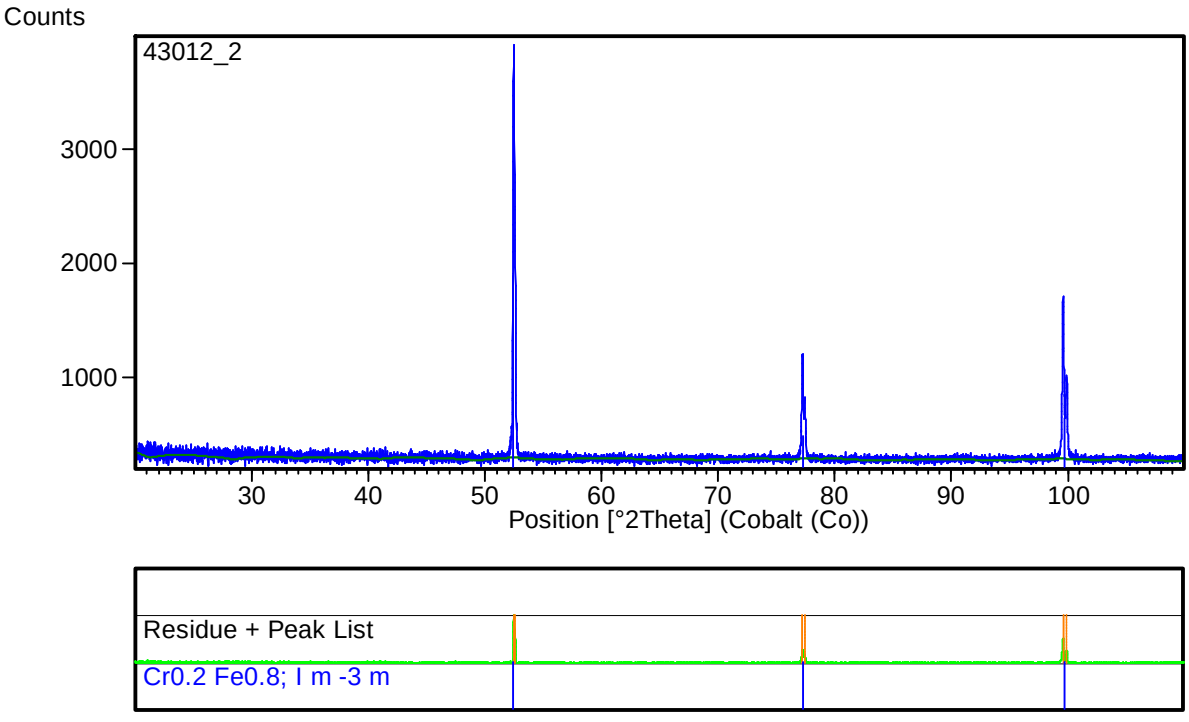


Figure 4.104. X-ray spectrum of the surface of Sample 430-2.

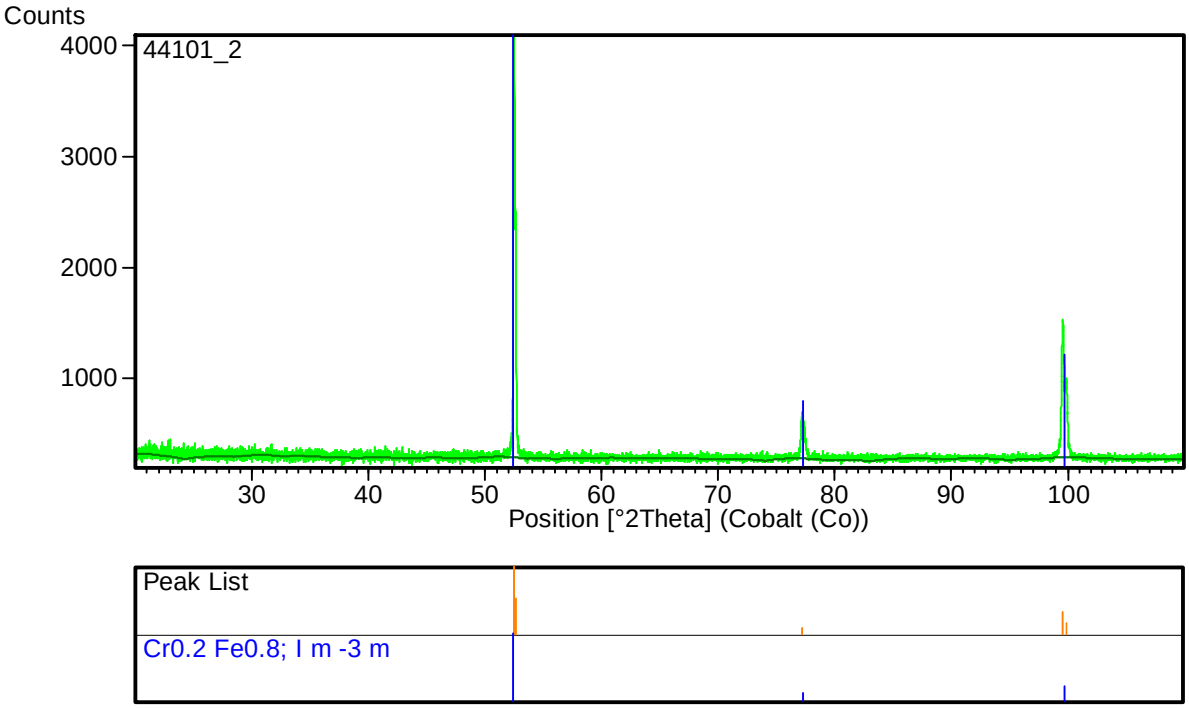


Figure 4.105. X-ray spectrum of the surface of Sample 441-2.

4.3. Fourteen day test

4.3.1. Visual examination

Significant coking was recorded on the samples that were exposed for fourteen days, as shown in Figure 4.106 and Figure 4.107. The coking was mainly associated with the austenitic materials, and in particular, the Type 316L samples. Figure 4.108 is a photograph of the Types 304L and 321 samples exposed for fourteen days. The Type 304L samples did not show significant tarnishing, although one of the 321 samples was covered with a black product, as shown in Figure 4.108 and Figure 4.109. This was probably coking, carburisation or even magnetite. Figure 4.110 is a photograph of the rear faces of the Types 304L and 321 samples. The only localised attack found was in one of the Type 304L samples.

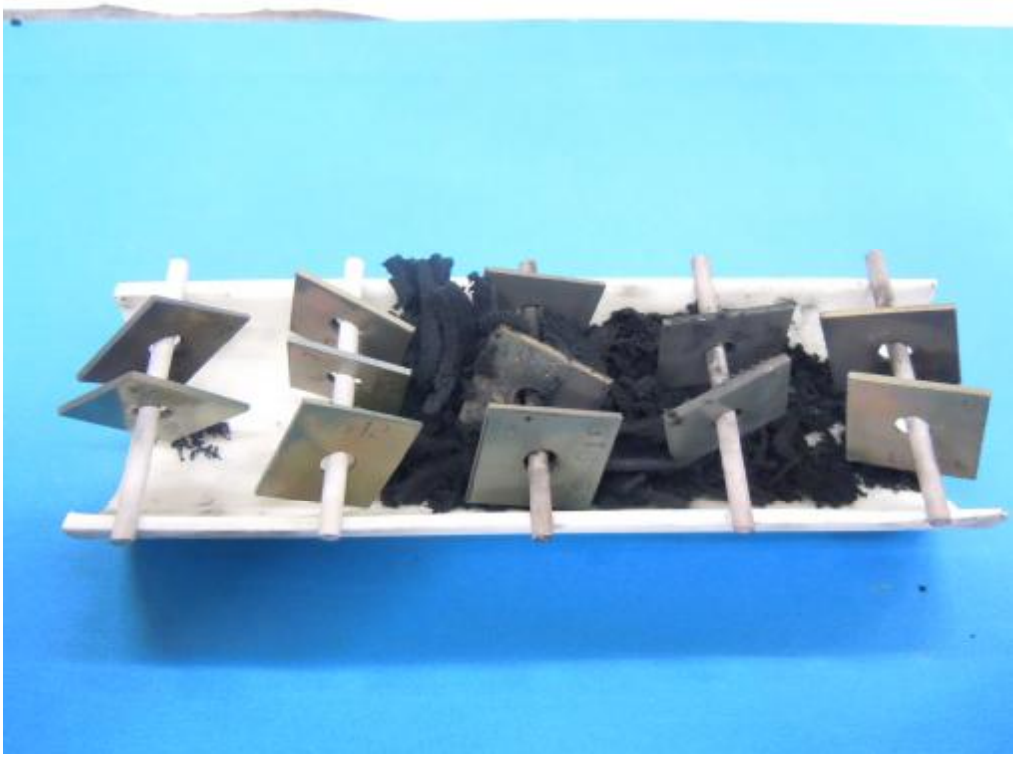


Figure 4.106. Photograph of all the coupons in the boat showing the extent of coke formation.



Figure 4.107. Close-up photograph of the coking shown in Figure 4.106.



Figure 4.108. Photograph of the 304L and 321 samples exposed in the 14-day test.

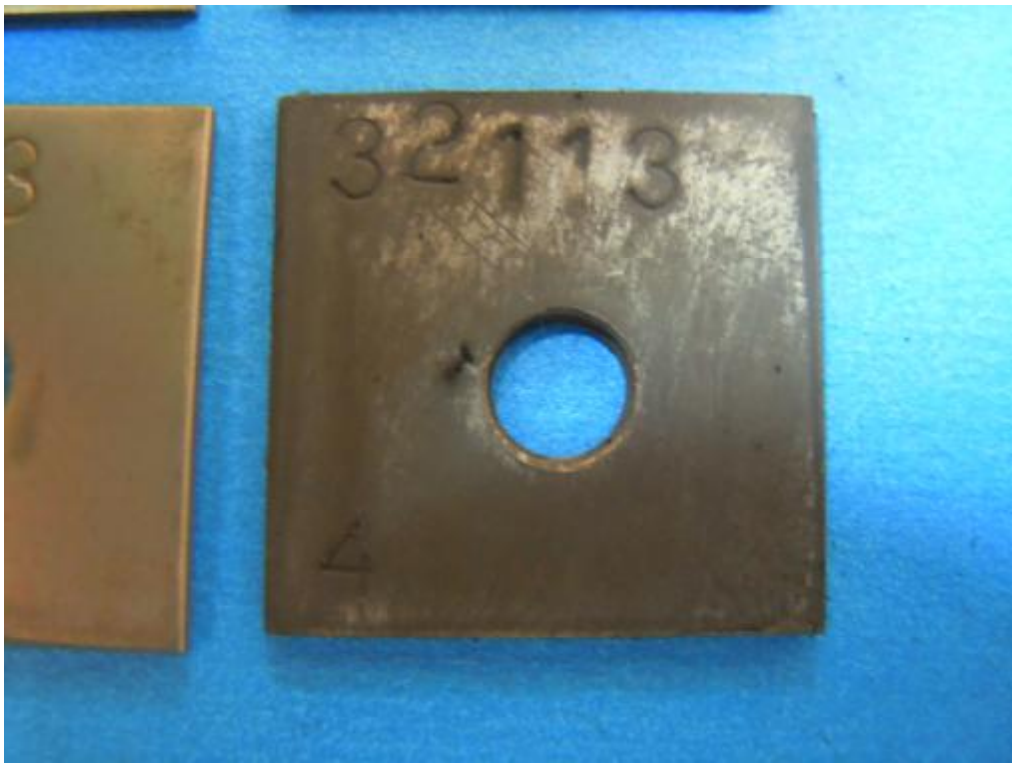


Figure 4.109. Close-up photograph of the 321-4 sample showing coke formation on the surface.



Figure 4.110. Photograph of the rear surfaces of the 304L and 321 samples shown in Figure 4.108, showing pit formation on 304-4 (arrow).

Figure 4.111 is a photograph of the Type 316L and 316Ti samples as removed from the furnace, illustrating the coking and filament growth associate with these alloys and “blueing” above the coke level. Figure 4.112 and Figure 4.113 are photographs of the coupons of the 316L and 316Ti samples showing the degree of coking and pitting attack on both the alloys. The attack appeared worse on the Type 316L samples. Figure 4.114 and Figure 4.115 are close-up photographs illustrating the extent of attack on Types 316L and 316Ti, respectively.



Figure 4.111. Close-up photograph of the 316L coupons after exposure showing coking and filament growth on the surface.



Figure 4.112. Photograph of the 316L and 316Ti samples exposed for 14-days.

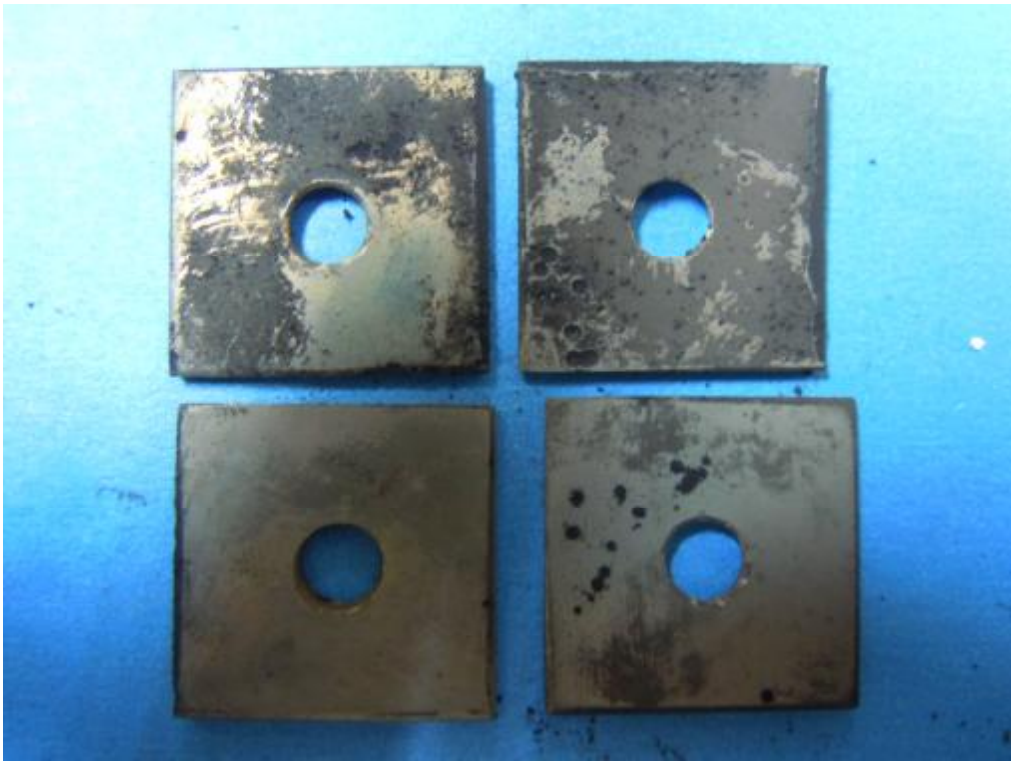


Figure 4.113. Photograph of the rear surfaces of the 316L and 316Ti samples showing coking and pitting on the surfaces.

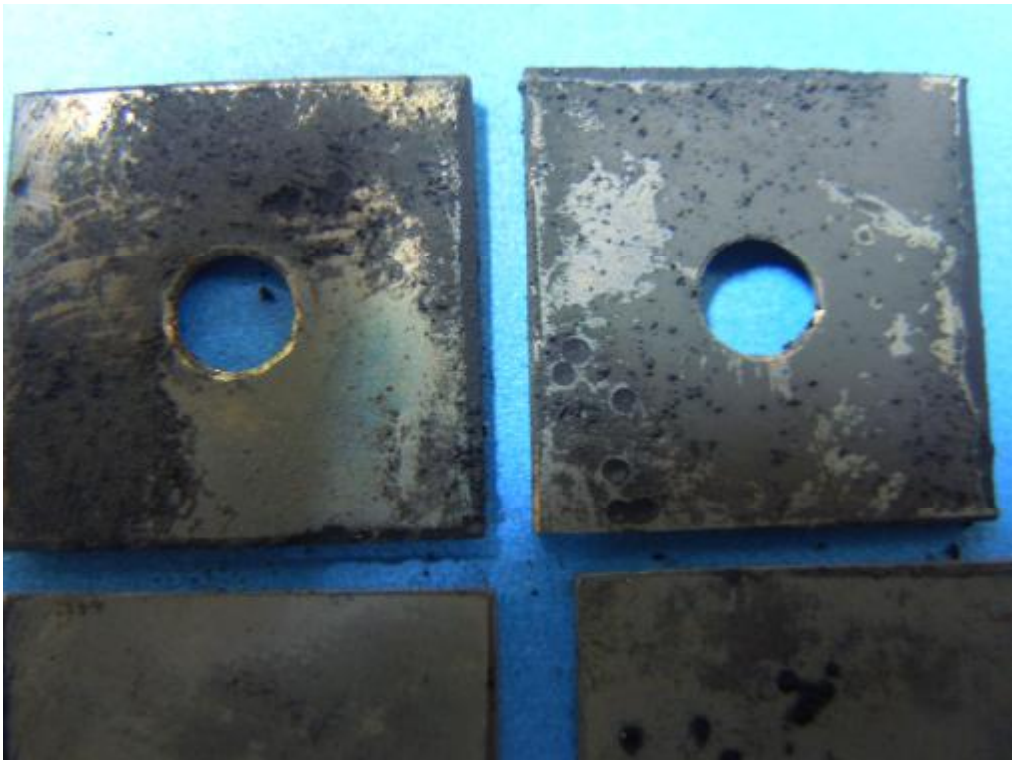


Figure 4.114. Close-up photograph of coking and pitting on the 316L samples.



Figure 4.115. Close-up photograph of coking on the 316Ti samples.

Figure 4.116 is a photograph of Types 430 and 441 samples after exposure for fourteen days. The degree of tarnishing seemed marginally greater on the Type 430 samples, but this was significantly less than for the 316L and 316Ti samples described above. Carbon filament growth was found at the whole chamfer on one of the Type 430 samples, as also shown in Figure 4.117. Figure 4.118 is a photograph of the coking associated with the ferritic samples, which was significantly different in appearance from the coking associated with the austenitic samples, as shown in Figure 4.107 and Figure 4.111.



Figure 4.116. Photograph of the Types 430 and 441 samples exposed for 14 days.



Figure 4.117. Photograph of Sample 430-3 showing filament growth.



Figure 4.118. Photograph of the coke formation associated with the ferritic samples (430 in this instance).

4.3.2. Mass loss

Based on the mass changes shown in Table 4.3, both Types 304L and 321 gained weight slightly, indicating that no significant metal loss was experienced on any of the samples. However, the molybdenum containing grades, namely Types 316L and 316Ti, revealed significant corrosion rates in comparison. Type 316Ti performed better than 316L regarding corrosion rate and coking rate. No significant mass changes occurred on either of the two ferritic grades, namely Types 430 and 441, indicating that these alloys are relatively resistant in the test conditions for these exposure periods.

Table 4.3. Mass change data for the 14-day test.

Sample		304L	304L	321	321	316L	316L	316Ti	316Ti	430	430	441	441
		3	4	3	4	3	4	3	4	3	4	3	4
Density	**g/cm^3**	7.9	7.9	7.8	7.8	8.0	8.0	8.0	8.0	7.8	7.8	7.7	7.7
Length	**mm**	20.30	20.09	20.57	20.44	20.83	20.45	20.77	20.58	20.33	20.50	20.50	20.49
Width	**mm**	19.30	19.31	20.50	20.36	20.35	20.26	20.40	20.46	20.31	20.46	20.34	20.42
Thickness	**mm**	1.19	1.15	1.32	1.30	1.44	1.45	1.82	1.76	1.43	1.46	1.40	1.42
Radius	**mm**	5.00	5.20	5.00	5.00	5.00	5.00	5.13	5.12	1.17	5.15	5.00	5.00
Area	**cm^2**	8.31	8.14	9.05	8.91	9.19	9.00	9.47	9.36	9.45	9.07	9.01	9.06
Mass before	**g**	3.3143	3.1592	4.0542	3.9368	4.3362	4.3305	5.5771	5.4360	4.1752	4.2409	4.0742	4.1658
Mass after	**g**	3.3145	3.1582	4.0547	3.9375	4.3182	4.2853	5.5768	5.4343	4.1752	4.2414	4.0743	4.1659
Mass loss	**g**	-0.0002	0.0010	-0.0005	-0.0007	0.0180	0.0452	0.0003	0.0017	0	-0.0005	-0.0001	-0.0001
Time	**h**	336	336	336	336	336	336	336	336	336	336	336	336
Corr. rate	**mm/y**	-0.0008	0.0041	-0.0018	-0.0026	0.0638	0.1637	0.0010	0.0059	0	-0.0018	-0.0004	-0.0004
Corr. rate	**Average**	**0.0016**		**-0.0022**		**0.1138**		**0.0035**		**-0.0009**		**-0.0004**	
Cleaned mass	**g**	3.3145	-	4.0547	-	4.3157	-	5.5765	-	-	-	4.0742	-
Cleaned mass loss	**g**	-0.0002	-	-0.0005	-	0.0205	-	0.0006	-	-	-	0.0000	-
Cleaned corr. rate	**mm/y**	**-0.0008**	**-**	**-0.0018**	**-**	**0.0727**	**-**	**0.0021**	**-**	**-**	**-**	**0.0000**	**-**
Coking mass	**g**	0.0000	-	0.0000	-	0.0025	-	0.0003	-	-	-	0.0001	-
Coking rate	**mg/cm^2/day**	**0.0000**	**-**	**0.0000**	**-**	**0.0194**	**-**	**0.0023**	**-**	**-**	**-**	**0.0008**	**-**

4.3.3. Metallography

No attack was evident on the Types 304L and 321 samples exposed for fourteen days, although the oxide layer on the surface was generally thicker than for the shorter exposure times, as shown in Figure 4.119. There was also some internal oxidation in the Type 304L sample, as shown in Figure 4.119. Other than for the samples exposed for shorter time periods, the attack on the Type 316L stainless steel was not localised (pitting), but was widespread over the surfaces of the samples, as shown in Figure 4.120 to Figure 4.123. The attack was intergranular, with associated grain dropping. Some copper from the copper plating process also plated between the loose grains. On the duplicate sample, there were also different zones that were attacked, and where the layers detached from the substrate, as shown in Figure 4.124. Figure 4.125 to Figure 4.129 are micrographs of localised attack found in a Type 316Ti sample. The attack was similar to that found in the Type 316L sample, in that the attack was initially intergranular, and then followed by complete attack/consumption of the individual grains, which occurred in layers. However, the attack on the 316Ti samples was not as extensive as on the 316L samples and was more concentrated at the edges.

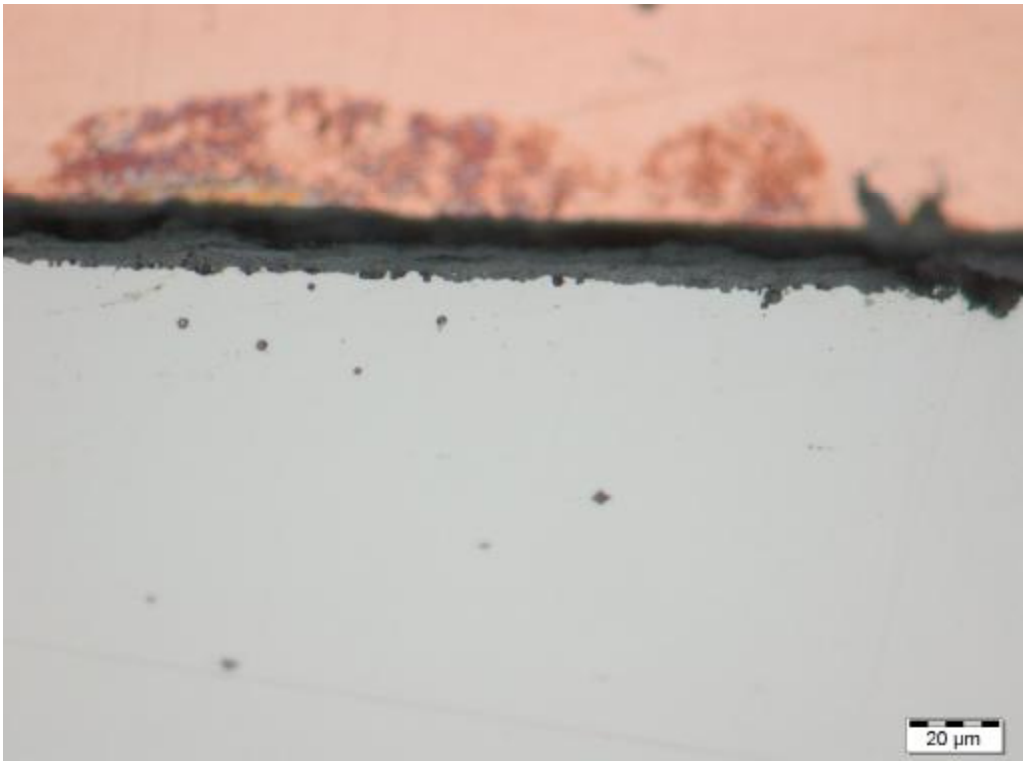


Figure 4.119. Micrograph of a cross-section through Sample 304-3.

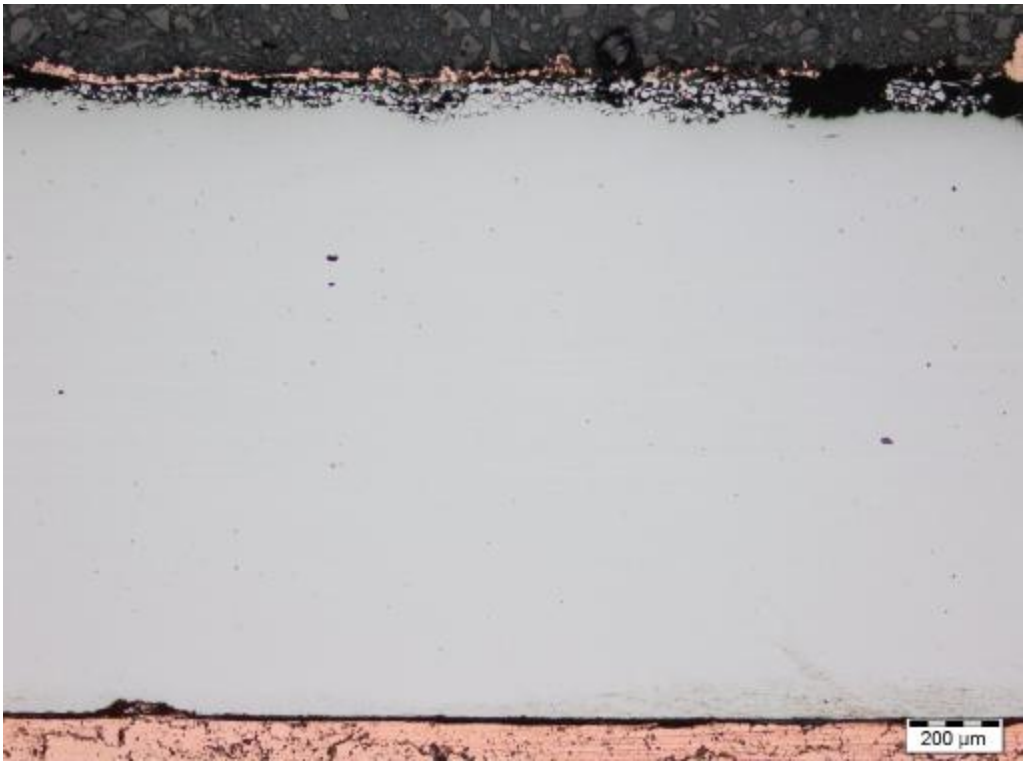


Figure 4.120. Micrograph of a cross-section through Sample 316-3 showing significant metal wastage by intergranular attack.

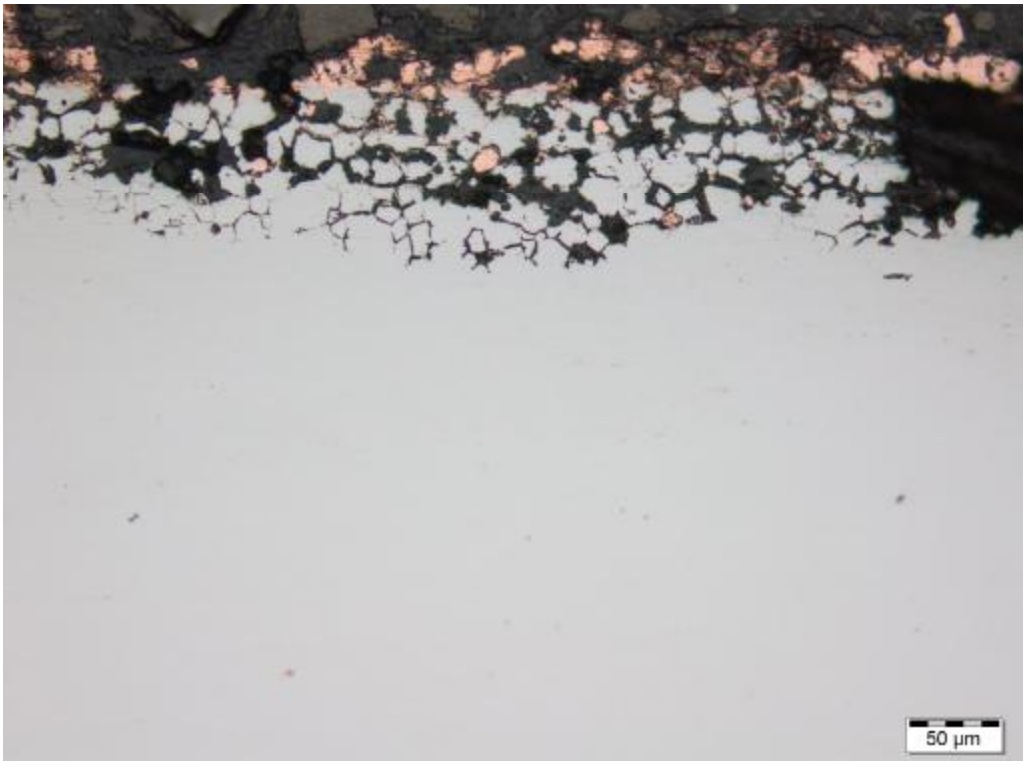


Figure 4.121. Higher magnification micrograph of intergranular attack in Sample 316-3 shown in Figure 4.120.

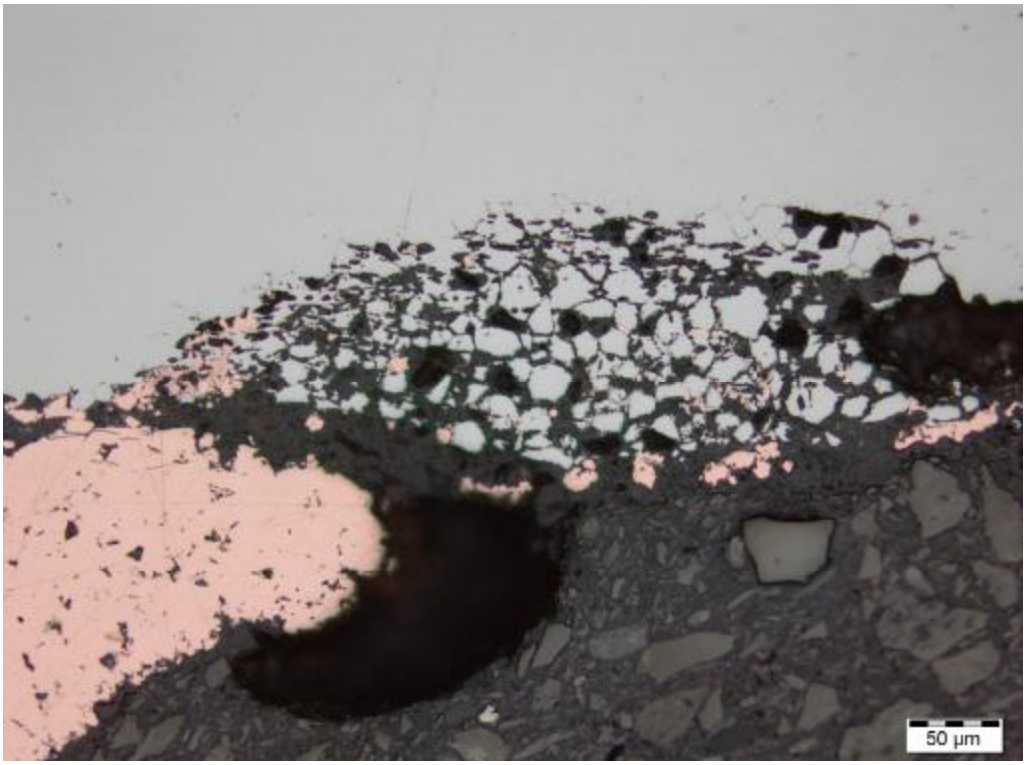


Figure 4.122. Micrograph of localised intergranular attack in Sample 316-3.

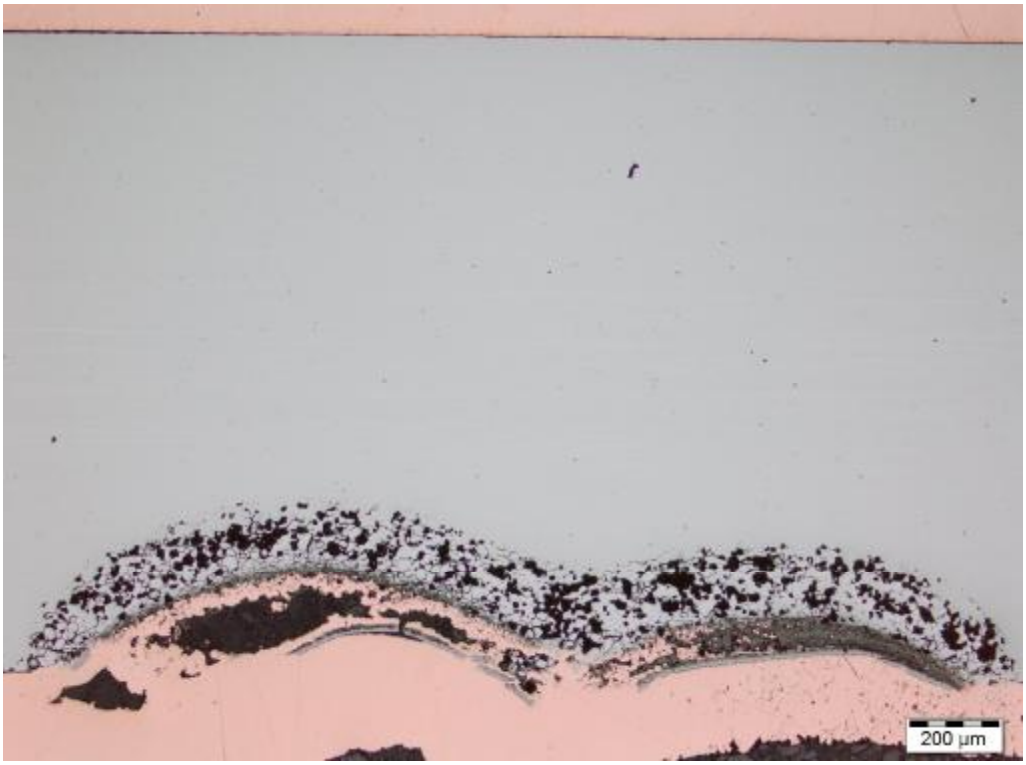


Figure 4.123. Micrograph of localised intergranular attack in Sample 316-4.

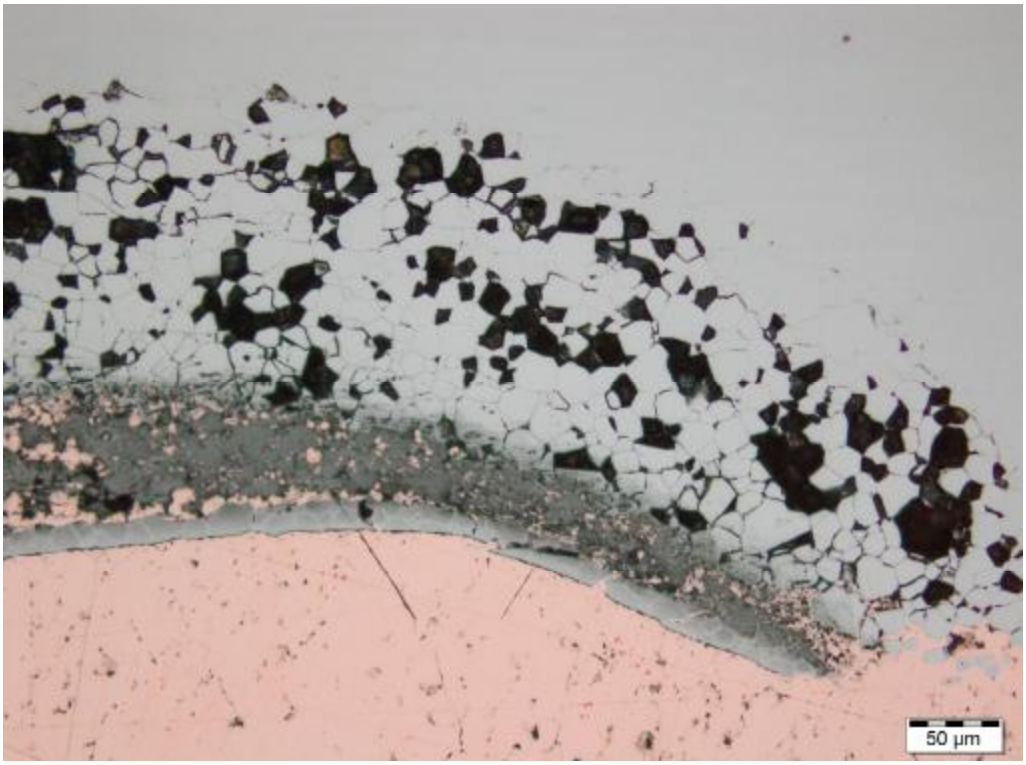


Figure 4.124. Higher magnification micrograph of the metal wastage on Sample 316-4 shown in Figure 4.123.

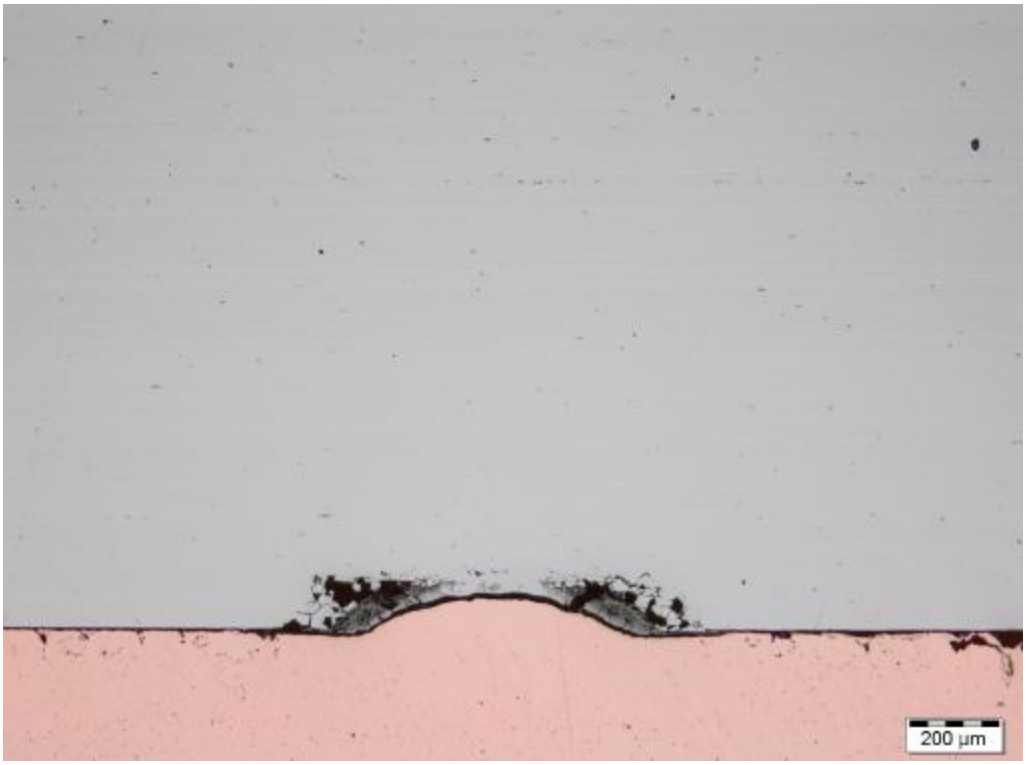


Figure 4.125. Micrograph of a pit in Sample 316Ti-3.

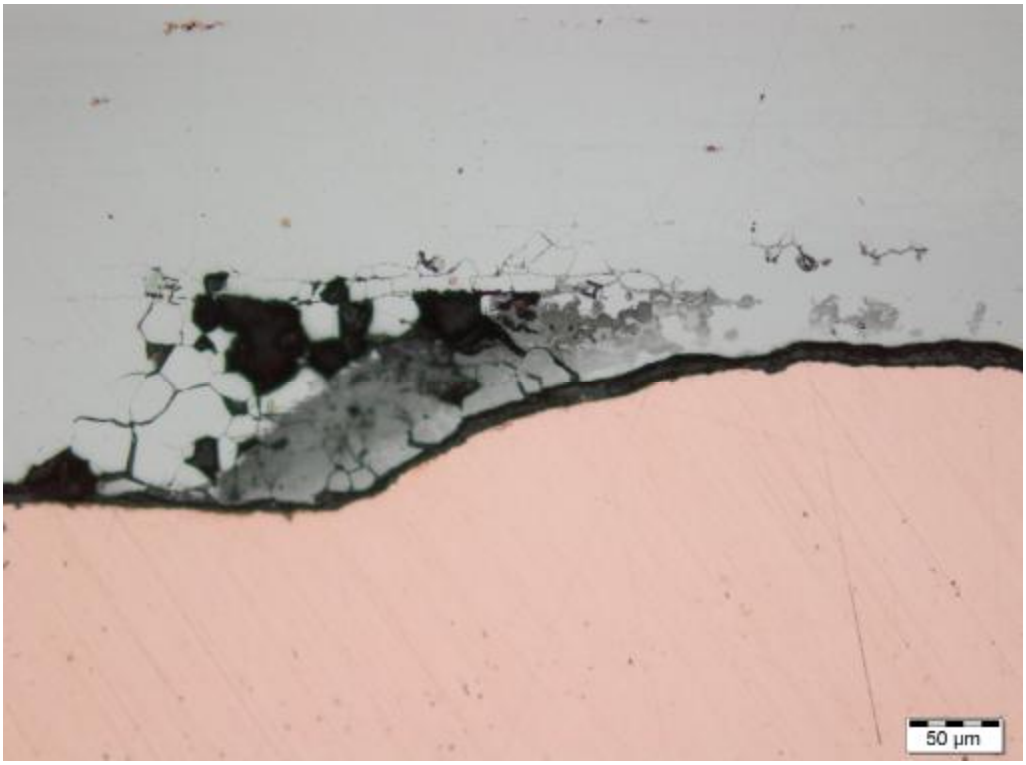


Figure 4.126. Micrograph of Sample 316Ti-3 shown in Figure 4.125.



Figure 4.127. Higher magnification of the intergranular attack and metal wastage in Sample 316Ti-3 shown in Figure 4.126.



Figure 4.128. Micrograph of localised attack in Sample 316Ti-4.



Figure 4.129. Higher magnification micrograph of intergranular attack in Sample 316Ti-4 shown in Figure 4.128.

Figure 4.130 is a micrograph through the Type 430 sample in the region associated with coke formation, with minor attack and broken oxides evident on the surface. No attack was evident on the rest of the surface, as shown in Figure 4.131. Figure 4.132 is an etched microstructure showing the carbides towards the centre of the sample. Figure 4.133 is a micrograph of the Type 441 sample showing no significant attack on the surface, and Figure 4.134 shows Type 441 in the etched condition with the titanium carbo-nitride precipitate distribution both on the grain boundaries and within the grains. Figure 4.135 is a higher magnification of the coking or carburisation associated with the titanium carbo-nitride precipitates, and Figure 4.136 is a micrograph showing much finer carbides than in Type 430 (as shown in Figure 4.132). These micrographs also show carbide precipitation on the grain boundaries, with a carbide-free zone around the grain boundaries. This is similar to sensitisation mechanism, indicating that the chromium content in the area adjacent to the grain boundaries is lower, giving rise to the intergranular attack observed.

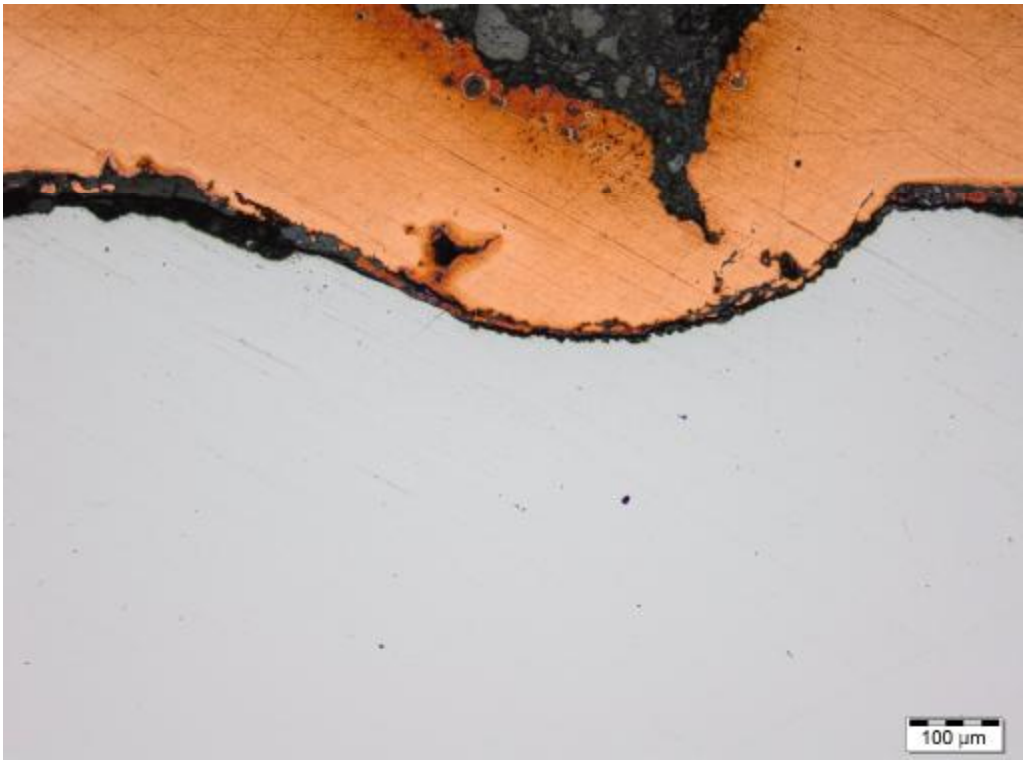


Figure 4.130. Micrograph of attack in Sample 430-3 associated with the coke formation shown in Figure 4.117.



Figure 4.131. Etched micrograph of Sample 430-3 showing carburisation at the surfaces of the sample.

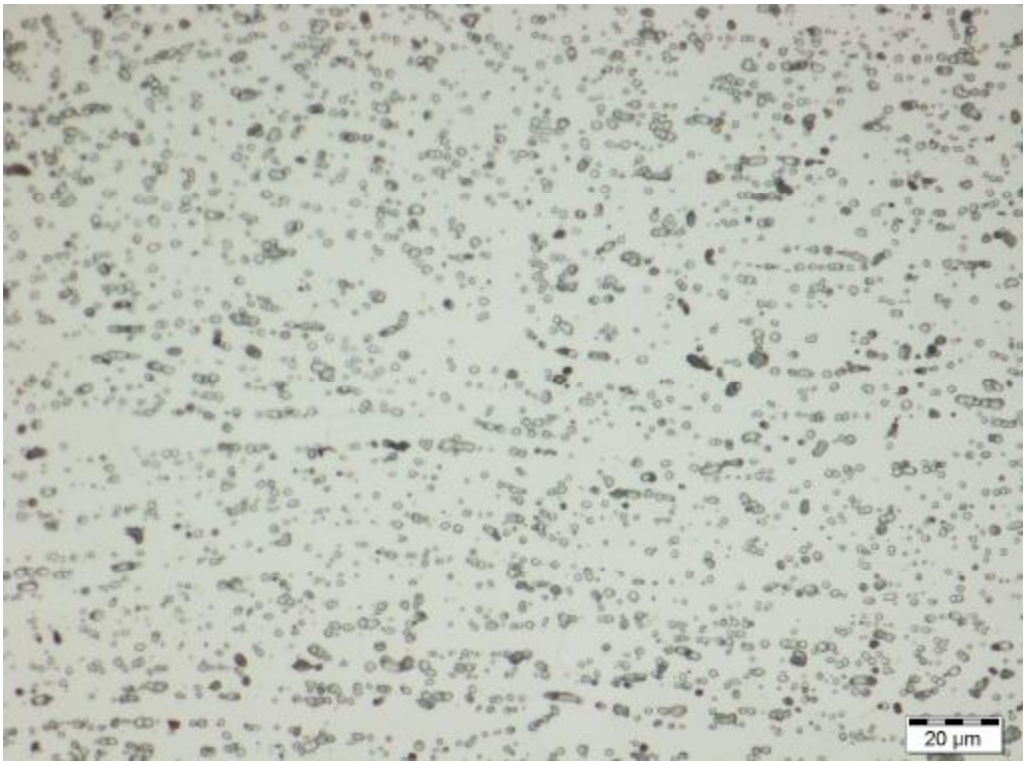


Figure 4.132. Etched micrograph of Sample 430-3 showing the carbide distribution in the centre through the thickness.



Figure 4.133. Micrograph of unetched Sample 441-3 showing no attack.



Figure 4.134. Etched microstructure of Sample 441-3 showing the titanium carbo-nitride distribution.

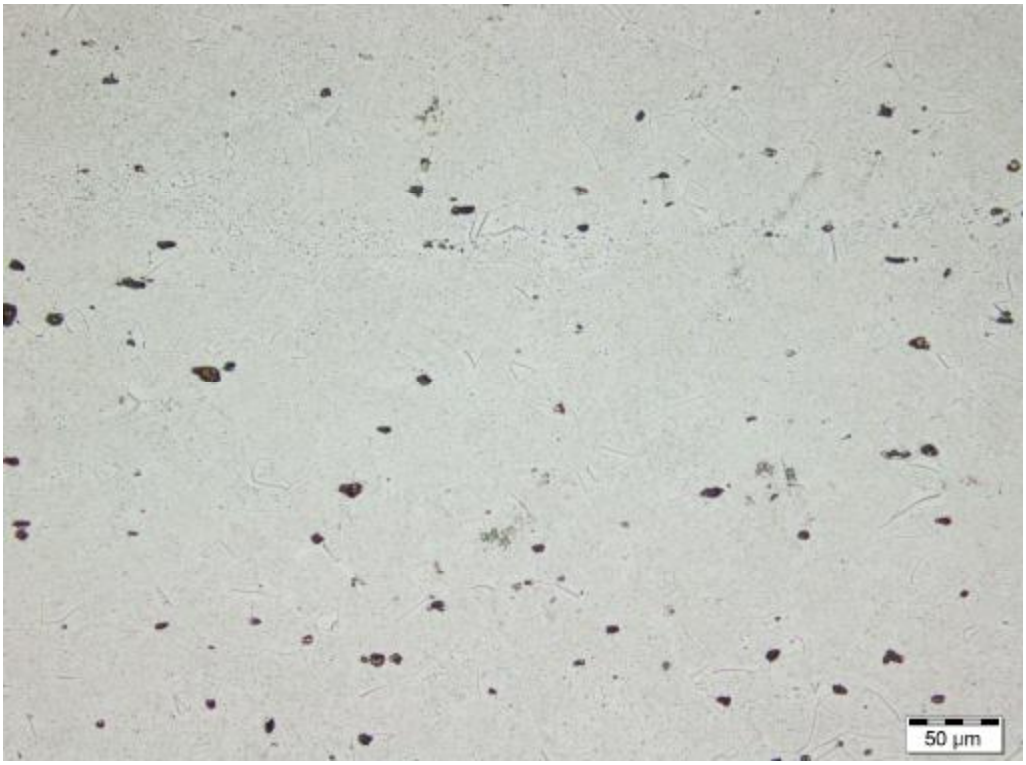


Figure 4.135. Higher magnification of the distribution of the titanium carbo-nitride precipitates in Sample 441-3.



Figure 4.136. High magnification micrograph of the carbide distribution and titanium carbo-nitride precipitation (arrows) in Sample 441-3 and associated coking (dark).

4.3.4. Scanning Electron Microscopy

Figure 4.137 is an SEM image of the base of a 'filament growth' at the centre of the Type 430 sample exposed for fourteen days. The filament broke off during sample preparation, leaving only the base at the surface. This 'filament growth' consisted of a large network of carbon nanotubes. The shape indicates that tensile stresses could be associated with the outside surface, giving rise to the "peel back" observed after fracture. Figure 4.138 and Figure 4.139 are SEM images of the surface of a 430 sample, showing light spheroidal particles, darker chunky and faceted particles, as well as needle-like particles on the surface. Figure 4.140 is a SEM image of the surface near an area that appears to be pitted. The light particles in this area appeared larger than elsewhere on the surface. Figure 4.141 and Figure 4.142 are SEM images of the coke filaments found on the surface. Analysis of the light particle on the end of the filaments by EDX detected primarily carbon and iron, as shown in Figure 4.143. Due to the small size of the particle (magnification of 100 000X), the carbon filaments were also included in the analysis. It can therefore not conclusively be said from this analysis whether the particles are pure iron, or iron carbide (such as cementite – Fe_3C).

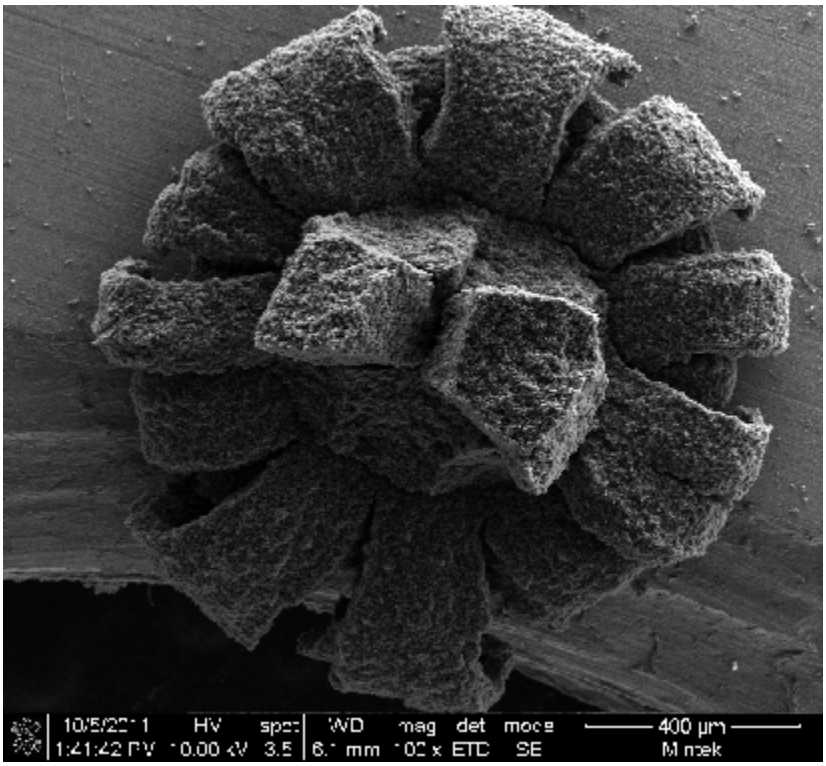


Figure 4.137. SEM-SE image in secondary mode showing coke filaments shown in Figure 4.117, with filaments fractured during sample preparation for SEM, leaving the "base" of the growth.

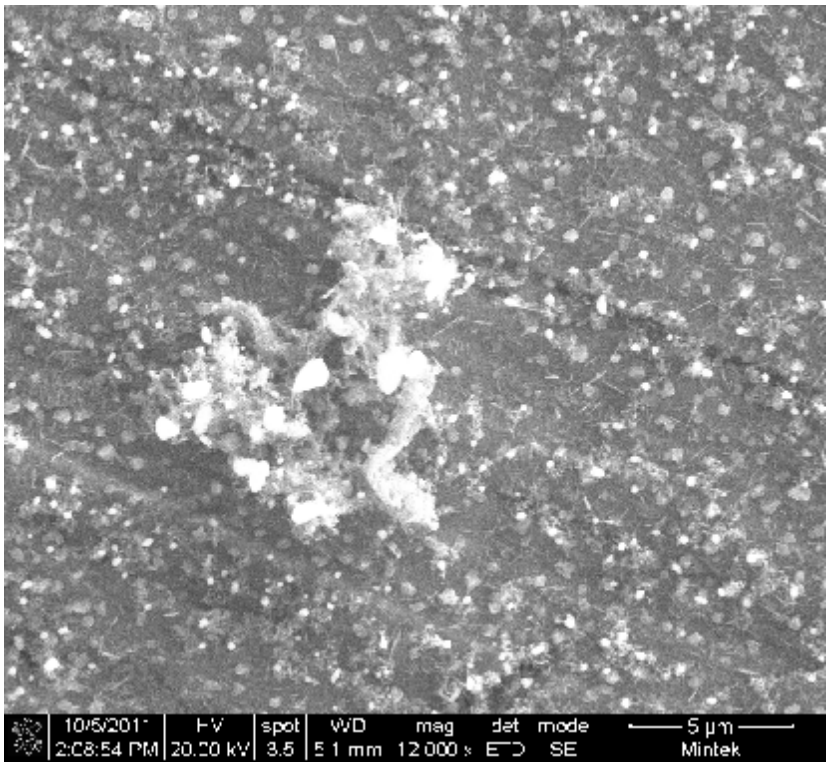


Figure 4.138. SEM-SE image of the surface of Sample 430-4.

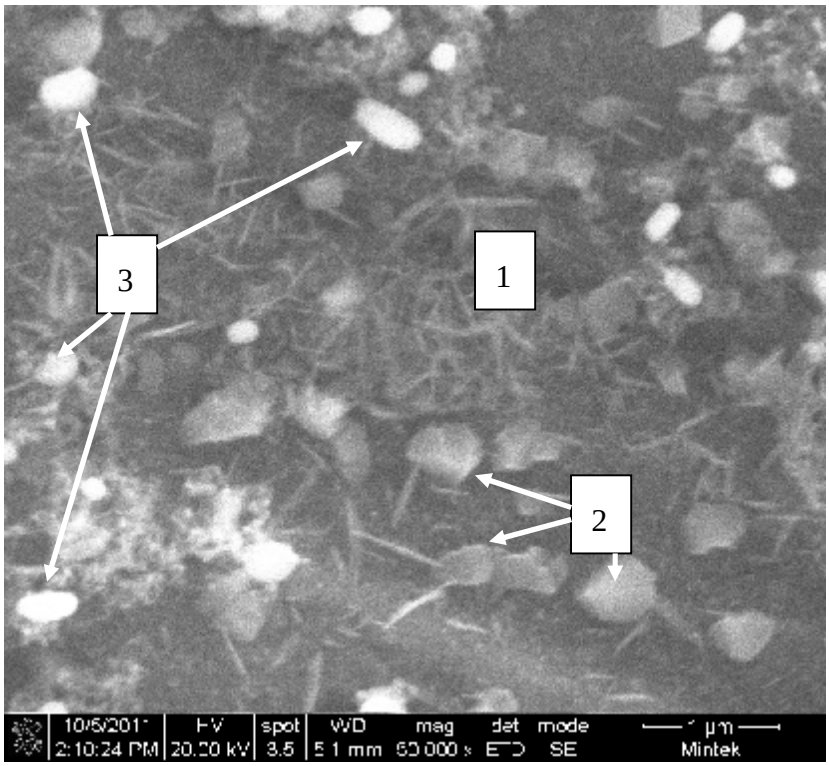


Figure 4.139. Higher magnification SEM-SE image of Sample 430-4 shown in Figure 4.138 showing different particles [(1) fine needles, (2) chunky and faceted particles and (3) light particles].

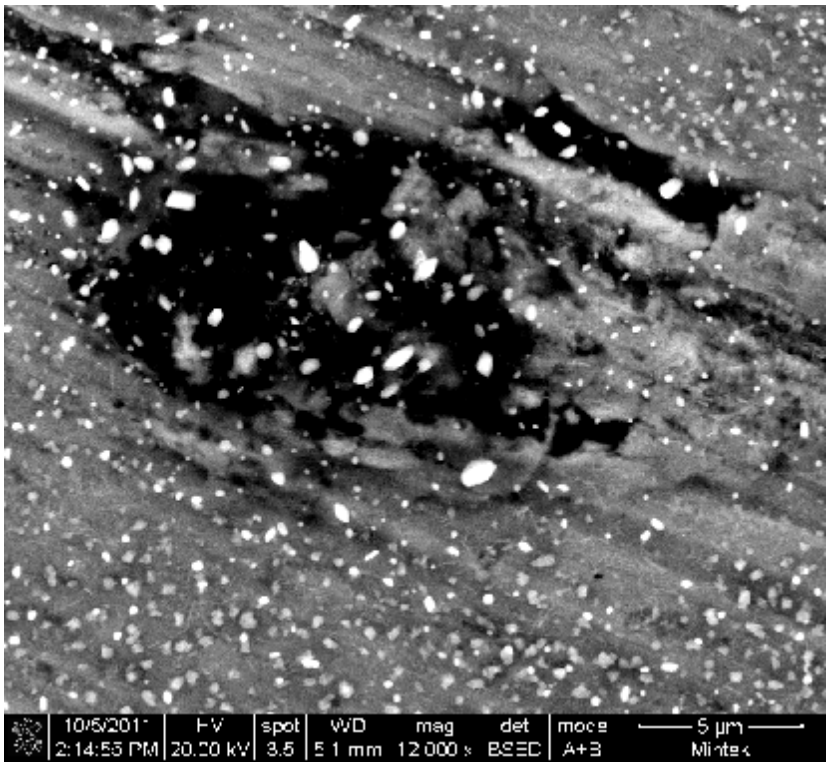


Figure 4.140. SEM-BSE image of coking and possible pit initiation on the surface in Sample 430-4.

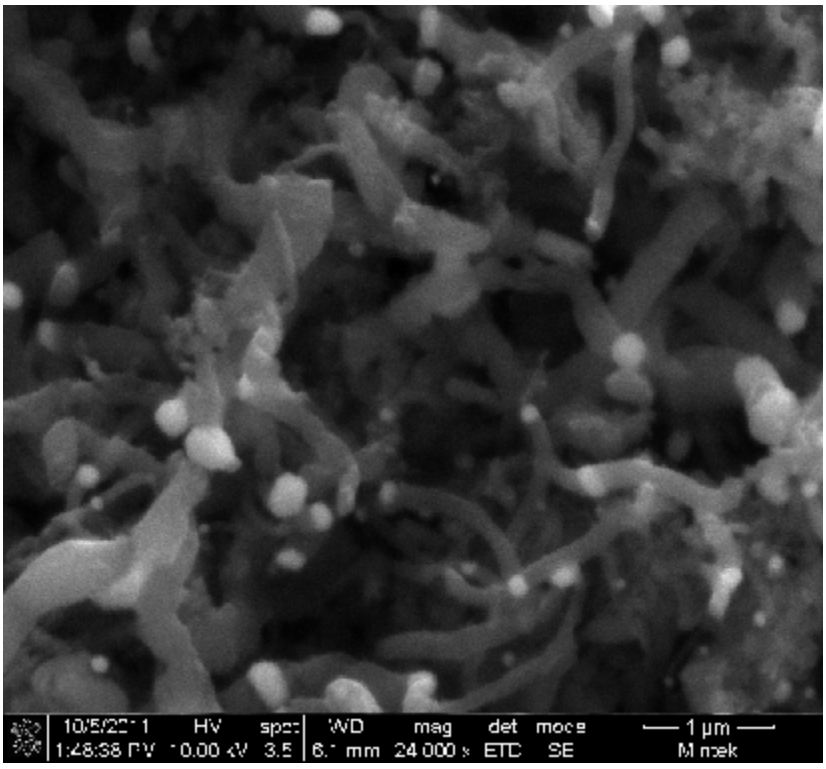


Figure 4.141. SEM-SE image in secondary mode of coke filaments shown in Figure 4.118, with carbide particles at the tips.

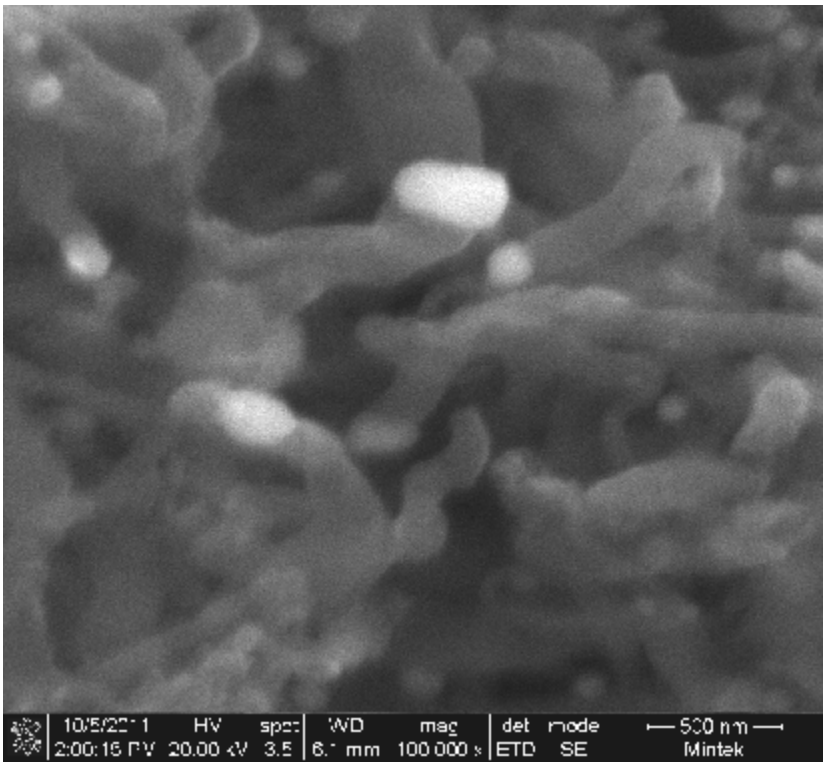


Figure 4.142. Higher magnification SEM-SE image of the region shown in Figure 4.141.

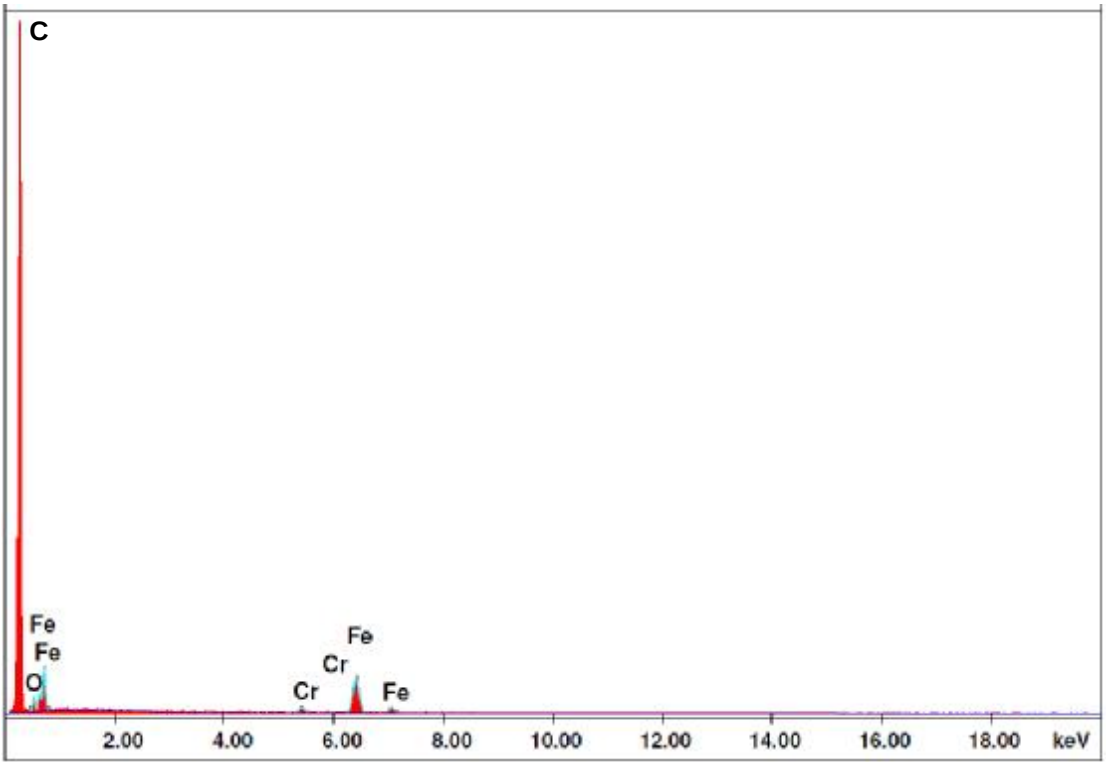


Figure 4.143. EDX spectrum of "metal dust" particles shown in Figure 4.142.

Figure 4.144 is an SEM image of a pit in a Type 316L sample exposed for fourteen days, after cleaning to remove coking and corrosion products. No significant attack was evident away from the pit. Figure 4.145 is an SEM image of a sample that was not cleaned, revealing some of the products still in the pit. Figure 4.146 and Figure 4.147 are SEM images of the coking in the pit, also showing the filament growths with particles at the ends.

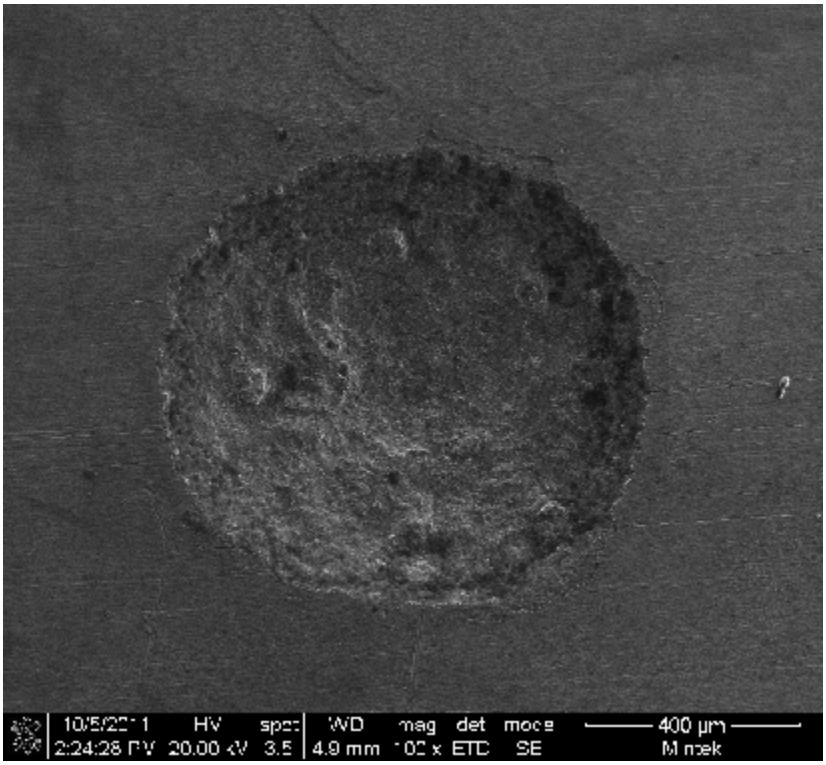


Figure 4.144. SEM-SE image of a pit on the surface in Sample 316-3 (after cleaning).

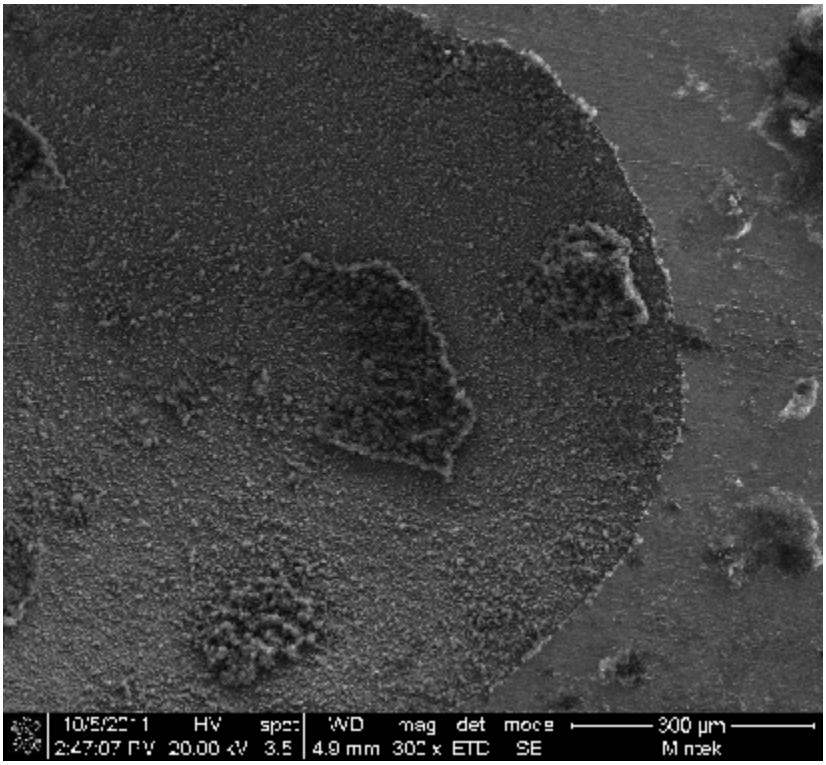


Figure 4.145. SEM-SE image of a pit in Sample 316-4 (not cleaned).

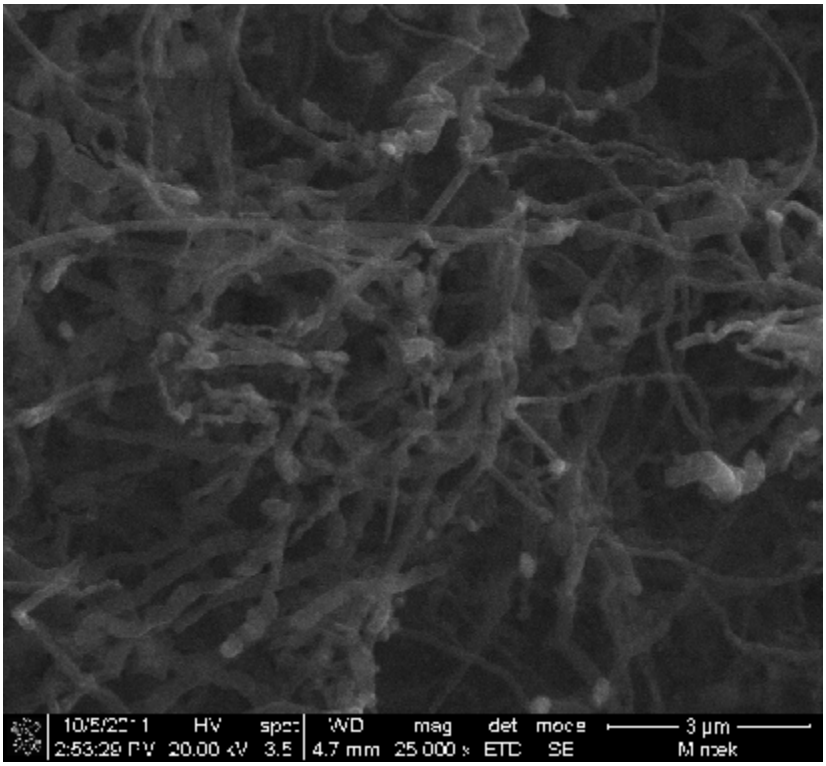


Figure 4.146. SEM-SE image of the carbon products inside the pits shown in Figure 4.145 showing the carbon filaments with carbide particles at tips.

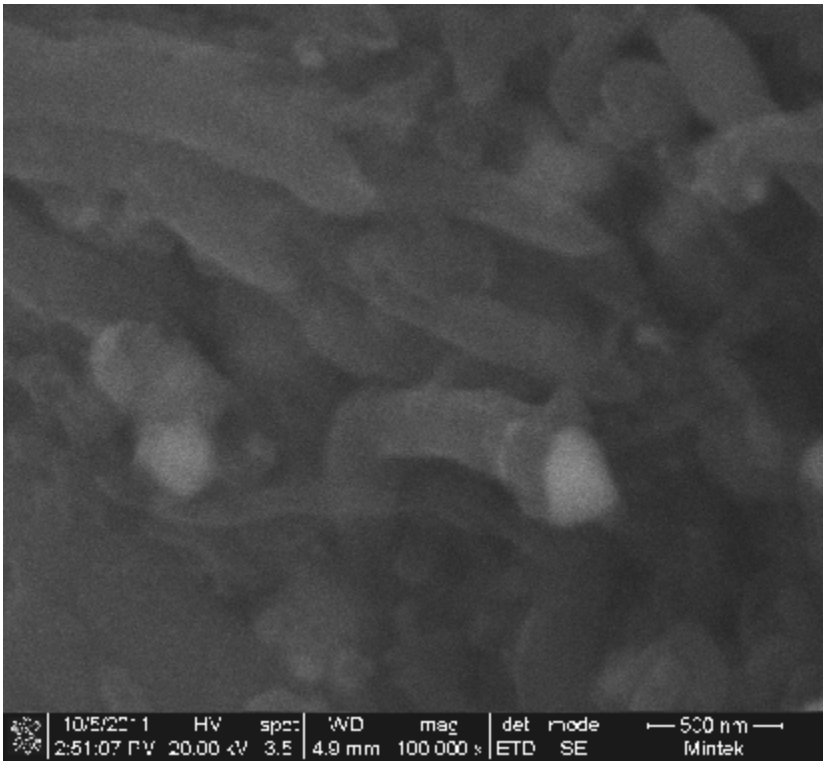


Figure 4.147. Higher magnification SEM-SE image of Figure 4.146.

Figure 4.148 and Figure 4.149 are TEM images of the coke that was removed from the boat. The TEM images clearly demonstrate that the carbon filaments were carbon nanotubes – i.e. they were hollow, although these filaments appeared to be more irregular in shape than for those removed from the austenitic alloys. The diameter of the filaments was less than 100 nm. The metal carbides were further characterised by EDX on the TEM, which allowed for more accurate analyses than on the SEM. Figure 4.150 shows X-ray maps for iron, chromium and nickel of several particles that were analysed. These images clearly show that the particles/carbides consisted predominantly of iron, and some particles contained nickel, and others chromium, or both for the larger particles. However, this finding might be an artefact from the analysis of very fine particles.

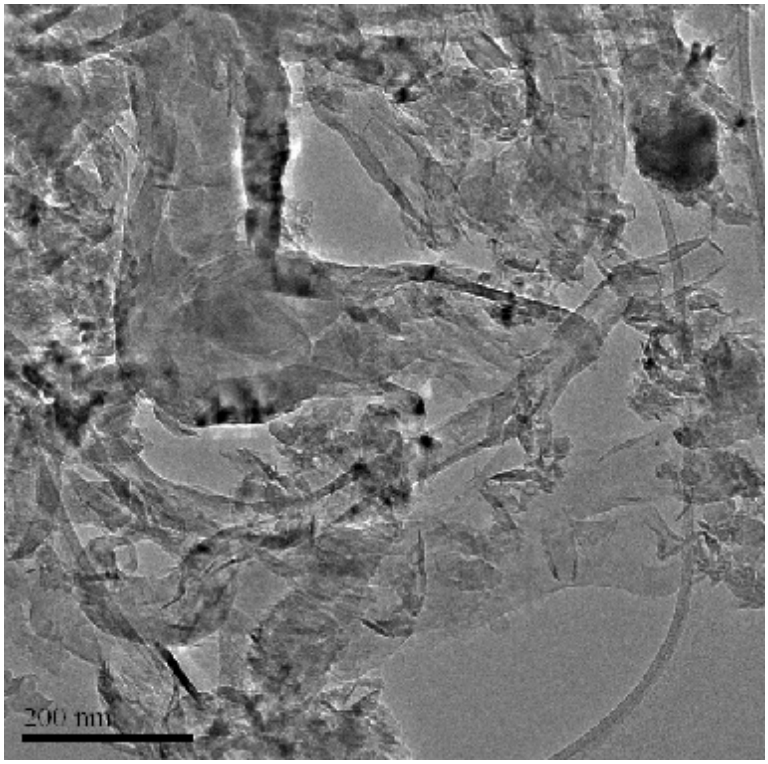


Figure 4.148. TEM image of some of the carbon filaments shown in Figure 4.141, with the dark particle in top right hand corner being a carbide "metal dust".

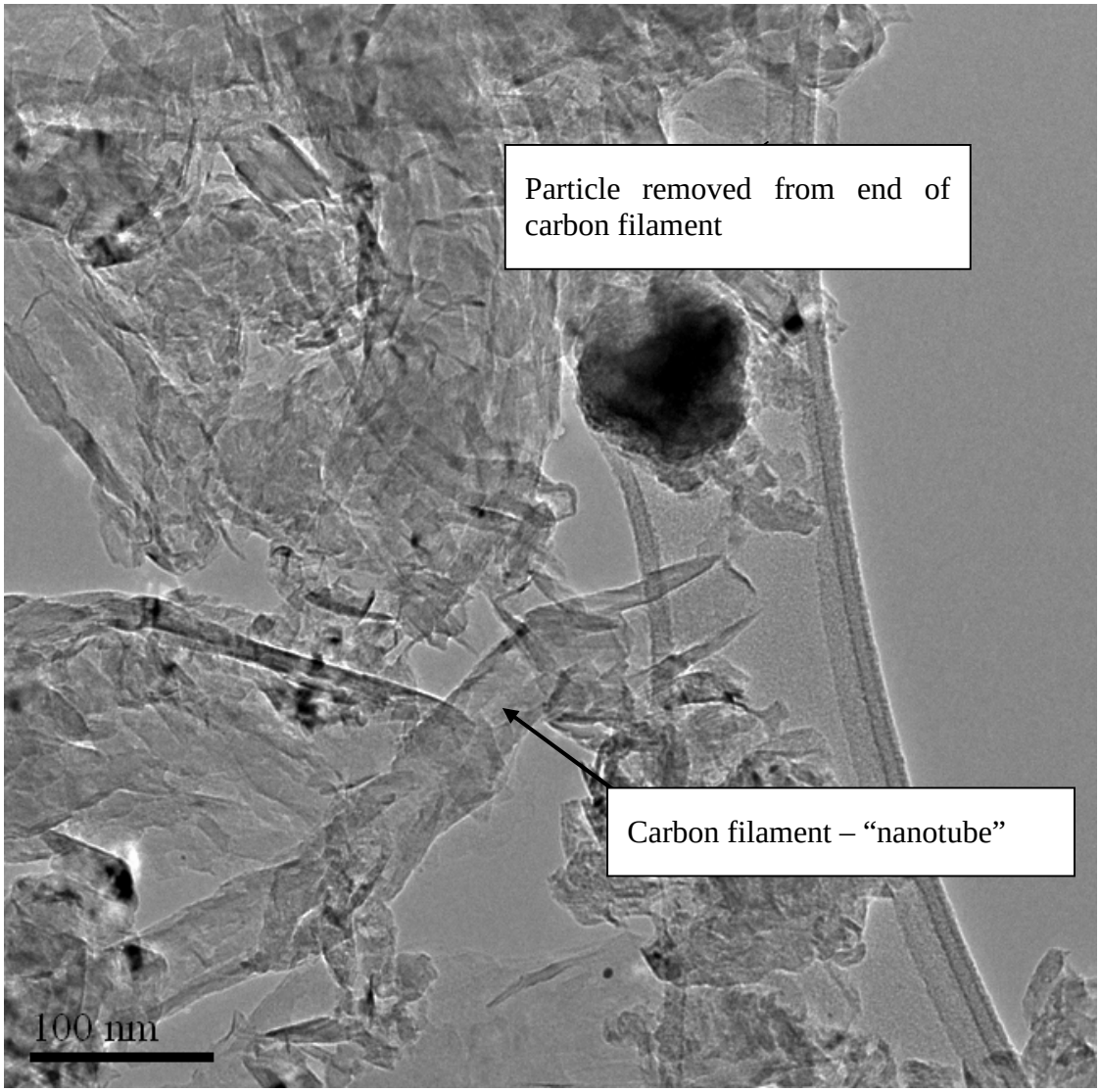
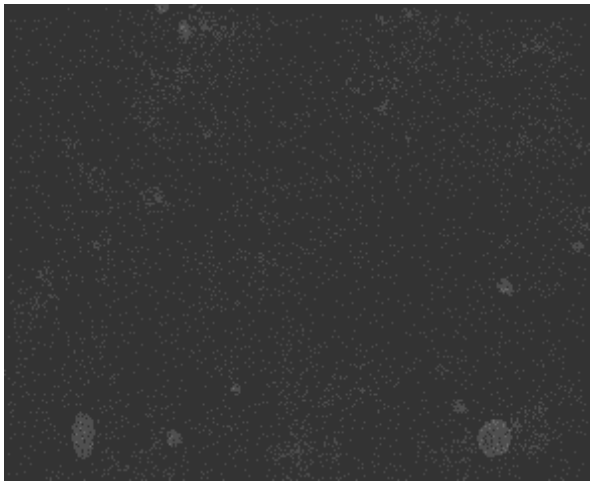
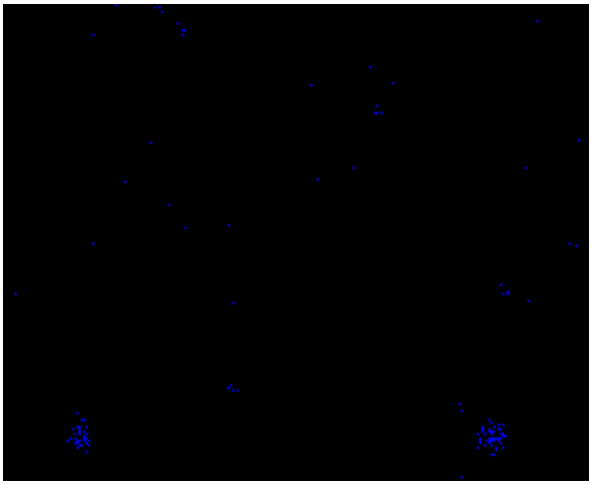


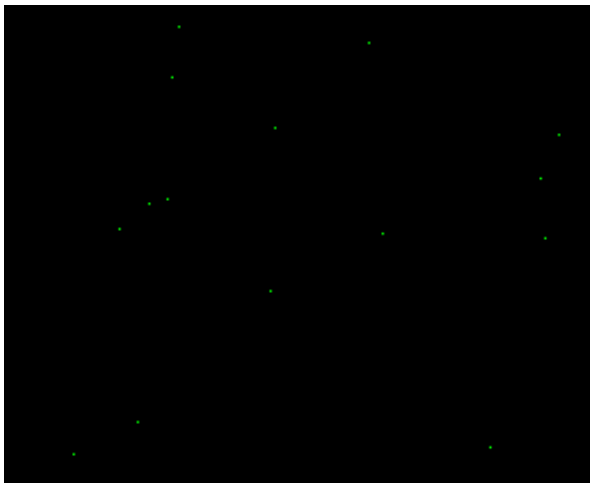
Figure 4.149. TEM image showing a higher magnification of the region in Figure 4.148, clearly showing that the carbon filaments are tubular.



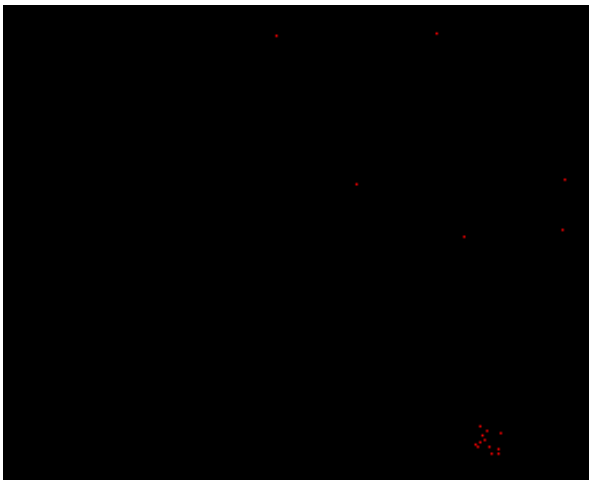
a) TEM image of metal particles – i.e. DUST



b) Fe



c) Cr



d) Ni

Figure 4.150. (a) is an BSE image of the region, and associated X-ray maps of (b) iron, (c) chromium and (d) nickel.

4.3.5. X-ray diffraction

X-ray diffraction of the un-cleaned surfaces of the samples exposed for fourteen days did not show any significant changes compared to the samples in the original condition, as shown in Figure 4.151 to Figure 4.156. The austenitic alloys consisted predominantly of austenite and

some ferrite, whereas the ferritic sample consisted primarily of ferrite, as expected. A trace amount of magnetite was also detected with both the Types 430 and 441 samples.

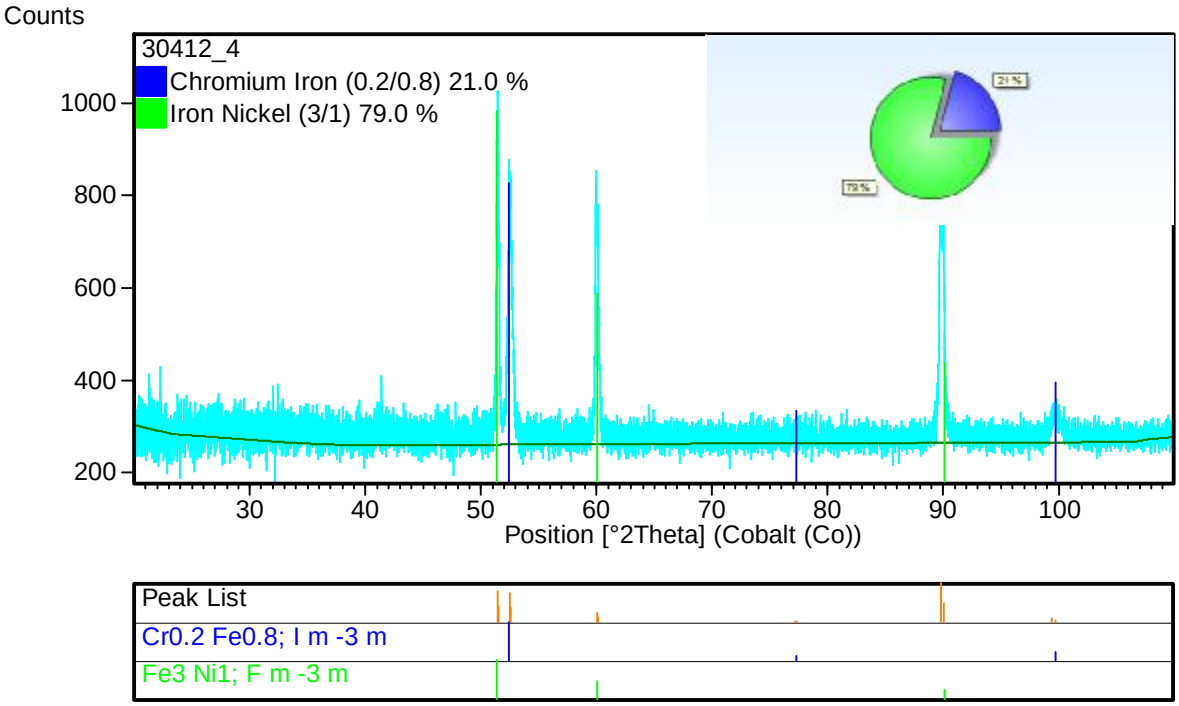


Figure 4.151. X-ray spectrum and volume % of the surface of Sample 304-4.

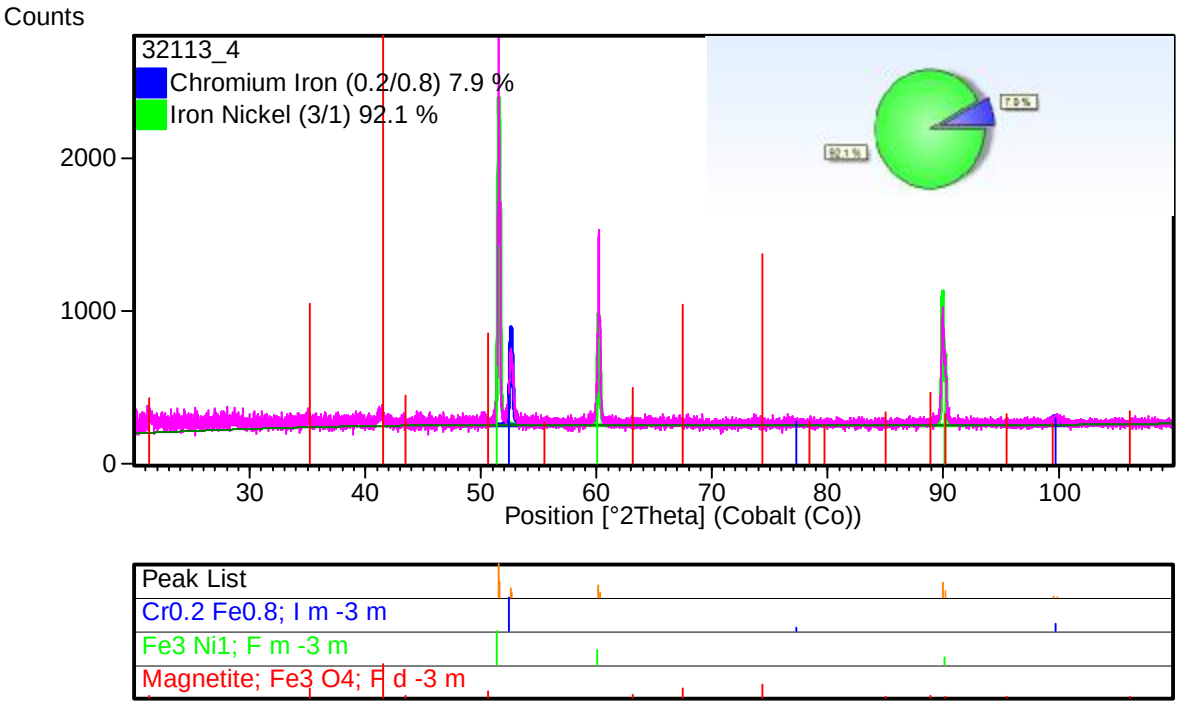


Figure 4.152. X-ray spectrum and volume % of the surface of Sample 321-4.

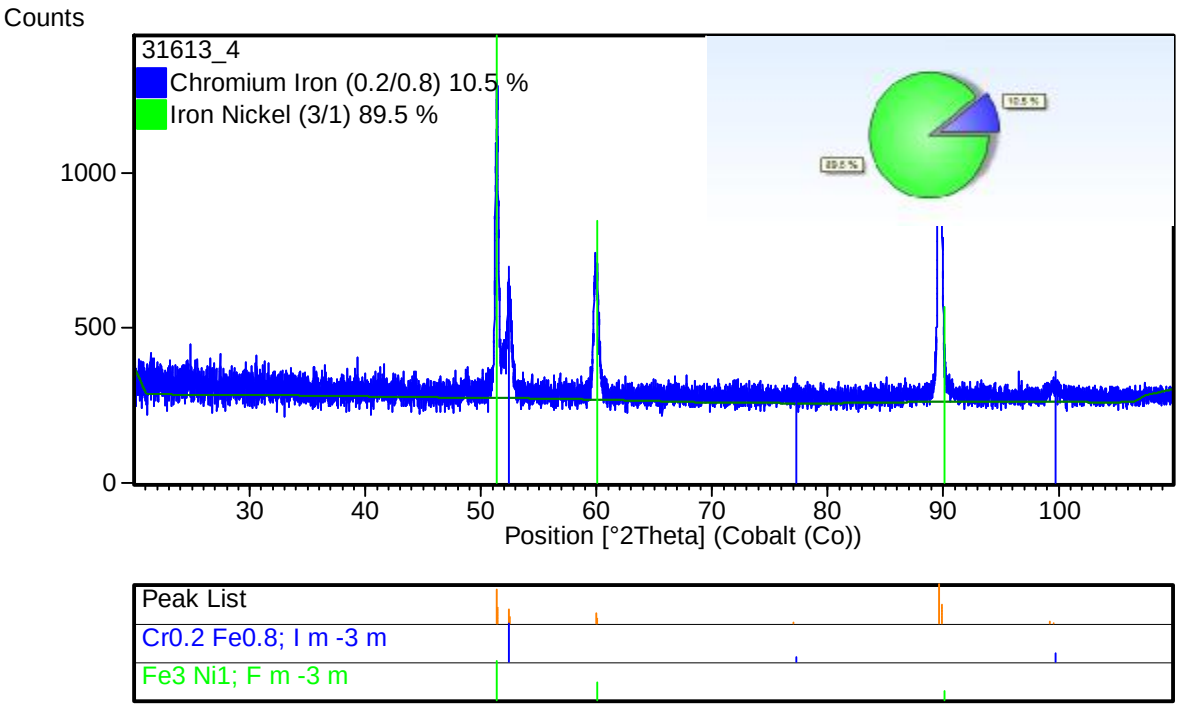


Figure 4.153. X-ray spectrum and volume % of the surface of Sample 316L-4.

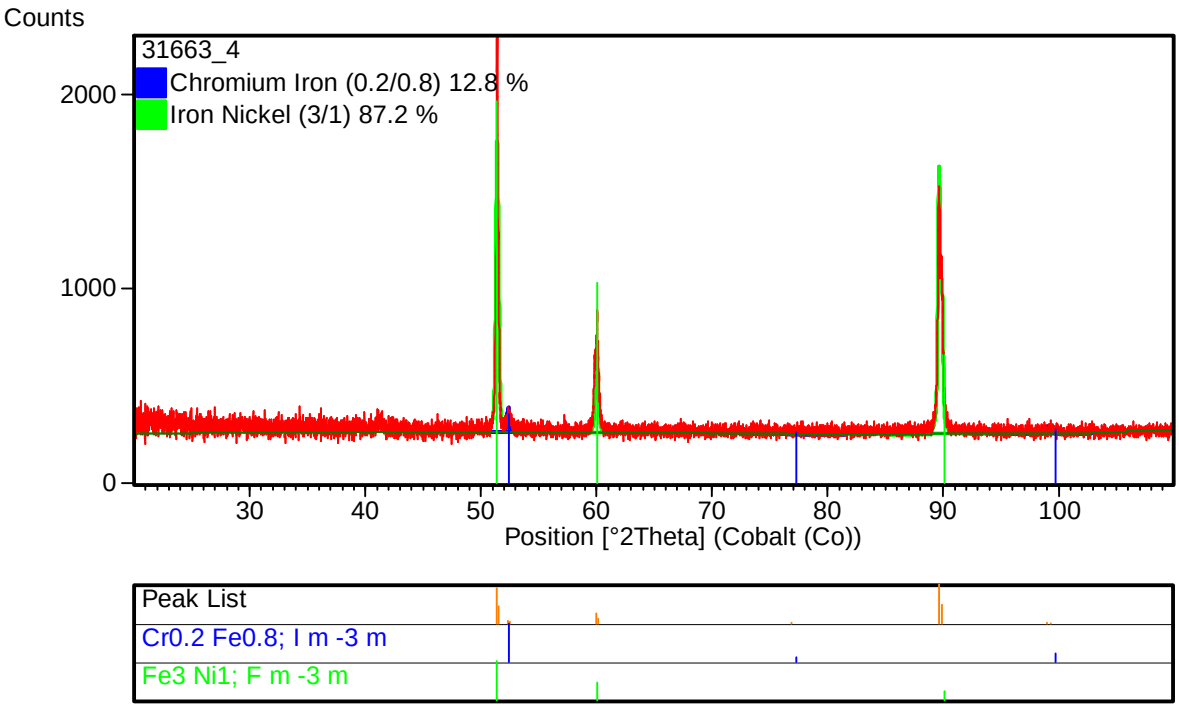


Figure 4.154. X-ray spectrum of the surface of Sample 316Ti-4.

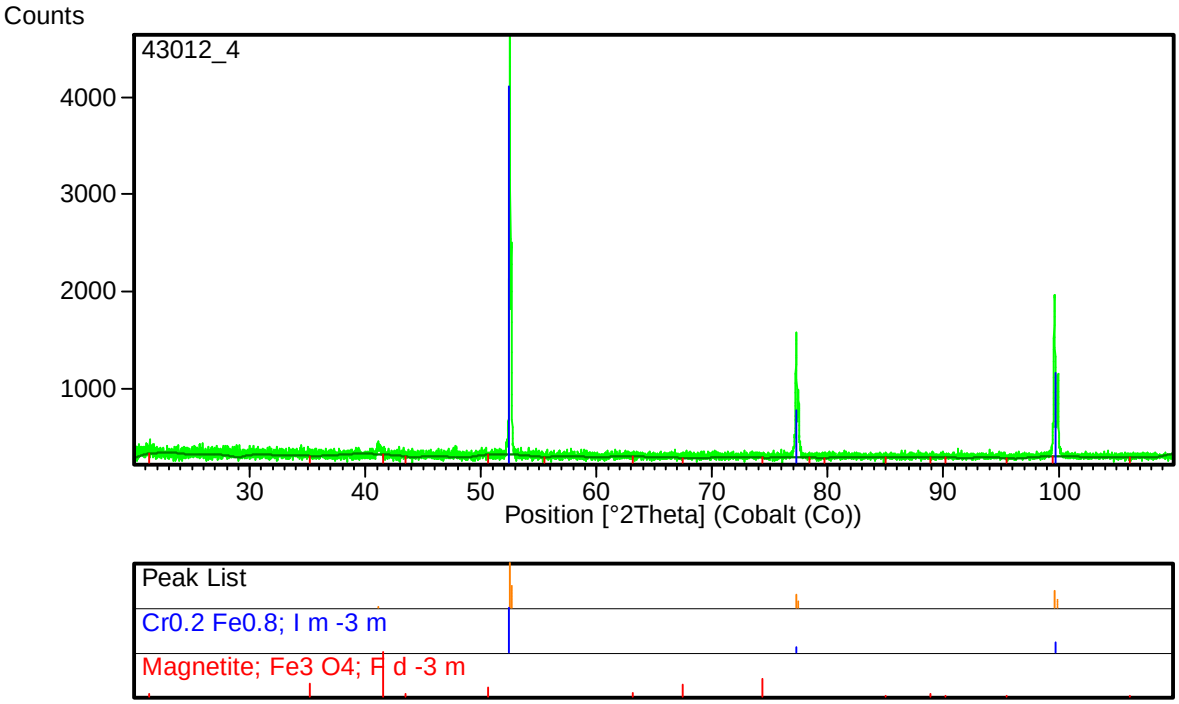


Figure 4.155. X-ray spectrum of the surface of Sample 430-4.

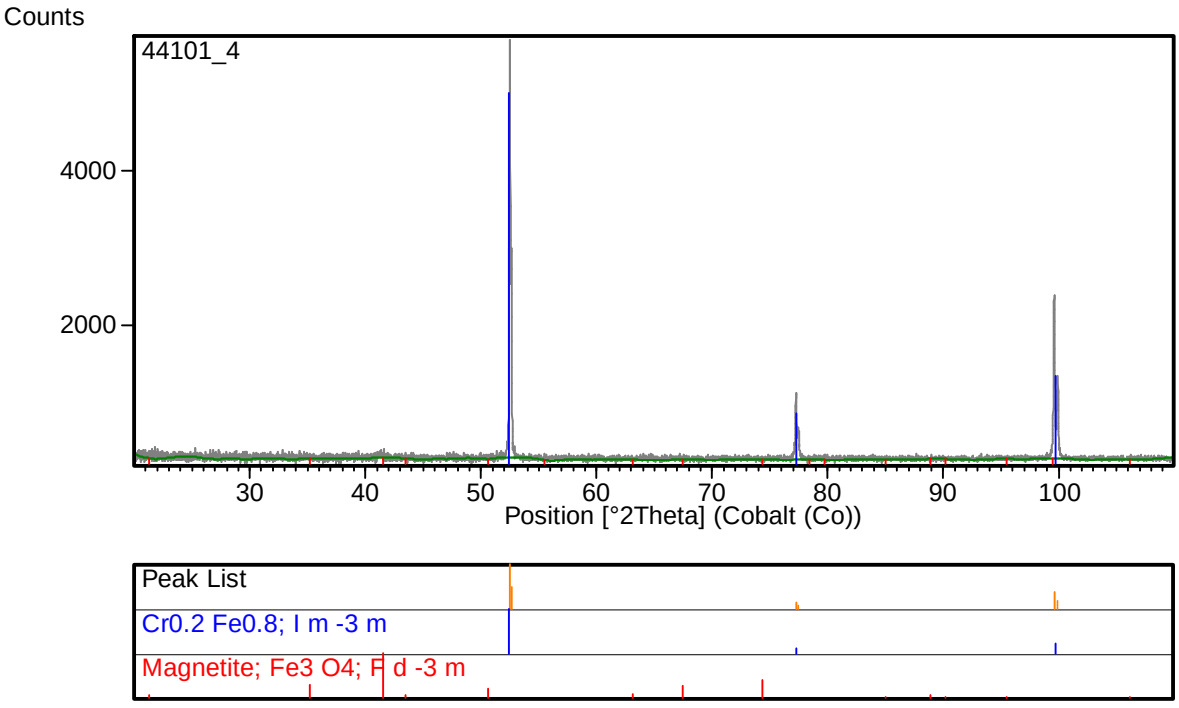


Figure 4.156. X-ray spectrum of the surface of Sample 441-4.

4.4. Thirty day Test

4.4.1. Visual examination

Figure 4.157 is a photograph of the samples removed from the furnace after the thirty day exposure test. Significant coking was again associated with the austenitic alloys, with the ferritic alloys showing significantly less coking. Figure 4.158 and Figure 4.159 are close-up photographs showing the extent of the coke formation on the samples. The coke associated with the ferritic alloys was finer than the coke associated with the austenitic samples. Figure 4.160 is a photograph of the Types 304L and 321 samples that were exposed for thirty days, showing the extent of coking on each material type. The surface of the Type 304L sample could be easily cleaned with a soft bristle brush, and revealed no significant corrosive attack, as shown in Figure 4.161. However, the Type 321 sample could not be easily cleaned, with a relative thick shiny black product on the surface, as shown in Figure 4.162 and Figure 4.163. This product appeared to be an oxide scale.



Figure 4.157. Photograph of the samples in the ceramic boat after the 30-day exposure test.

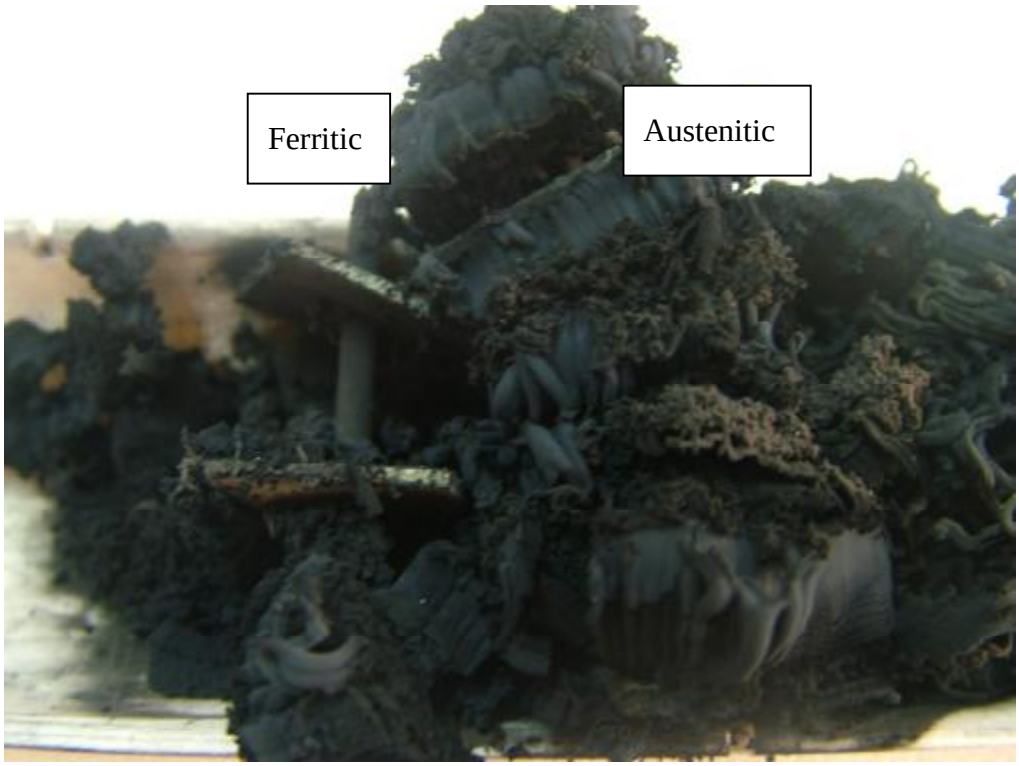


Figure 4.158. Close-up photograph of the coking comparing the austenitic alloys to the ferritic alloys.

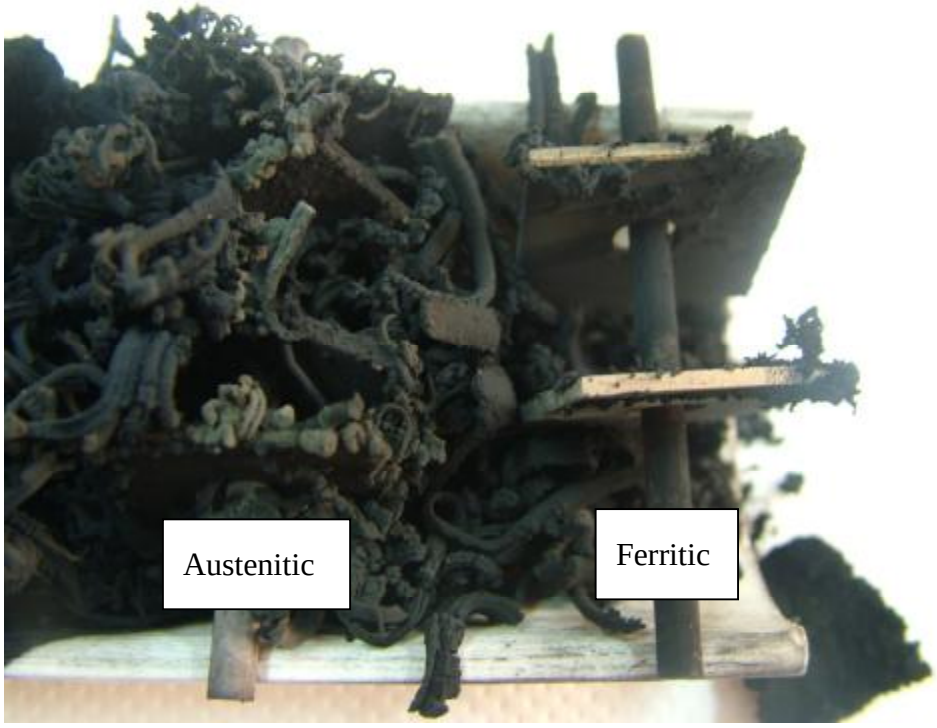


Figure 4.159. Close-up photograph of the coking comparing the austenitic alloys to the ferritic alloys.



Figure 4.160. Photograph of the 304L and 321 samples after the 30-day exposure. The samples on the left-hand side have been cleaned with a soft nylon brush.



Figure 4.161. Close-up photograph of the cleaned 304-7 sample showing pitting at the edges.



Figure 4.162. Photograph of the 321-8 sample that was not cleaned, showing a uniform coke layer.

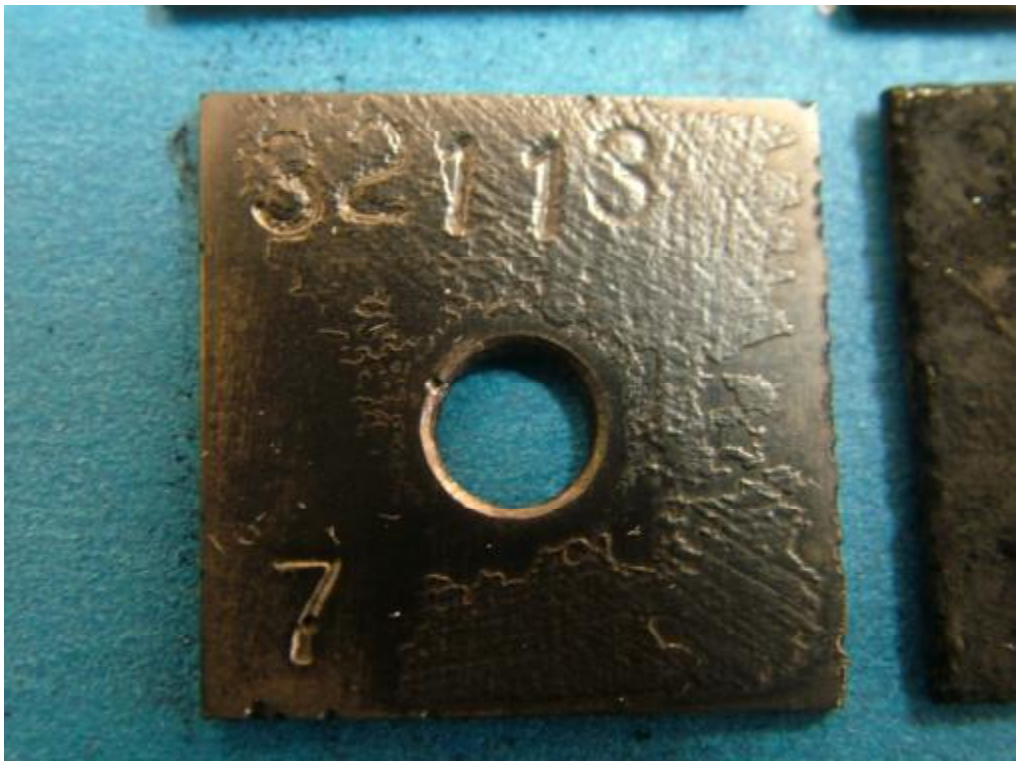


Figure 4.163. Photograph of Sample 321-7 after being cleaned with a brush in running water, showing the shiny black layer retained on the surface.

Figure 4.164 is a photograph of the Types 316L and 316Ti samples after exposure for thirty days, showing coking and the extent of metal wastage on the surface. The attack was in the form of extensive pitting attack. Figure 4.165 is a close-up photograph of the 316L sample and Figure 4.166 after the coupon was cleaned. Figure 4.167 is a photograph of the pitting attack on the 316Ti sample.



Figure 4.164. Photograph of the 316L and 316Ti samples exposed for 30 days. The samples on the LHS have been cleaned, and show extensive pitting.



Figure 4.165. Photograph of Sample 316-8 that was not cleaned.



Figure 4.166. Photograph of Sample 316-7 after cleaning, showing the extent of the pitting.

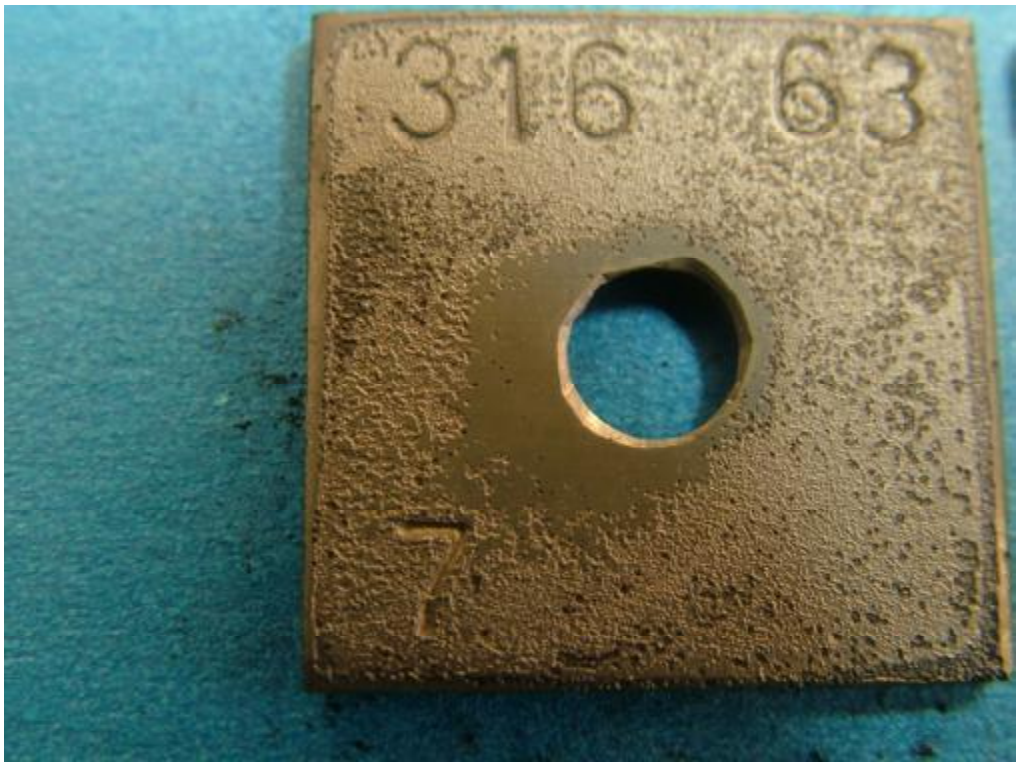


Figure 4.167. Photograph of Sample 316Ti-7 after cleaning, showing the extent of the pitting.

Figure 4.168 is a photograph of the Types 430 and 441 samples after exposure for 30 days. Figure 4.169 is a photograph of one coupon from each alloy after cleaning, showing the extent of coking and metal wastage. The coking appeared similar for the alloys, but the attack on the Type 430 was by single pits (Figure 4.170), whereas the pitting attack was more widespread on the 441 samples, albeit in a localised area of the samples (Figure 4.171). There was also a black product on the 441 sample surfaces associated with the pitting attack, which could not be easily removed.



Figure 4.168. Photograph of the 430 and 441 samples after exposure for 30 days.



Figure 4.169. Photograph showing the difference between the 430 and 441 samples that were cleaned (LHS) and those that were not cleaned (RHS).



Figure 4.170.Close-up photograph of the 430-7 sample that was cleaned, showing attack on the edges.



Figure 4.171. Close-up photograph of Sample 441-7 after being cleaned, showing tenacious carbon build-up and associated pitting.

4.4.2. Mass loss

The changes in the weights of the samples after the 30 day exposure test are given in Table 4.4. Both the Types 304L and 321 samples gained weight, but the 321 sample gained significantly more. This was attributed to the relatively thick black product that appeared to be an oxide scale. The 316L and 316Ti samples lost a significant amount of weight during the test, which was obviously due to the metal wastage. The 316Ti sample exhibited a higher weight loss than the 316L samples. The mass loss on the Type 441 samples was the lowest of all the samples, suggesting that this alloy performed the best. The amount of coking on the ferritic samples was lower than for the austenitic samples.

Table 4.4. Mass change data for the 30-day test.

Sample		304L	304L	321	321	316L	316L	316Ti	316Ti	430	430	441	441
		7	8	7	8	7	8	7	8	7	8	7	8
Density	**g/cm^3**	7.9	7.9	7.8	7.8	8.0	8.0	8.0	8.0	7.8	7.8	7.7	7.7
Length	**mm**	20.41	20.46	20.47	20.64	20.43	19.87	20.92	20.78	20.54	20.65	20.69	20.83
Width	**mm**	19.54	20.37	20.13	20.51	20.19	19.77	20.62	20.48	20.40	20.13	20.52	20.64
Thickness	**mm**	1.24	1.29	1.31	1.42	1.40	1.40	1.85	1.83	1.47	1.42	1.39	1.43
Radius	**mm**	5.00	5.05	5.00	5.00	5.20	5.00	5.00	5.12	5.03	5.03	5.00	5.00
Area	**cm^2**	8.50	8.90	8.83	9.16	8.86	8.50	9.68	9.22	9.11	9.00	9.17	9.31
Mass before	**g**	3.4582	3.9261	4.0132	4.3227	4.1247	3.9697	5.7779	5.6501	4.2866	4.1911	4.1089	4.2224
Mass after	**g**	3.4601	3.9292	4.0647	4.3697	4.0730	3.9376	5.6669	5.5336	4.2769	4.1994	4.1121	4.2323
Mass loss	**g**	-0.0019	-0.0031	-0.0515	-0.047	0.0517	0.0321	0.111	0.1165	0.0097	-0.0083	-0.0032	-0.0099
Time	**h**	720	720	720	720	720	720	720	720	720	720	720	720
Corr. rate	**mm/y**	-0.0034	-0.0054	-0.0909	-0.0800	0.0887	0.0575	0.1745	0.1921	0.0166	-0.0144	-0.0055	-0.0168
Corr. rate	**Average**	**-0.0044**		**-0.0855**		**0.0731**		**0.1833**		**0.0011**		**-0.0112**	
Cleaned	**g**	3.453	-	4.011	-	4.0679	-	5.6597	-	4.2745	-	4.1083	-
Cleaned mass loss	**g**	0.0052	-	0.0022	-	0.0568	-	0.1182	-	0.0121	-	0.0006	-
Cleaned corr. rate	**mm/y**	**0.0094**	**-**	**0.0039**	**-**	**0.0975**	**-**	**0.1858**	**-**	**0.0207**	**-**	**0.0010**	**-**
Coking mass	**g**	0.0071	-	0.0537	-	0.0051	-	0.0072	-	0.0024	-	0.0038	-
Coking rate	**mg/cm^2/day**	**0.0279**	**-**	**0.2026**	**-**	**0.0192**	**-**	**0.0248**	**-**	**0.0088**	**-**	**0.0138**	**-**

4.4.3. Metallography

Figure 4.172 to Figure 4.174 are cross-sections through samples of Types 304L, showing relatively minor attack at the surfaces. Figure 4.175 is a micrograph showing internal carburisation in a 304L sample which penetrated to at least 300 µm internally, with some associated metal wastage. Figure 4.176 is a micrograph of a Type 321 sample showing very little attack over most of the surface, although there was carburisation and associated attack at other areas of the samples, as shown in Figure 4.177 to Figure 4.179. Although there were local areas that were attacked deeper, the attack was more general over the surfaces of the samples. A light second phase formed on the grain boundaries, as well as inside the grains. This phase does not seem to be attacked, but was left seemingly unaffected inside the corrosion products.



Figure 4.172. Micrograph of a cross-section through Sample 304-7 showing localised attack.



Figure 4.173. Micrograph of Sample 304-7 showing more widespread attack.

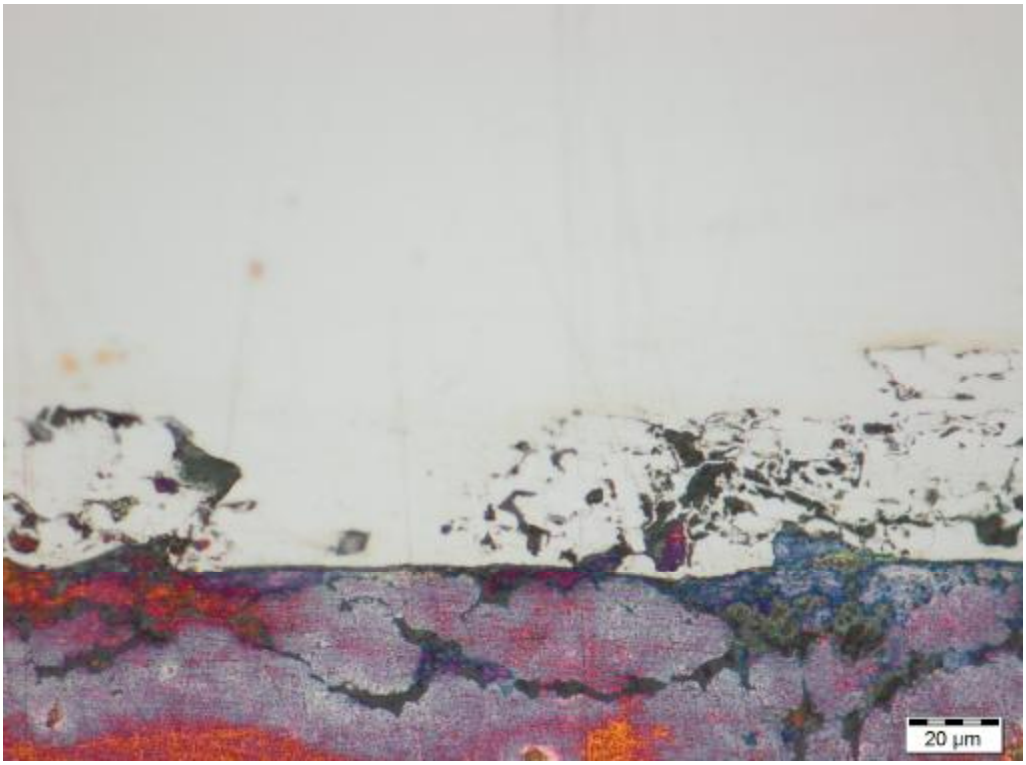


Figure 4.174. Higher magnification micrograph of the attack in Sample 304-7.



Figure 4.175. Micrograph of carburisation and associated attack in Sample 304-7.

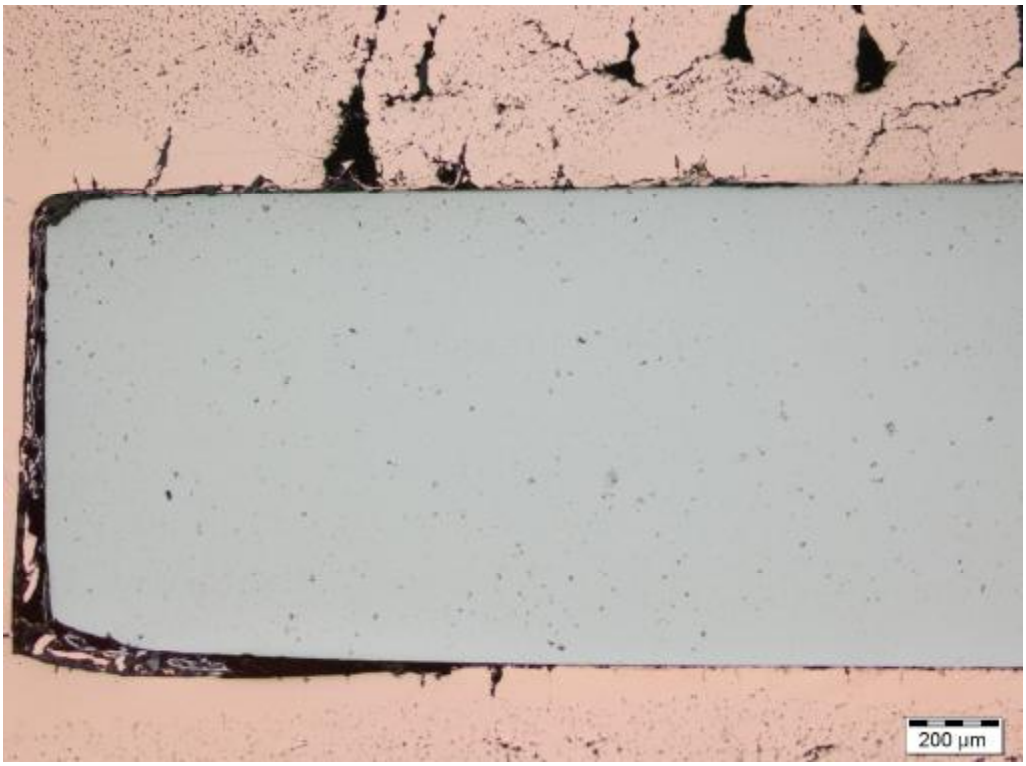


Figure 4.176. Micrograph of a cross-section through Sample 321-7 showing no localised attack.



Figure 4.177. Micrograph of carburisation and widespread attack in Sample 321-8.

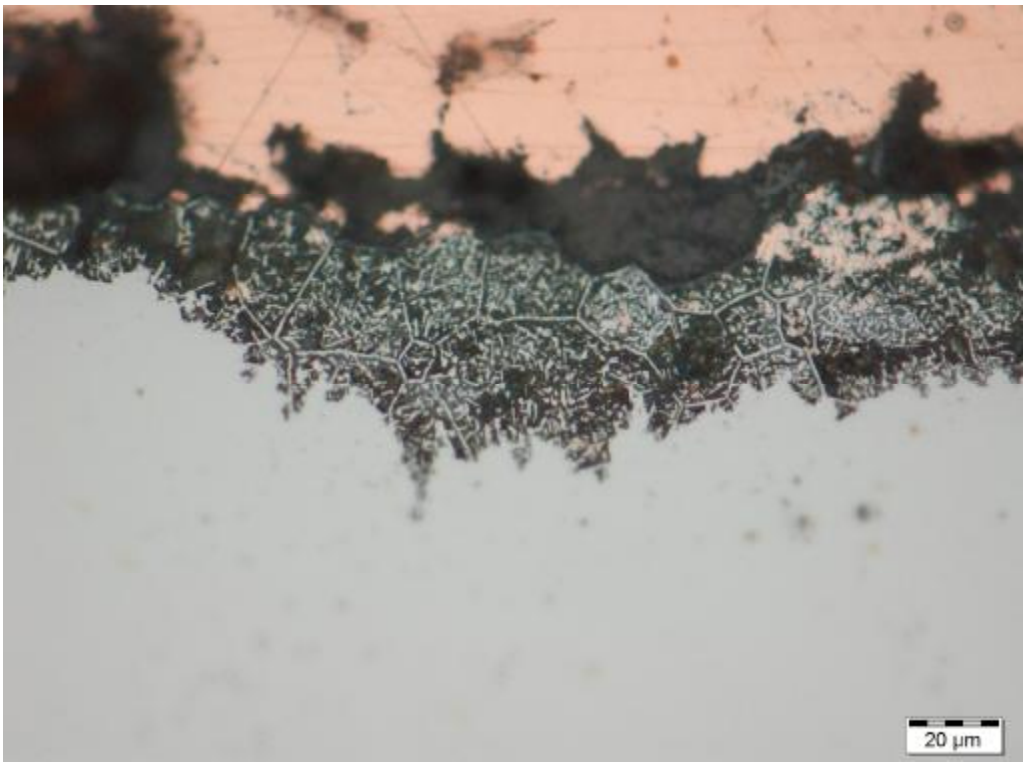


Figure 4.178. Higher magnification of the carburisation and attack in Sample 321-8 shown in Figure 4.177.

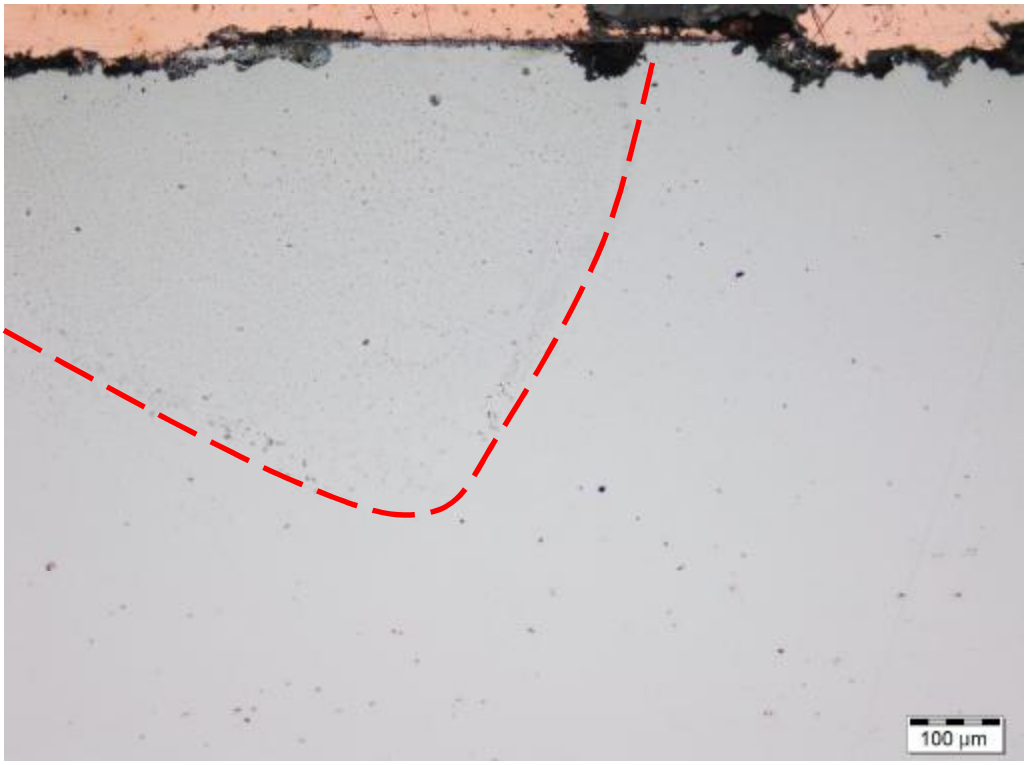


Figure 4.179. Micrograph in the unetched condition showing the internal carburisation in Sample 321-8 (inside dashed line).

The pitting attack in the Type 316L samples was so extensive that the attack became general (uniform), as the pits grew together. However, these areas had generally smooth surfaces, even though the mechanism of attack over most of the surfaces was intergranular, as shown in Figure 4.180 to Figure 4.185. Figure 4.186 to Figure 4.188 are micrographs of the 316Ti samples showing similar attack to that of the 316L samples. The progressive degradation of the grains, starting from the grain boundaries, is demonstrated. There was no evidence of a protective oxide film in the areas exhibiting attack.



Figure 4.180. Micrograph of a cross-section through Sample 316-7 showing wide-spread attack.

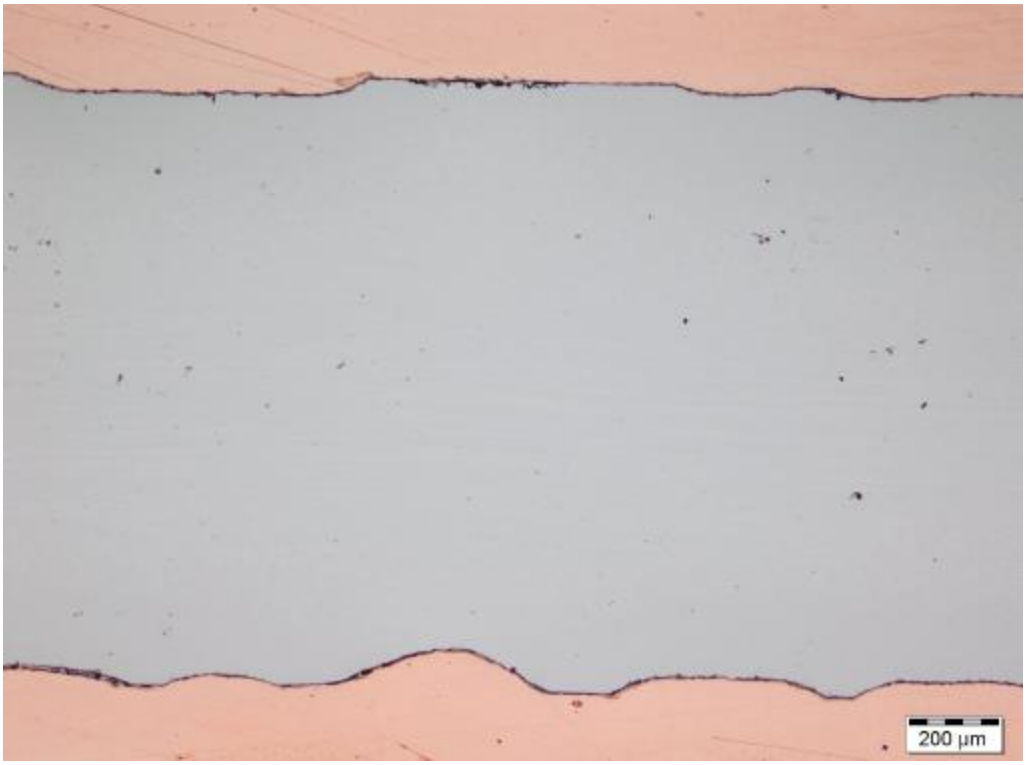


Figure 4.181. Micrograph of Sample 316-7 in another area as shown in Figure 4.180 showing uniform nature of attack.

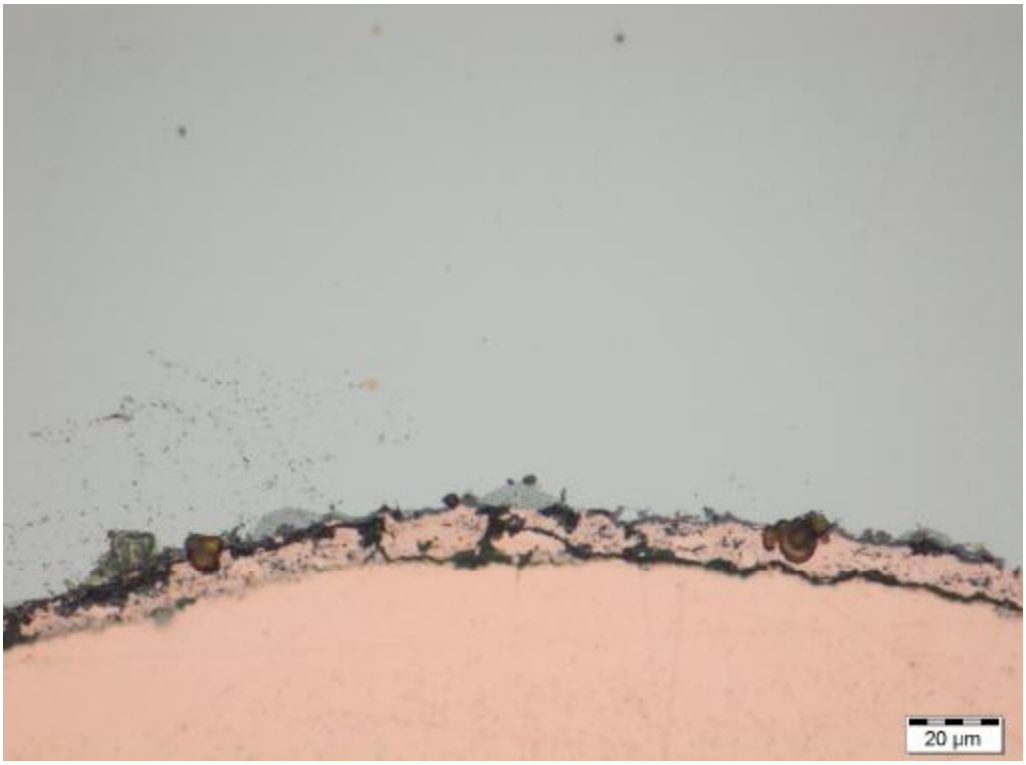


Figure 4.182. Higher magnification micrograph of Sample 316-7 showing uniform nature of attack.



Figure 4.183. Micrograph of Sample 316-7 showing intergranular attack and grain dropping.

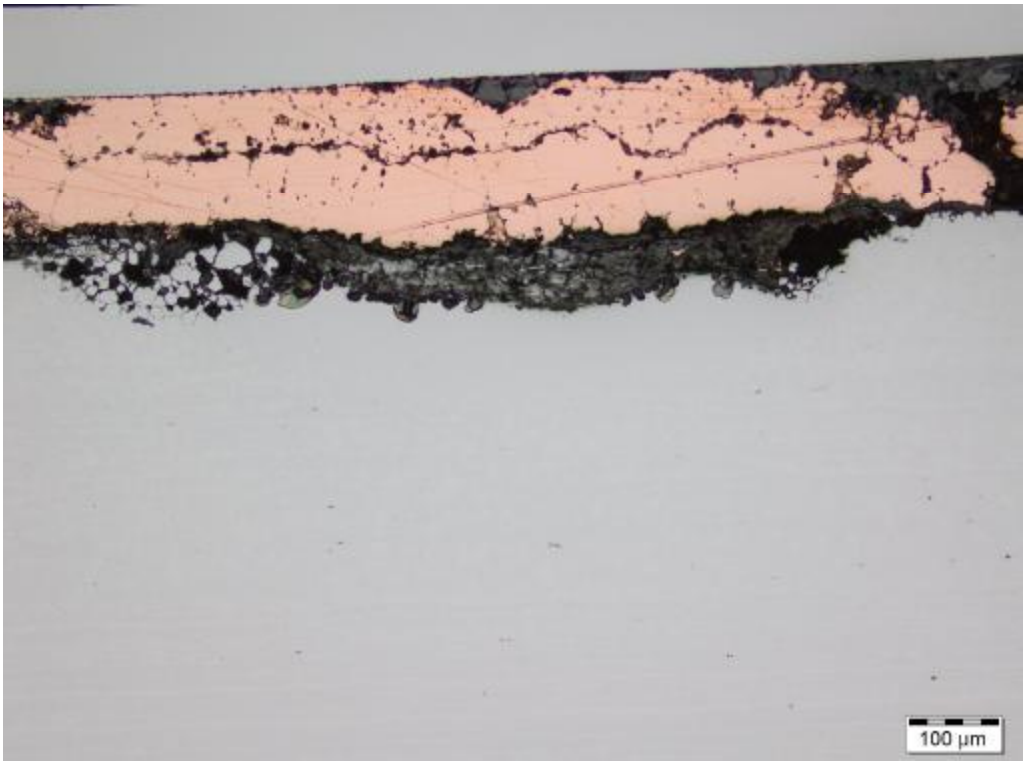


Figure 4.184. Micrograph of attack in Sample 316-8.

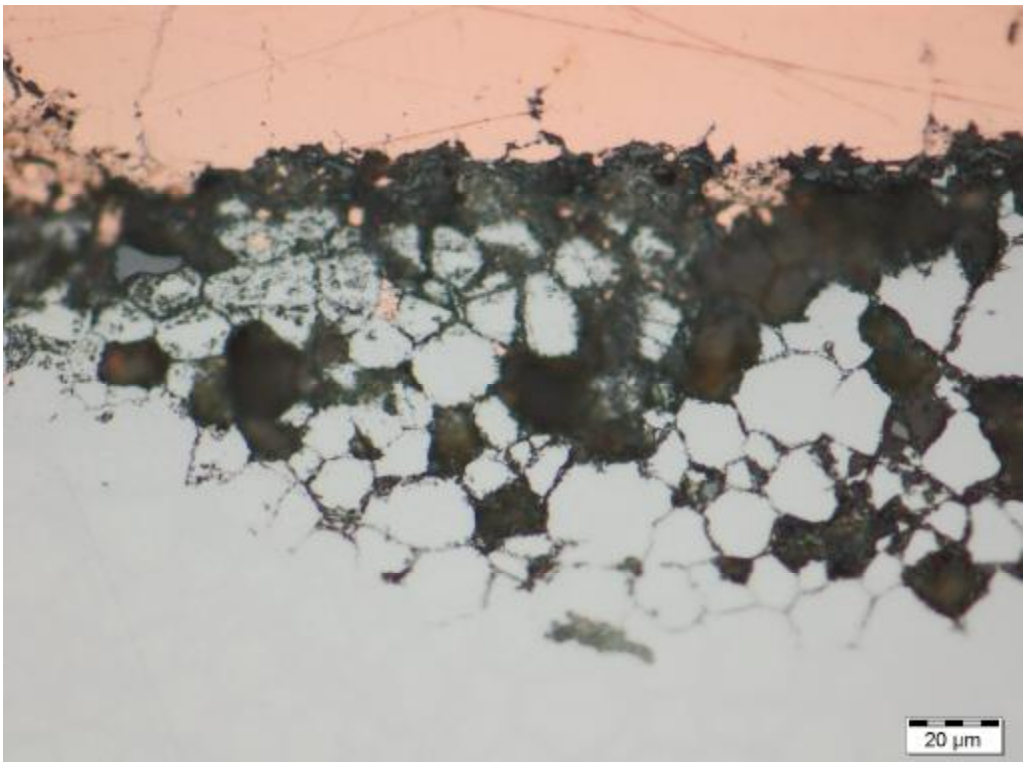


Figure 4.185. Higher magnification micrograph of Sample 316-8 showing intergranular attack.



Figure 4.186. Micrograph of attack in Sample 316Ti-8.

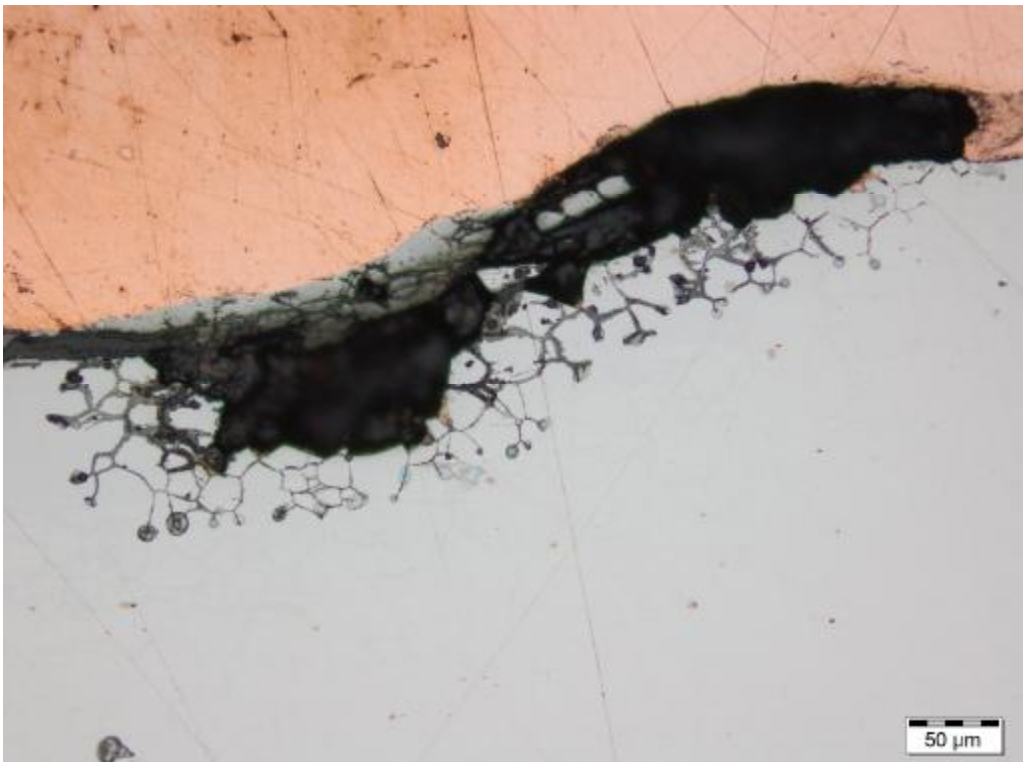


Figure 4.187. Higher magnification micrograph of Sample 316Ti-8 shown in Figure 4.186.

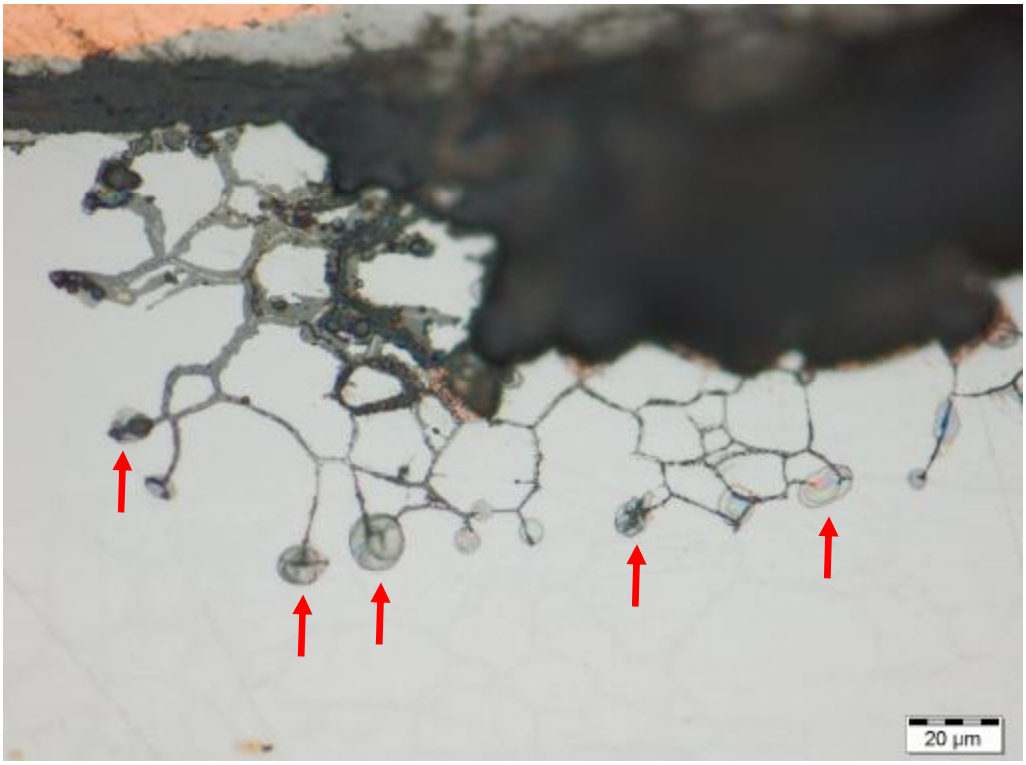


Figure 4.188. Higher magnification micrograph of Sample 316Ti-8 shown in Figure 4.187 (the globular features (arrows) are alcohol stains, seeping from the intergranular attack).

Figure 4.189 is of etched Type 430 at an area that revealed minor pitting/attack on the surface. However, three zones were apparent subsurface: i) the matrix that was slightly carburised throughout, ii) a dark layer of carburisation surrounding the attack, and iii) a lighter area inside the carburised zone. Figure 4.190 is a higher magnification of the different areas and Figure 4.191 is an area between two regions of attack, showing a similar extent of carburisation as shown in Figure 4.189. Figure 4.192 is a higher magnification of the material below the surface, Figure 4.193 is a micrograph of the carburised layer, Figure 4.194 shows the interface between the carburised zone and the matrix, and Figure 4.195 is a micrograph near the centre of the sample, showing the general carbide distribution. The dark carburised zone (Figure 4.193) shows significant grain boundary precipitation, probably a chromium carbide. The carbides in the matrix were spheroidal, but they become finer and plate-like (Widmanstätten structure) in the carburised zone. Near the surface in the carburised zone (Figure 4.192), there were no plates, but all had broken down as finely distributed carbides. The most significant corrosion attack was associated with the fine carburised zone, as well as with the grain boundary carbide precipitation zone.

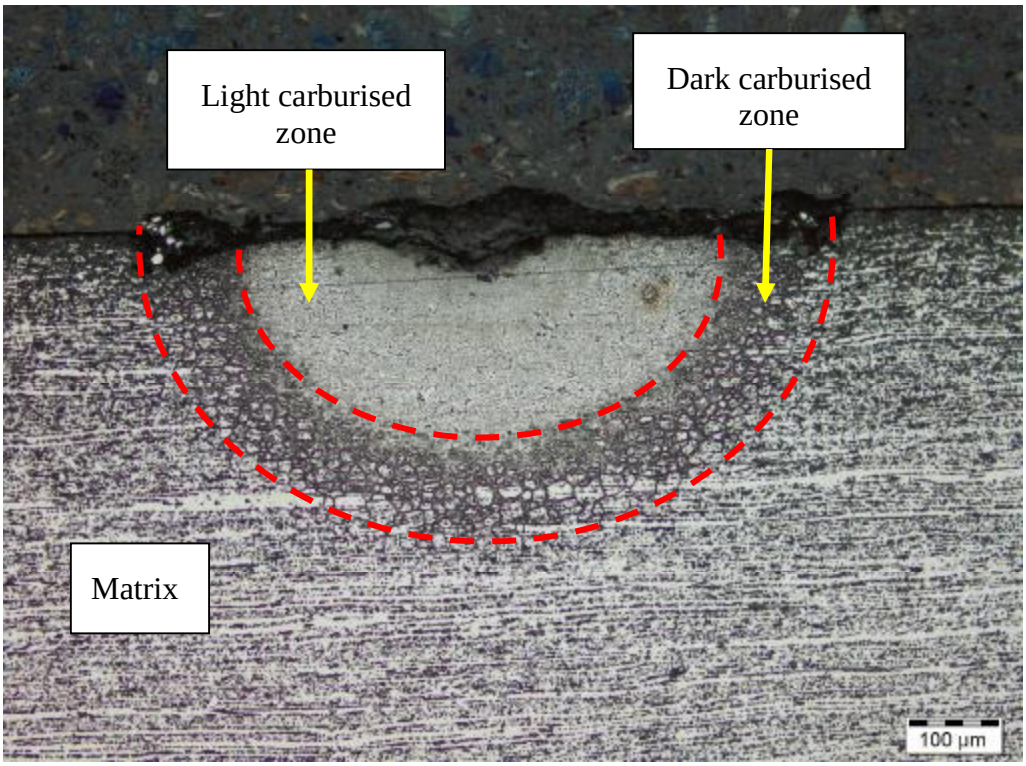


Figure 4.189. Micrograph of internal carburisation and attack in Sample 430-7 (etched).



Figure 4.190. Higher magnification micrograph of Sample 430-7 shown in Figure 4.189 (etched).

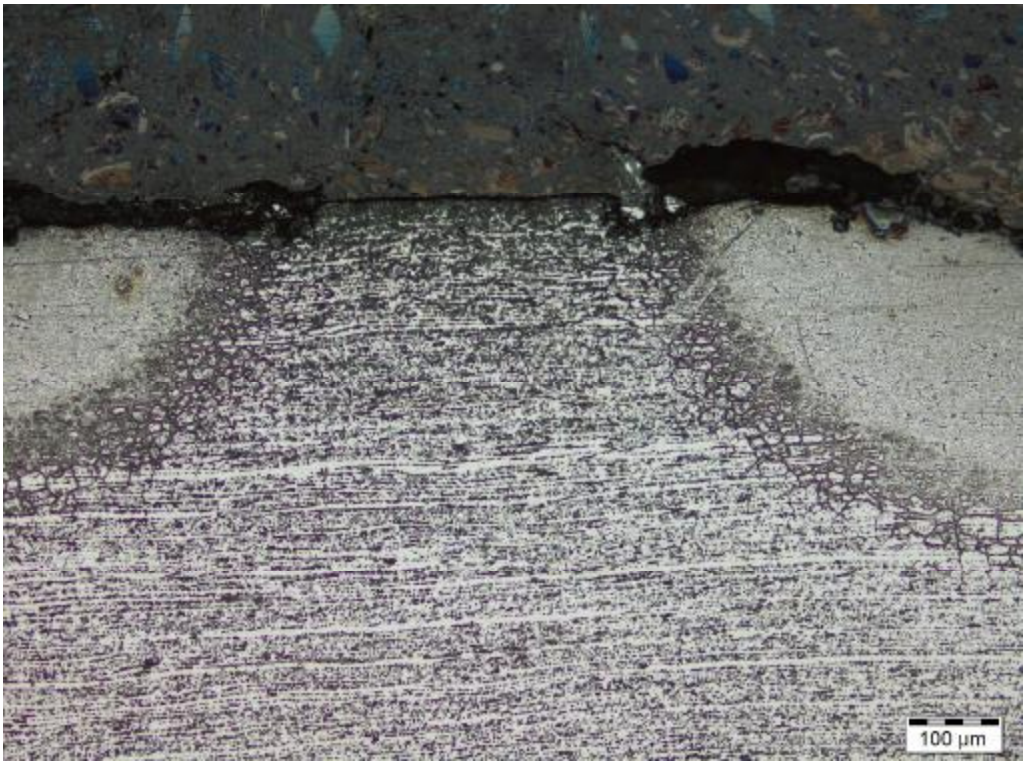


Figure 4.191. Micrograph between two areas of localised attack in Sample 430-7 (etched).

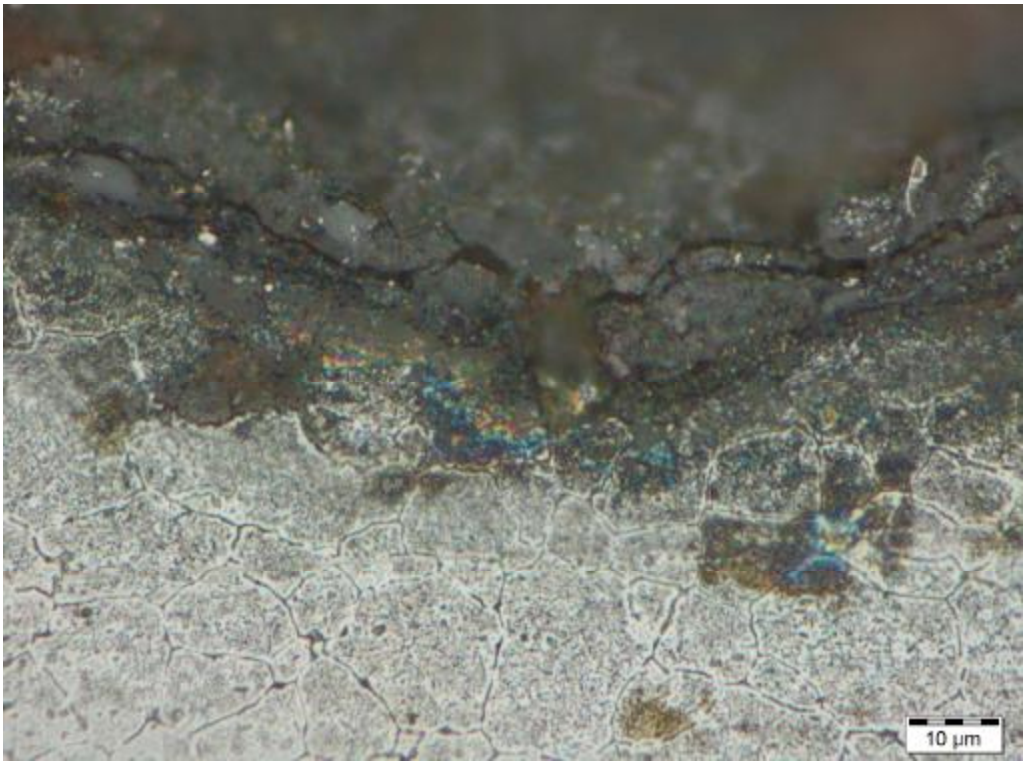


Figure 4.192. Higher magnification micrograph near the surface just below the pit in Sample 430-7 (etched).

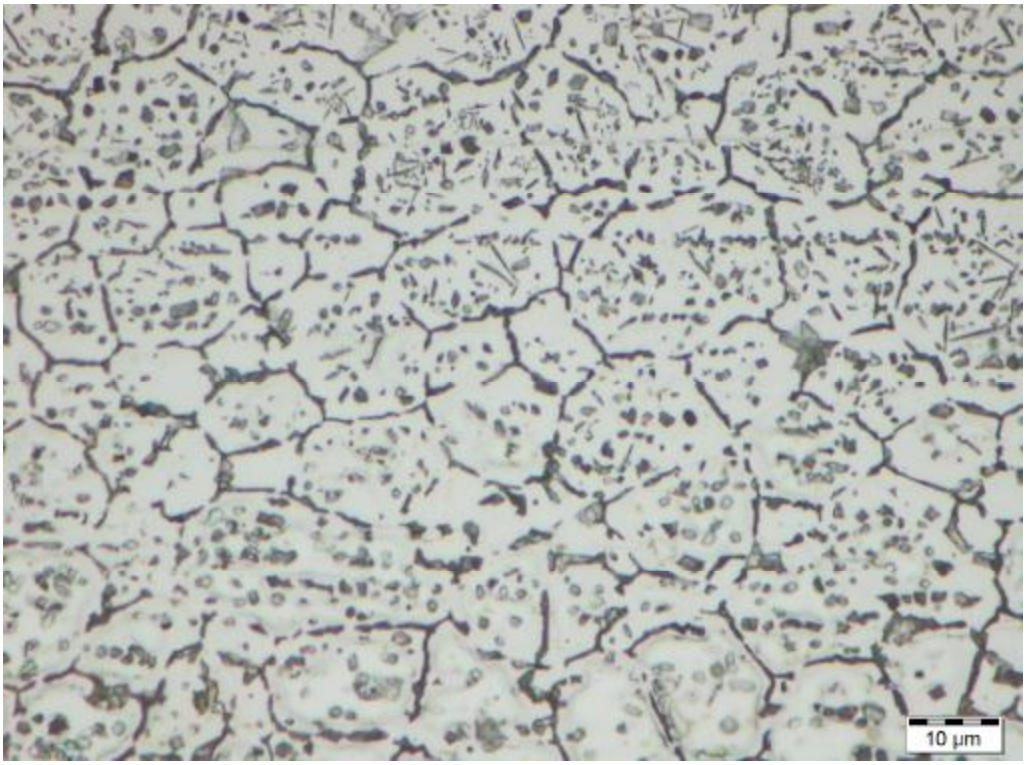


Figure 4.193. Micrograph of Sample 430-7 in the carburised zone (etched).

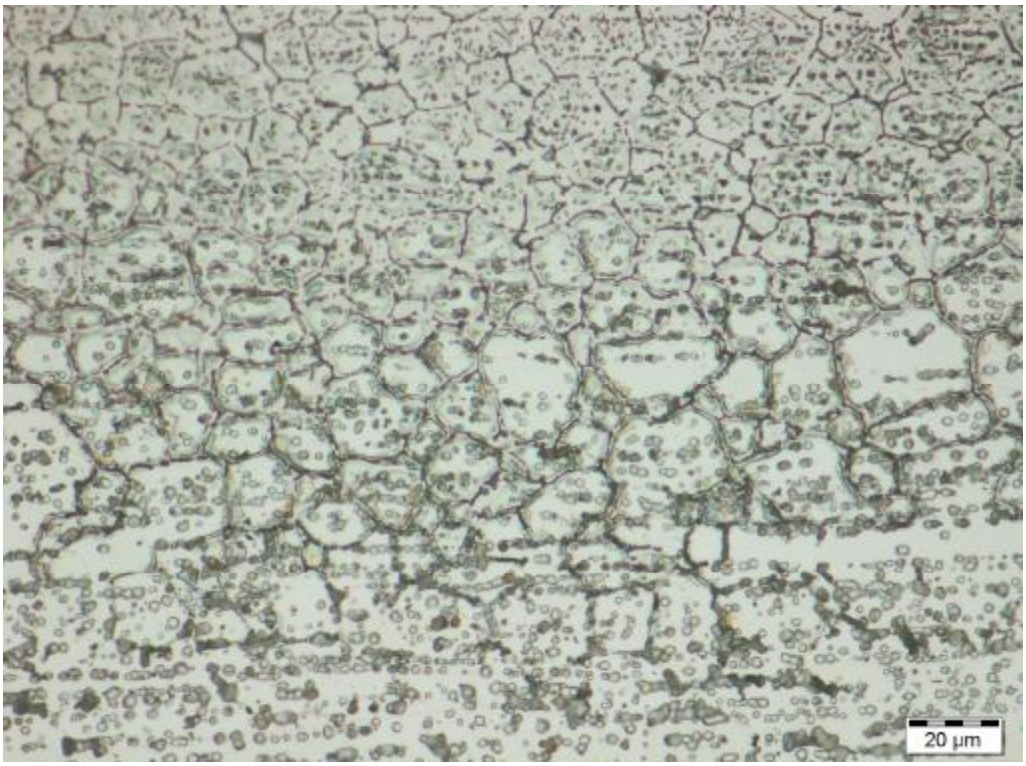


Figure 4.194. Micrograph of the interface between the carburised zone and matrix in Sample 430-7 (etched).

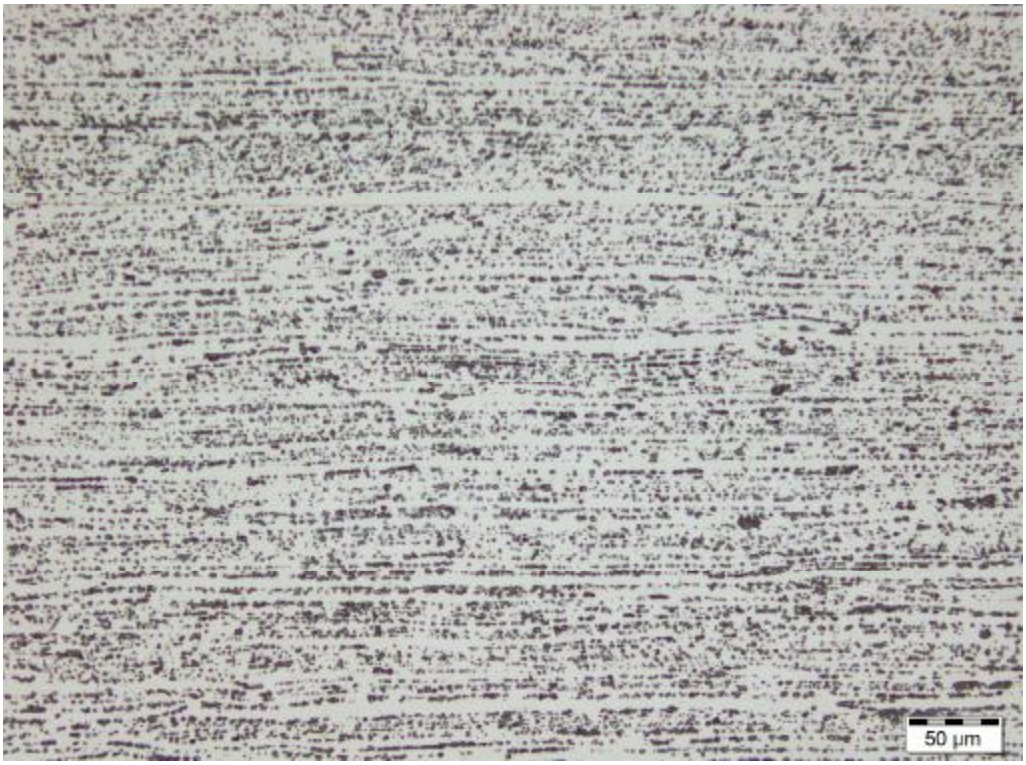


Figure 4.195. Micrograph of sample near the centre of Sample 430-7 showing the general carbide distribution (etched).

Figure 4.196 to Figure 4.198 are micrographs of cross-sections through the Type 441 samples that were exposed for 30 days. No significant pitting or other attack was evident on the surface, except on one corner of one sample. However, a dark layer was evident around the circumference of the sample, which was also accompanied by surface relief around the edges. This is akin to poor edge retention, generally associated with over-polishing during sample preparation for metallography, although this sample was mechanically polished with other alloys that did not show this phenomenon. Figure 4.199 is a micrograph showing several places of local oxide breakdown and consequent carburisation, and Figure 4.200 shows an area of the sample exhibiting continuous carburisation. Figure 4.201 is a micrograph of an etched sample showing the same area as Figure 4.196 (rotated 180°), explaining the edge effect observed, i.e. being due to carburisation. Figure 4.202 to Figure 4.204 are higher magnification micrographs at different positions of the carburisation. The carburisation initiated on the grain boundaries, and then propagated to the entire grains. The carbide precipitation differed from the Type 430 samples, with the precipitation associated with the grain boundaries being more extensive in the Type 441 samples. The internal carburisation of the grains was also more severe, and occurred by the precipitation of fine carbides. Figure 4.205 and Figure 4.206 are micrographs showing the carburisation and/or

coking associated with the titanium carbo-nitride precipitates in the 441 samples away from the surface.

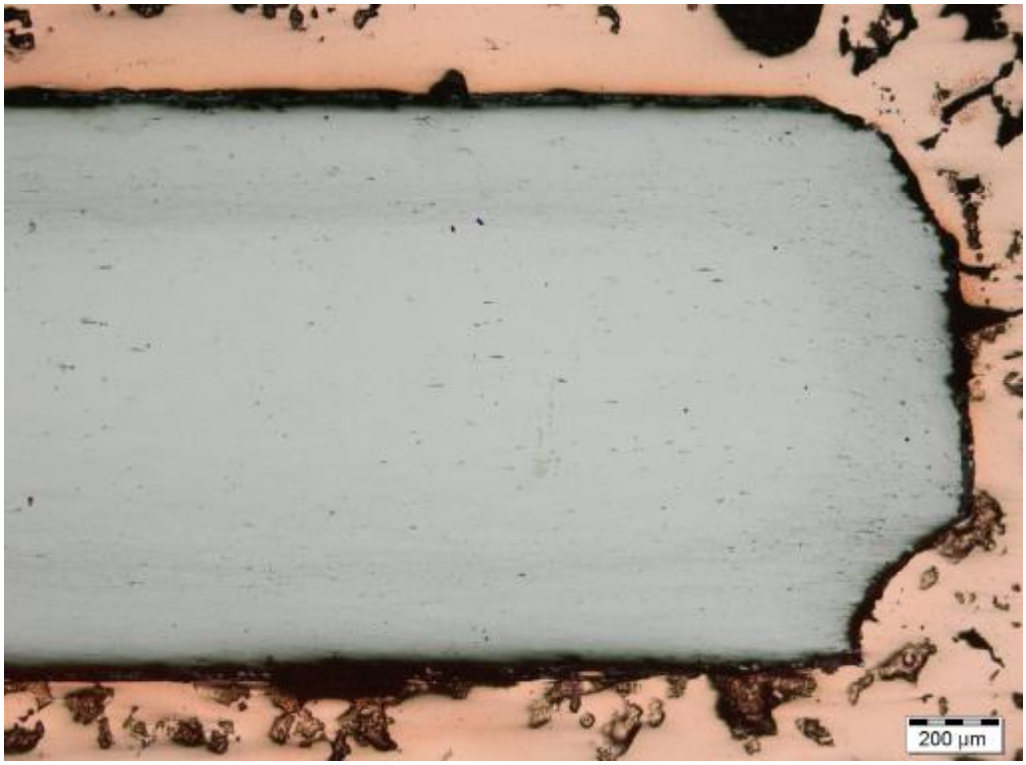


Figure 4.196. Micrograph of Sample 441-7, showing significant surface relief near the edges after polishing.

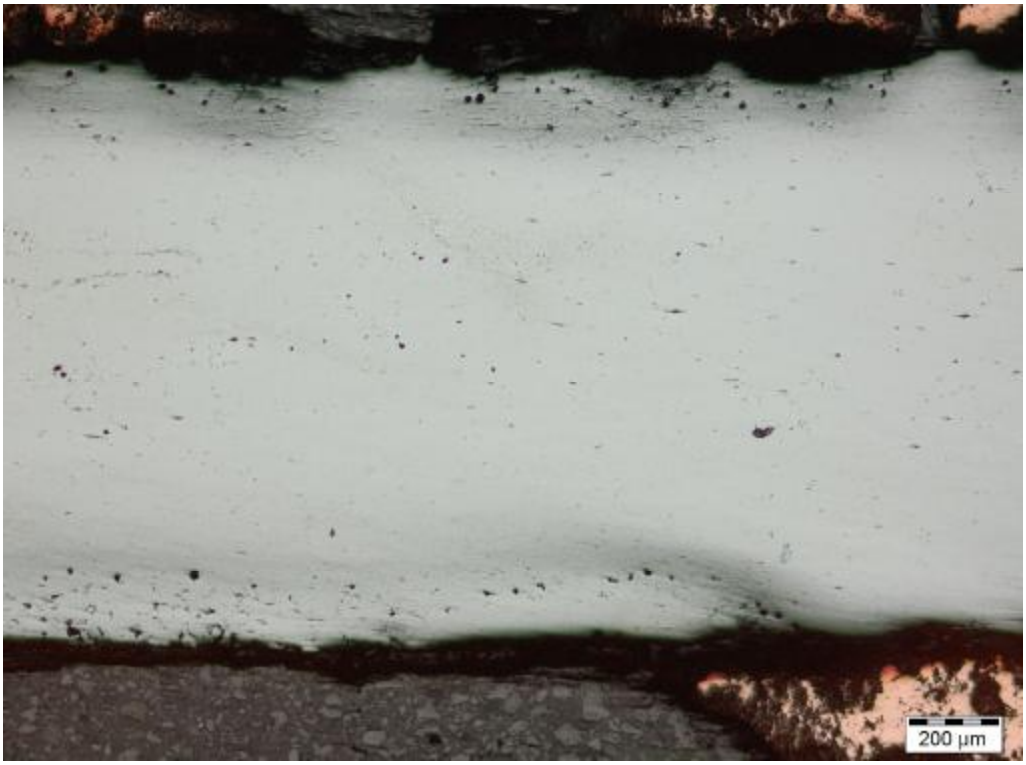


Figure 4.197. Micrograph of Sample 441-7 showing relief around the edges, due to poor edge retention from polishing and associated coking.



Figure 4.198. Micrograph of a cross-section through Sample 441-7 (etched).



Figure 4.199. Micrograph showing extensive carburisation in Sample 441-7 (etched), initiating from localised sites.

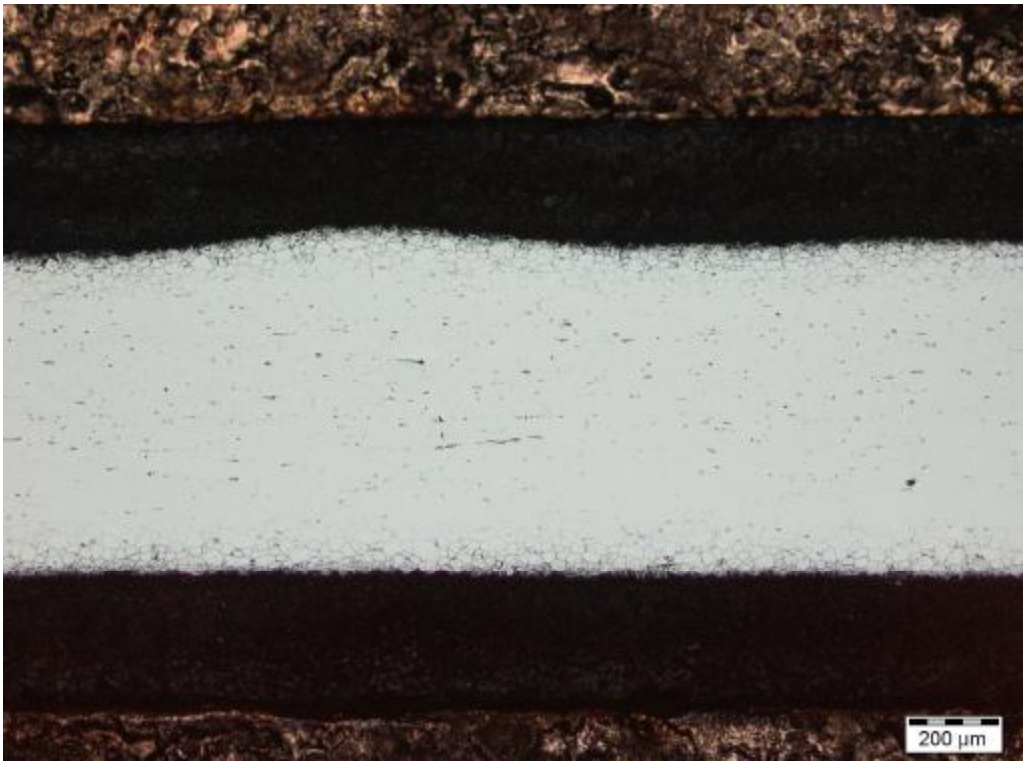


Figure 4.200. Micrograph in another area of Sample 441-7 (etched), showing uniform carburisation.

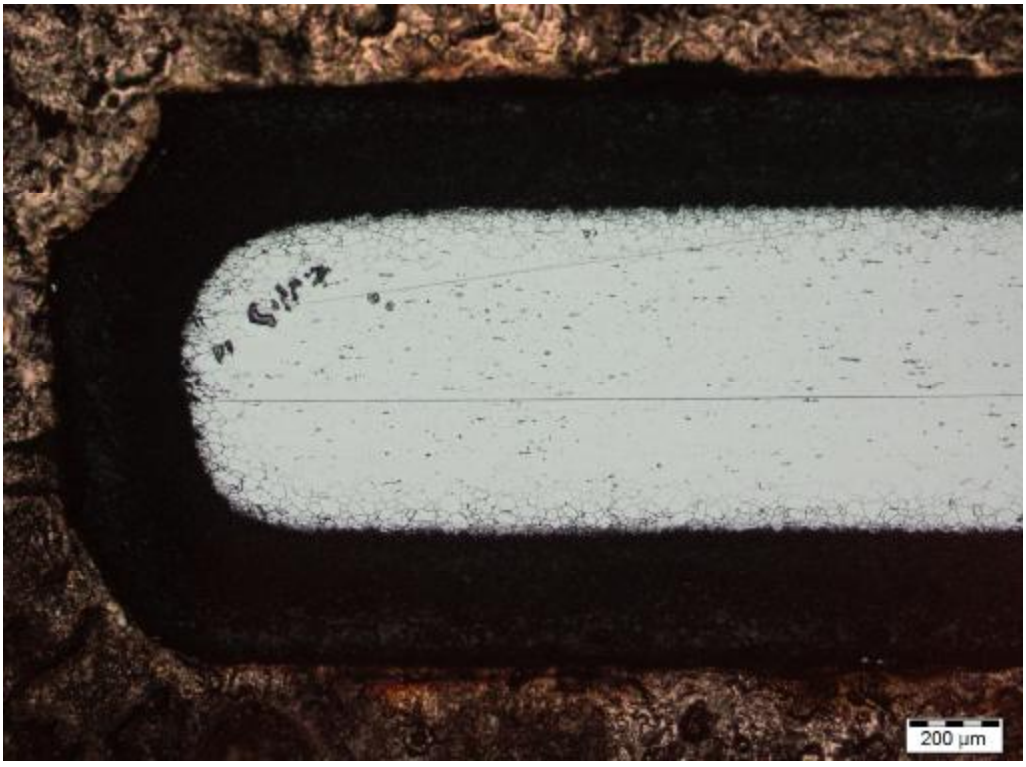


Figure 4.201. Micrograph showing uniform carburisation at the edge of Sample 441-7 (etched) (this area is similar to Figure 4.196).



Figure 4.202. Higher magnification micrograph of carburisation in Sample 441-7 initiating from localised sites.

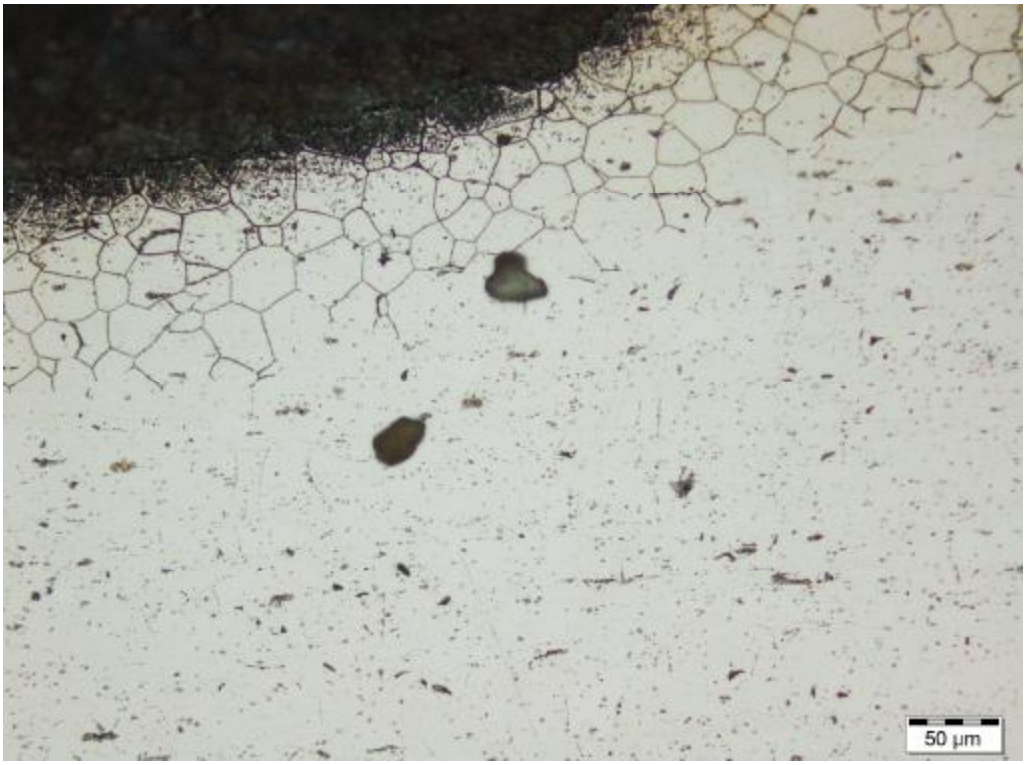


Figure 4.203. Higher magnification image of Sample 441-7 of the intergranular nature at the progressing front shown in Figure 4.202.

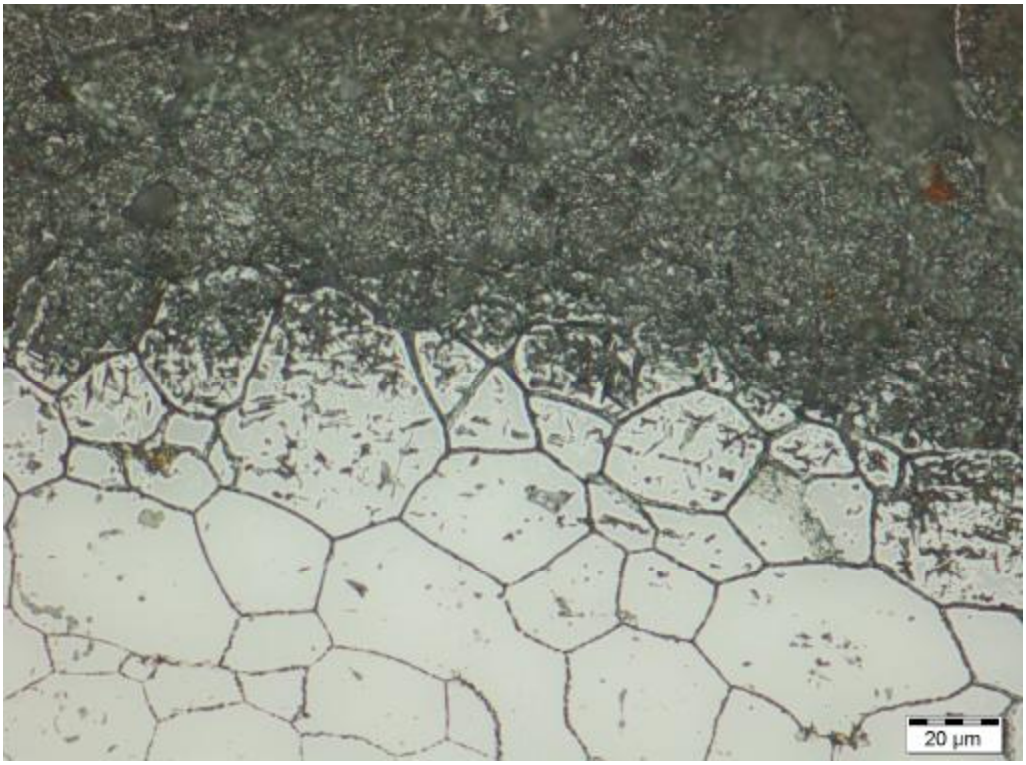


Figure 4.204. Higher magnification image of the carburisation near the edge of Sample 441-7.

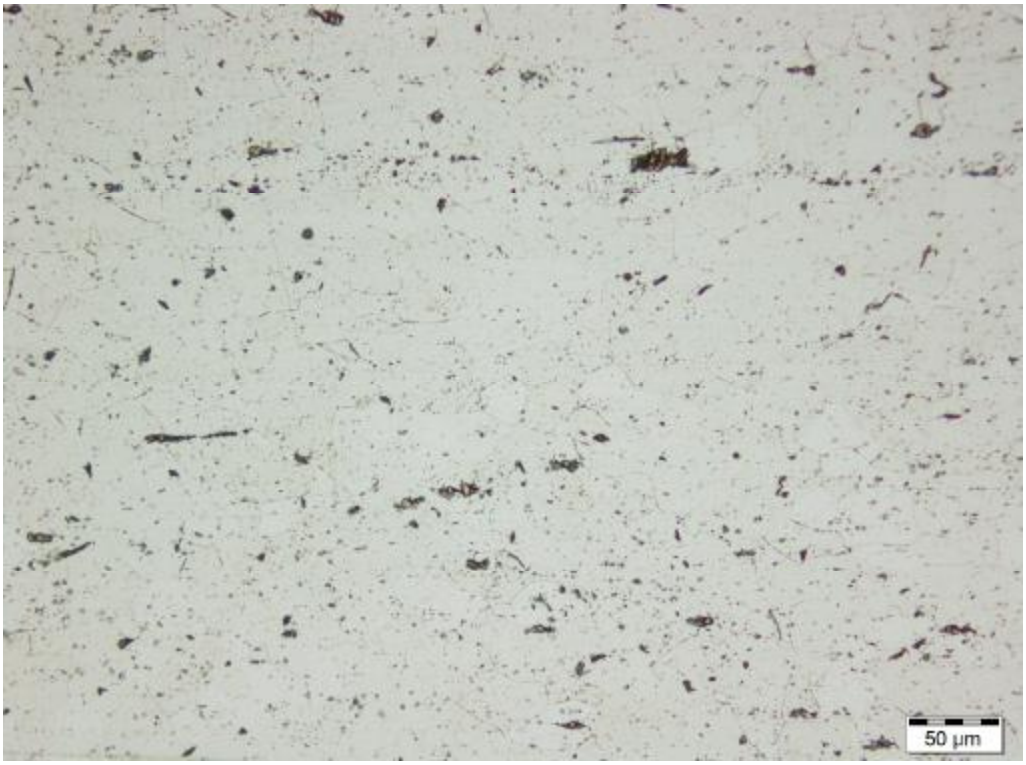


Figure 4.205. Micrograph of the attack associated with the titanium carbo-nitride precipitates in Sample 441-7.

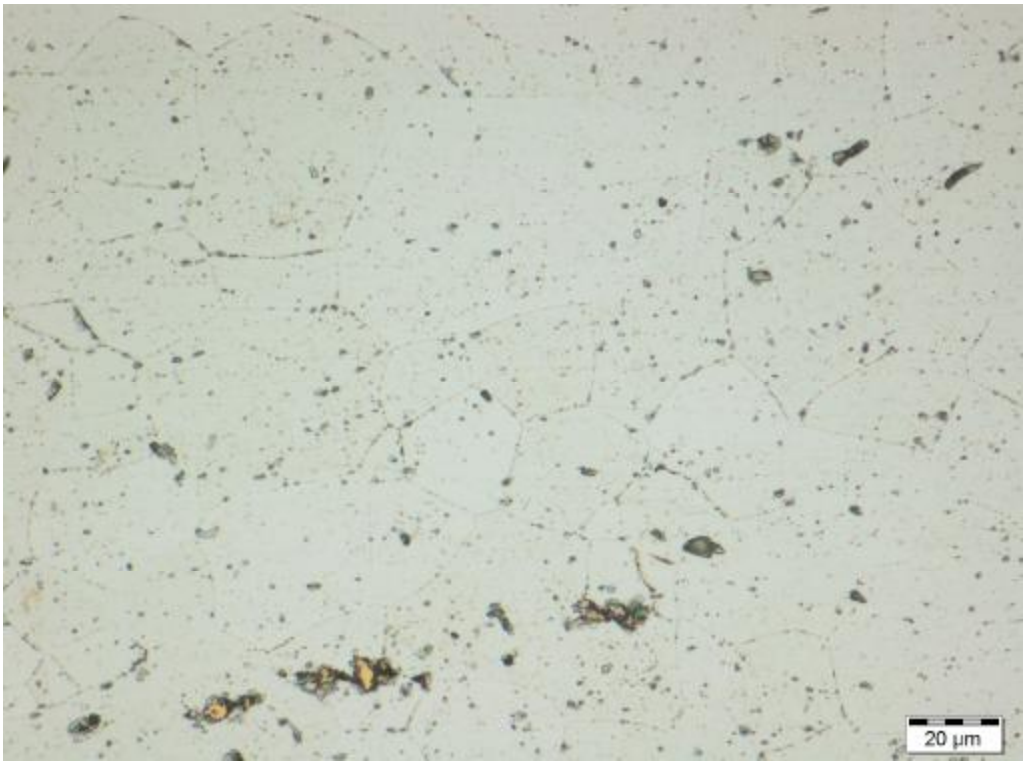


Figure 4.206. Higher magnification image of Sample 441-7 shown in Figure 4.205.

4.4.4. Scanning Electron Microscopy

Figure 4.207 and Figure 4.208 are SEM images of the surface of a Type 304L sample that was exposed for 30 days. Numerous graphite protrusions were observed on the surface. Figure 4.209 is an image showing the general appearance of the surface of the sample, with a degree of intergranular attack evident. Figure 4.210 is an SEM image of a pit found on the surface. This pit was covered with a relatively thick and very tenacious product. Figure 4.211 is an EDX spectrum of the product illustrating that it predominantly consisted of an iron-chromium oxide. The carbon peak in particular was low, indicating that it was not a graphite layer.

Figure 4.212 is an SEM image of the black product on the surface of the Type 321 samples, after it was cleaned with running water. Figure 4.213 is an SEM image of the surface, illustrating that no very different features were evident on the surface, apart from a light particle. Figure 4.214 and Figure 4.215 are SEM images of the surface away from the black product, illustrating the degree of attack. Figure 4.216 is an EDX spectrum of the surface

showing a chromium-enriched iron oxide layer, with a relatively high carbon peak. Figure 4.217 is an EDX spectrum in another area of the sample, illustrating that the black product consisted only of carbon (i.e. coke formation).

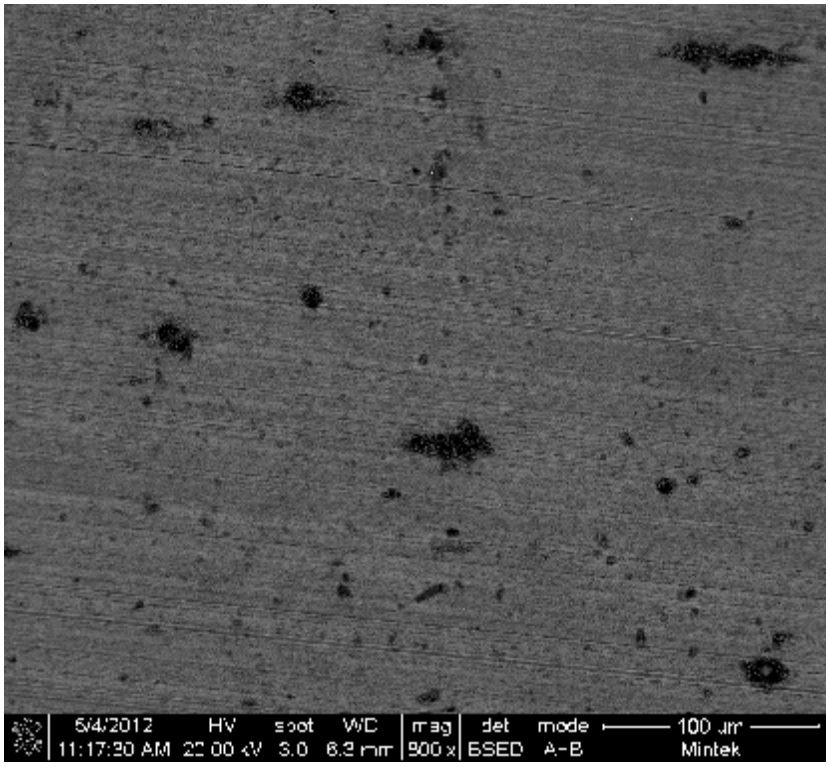


Figure 4.207. SEM-BSE image of the surface of Sample 304-8.

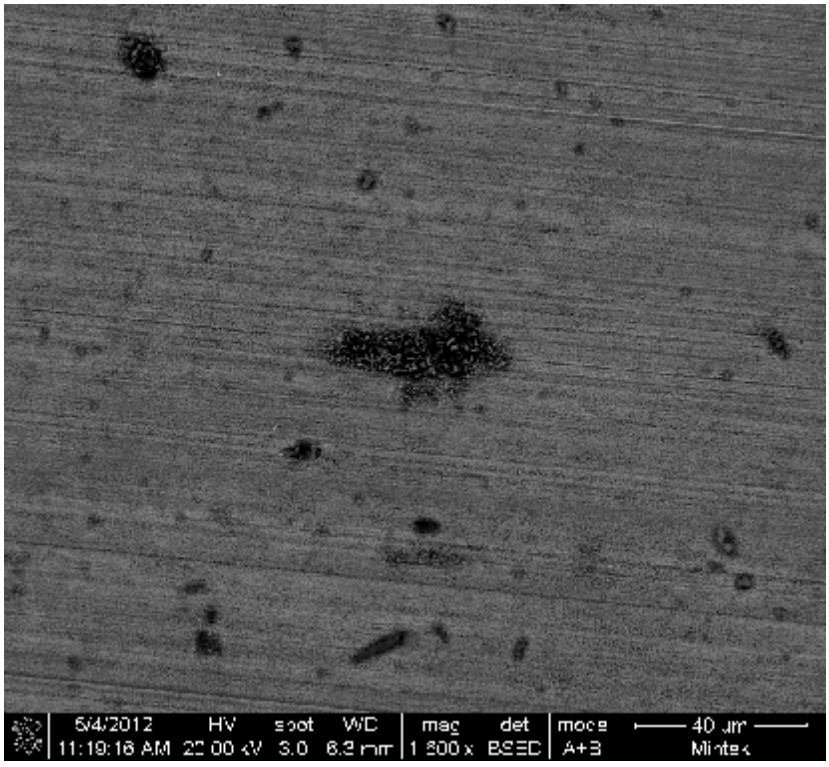


Figure 4.208. Higher magnification SEM-BSE image of the surface of Sample 304-8 showing protrusions on the surface and individual particles.

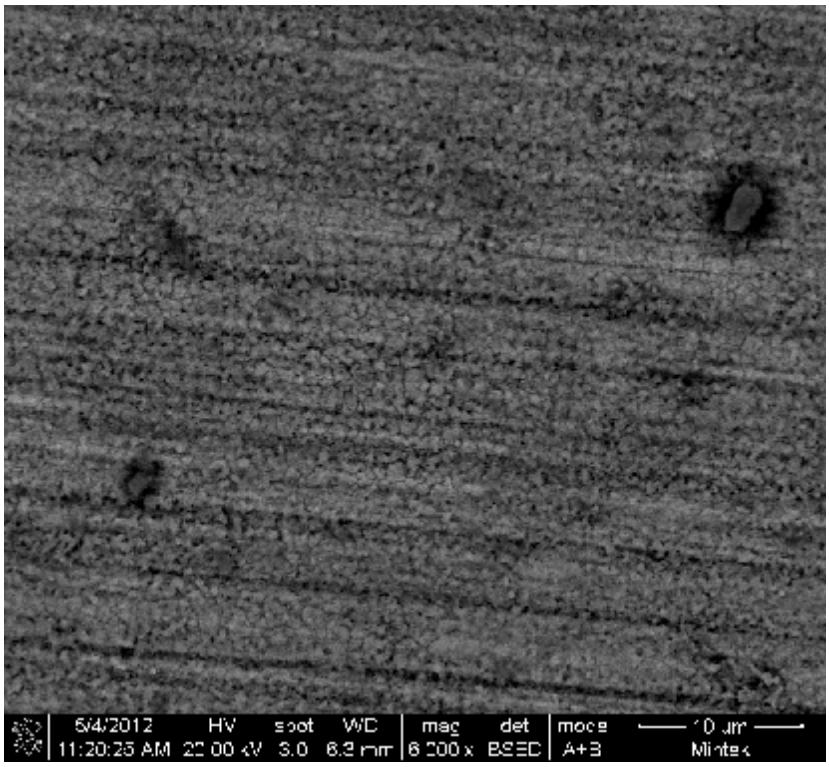


Figure 4.209. Higher magnification SEM-BSE image of the surface of Sample 304-8.

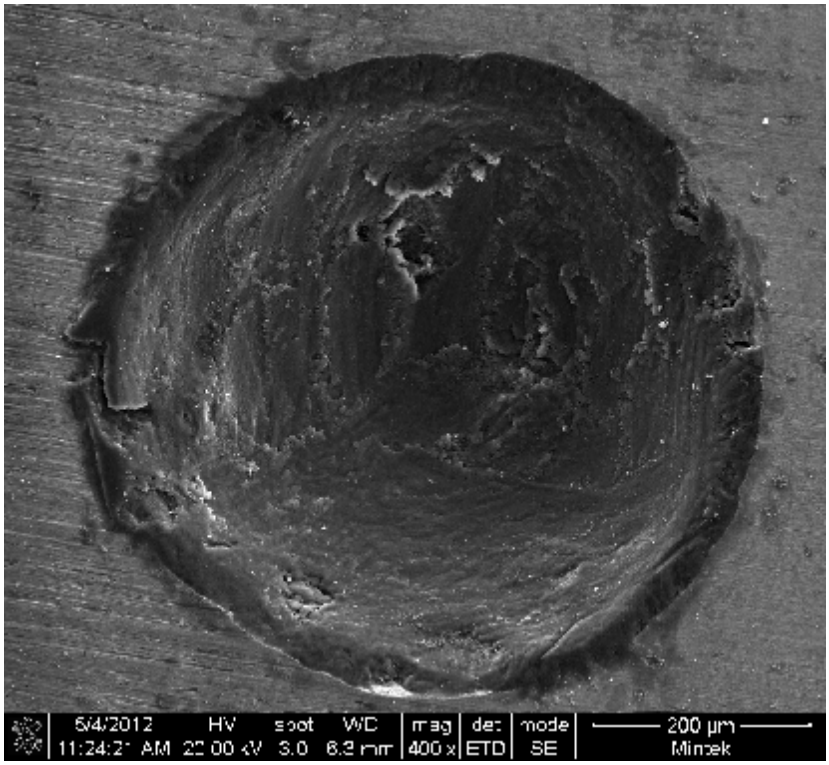


Figure 4.210. SEM-SE image of a pit in the surface in Sample 304-8 that was covered with corrosion product, which was an oxide (i.e. not coke), as shown in Figure 4.211.

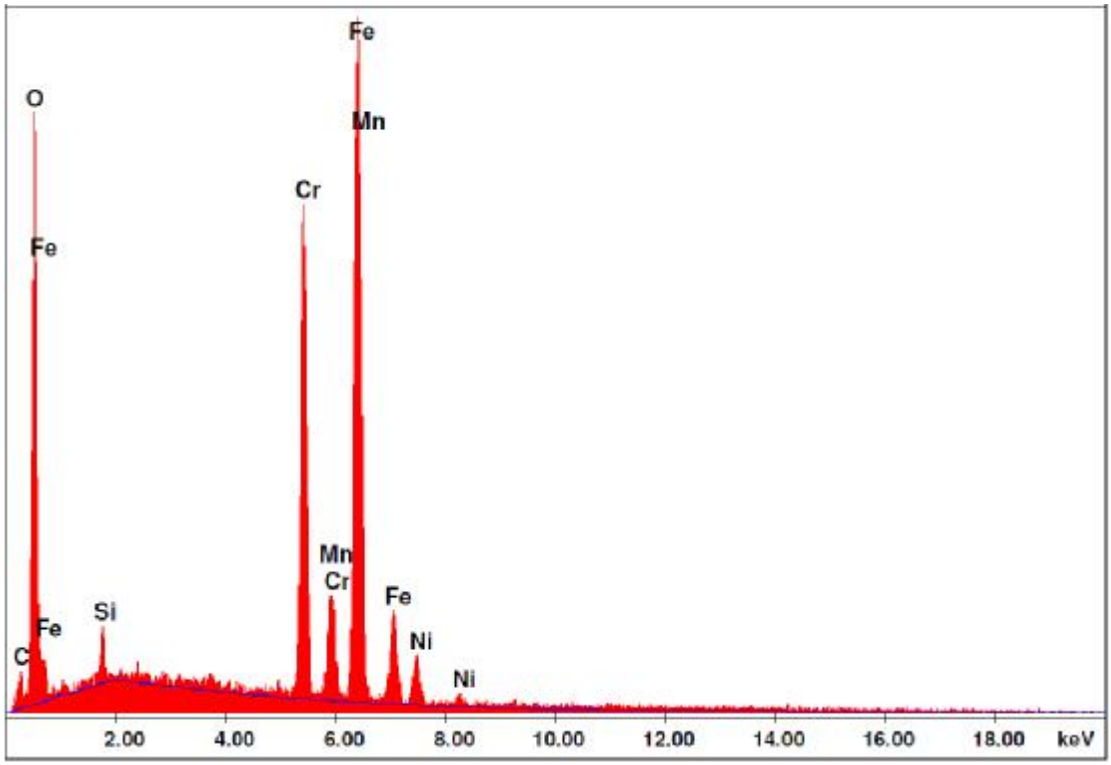


Figure 4.211. EDX spectrum of product inside pit shown in Figure 4.210.

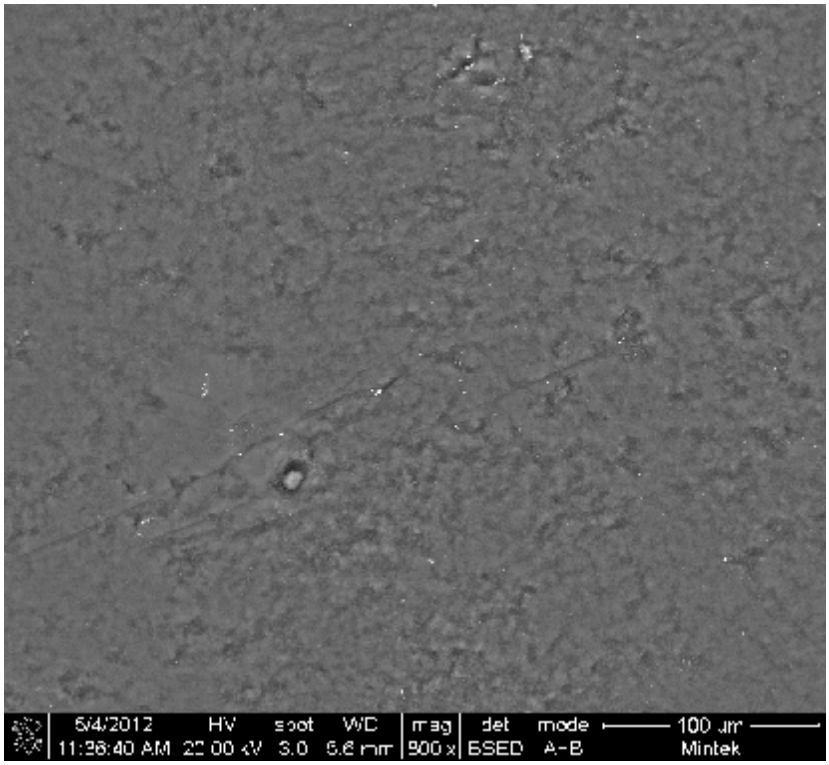


Figure 4.212. SEM-BSE image of the surface of Sample 321-8.

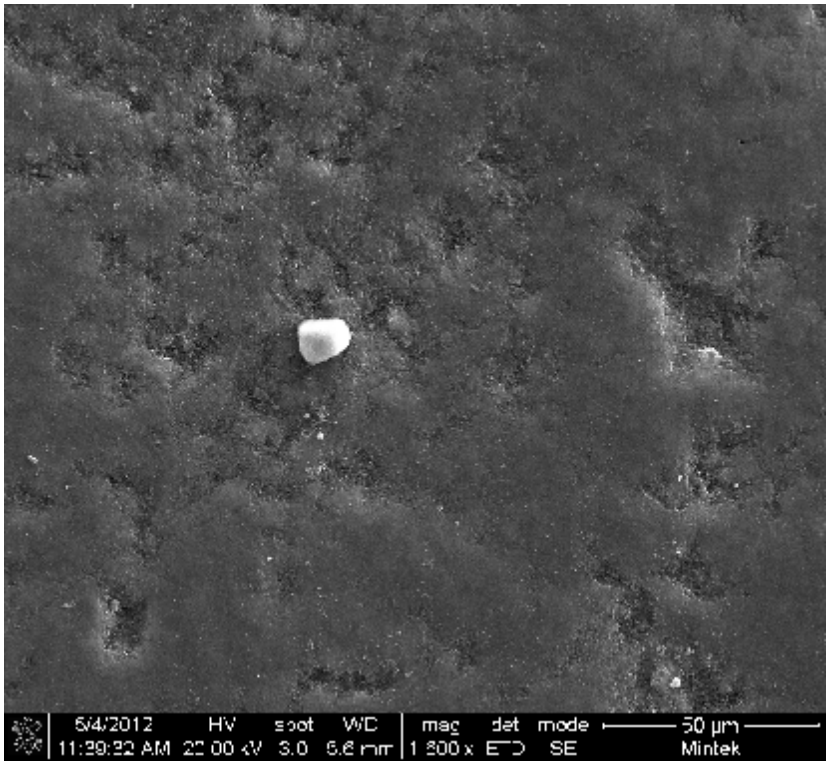


Figure 4.213. SEM-SE image of the coke layer covering parts of the surface on Sample 321-8 (the light particle near the centre was not analysed).

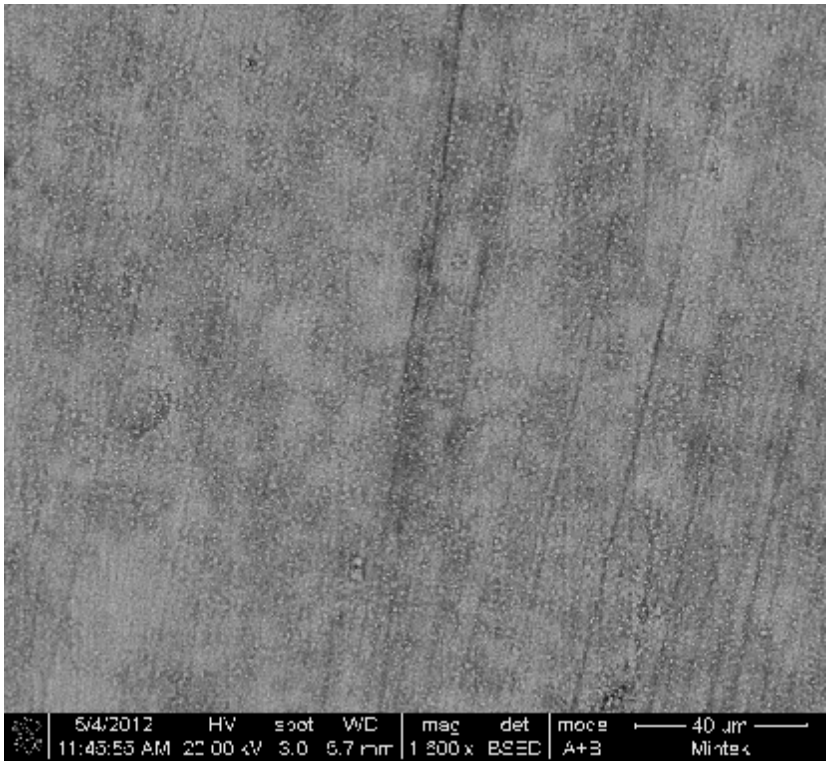


Figure 4.214. SEM-BSE image of the surface of Sample 321-8.

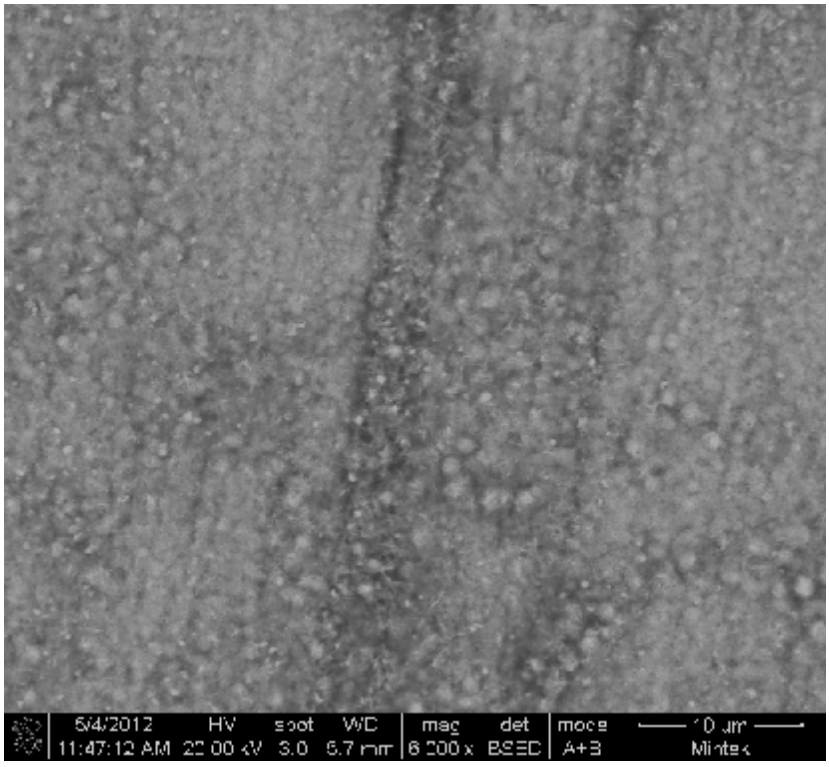


Figure 4.215. Higher magnification SEM-BSE image of the surface of Sample 321-8.

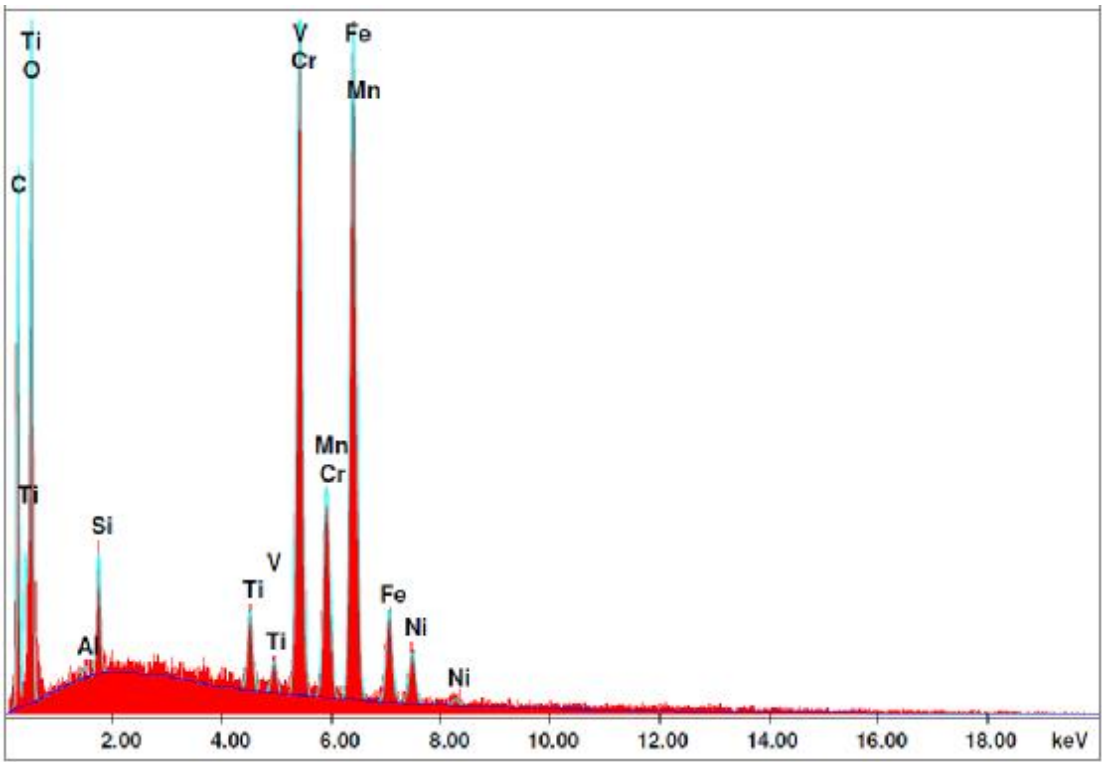


Figure 4.216. EDX spectrum of the surface of Sample 321-8 shown in Figure 4.215.

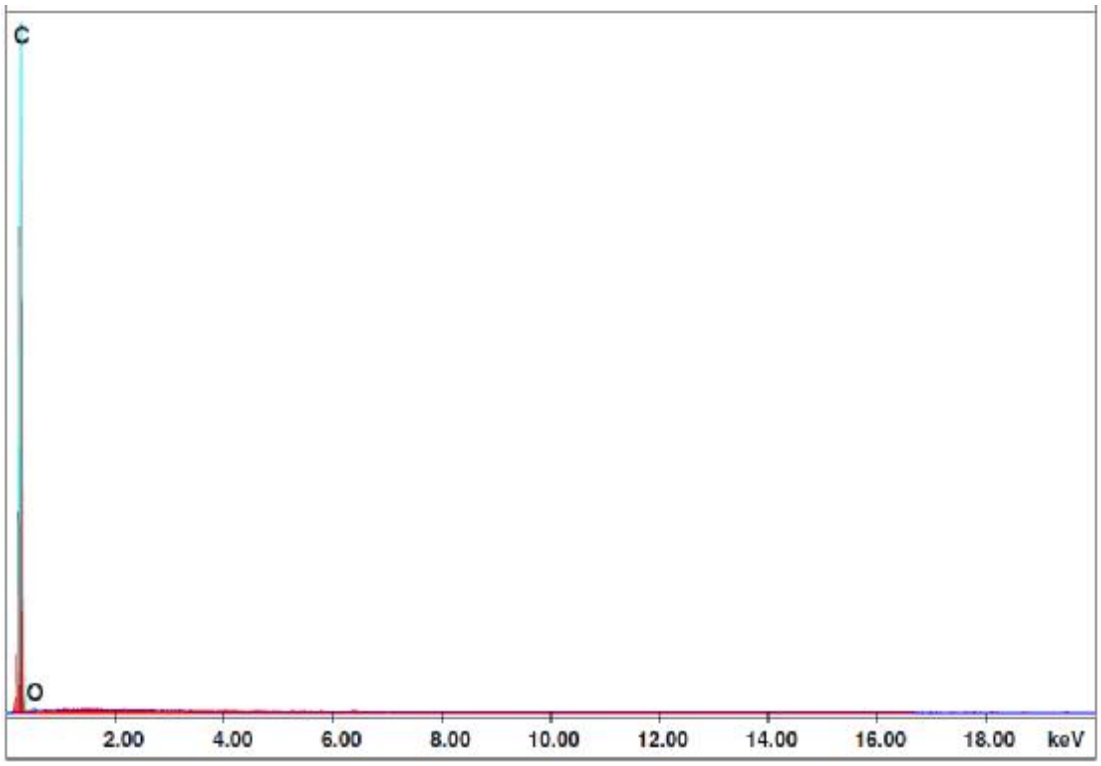


Figure 4.217. EDX spectrum of the coke layer on Sample 321-8, shown in Figure 4.213.

Figure 4.218 is a SEM image showing the extent of pitting on the surface of a Type 316L sample that was exposed for 30 days. The pits were different than previous, as they did not contain a tenacious oxide layer. There were numerous pits that grew together to form general (uniform) attack on the surface. Figure 4.219 is a higher magnification SEM image of the surface away from the pitting, showing the formation of a product (either oxide layer or carbides). Figure 4.220 and Figure 4.221 are SEM images of the surface inside the pits, showing that the grain boundaries were preferentially attacked. Figure 4.222 is an EDX spectrum of the surface of the 316L specimen away from the pitting (Figure 4.219) and Figure 4.223 is an EDX spectrum of the inside a pit (Figure 4.220). The chromium content on the surface of the specimen was higher than the bulk (comparing the ratio of the iron and chromium peaks), and the chromium content was even higher inside the pit (specifically compared to iron peak).

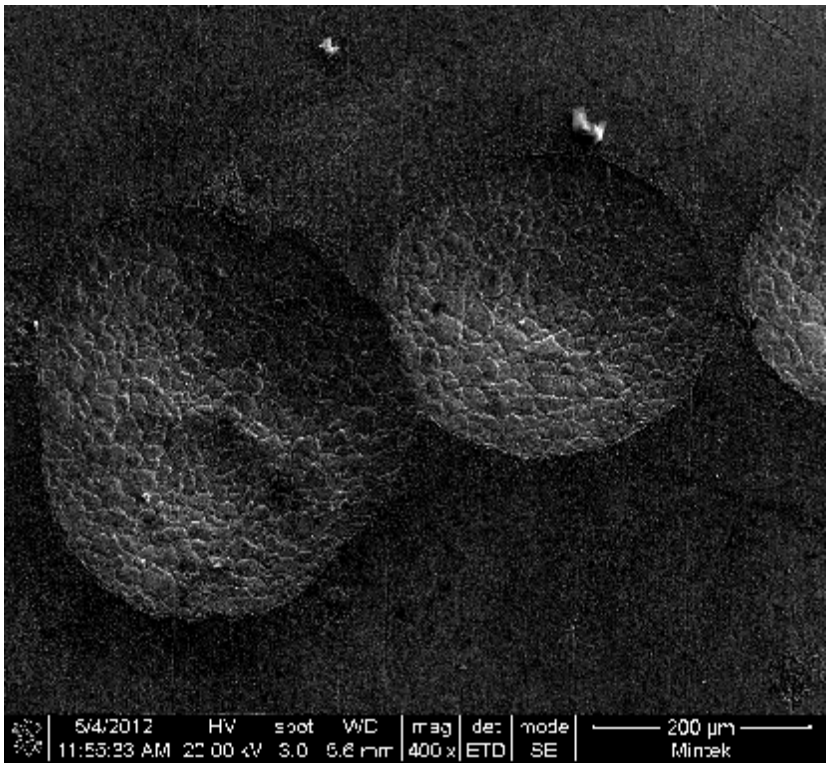


Figure 4.218. SEM-SE image of pitting on the surface of Sample 316-8.

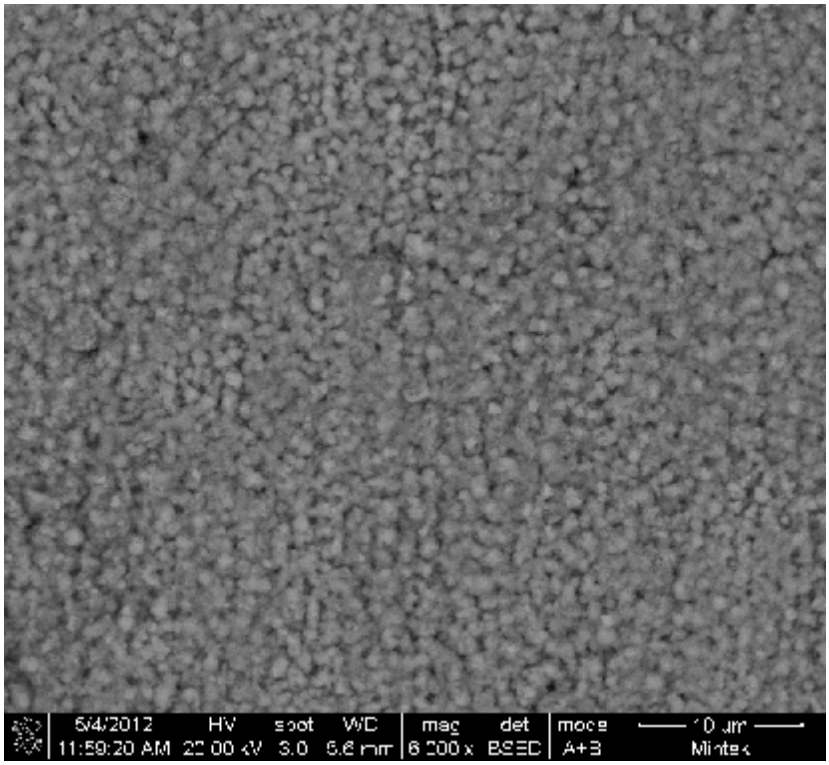


Figure 4.219. SEM-BSE image of the surface of Sample 316-8.

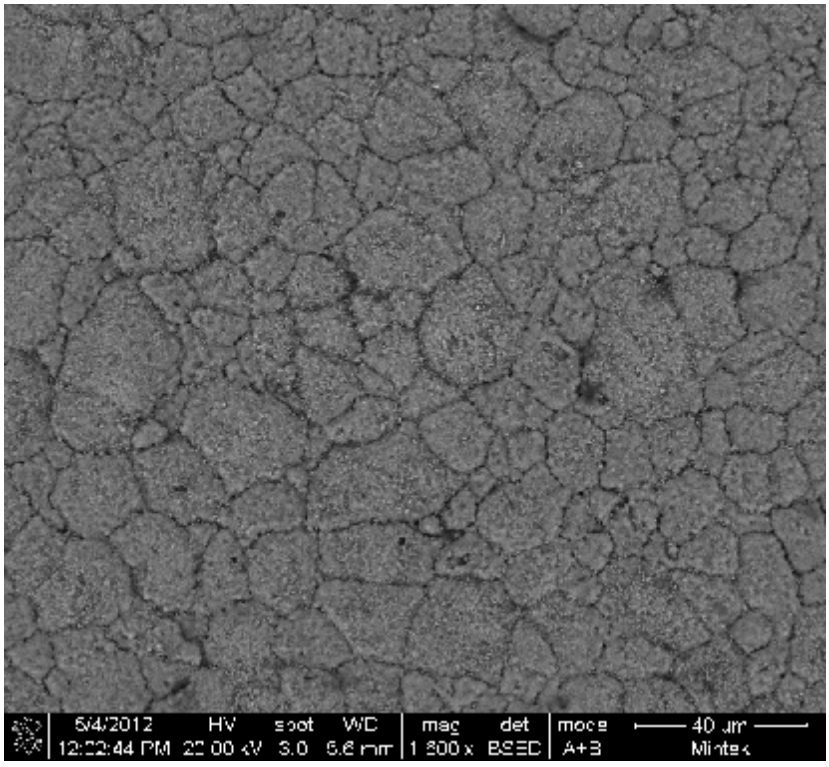


Figure 4.220. SEM-BSE image inside a pit of Sample 316-8.

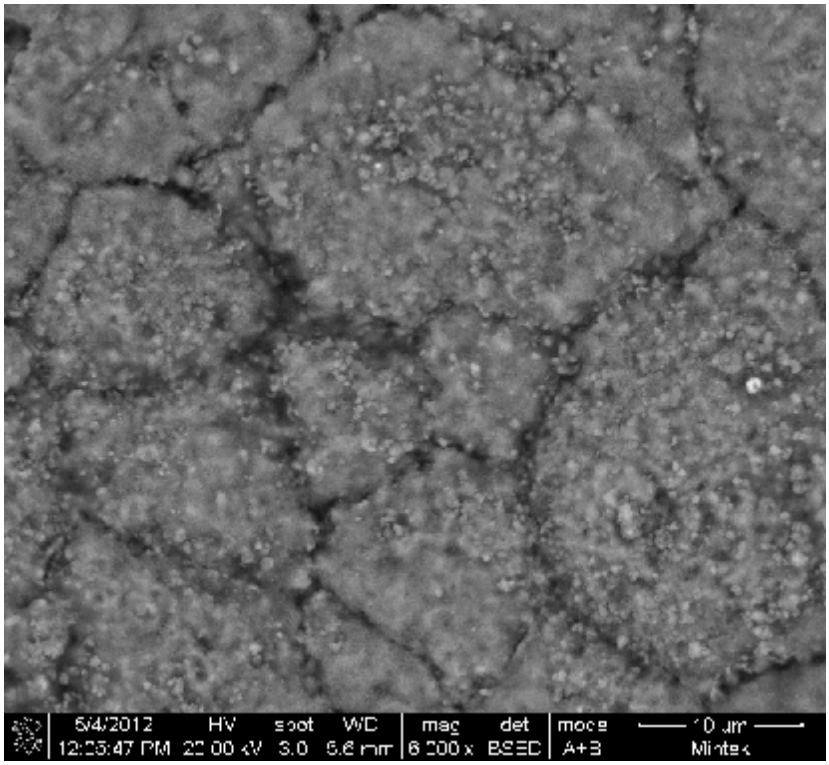


Figure 4.221. Higher magnification SEM-BSE image of Sample 316-8.

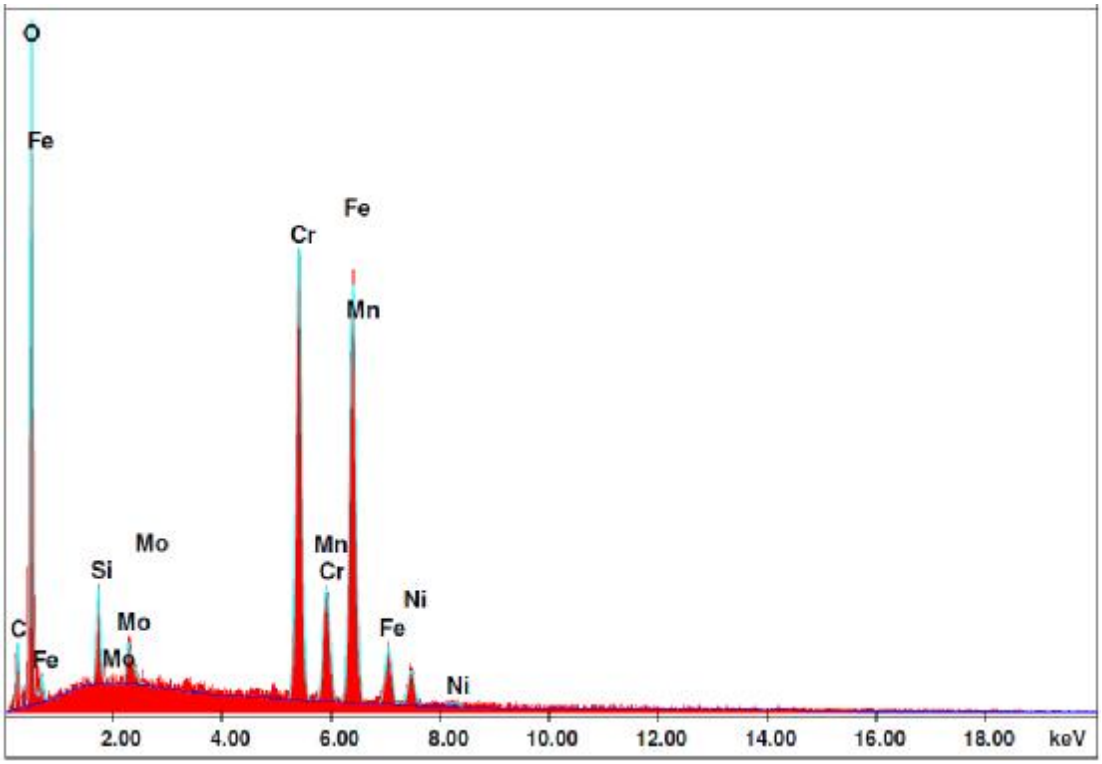


Figure 4.222. EDX spectrum of the surface of Sample 316-8.

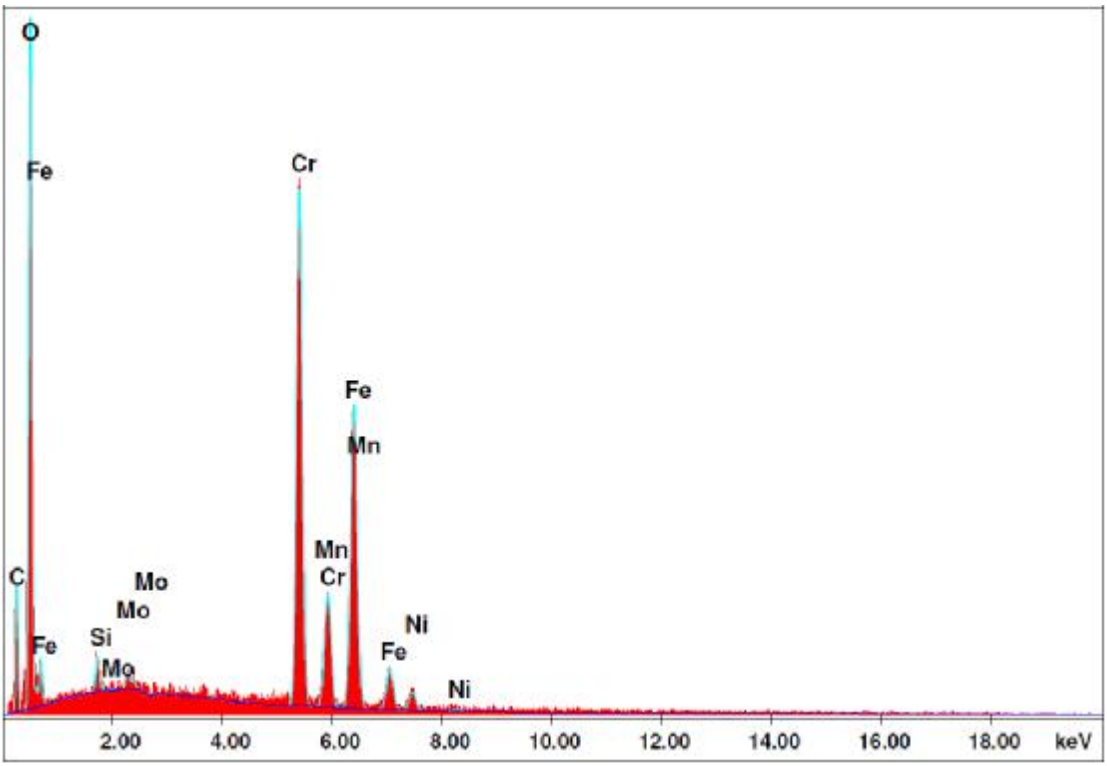


Figure 4.223. EDX spectrum of the surface of a pit on Sample 316-8.

Figure 4.224 is an SEM image showing the pitting attack on a Type 316Ti sample that was exposed for 30 days. Numerous graphite/coke protrusions were also evident, from where shallow pits also initiated. Figure 4.225 is a higher magnification image of the attack, showing general attack over most of the surface, also associated with deeper pits. Figure 4.226 and Figure 4.227 are SEM images showing that the grain boundaries acted as local sites for preferred attack, although the attack was not exclusively intergranular. Figure 4.228 is a SEM image of the surface of the 316Ti sample showing localised sites where corrosion attack initiated. Figure 4.229 is an EDX spectrum of a uniformly corroded area, and Figure 4.230 is a spectrum of the surface at a localised corroded area. The surface was generally enriched with chromium, but the surface at the pitted areas (i.e. more severely attacked areas) contained a higher amount of chromium – specifically compared to the iron peak.

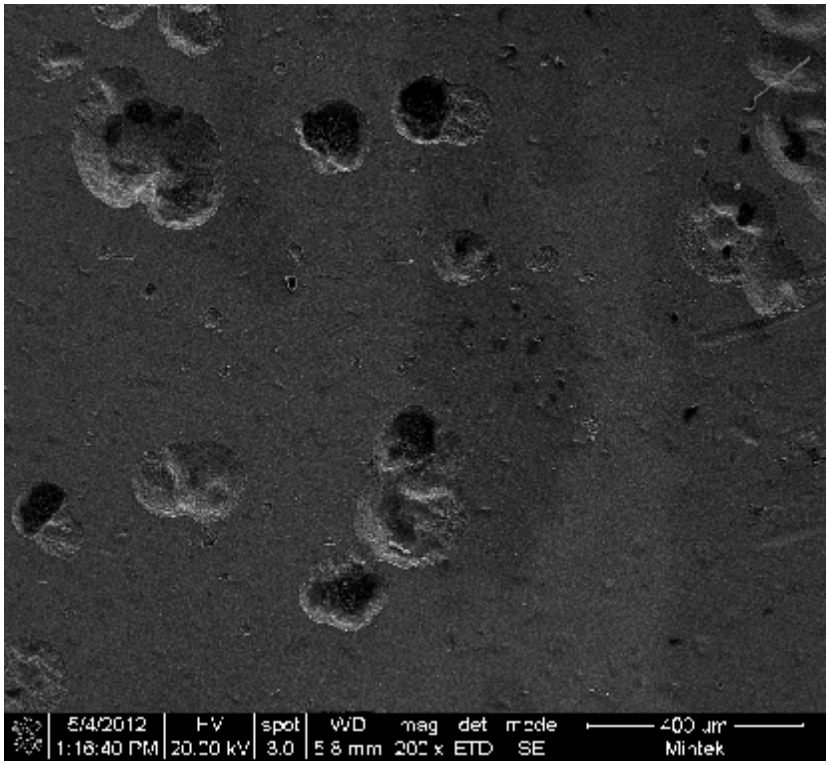


Figure 4.224. SEM-SE image of pitting on the surface on Sample 316Ti-8.

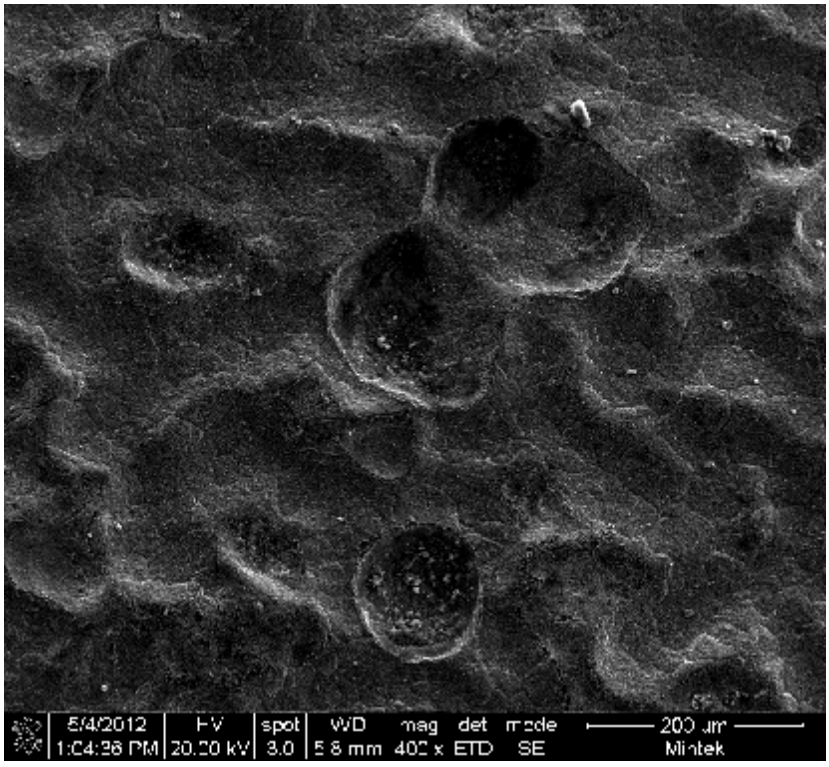


Figure 4.225. SEM-SE image of general attack and pitting on Sample 316Ti-8.

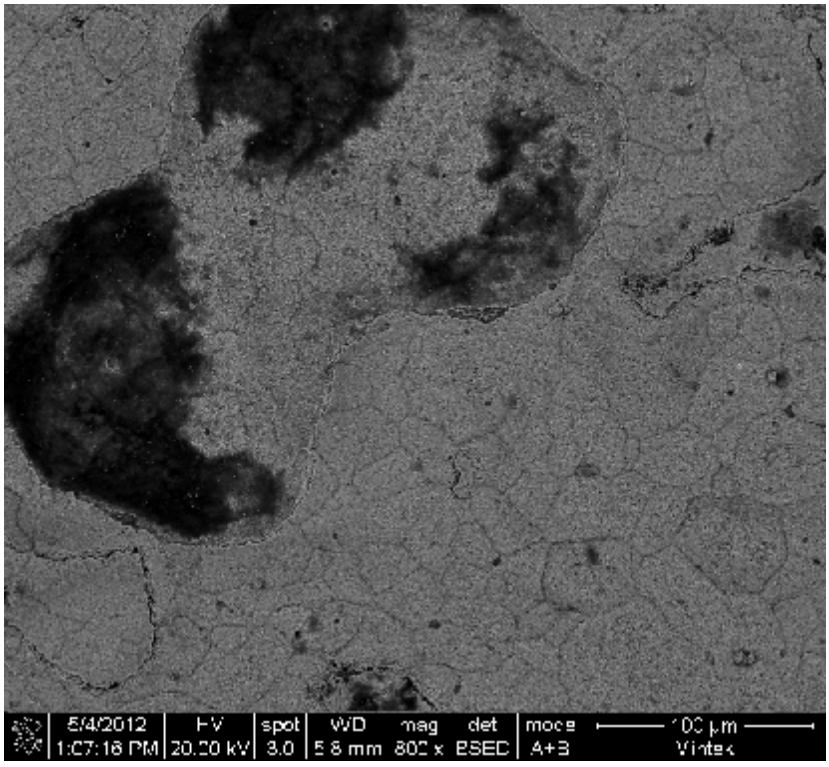


Figure 4.226. SEM-BSE image of the pitting and uniform attack on the surface of Sample 316Ti-8.

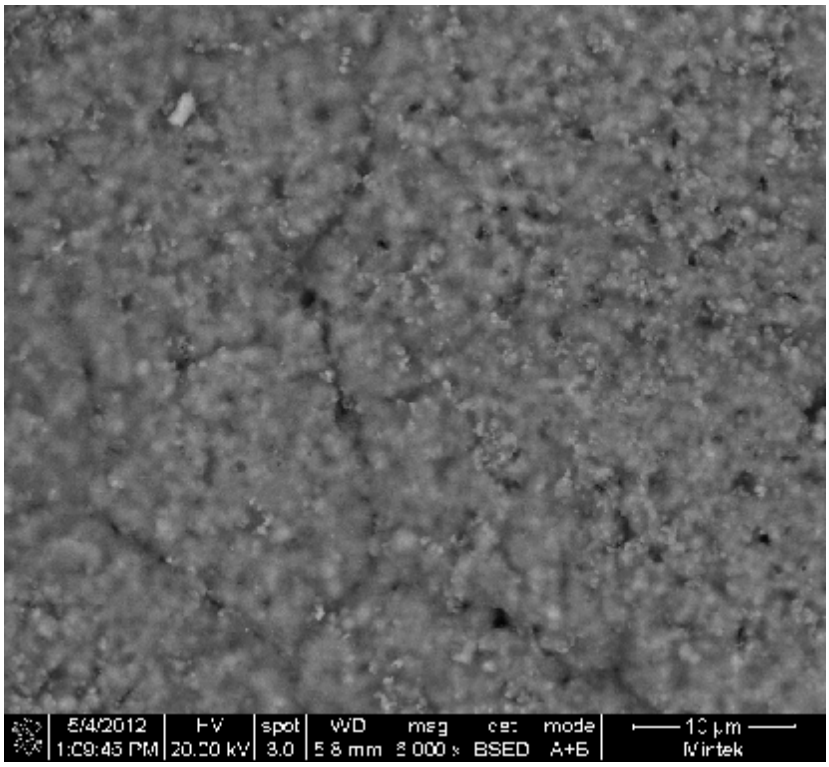


Figure 4.227. Higher magnification SEM-BSE image of the surface of Sample 316Ti-8.

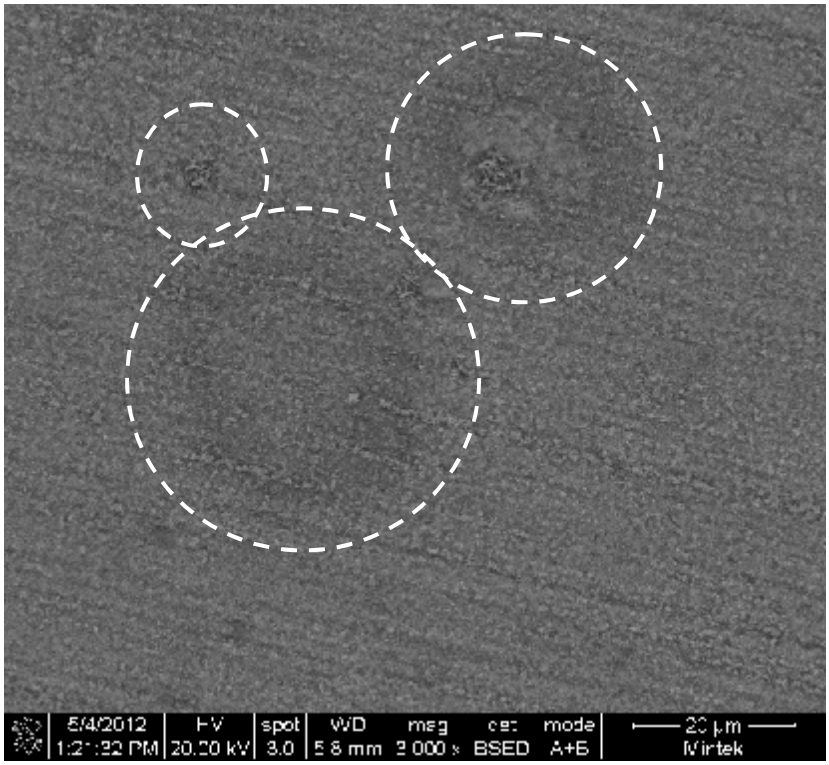


Figure 4.228. SEM-BSE image of the surface of Sample 316Ti-8 showing the initiation of pitting.

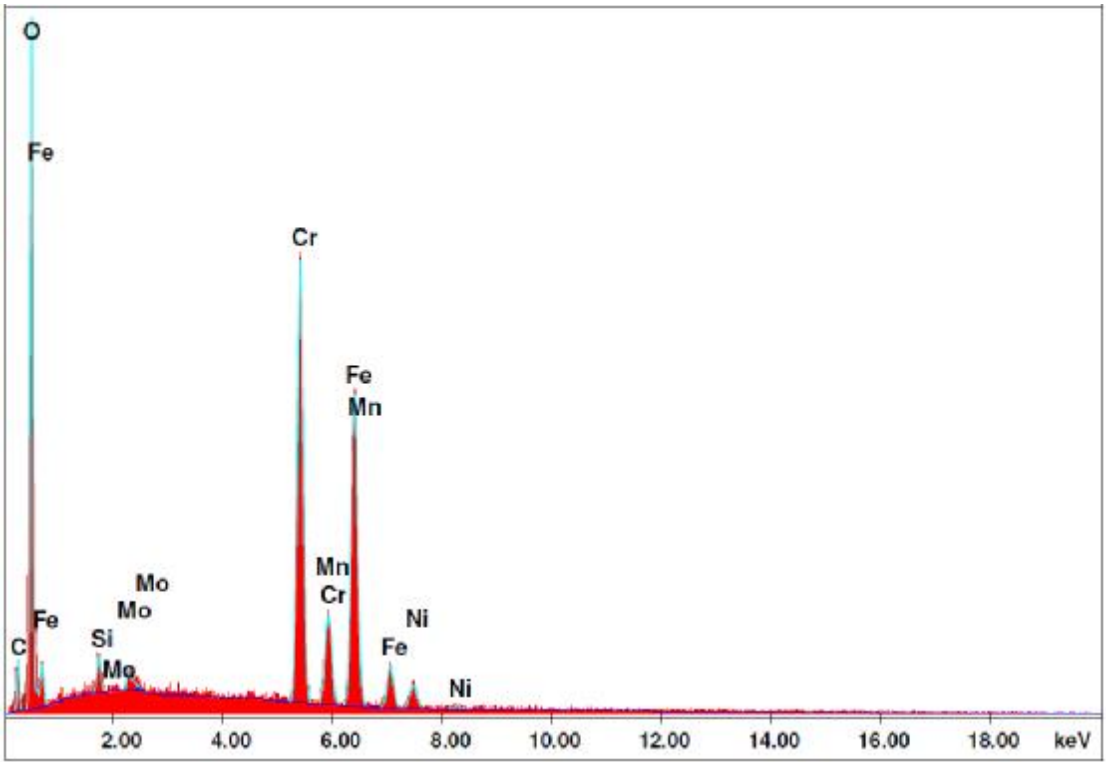


Figure 4.229. EDX spectrum of the uniform corroded surface of Sample 316Ti-8.

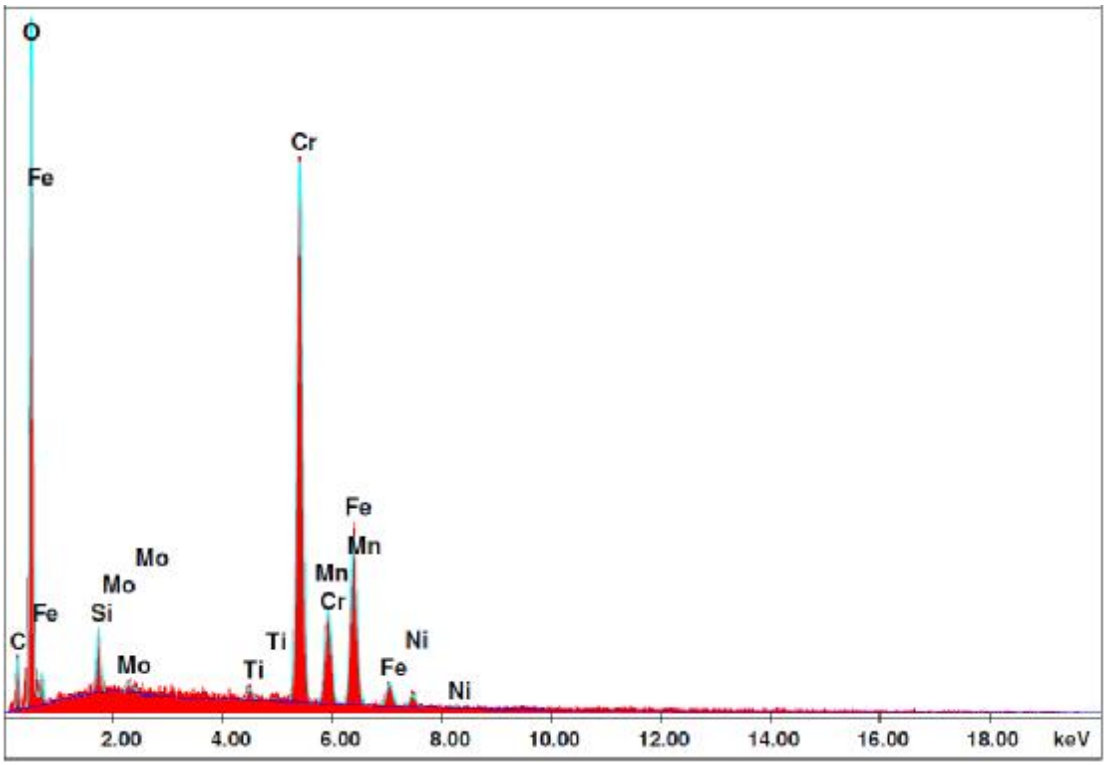


Figure 4.230. EDX spectrum of the darker areas on the surface of Sample 316Ti-8 shown in Figure 4.228.

Figure 4.231 and Figure 4.232 are SEM images of a Type 430 sample that was exposed for 30 days. Graphite/coke protrusions were evident on the surface, as well as round particles, as shown in Figure 4.233. These particles seemed to be larger on (what is assumed to be) the grain boundaries. Figure 4.234 is a SEM image of a pit in a Type 430 sample, and Figure 4.235 is an image taken in BSE mode, showing the intergranular nature of the attack, and black products inside the pit. Figure 4.236 is a higher magnification SEM image showing a second phase associated with the grain boundaries – probably a carbide. These phases were too small to positively identify by EDX analysis. Figure 4.237 is an EDX spectrum of the general surface, and Figure 4.238 is an EDX spectrum taken inside the pit. The chromium to iron ratio was significantly higher inside the pit. The carbon content was also higher inside the pit, which could be due to coking, or an indication that the higher local chromium content was due to the formation of chromium carbides. The oxide peak was relatively low in comparison, indicating that the chromium was not primarily present as a chromium oxide layer.

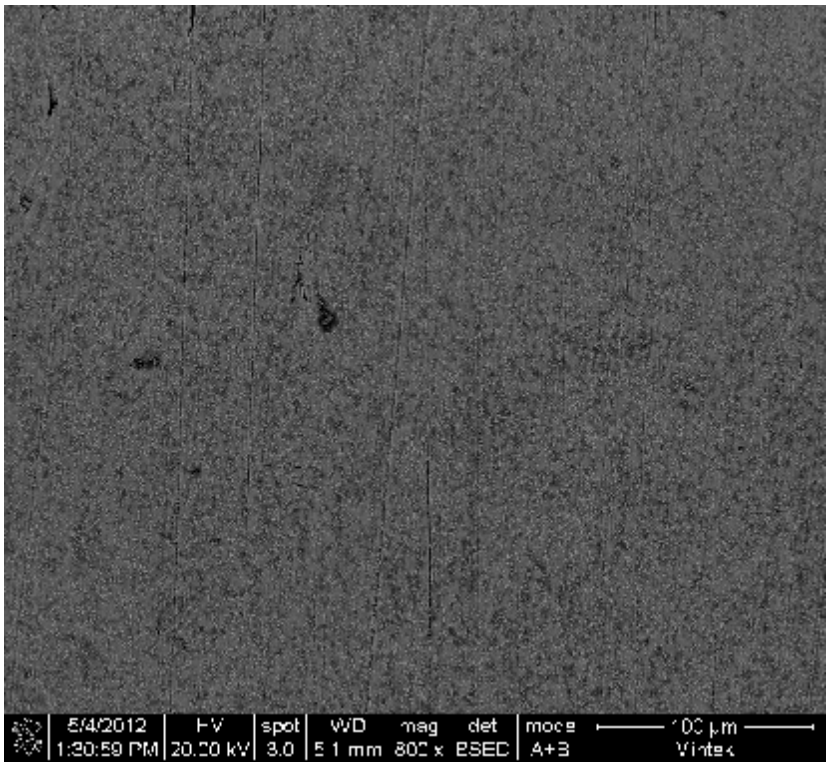


Figure 4.231. SEM-BSE image of the surface of Sample 430-8.

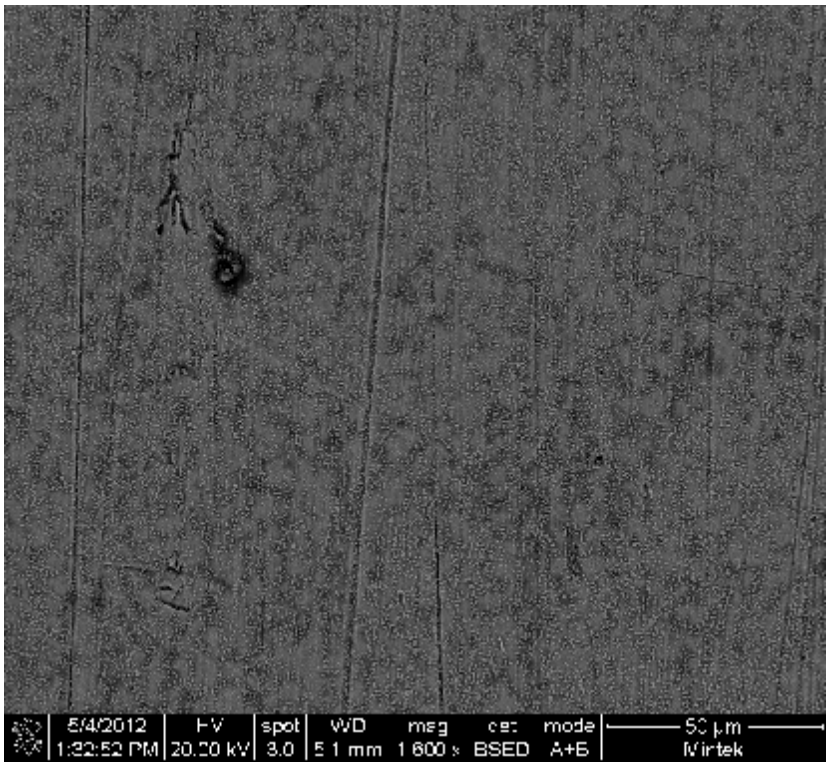


Figure 4.232. Higher magnification image of the surface of Sample 430-8.

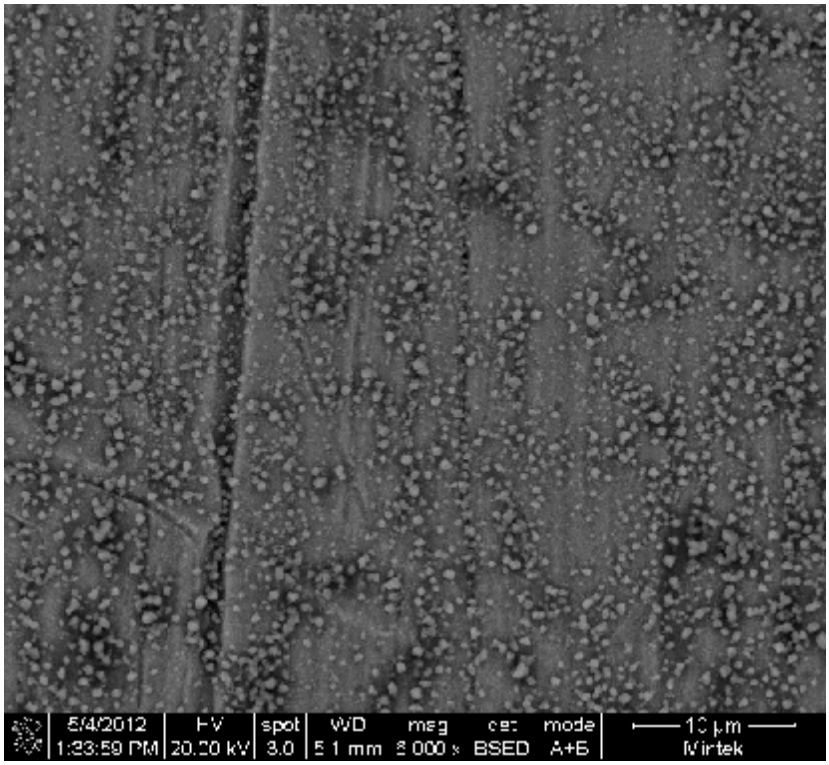


Figure 4.233. Higher magnification SEM-BSE image of the surface of Sample 430-8.

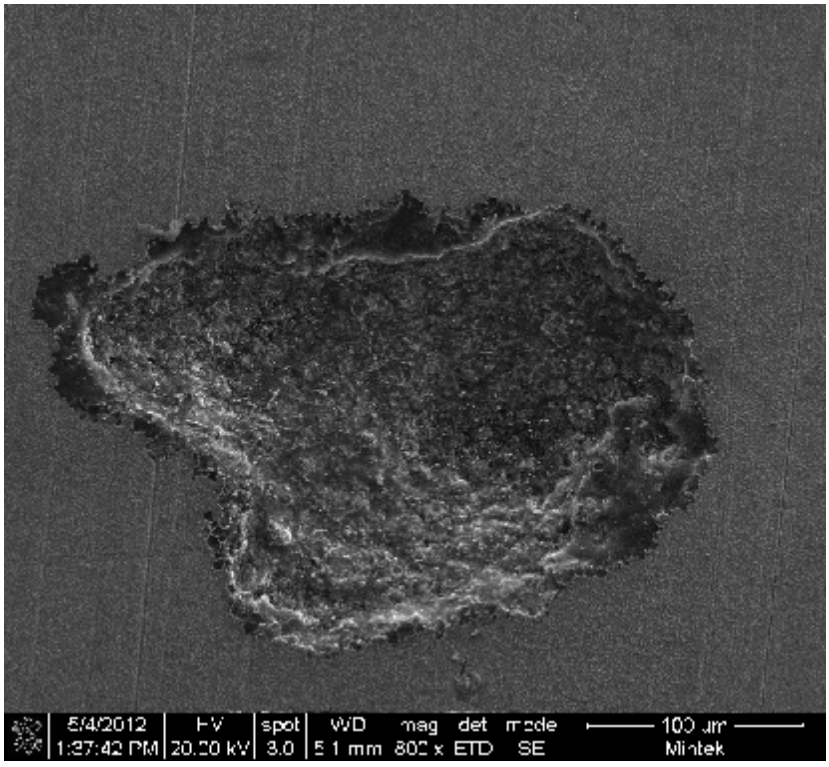


Figure 4.234. SEM-SE image of a pit in Sample 430-8.

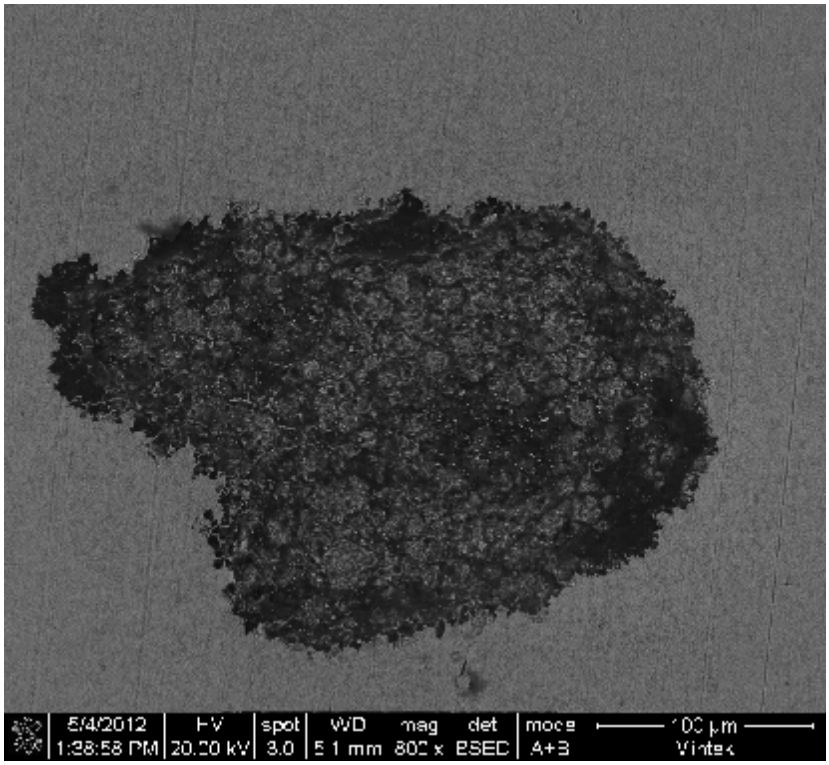


Figure 4.235. SEM-BSE image of the same pit in Sample 430-8 (Figure 4.234).

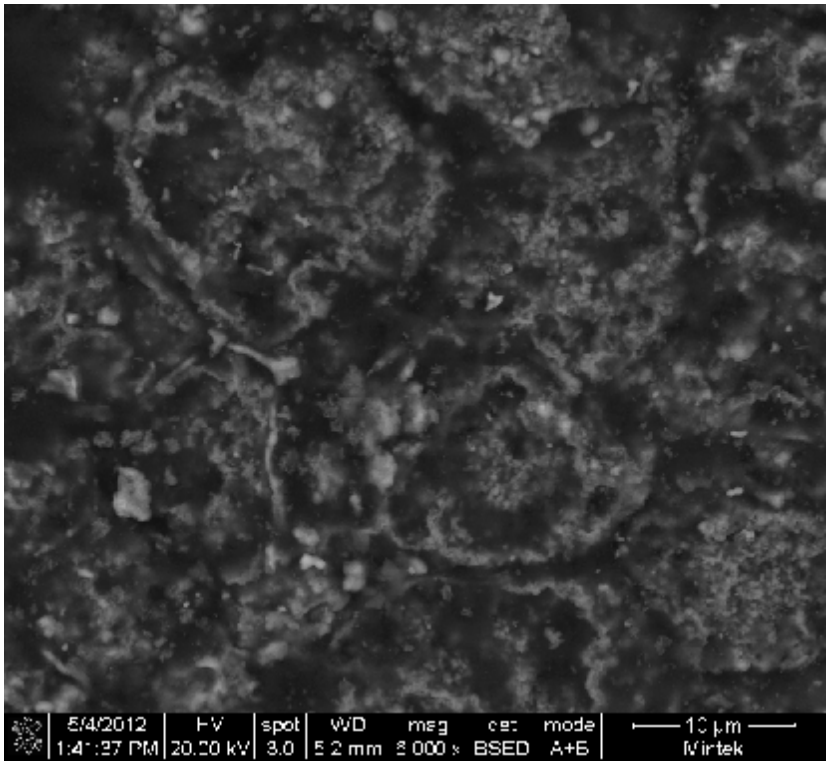


Figure 4.236. Higher magnification SEM-BSE image of inside the pit in Sample 430-8.

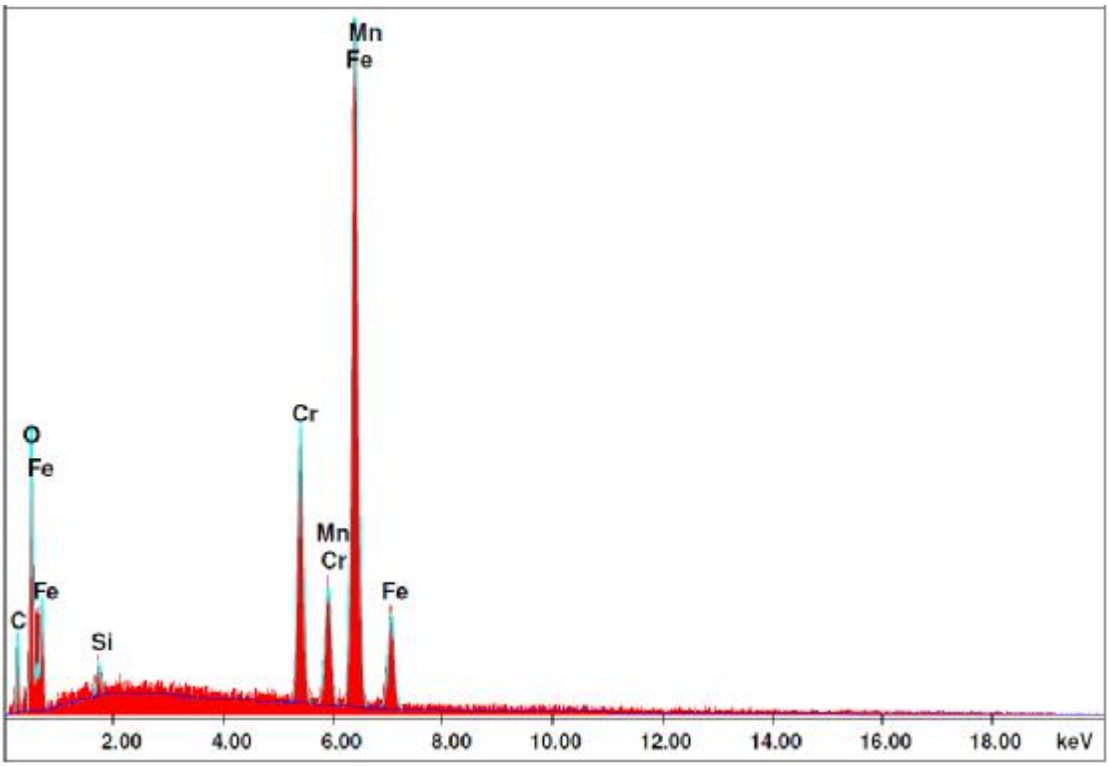


Figure 4.237. EDX spectrum of the surface in Sample 430-8.

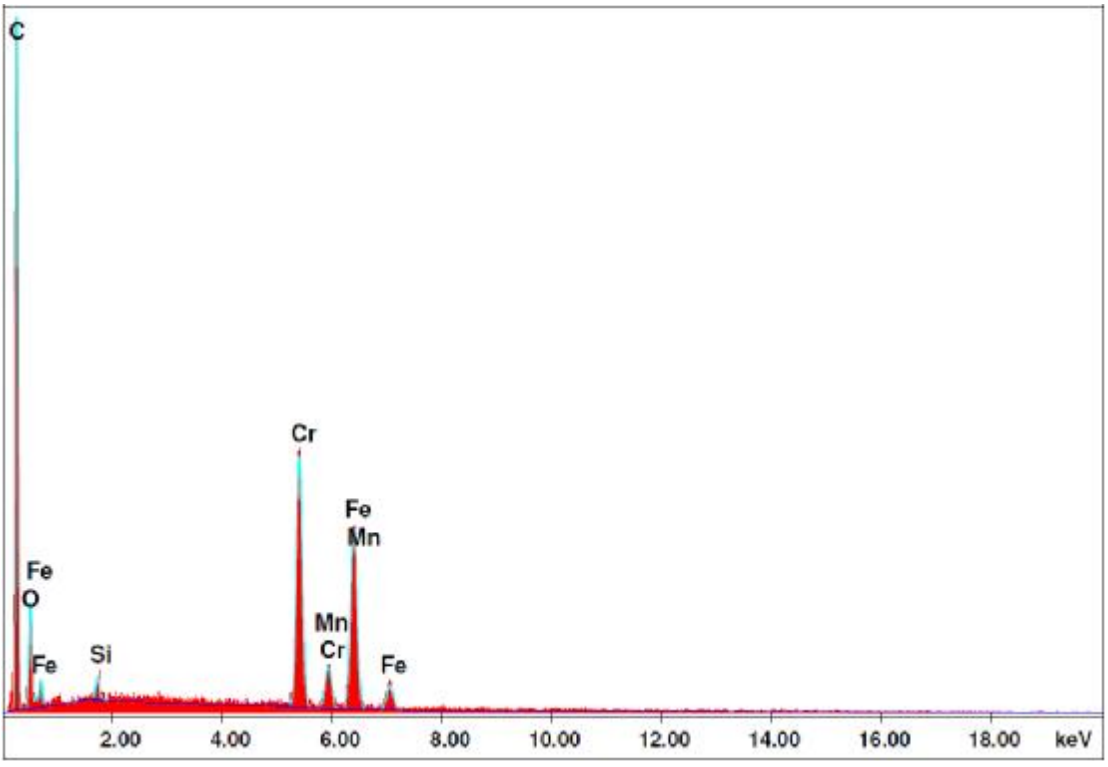


Figure 4.238. EDX spectrum of the pit in Sample 430-8 shown in Figure 4.236.

Figure 4.239 and Figure 4.240 are SEM images of the surface of a Type 441 sample that was exposed for 30 days. Localised break-down where pitting initiated and light particles were also evident on the surface. Figure 4.241 is a SEM image of an area showing extensive pitting on the surface. Similar to the pitting found on the other ferritic material (i.e. Type 430), these pits were more irregular in shape – opposed to the hemispherical pitting generally associated with the austenitic alloys in this study. Figure 4.242 is a higher magnification SEM image of the pitting in the Type 441 sample. Figure 4.243 is an EDX spectrum of the general surface of a Type 441 sample, and Figure 4.244 is a spectrum taken inside a pit. The analysis in the pit revealed a higher chromium and carbon content, compared to the general analysis of the surface (where the oxygen content was higher).

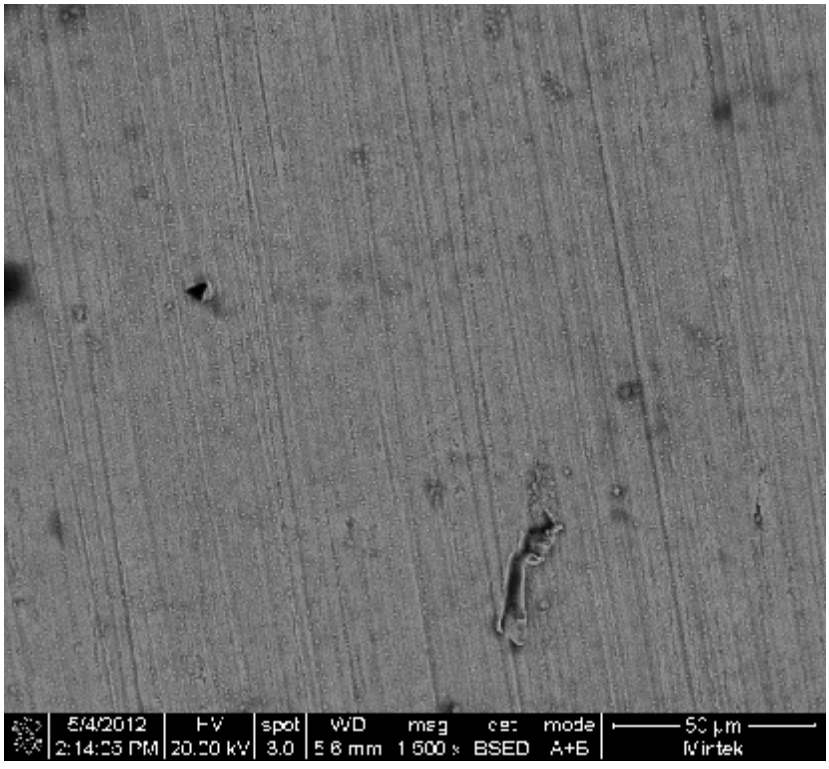


Figure 4.239. SEM-BSE image of the surface of Sample 441-8.

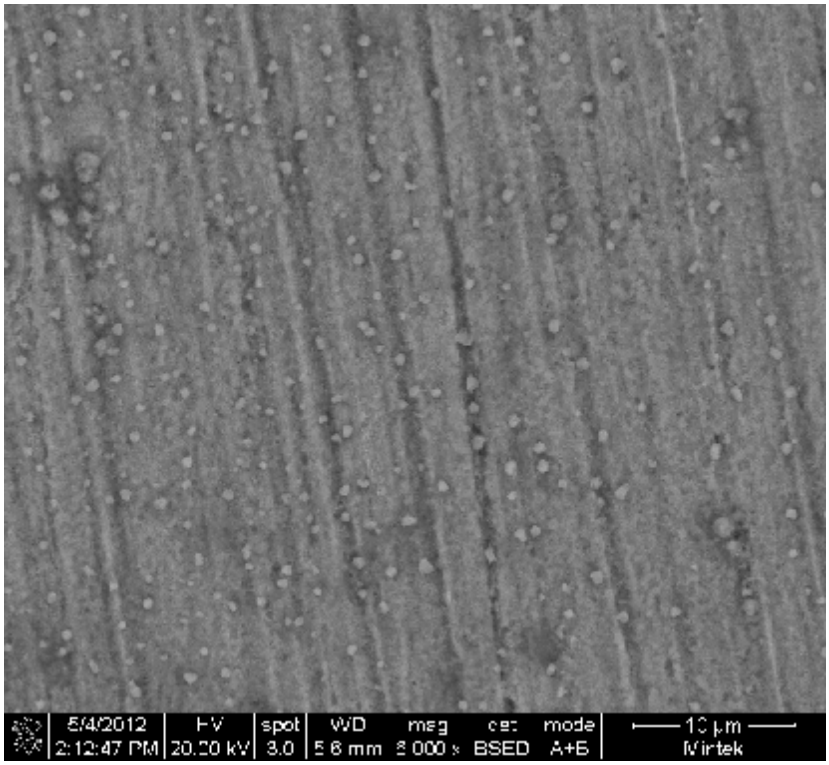


Figure 4.240. Higher magnification SEM-BSE image of the surface of Sample 441-8.

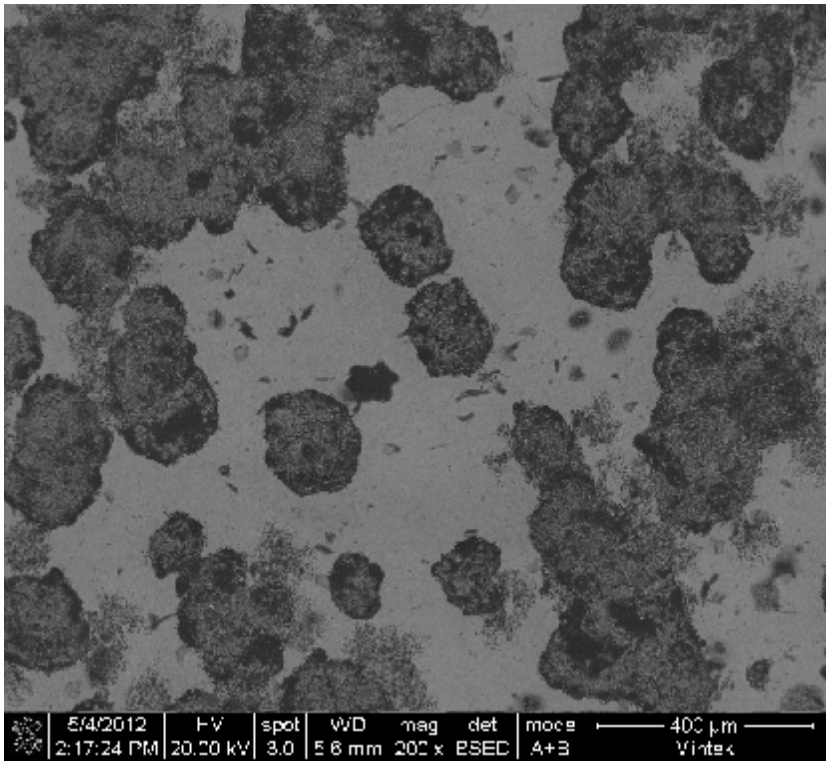


Figure 4.241. SEM-BSE image of pitting in Sample 441-8.

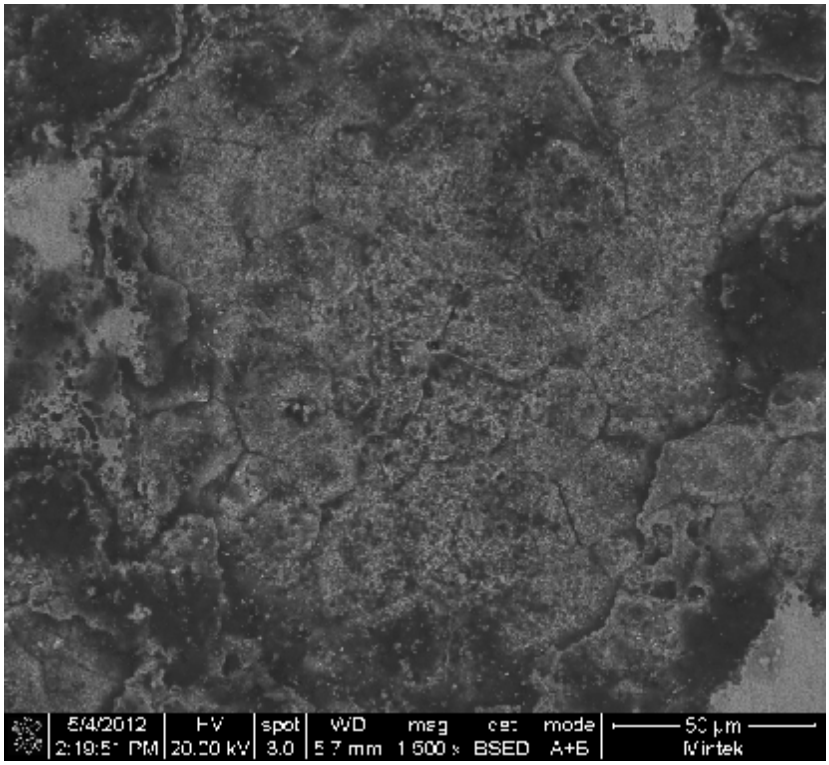


Figure 4.242. Higher magnification SEM-BSE image of a pit in Sample 441-8.

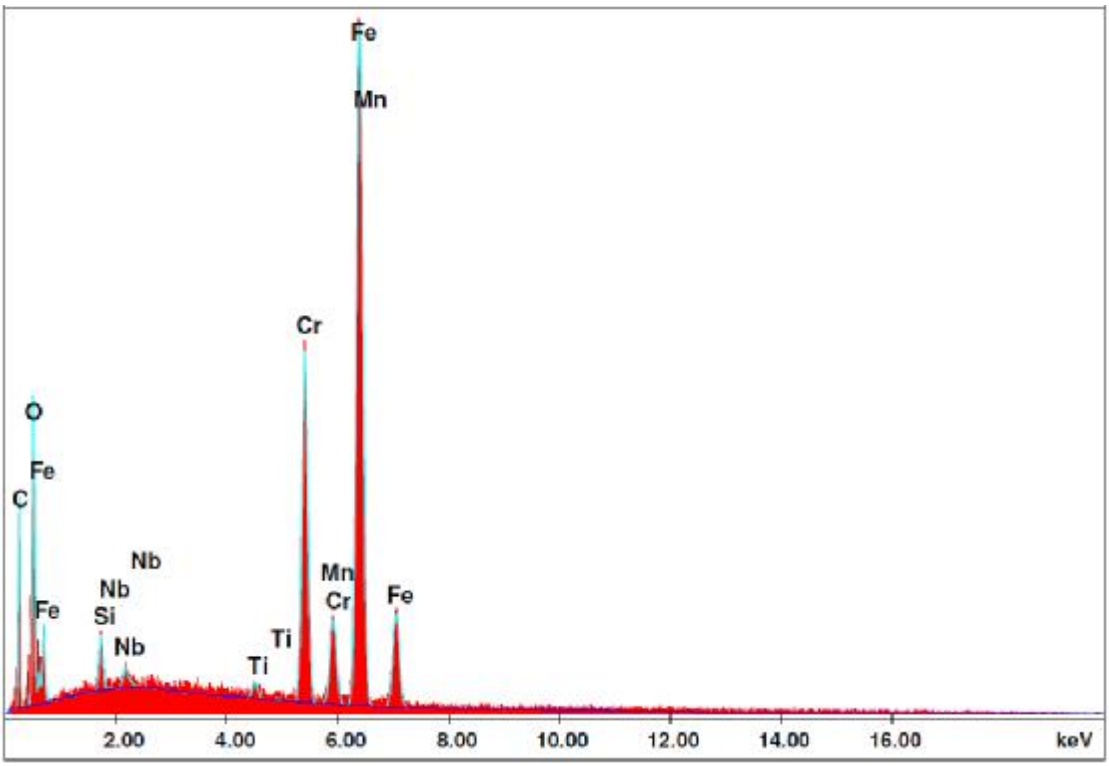


Figure 4.243. EDX spectrum of the surface of Sample 441-8.

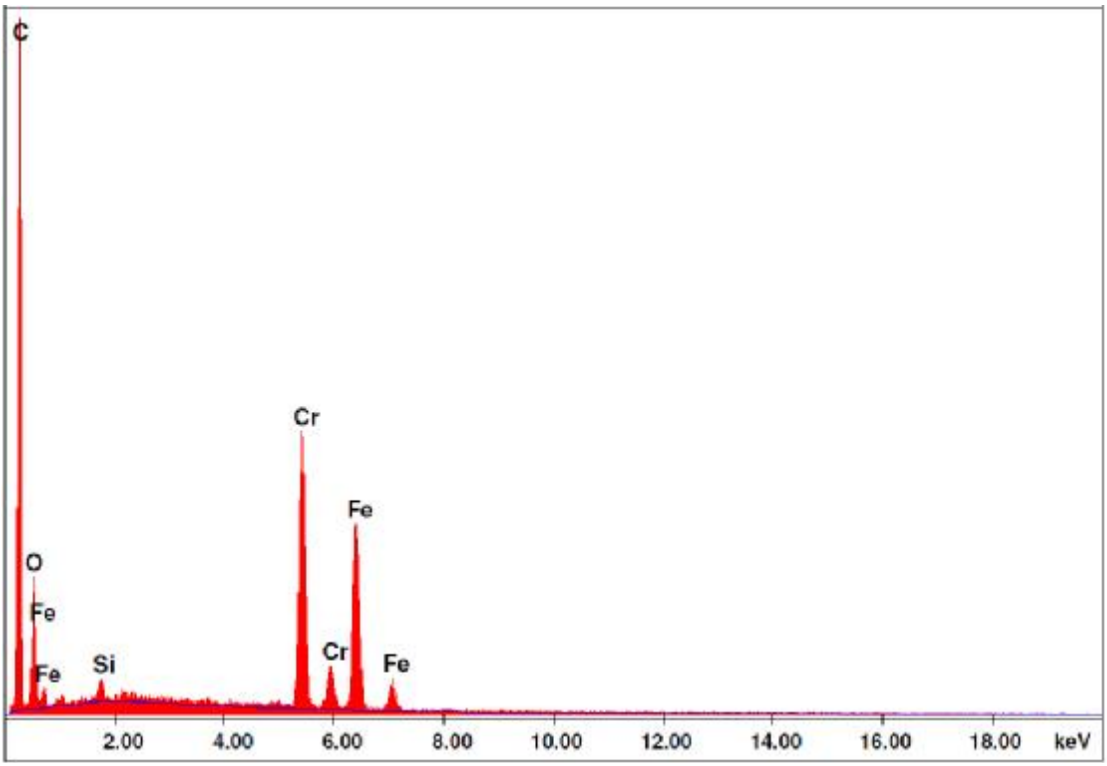


Figure 4.244. EDX spectrum inside a pit (area analysis) in Sample 441-8.

Figure 4.245 is a SEM image of a cross-section through a corroded area in a Type 304L sample. The white particle, labelled A in the image, was analysed by EDX, and found to be similar to the base material, as shown in Figure 4.246. An EDX line-scan was performed near the corroded area, as indicated on Figure 4.245, and is shown in Figure 4.247. The layer on the surface consisted primarily of chromium, probably as chromium oxide. There was no significant chromium de-alloyed layer subsurface. The nickel and other elements also did not vary considerably.

Figure 4.248 is an SEM image through a cross-section of the Type 304L sample, showing a sound area. There was a layer on the surface of the specimen, and a light phase just below the surface. An EDX line-scan was performed from the surface inwards, as shown in Figure 4.248, and is shown in Figure 4.249. The outer layer consisted predominantly of chromium, probably as chromium oxide. This is the protective layer that protected the substrate material from metal dusting, by preventing carbon ingress. The light phase present underneath the oxide layer was probably chromium carbides, but this could not be substantiated by EDX analysis, due to their small size.

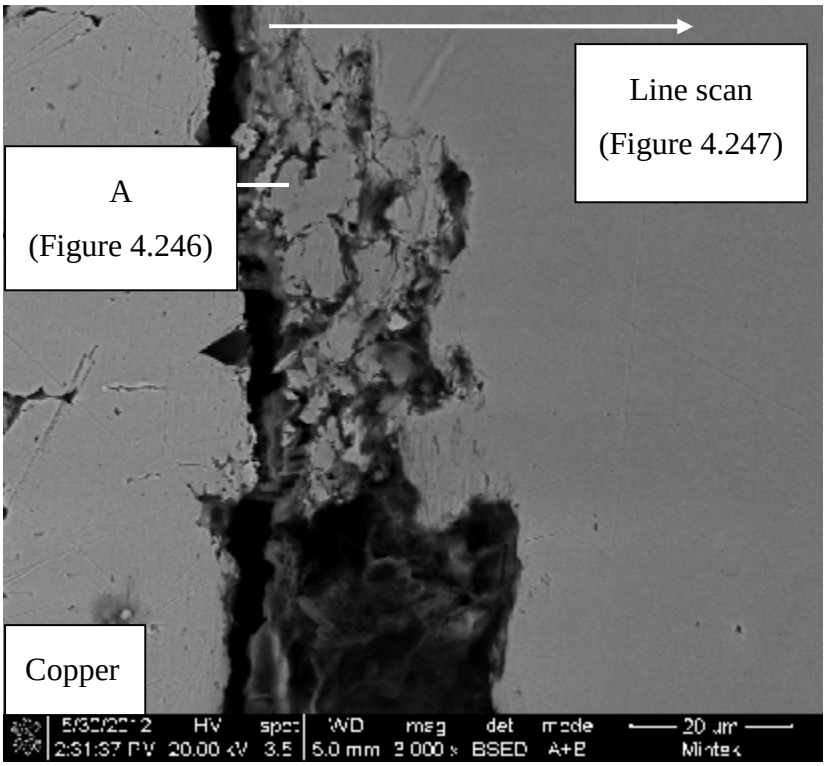


Figure 4.245. SEM-BSE image of a cross-section through a corroded area of Sample 304-7.

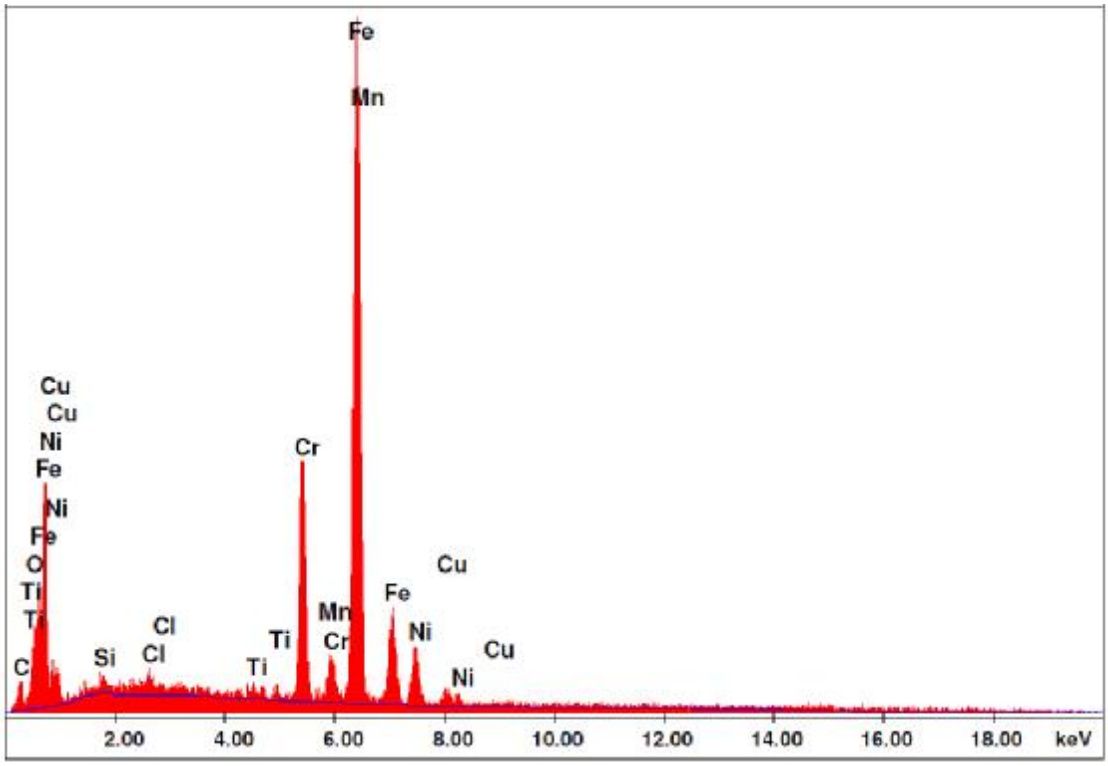


Figure 4.246. EDX spectrum of position A shown in Figure 4.245 of Sample 304-7.

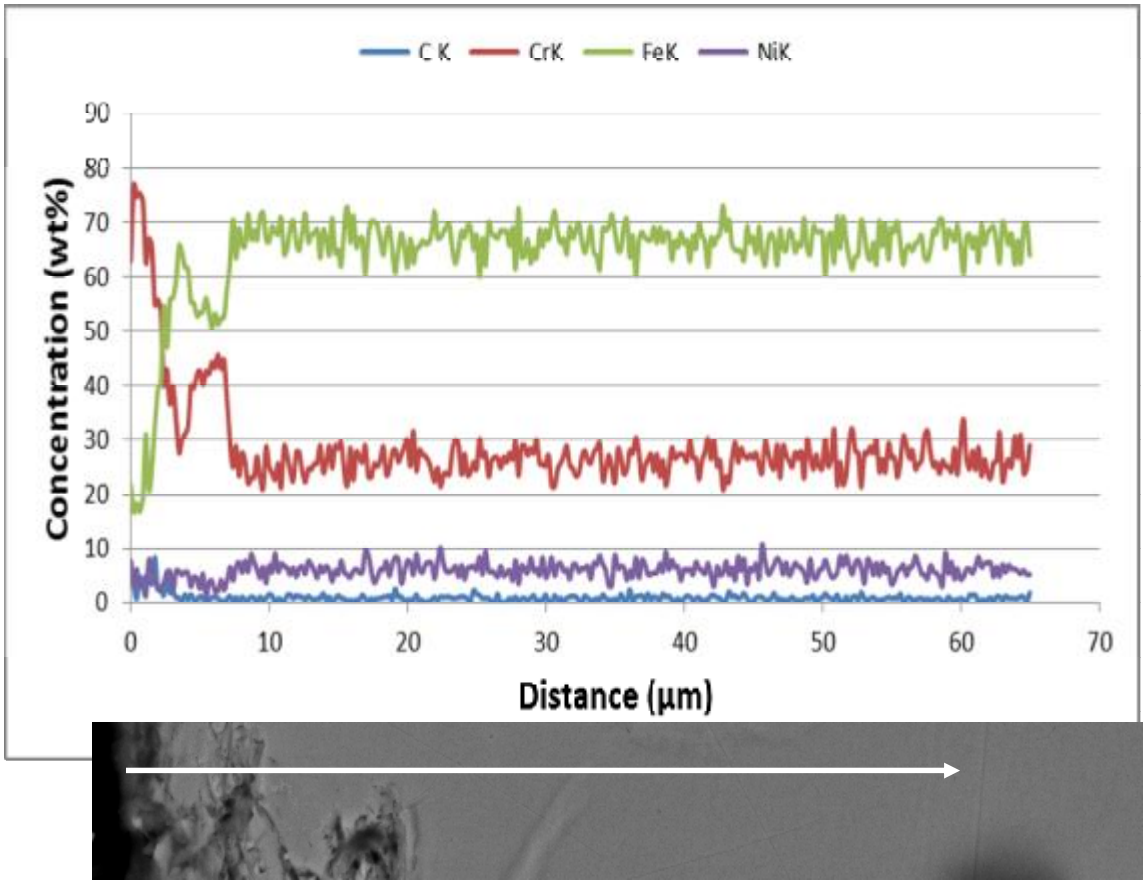


Figure 4.247. EDX line scan on Sample 304-7 as shown in Figure 4.245.

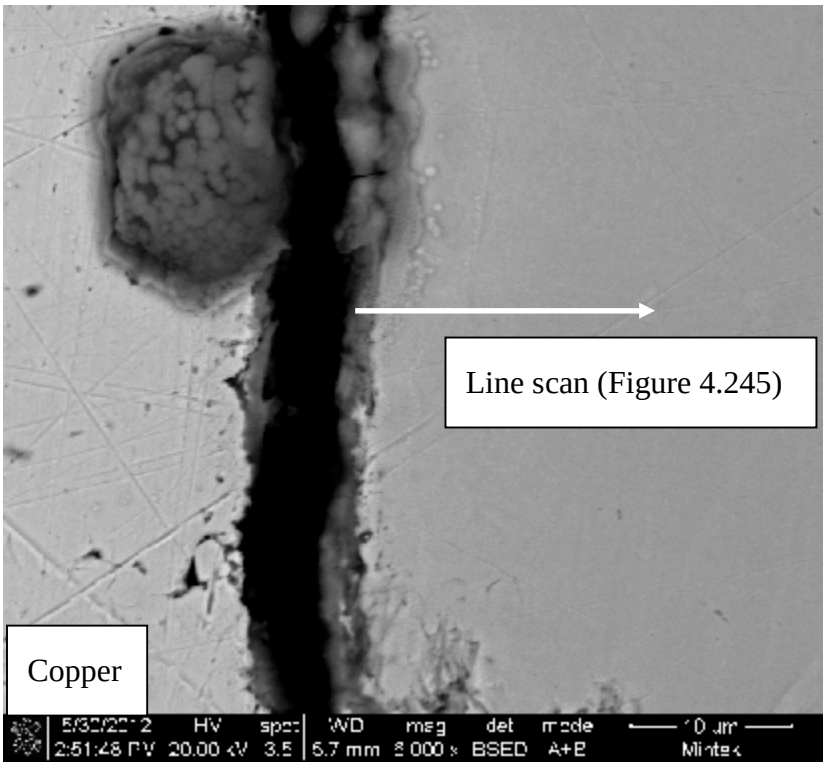


Figure 4.248. SEM-BSE image of the protective oxide layer on Sample 304-7.

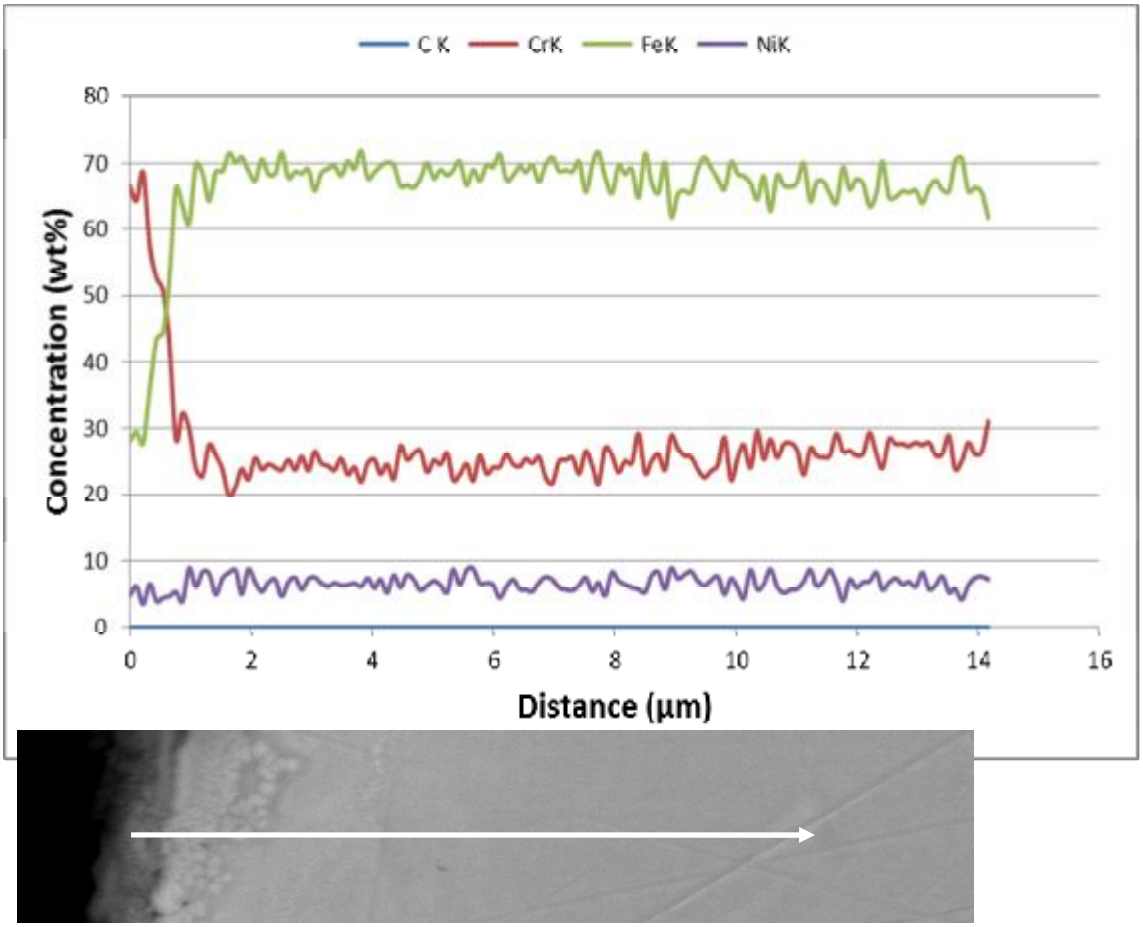


Figure 4.249. EDX line scan through Sample 304-7 as shown in Figure 4.248.

Figure 4.250 is an SEM image showing the fairly uniform nature of the attack on a Type 321 sample that was exposed for 30 days. Significant internal carburisation was also evident; both on the grain boundaries as well as inside the grains. Figure 4.251 is a higher magnification image of the attack, showing carbides on the grain boundaries, as well as inside the grains, that were seemingly unaffected by the attack. A product was also evident on the surface that consisted of two phases, a lighter phase and a darker phase. An EDX line-scan was performed from the product layer inwards, as shown in Figure 4.251, and is shown in Figure 4.252. Five distinctly different zones were identified by the line-scan, labelled A to E. Section A on the outside was primarily an iron oxide, followed by a chromium oxide (Section B). Section C consisted predominantly of iron and chromium, with concentration levels similar to the base alloy but with higher oxygen, as shown in Section E. Section D consisted of a phase with equal quantities of iron and chromium, and a higher level of carbon than the matrix, indicting iron chromium carbide also with some (but less) oxygen. Much less carbon and oxygen was detected in Section E, but it consisted primarily of iron

and chromium. The profile plot was very irregular, with the iron and chromium contents varying inversely, due to the extensive chromium carbide precipitation. Dark globular precipitates were also evident towards the end of Section E, which were identified as niobium- and titanium-rich precipitates (white phases). Figure 4.253 is a higher magnification image of the extensive carbide precipitation at the grain boundary and with Widmanstätten morphology within the grain. The nature of the corrosive attack around the carbides is also shown. The chromium oxide layer that protected the original surface layer was also still evident. An EDX spectrum of this layer is shown in Figure 4.254, and an EDX spectrum of the iron-rich oxide layer on the outside surface is shown in Figure 4.255.

Figure 4.256 is a SEM image near the centre of the Type 321 sample, showing extensive carburisation on the grain boundaries and larger titanium carbo-nitride precipitates. Coking was also evident at the interface between the titanium carbo-nitride and the matrix. Figure 4.257 is an EDX spectrum of the precipitates, indicating that it primarily consisted of titanium with some niobium. Figure 4.258 is a bulk EDX spectrum (area analysis), showing the general composition of the Type 321 sample. It is interesting that no nickel was detected in this sample; this needs to be further investigated, but agreed with Section 4.2.5 which indicated that the structure was ferritic. The nickel is expected to be at least 8wt%.

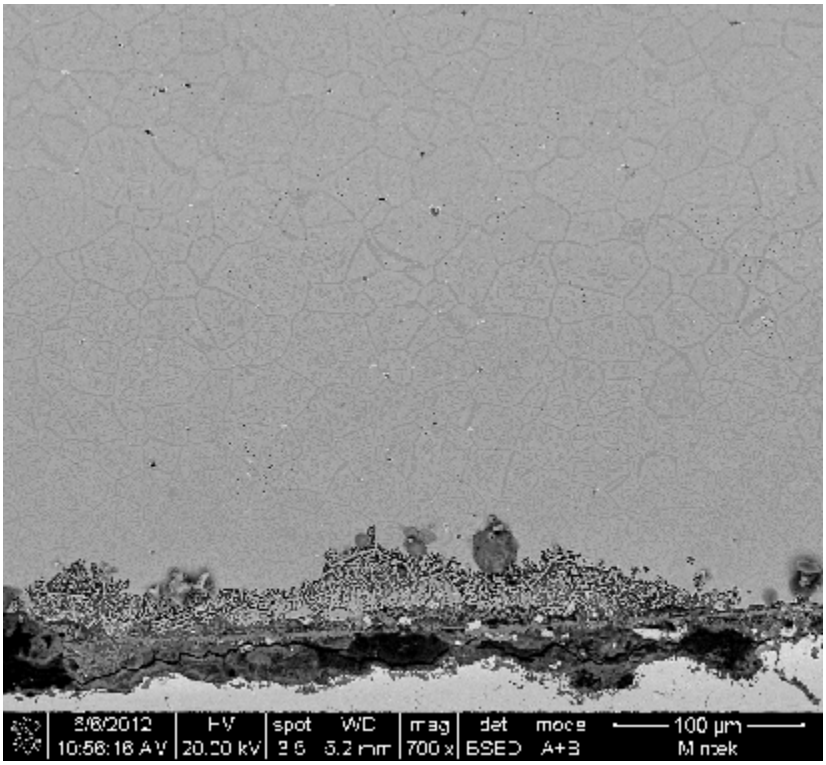


Figure 4.250. SEM-BSE image of attack in Sample 321-8.

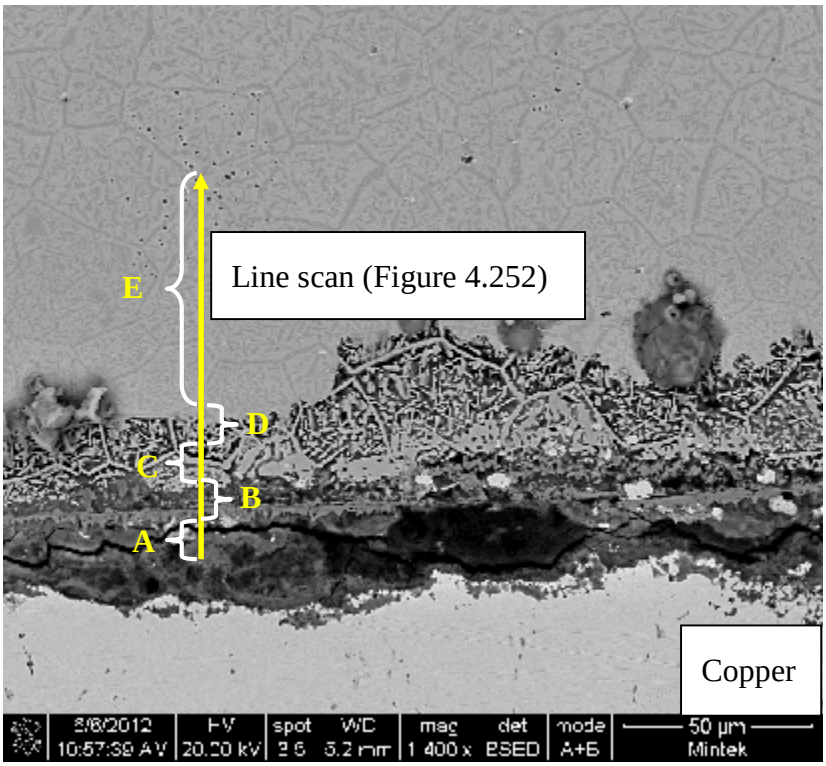


Figure 4.251. Higher magnification SEM-BSE image of attack on Sample 321-8.

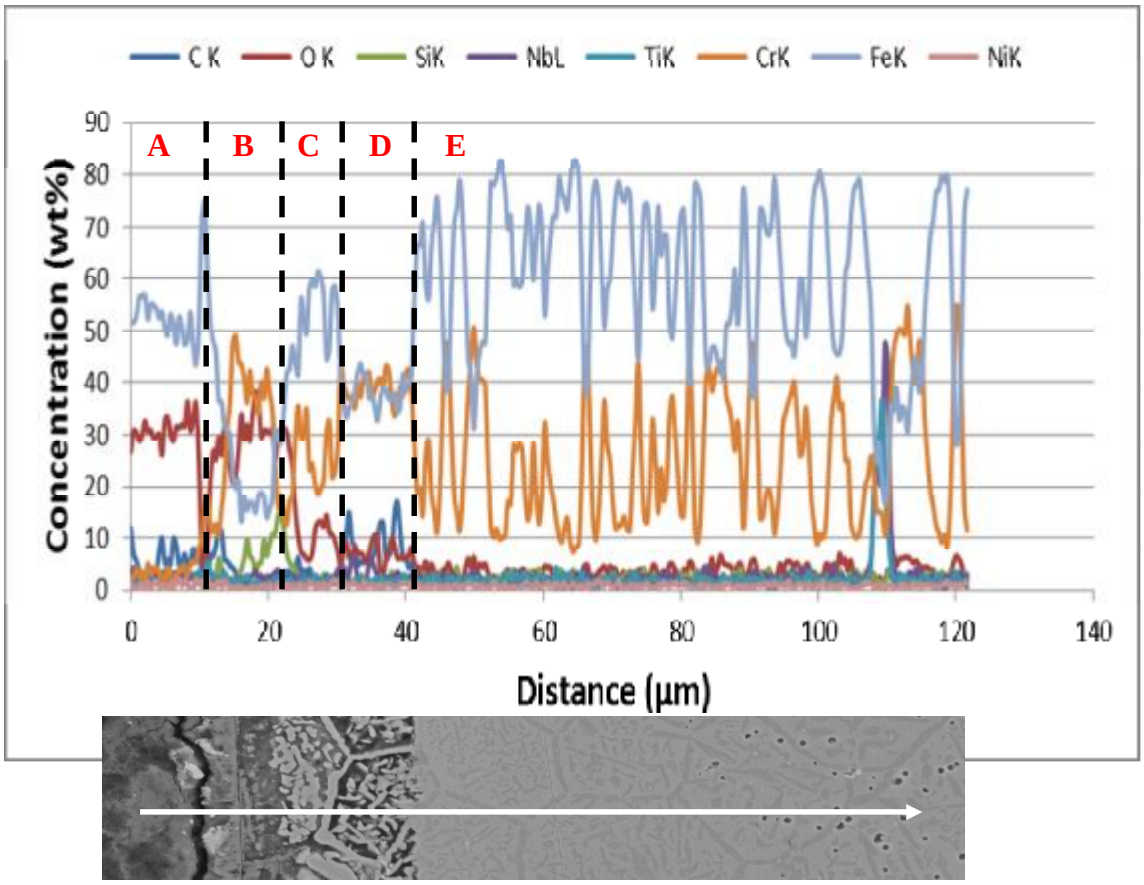


Figure 4.252. EDX line scan of Sample 321-8 as shown in Figure 4.251.

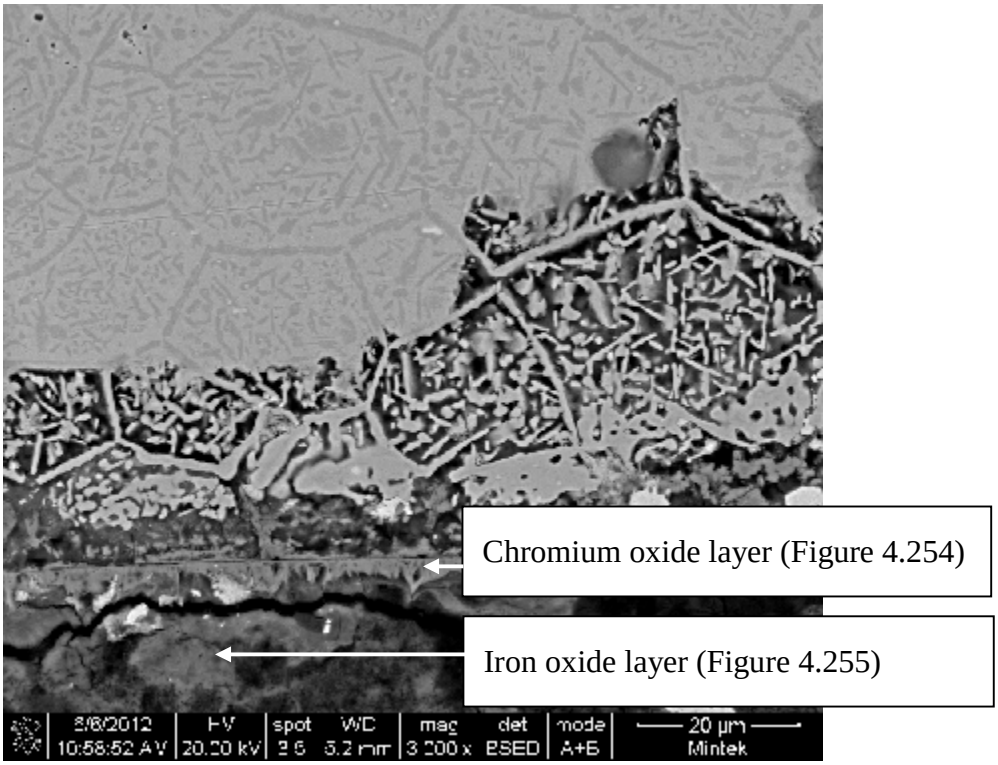


Figure 4.253. Higher magnification (SEM-BSE) of the uniform attack in Sample 321-8.

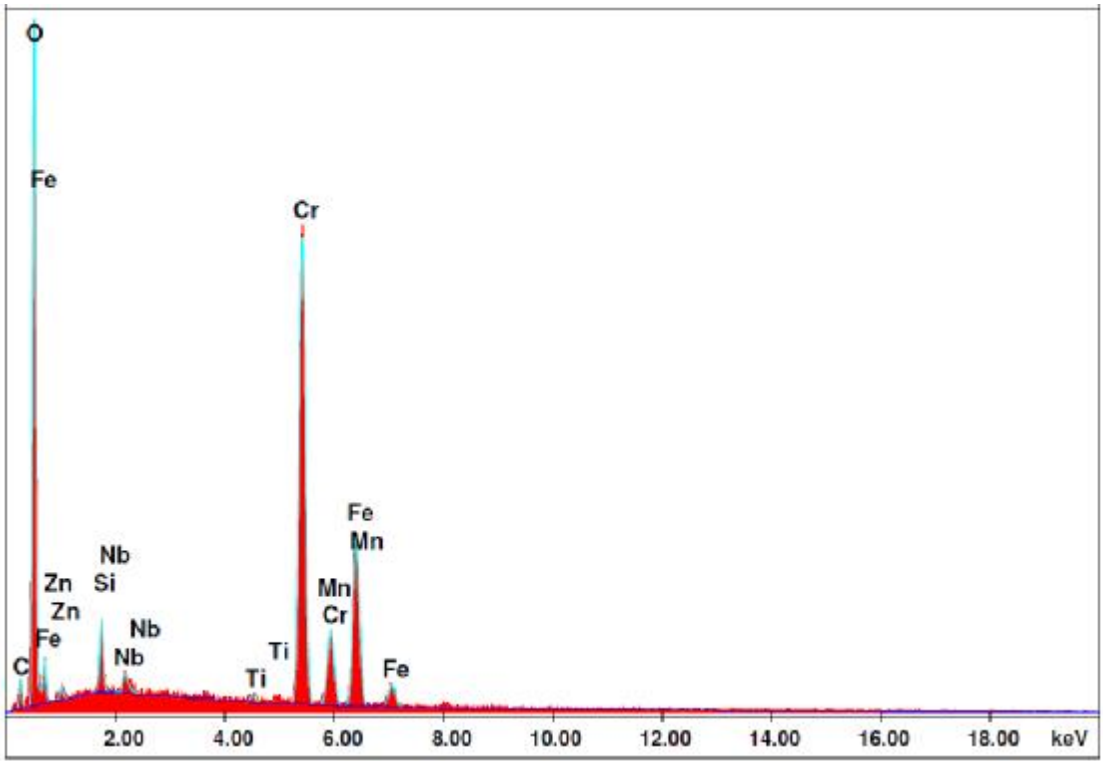


Figure 4.254. EDX spectrum of the protective chromium oxide layer on Sample 321-8 as shown in Figure 4.253.

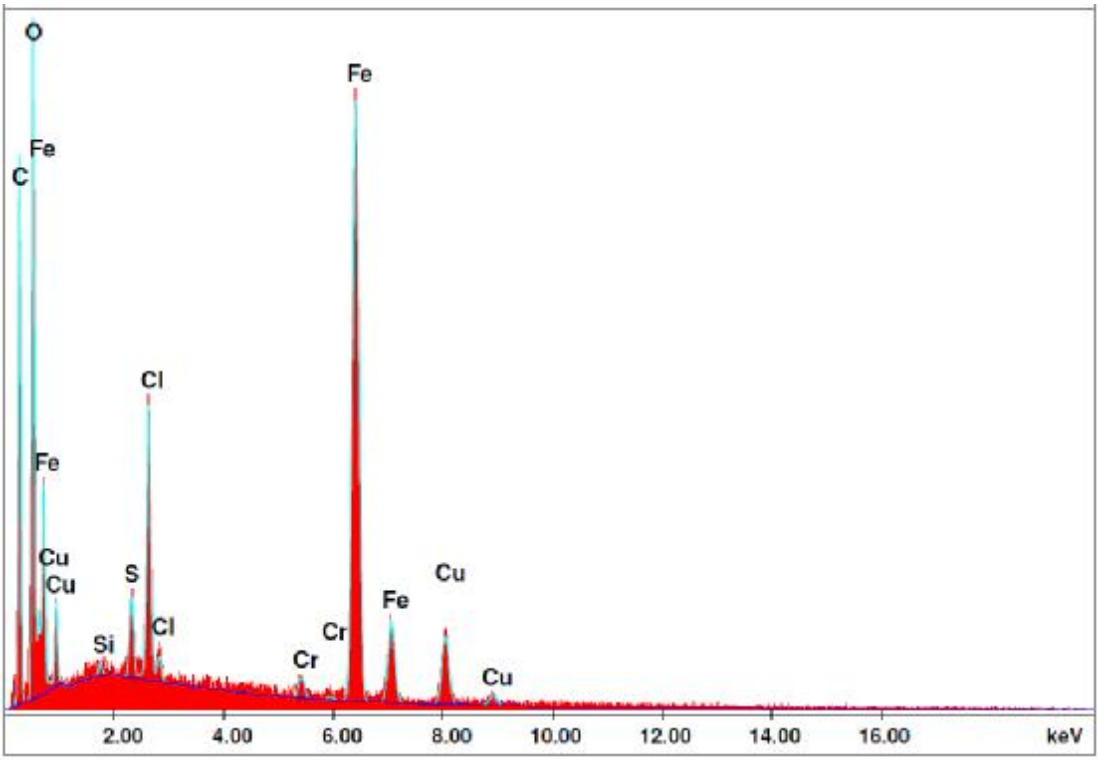


Figure 4.255. EDX spectrum of the oxide outside the chromia layer of Sample 321-8 as shown in Figure 4.253.

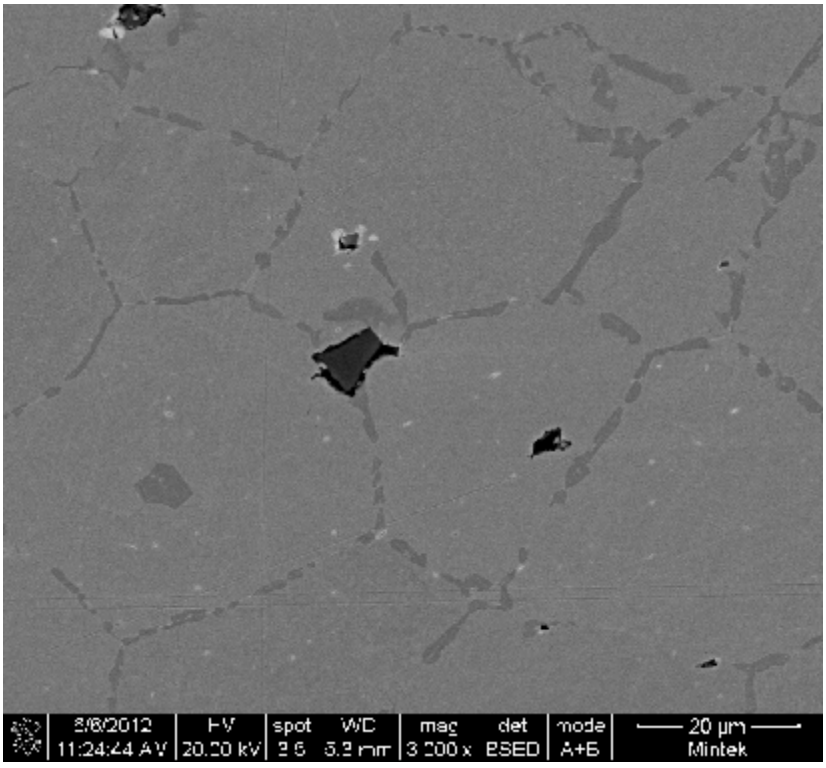


Figure 4.256. SEM-BSE image of the matrix of Sample 321-8 showing carburisation on the grain boundaries and attack around the titanium carbo-nitride precipitate.

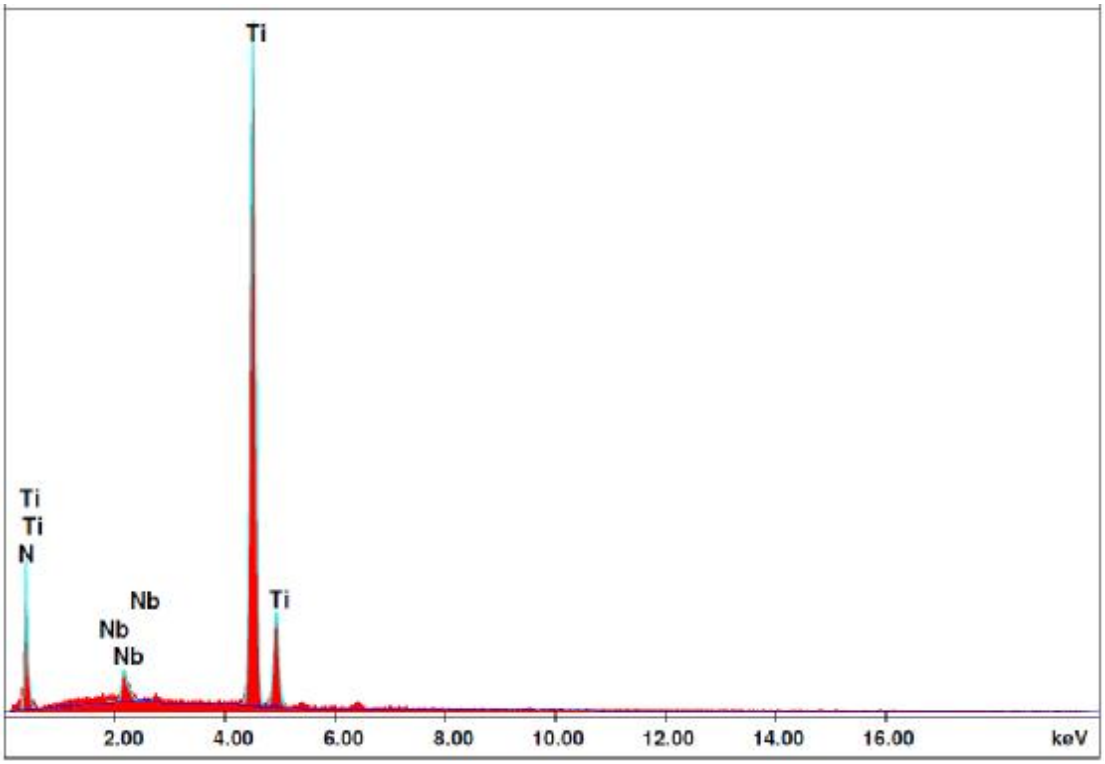


Figure 4.257. EDX spectrum of the titanium carbo-nitride precipitate in Sample 321-8 (Figure 4.256).

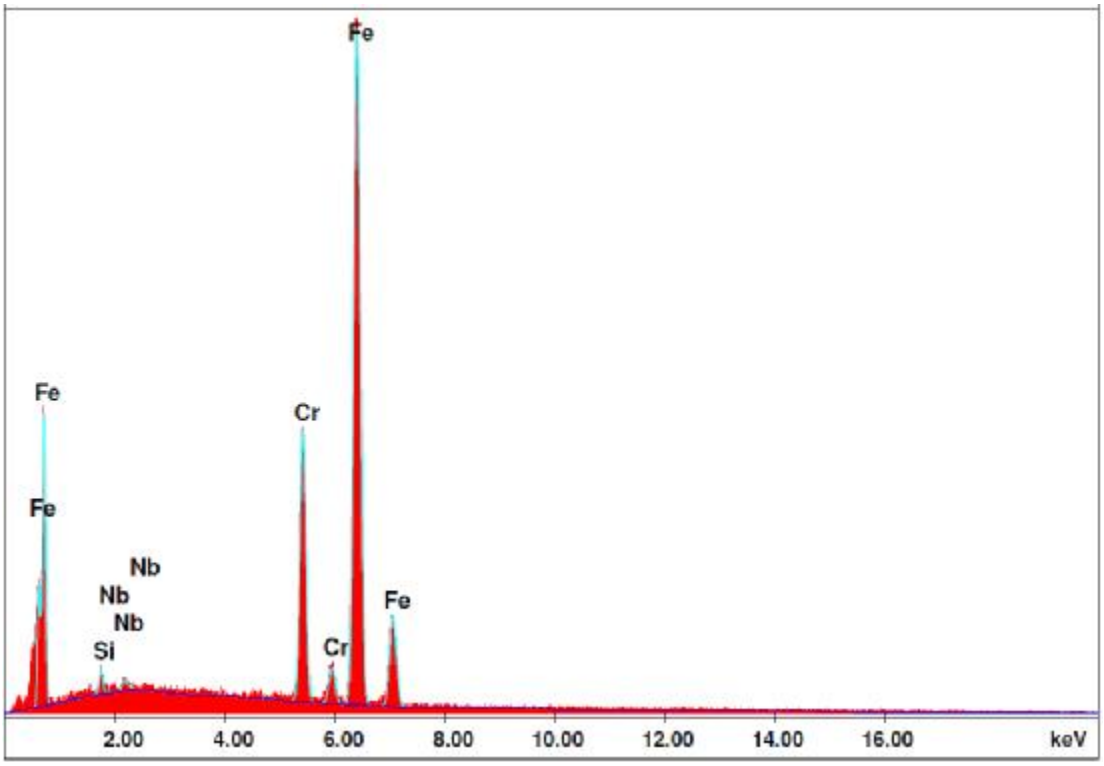


Figure 4.258. Bulk analysis of Sample 321-8 showing no evidence of nickel.

Figure 4.259 is an SEM image of the uniform attack on the surface of a Type 316L sample that was exposed for 30 days. Figure 4.260 is a higher magnification image showing the intergranular nature of the attack, as well as a white second phase on the grain boundaries. The grains near the outside surface were completely corroded at certain areas, whereas at the reaction front, only the grain boundaries were attacked. This suggests that the attack initiated on the grain boundaries, and then propagated to "consume" the entire grains. Figure 4.261 and Figure 4.262 are higher magnification images of this process. The light phase apparent on the grain boundaries was also evident as smaller precipitates inside the grains, and did not appear the be attacked. Figure 4.263 is an EDX spectrum of the light phase, indicating that it was enriched in chromium, molybdenum and carbon, so is probably an iron molybdenum carbide (although some matrix would also have been included).

Figure 4.264 is another SEM image showing the significant general (uniform) attack, with the white phase evident on the grain boundaries, seemingly unaffected by the attack. Figure 4.265 is a higher magnification of the attack at the reaction front (interface with sound substrate material), showing the white phase on the grain boundaries. An EDX line-scan was performed across this phase as illustrated in this figure, and is plotted in Figure 4.266. The particle was significantly enriched in chromium at the expense of iron. The molybdenum content also increased from 2% to about 10%. It is interesting to note that the chromium and molybdenum concentration increased gradually from a distance corresponding with the attacked region shown in Figure 4.265. Figure 4.267 is a line scan in the same location as shown above, but over a longer distance into the substrate material to identify any gradients in element concentration. No significant gradients were observed, indicating that chromium and molybdenum did not diffuse over large distances to enrich the grain boundary regions, unless all had diffused. Figure 4.268 is an EDX spectrum of the light phase on the grain boundary, and Figure 4.269 is an EDX spectrum of the area adjacent to the grain boundary. Both these figures confirm that these areas were enriched with chromium and molybdenum, with the iron content higher in the area next to the carbide on the grain boundary (even though the areas were too small to be analysed without pick-up from the surrounding area). It is possible that the light phase is sigma, being rich in chromium and molybdenum, and with the sample being exposed at elevated temperatures for 30 days.

Figure 4.270 is an SEM image of attack with four areas labelled that were analysed by EDX. Position 1 was taken in the uniformly attached area and Position 2 on the light phase on a grain boundary. These two areas were similar (the EDX analysis of Position 2 would also have included some matrix), being enriched with chromium and molybdenum, as shown in Figure 4.271 and Figure 4.272. The EDX analysis of Positions 3 and 4 were similar, esentially resembling the substrate analysis of 316L stainless steel, as shown in Figure 4.273 and Figure 4.274 respectively. A light phase is also present in the matrix, but this was not characterised.

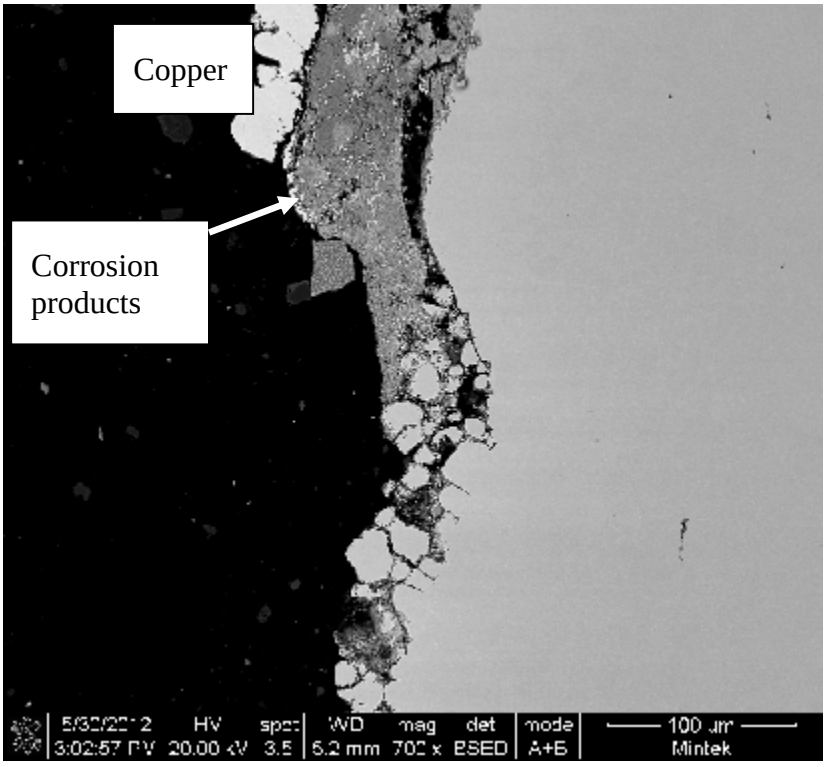


Figure 4.259. SEM-BSE image of uniform corrosion by intergranular attack, and subsequent degradation of the grains in Sample 316-8.

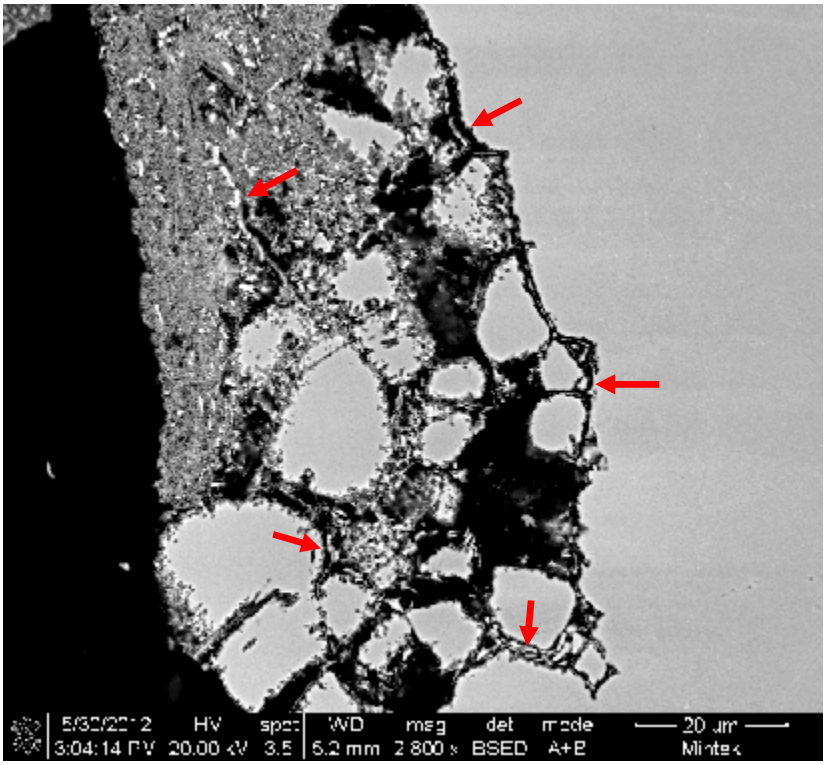


Figure 4.260. Higher magnification SEM-BSE image of the carbides (arrows) and attack on Sample 316-8.

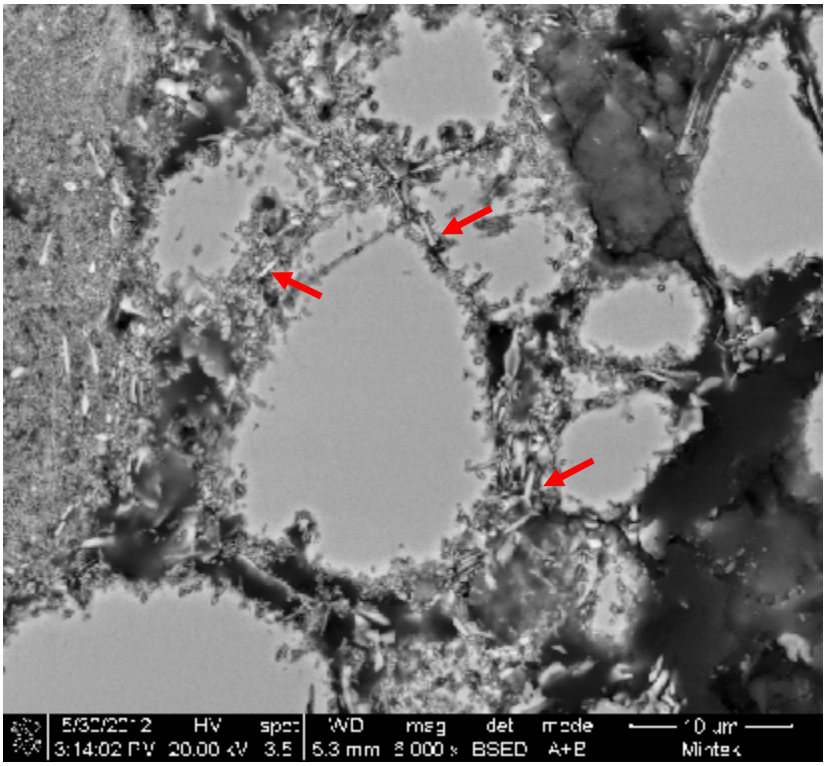


Figure 4.261. Higher magnification SEM-BSE image of the carbides (arrows) and associated attack in Sample 316-8.

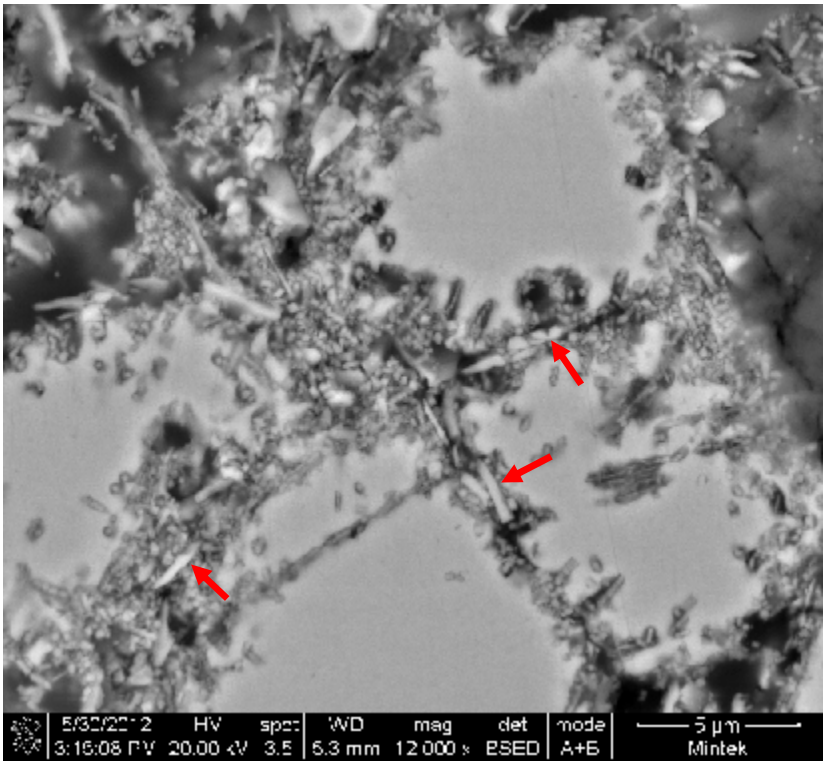


Figure 4.262. High magnification SEM-BSE image of the carbides (arrows), grain boundary attack and progressive attack of the grains in Sample 316-8.

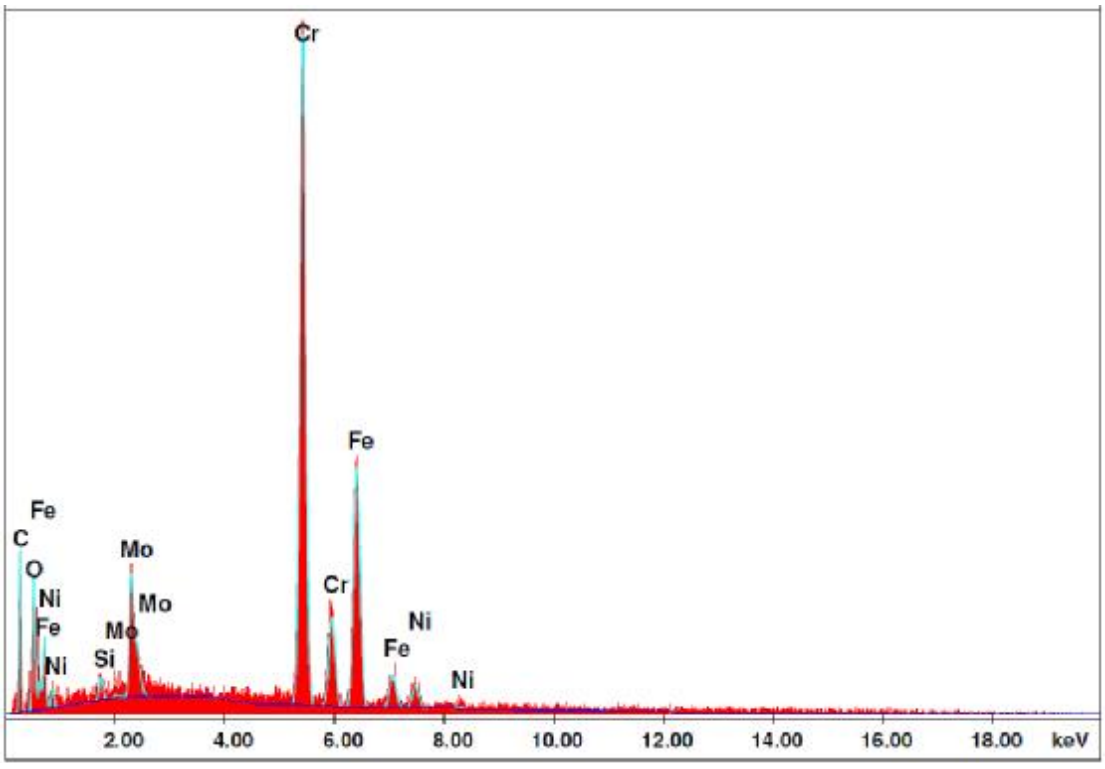


Figure 4.263. EDX Spectrum of products (white phase) on the grain boundaries of Sample 316-8 (including some matrix).

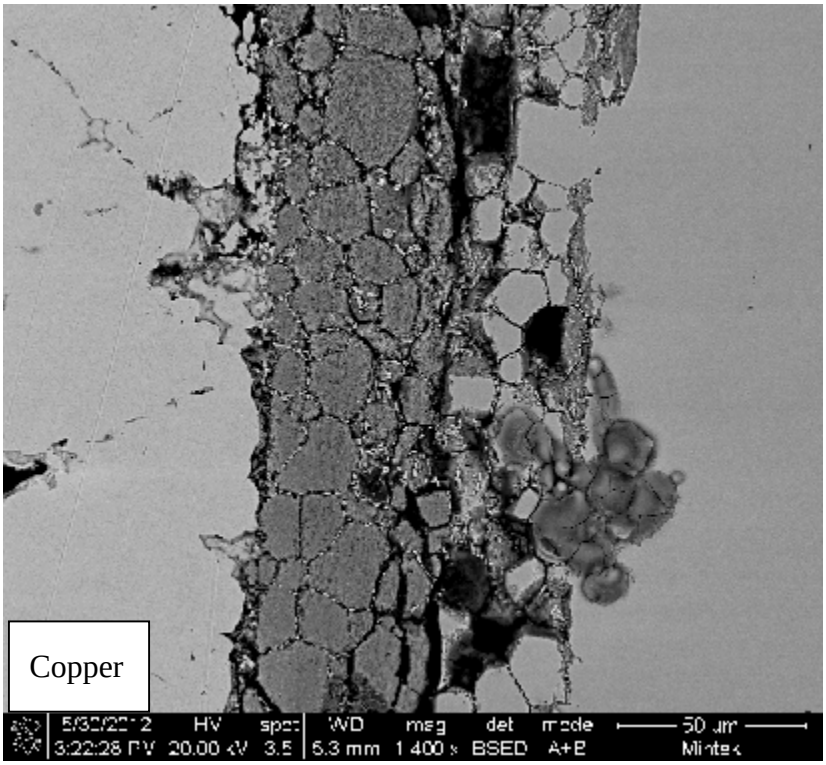


Figure 4.264. SEM-BSE image of the general nature of the metal wastage on Sample 316-8, showing the white phase on the grain boundaries was still evident in the corroded area.

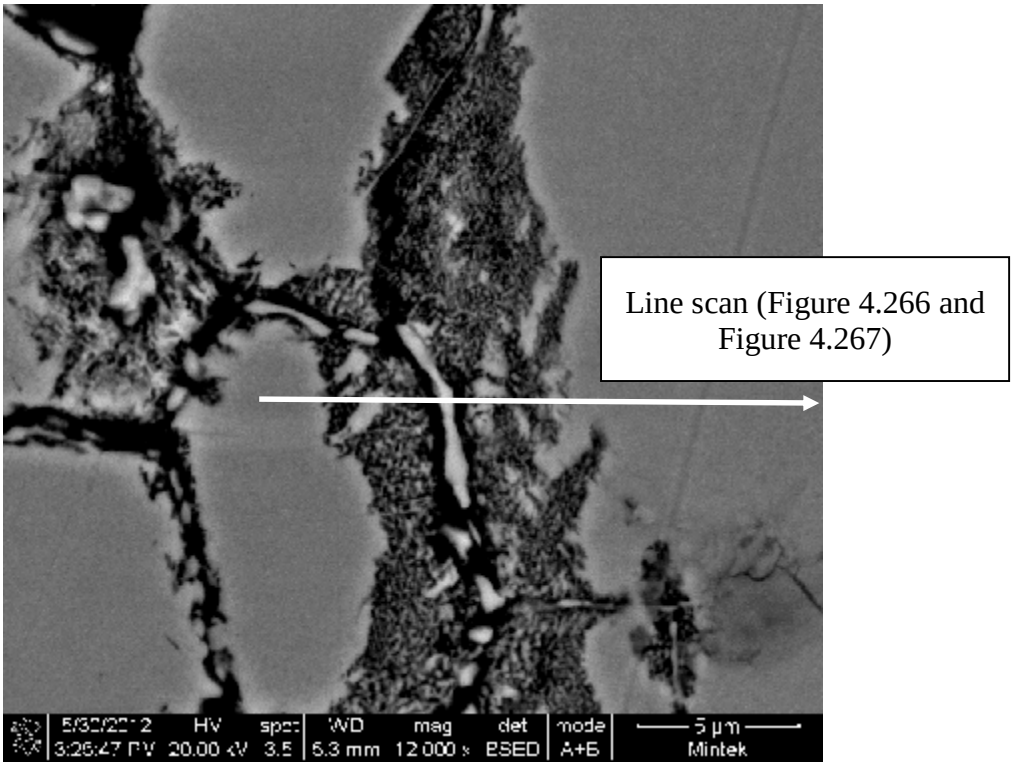


Figure 4.265. Higher magnification image of the attack on Sample 316-8.

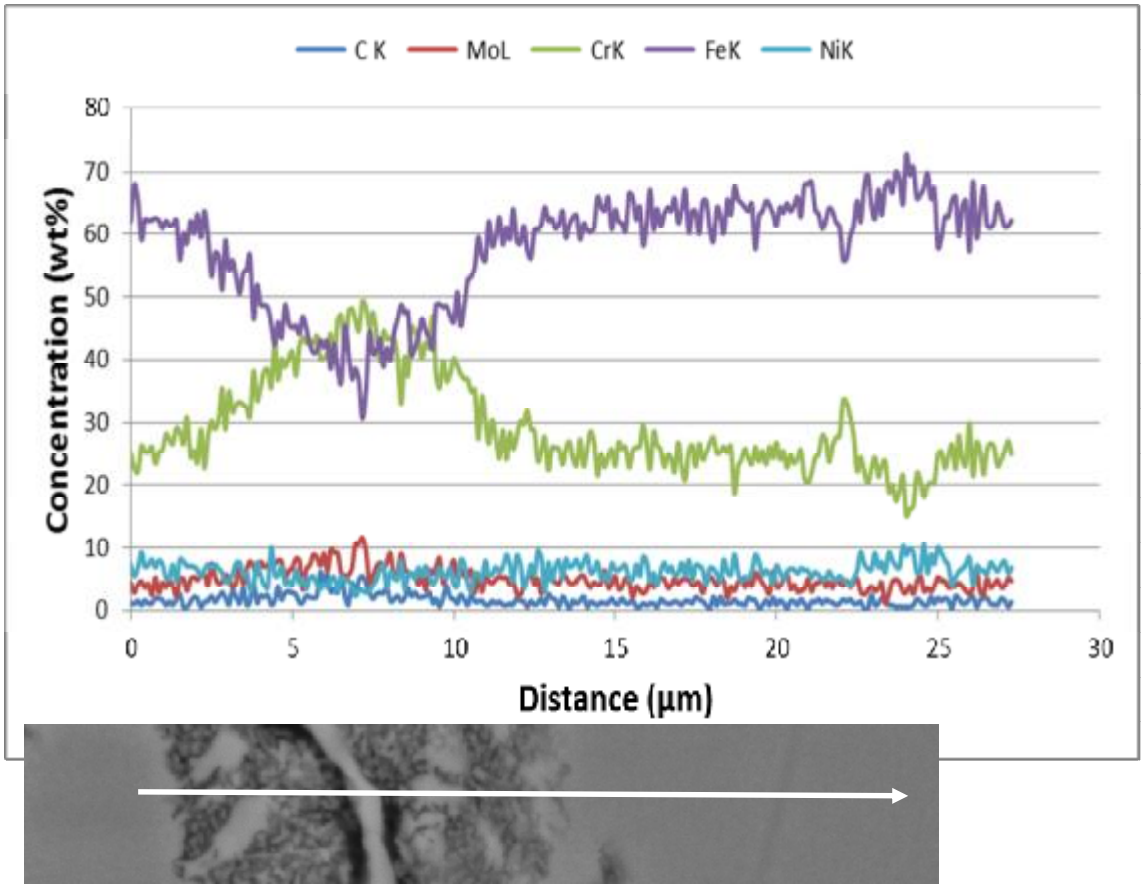


Figure 4.266. EDX line scan of Sample 316-8 as shown in Figure 4.265.

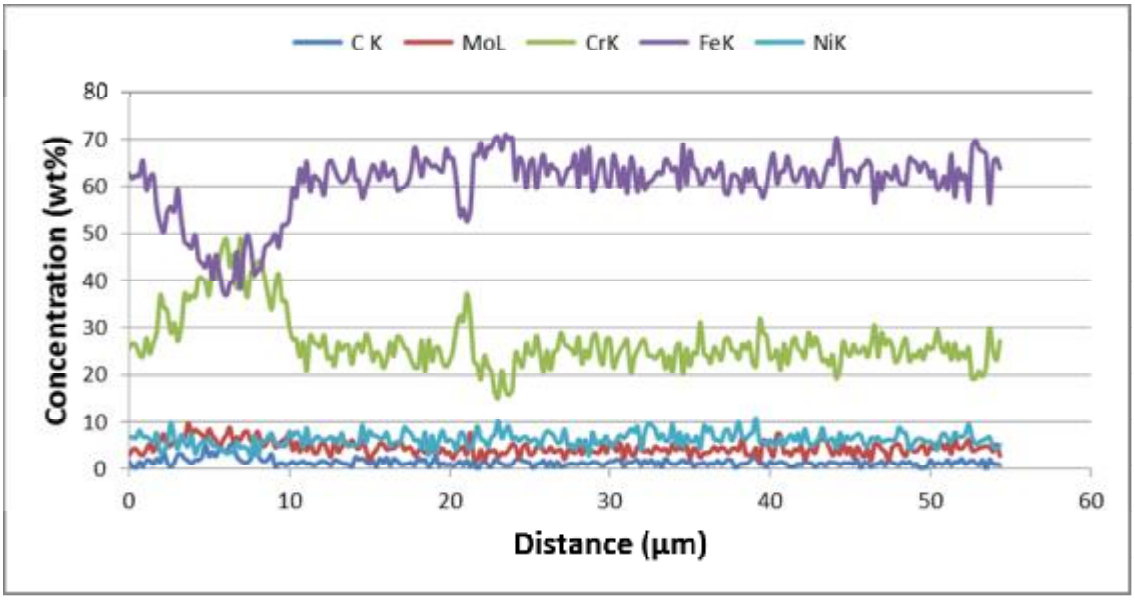


Figure 4.267. EDX line scan in similar area as shown in Figure 4.266, but over a longer distance.

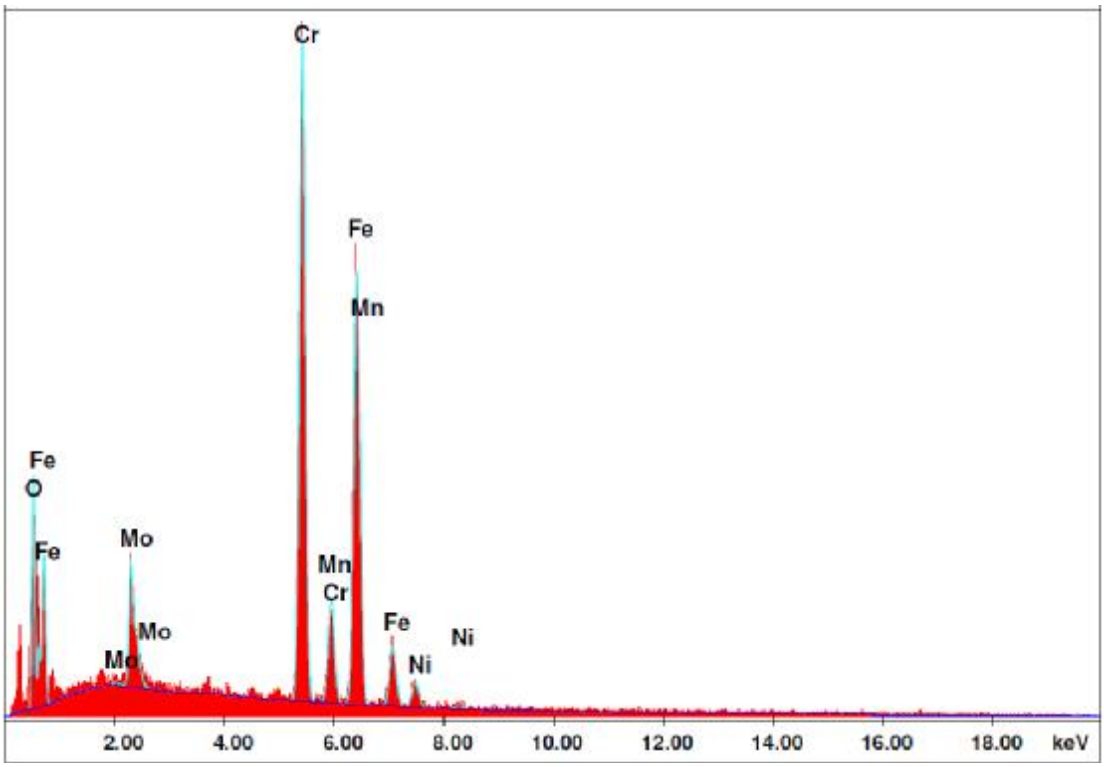


Figure 4.268. EDX spectrum of the large light phase on the grain boundary of Sample 316-8 as shown in Figure 4.265.

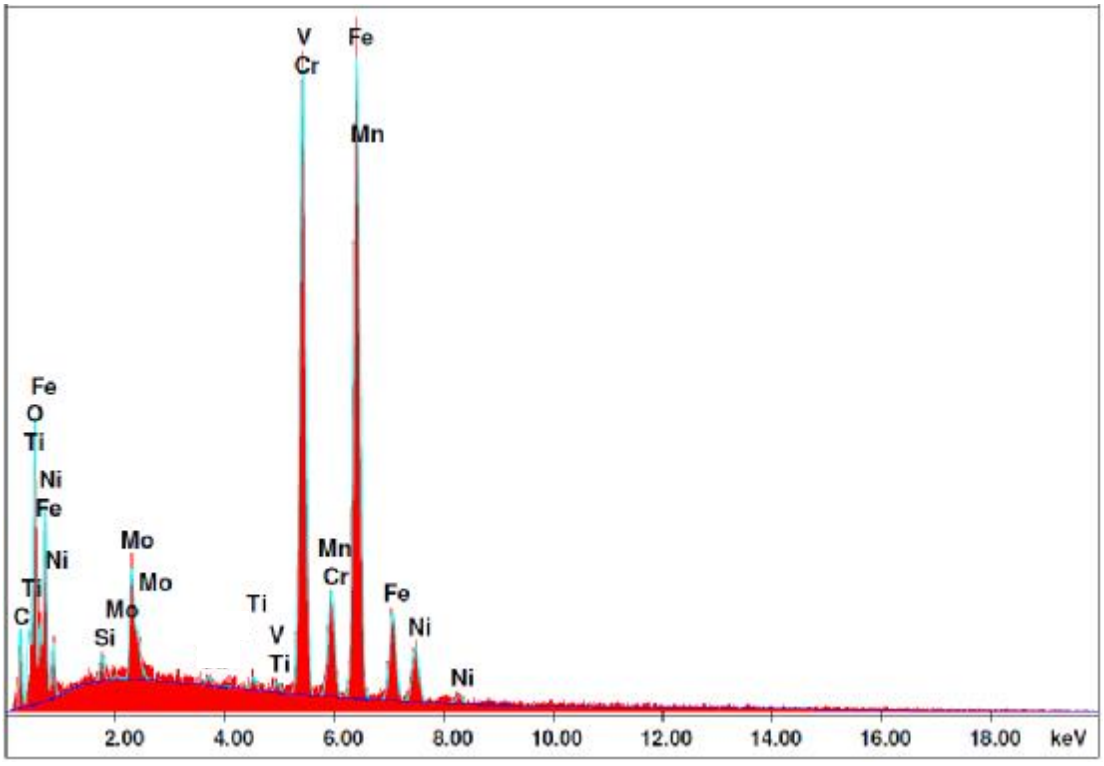


Figure 4.269. EDX spectrum of the corroded region adjacent to the large light phase on the grain boundary of Sample 316-8 as shown in Figure 4.265.

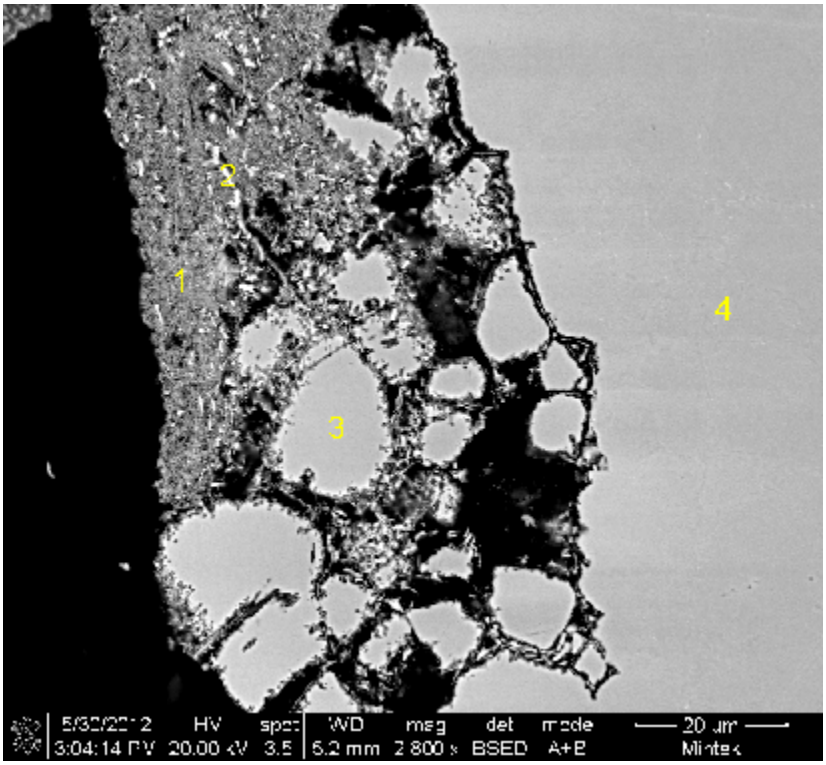


Figure 4.270. SEM-BSE image of Sample 316-8 indicating positions where various EDX analyses were made.

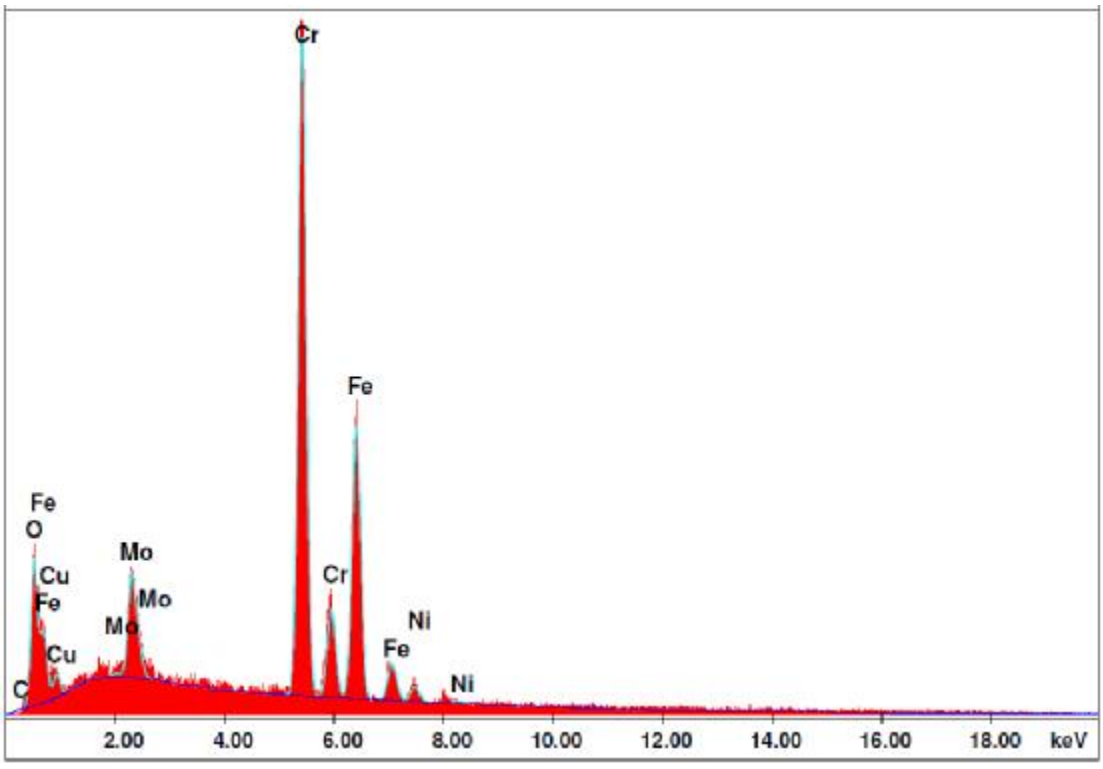


Figure 4.271. EDX analysis of Point 1 in Sample 316-8 as shown in Figure 4.270.

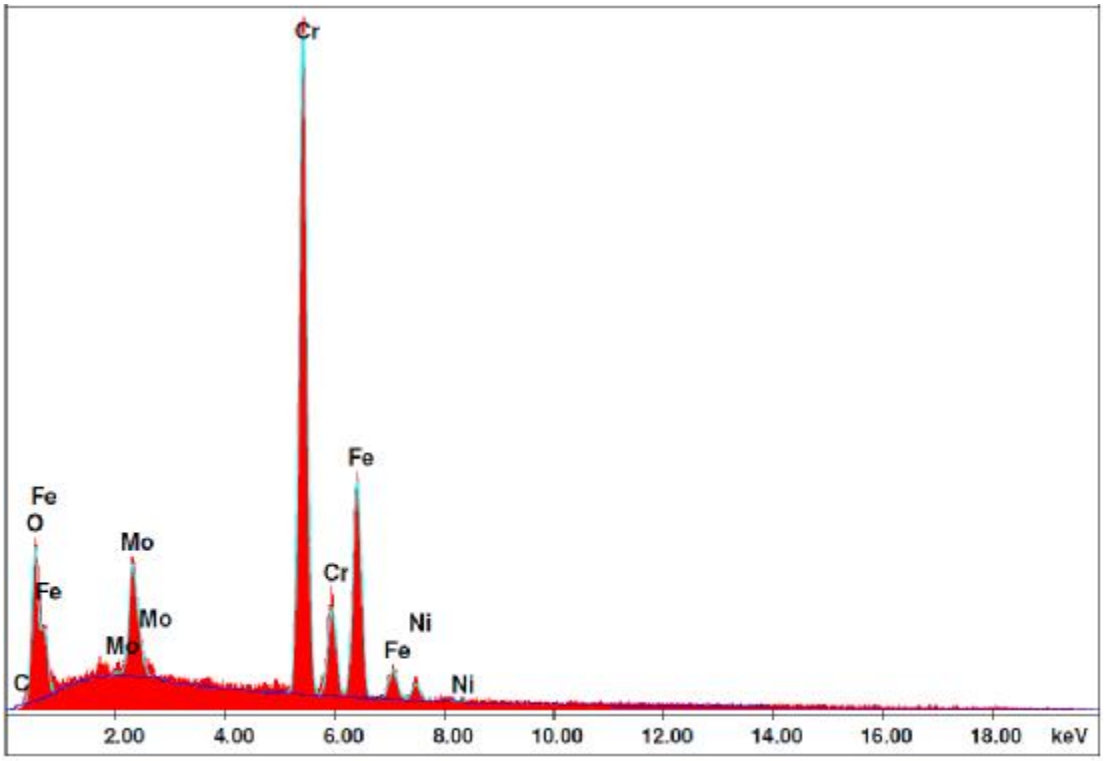


Figure 4.272. EDX analysis of Point 2 in Sample 316-8 as shown in Figure 4.270.

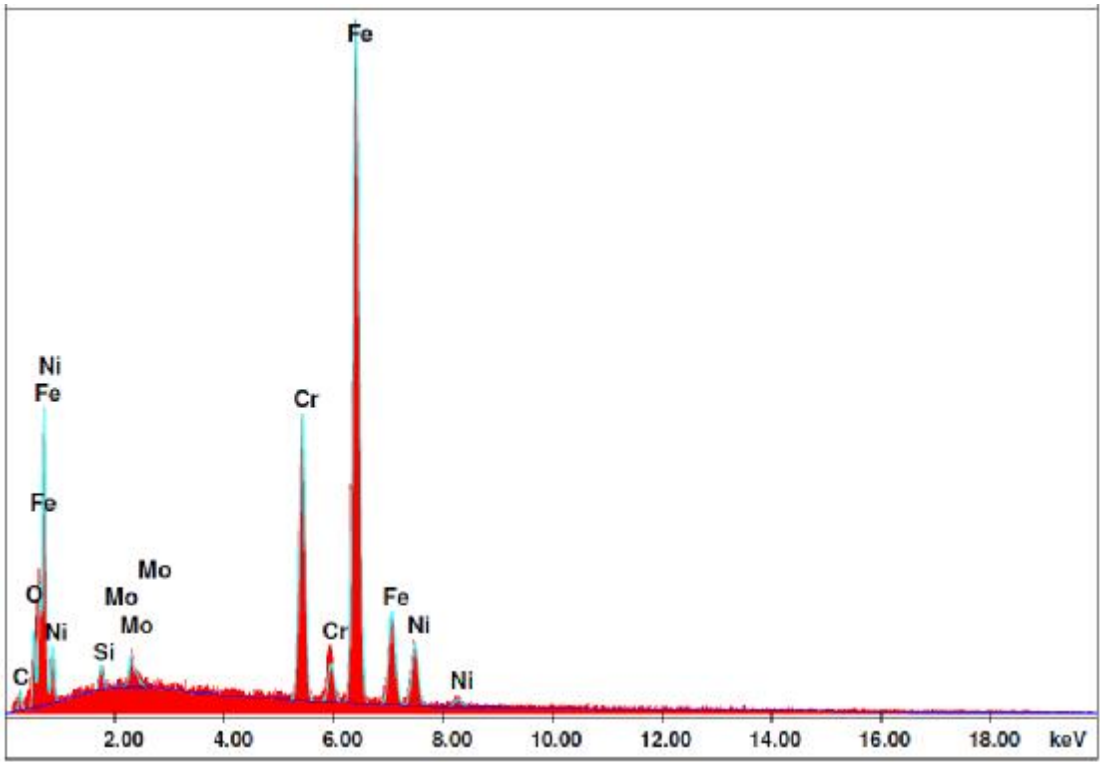


Figure 4.273. EDX analysis of Point 3 in Sample 316-8 as shown in Figure 4.270.

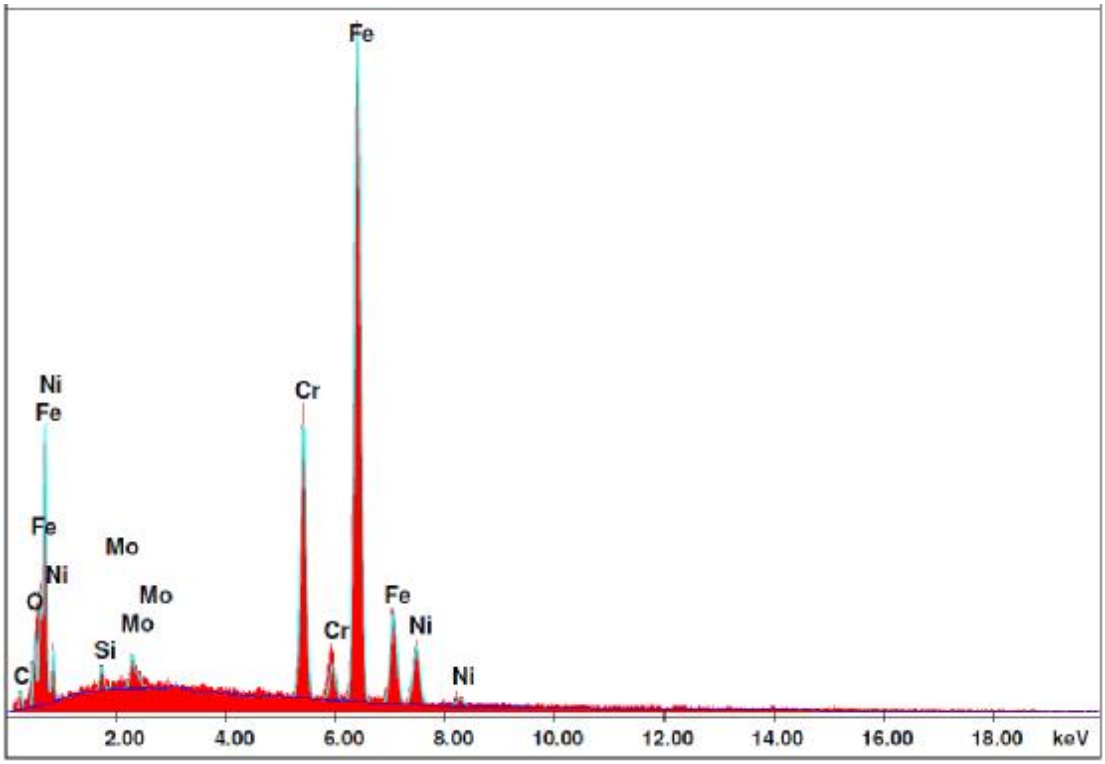


Figure 4.274. EDX analysis of Point 4 in Sample 316-8 as shown in Figure 4.270.

Figure 4.275 and Figure 4.276 are SEM images of a 316Ti sample that was exposed for 30 days, showing the extent of the corrosive attack. The attack was also intergranular. Figure 4.277 is an image at a higher magnification, demonstrating that several grains had dropped out and a white phase was apparent on the grain boundaries. The removal of the grains appeared to be influenced more by a mechanical action, than due to a corrosion process, as the facets of the grains were relatively smooth and straight.

Figure 4.278 is a SEM image of the oxide layer on the outside surface, showing that the light phase on the grain boundaries was still seemingly unaffected. Figure 4.279 and Figure 4.280 are images of the light phase at the reaction front, showing its formation and the initiation of the attack from the grain boundaries inwards into the grains. Figure 4.281 is an EDX spectrum of the oxide on the outside surface, indicating that it is enriched with chromium. Figure 4.282 and Figure 4.283 are EDX spectra of the light phase on the grain boundaries in the outside oxide scale, and inside the metal substrate, respectively (although the areas were too small to be analysed accurately and collected the matrix too). The spectra are similar, indicating that they are from carbides enriched with chromium and molybdenum. The

carbides were similar, since they had not been attacked/degraded further by the metal dusting mechanism.

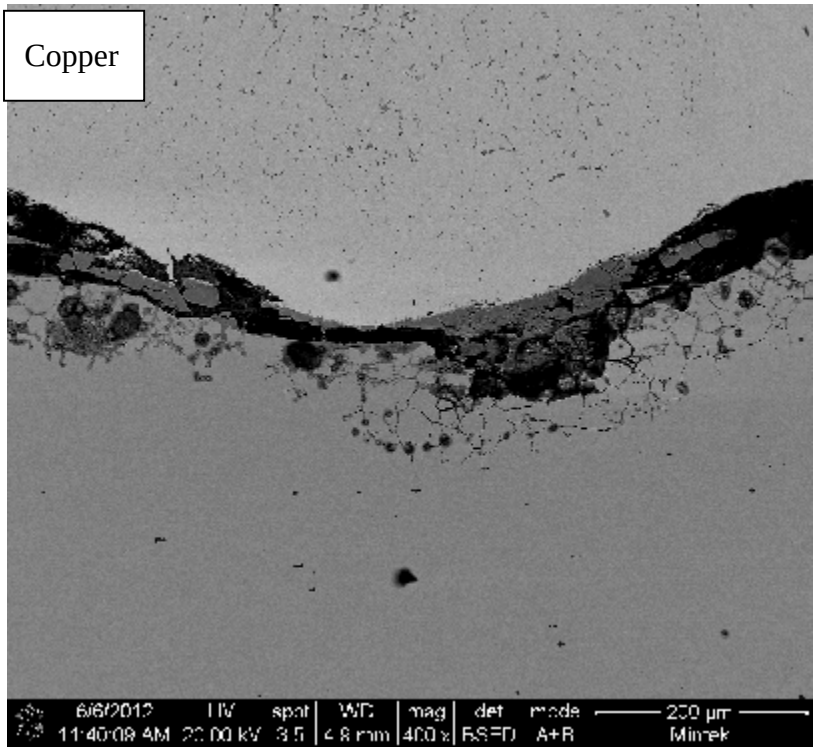


Figure 4.275. SEM-BSE image of attack in Sample 316Ti-8.

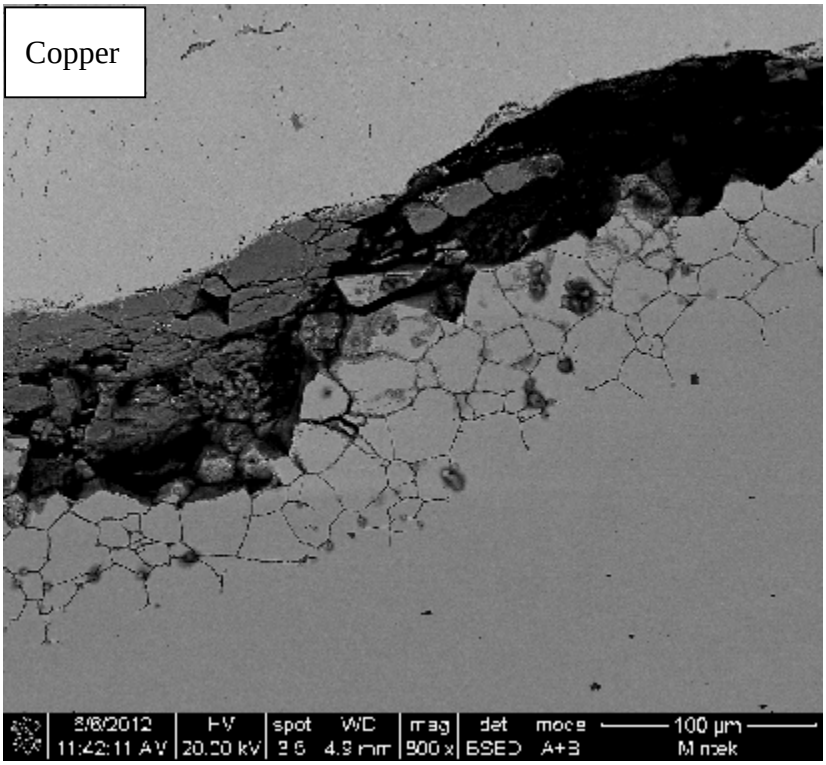


Figure 4.276. Higher magnification SEM-BSE image of attack in Sample 316Ti-8.

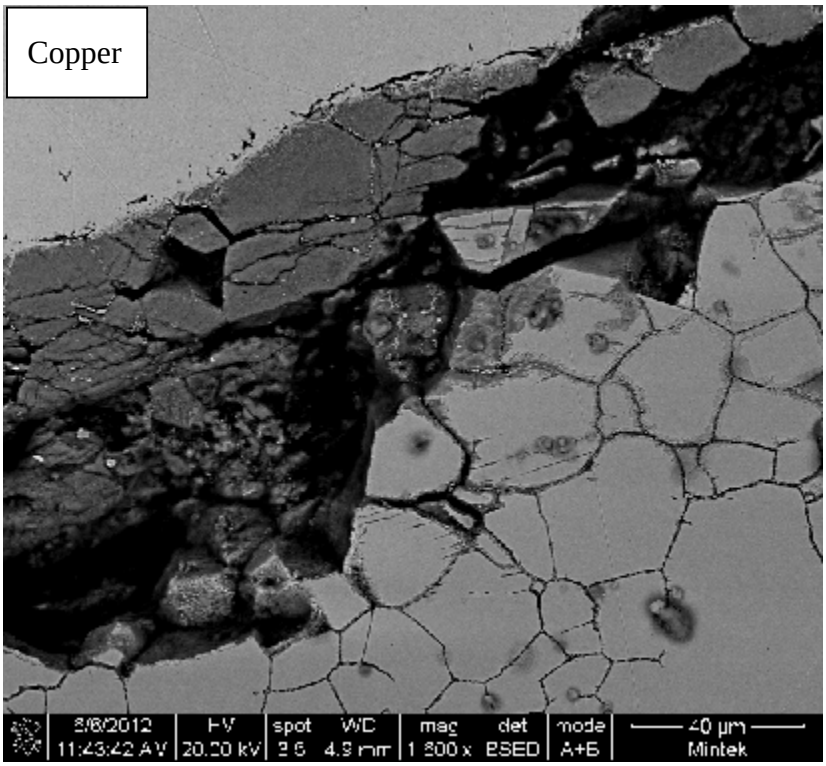


Figure 4.277. Higher magnification SEM-BSE image of grain boundary precipitation and associated attack in Sample 316Ti-8.

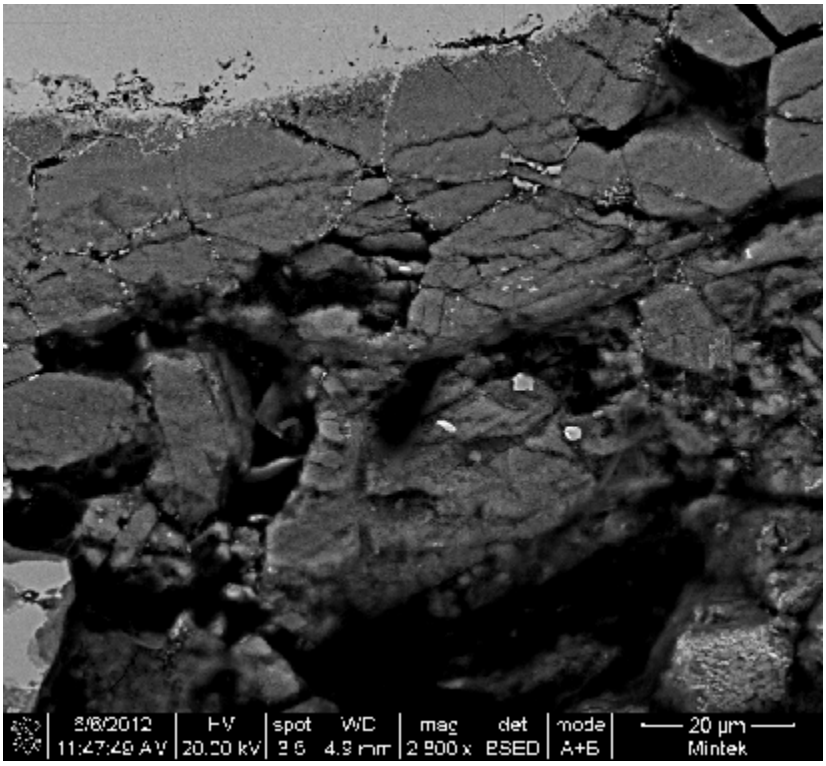


Figure 4.278. Higher magnification SEM-BSE image of products on the surface of Sample 316Ti-8.

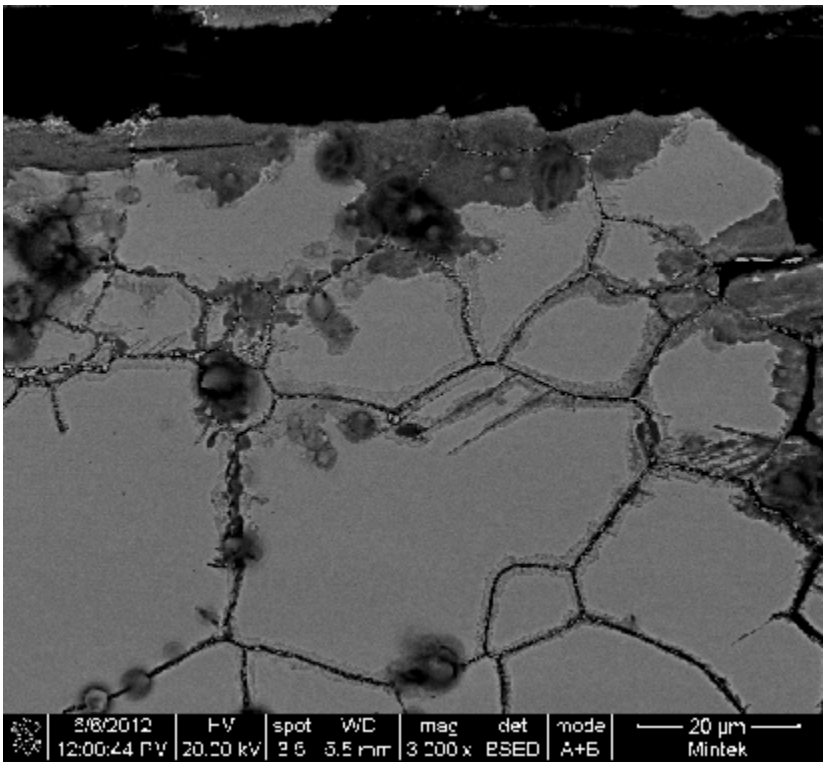


Figure 4.279. SEM-BSE image of grain boundary attack in Sample 316Ti-8.

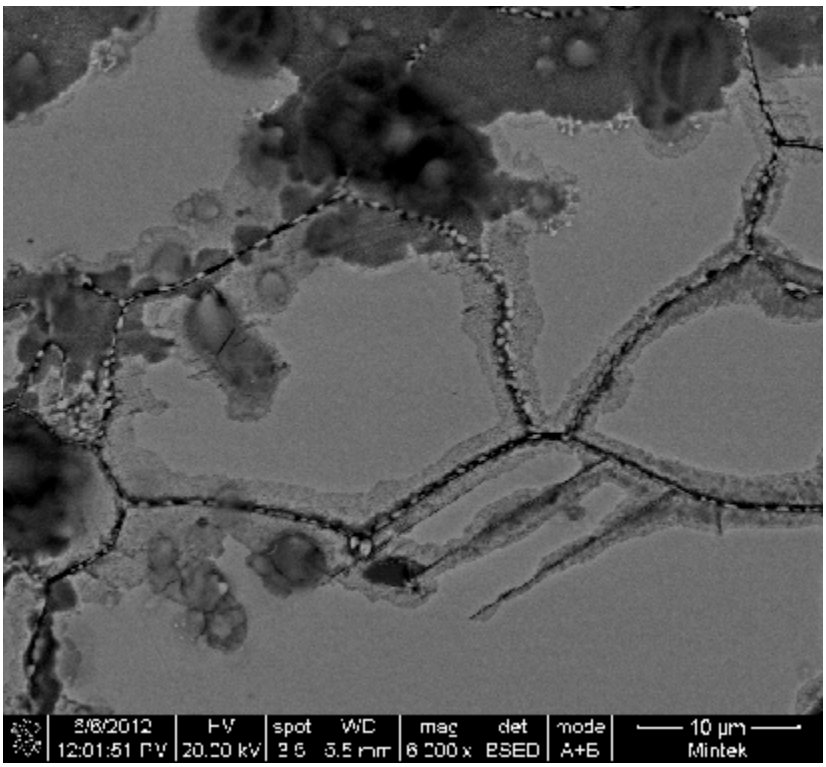


Figure 4.280. Higher magnification SEM-BSE image of attack in Sample 316Ti-8 as shown in Figure 4.279.

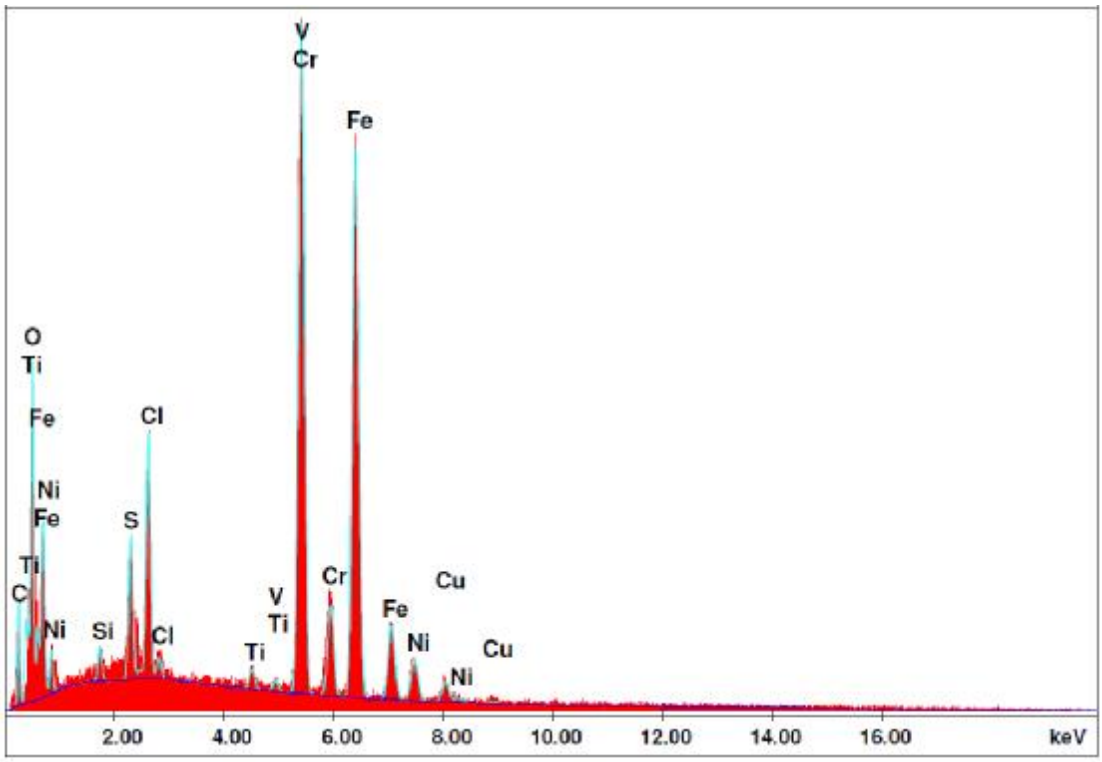


Figure 4.281. EDX spectrum of the outside oxide on Sample 316Ti-8 as shown in Figure 4.278.

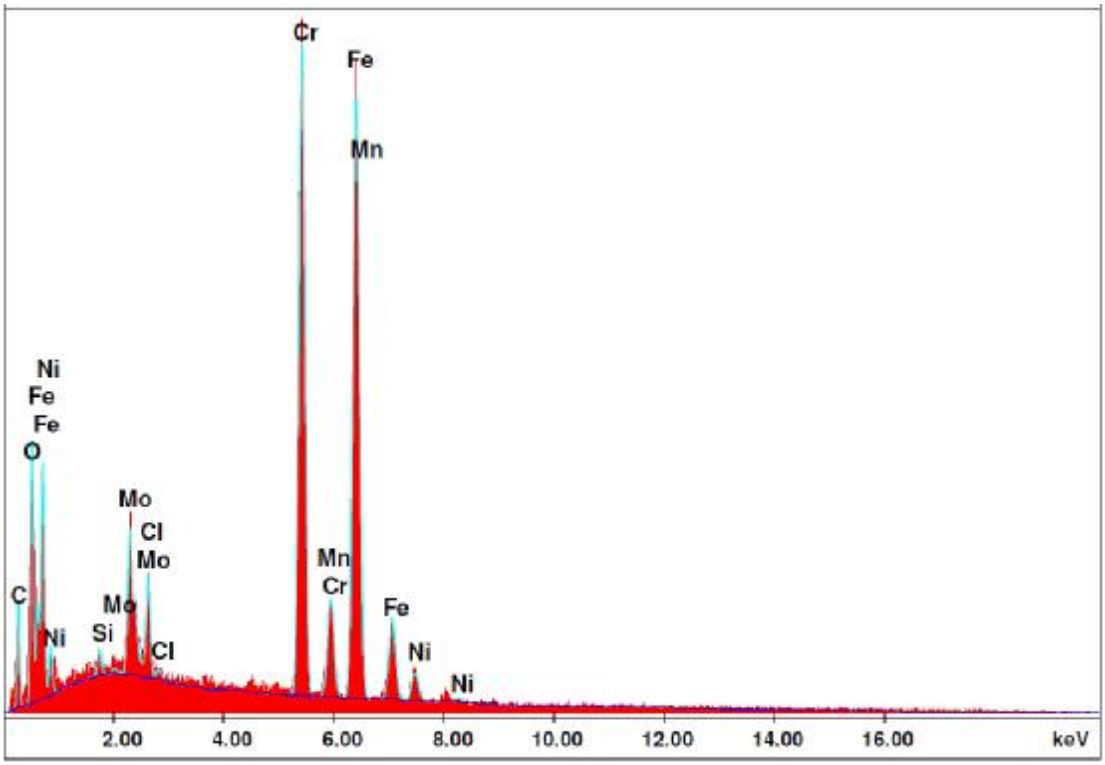


Figure 4.282. EDX spectrum of the white phase in the outside oxide layers in Sample 316Ti-8 as shown in Figure 4.278.

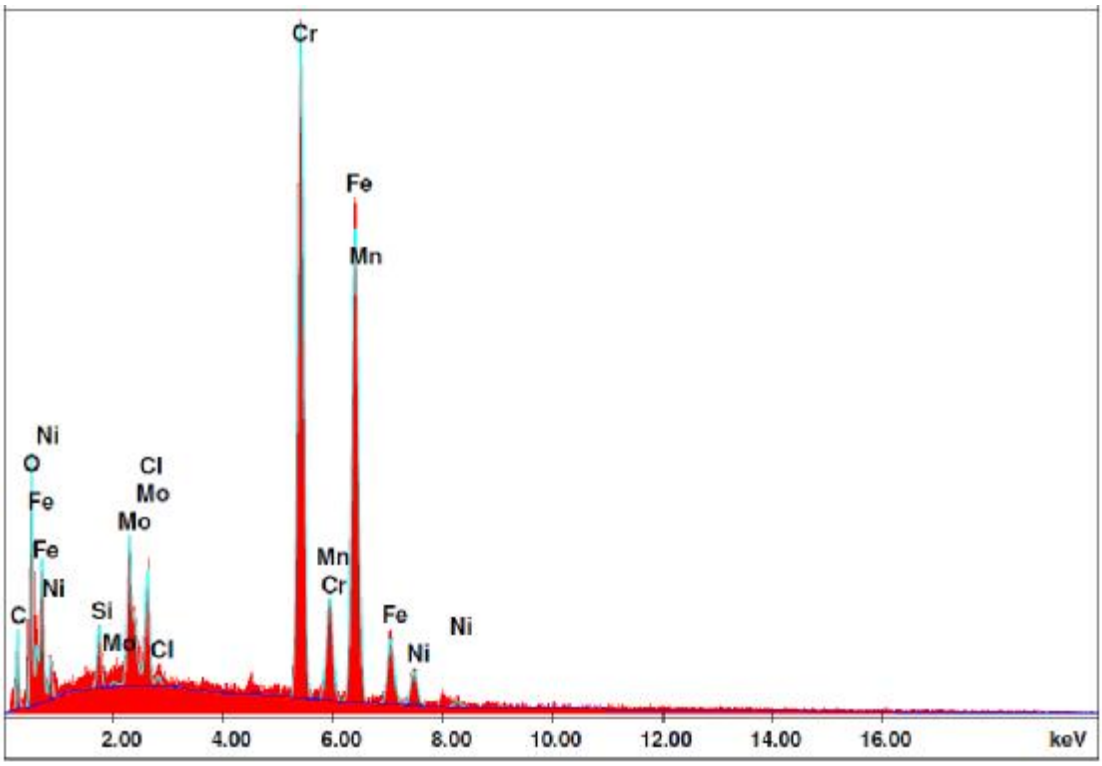


Figure 4.283. EDX spectrum of the white phase on the grain boundaries in Sample 316Ti-8 as shown in Figure 4.280.

Figure 4.284 is an SEM image of a cross-section through a localised break in the oxide layer, in a Type 430 sample that was exposed for 30 days. There had not been a significant amount of metal loss in this region, but a clear zone of hemispherical carburisation is shown, showing the extent of carbon ingress, as well as some products on the surface. Figure 4.285 to Figure 4.288 are images showing the corrosive attack, and the structure of the material below the surface. The carbides in this area appeared smaller than at the interface between the carburised zone and the substrate material. Figure 4.289 is a SEM image of the carbides near the interface with the substrate. The Widmanstätten morphology of the carbides is shown, similar to Figure 4.193, whereas the larger facetted carbides were probably those that were present after rolling (although they might have grown). The carbides were both on the grain boundaries, as well as inside the grains. Figure 4.290 is a SEM image of the general carbide distribution in the substrate material in lines.

EDX analysis of the substrate material in the carburised zone detected predominantly iron, with <5% chromium present, as shown in Figure 4.291. The original chromium content was

about 17%, indicating that a significant amount of chromium had been lost. Figure 4.292 is an EDX spectrum of the light phase on the surface, indicating that this is a chromium-rich phase. Figure 4.293 is an EDX spectrum of the oxide close to the surface, consisting predominantly of iron, and Figure 4.294 is an EDX spectrum of the corrosion product on the outer layer, being rich in chromium. All of these EDX analyses were taken on very small areas, and so might not be accurate, but they were used in comparison.

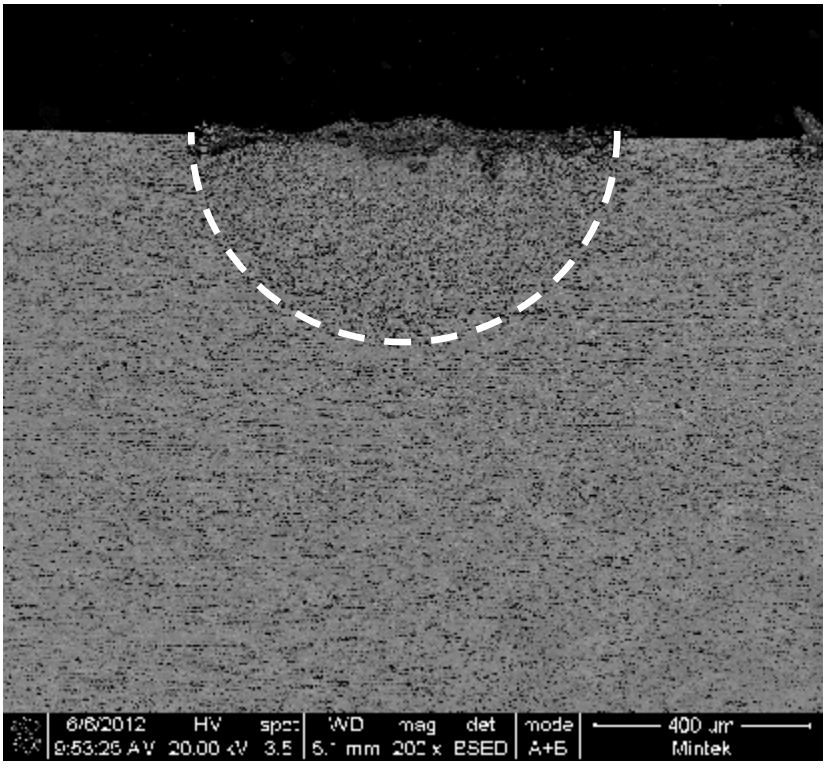


Figure 4.284. SEM-BSE image of carburisation at local breakdown of the protective oxide layer in Sample 430-7, and the onset of metal wastage by metal dusting.

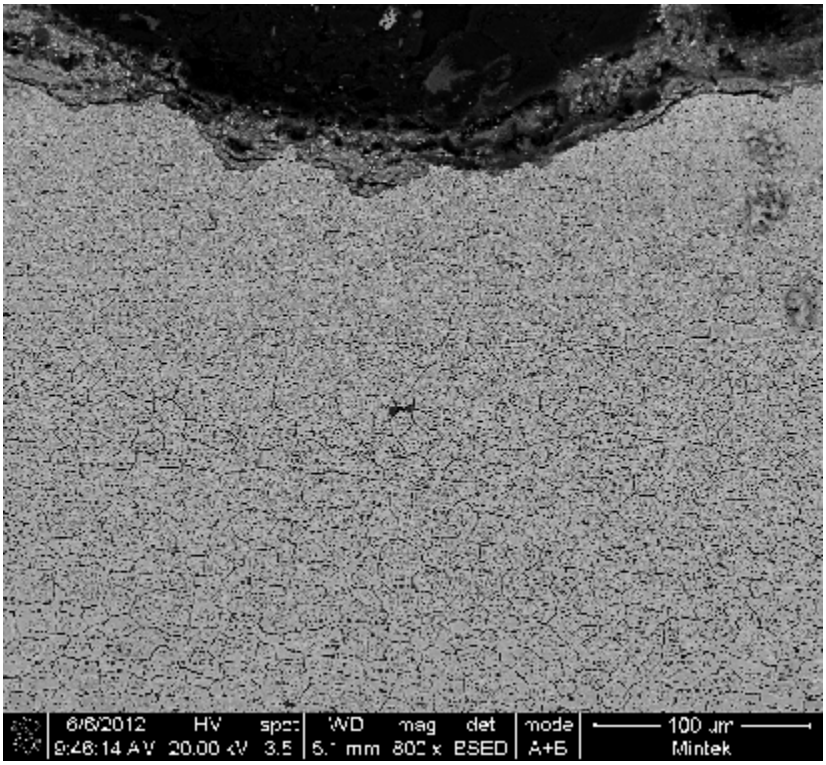


Figure 4.285. Higher magnification SEM-BSE image of pitting and carburisation in Sample 430-7.

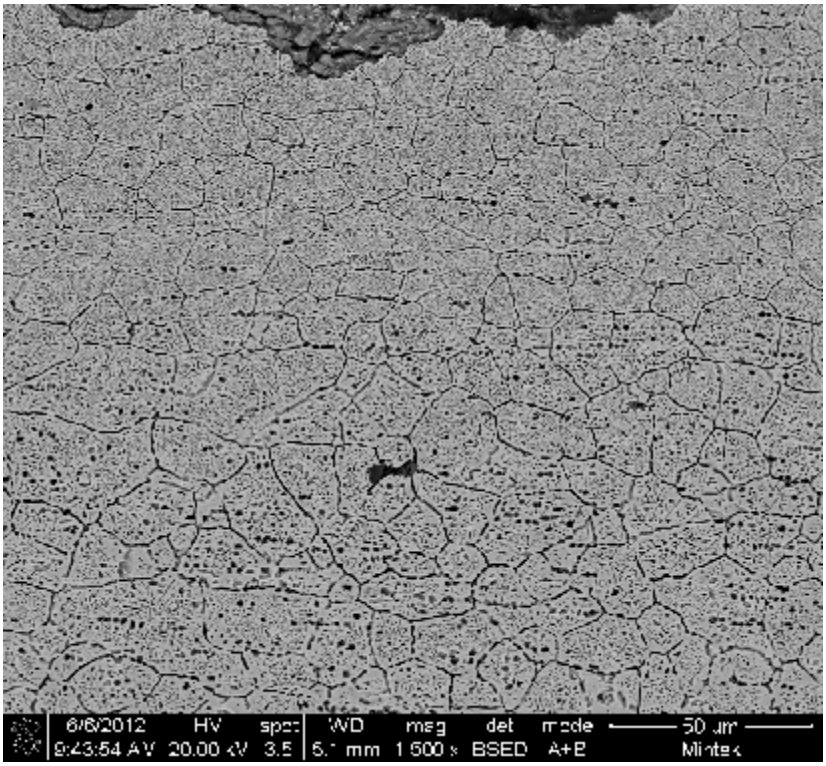


Figure 4.286. Higher magnification SEM-BSE image of carburisation at the pitting of Sample 430-7 shown in Figure 4.285.

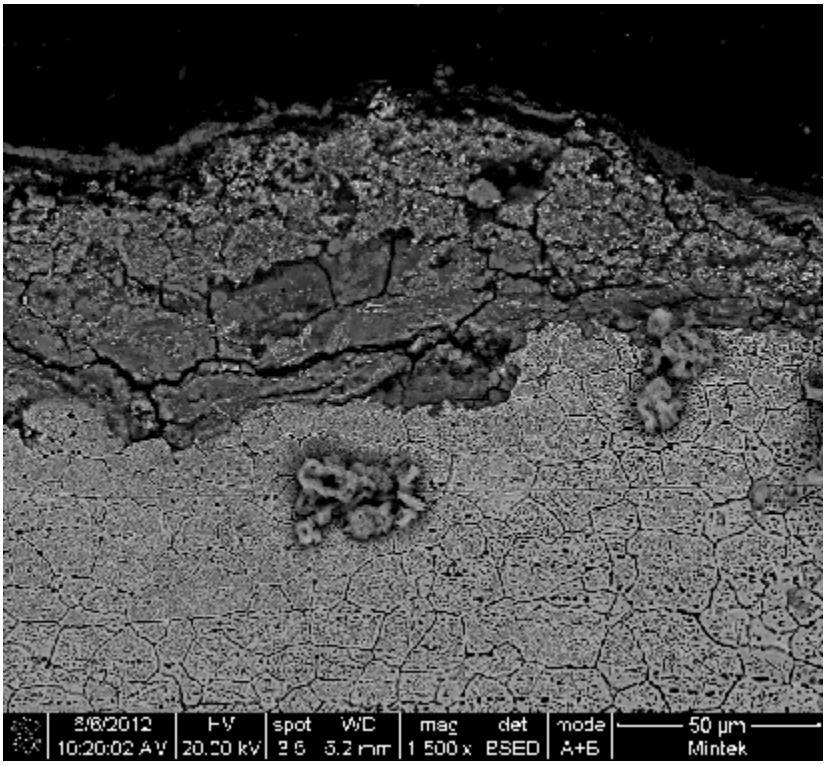


Figure 4.287. SEM-BSE image of the oxide associated with the pit on Sample 430-7.

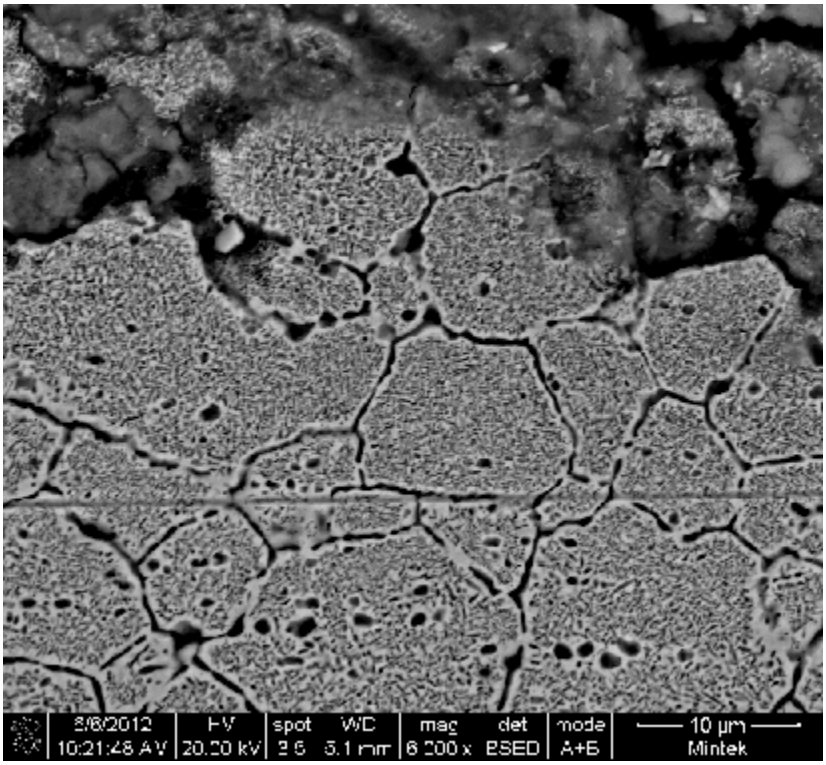


Figure 4.288. High magnification SEM-BSE image of carburisation below the pit in Sample 430-7.

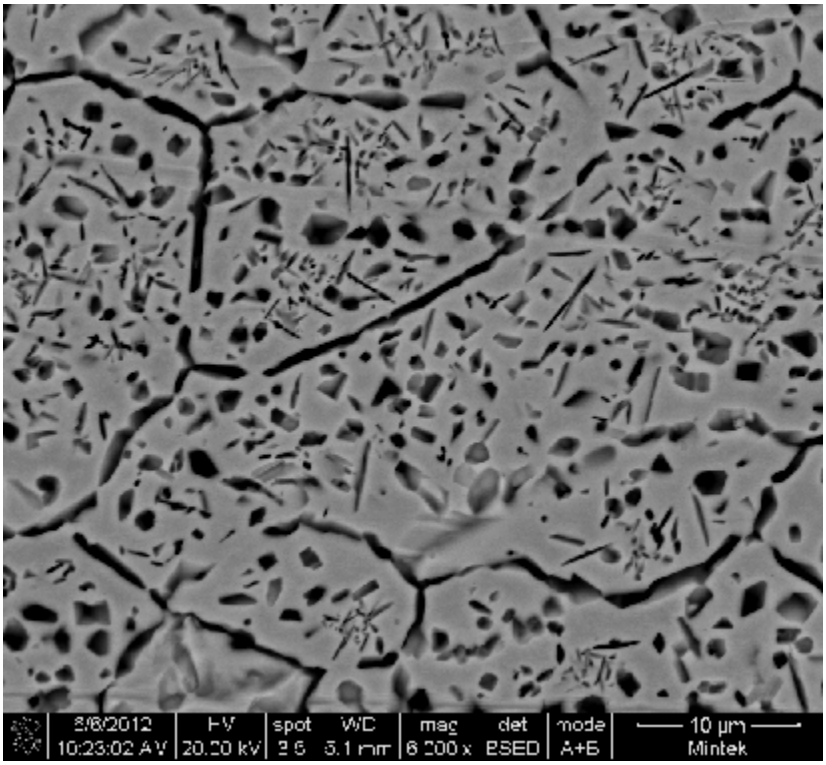


Figure 4.289. SEM-BSE image in carburised zone in Sample 430-7 showing the carbide morphology.

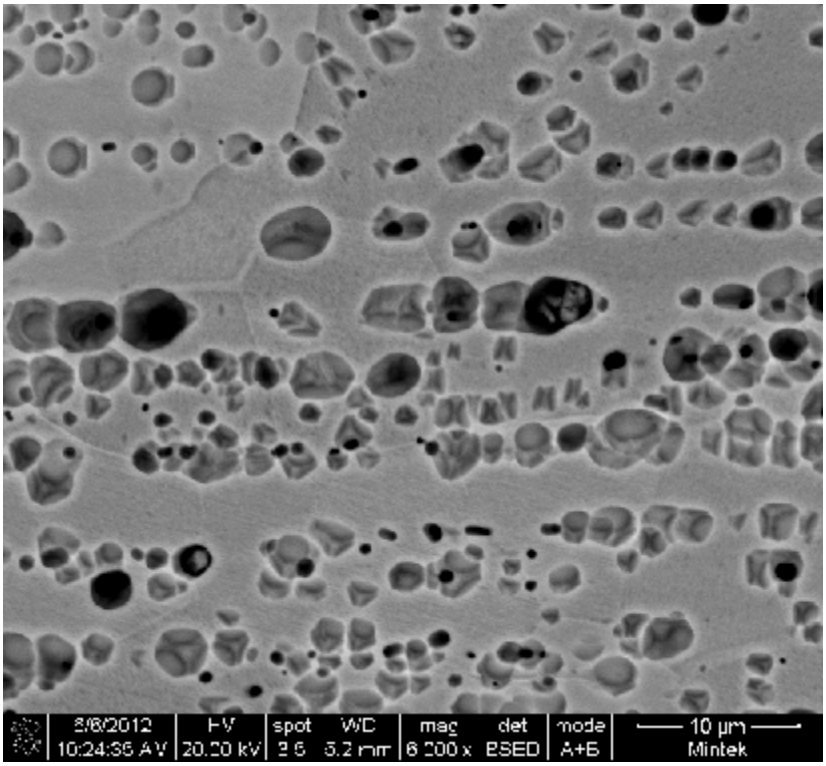


Figure 4.290. SEM-BSE image of carbides in the matrix of Sample 430-7.

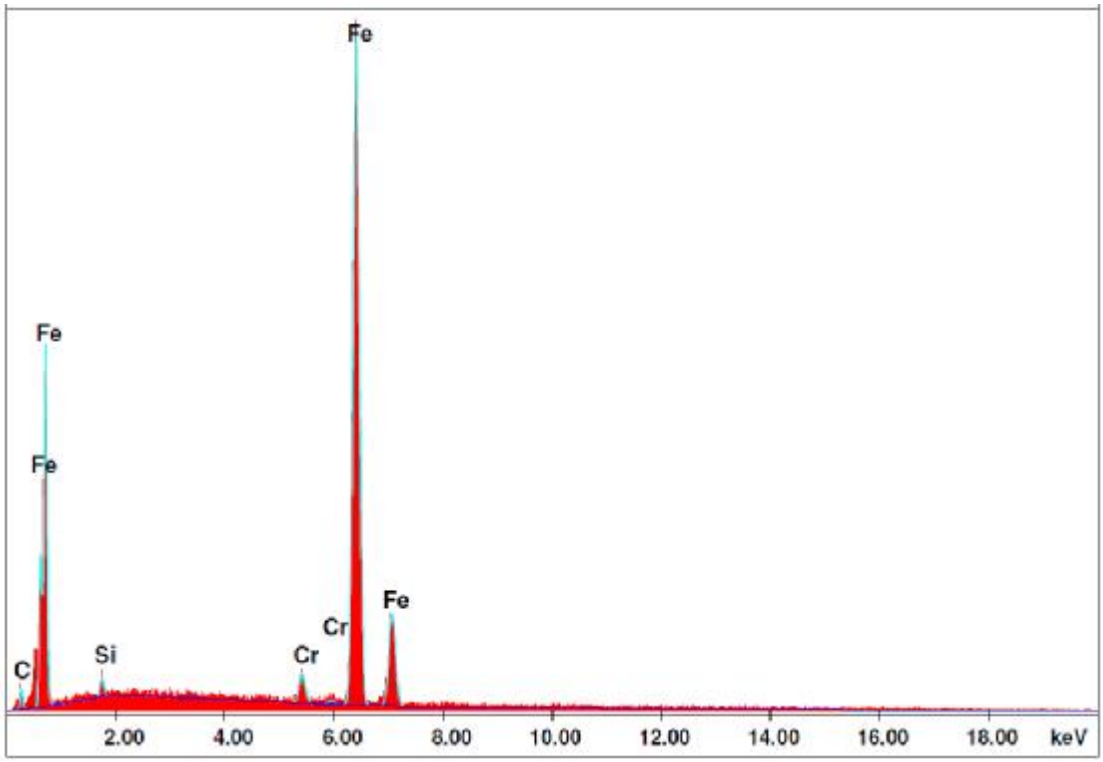


Figure 4.291. EDX spectrum in the carburised zone, close to the surface in Sample 430-7.

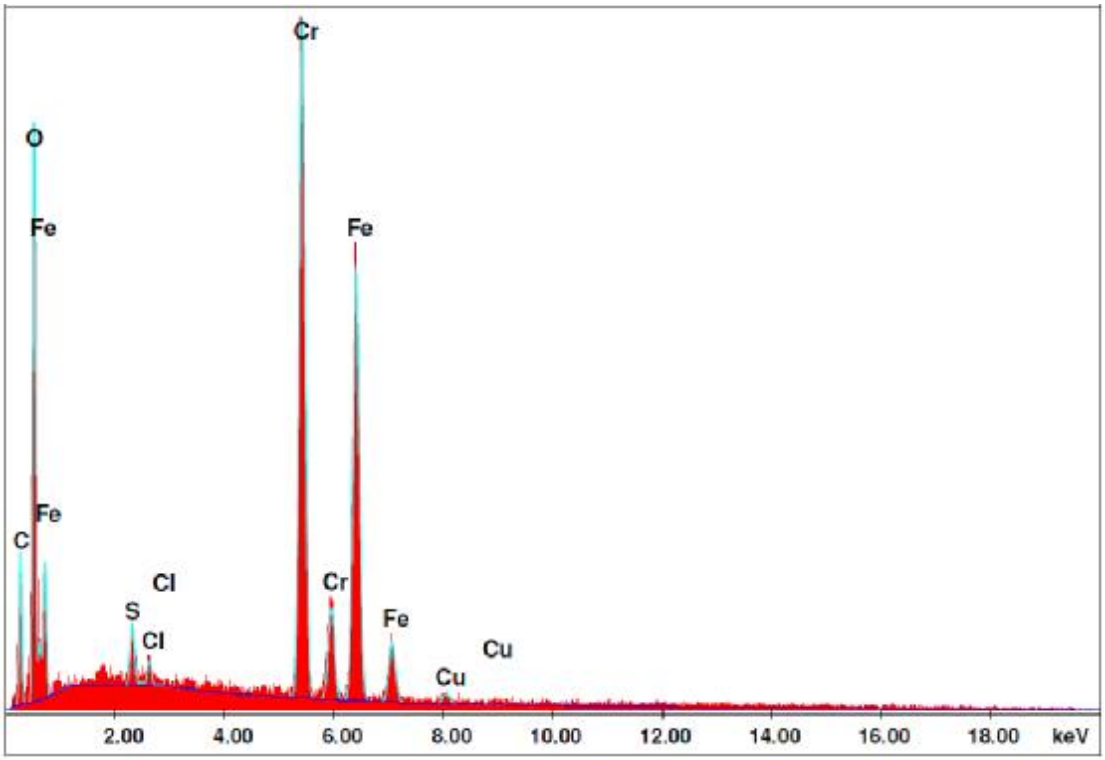


Figure 4.292. EDX spectrum of white phase in oxide layer in Sample 430-7 as shown in Figure 4.287.

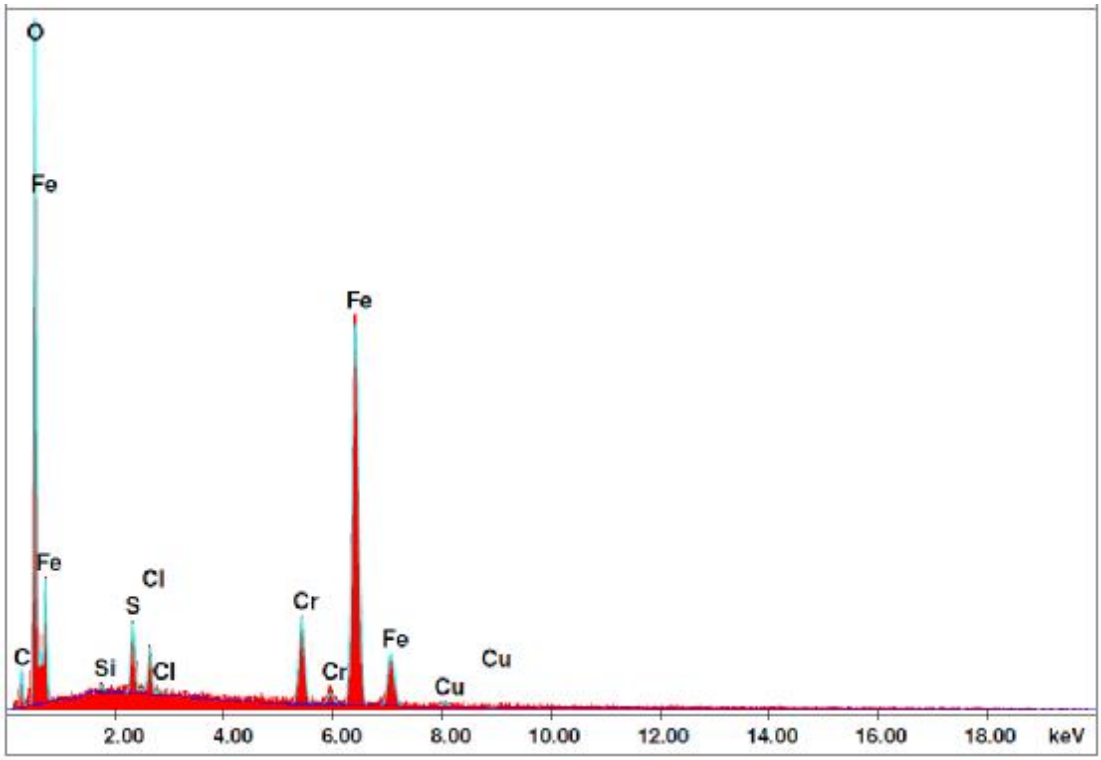


Figure 4.293. EDX spectrum of the oxide layer close to the metal surface in Sample 430-7 as shown in Figure 4.287.

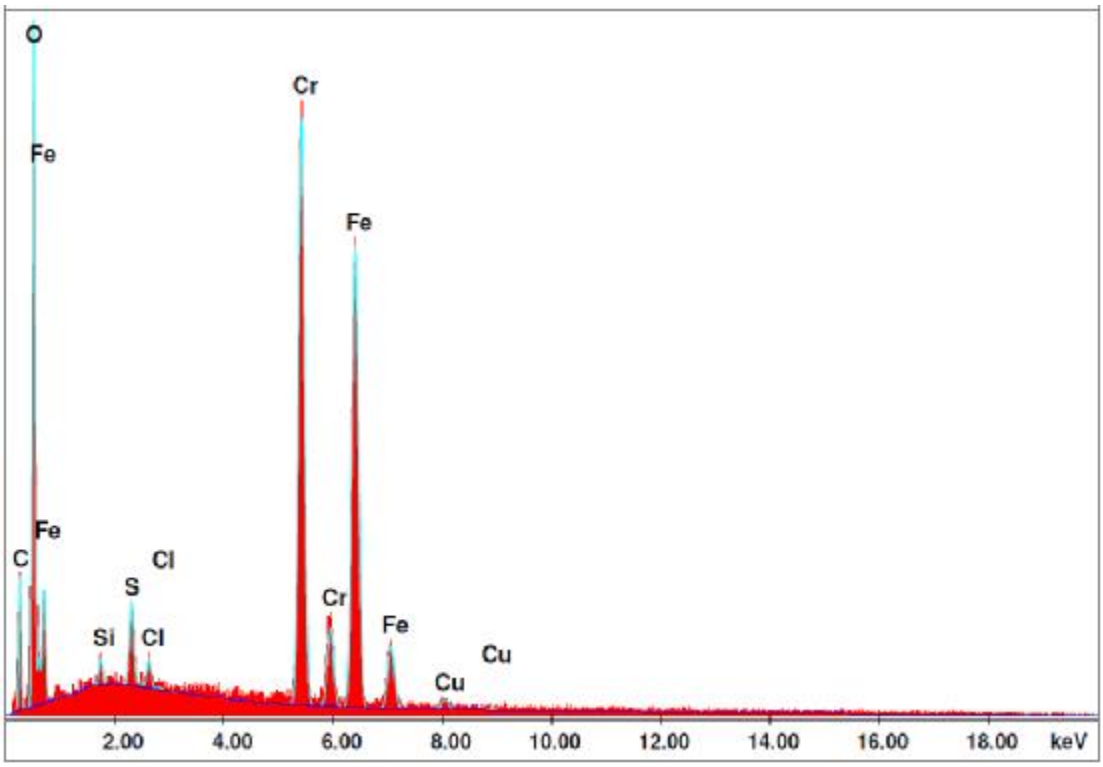


Figure 4.294. EDX spectrum of the outside oxide layer in Sample 430-7 as shown in Figure 4.287.

Figure 4.295 is an SEM image of the same area shown in Figure 4.284 to Figure 4.289, indicating the path of an EDX line scan that was performed from the oxide layer on the surface, through the carburised zone, to the substrate material. The scan is shown in Figure 4.296. The initial part of the line scan shows an iron, chromium oxide, followed by an iron oxide, with less chromium. The substrate material, just below the oxide, contained only about 5% chromium. This level of chromium was maintained for about 150 µm. The chromium depleted zone was about 350 µm deep. This is the depth from where chromium diffused to the surface to repair the break in the passive oxide layer.

Figure 4.297 is an SEM image of an area on the Type 430 sample that showed uniform corrosion, but where the passive chromium oxide layer was still intact. Figure 4.298 is a higher magnification image of the oxide layer, showing that it was significantly thickened in this area, but had not failed completely yet. Apart from the continuous oxide layer, there were also spheres on the surface, which were like the light particles on the surface, shown in Figure 4.233. Figure 4.299 is an EDX spectrum of the oxide layer, showing that it was significantly enriched with chromium. Figure 4.300 is an EDX spectrum of the dark product on the outside of the scale, indicating that it was coke (carbon), and Figure 4.301 is a spectrum of the substrate material just below the surface, where the chromium content was slightly lower, compared to the bulk content (15% chromium compared to the original content of 17%).

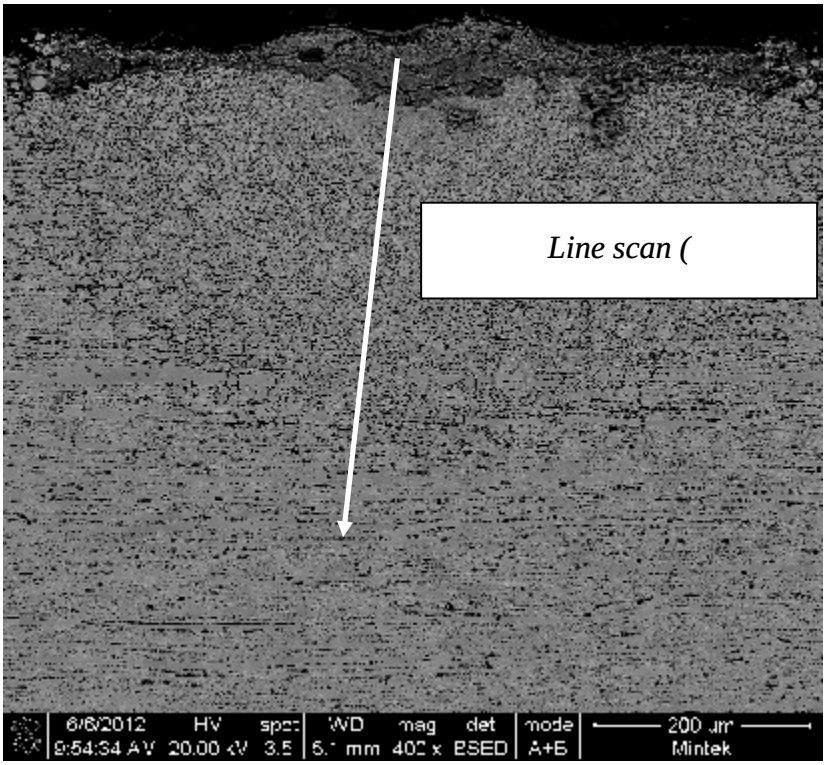


Figure 4.295. SEM-BSE image of localised carburisation and associated initiation of a pit in Sample 430-7, showing the position of the line scan performed.

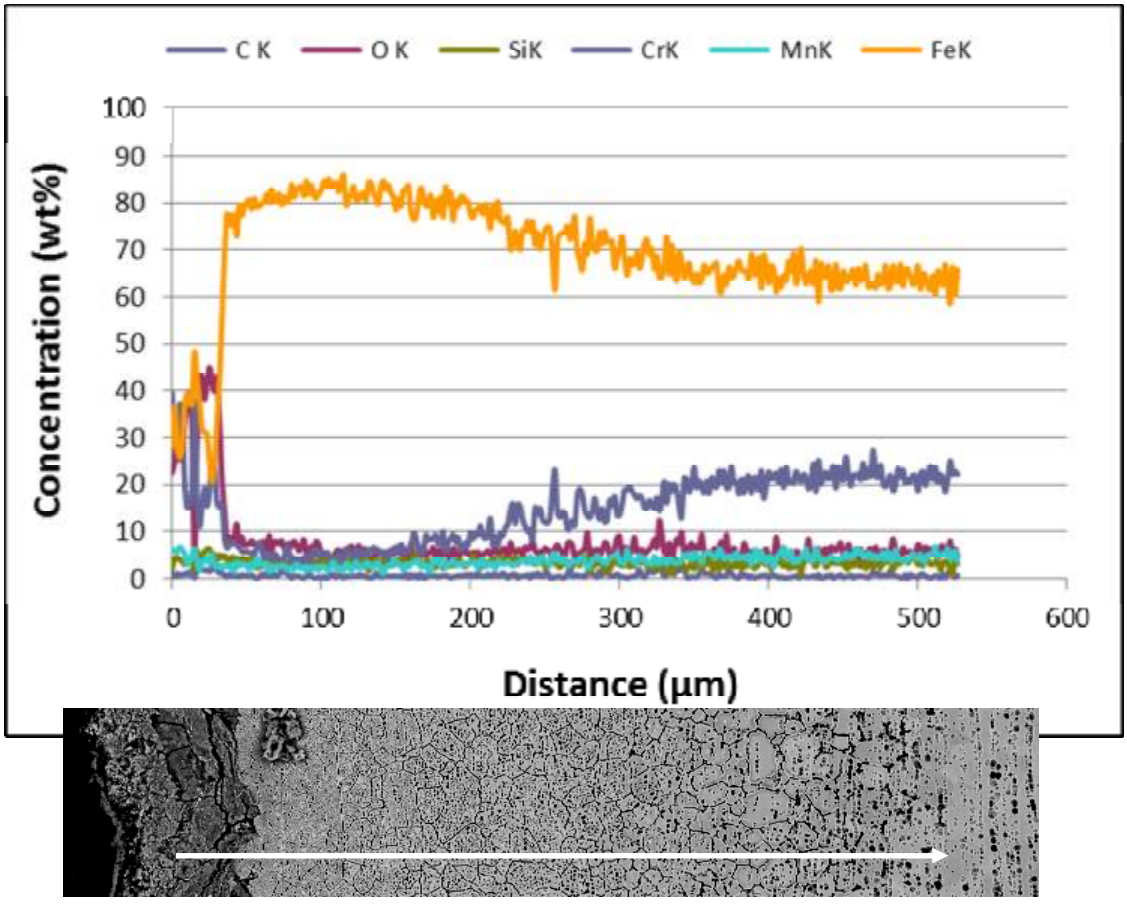


Figure 4.296. EDX line scan in Sample 430-7 as shown in Figure 4.295.

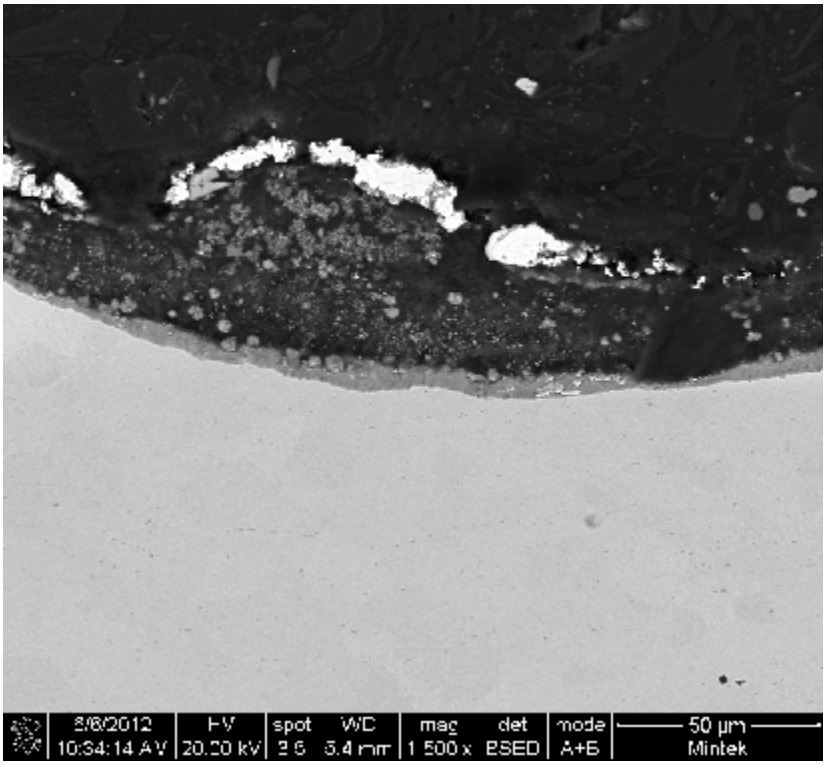


Figure 4.297. SEM-BSE image of general (uniform) attack in Sample 430-8.

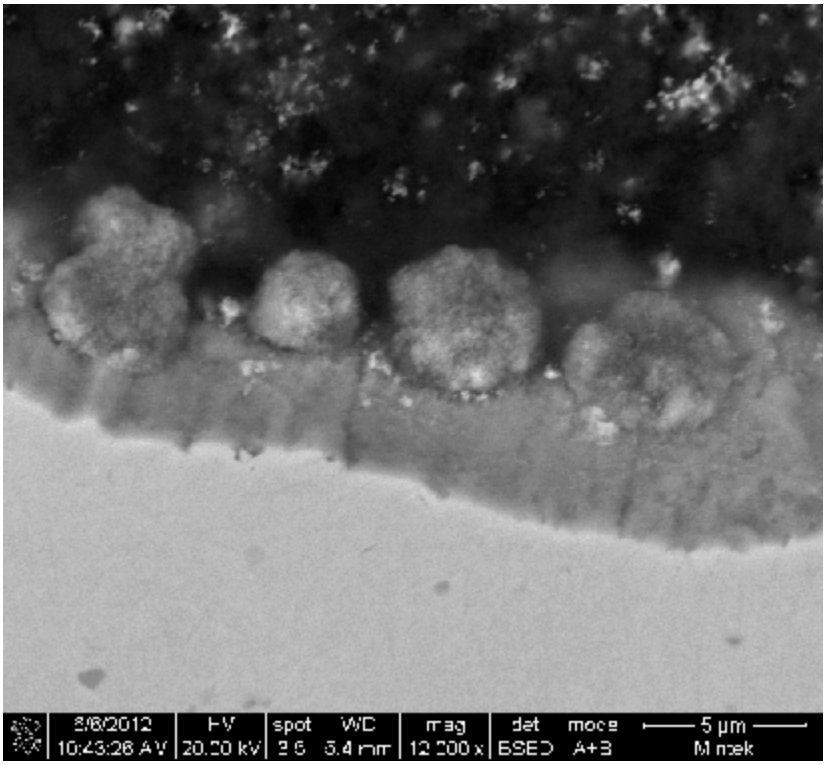


Figure 4.298. High magnification SEM-BSE image of the oxide layer in Sample 430-8 shown in Figure 4.297.

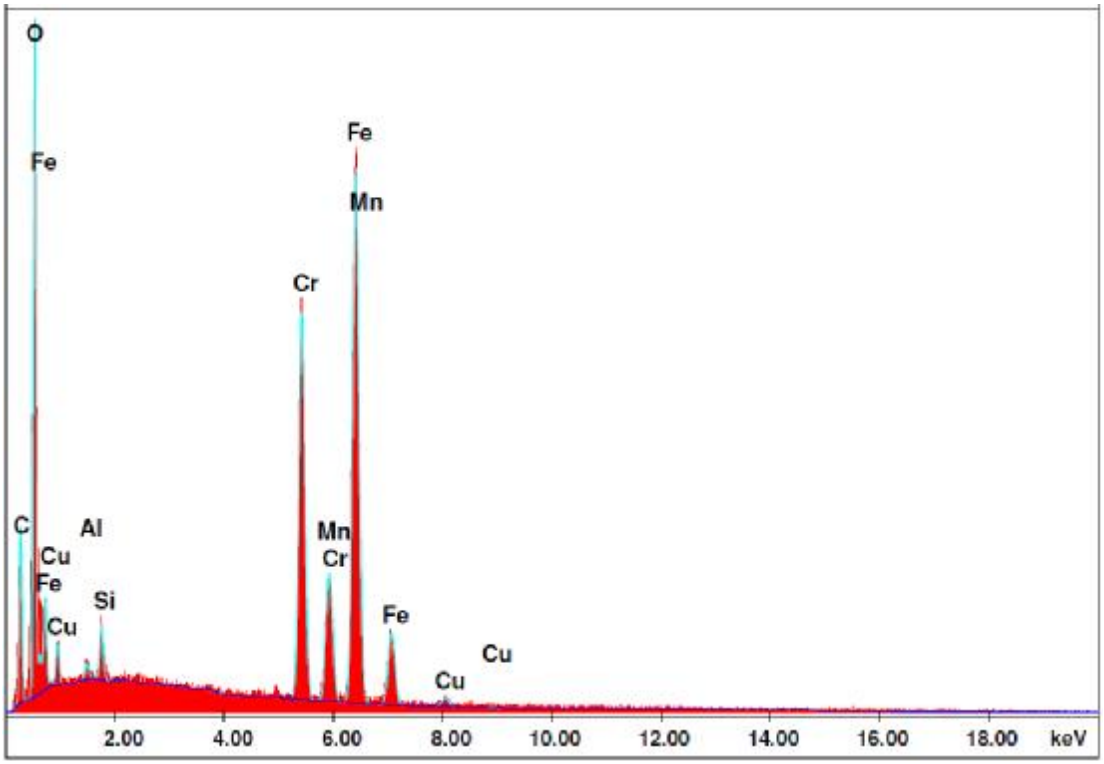


Figure 4.299. EDX spectrum of the oxide layer on Sample 430-8 as shown in Figure 4.298.

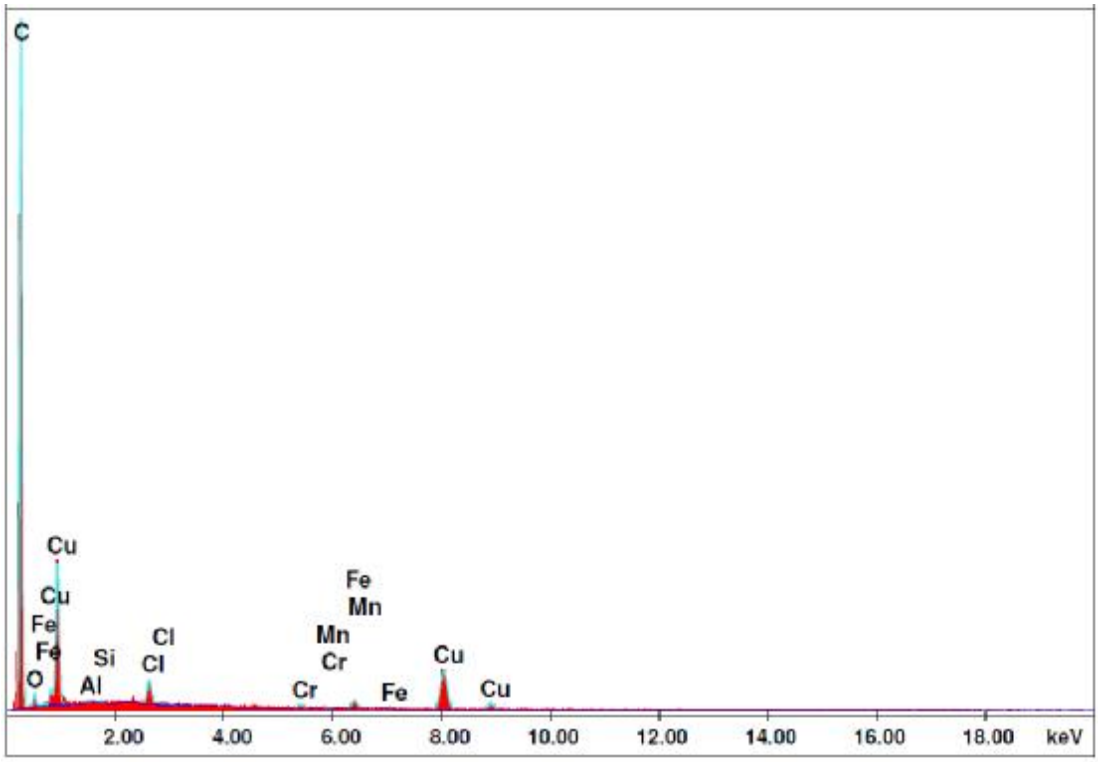


Figure 4.300. EDX spectrum of the coke above the oxide layer in Sample 430-8 as shown in Figure 4.297.

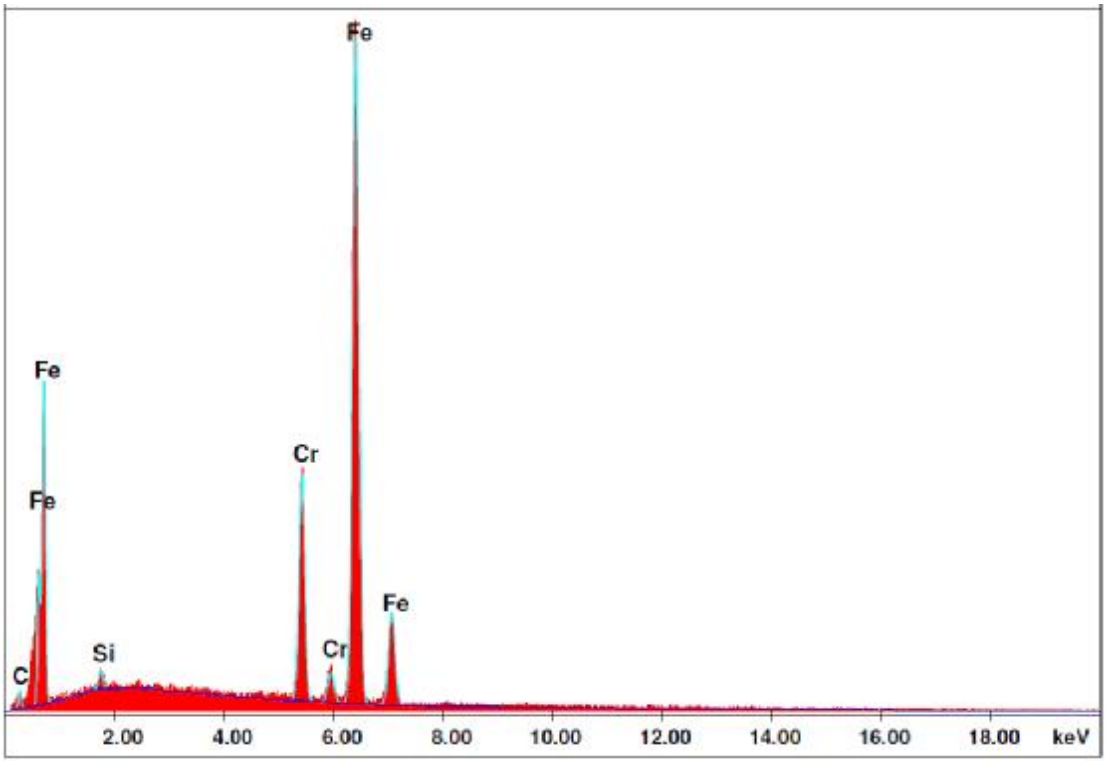


Figure 4.301. EDX spectrum of the metal below oxide layer of Sample 430-8 containing about 15% chromium.

Figure 4.302 is an SEM image of the general microstructure of the Type 441 sample that was exposed for 30 days. The microstructure consisted of titanium carbo-nitrides in a matrix of equiaxed ferrite. Figure 4.303 is a higher magnification image of a titanium carbo-nitride precipitate. The light phase associated with the precipitate, and in the matrix, was rich in niobium. The dark product surrounding the precipitate consisted of carbon, indicating preferential coke formation at the interface. Figure 4.304 is an SEM image of an area where the oxide layer failed, with subsequent internal carburisation, with a line scan performed from the oxide layer on the surface to the substrate material. The resultant EDX spectrum is shown in Figure 4.305. The oxide consisted predominantly of iron and chromium, with a high carbon peak also identified near the metal interface (surface). Similar to the Type 430 sample, the chromium in the carburised zone was below 10% to a depth of about 215 µm, indicating the depth from where chromium diffused to the surface to repair the chromium oxide passive layer. This carburised zone also contained several iron oxide particles, as shown by the oxygen spikes (peaks) in the EDX line scan. The iron correspondingly decreased at these positions, but no other elements increased, indicating that iron oxidised. The distance between the peaks was roughly 25 µm, which correlates with the size of the grains in this region. This indicates that the iron on the grain boundaries could be

preferentially oxidised. There was a proceeding front of preferential grain boundary carburisation around the fully internal carburised zone. Similar grain boundary carburisation was not present on the Type 430 sample. The was an example of SiO_2 at ~390µm.

Figure 4.306 is an SEM image of the carburised metal below the oxide scale, Figure 4.307 is an image at the end of the internal carburisation, and Figure 4.308 is an image of the grain boundary carburisation. Areas where grains have been removed by the polishing action is shown in Figure 4.307.

Figure 4.309 is an EDX spectrum of the substrate material below the oxide layer, indicating that the chromium content was very low (<5%), Figure 4.310 and Figure 4.311 are EDX spectra of the chromium and silica rich oxide, and Figure 4.312 is a spectrum of iron oxide in the scale (deficient of chromium).

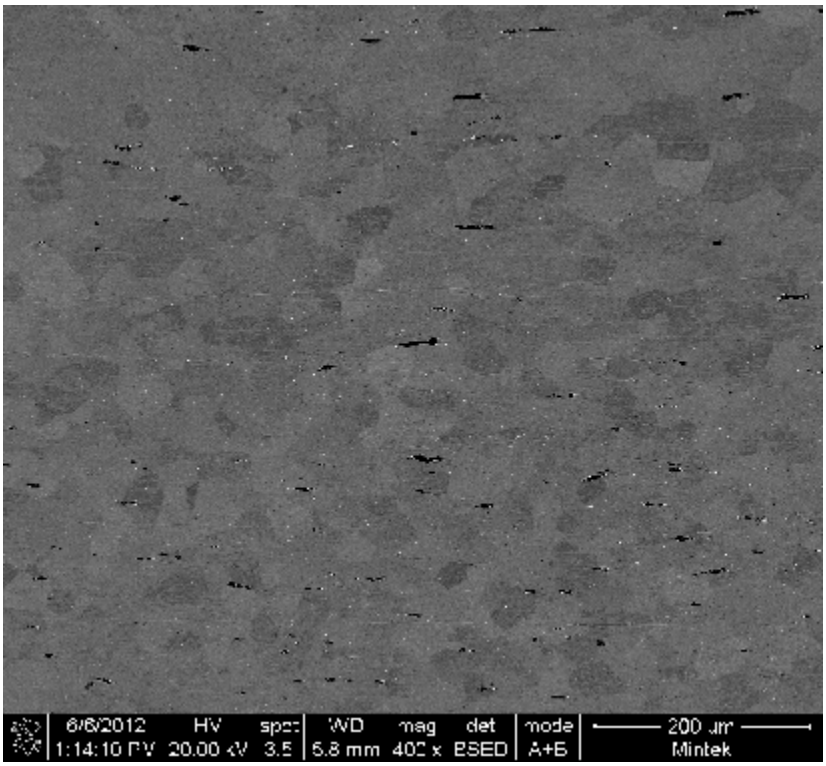


Figure 4.302. SEM-BSE image of the matrix of Sample 441-7.



Figure 4.303. Higher magnification SEM-BSE image of internal attack forming coke (black) associated with titanium carbo-nitride precipitates (dark) in Sample 441-7.

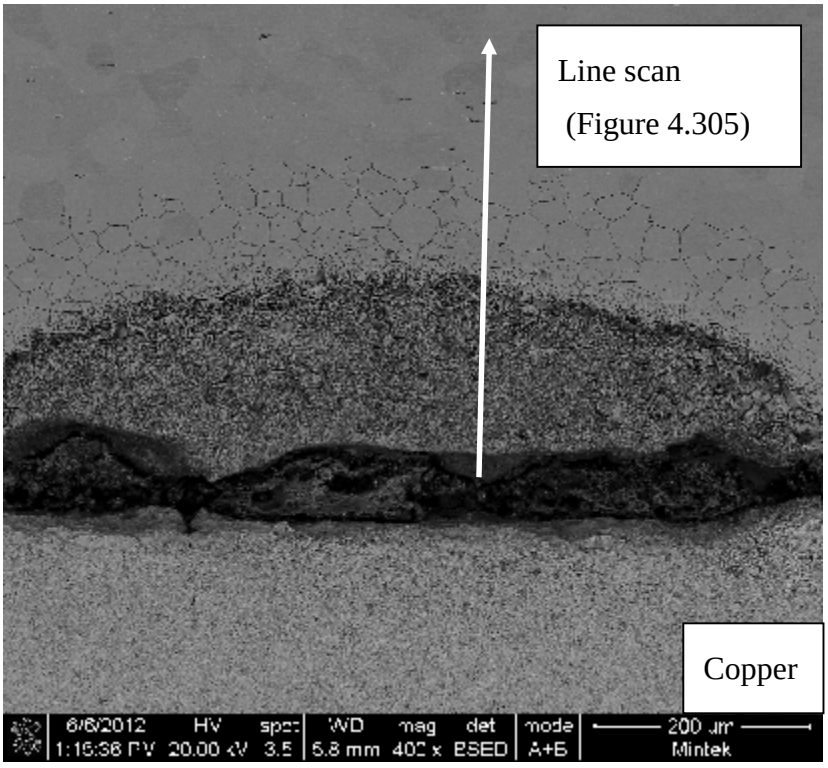


Figure 4.304. SEM-BSE image of localised carburisation in Sample 441-7.

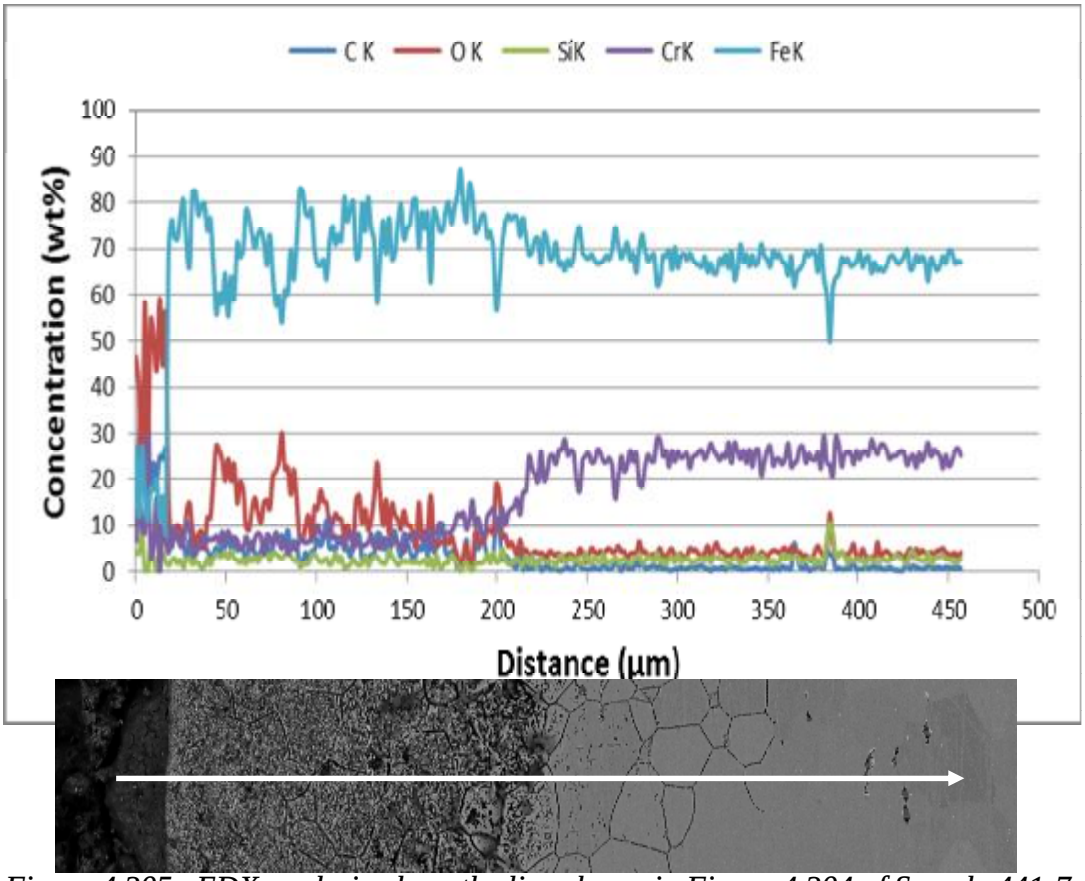


Figure 4.305. EDX analysis along the line shown in Figure 4.304 of Sample 441-7.

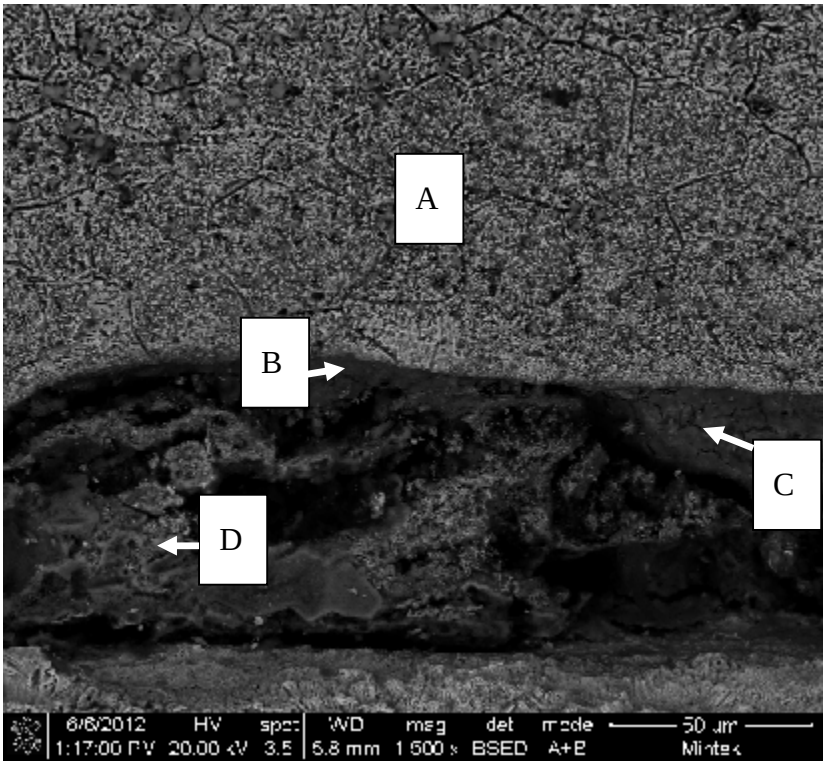


Figure 4.306. SEM-BSE image of oxide in a pit and associated carburisation in Sample 441-7, showing positions where EDX analyses were performed.

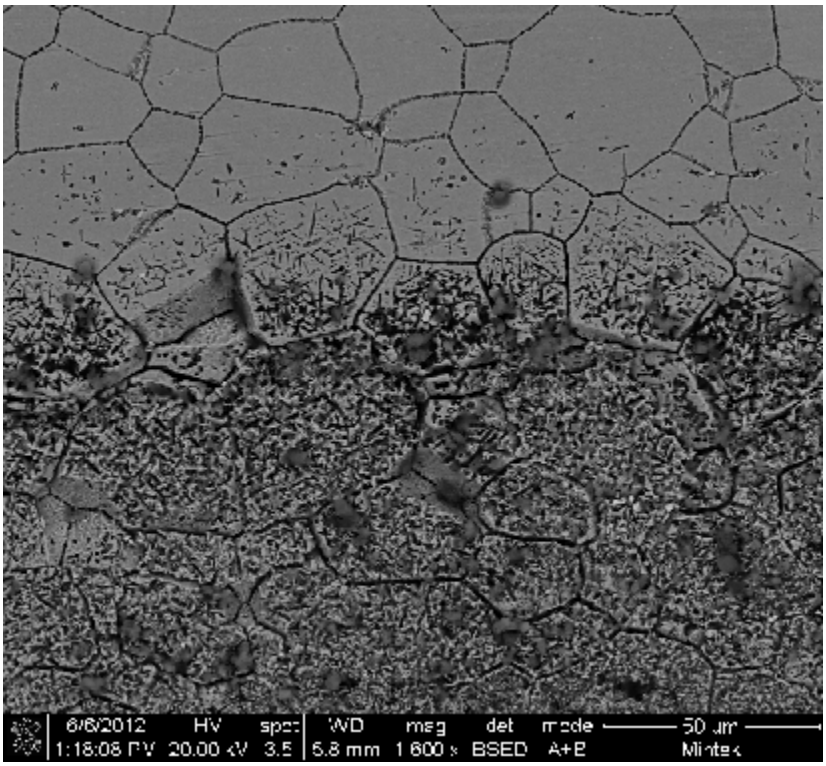


Figure 4.307. SEM-BSE image of the interface between the grain boundary and internal carburisation in Sample 441-7.

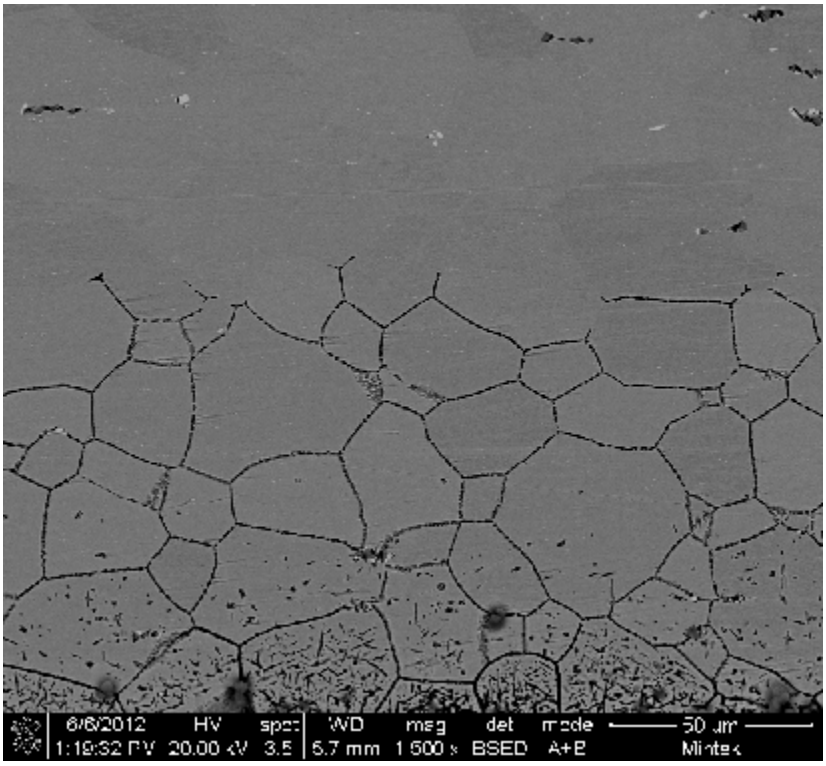


Figure 4.308. SEM-BSE image of interface between grain boundary carburisation and matrix structure in Sample 441-7.

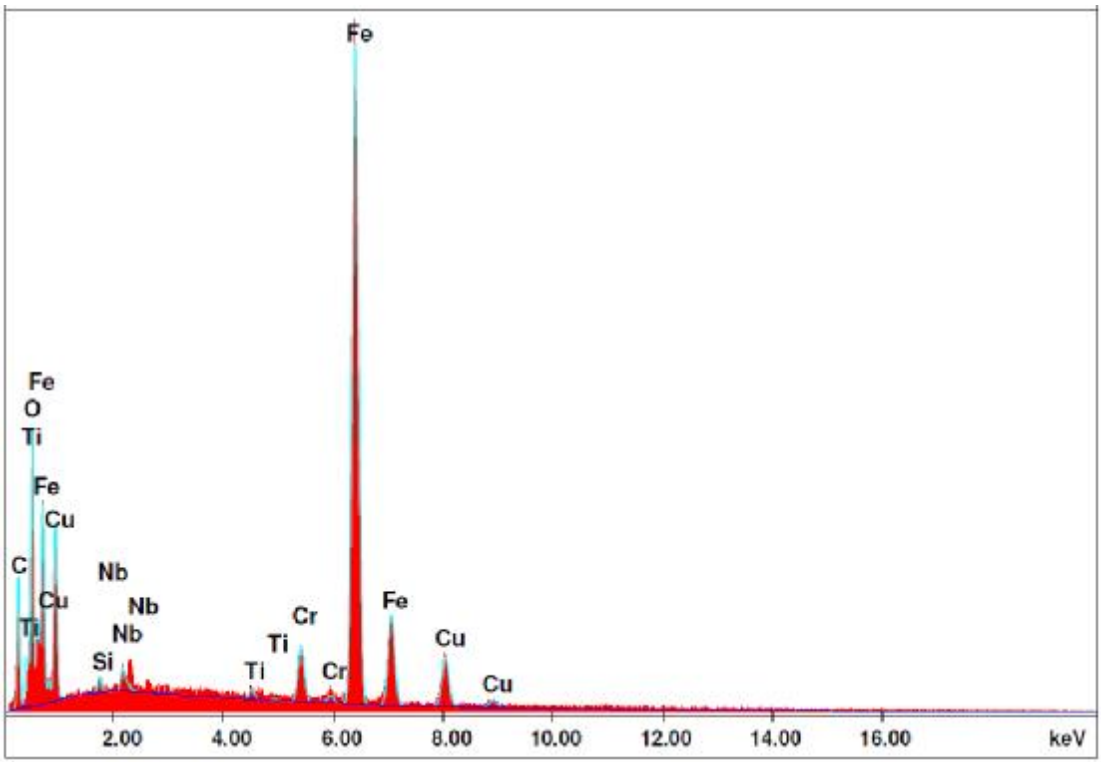


Figure 4.309. EDX analysis of the substrate underneath the oxide layer in Sample 441-7 shown in Figure 4.306 (Position A).

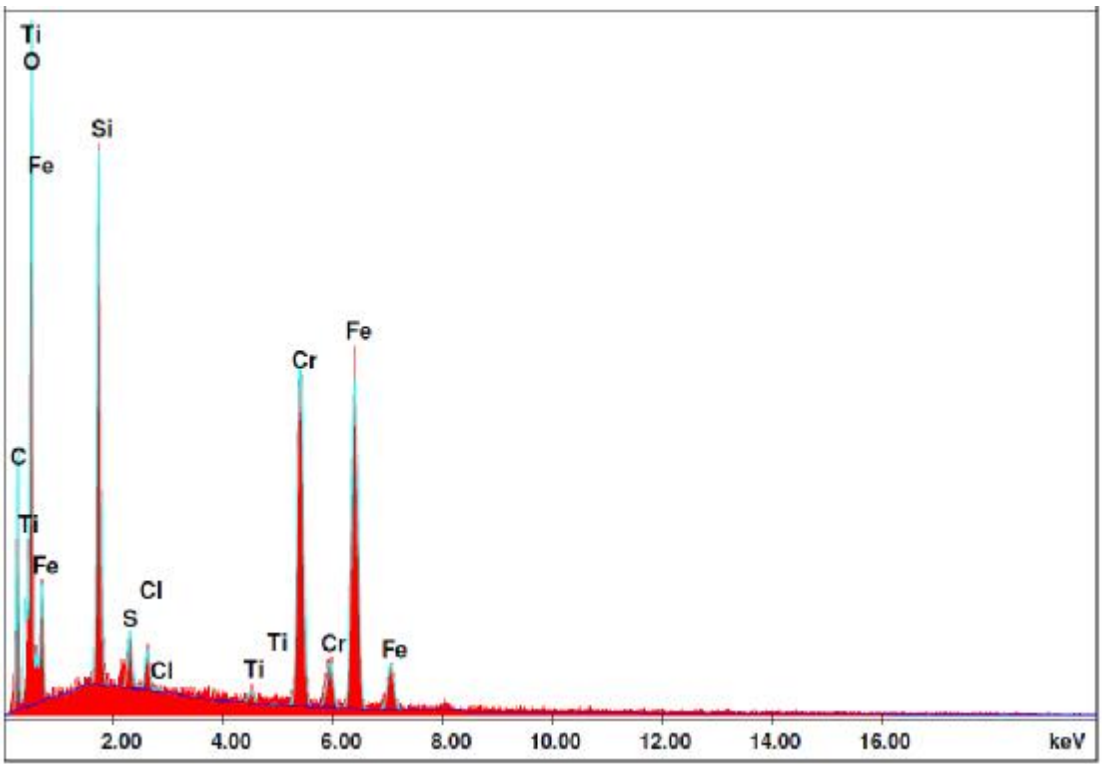


Figure 4.310. EDX analysis of a chromium- and silicon-rich phase in the oxide layer on Sample 441-7 shown in Figure 4.306 (Position B).

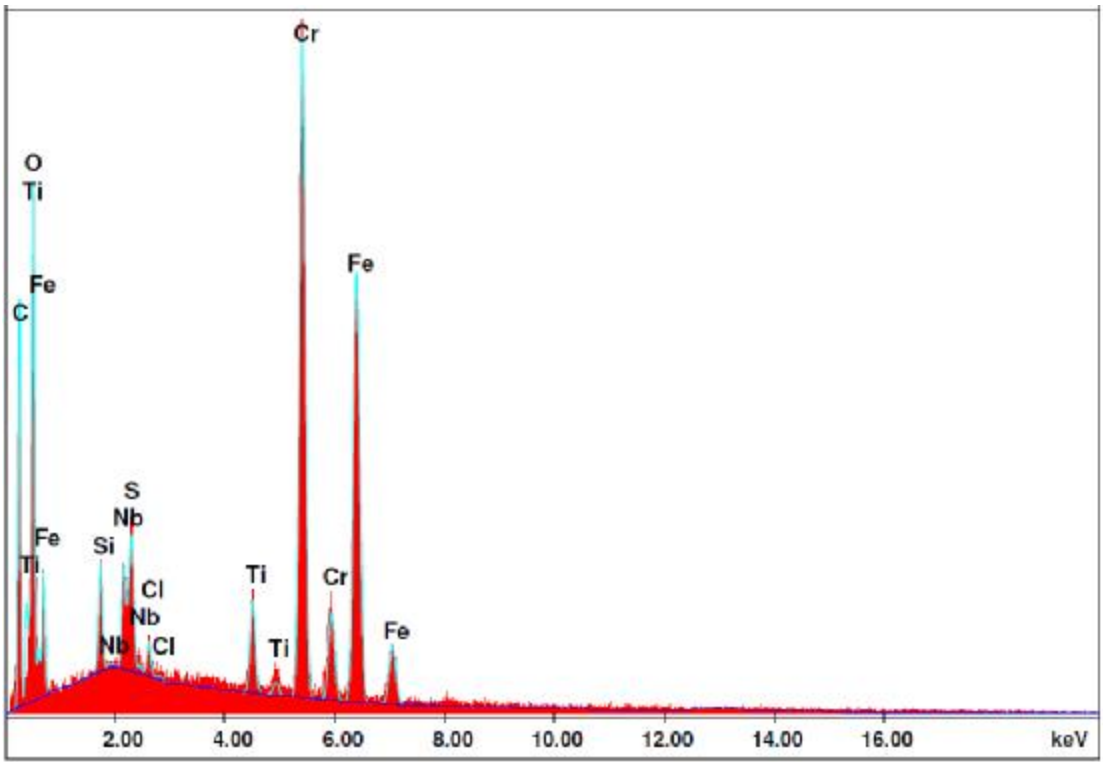


Figure 4.311. EDX analysis of the chromium-rich phase in the oxide layer in Sample 441-7 shown in Figure 4.306 (Position C).

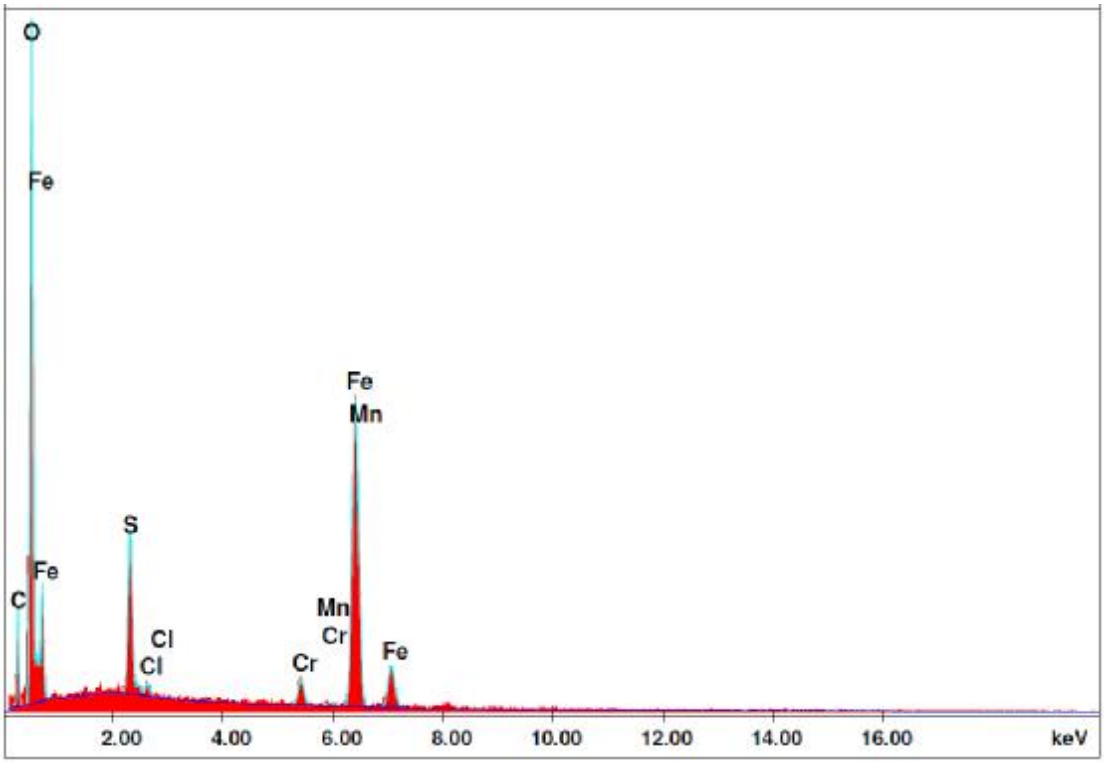


Figure 4.312. EDX analysis of the iron-rich phase in the oxide layer in Sample 441-7 shown in Figure 4.306 (Position D).

Figure 4.313 is an SEM image of a Type 441 sample in an area where the surface oxide layer provided sufficient protection, and no corrosive attack was evident. Figure 4.314 is an SEM image of an area at the corner of the sample where corrosive attack occurred by intergranular corrosion, as well as attack in possible precipitates on parallel crystallographic planes. The oxide associated with this attack was enriched with chromium, as shown in Figure 4.315 and Figure 4.316. Figure 4.317 is an EDX spectrum of the precipitates on the grain boundaries, preceding the corrosive attack, showing that the precipitates were high in chromium. Once again, the areas analysed were small, and so are not accurate, but the results were used for comparison.

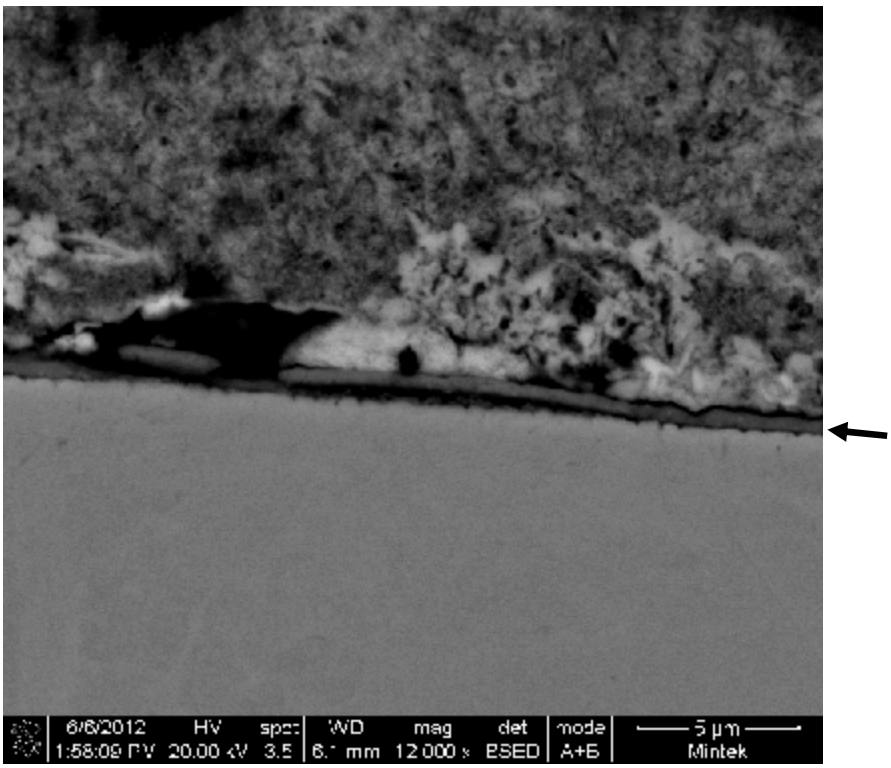


Figure 4.313. SEM-BSE image of an area where the protective chromium oxide layer (arrow) was still relatively intact on Sample 441-8.

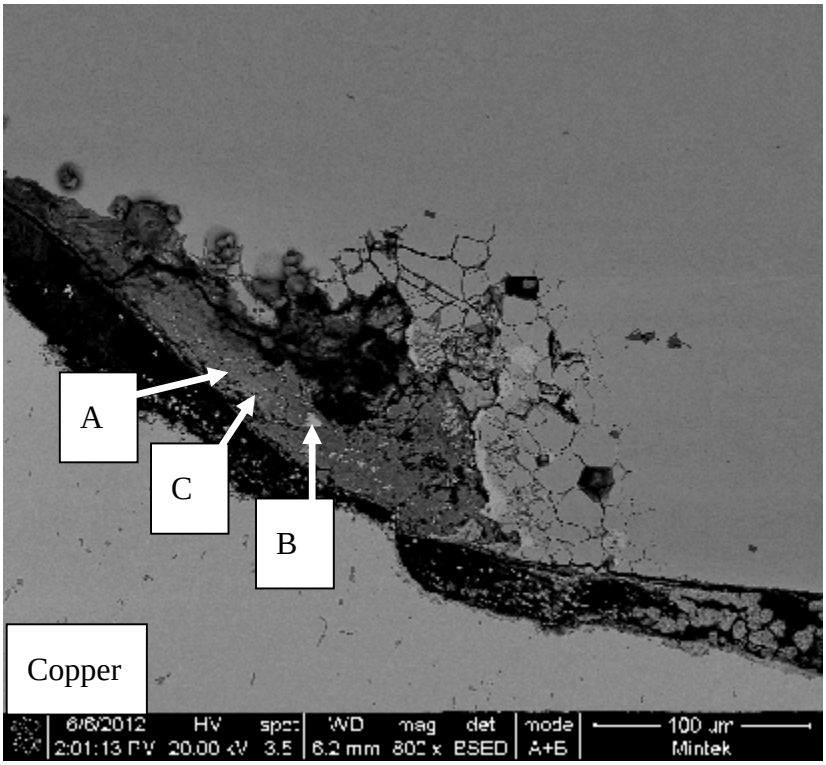


Figure 4.314. SEM-BSE image of localised attack in Sample 441-8.

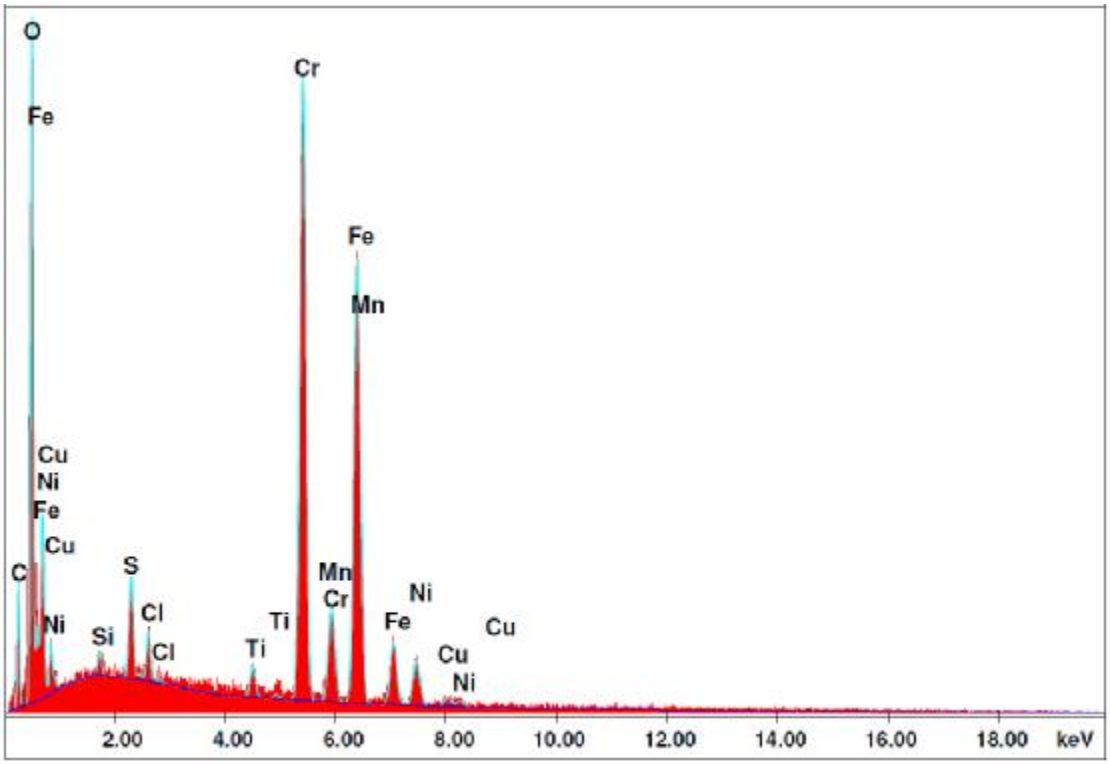


Figure 4.315. EDX spectrum of the oxide associated with the attack on Sample 441-8 as shown in Figure 4.314 (Position A).

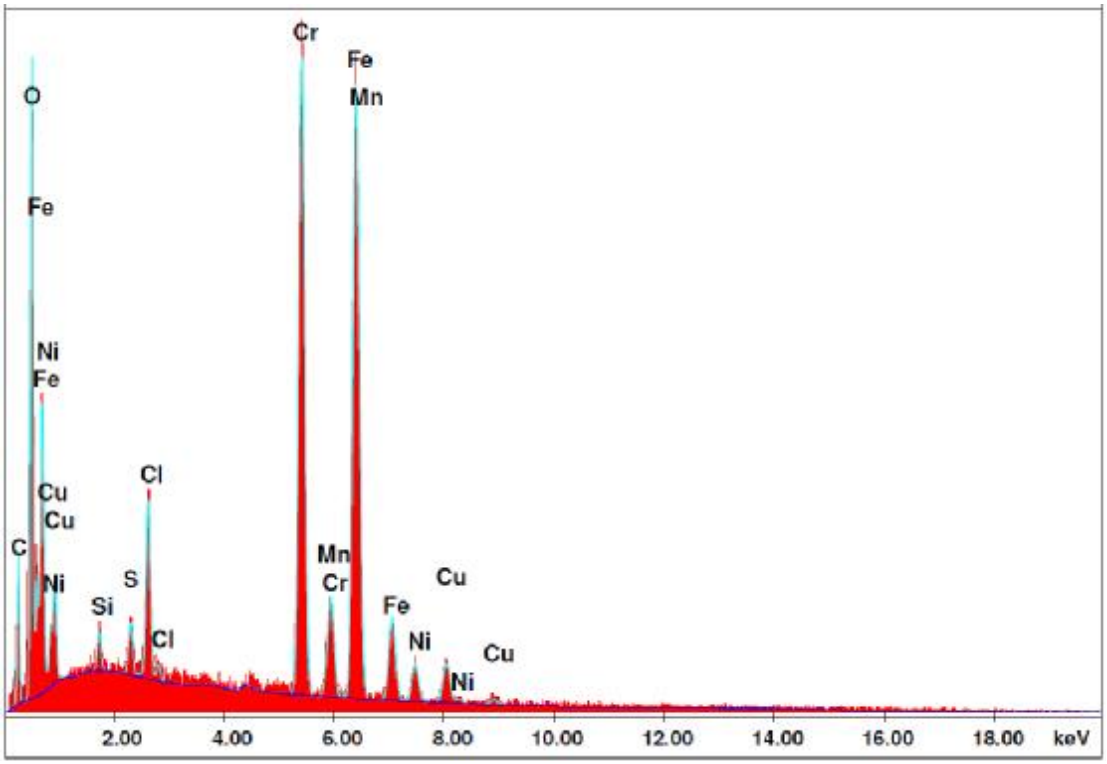


Figure 4.316. EDX spectrum of the white product in the oxide shown in Figure 4.314 in Sample 441-8 (Position B).

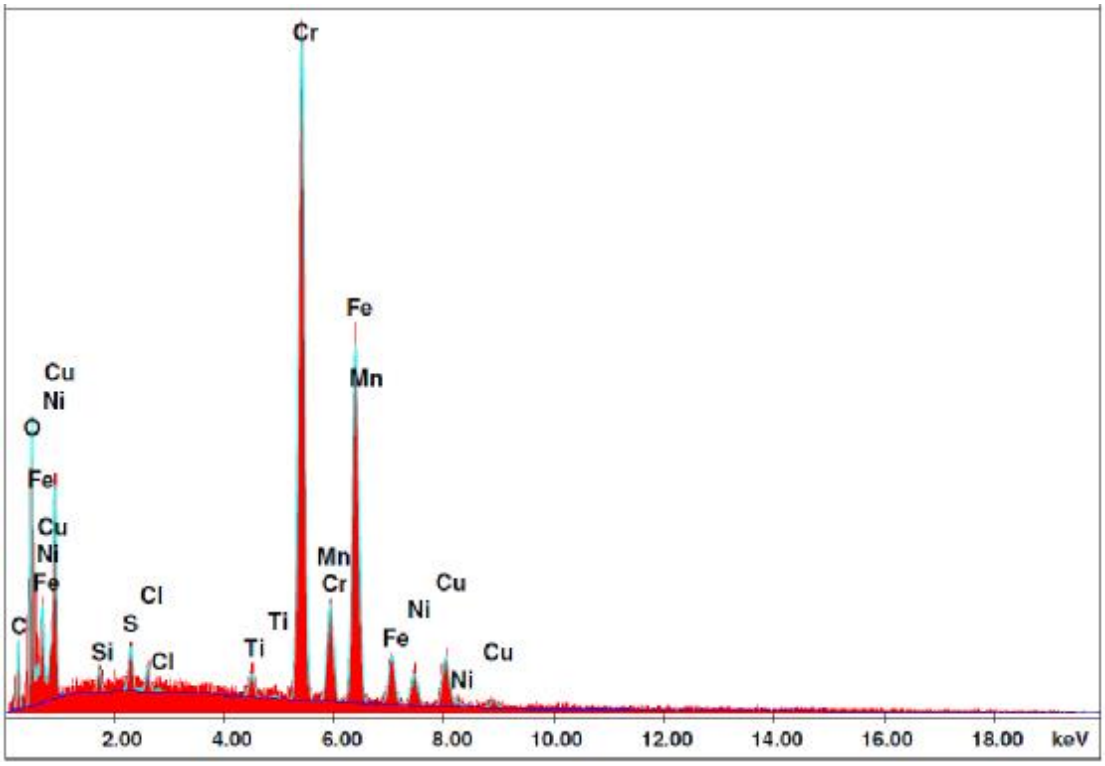


Figure 4.317. EDX spectrum of the particles at the grain boundaries of Sample 441-8 (Position C).

Figure 4.318 and Figure 4.319 are SEM images at an area where attack initiated on the surface, but did not propagate deeply. A lighter contrast layer was evident on the surface. An accurate analysis of the phase could not be performed to positively characterise it, because it was too small. Figure 4.320 is an SEM image at an area where no attack occurred. The lighter phase here was not present as a continuous layer, as in the preceding two images, but as discreet particles.

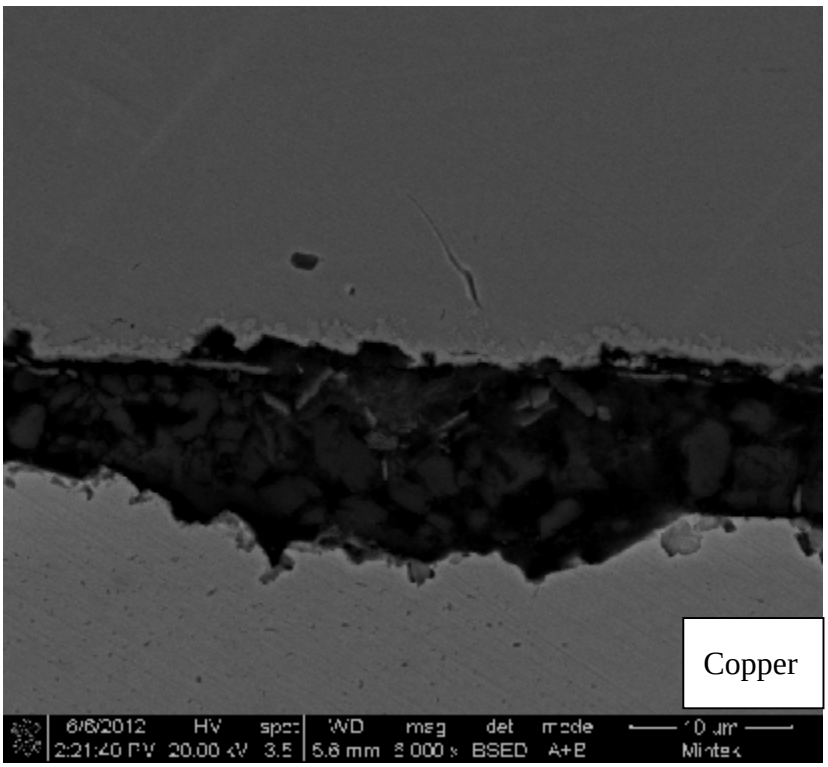


Figure 4.318. SEM-BSE image of the initiation of metal dusting and the surface of Sample 441-8.

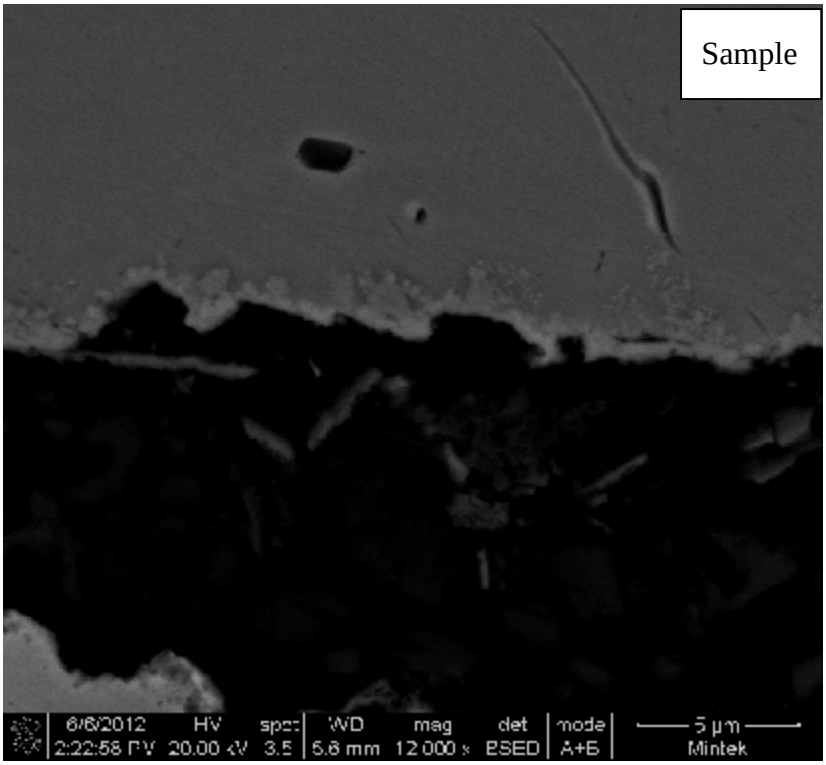


Figure 4.319. Higher magnification SEM-BSE image of the white phase at the surface of Sample 441-8 shown in Figure 4.318.

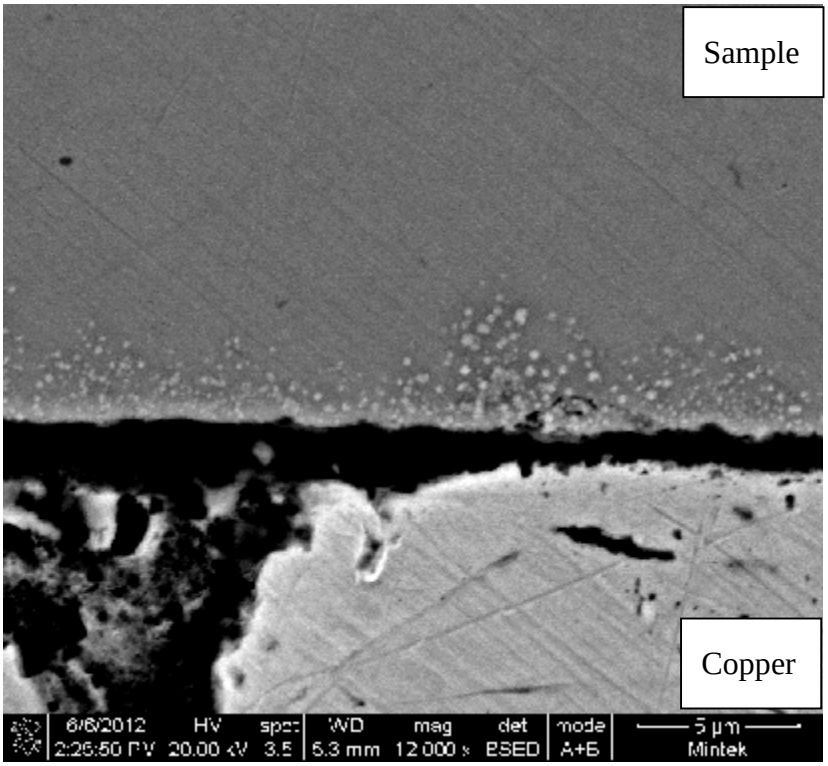


Figure 4.320. SEM-BSE image of the white phase at the surface of Sample 441-8.

4.4.5. X-ray diffraction

Figure 4.321 is an X-ray diffraction pattern from the surface of a Type 304L sample that was exposed for 30 days. No significant changes were recorded, except for perhaps a minor amount of graphite. The Type 321 sample showed a major graphite peak, confirming that the black product layer that formed was graphite, as shown in Figure 4.322. The Type 316L sample revealed significantly less austenite on the surface, as shown in Figure 4.323, although the pattern was poor. Predominantly ferrite and graphite were detected. Similarly, the Type 316Ti sample also showed a significant increase in the ferrite content, as well as graphite, as shown in Figure 4.324. Due to the extent of the attack that produced a rough surface, this spectrum had low counts and a high background.

For the ferritic materials tested, the Type 430 sample did not show any significant change throughout all the test durations. Only a minor amount of graphite was detected, in addition to the ferrite, as shown in Figure 4.325. However, a significant amount of magnetite and graphite was detected in the Type 441 sample, as shown in Figure 4.326. It is therefore likely that this sample analysed were removed from an area similar to that shown in Figure 4.200. The roughness of this surface also produced a spectrum with relatively low counts and a high background.

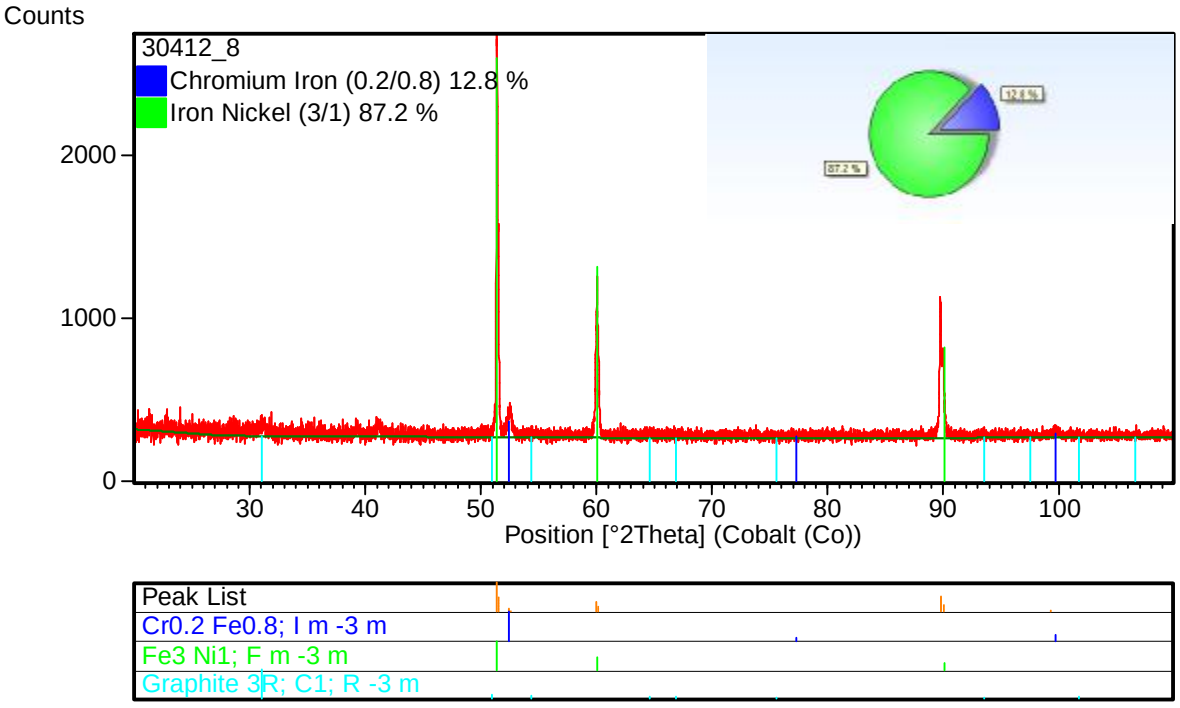


Figure 4.321. X-ray spectrum of the surface of Sample 304-8 showing peaks and volume %.

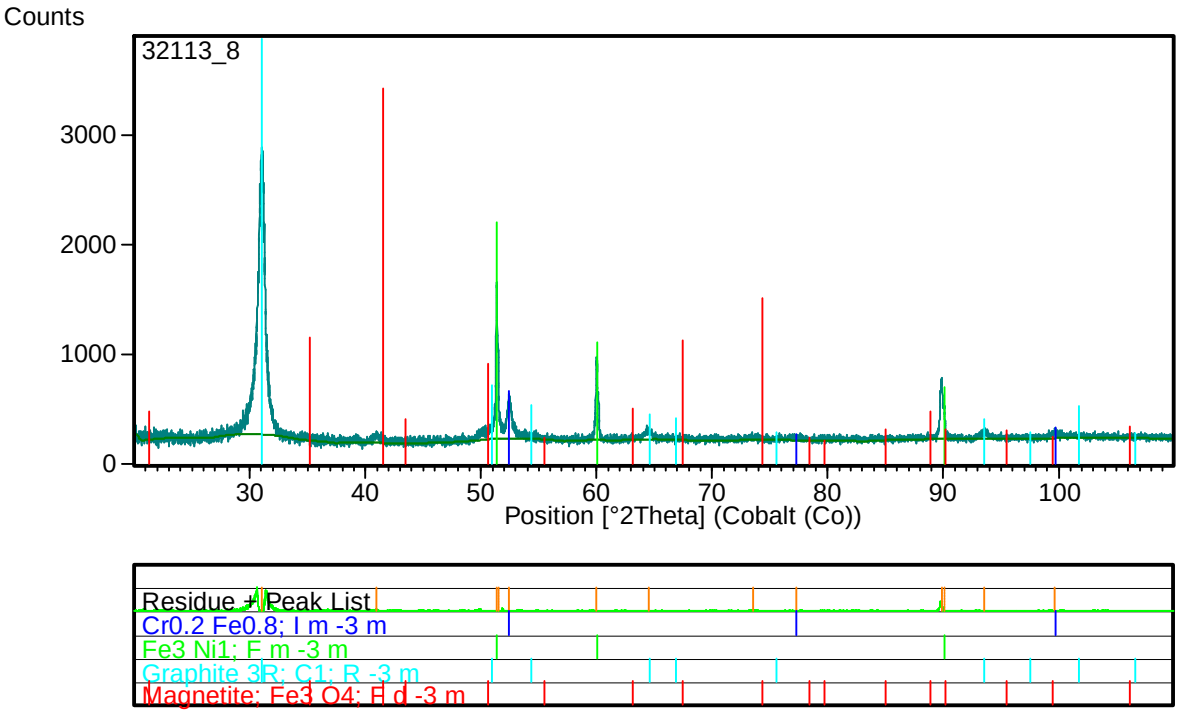


Figure 4.322. X-ray spectrum of the surface of Sample 321-8.

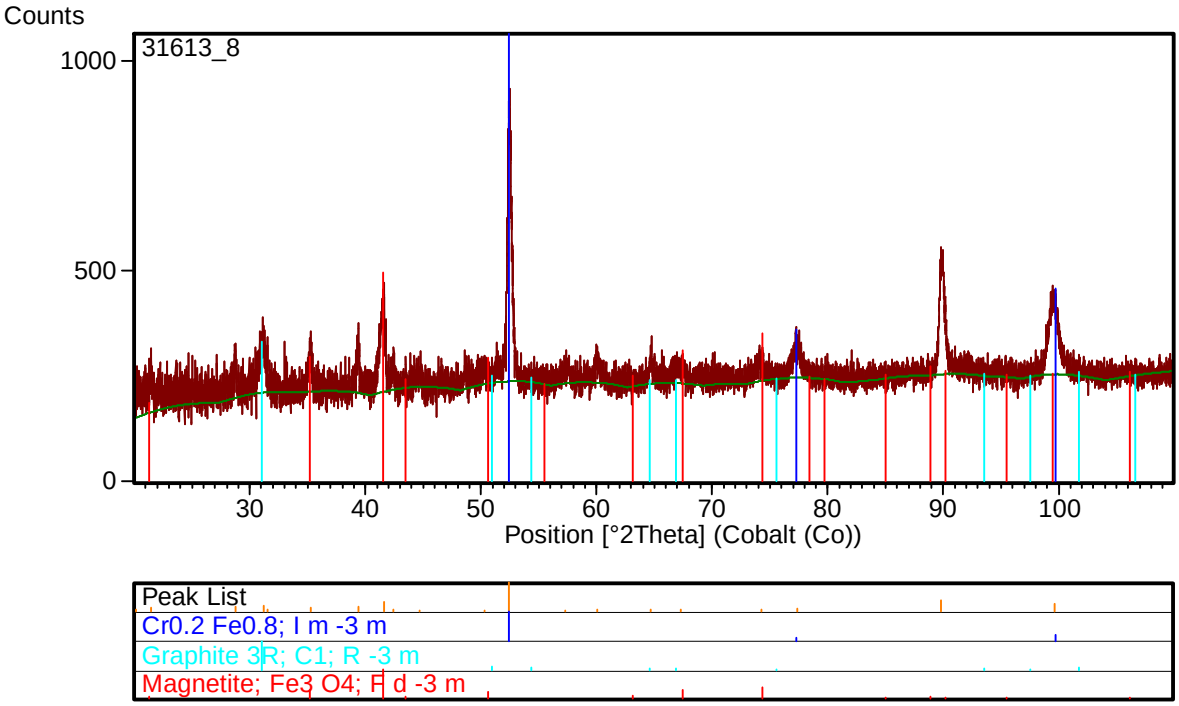


Figure 4.323. X-ray spectrum of the surface of Sample 316-8.

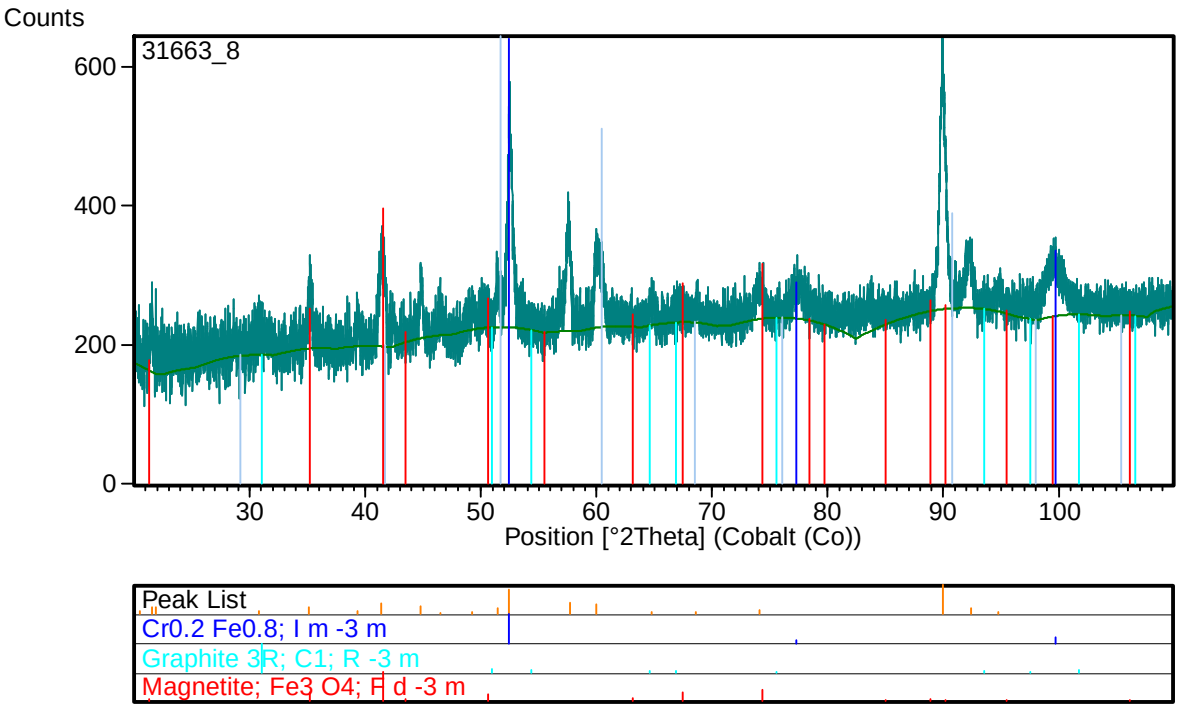


Figure 4.324. X-ray spectrum of the surface of Sample 316Ti-8.

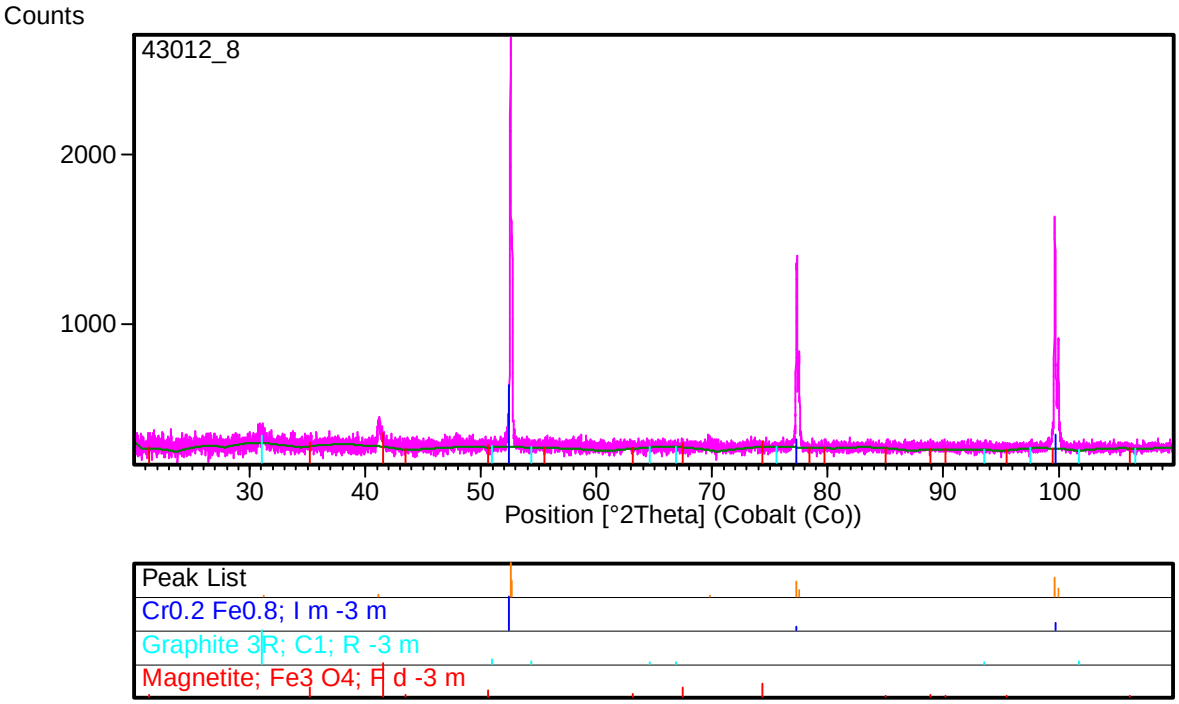


Figure 4.325. X-ray spectrum of the surface of Sample 430-8.

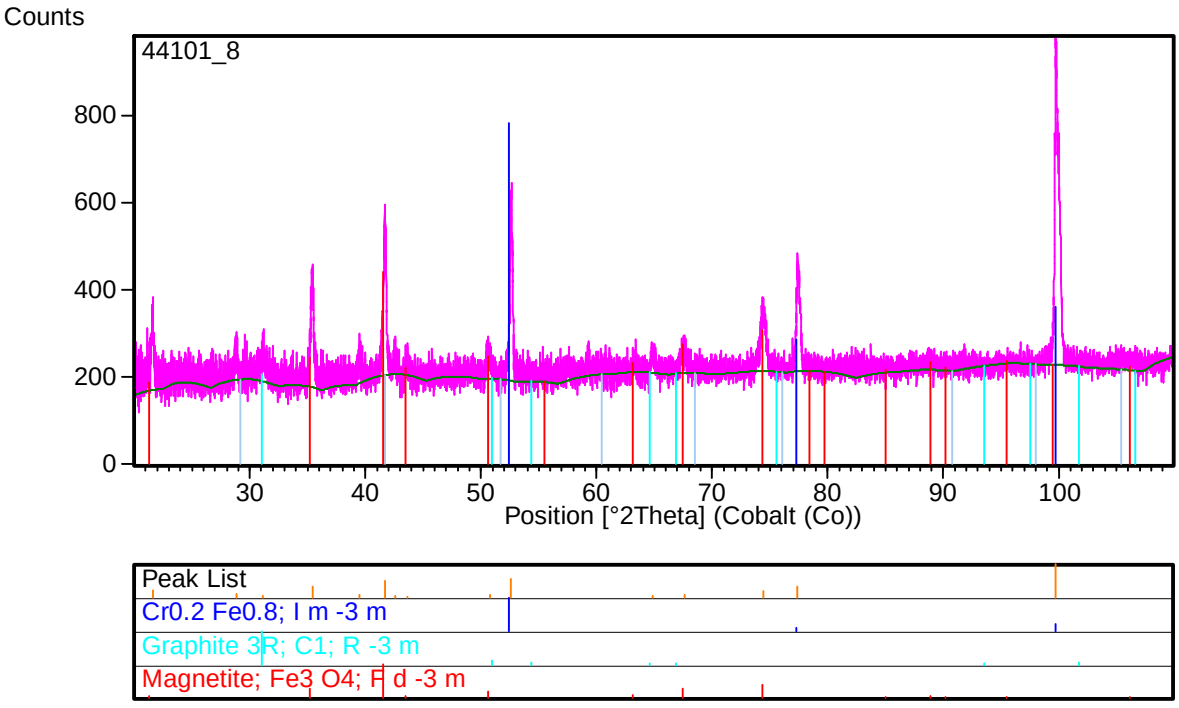


Figure 4.326. X-ray spectrum of the surface of Sample 441-8

4.4.6. Characterisation of coke

The black product removed from the boat after the thirty day test (as shown in Figure 4.157 and Figure 4.158) was also analysed by X-ray diffraction to confirm the composition of the products. Figure 4.327 is an X-ray spectrum obtained, confirming that the products predominantly consisted of graphite.

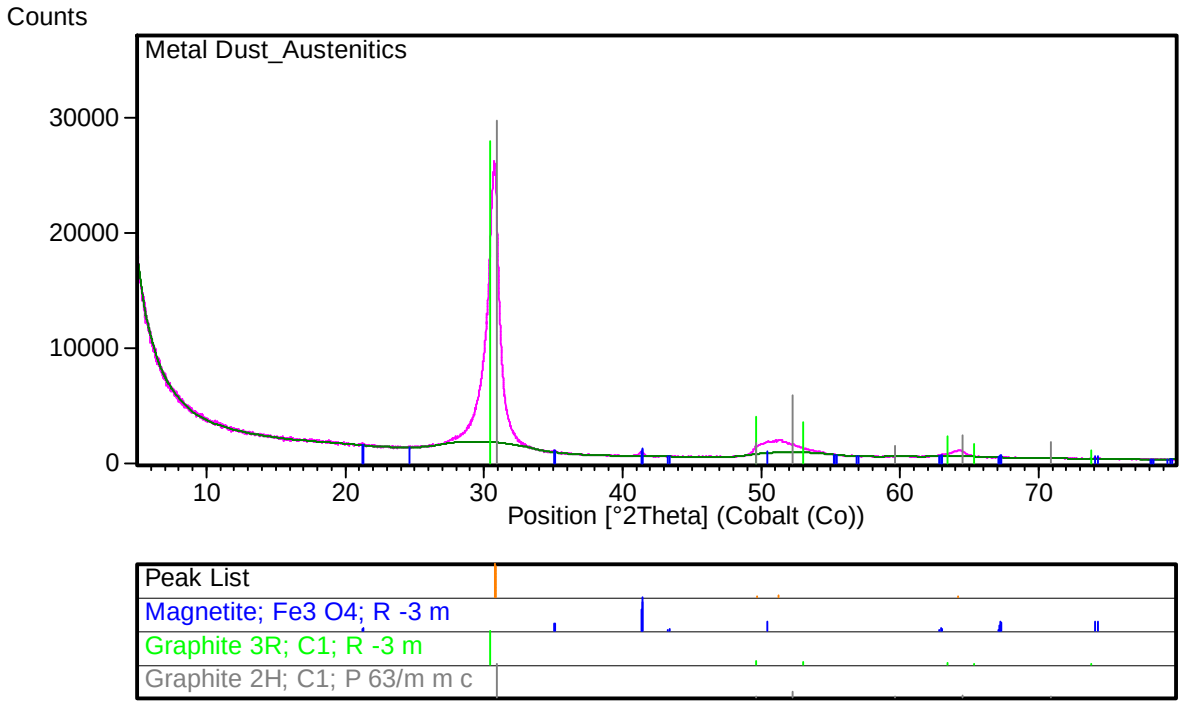


Figure 4.327. X-ray spectrum of the coke associated with the austenitic samples.

The graphite (coke) sample removed from the boat was also analysed by Raman spectroscopy. The sample was analysed together with potassium bromide (KBr) as reference sample, together with single walled carbon nanotubes (SWCNT) and multi-walled carbon nanotubes (MWCNT) – both purchased as reference materials. The resultant spectrum is shown in Figure 4.328 confirming that the graphite formed as MWCNTs. This is agreement with the TEM images obtained on coke products, as shown in Figure 4.24 and Figure 4.25.

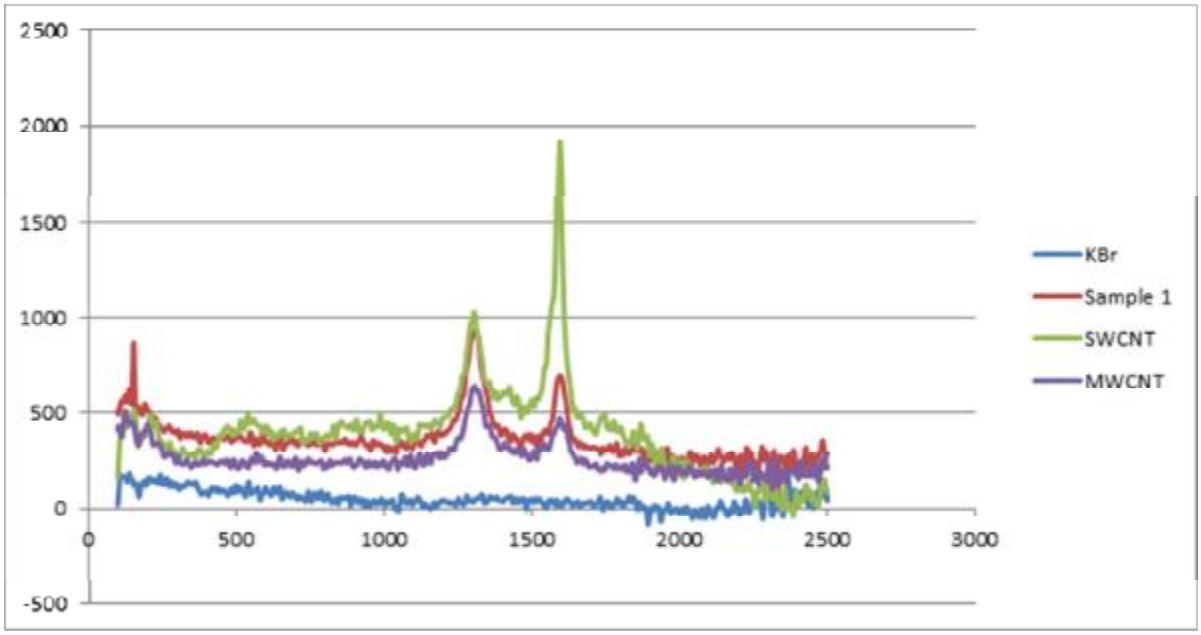


Figure 4.328. Raman spectrograph of the coke associated with the austenitic samples (labelled as Sample 1).

5. DISCUSSION

The phenomenon of metal dusting, as a form of high temperature degradation, was succesfully simulated in the test rig. Based on the degree of tarnish on the samples after testing, it appeared that all the grades with carbide-forming elements (Types 321, 316Ti and 441) performed better than the respective standard grades (i.e. Types 304L, 316L and 430), as shown in Figure 4.30, Figure 4.33 and Figure 4.36, respectively. This assessment only applied to the exposure times of up to fourteen days, since the coking and attack after the thirty day exposure period was too severe to make a similar comparison. Initially, the mass-loss data confirmed this observation, although the microstructural analyses indicated that various degrees of degredation had already initiated. Figure 5.1 is a graph illustrating the corrosion rates of all the samples over the test durations. Figure 5.2 is a graph on an expanded y-axis to show the relative performance of the other alloys (only one sample was weighed, so no statistical analysis is included). The data suggests that Type 321 performed better than 304L, and Type 441 performed better than 430.

Type 304L stainless steel performed well in the test, particularly compared to Type 316L, and revealed less metal wastage than the 321 sample. Although the mass-loss data indicated that Type 304L was attacked to a greater degree, cross-sections revealed greater attack in the 321 sample, where the corrosion products were also weighed and included as “unaffected material” (Figure 4.250). It was clear from the microstructures that the titanium precipitates were preferentially attacked (Figure 4.256), although the effect was not as marked as on the 316L samples where molybdenum carbides formed (Figure 4.264).

The Type 316L and 316Ti samples were attacked significantly more than all the other alloys. Initially, the Type 316Ti performed better than 316L, but once the corrosion started, the rate of attack was significantly greater than for the 316L samples. This could be due to the effect of titanium that initially tied up the carbon to prevent carburisation, and left chromium free to provide protection. However, these phases (refractory metal carbides) subsequently oxidised to increase the metal dusting rate significantly, as shown in Figure 4.278 [2010You]. This effect could also explain the significant difference between the 304L and 316L samples.

Apart from the addition of molybdenum in the 316L samples, the alloys were very similar. The carbides on the grain boundaries of the 316L material were enriched with chromium and molybdenum. Therefore, apart from resulting in de-alloyed chromium zones around the grain boundaries that were preferentially attacked, the expansion of the carbides upon subsequent oxidation resulted in mechanical stresses in the protective coating that caused breakage and allowed carbon ingress (Figure 4.259 to Figure 4.262) [2010You]. The use of alloys containing molybdenum is therefore not recommended in metal dusting environments.

Type 441 also initially performed better than the 430 samples, but again, coke formation was associated with the titanium carbo-nitride precipitates, which would likely cause an increased rate of attack over extended periods – similar to that shown in the 321 and 316L and 316Ti samples. The greater mobility of chromium in the ferritic material, compared to austenitic structures, also helped to provide better resistance of the ferritic materials than the austenitics used (all with approximately the same chromium content). Areas associated with breaks in the oxide scale in both the Types 430 and 441 had essentially no chromium to a depth of 200 to 300 µm, which was the radius from where chromium diffused to the surface to heal/repair the oxide. Although this effect provided greater resistance of the ferritic alloys to metal dusting in these tests for a period of 30 days, extended use would probably lead to rapid degradation and these zones would then behave similarly to carbon steel.

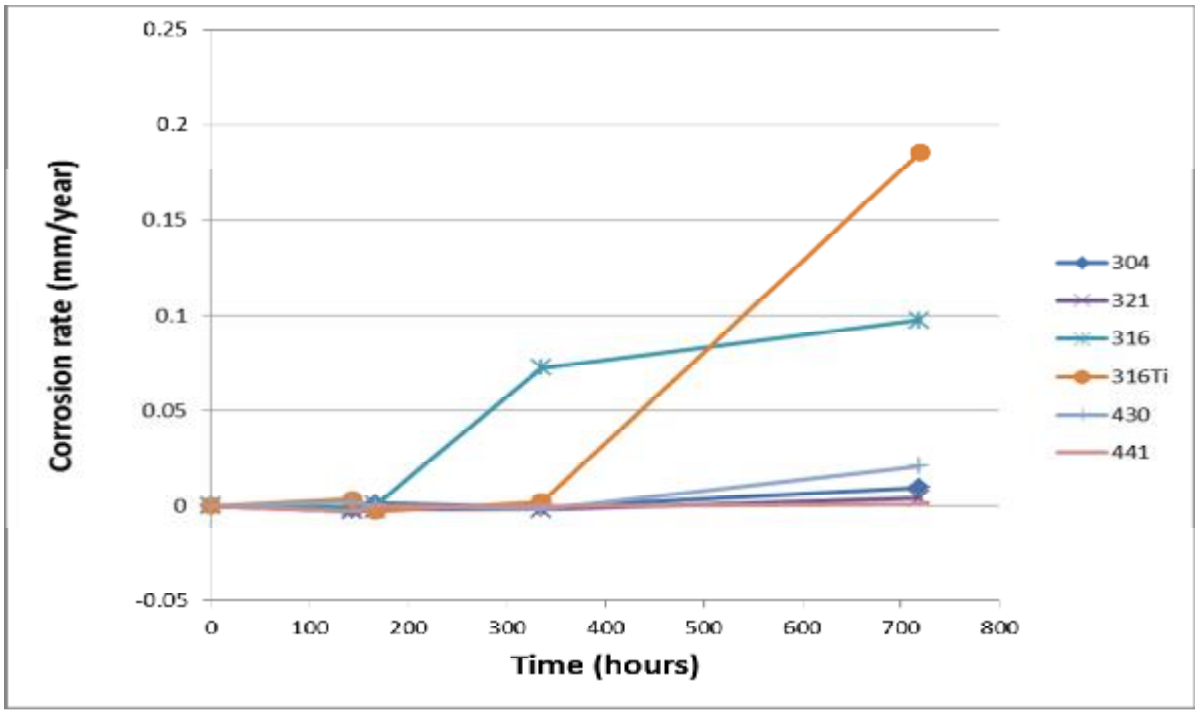


Figure 5.1. Graph of the corrosion rates for up to 30 days.

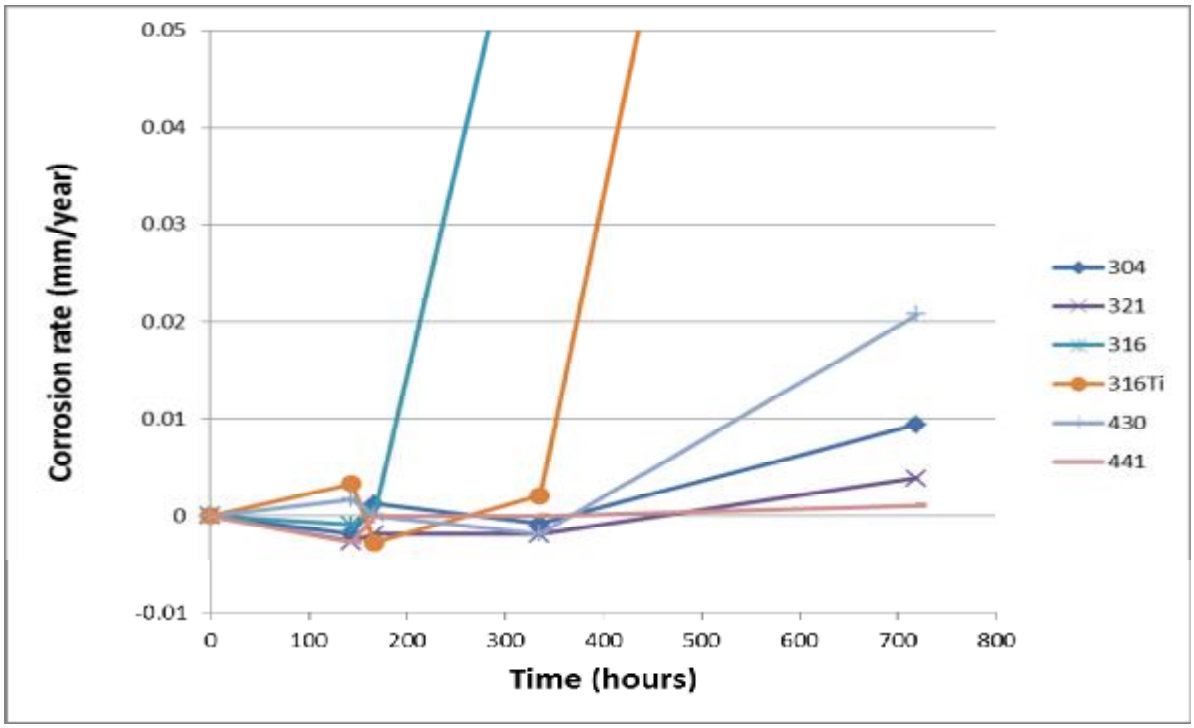


Figure 5.2. Corrosion rates of the 304L, 321, 430 and 441 samples exposed for up to 30 days.

Figure 5.3 is a compilation of all the X-ray spectra performed on the Type 304L over the test period. This confirms that no major changes occurred on the surface of the Type 304L sample. A higher ferrite peak was detected for the sample that was exposed for fourteen days. This could be related to an area of localised metal dusting. The reason for the relatively high ferrite peak in the un-exposed sample is not known.

Figure 5.4 is a compilation of all the X-ray spectra related to the Type 321 samples. The only noteworthy change was the significant graphite peak for the 30 day test. Figure 5.5 shows the X-ray spectra for the Type 316L samples exposed for increasingly longer times, illustrating that the changes on the surface mainly occurred after the 30 day test, i.e. less austenite and more ferrite and graphite. Similarly, Figure 5.6 shows the X-ray spectra for the 316Ti samples, illustrating that significant levels of ferrite, magnetite and graphite were detected after the thirty day exposure. Figure 5.7 and Figure 5.8 are X-ray spectra of both the ferritic alloys, illustrating that no significant change occurred to the Type 430 sample over the test duration, but that magnetite and graphite were detected on the Type 441 samples after the 30 day exposure.

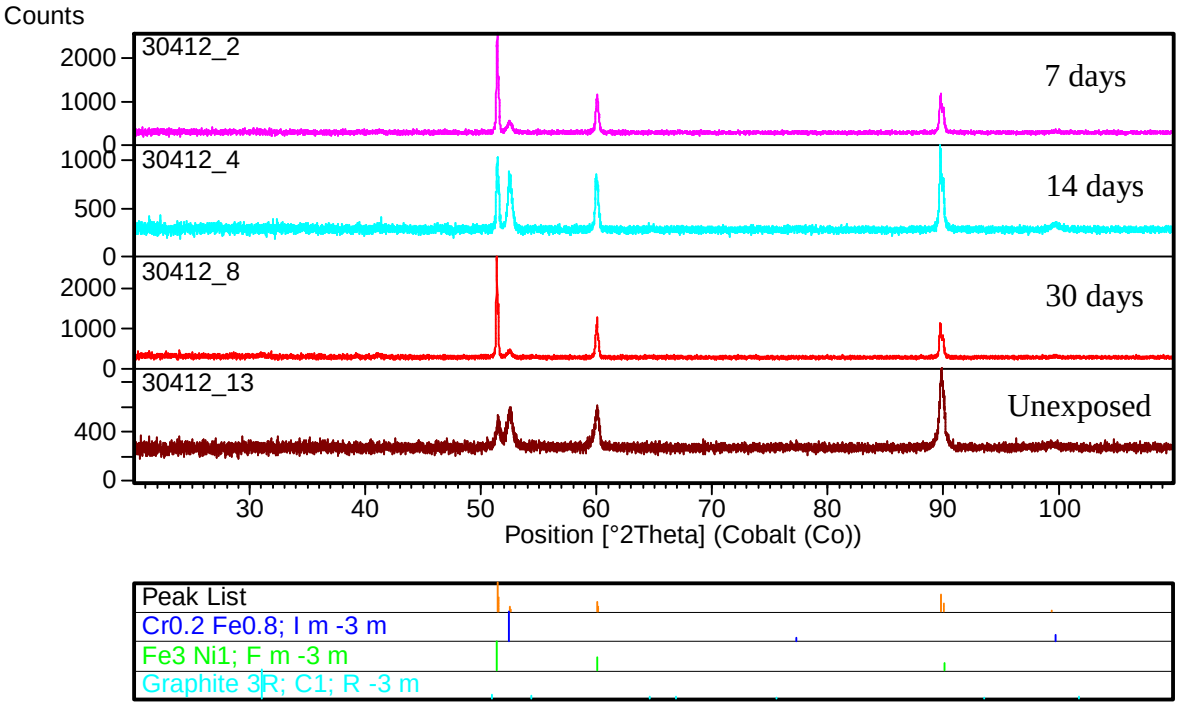


Figure 5.3. X-ray spectra of the 304L samples exposed for 7 days, 14 days, 30 days and un-exposed (from top to bottom respectively)

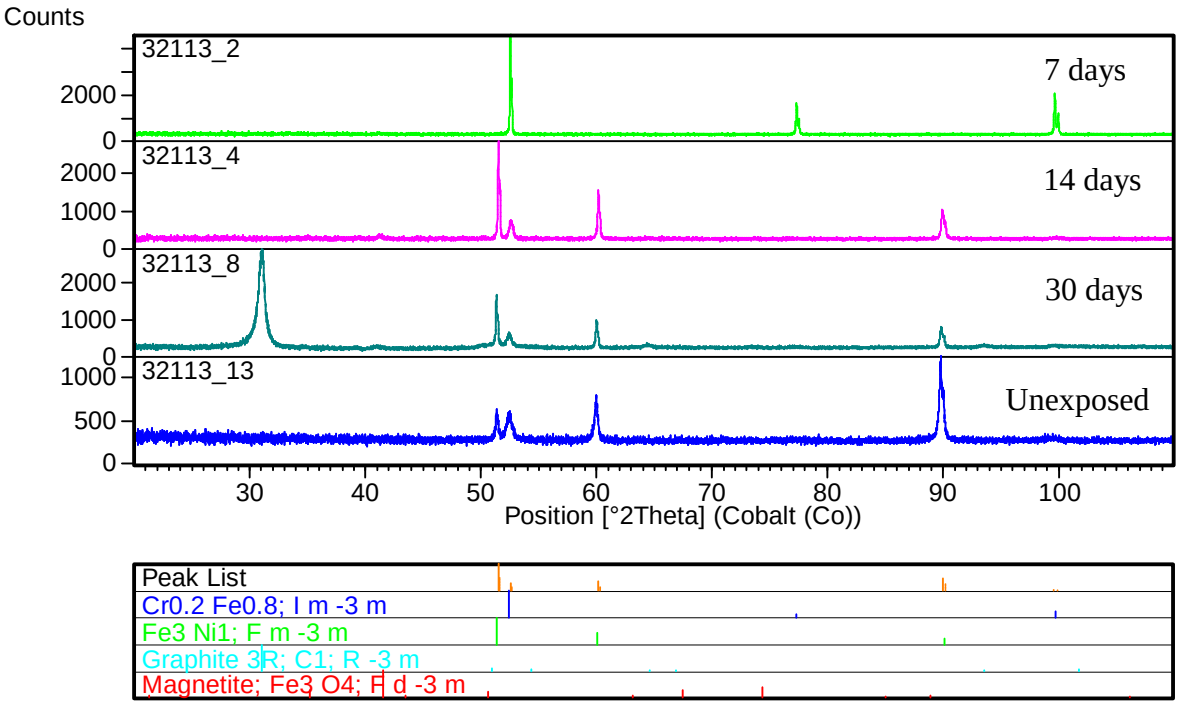


Figure 5.4. X-ray spectra of the 321 samples exposed for 7 days, 14 days, 30 days and un-exposed (from top to bottom respectively)

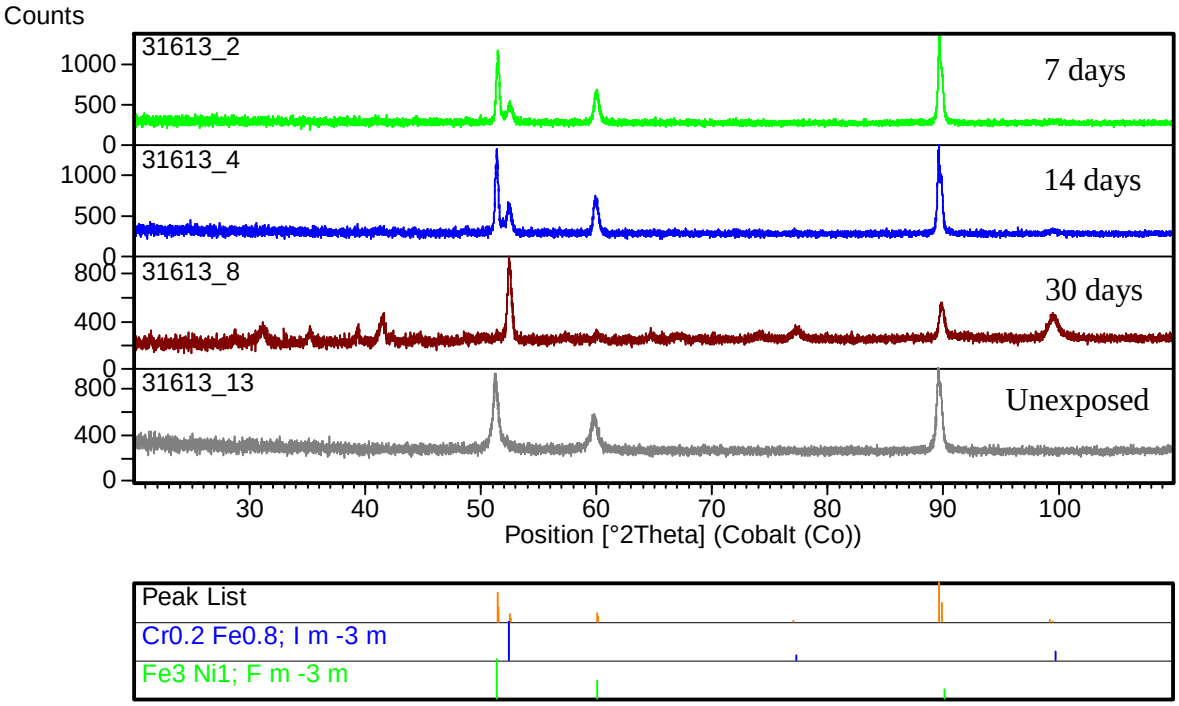


Figure 5.5. X-ray spectra of the 316L samples exposed for 7 days, 14 days, 30 days and un-exposed (from top to bottom respectively)

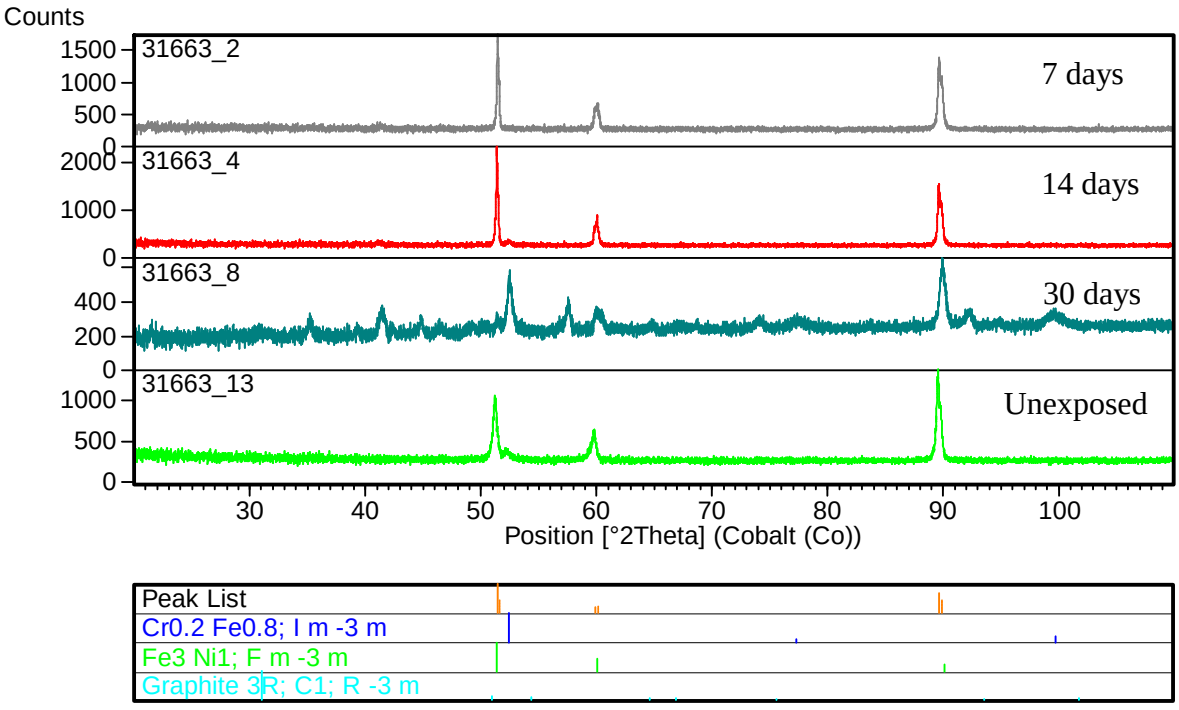


Figure 5.6. X-ray spectra of the 316Ti samples exposed for 7 days, 14 days, 30 days and un-exposed (from top to bottom respectively)

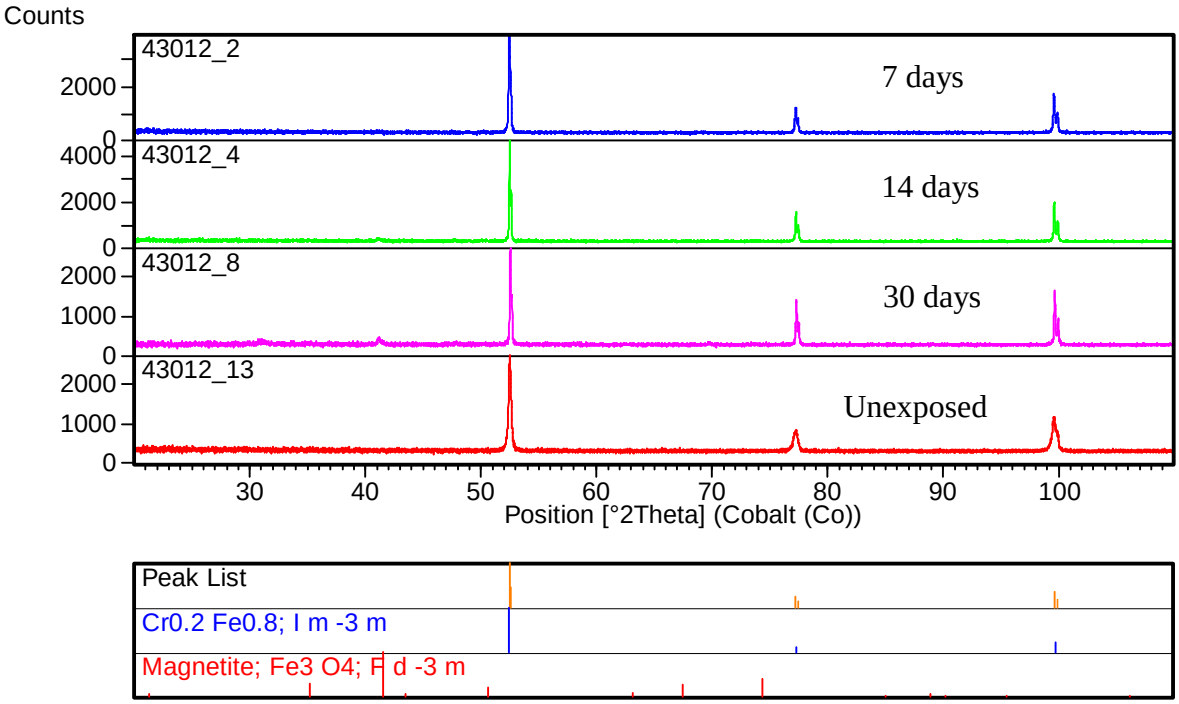


Figure 5.7. X-ray spectra of the 430 samples exposed for 7 days, 14 days, 30 days and unexposed (from top to bottom respectively)

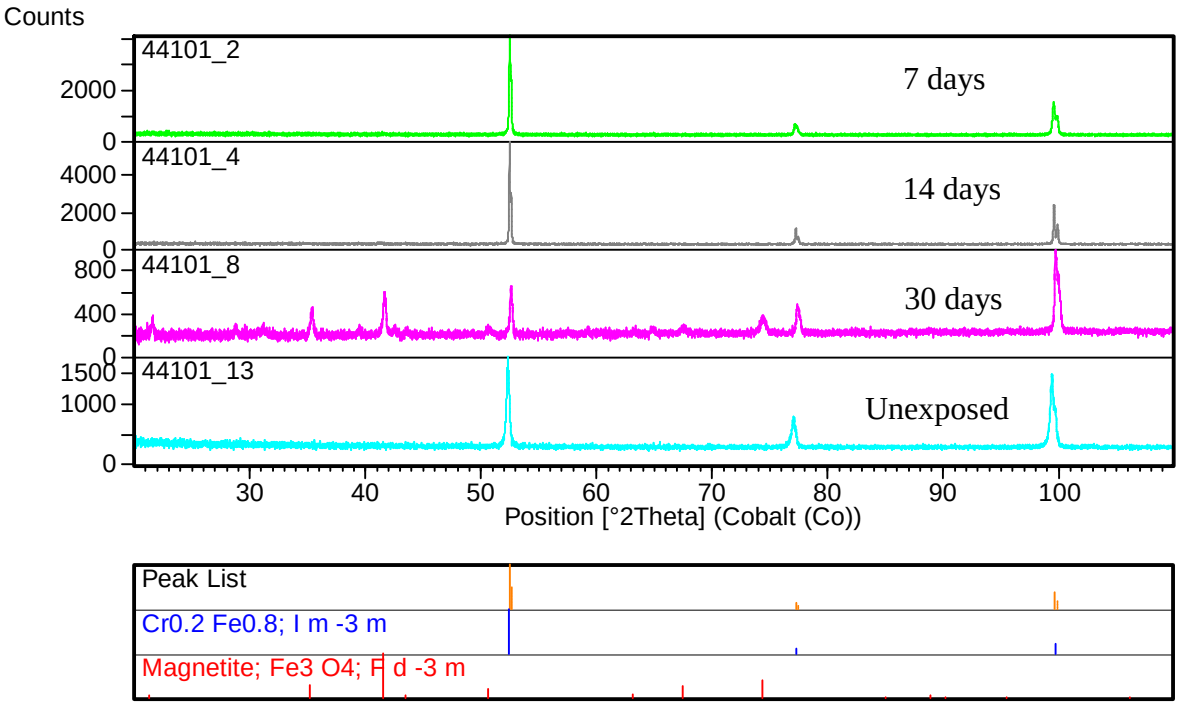


Figure 5.8. X-ray spectra of the 441 samples exposed for 7 days, 14 days, 30 days and unexposed (from top to bottom respectively)

A phase formed on the surfaces of the alloys (Figure 4.248, Figure 4.319 and Figure 4.320) which could have been $M_{23}C_6$ and/or M_7C_3, referring to the compositions in Figure 4.247, in contrast to cementite (Fe_3C) which is formed during metal dusting of low alloy steels, as shown in Figure 2.3 [1966Hoc, 1972Hoc, 1995Gra1, 1998Gra1]. However, Grabke [1995Gra1, 2003Gra] did discuss these mixed carbides. Unfortunately this layer was too thin to characterise in this study by EDX, but was interpreted as a mixed metal carbide, since it had the same appearance as behaviour as reported before [2002Sza1, 2002Sza2, 2002Sza3]. This, together with the high metal dusting rate of 316L and 316Ti grades, due to the formation and subsequent oxidation of chromium- and molybdenum-rich carbides, confirms that the predominant metal dusting mechanism in all the samples was Type III, i.e. selective oxidation of alloy carbides [2002Sza1, 2002Sza2, 2002Sza3]. The metal dusting of the ferritic alloys was similar to the models given by Grabke [2003Gra] in Figure 2.7 (b) and also Young [2011You] in Figure 2.9. The structure shown in Figure 4.137 is likely to be the coke structure in Figure 2.7 (b) (d) [2003Gra].

The importance of maintaining a passive oxide layer to prevent carbon deposition and diffusion into the metal was clearly demonstrated. The oxide layers were catalytically inactive and did not promote the deposition of carbon from the carbon-oversaturated gases. Furthermore, due to the low solubility of carbon in the oxide layer, carbon could not diffuse readily through the oxide layer into the substrate material. The ferritic materials revealed significantly less coking compared to Types 316L and 316Ti. This is due to the ease at which chromium can diffuse through the ferritic matrix to heal breaks in the passive oxide layer, and thereby preventing carbon deposition from the carbon oversaturated gas mixture. The importance of a high chromium content, as well as a ferritic structure, are highlighted as possibilities to develop alloys to mitigate attack by metal dusting, is therefore demonstrated.

The advantage of using austenitic alloys to prevent metal dusting, is that the carbon diffusion rate is slow. For the relatively low nickel concentration ranges used in this study (8 to 10 wt%), the slow carbon diffusion rate of the austenite structure was not as effective to mitigate metal dusting as the advantage provided by an increased chromium diffusion rate in ferritic alloys. It must be noted that the exposure period of 30 days was relatively short, and an accelerated rate of attack for the ferritic alloys can be expected for longer exposure periods.

Alloys should also not contain any precipitates, since these provide sites where coke deposits. The formation of phases at elevated temperatures should also be avoided. These phases oxidise and the resultant mechanical stresses cause breaks in the protective oxide layer, which allows carbon deposition and ingress (i.e. internal carburisation).

6. CONCLUSIONS AND RECOMENDATIONS

While carbide-forming elements (titanium and niobium) initially provided protection against metal dusting, the rate of attack increased subsequently. The initial good protection was ascribed to the fact that these elements tied up the carbon ingress, to leave the chromium in the alloy, free to protect the material. However, subsequent oxidation of these refractory metal carbides increased the rate of attack.

Type 316L performed significantly worse than 304L. Since molybdenum is also a carbide-former, the effect was probably similar to that described above for titanium and niobium. Thus, molybdenum alloys should therefore not be used in metal dusting applications.

Thus, the use of alloys containing carbide-forming elements such as molybdenum, titanium and niobium are not recommended for metal dusting environments.

The ferritic materials initially performed better than the austenitic materials with similar chromium contents (18wt%). This was due to the greater mobility of chromium that diffused towards the surface to heal breaks in the oxide layer. However, this resulted in essentially a layer of carbon steel on the substrate surface that could increase the metal dusting rate significantly during prolonged use. Although this demonstrated the advantage that ferritic alloys offer, this should be explored by further improving the resistance of these alloys by the addition of other elements to provide a stable oxide film to prevent carbon ingress.

The importance of a stable oxide layer to prevent carbon deposition was clearly demonstrated, as major coking was only associated with the alloys that exhibited corrosion. The ferritic alloys were able to repair breaks in the film more effectively, by chromium diffusion over relative long distances (~300 μm), thereby preventing coke formation at the metal surface.

The formation and maintenance of a protective oxide film was shown as key to prevent metal dusting. The oxide layers were catalytically inactive and did not promote the deposition of carbon from the carbon-oversaturated gases. Alloys containing chromium, aluminium and silicon should therefore perform well.

Due to the low solubility of carbon in the oxide layer, carbon could not diffuse readily through the oxide layer into the substrate material. Alloys should therefore be designed to provide optimum oxide integrity at the targeted environments (combination of temperature and gas composition).

The high chromium diffusion coefficient in ferritic materials and the low carbon diffusion rate in austenitic materials should also be considered, at the particular temperatures, to specify an optimum alloy to resist metal dusting.

The higher ferrite content in some of the austenitic alloys, as determined by X-ray diffraction, needs to be further investigated.

Preferential attack occurred at the titanium carbo-nitrides, with indications of associated coke formation. It was clear that the titanium-carbo-nitrides initially reduced the metal dusting rate, but that the degradation rate thereafter accelerated. The processes involved should be further characterised to clarify the mechanisms, and could involve TEM.

Indications are that the filaments associated with the ferritic alloys were different, compared to the austenitic alloys. Separate metal dusting tests should be performed with the respective alloys, and the coke filaments characterised and compared, probably using TEM.

The light-contrast phase that formed at the surfaces could not be characterised by SEM in this study. Thin films should be prepared to further characterise this phase by TEM. Glow discharge optical emission spectrometry can also be employed.

All scans and precipitates could be done analysing for oxygen as well.

7. REFERENCES

[1953Hul] A. Hultgren and M. Hillert, Betingelser för Bildning av Cementit vid Uppkolning av Nickelstål, Jernkont. Ann, Vol. 137, No 7, (1953).

[1959Bet] W. Betteridge, The Nimonic Alloys, E Arnold, London (1959).

[1966Hoc] R.F. Hochman and J.H. Burson, The Fundamentals of Metal Dusting, American Petroleum Institute, Division of Refining, Proceedings, Vol. 46, (1966), pp. 331-344.

[1967Fon] M.G. Fontana, N.D. Greene, Corrosion Engineering, McGraw-Hill, Inc, New York, USA, (1967).

[1972Hoc] R.F. Hochman, Basic Studies of Metal Dusting Deterioration in Carbonaceous Environments at Elevated Temperatures, Proc. of the 4th International Congress on Metal Corrosion, Amsterdam, The Netherlands, 1969, (1972), pp. 258-263.

[1985Wol] I. Wolf and H.J Grabke, Solid State Communication, Vol. 54, (1985), pp. 5-10.

[1986Gut] J. Gutzeit, High Temperature Sulfidic Corrosion of Steels, Process Industries Corrosion-The Theory and Practice, NACE, 1986.

[1987Atk] A. Atkinson and D.W. Smart, Report AERE R 2762, United Kingdom Atomic Energy Authority, Harwell, (1987).

[1987Kha] A.S. Khanna and B.B. Jha, Oxidation of Metals, Vol. 27 (1-2), (1987), pp. 95-102.

[1987Scu] M. Shutze, Protective Oxide Scales and Their Breakdown, John Wiley & Sons Ltd, Chichester, England, (1987).

[1988Lit] J. Litz, A. Rahmel and M. Schorr, Oxidation of Metals, Vol. 29, (1988), pp. 99-105.

[1992Ree] E. Reese and H.J. Grabke, Effects of Chlorides on the Oxidation of the 2.25Cr-1Mo Steel, Materials and Corrosion, Vol. 43, (1992), pp. 547-557.

[1993Gra1] H.J. Grabke, R. Krajak and J.C. Nava Paz, Corrosion Science, Vol. 35, (1993), pp. 1141-1150.

[1993Gra2] H.J. Grabke, R. Krajak and E.M. Müller-Lorenz, Werkstoffe und Korrosion, Vol. 44, (1993), pp. 89-97.

[1994Gra1] H.J. Grabke, C.B. Bracho-Troconis and E.M. Müller-Lorenz, Werkstoffe und Korrosion, Vol. 45, (1994), pp. 215-221.

[1994Gra2] H.J. Grabke and R. Krajak, Härterei-Techn. Mitteilungen, Vol. 49, (1994), page 150.

[1995Gra1] H.J. Grabke, Metal Dusting of Low- and High-Alloy Steels, Corrosion, Vol. 51, 9, (1995), pp. 711-720.

[1995Gra2] H.J. Grabke and E.M. Müller-Lorenz, Steel Research, Vol. 66, (1995), 252-258.

[1995Pip] E. Pippel, J. Woltersdorf, H.J. Grabke and S. Strauss, Microprocesses of Metal Dusting on Iron, Steel Research, Vol. 66, No. 7, (1995), pp. 217-221.

[1996Gra] H.J. Grabke, R. Krajak, E.M. Muller-Lorenz, S. Strauss, Materials and Corrosion, Vol. 47, (1996), pp. 495-504.

[1997Klo] J. Klower, H.J. Grabke, E.M Muller-Lorenz and D.C Agarwal, Metal dusting and carburisation resistance of Ni-base alloys, Paper No 139, Corrosion 97, NACE, (1997).

[1998Gra1] H.J. Grabke, Thermodynamics, Mechanisms and Kinetics of Metal Dusting, Materials and Corrosion, Vol. 49, (1998), pp. 303-308.

[1998Gra2] H.J. Grabke, E.M. Müller-Lorenz, J. Klöwer and D.C. Agarwal, Materials Performance, Vol. 37, (1998), pp. 58-63.

[1998Gra3] H.J. Grabke and E.M. Müller-Lorenz, Materials and Corrosion, Vol. 49, (1998), pp. 317-320.

[1998Pip] E. Pippel, J. Woltersdorf and R. Schneider, Micromechanisms of Metal Dusting on Fe-base and Ni-base Alloys, Materials and Corrosion, Vol. 49, No. 5, (1998), pp. 309-316.

[1998Stra] S. Strauss, H.J. Grabke, Materials and Corrosion, Volume 49, (1998), pp. 321-327.

[1999Mai] M. Maier and J.F. Norton, Corrosion 99, NACE, Houston, TX, Paper 75 (1999).

[1999Sza] P. Szakálos, J. Lindblom and L. Lindé, Carburizing of Chromia and Alumina Forming Stainless Steels at 750°C, 14th International Corrosion Congress (ICC), Paper 153, Cape Town, South Africa, September 1999.

[2000Bak] B.A. Baker, G.D. Smith, Corrosion 2000, NACE, Houston, TX, Paper 257, (2000).

[2000Mai] M. Maier, J.F. Norton, P. Puschek, Materials for High Temperature, Vol. 17, (2000).

[2000Sch1] A. Schneider, G. Inden, H.J. Grabke, Q. Wei, E. Pippel and J. Woltersdorf, Steel Research, Vol. 71, No. 5, (2000), pp. 179-184.

[2000Sch2] A. Schneider, G. Inden and H.J. Grabke, Interface Controlled Materials, Vol. 9, EUROMAT 99, M. Rühle; H. Gleiter (Eds), Wiley-VCH, (2002), pp. 30-37.

[2001Gra] H.J. Grabke, E.M. Müller-Lorenz and A. Schneider, Iron and Steel Institute of Japan International., Vol. 41, (2001), Supplement S1-S8.

[2002Sza1] P. Szakálos, R. Pettersson and S. Hertzman, An Active Corrosion Mechanism for Metal Dusting on 304L Stainless Steel, Corrosion Science, Vol. 44, No. 10, (2002), pp. 2253-2270.

[2002Sza2] P. Szakálos and L. Liu, Mechanisms of Metal Dusting – Application to Alloy Composition, Temperature and Pressure, 15th International Corrosion Conference (ICC), Paper 806, Granada, September, (2002).

[2002Sza3] P. Szakálos, Mechanisms of Metal Dusting on Stainless Steels, Licentiate Thesis, ISBN 91-7283-260-6, Stockholm, Sweden, (2002).

[2002Toh] C. Toh, P.R. Munroe and D.J. Young, Oxidation of Metals, Vol. 58 (2002), pp. 1-21.

[2003Gra] H.J. Grabke, Metal Dusting, Materials and Corrosion, Vol. 54, No. 10, (2003), pp. 736-746.

[2003Gra2] H.J. Grabke, E.M. Muller-Lorenz and M. Zinke, Metal dusting behaviour of welded Ni-base alloys with different surface finishes, Materials and Corrosion, Vol. 34, (2003), page 785-792.

[2003Sza] P. Szakálos, Mechanisms and Driving Forces of Metal Dusting, Materials and Corrosion, Vol. 54, No. 10, (2003), pp. 752-762.

[2003Toh] C.H. Toh, P.R. Munroe, D.J. Young, Material for High Temperature, Vol. 20, (2003), pp. 527-534.

[2004McE] Corrosion Control in Southern Africa, J.J. McEwan (Ed), page vii, Corrosion Institute of Southern Africa, (2004).

[2004Sza] P. Szakálos, Mechanisms of Metal Dusting, PhD Thesis, Royal Institute of Technology and Swedish Institute for Metals Research, Stockholm, Sweden, (2004).

[2004Zen] Z. Zeng, K. Natesan and M. Grimoditch, Corrosion 2004, Volume 60, (2004), Page 632.

[2005Nis] Y. Nishiyama, K. Moriguchi, N. Otsuka, T. Kudo, Materials and Corrosion, Vol. 56, (2005), pp. 806.

[2005Out] High Temperature Ferritic Stainless Steel, Outokumpu, http://www.outokumpu.com/SiteCollectionDocuments/High_temperature_ferritic_grades.pdf , (Accessed 19 June 2012).

[2006Sza] P. Szakálos, M. Lundberg and R. Pettersson, Metal Dusting on an Alumina Forming Ni-base Alloy, Corrosion Science, Vol. 48, (2006), pp. 1679-1695

[2007Roh] D. Rohnert, F. Phillip, H. Reuther, T. Weber, E. Wessel and M Shutze, Oxidation of Metals, Vol. 68, 271, (2007), pp. 271-293.

[2007Lai] G.Y. Lai, High-Temperature Corrosion and Materials Applications, ASM International, United States of America, (2007).

[2010You] D.J. Young, Carburisation and Metal Dusting, Shreir's Corrosion, Fourth Edition, (Ed) B. Cottis, M. Graham, R. Lindsay, S. Lyon, T. Richardson, D. Scantlebury and H. Stott, Elsevier B.V., The Netherlands, (2010), Volume 1, pp. 273-301.

[2011You] D.J. Young, J. Zhang, C Geers and M. Shutze, Recent advances in understanding metal dusting: A review, Materials and Corrosion, Vol. 62, No 1, (2011), pp. 7-28

[NiI1] The Role of Stainless Steels in Petroleum Refining, Nickel Institute, http://www.nickelinstitute.org/~/Media/Files/TechnicalLiterature/RoleofStainlessSteelinPetroleumRefining_9021_.pdf#page=, (accessed 19 June 2012).

[NiI2] High-Temperature Characteristics of Stainless Steels, A Designers' Handbook Series, No 9004, Nickel Institute, http://www.nickelinstitute.org/~/Media/Files/TechnicalLiterature/High_TemperatureCharacteristicsofStainlessSteel_9004_.pdf, (accessed 19 June 2012).

[2012Hol] Refinery Damage Mechanisms (Based on API 571), Course presented by M.L. Holland, Corrosion Institute of Southern Africa, 2012.

APPENDIX 1

Publications

Results of this project were presented at the following conferences (where the first three were testing the rig, and the rest were for this work):

"A study of metal dusting on alloys 602CA and 800", F.M.L. Mulaudzi, L.A. Cornish, G.A. Slabber and M.J. Papo, ZrTa 2011 New Metals Development Network Conference, Magaliesburg, South Africa, October 2011.

"Microstructural investigation of metal dusting on alloys 602CA and 800", F.M.L. Mulaudzi, L.A. Cornish, G.A. Slabbert, M.J. Papo and J. Zhang, 49th Annual Conference of the Microscopy Society of Southern Africa, CSIR International Convention Centre, December 2011.

"An investigation of metal dusting corrosion of alloys N06025 and N08800", F.M.L. Mulaudzi, L.A. Cornish, G.A. Slabbert, M.J. Papo and J. Zhang, NACE International Corrosion Conference & Expo, Salt Lake City, Utah, USA, March 2012.

"The effect of carbide-forming elements on the metal dusting rate in hydrocarbon environments", G.A. Slabbert, F.M.L. Mulaudzi, L.A. Cornish, M.J. Papo and J. Zhang, Poster Presentation, DST/NRF Centre of Excellence for Strong Materials, Annual Students Presentations, 30 May 2012.

The effect of the matrix structure on the metal dusting rate in hydocarbon environments, GA Slabbert, F.M.L. Mulaudzi, L.A. Cornish, M.J. Papo, V. Morudu and J. Zhang, AMI Ferrous 2012, Ferrous Metals Development Network Conference, Magaliesburg, South Africa, 15-17 October 2012 – Abstract accepted and paper under review for Oral Presentation.

"The effect of carbide-forming elements on the metal dusting rate in hydrocarbon environments", G.A. Slabbert, F.M.L. Mulaudzi, L.A. Cornish, M.J Papo and J. Zhang, Corrosion and Prevention 2012, Melbourne, 11-14 November 2012 – Paper accepted for Oral Presentation.